Diversity in emotion language across cultures pp. 1444 & 1517

A crushing approach to redox catalysis pp. 1451 & 1500

Bioscience, law, and being "human" p. 1455

Science

$15
20 DECEMBER 2019
SPECIAL ISSUE
sciencemag.org

AAAS

2019 BREAKTHROUGH *of the* YEAR

CONTENTS

20 DECEMBER 2019 • VOLUME 366 • ISSUE 6472

SPECIAL SECTION
BREAKTHROUGH *of the* YEAR

WINNER
1434 Darkness made visible

RUNNERS-UP
1436 A killer impact and its aftermath

1437 Face to face with the Denisovans

1437 Hope for Ebola patients, at last

1438 Quantum supremacy attained

1438 A 'missing link' microbe emerges

1439 A close-up of a far-out object

1440 In a first, drug treats most cases of cystic fibrosis

1440 Microbes combat malnourishment

1441 Artificial intelligence masters multiplayer poker

SEE ALSO EDITORIAL p. 1423; PODCAST; VIDEO

BREAKDOWNS OF THE YEAR
1442 The Amazon ablaze

1442 Measles resurgent

1443 Bird counts dwindling

1443 An eleventh hour climate awakening?

ON THE COVER

In *Science*'s 2019 Breakthrough of the Year, the Event Horizon Telescope (EHT) imaged superheated matter ringing the supermassive black hole in the galaxy M87. Here it is seen, outlined by the glowing ring, from an imaginary nearby planet. Hot gas and radiation jet from its pole, and its titanic gravity stretches background stars into so-called Einstein rings. Dimitrios Psaltis, EHT project scientist, advised on the illustration. See page 1434. *Illustration: Mark A. Garlick*

An illustration suggests how data from multiple radio telescopes made a black hole visible.

NEWS

IN BRIEF
1424 News at a glance

IN DEPTH
1427 Australia's vulnerable species hit hard by fires
Endangered plants and animals with small ranges and few individuals are at high risk
By J. Pickrell

1428 U.S. takes aim at foreign influence
Defining "sensitive research" remains a sticking point *By J. Mervis and D. Malakoff*

1429 NIH director pledges action on harassment after report
Panel recommends a process parallel to one for research misconduct *By J. Kaiser*

1430 To help the 'disadvantaged,' NIH refines its definition
Agency aims to help economically stressed groups *By J. Mervis*

1431 'Polygenic' analyses may sharpen disease risk predictions
Genetic background modifies impact of single disease genes *By J. Kaiser*

1432 Two Asian American women allege bias by HHMI
Powerhouse institute rejects claims of race, sex bias in separate legal actions
By M. Wadman

1433 Rude reviews are pervasive and sometimes harmful, study finds
Survey finds that "unprofessional" comments abound *By C. Wilcox*

INSIGHTS

PERSPECTIVES
1444 Mapping words reveals emotional diversity
Semantic networks reveal cultural variability in emotion *By A. Majid*
REPORT p. 1517

1445 Mitochondrial DNA promotes autoimmunity
Stressed mitochondria leak DNA fragments that induce inflammation *By M. K. Crow*
REPORT p. 1531

1447 Producing adipic acid without the nitrous oxide
Synthesis of nylon monomer from butadiene avoids emission of a potent greenhouse gas
By T. Schaub
REPORT p. 1514

ILLUSTRATION: CHARIS TSEVIS

Published by AAAS

1448 Bypassing the blood-brain barrier
The meninges membranes surrounding the brain are an immune-blood-brain interface in homeostasis and disease
By J. Rustenhoven and J. Kipnis

1450 Free at last: Bose metal uncaged
A metallic phase disrupts the classic two-state superconductor-insulator picture
By P. W. Phillips
REPORT p. 1505

1451 Piezoelectricity drives organic synthesis
Ball milling allows for solvent-free mechanoredox catalysis *By H. Xia and Z. Wang*
REPORT p. 1500

1452 Targeted drugs ramp up cancer mutability
Drug-induced mutagenesis may accelerate cancer evolution and resistance
By M. Gerlinger
RESEARCH ARTICLE p. 1473

1454 Peptidic catalysts for macrocycle synthesis
A heptapeptide pulls aldehyde groups of a molecule together for elusive ring-closing reactions *By A. Gutiérrez Collar and T. Gulder*
REPORT p. 1528

POLICY FORUM

1455 Biotechnologies nibbling at the legal "human"
Recent advances in the biosciences invite reconsideration of fundamental legal concepts such as the definition of "human"
By B. M. Knoppers and H. T. Greely

BOOKS *ET AL.*

1458 More than a merchant's trading route
A vividly illustrated tome traces the cultural impacts of the Silk Road *By A. Robinson*

1459 The ongoing quest for pure foods
Early adulteration sowed mistrust in the food production system that endures today
By D. Blum

LETTERS

1460 Retraction
By E. Berret et al.

1460 Genome studies reveal flaws in broad consent
By S. Holm and T. Ploug

1461 Genome studies must account for history
By S. S. Richardson et al.

1461 Response
By A. Ganna et al.

1462 Technical Comment abstracts

1462 Errata

RESEARCH

IN BRIEF

1467 From *Science* and other journals

RESEARCH ARTICLES

1470 Molecular biology
The biochemical basis of microRNA targeting efficacy *S. E. McGeary* et al.
RESEARCH ARTICLE SUMMARY; FOR FULL TEXT: DX.DOI.ORG/10.1126/SCIENCE.AAV1741

1471 Transcriptomics
A genome-wide transcriptomic analysis of protein-coding genes in human blood cells *M. Uhlen* et al.
RESEARCH ARTICLE SUMMARY; FOR FULL TEXT: DX.DOI.ORG/10.1126/SCIENCE.AAX9198

1472 Infection
Host monitoring of quorum sensing during *Pseudomonas aeruginosa* infection
P. Moura-Alves et al.
RESEARCH ARTICLE SUMMARY; FOR FULL TEXT: DX.DOI.ORG/10.1126/SCIENCE.AAW1629

1473 Cancer
Adaptive mutability of colorectal cancers in response to targeted therapies
M. Russo et al.
PERSPECTIVE p. 1452

1480 Superfluidity
Coherent vortex dynamics in a strongly interacting superfluid on a silicon chip
Y. P. Sachkou et al.

1486 Neurodevelopment
Potassium channel dysfunction in human neuronal models of Angelman syndrome
A. X. Sun et al.

REPORTS

1492 Materials science
Intragranular three-dimensional stress tensor fields in plastically deformed polycrystals *Y. Hayashi* et al.

1496 Quantum gases
Dissipation-induced structural instability and chiral dynamics in a quantum gas *N. Dogra* et al.

1500 Mechanochemistry
Redox reactions of small organic molecules using ball milling and piezoelectric materials *K. Kubota* et al.
PERSPECTIVE p. 1451

1505 Solid-state physics
Intermediate bosonic metallic state in the superconductor-insulator transition
C. Yang et al.
PERSPECTIVE p. 1450

1509 Solar cells
Constructive molecular configurations for surface-defect passivation of perovskite photovoltaics *R. Wang* et al.

1514 Organic chemistry
Direct synthesis of adipic acid esters via palladium-catalyzed carbonylation of 1,3-dienes *J. Yang* et al.
PERSPECTIVE p. 1447

1517 Emotion and language
Emotion semantics show both cultural variation and universal structure
J. C. Jackson et al.
PERSPECTIVE p. 1444

1522 Immunology
A class of γδ T cell receptors recognize the underside of the antigen-presenting molecule MR1 *J. Le Nours* et al.

1528 Organic chemistry
Foldamer-templated catalysis of macrocycle formation *Z. C. Girvin* et al.
PERSPECTIVE p. 1454

1531 Mitochondrial biology
VDAC oligomers form mitochondrial pores to release mtDNA fragments and promote lupus-like disease
J. Kim et al.
PERSPECTIVE p. 1445

DEPARTMENTS

1423 Editorial
Seeing is believing *By H. Holden Thorp*
BREAKTHROUGH OF THE YEAR p. 1434

1574 Working Life
Learning to teach *By Firdous A. Khan*

AAAS News & Notes 1464
New Products 1537
Science Careers 1538

SCIENCE (ISSN 0036-8075) is published weekly on Friday, except last week in December, by the American Association for the Advancement of Science, 1200 New York Avenue, NW, Washington, DC 20005. Periodicals mail postage (publication No. 484460) paid at Washington, DC, and additional mailing offices. Copyright © 2019 by the American Association for the Advancement of Science. The title SCIENCE is a registered trademark of the AAAS. Domestic individual membership, including subscription (12 months): $165 ($74 allocated to subscription). Domestic institutional subscription (51 issues): $1971; Foreign postage extra: Mexico, Caribbean (surface mail) $55; other countries (air assist delivery): $98. First class, airmail, student, and emeritus rates on request. Canadian rates with GST available upon request, GST #125488122. Publications Mail Agreement Number 1069624. **Printed in the U.S.A.**
Change of address: Allow 4 weeks, giving old and new addresses and 8-digit account number. **Postmaster:** Send change of address to AAAS, P.O. Box 96178, Washington, DC 20090–6178. **Single-copy sales:** $15 each plus shipping and handling; bulk rate on request. **Authorization to reproduce** material for internal or personal use under circumstances not falling within the fair use provisions of the Copyright Act can be obtained through the Copyright Clearance Center (CCC), www.copyright.com. The identification code for *Science* is 0036-8075. *Science* is indexed in the *Reader's Guide to Periodical Literature* and in several specialized indexes.

Published by AAAS

EDITORIAL

Seeing is believing

Scientists can often make indirect measurements that tell us about things we can't actually see. For scientists who work on molecules, such as myself, this is especially true: Many of the small and large molecules that dance in my head are objects that I've never actually looked at. But for many outside of science, seeing is believing.

In my first administrative job at the University of North Carolina, I learned about this while running the campus planetarium. On clear nights, we would set up telescopes for public viewings. It was common for people to see Saturn through the telescope for the first time and then frantically look to see whether we had taped a cartoon of the ringed planet to the end of the telescope. They had assumed that Saturn didn't really look like the pictures in their grade-school classrooms.

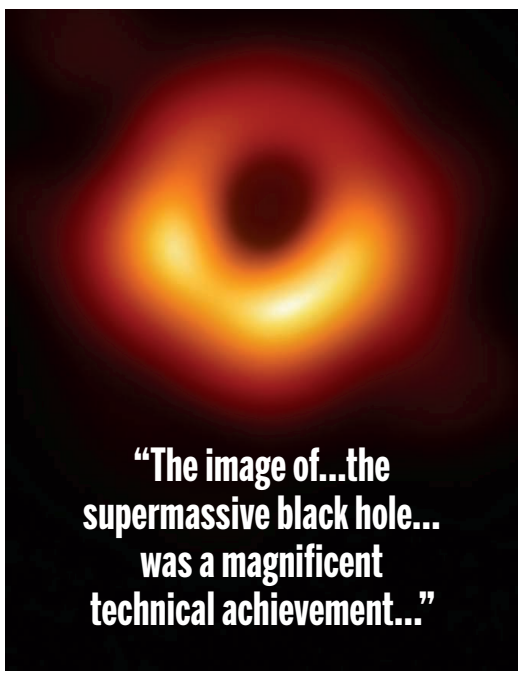

While I was in that job almost 20 years ago, I was fortunate enough to convince the authors Will and Mary Pope Osborne to work with the university on a planetarium show based on their blockbuster children's book series *Magic Tree House*. At the most suspenseful part of the show, the protagonists Jack and Annie end up dangerously close to the event horizon of a black hole—the point beyond which not even light can escape. That meant we had to project a convincing and exciting image of a black hole onto the planetarium dome.

Most of today's planetariums project a continuous digital image. Back then, planetarium operators had to be wizards of improvisation with baby food jars, filmstrip projectors, and various kinds of motors. Our projector genius, Richard McColman, created an ominous black hole by using a simulated image of what was then the most current idea of an accretion disk orbiting an event horizon; he printed the image on transparent film and rotated it on top of a projector bulb that moved closer and closer to the image. Combined with dramatic music, it was enough to create substantial suspense, including for my 5-year-old daughter, who is still scared to talk about it today. (Spoiler alert: Jack and Annie are rescued from spaghettification at the event horizon by Mary Pope Osborne herself.)

If we made the show today, we wouldn't have to guess at what the black hole looks like. The image of the event horizon of the supermassive black hole in the nearby galaxy Messier 87 was a magnificent technical achievement and a worthy Breakthrough of the Year. But it is more than that. For a skeptical public that often rolls their eyes when they hear scientists say that they know things exist even though they cannot be seen, this is one more important object that we can see. Given the influence of black holes on the evolution of galaxies, this is a remarkable milestone in every respect.

There were also some extraordinary runners-up this year. When I was at Washington University in St. Louis, I had the privilege of watching research progress on restoring the gut microbiome in malnourished children. It's intensely encouraging to know that there is a way to do this, and the companion papers that show how the microorganisms develop make it great science, as well. This has implications for public health in the developed world, too: Children need to start with excellent nutrition, and when they don't, it isn't enough just to get food to them—it has to be the right food.

A series of papers that reveal details of how the Chicxulub asteroid impact wiped out the dinosaurs and how mammals reemerged afterward provide very important pieces of science about the history of life on Earth. Like the black hole image, seeing is believing. The mammal fossils recovered in Colorado tell a story that needs to be shared widely as scientists make the case for preserving life on Earth. Objective science such as these discoveries creates a powerful narrative that can compel society to consider the trajectory of Earth in the aftermath of tremendous ecological upheavals—those of the past as well as those that may yet come.

– H. Holden Thorp

H. Holden Thorp
Editor-in-Chief, *Science* journals.
hthorp@aaas.org;
@hholdenthorp

10.1126/science.aba5359

PHOTOS (TOP TO BOTTOM): CAMERON DAVIDSON; EHT COLLABORATION/CC 4.0

Published by AAAS

NEWS

> “Very exciting for the louse community.”
>
> **Evolutionary biologist Julie Allen,** about the discovery by paleontologists in China of fossilized lice that, when alive, appeared to have feasted on dinosaurs' feathers. Lice are thought to have evolved during the age of dinosaurs but rarely fossilized; these were preserved in amber.

IN BRIEF

Edited by **Jeffrey Brainard**

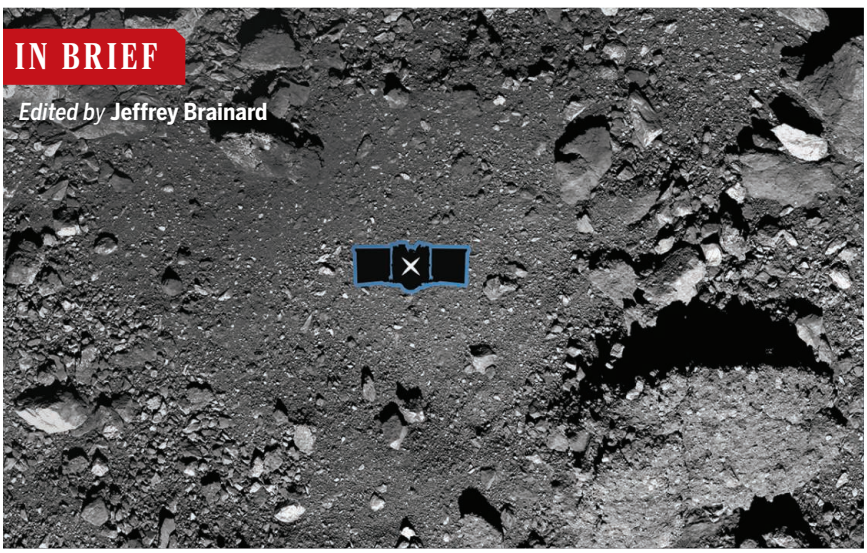

Scientists modified the OSIRIS-REx probe (illustrated in photo) to better navigate a difficult landing.

PLANETARY SCIENCE

Risky site picked for asteroid sample grab

Mission leaders last week announced they picked a challenging landing site on the asteroid Bennu for a spacecraft to suck up fine grit and return it to Earth for analysis. The 16-meter-wide target is among the most flat and accessible places on the boulder-strewn surface. Even so, the NASA-funded space probe—the Origins, Spectral Interpretation, Resource Identification, Security, Regolith Explorer (OSIRIS-REx)—must avoid nearby tall rocks nicknamed “Mount Doom” during its visit, planned in August 2020. The crater's location, toward the north pole of the 500-meter-wide body, keeps it cool, which may have preserved water and organic materials from the Solar System's earliest days. Another spacecraft, Japan's Hayabusa-2, this year successfully navigated around boulders on a different asteroid, Ryugu, to collect surface samples for return to Earth.

Map reveals Antarctic terrain

GLACIOLOGY | The lowest land canyon on Earth is in East Antarctica, plunging 3.5 kilometers below sea level, according to a new map of the land below the continent's ice sheets. The canyon is seven times deeper than the shores of the Dead Sea, the lowest exposed spot on Earth's surface. The map, called BedMachine Antarctica and published last week in *Nature Geoscience*, was inferred using the flow and volume of ice. It reveals previously unknown ridges that sit above sea level in the deep valleys that drain the Transantarctic Mountains, stabilizing glaciers there. Researchers had hoped the map would reveal similar ridges under West Antarctica's fastest melting glacier that might stabilize it as well. But none beyond the two already known was found.

U.S. science gets spending boost

FUNDING | Most U.S. research agencies will receive healthy budget increases in 2020 after Democrats and Republicans resolved a 3-month stalemate. The spending levels for the fiscal year ending on 30 September 2020, expected to become law this week, also reject the deep cuts proposed by President Donald Trump in his 2020 budget request in February. The National Institutes of Health will receive by far the largest increase in absolute dollars, as legislators approved a fifth year of annual budget hikes of at least $2 billion. Congress also allocated $25 million for gun violence research, ending a 23-year de facto federal spending freeze, and extended for 10 years a government-funded nonprofit that studies the relative benefits of medical treatments. Climate, energy, and space science also fared well: Legislators again rejected Trump's request to kill the Advanced Research Projects Agency-Energy, for example, and they gave NASA a $36 million down payment for a new mission to monitor near-Earth objects. The National Science Foundation got less love, as its $203 million increase fell below what appropriators in the Senate and House of Representatives had previously approved.

▲ What selected agencies got

AGENCY/PROGRAM	2020 BUDGET ($ BILLION)	INCREASE OVER 2019
National Institutes of Health	$41.684	7%
National Science Foundation	**$8.278**	**2.5%**
NASA science office	$7.139	3.4%
Department of Energy science office	$7	6.3%
Department of Defense basic science	**$2.603**	**3%**
U.S. Geological Survey	**$1.271**	**9.5%**
National Institute of Standards and Technology labs	$0.754	4.1%
EPA science programs	$0.716	1.4%
NOAA	$0.590	4.3%

CREDITS: (PHOTO) NASA/GODDARD/UNIVERSITY OF ARIZONA; (GRAPHIC) J. BRAINARD/*SCIENCE*; (DATA) U.S. CONGRESS

Published by AAAS

French Polynesia's reefs benefit in part from its remoteness.

PHOTO: © MICHELE WESTMORLAND/ILCP

MARINE ECOLOGY

Coral surprise in French Polynesia

Even as coral reefs almost everywhere are dying, those in French Polynesia stand out as an exception, a study has found. Six years ago, the Khaled bin Sultan Living Oceans Foundation in Annapolis carried out censuses of fish and coral and developed detailed satellite and underwater maps of reefs around 29 of that country's islands. On some atolls, live coral covers 70% of the reef's surface, the highest coverage in the world, according to a final report released 12 December. In comparison, coral coverage on the iconic Great Barrier Reef reaches only about 45%. And big fish such as grouper and barracuda that have almost disappeared elsewhere are thriving in French Polynesia. The country's remoteness and milder climate likely account for why many reefs were doing so well, although scientists say some have declined since the surveys.

Climate talks bog down

SUSTAINABILITY | A Madrid meeting of nations that have signed the Paris climate pact ended in disappointment on 15 December. Climate activists had hoped nations would rachet up commitments to cut carbon emissions and agree on how to set up a global market that would help create financial incentives for reducing emissions. Poorer nations also wanted to nail down how richer countries will compensate them for damages caused by climate change. But delegates failed to reach agreement on these and other issues, delaying action until next year's talks in Glasgow, U.K.

U.S., Iran swap detainees

INTERNATIONAL AFFAIRS | A harrowing saga has ended for four researchers ensnared in the poisonous politics of U.S.-Iranian relations. In a prisoner swap at an airport in Zurich, Switzerland, on 7 December, Iran released Xiyue Wang, a U.S. citizen and graduate student in history at Princeton University who was arrested in Tehran in 2016 while conducting archival research on Persia's Qajar Dynasty. Wang was convicted in 2017 of espionage and sentenced to 10 years of prison. In the exchange, the United States handed over Masoud Soleimani, a stem cell researcher at Tarbiat Modares University in Tehran detained in Chicago, Illinois, in October 2018—en route to a stint at the Mayo Clinic—on charges of attempting to evade trade sanctions by smuggling U.S.-made growth factors into Iran. Two of Soleimani's former students who purchased and transported the proteins are also in the clear: On 11 December, a U.S. federal judge approved a motion by prosecutors to dismiss charges against the Iranian American scientists "in the interest of justice."

Name that exoplanet

PUBLIC ENGAGEMENT | The International Astronomical Union (IAU) this week announced a set of evocative names for 112 exoplanets and their stars. Each pair of names was suggested by a different country from ideas offered by 780,000 people across the world. Exoplanets are routinely named after the star they orbit or the telescope that discovered them, such as 51 Pegasi b or Kepler-62e. In response to IAU's call, Irish participants suggested two mythological dogs, Bran and Tuiren, for their planet-star pair. Jordanians honored famed historic places, the ancient city Petra and desert site Wadi Rum, whereas the stargazers of Burkina Faso picked prominent rivers, Nakambé and Mouhoun. Names in Indigenous languages were encouraged, so Argentinians suggested Naqaya and Nosaxa in the Moqoit language. With more than 4000 worlds now discovered,

Published by AAAS

there will be plenty of opportunities for additional creative naming.

H. erectus lingered late on Java

PALEOANTHROPOLOGY | The extinct human ancestor *Homo erectus* likely lived out its final days on the Indonesian archipelago approximately 100,000 years ago, according to a new analysis of fossils from a site in Central Java. A dozen partial skulls and two leg bones of *H. erectus* were first identified at the riverside site known as Ngandong in the 1930s. But those fossils proved notoriously difficult to date, so paleoanthropologists returned to the original bone bed and uncovered hundreds of animal bones from the same layers. Combining five methods to date those bones, the researchers concluded this week in *Nature* that the *H. erectus* fossils date from 117,000 to 108,000 years ago—the latest known reliable evidence for the species. The authors suggest a climate shift significantly transformed the island's landscape, dooming *H. erectus* before our own species arrived on the island. *H. erectus*'s long presence in Southeast Asia supports the hypothesis that the species gave rise to at least two others, *H. floresiensis* and *H. luzonensis*, as it migrated across Southeast Asia's necklace of islands.

Exxon wins climate lawsuit

LEGAL AFFAIRS | Exxon Mobil did not fraudulently downplay the financial costs it faces from possible regulations to control climate change, a New York state judge ruled last week. The state attorney general had alleged in a civil lawsuit that the company duped investors and inflated its share price by low-balling those costs. Judge Barry Ostrager said that his decision was based on securities fraud law and did not settle whether the company had contributed to climate change through greenhouse gas emissions from its products. Other state and city governments are suing Exxon Mobil and other energy companies under a different legal theory, alleging that the emissions worsened floods and hurricanes and that the companies must pay for damages they caused and for reducing the risks of future ones.

Tool tracks threatened species

CONSERVATION | Collaborators from Google and conservation organizations on 17 December unveiled a tool to analyze photos of endangered and threatened species to generate useful information about their population trends. The website, Wildlife Insights, relies on crowdsourcing: Users upload photos of passing fauna taken by motion-sensing cameras stationed in the wild. The system employs artificial intelligence to identify and count unique individuals in the photos, based on a tiger's unique pattern of stripes, for example—automating a task that is time-consuming for ecologists who examine the photos one by one. Uploaded images will become part of a worldwide public database that researchers can study. There are countless "hard drives around the world full of very, very useful data just sitting there, unused," says Margaret Kinnaird, a wildlife practice leader at the World Wildlife Fund.

Researchers fitted more than 1 million butterflies with tags like this one.

PHOTO: LYNN M. STONE/MINDEN PICTURES

ANIMAL BEHAVIOR

Sun's angle may spark monarch migrations

Data from tagged monarch butterflies (above) indicate they begin and end their 4000-kilometer migrations from Canada and the United States to Mexico based on a surprising cue: the angle of the noon Sun above the horizon, which changes with the seasons and with latitude. Researchers knew these butterflies navigate using the horizontal movements of the Sun. Now, in the 10 December issue of *Frontiers in Ecology and Evolution*, Orley Taylor from the University of Kansas in Lawrence and colleagues propose that the butterflies also read changes in the Sun's vertical position. Each summer they launch their migrations, and continue to fly south, when it dips between 48° and 57° above the horizon.

AWARDS

Science wins journalism prizes

Members of our visuals and news teams were honored for work published in 2018.

"Starry eyes," an online feature about NASA's proposed space telescopes with graphics and design by **Jia You** and **Chris Bickel** and text by **Daniel Clery**, won an Ozzie Award from Folio for visual digital storytelling and a bronze EXCEL Award from Association Media and Publishing for website design excellence. (See the presentation at https://scim.ag/StarryEyes.)

Chrystal Smith won a gold EXCEL Award from Association Media and Publishing for the design of the 29 June 2018 issue's cover, "Tomorrow's Earth." The visuals team also won a gold EXCEL Award for design excellence for three issues of *Science* that appeared in December 2018.

Val Altounian received an Award of Excellence from the Society for News Design for a 19 April 2018 illustration about kidney disease.

Martin Enserink won the American Society of Tropical Medicine and Hygiene's Communications Award for his 19 July 2018 article, funded by the Pulitzer Center, on a young doctor's quest to eradicate yaws, a forgotten tropical disease that still takes a major toll.

SCIENCEMAG.ORG/NEWS
Read more news from *Science* online.

Published by AAAS

Fires, such as this one in New South Wales, have burned more than 3 million hectares in Australia.

PHOTO: WOLTER PEETERS/*THE SYDNEY MORNING HERALD* VIA GETTY IMAGES

CONSERVATION BIOLOGY

Australia's vulnerable species hit hard by fires

Endangered plants and animals with small ranges and few individuals are at high risk

By **John Pickrell**, *in Sydney, Australia*

Until recently, the Ngunya Jargoon Indigenous Protected Area here in the state of New South Wales (NSW) had the healthiest remaining population of the northern long-nosed potoroo, a hare-size wallaby that feeds on truffles that grow around the roots of gum trees. But in October, after an unprecedented drought reduced the forest to tinder, an intense blaze incinerated the preserve. When ecologists and rangers returned to survey the damage they found no sign of the endangered marsupial, which had declined to a few hundred animals. Now, "The future of the largest known population is in serious doubt," says Mark Graham, an ecologist with NWS's Nature Conservation Council, who has worked for 20 years to protect the potoroo.

It isn't the only Australian species facing potentially catastrophic losses as a result of the unusually severe and widespread wildfires that have so far burned some 3 million hectares in the eastern states of Queensland and NSW—an area nearly the size of Belgium. The blazes, which have hit both arid, fire-prone ecosystems and typically fireproof wetlands and rainforests, have already destroyed the habitats of dozens of rare animals and plants. Worse news may be coming: Peak summer fire season still has 2 months to go, and as *Science* went to press, the already parched region was bracing for another heat wave.

"There's little question that threatened species are going to be affected; even common species are being pushed towards becoming vulnerable by the size of these fires," says Euan Ritchie, an ecologist at Deakin University in Melbourne.

The fires have prevented researchers from reaching many study sites to fully assess the damage. As a result, "We are in the fog of war," says David Bowman, director of the Fire Centre Research Hub at the University of Tasmania in Hobart. But satellite images and other data sources paint a grim picture. Some scientists have even watched in horror as the automated camera traps they use to monitor wildlife instead have captured flames reducing their study sites to ash.

In NSW, which covers a large part of southeastern Australia, at least 20% of the area protected by national parks has gone up in flames. Affected areas include at least 35 of the 41 total reserves scattered across both the Greater Blue Mountains World Heritage Area, west of Sydney, and much of the Gondwana Rainforests of Australia World Heritage Area in the north of the state. Officials estimate about 48% of the iconic Gondwana reserves, which include rainforests that have existed since the time of the dinosaurs, have now burned.

Maurizio Rossetto, an evolutionary ecologist at the Royal Botanic Garden Sydney, says that in Nightcap National Park, one of the Gondwana reserves, he fears for about 30 rare tree species and a similar number of rare animals, because their habitats have likely been destroyed. The park has some of Australia's most biodiverse forests, "with high proportions of [species from] ancient, endemic lineages that go back to Gondwanan times" more than 60 million years ago. And it is precisely the absence of fire in the forests of Nightcap and nearby reserves that has allowed rare tree species to persist there, Rossetto notes. "Many of these trees have thin bark that does not provide protection against fire," he says.

Published by AAAS

He is particularly concerned about three species, each of which has just a few hundred remaining trees "tightly grouped in a single population."

The Gondwana rainforest's frogs are also under threat. One species, the pouched or hip pocket frog, is a delicate, 2-centimeter-long amphibian that raises its tadpoles in pouches on its hips. It needs moist leaf litter to survive and "has no tolerance to fire," Graham says. He suspects the fires have caused "mass mortality" and wonders whether NSW officials will have to reclassify the frog, now listed as vulnerable, as endangered.

In the Greater Blue Mountains, flames have ravaged about 50% of its heritage reserves, threatening regions inhabited by endangered species with small ranges, including a shrub called the Kowmung hakea, a lizard known as the Blue Mountains water skink, and the Wollemi pine, a "living fossil" discovered in 1994.

Ross Crates, an ecologist at the Australian National University in Canberra, notes the mountains are also the "final stronghold" of a critically endangered bird, the

Fires have wiped out prime habitat used by one of the largest populations of the long-nosed potoroo.

regent honeyeater. Just 250 to 400 of these striking black-and-yellow nectar feeders remain, and an estimated 80% of breeding pairs nest in the Greater Blue Mountains. The fires have so far destroyed honeyeater nesting sites in at least five valleys; some had nests that still held chicks. He's also lost about 10% of the 1200 honeyeater monitoring stations he set up over the past 5 years, which can include cameras and other sensors.

Farther west in NSW, well into Australia's inland, another endangered bird faces new peril. The Australasian bittern inhabits the Macquarie Marshes, an internationally significant protected wetland that supports hundreds of thousands of water birds during times of plenty. But Australia's lengthy drought has deprived the marsh of water, and in October fire burned through 3000 hectares, eliminating 90% of the reed bed, the bittern's key nesting habitat.

In Queensland, which covers northeastern Australia, researchers fear fires have consumed key habitats within Bulburin National Park, which harbors an endangered native macadamia reduced to fewer than 150 remaining trees. Satellite images suggest fire may have reached all three parts of the park that have the trees, says Diana Fisher, a mammal ecologist at the University of New England in Armidale. The Bulburin fires also menace the silver-headed antechinus, an endangered shrew-size marsupial carnivore. Just a few hundred individuals remain, and Bulburin has the largest of the three known populations.

Researchers say even animals that survive the fires are likely to face long-term challenges. Some silver-headed antechinus, for instance, might have escaped the heat by squeezing into rock crevices, Fisher says. But they may emerge to find little shelter or food. "If they lose all of their leaf litter and ground cover, then they're not going to persist," she says. In the past, antechinus from other areas might have repopulated vacated territories, she adds, but habitat fragmentation now makes that nearly impossible.

Surviving potoroos, too, will likely have to avoid cats and foxes, introduced predators that move into disturbed forests "and quickly mop up ground-living wildlife," says Mike Letnic, an ecologist at the University of New South Wales here. "It's like a double whammy."

More mobile animals, such as adult honeyeaters, probably fled from trouble. But the specific types of rare gum tree blossoms that the honeyeaters prefer to feed on, and nest near, could be in short supply. "It's about the long-term cumulative impacts on breeding success, rather than death of individuals," Crates says. "For a species already on the brink of extinction, it's not great."

The fires have amplified many scientists' complaints that Australia's current government, led by Prime Minister Scott Morrison, has failed to acknowledge the role of climate change in the drought and fires, and has done little to cut national greenhouse gas emissions. The looming question, scientists say, is whether climate change will make catastrophic fire seasons like this one—which started unusually early—the norm in Australia. If so, Ritchie and other researchers say, even Australian species and habitats with some level of fire tolerance may face existential threats. ■

John Pickrell is a journalist in Sydney, Australia.

PHOTOS: (LEFT TO RIGHT) DAVE WATTS/MINDEN PICTURES; AGU/EPNAC

SCIENCE & SECURITY

U.S. takes aim at foreign influence

Defining "sensitive research" remains a sticking point

By **Jeffrey Mervis** *and* **David Malakoff**

U.S. policymakers are making headway on the thorny question of how to deal with foreign threats to U.S. research. Congress has created two new panels to wrestle with the topic and an influential panel has recommended steps that the National Science Foundation (NSF) should take. But there is no consensus on the core issue of whether protecting national security and U.S. innovation requires new restrictions on basic research.

Concern is rising across the U.S. government that foreign entities, especially the Chinese government and affiliated institutions, are making systematic efforts to steal the fruits of U.S.-funded research. The National Institutes of Health (NIH) has led the charge among federal funding agencies by cracking down on grantees who have failed to disclose foreign ties or have violated the confidentiality of peer review. NIH has examined 140 such cases to date, says Michael Lauer, head of NIH's Office of Extramural Research in Bethesda, Maryland, and has found "a substantial compliance issue" in 75% of them.

In a bid to address those concerns, a major defense bill that Congress approved this

Published by AAAS

Presidential science adviser Kelvin Droegemeier will lead a new panel on foreign influences.

week creates two high-level bodies—one inside and one outside the government—to search for the right balance between scientific openness and security. One panel, led by the White House Office of Science and Technology Policy, will try to harmonize actions by more than a dozen agencies to protect federally funded research projects from cyberattacks, theft, and other foreign threats. The other group, a roundtable convened by the National Academies of Sciences, Engineering, and Medicine, will bring together officials from academia, government, and industry for discussions on how to assess and mitigate the risks posed by foreign collaborations involving U.S. researchers.

U.S. higher education organizations lobbied hard for both bodies. They are hoping the White House panel will eliminate mixed messages from research agencies about what they expect from grantee institutions. The roundtable, meanwhile, could help build consensus between the research and intelligence communities, whose cultures and missions differ sharply.

The defense bill, which also authorizes some $738 billion in military spending for the current fiscal year, contains a provision that raises the hackles of most scientists. It orders the director of national intelligence to produce an annual report that assesses the extent to which foreign entities are trying to obtain "sensitive research" done at U.S. universities.

But that exercise will likely inflame the long-running debate over what research should be protected. In 1985, then-President Ronald Reagan issued an order, known as National Security Defense Directive 189, that creates a bright line: The government should classify federally funded fundamental research that it feels poses a security risk, but leave the rest in the open. It also said that fundamental research should "remain unrestricted … to the maximum extent possible." Even so, former President George W. Bush alarmed many scientists in 2008 by creating a new category of controlled unclassified research (CUI). Two years later, former President Barack Obama preserved that category but suggested it should be a last resort.

That's not what has happened, however. "Despite good intentions, the number of CUI categories has continued to proliferate and now stands at 125," according to the new report, prepared by an independent group of prominent scientists, known as Jason, which advises the government on technical issues. The report, prepared at NSF's request, says it would be a bad idea for the government to limit fundamental research that is not already classified in hopes of thwarting foreign access.

"Take a topic like quantum properties—any attempt to fence off some aspects of that work would strangle basic research across a huge swath," says Ellen Williams, a materials scientist at the University of Maryland in College Park and chair of Jason. (She did not participate in the study.) "It's just crazy."

Despite warning against additional restrictions, the report agrees the threat to U.S. research is serious. It suggests universities and funders treat failures to disclose foreign ties as violations of research integrity rules, although it does not spell out how investigations or punishments might work.

Citing anecdotal evidence, the Jason report asserts that some foreign scientists may not be familiar with U.S. norms of what constitutes research integrity. Some Chinese students and scientists working in the United States might consider it acceptable to share confidential research information with their government, it says, referring to a Chinese law that "requires a degree of cooperation from citizens in ways the United States does not." At the same time, the report chides U.S. intelligence agencies for assuming theft in cases that "actually appear to be the collegial sharing of academic work."

Jason admits it doesn't know the magnitude of the problem, nor whether rule violations are due to simple ignorance or deliberate subterfuge. In either case, it says NSF should insist that grantee institutions implement "more robust" training in ethical research practices.

Lauer agrees that the foreign influence problem hasn't been quantified. And although he supports more education, he thinks enforcement is at least as important. "We have seen so much deception and heard so many lies," Lauer says, "that it's clear to us this is mostly willful activity." ■

SCIENCE POLICY

NIH director pledges action on harassment after report

Panel recommends a process parallel to one for research misconduct

By **Jocelyn Kaiser**

In a widely anticipated report, an advisory group last week issued sweeping recommendations for cracking down on sexual harassment in labs funded by the National Institutes of Health. NIH Director Francis Collins said he "will make every effort" to follow the group's advice. However, he said NIH does not have the legal authority to take some key steps, which could blunt the report's impact.

NIH is already acting on some interim recommendations the group made in June (*Science*, 21 June, p. 1117). The agency will soon release a procedure it will follow when it receives an allegation of sexual misconduct, and it has set up a phone and web hotline for complaints. It has also stepped up enforcement. Since January, NIH has received 105 inquiries (compared with 28 in 2018), removed 12 principal investigators (PIs) from grants, and barred 55 from peer review. But Collins said the agency may need to go through a formal policymaking process to take other steps the report recommended. These include requiring grant personnel to undergo training to prevent sexual harassment and mandating that grant personnel check a box on grant applications and annual progress reports to attest that there have been no sexual harassment findings against them.

Still, observers welcomed the report from a 21-member working group that included NIH officials, NIH-funded researchers, and victims of sexual harassment. The report "addresses sexual harassment at all levels, from institutional leadership to protecting the safety and careers of targets of harassment," said Heather Pierce, senior director of science policy for the Association of American Medical Colleges in Washington, D.C. "I really appreciate your attention to these issues," neuroscientist

Published by AAAS

and #MeTooSTEM advocacy organization leader BethAnn McLaughlin told the working group.

NIH had come under fire for responding slowly to rising concerns about harassment. By contrast, in fall of 2018, the National Science Foundation (NSF) began to require that funded institutions report sexual misconduct findings and notify the agency when an investigator is put on leave because of a harassment investigation. After several high-profile harassment cases involving federally funded investigators made headlines, Collins created the working group.

It followed advice from a National Academies of Sciences, Engineering, and Medicine (NASEM) panel that sexual misconduct be treated "as seriously as research misconduct" by establishing "parallel processes" for reporting and handling the two kinds of misbehavior. "Institutions have paid attention to research misconduct because NIH has tied dollars and funding to it," said working group member Carol Greider, a biologist at Johns Hopkins University in Baltimore, Maryland. The report calls for similar incentives for confronting harassment.

The report includes dozens of other recommendations for NIH, scientific societies, and institutions—including that NIH restructure awards to give trainees independence from investigators, survey staff on every grant about workforce climate, and provide victims of harassment with funding to resume their careers.

It also urges NIH to work toward reducing the concentration of funding among straight white male investigators, because, as the NASEM report noted, this contributes to the risk of sexual harassment by creating "hierarchical work environments." That shift could be accomplished in many ways, the report said, from working to reduce bias in peer review to rewarding institutions that support diversity.

But legal constraints that NSF, an independent agency, did not face preclude NIH from acting on several key recommendations, among them that NIH require institutions to notify the agency within 2 weeks when a PI is found guilty of sexual misconduct. Another is the advice that when a PI is put on leave because of an investigation, institutions inform NIH that the reason is sexual harassment concerns. NIH officials say they hope the working group's report will help them make the case to Trump administration officials for new legal authority. "In the meantime," said NIH Associate Director for Science Policy Carrie Wolinetz, "we're going to see how close we can get with the authorities that we have." ■

WORKFORCE DIVERSITY

To help the 'disadvantaged,' NIH refines its definition

Agency aims to help economically stressed groups

By **Jeffrey Mervis**

Living in near poverty can be a huge obstacle for someone who wants to become a biomedical researcher. So can a confusing definition of "economically disadvantaged" from the National Institutes of Health (NIH), which wants to increase the diversity of the scientific workforce. Now, the agency has sharpened its definition.

NIH has long offered existing grantees additional funding to mentor students and early-career scientists belonging to specified groups underrepresented in biomedical research. The list of groups targeted by these "diversity supplements" includes Hispanics, African Americans, American Indians, and Native Hawaiians, as well as people with a disability and the disadvantaged. NIH found some 84% of supplement applications last year were focused on African American or Hispanic students, and they represented 90% of all awards. Fewer than 1% of proposals cited disadvantaged students.

<1%
of applications are in the disadvantaged category

NIH officials blame the agency's old definition of disadvantaged for that tiny number. It defined economically disadvantaged students as those living in "an educational environment such as that found in certain rural or inner-city environments." "What does [that] mean?" asked Michael Lauer, who leads NIH's Office of Extramural Research in Bethesda, Maryland, in a 26 November blog describing the change. The phrase "is nearly impossible to evaluate."

NIH's new definition has seven components. Persons are disadvantaged if they have been homeless, or if they qualified for a free or reduced priced lunch in school or a federal Pell Grant for college. NIH also invites in those who were in foster care, whose parents never graduated from college, or who grew up in a rural area or a region with a shortage of health professionals. The change applies to all the agency's diversity programs, which serve those from high school through postdoctoral training.

"We wanted to make it easy for students to self-identify while not being overly redundant," says Jon Lorsch, director of NIH's National Institute of General Medical Sciences in Bethesda, the hub of NIH's diversity activities.

Wonder Drake, a professor of medicine at Vanderbilt University in Nashville, has received several diversity supplements and applauds NIH's move. The new definition "may attract more students who are immigrants, or poor Caucasians," she says. "Just think how useful their input would be in finding solutions to the opioid crisis, which is ravaging so many low-income communities."

Drake notes that, as a student, she would have met several of the new eligibility criteria. "I certainly grew up disadvantaged," she says, noting she was raised in rural Alabama by a single mother who never graduated from high school. She is also African American, however, so she would have qualified in that category as well.

For her diversity supplements, Drake typically chooses students from a racial or ethnic minority "because it's obvious," she says, and because students of color at Vanderbilt who want a research experience tend to seek her out. But she also contacts nearby colleges with large numbers of students who fit NIH's criteria. "I call up the chair of the basic science department and I tell them, 'I need your best student,'" she says. The goal is to have them complete a research project over the summer and then present a poster at a scientific conference. "Based on my experience," she says, "the economically disadvantaged students are sometimes the most talented because they have had to overcome so much adversity."

Lorsch estimates that NIH could accommodate a 10-fold increase in the number of applications that cite the disadvantaged category—in 2018 there were fewer than 11—without straining its budget. Given that NIH funds nearly two-thirds of the proposals it receives for diversity supplements, Drake doesn't understand why more of her colleagues don't apply.

"I think [the diversity supplements] are one of the best kept secrets at NIH," she says. "And we're doing everything we can at [Vanderbilt] to spread the word." ■

Published by AAAS

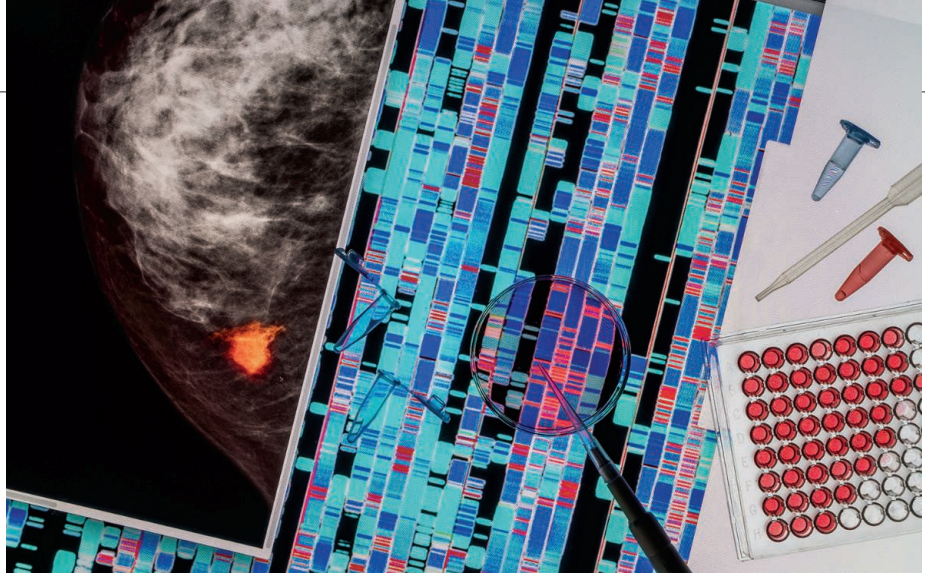

PHOTO: VOISIN/SCIENCE SOURCE

A woman's genetic background can powerfully modify her cancer risk from a *BRCA1* mutation.

BIOMEDICINE

'Polygenic' analyses may sharpen disease risk predictions

Genetic background modifies impact of single disease genes

By **Jocelyn Kaiser**

Women who learn that they have a mutation in the breast cancer gene *BRCA1* face a wrenching decision. Their doctor or genetic counselor will likely tell them that women with such mutations have, on average, a 72% lifetime risk of breast cancer and a 44% risk of ovarian cancer. Given that, up to half decide to have prophylactic mastectomies, and many have ovaries removed, too.

But recent studies show a woman could receive a more individualized, accurate cancer risk estimate by factoring in other gene variants. A preprint posted last month finds that a person's "polygenic" background influences not only the disease risk conferred by a *BRCA1* defect, but also risks from single gene mutations linked to colorectal cancer and heart disease. Some individuals were very likely to develop cancer or heart disease by age 75, the analysis showed, whereas in others the risk was not much greater than in a person without the high-risk mutation.

"It's pretty striking," says cardiologist and geneticist Amit Khera of Massachusetts General Hospital (MGH) in Boston, leader of the study, which is on the medRxiv preprint server. "It's become clear that there are both monogenic and polygenic [disease] drivers. The future is to assess both."

"The message is a very important one for patients and clinicians," says Teri Manolio of the National Human Genome Research Institute in Bethesda, Maryland. "Carriers of *BRCA1* mutations or other pathogenic variants don't invariably develop disease, and genomics can be used to help parse carriers who are at lower risk." Others caution, however, that risk scores summing how dozens to thousands of other genetic variants interact with a single major disease gene aren't yet accurate enough to use in the clinic. The new paper "is teasing at the possibility, but there's a lot of work to be done," says Harvard University epidemiologist Peter Kraft.

MGH cardiology fellow Akl Fahed and others in Khera's group explored polygenic influences on the three important single-gene disorders in the United States: familial hypercholesterolemia, which leads to sky-high cholesterol levels and dramatically elevates risk of heart disease; Lynch syndrome, a flaw in DNA repair that brings a lifetime risk of colorectal cancer of about 60%; and inherited breast cancer, caused by variants in *BRCA1* or *BRCA2*. They took advantage of databases that combine medical and genomic information from thousands of people, enabling researchers to tally how the many genetic variants with subtle effects modify disease risks and complex traits such as height.

Drawing on some 50,000 participants in the UK Biobank and 19,000 women tested for *BRCA* genes by the company Color Genomics, the team found that polygenic background strongly modified the risk of carrying a mutation in the key genes for the three disorders. For a small proportion of major disease gene carriers, other genetic variants boosted their overall risk of cancer or heart disease to about 80%, well above the average of 30% to 40% that Khera's group estimated for its study populations based on just the single disease gene mutations. (The team's monogenic disease risk predictions are lower than many other estimates for several possible reasons, Khera notes, including that the UK Biobank participants are healthier than the general population.) At the other extreme, the polygenic analysis suggested that a few people with those mutations have much lower risks than predicted by their single mutation alone, as low as 11% for colon cancer, 13% for breast cancer, and 17% for heart disease—not much higher than other people in general.

Khera's group says adding polygenic data to single-gene tests could help people decide whether to take aggressive steps to head off disease—mastectomy or removal of the ovaries for women carrying *BRCA* mutations or frequent colonoscopies for people with Lynch syndrome. But the new study does not include enough data for clinical decisions, says genetic epidemiologist Antonis Antoniou of the University of Cambridge in the United Kingdom. Only 116 women in the UK Biobank sample had *BRCA* mutations, which he notes "is an extremely small number to make inferences about risks."

Two years ago, Antoniou led a study that reported on how polygenic scores influence risks in 25,000 carriers of *BRCA* mutations and found nearly as wide a range of overall cancer risks. His team has incorporated those data into a breast cancer risk estimator along with factors such as family history.

The MGH study is "an important and exciting paper" that complements other work, says David Ledbetter, chief scientific officer for the Geisinger Health System in Danville, Pennsylvania. His team recently looked at 92,000 participants in an ongoing genomic medicine study called MyCode, focusing on those who carried mutations predisposing them to 11 rare disorders that affect traits such as height, weight, and cholesterol levels. Incorporating polygenic scores helped predict those traits, the group reported on 25 October in *Nature Communications*.

It may be a while before physicians are comfortable telling patients how genetic backgrounds modify the risk posed by a major disease gene mutation. But some companies already offer polygenic scores for cancer and other diseases, and tests that combine both kinds of information are imminent. Before insurance companies agree to pay for such tests, Ledbetter cautions, "They're going to want to see much more clinical validation"—including for minorities, because current polygenic analyses draw on data primarily from people of European ancestry. ■

Published by AAAS

SCIENTIFIC COMMUNITY

Two Asian American women allege bias by HHMI

Powerhouse institute rejects claims of race, sex bias in separate legal actions

By **Meredith Wadman**

Two Asian American women biologists who failed to win renewals of plum awards from the Howard Hughes Medical Institute (HHMI) are suing the private medical research funder, alleging discrimination on the basis of sex and race or national origin.

Jeannie Lee, 55, an epigeneticist at Harvard Medical School and Massachusetts General Hospital in Boston and a naturalized U.S. citizen of Taiwanese origin, failed in 2016 to win a third renewal of her 5-year HHMI Investigator Award. She sued in August, asserting that a significantly lower percentage of Asian American women than whites win renewals of these generous employment contracts. She is also suing for age and sex discrimination; the suit claims that women aged 50 or older are less likely to be renewed than their male peers. It also alleges that Thomas Cech, 72, a white biochemist and former HHMI president with whom Lee is in a scientific dispute, undermined HHMI's review of Lee's work.

Separately, Vivian Cheung, 52, an RNA biologist at the University of Michigan in Ann Arbor, in March filed a Charge of Discrimination against HHMI with the U.S. Equal Employment Opportunity Commission (EEOC). This month, she received an EEOC notice giving her the right to sue, which she plans to do soon. Her EEOC filing alleges that HHMI's failure to renew her Investigator Award in 2018 was due to discrimination based on race, sex, and disability. (Cheung has a rare genetic disorder causing progressive vision loss.)

"Who is going to fight this fight for many minority women if I don't?" Cheung asks.

Lee said in a statement: "I'd rather not have to pursue this, but it's important to speak out because any kind of discrimination slows scientific progress."

HHMI President Erin O'Shea said in a written statement, "We are fully confident in the integrity of our review process." She added: "We respect Drs. Lee and Cheung and value their contributions during their tenures as HHMI Investigators. ... While we cannot provide details of personnel matters, particularly in cases of litigation, we have investigated these claims and believe they have no merit."

HHMI last month moved to dismiss parts of Lee's lawsuit that allege that it breached its contract with her by not renewing her and underpaying her. HHMI declined to share data on renewal rates by race, gender, and age, and publicly available data are incomplete.

With its $20.1 billion endowment, HHMI currently supports 260 scientists with coveted Investigator Awards, which now provide 7 years of salary and research support, making each award worth about $8 million. Investigators run their labs at their home institutions but are employed by HHMI. Investigators seeking renewal present their work to a peer-review panel and HHMI leaders at the institute's Chevy Chase, Maryland, headquarters.

Jeannie Lee received the $100,000 Lurie Prize in Biomedical Sciences in 2016, the year the Howard Hughes Medical Institute decided to end her Investigator Award.

In September 2016, Lee, an expert in how one of two X chromosomes is turned off during female development, was judged for renewal. During the award term from 2011 to 2016, she had published 18 research papers as senior author, five of them in *Nature*, *Science*, or *Cell*; applied for 24 patents; and, in 2015, been elected to the National Academy of Sciences.

She had also clashed publicly with Cech over the workings of an enzyme, polycomb repressive complex-2, which helps silence gene expression by binding to RNA during development and cancer. Lee argued that the enzyme binds RNA at specific sites with critical functions; Cech, now an HHMI investigator at the University of Colorado in Boulder, argued that the enzyme binds "promiscuously" to RNA.

Lee's lawsuit in U.S. District Court in Massachusetts alleges that Cech, who made the case for his own renewal to HHMI peer reviewers earlier on that September day, told them that Lee's model had been supplanted by his own. When Lee's turn came, the HHMI reviewers repeatedly questioned the legitimacy of her model, according to the lawsuit. It adds that their written comments accused her of being dogmatic and "undermin[ing] ... resolution" of the dispute with Cech. But according to the lawsuit, data from Lee's lab and dozens of articles by other scientists had confirmed her model at the time. Cech declined to comment on Lee's science, but their dispute continues.

Lee earned a "C" from the HHMI peer reviewers and lost her award, whereas Cech earned an "A," the lawsuit states. "HHMI applied a different standard to Dr. Cech, choosing to credit, reward and renew a white man and to discredit, not renew and criticize an Asian woman, where both had strongly held scientific views on a common subject," the lawsuit alleges.

Cech, a 1989 Nobel laureate in chemistry, says he can't comment on active litigation. But he notes that as president of HHMI from 1999 to 2009, he opened Investigator Award applications to all, ending institutional nominations with the goal of drawing more diverse applicants. "Encouraging diversity is a core value for me," Cech wrote in an email. O'Shea's statement also notes that several HHMI programs aim to boost diversity and that HHMI is "committed to progress" in this area.

Cheung, who studies RNA processing in human cells, won an Investigator Award in 2008 and was renewed in 2013. Her

PHOTO: FOUNDATION FOR THE NATIONAL INSTITUTES OF HEALTH

Published by AAAS

Charge of Discrimination alleges that after she was diagnosed in 2014, HHMI refused at first to grant her accommodations—an extra assistant and the ability to work remotely—and threatened to terminate her contract. Then, before her second renewal review, the charge states, HHMI officials pressured her to accept a 5-year phaseout award. She refused.

Joan Williams of the University of California (UC) Hastings College of the Law in San Francisco, who has written on gender bias faced by female scientists of color, notes that both Cheung and Lee bucked authority, Cheung by refusing to accept HHMI's 5-year phaseout funding, and Lee by publicly taking on Cech's science. "The research shows that Asian Americans who behave in dominant ways rather than deferential ones often trigger dislike by whites in the United States," she says.

Williams adds that the scientific dispute between Lee and Cech may have worked against her. "It's a very, very common pattern where if there are questions raised about the quality of somebody's work, they can be much more corrosive to a person's career if you are not a majority man."

Several other Asian American women who were discontinued as HHMI investigators—one in her late 40s and others in their early 50s—spoke to *Science* of their shock and dismay when they were not renewed. "Were they prejudiced against me as Asian? I think it's kind of a given. If you are Asian, you have to do so, so much better, and that's not even enough. You have to have friends," recalls one, who was senior author on two papers in *Science*, and many others, in the term before she lost her award.

Says another, whose many publications included four papers in *Nature*, *Cell*, or *Science* in the term before she was discontinued: "I was really shocked. … For me the glass ceiling was everywhere."

Still another, Xuemei Chen, 52, is a naturalized U.S. citizen who grew up in China and studies RNA biology at UC Riverside. She says she was devastated in 2017 when her initial Investigator Award was not renewed. The two white men in her field who were also up for review won renewals. "My work is no less groundbreaking," Chen says.

But neuroscientist Amita Sehgal of the University of Pennsylvania's Perelman School of Medicine, who grew up in India, says: "I cannot remember a single instance where at HHMI I felt discriminated against or overlooked because of being Asian American." Her HHMI award was renewed for the fourth time in 2017, when she was 56. After each renewal, she says, "I have basically walked away feeling like the process was fair." ■

PEER REVIEW

Rude reviews are pervasive and sometimes harmful, study finds

Survey finds that "unprofessional" comments abound

By **Christie Wilcox**

There's a running joke in academia about Reviewer 2. That's the reviewer who doesn't bother to read the manuscript a journal has sent out for evaluation, offers condescending or offensive comments, and urges the irrelevant citation of their own work. Such unprofessional conduct is so pervasive there's even a Facebook group, 25,000 members strong, named "Reviewer 2 Must Be Stopped!" But it is no laughing matter, concludes a new study that finds boorish reviews can have serious negative impacts, especially on authors belonging to marginalized groups.

Peer reviewers are supposed to help journals publish high-quality science by evaluating manuscripts and offering suggestions for improvement. But referee comments often stray far from that mission, found the study, published 12 December in *PeerJ*, which surveyed 1106 scientists from 46 countries and 14 disciplines. More than half of the respondents—who were promised anonymity—reported receiving at least one "unprofessional" comment, which the study defined as those that personally targeted a scientist, lacked constructive criticism, or were just unnecessarily cruel. About 40% said they had received more than one such comment.

"I didn't read the manuscript because I'm sure it's full of bad English."
Anonymous reviewer

One author, for example, received a review that stated: "The phrases I have so far avoided using in this review are 'lipstick on a pig' and 'bullshit baffles brains.'" Another reported this missive: "The author's last name sounds Spanish. I didn't read the manuscript because I'm sure it's full of bad English."

"It wasn't like it was just a certain group receiving these comments—everybody was getting them," says ecologist Amber Stubler of Occidental College in Los Angeles, California, a lead author of the study. "That is really very disturbing in and of itself."

What wasn't equal was the toll these reviews exacted. White men reported being "the least impacted" by rude comments, says co–lead author Nyssa Silbiger, an ecologist at California State University in Northridge. But women, nonbinary individuals, and people of color were all more likely to report that rude reviews increased feelings of self-doubt and harmed their scientific productivity. People of color were also more likely to say such reviews delayed their career advancement.

Those reports align with other findings on what is called stereotype threat—the psychological harm caused by pervasive negative stereotypes, says psychologist Denise Sekaquaptewa of the University of Michigan in Ann Arbor. Receiving a review that reinforces a harmful stereotype—such as that women or people of color are less intelligent—can create distress that results in self-doubt and impaired work performance.

The authors hope their findings will spur efforts to curb rude comments, and researchers already have some ideas. Linda Beaumont, a climate scientist at Macquarie University in Sydney, Australia, views nasty reviews as "another form of bullying" that should be exposed. More journals, she says, should take the step of publishing reviewer comments, which are typically kept private, alongside the final paper. (Silbiger and Stubler note that less than 3% of the problematic reviews they found involved journals with such policies.) Beaumont has also called on journals to adopt specific codes of conduct for reviewers. Ideally, Silbiger says, those codes would also specify "serious consequences" for violations, including bans.

Others want journals to end anonymity for referees. They note studies have found that such "open peer review" can increase the quality and professionalism of comments. But some early-career researchers oppose that idea, fearing it could expose them to retaliation from senior colleagues displeased by their critiques. They'd prefer journals use double-blind peer review, which hides the identities of both authors and reviewers.

In the meantime, the study's authors are hoping to dive deeper into reviewer comments, for example to better understand the effects of nasty comments, that specifically target gender or ethnicity. The current study, Stubler says, "sort of scratches the surface." ■

Christie Wilcox is a journalist based in Washington.

Published by AAAS

DARKNESS MADE VISIBLE

An international team of astronomers has produced the first ever image of a black hole

By **Daniel Clery**

3 PEOPLE'S CHOICE

Massive, ubiquitous, and in some cases as big as our Solar System, black holes hide in plain sight. The effect of their gravity on objects around them and, lately, the gravitational waves emitted when they collide reveal their presence. But no one had ever seen one directly—until April. That's when an international team of radio astronomers released a startling close-up image of a black hole's "shadow," showing a dark heart surrounded by a ring of light created by photons zipping around it. Heino Falcke of Radboud University in Nijmegen, the Netherlands, a member of the team that produced the image, said the first glimpse felt like "looking at the gates of hell." That evocative image is *Science*'s 2019 Breakthrough of the Year.

The iconic image of galaxy Messier 87's central black hole, showing a ring of photons bent by its gravity.

For astronomers, the image is a validation of decades of work theorizing about esoteric objects they couldn't see. "I'm still kind of stunned," says astrophysicist Roger Blandford of Stanford University in Palo Alto, California. "I don't think any of us imagined the iconic image that was produced." In fact, until recently few astronomers imagined such an image was even possible. Black holes are very small by cosmic standards and by definition emit no light. When they grow to gargantuan masses, as happens in the centers of galaxies, the swirling mayhem of gas, dust, and stars stirred up by their extreme gravity creates an additional barrier.

But 2 decades ago, a handful of astronomers began to wonder whether the hot swirling gases close to a giant black hole's edge, or event horizon, might make it visible. They glow at many wavelengths, including

IMAGES: (TOP TO BOTTOM) LIA MEDEIROS/CHI-KWAN CHAN/DIMITRIOS PSALTIS/FERYAL OZEL/UNIVERSITY OF ARIZONA/INSTITUTE FOR ADVANCED STUDY; EHT COLLABORATION/CC 4.0

Published by AAAS

A simulation of matter swirling around the black hole at the center of Messier 87 and radiating at different wavelengths. A bright ring of light orbiting the black hole's shadow shines through the haze, and green tendrils of a powerful jet stream from its pole.

millimeter waves—short-wavelength radio waves that can pierce the gas and dust surrounding a galactic center. Developments in technology promised to help. A technique known as very-long-baseline interferometry (VLBI), which combines data from widely spaced radio dishes to simulate a much larger telescope, was revealing distant objects in finer detail. And improvements in receivers, antenna design, and digital electronics were allowing radio astronomers to capture millimeter waves. By observing at those wavelengths, using dishes spread as far apart as possible to boost resolution, could they make out the details of a black hole?

ON OUR WEBSITE

For more on the Breakthrough of the Year, including a video and a podcast, go to: https://scim.ag/Breakthrough2019

Maybe, if it were a monster with the mass of millions of suns, and relatively close by. The 4-million-solar-mass black hole at the center of our Milky Way Galaxy, known as Sagittarius A* (Sgr A*), was an obvious contender, being the closest to Earth at just 26,000 light-years away. Despite its heft, it is a tiny object in galactic terms—it would fit inside the orbit of Mercury—and imaging it would push VLBI to the limit.

Early attempts about a dozen years ago using telescopes in Hawaii and the mainland United States revealed scraps of detail of the superheated gas close to Sgr A*. The telescopes also got a glimpse of a second potential target: the supermassive black hole at the center of the nearby galaxy Messier 87. Although M87 is 2000 times farther from Earth than Sgr A*, its black hole, M87*, has more than 1000 times the mass so it appears roughly the same size in the sky. With observations beginning to bear fruit, funding agencies started to chip in, and the international Event Horizon Telescope (EHT) was born.

Despite its name, EHT is not a telescope, but a consortium involving more than 200 scientists from across the globe. It applies for time on existing telescopes—as many and as widely spaced as possible. At most telescopes, EHT members must install their own equipment, including high data rate digital processors and atomic clocks, to make the instrument VLBI-friendly. A turning point came when EHT enlisted the Atacama Large Millimeter/submillimeter Array (ALMA). Made up of 66 dishes high in the desert mountains of northern Chile, it is by far the largest observatory at millimeter wavelengths. Allowing the EHT team to come in, open up the hood, and tinker with the engine of this $1.5 billion U.S.-European-Japanese collaboration took years of persuasion and several rejected designs, but adding ALMA boosted EHT's sensitivity 10-fold.

In April 2017, everything was in place for a major 10-night observing run. ALMA, along with seven other observatories in the United States, Mexico, Chile, Spain, and at the South Pole, took repeated nightlong exposures of both Sgr A* and M87*. "We lucked out with the weather," says EHT's founding director Shep Doeleman of the Harvard-Smithsonian Center for Astrophysics in Cambridge, Massachusetts. But it would be almost 2 years before the EHT team knew what, if anything, it had achieved.

Working in parallel at data centers in Germany and the United States, separate teams calibrated and processed the data, using several different methods, while other teams independently checked the results. No image was produced until the very end, to avoid biasing the outcome. The teams began to work on Sgr A* and M87* in parallel, but focused on M87* when they found that the material swirling around Sgr A* changed by the hour, blurring the image. The action around the giant M87* moves at a stately pace, changing little over the course of a night. In April, the team revealed an image of M87*. The black hole's silhouette—outlined in a ring of light—adorned front pages and news reports across the globe, and became the most downloaded image in the history of the National Science Foundation's website. A description of the effort and its implications filled six papers in *Astrophysical Journal Letters*.

For black hole theorists, that first, rather blurry image sprang few surprises, but just seeing it was "a glorious affirmation of theory," Blandford says. Albert Einstein's description of gravity, general relativity, predicts a black hole's shadow should be perfectly round—a prediction confirmed to within 10% by the M87* image. That may rule out a few of the wildest alternative theories of gravity that aim to supplant relativity, but the EHT team will need to squeeze down the error bars in future observations to put Einstein to more stringent tests.

The best tests of general relativity could come from an image of Sgr A*, which the team hopes to finish in 2020. Researchers have much more precise data on the mass, size, and distance of Sgr A* than of M87*. "That will immediately improve the quality of constraints [on general relativity]," says team member Feryal Özel of the University of Arizona in Tucson. First, though, the team needs to sharpen its view of Sgr A*. "We're trying to finalize the analysis tools to deal with its quirkiness," she says.

EHT has 11 facilities lined up for the next round of observing in 2020, including new dishes in Greenland and Arizona and an upgraded array in France. Observations will soon move to even shorter wavelengths—0.86 millimeters instead of the 1.3 millimeters used so far. Further in the future, the team hopes to add a dozen or so purpose-built dishes scattered across the globe and some in space, to increase the resolution still further. A dish one-third of the way to the Moon, for example, would bring another 20 supermassive black holes into imaging range.

Such expansion would also enable EHT to graduate from making still images to "movies" of a black hole sucking in material and funneling it into high-powered jets that fire from its poles millions of light-years into space. How those jets are created "is the big astrophysical puzzle," Blandford says. This year's triumph, he adds, "is the beginning, not the culmination, of this research project." ■

PEOPLE'S CHOICE

Our readers weigh in with their picks for the top breakthrough of 2019

For readers of *Science* online, this was the year of the Denisovans. The ancient humans had been known only from scraps of fossils found in a cave in Siberia in Russia. But this year, researchers used evidence from proteins to identify a fossilized jaw from China's Tibetan Plateau as Denisovan, indicating they were widespread, and genetic evidence to reconstruct the face of a Denisovan girl. Those achievements are this year's People's Choice for Breakthrough of the Year.

We invited visitors to *Science*'s website to vote on 12 candidates for the breakthrough. A first round of voting narrowed the choices to four, and a second round, in which more than 34,000 votes were cast, determined the People's Choice. The Denisovan research was the clear winner, followed by the development of two promising drugs to treat Ebola, the first ever image of a black hole—*Science*'s choice—and a newly approved treatment for the majority of cystic fibrosis patients. The complete results:

1. Denisovans come into focus **49%**
2. Ebola drugs **25%**
3. Black hole image **15%**
4. Cystic fibrosis drug **11%**

Published by AAAS

A killer impact and its aftermath

After a giant asteroid hit Earth 66 million years ago, 76% of the world's species, including the big dinosaurs, disappeared. But exactly how and when they died, and how quickly ecosystems recovered, has been unclear. Now, a sediment core extracted from the site of the impact on Mexico's Yucatán Peninsula, together with several rich fossil finds in the United States, are bringing the cataclysm and its aftermath into sharp focus.

In 2016, the International Ocean Discovery Program drilled into the rugged hills around the center of the 193-kilometer-wide Chicxulub crater, which now lies mostly underwater on the Yucatán coast. The drilling extracted an 835-meter core, including 130 meters deposited the day the asteroid hit. An examination of the core, published this year, provides an almost minute-by-minute reconstruction of what happened after the impact. Molten rock filled the impact hole, followed by a hailstorm of debris. The ocean surged in, churning the deposits; then, by the end of the first day, a tsunami swept in more material, including charcoal from impact-induced wildfires. Even though sulfur-rich material was abundant at that site, there was little present in the core, suggesting it all vaporized and likely helped cause rapid global cooling and darkness.

Thousands of kilometers from ground zero, a new site in North Dakota captured the catastrophic effects of the impact on living things. In less than 1 hour, impact-induced seismic activity caused waves of water to rush up an ancient river system at the site, sweeping living things into tumbled deposits. Fossil fish bear a vivid fingerprint of the impact: Their gills are filled with glass particles, rich in iridium, from the impactor itself.

But life recovered faster than expected, as an analysis of pollen, plant fossils, mammal skulls, and other bones at another site, Colorado's Corral Bluffs, chronicles. Ferns and mammals no bigger than rats survived the impact, which ended the Cretaceous period and marked the beginning of the Paleogene, creating the K-Pg boundary. Palm trees replaced the ferns within 1000 years; by 300,000 years, walnutlike species dominated; and by 700,000 years after the impact, legumes showed up. Mammals doubled in size and diversity within the first 100,000 years, a trend that accelerated and continued, particularly after the legumes appeared; by 700,000 years, some mammals topped 50 kilograms.

Last year, an analysis of tiny shelled plankton called foraminifera in the Chicxulub drill core indicated that the marine ecosystem at the crater site was back up and running within 30,000 years, much faster than anticipated. But recovery was slower elsewhere. This year, analyses of foraminifera from the drill core and from sites around the world documented rapid acidification of the oceans following the impact and suggested a 50% reduction in the amount of organic material reaching the sea bottom, which may have suppressed marine life for 1 million years.

All these results made for a "superyear" in studies of the K-Pg mass extinction, says Vivi Vajda, a paleontologist at the Swedish Museum of Natural History in Stockholm.
—Elizabeth Pennisi

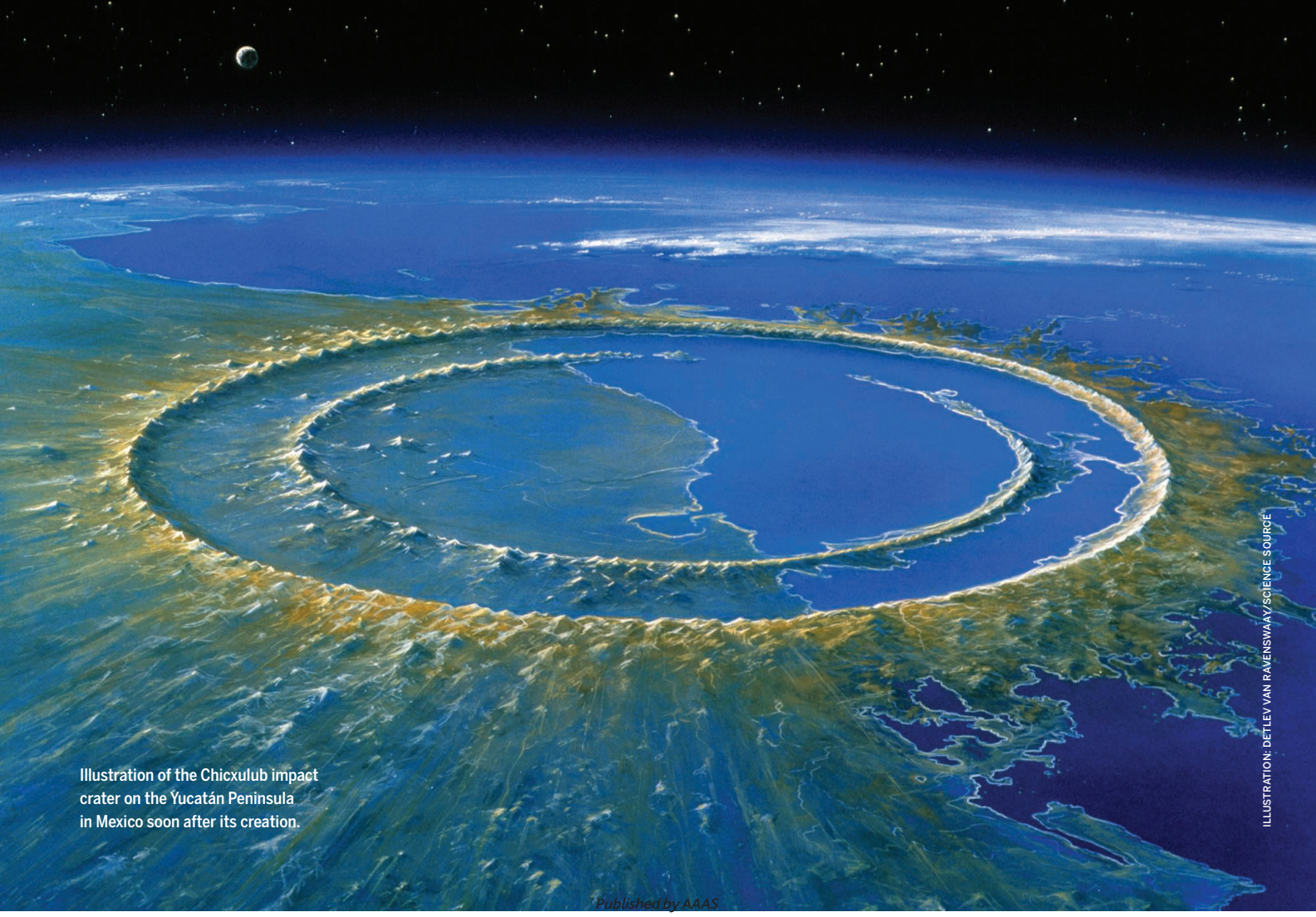

Illustration of the Chicxulub impact crater on the Yucatán Peninsula in Mexico soon after its creation.

ILLUSTRATION: DETLEV VAN RAVENSWAAY/SCIENCE SOURCE

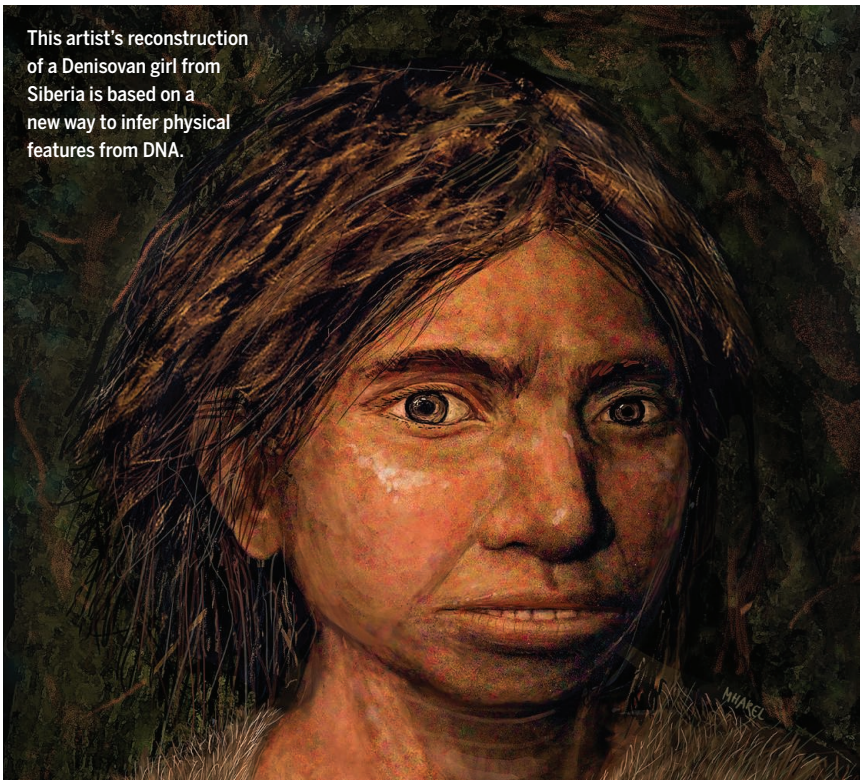

This artist's reconstruction of a Denisovan girl from Siberia is based on a new way to infer physical features from DNA.

1 PEOPLE'S CHOICE

Face to face with the Denisovans

Almost 40 years ago, a Buddhist monk found an odd human jaw bone in Baishiya Karst Cave, high on the edge of the Tibetan Plateau. Recognizing that the jaw, with its giant molars, was something special, he gave it to another monk, who donated it to scholars. But no one knew what to make of it. Then in May, scientists applied a new method of analyzing ancient proteins and identified the strange jaw as that of a Denisovan, a mysterious human ancestor who ranged across Asia until some 50,000 years ago, about the same time as the Neanderthals. The work brings these enigmatic ancient people into focus, and heralds a potential protein-based revolution in understanding ancient life.

The Denisovans have haunted human evolution researchers for 10 years. Back in 2010, researchers identified them by sequencing DNA from a fossilized pinkie bone found in Denisova Cave in Siberia. The DNA, which came from a girl, differed from that of Neanderthals and modern humans. Today, ghostly traces of Denisovans linger in the DNA of living people across Asia, suggesting the group was once widespread and mingled with both Neanderthals and modern humans. But until this year, only a few scraps of additional Denisovan fossils had been identified, all from Denisova Cave. Scientists were left guessing what the Denisovans looked like.

The 160,000-year-old Baishiya jaw yielded no DNA. But a Chinese and European team managed to extract collagen, a common protein, from the bone, and match it with collagen from the Denisova Cave girl. That suggested the jaw was Denisovan and that these mystery humans had robust jaws, big molars, and teeth with three roots.

In September, another team refined that picture by applying a new technique to the Denisova Cave girl's genome. They traced chemical modifications of the DNA called methylation, which can silence genes, then combined that information with a database that describes how missing or defective genes influence anatomy in living people. The results suggested how the methylation pattern of the girl's DNA might have shaped her body. The team concluded that she would have looked a lot like a Neanderthal, with a wide pelvis, sloping forehead, and protruding lower jaw. But she also had a wider face than modern humans or Neanderthals, and a longer arch of teeth along her jaw bone. When the researchers tested their view of the Denisovan smile against the newly identified Baishiya jaw bone, it fit almost perfectly. —*Elizabeth Culotta*

2 PEOPLE'S CHOICE

Hope for Ebola patients, at last

In 1976, a new virus emerged from the rainforest of the Democratic Republic of the Congo (DRC, then called Zaire). It killed 280 people in the village of Yambuku and disappeared, only to pop up again sporadically with devastating effect. Ever since, the name of that virus, adopted from a nearby river, has been synonymous with deadly, incurable infection: Ebola. This year, that characterization began to change.

In the midst of another outbreak, the deadliest in the DRC's history, scientists finally identified two drugs that dramatically reduce death rates from the disease. Both are antibodies, one isolated from a survivor of a 1996 Ebola outbreak, the other a mix of three antibodies produced in mice with humanized immune systems. In a randomized trial that pitted four different drugs against each other, about 70% of the patients who received one of those two medicines survived, compared with about 50% of those given either of the other two drugs. The result was so compelling that the trial was stopped early. Simply conducting the trial was a notable achievement in itself: It was carried out in makeshift treatment units in the midst of a devastating outbreak and in an area of violent conflict.

The result should help combat the disease not only by improving patients' chances of survival, but also by encouraging people to seek treatment early. With no effective drugs available, people with symptoms have often tried to evade detection and sought out traditional healers, which has fueled outbreaks.

More than 40 years after the threat from Ebola emerged, the world is finally better prepared to deal with the virus. And the architect of this victory, the principal investigator of the trial, was Jean-Jacques Muyembe-Tamfum, the Congolese virologist who was instrumental in the discovery of the virus in Yambuku. —*Kai Kupferschmidt*

A health worker dons protective gear during the ongoing Ebola outbreak in the DRC.

IMAGES: (TOP TO BOTTOM) MAAYAN HAREL; BAZ RATNER/REUTERS

Published by AAAS

Quantum supremacy attained

In October, the era of quantum computing dawned—maybe. Physicists with Google claimed they had used a quantum computer to calculate something no ordinary computer could, reaching a milestone known as quantum supremacy. Although a rival group disputed the claim, it was widely hailed as a major achievement. But a quantum computer that can solve practical problems could still remain decades away.

A conventional computer manipulates information encoded in bits that can be set to either zero or one. A quantum computer uses qubits that can be set to zero, one, or both zero and one at once. For certain problems, possible solutions can then be represented by different quantum waves sloshing simultaneously through the qubits. The wrong solutions can interfere to cancel one another, while the right solution pops out. Because the system explores a vast number of potential solutions at once, a full-fledged quantum computer could, for example, factor huge numbers much faster than conventional computers. That could enable a quantum computer to crack current internet security protocols.

Google researchers say they have taken a key step toward a functioning quantum computer by achieving quantum supremacy with an abstract test problem. Using a chip containing 53 qubits made of tiny circuits of superconducting metal, they implemented a set of randomly chosen interactions and showed, essentially, that the machine would output the correct quantum state. For calculations requiring a few qubits, they checked the result with supercomputer simulations. For larger numbers of qubits, they employed a statistical measure to help confirm the result. The comparisons showed that the quantum computer calculated in 200 seconds something that would take a supercomputer 10,000 years to figure out, the team says.

Immediately, however, IBM researchers questioned whether Google had truly reached its mark. They claimed that, with the right algorithm, a supercomputer could solve the problem in as little as 2 days. Other physicists say that to solve practical problems, a quantum computer will have to be able to correct errors in its own qubits, something that has yet to be achieved. Researchers also face massive practical challenges in scaling up from a single machine containing a few dozen qubits to a vast array of machines containing 100 million qubits—the number it would take to crack internet encryption. The era of quantum computing may have dawned, but we may be waiting a while for breakfast. —*Adrian Cho*

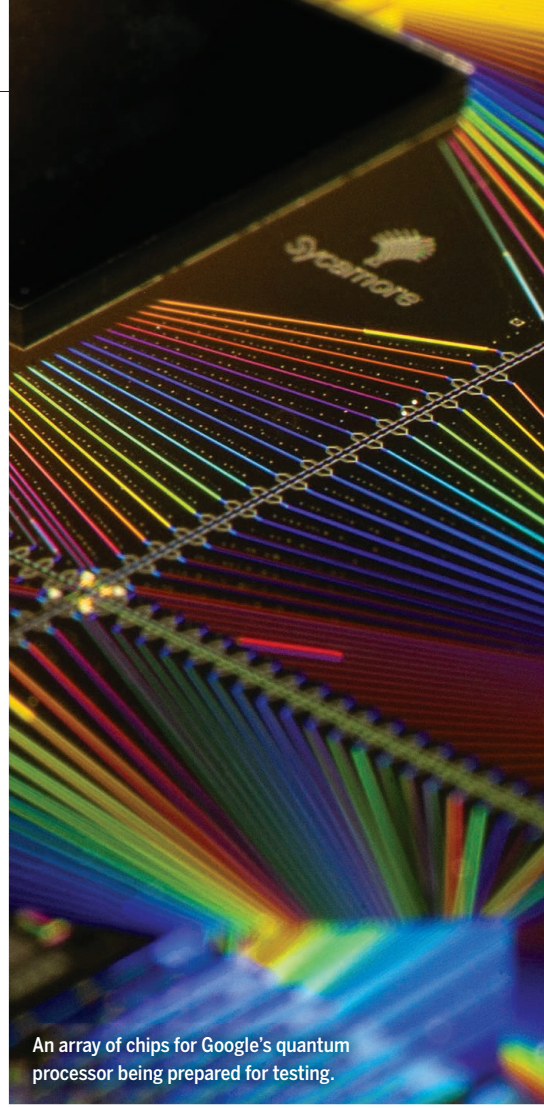

An array of chips for Google's quantum processor being prepared for testing.

A 'missing link' microbe emerges

This year, microbiologists took a major step toward resolving a controversy over the origin of eukaryotes, the group that encompasses all plants and animals—including humans. After 12 years of trying, a team in Japan succeeded in growing a mysterious microbe from deep-sea sediments and sequenced its genome. It could shed light on the ultimate ancestry of us all.

The organism, *Prometheoarchaeum syntrophicum* strain MK-D1, is a member of the recently recognized Asgard group of microbes, which are not bacteria but a completely separate branch of life called archaea. The Asgards were known only from DNA fragments isolated from deep-sea sediments and other extreme environments. Surprisingly, those fragments contain genes formerly thought to be found only in eukaryotes—organisms with cells that have nuclei and organelles such as mitochondria. Comparative DNA analyses indicated the Asgards, or an ancient relative, may have even given rise to eukaryotes. That radical idea would shrink the domains of life from three—archaea, eukaryotes, and bacteria—to two: bacteria and archaea, with eukaryotes reduced to a subset of archaea. But given the scant evidence, many researchers were skeptical.

It took 12 years to culture this tentacled deep-sea microbe (lighter color).

By growing an Asgard in culture, the team in Japan could sequence its full genome and confirm that it carries eukaryotic genes. The researchers also found that it seems to grow best in association with certain bacteria, and that it forms short tentacles that might engulf bacterial companions. If so, that could explain how an Asgard acquired the microbial guests that became mitochondria. (A paper detailing the findings was posted on the bioRxiv preprint archive; it has now been accepted for publication.)

Other studies this year have identified more eukaryotic genes in DNA fragments from other members of the Asgard group. And information derived from DNA about Asgard metabolism also bolsters the two-domain over the three-domain hypothesis. Proponents of both ideas agree, however, that events that happened almost 3 billion years ago will be hard to reconstruct, and that new ideas may emerge as more Asgards are studied—and, perhaps, cultured. But with one now in hand, researchers have a clearer window into that distant past. —*Elizabeth Pennisi*

PHOTOS: (TOP TO BOTTOM) GOOGLE; IMACHI AND NOBU *ET AL.*

Published by AAAS

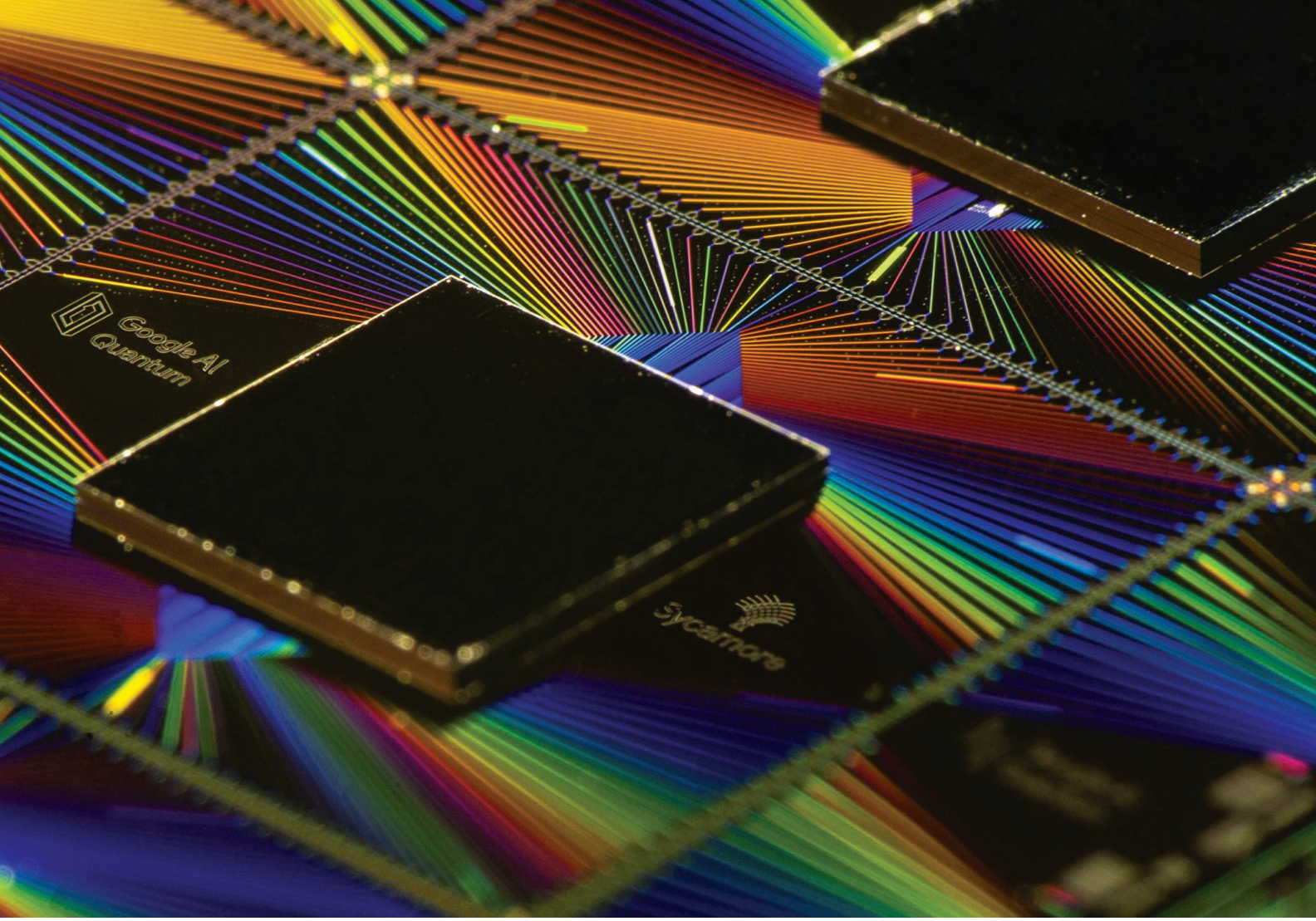

PHOTO: NASA/ROMAN TKACHENKO

A close-up of a far-out object

Last year, it was just a tiny gray spot in the blackness of space; now, it is Arrokoth. On the first day of this year, NASA's $800 million New Horizons spacecraft swept by 2014 MU69, a 36-kilometer-wide object some 6.6 billion kilometers from Earth, in a region beyond Neptune called the Kuiper belt. Astronomers have discovered thousands of objects lurking in the belt, which they believe harbors material little altered from the early years of the Solar System. But they have never had a close-up look.

New Horizons revealed that Arrokoth—MU69's new official name, after the Powhatan and Algonquian word for "sky"—consists of two pristine planetary building blocks that resemble lumpy pancakes, joined at a narrow neck. Relatively free of craters, Arrokoth's two icy lobes formed separately at the Solar System's beginning, likely condensing out of the same cloud of dust. Their odd shape and unmarred, homogenous surfaces support a new notion for how planetary building blocks form. They don't grow by collision after collision. Rather, soon after the Sun formed, static electricity drew together dusty grains into centimeter-size pebbles; the swirl of the primordial nebula then caused the pebbles to flock together into gathering clouds, which gravitationally collapsed into kilometer-size lumps. This "streaming instability" can explain why Arrokoth has two lobes: The pebble cloud rotated faster as it collapsed, developing turbulence that fractured it. Two of the pieces drew close until their axes aligned, and mutual attraction pulled them together in a gentle kiss.

Much work remains to be done; the spacecraft will not even finish beaming back all its observations of Arrokoth until the end of 2020. Even then, its mission may not be over: The New Horizons team is now using the probe's telescope to search for a new Kuiper belt target to visit, one too small for any telescope on Earth to see. —*Paul Voosen*

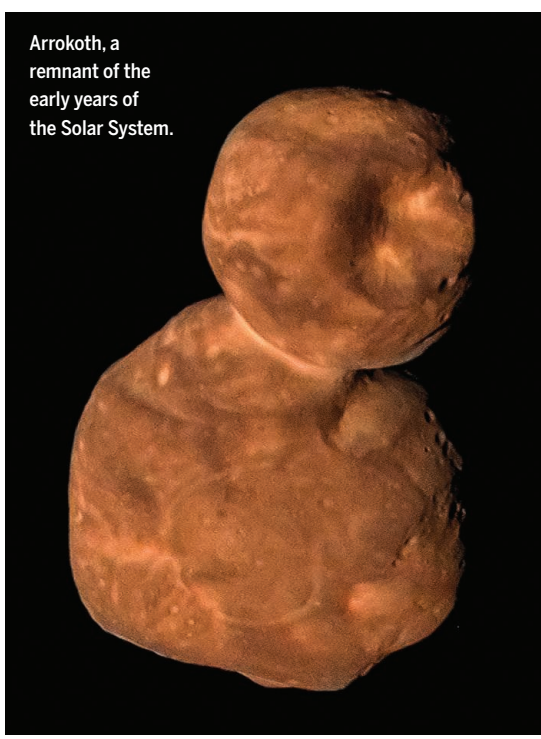

Arrokoth, a remnant of the early years of the Solar System.

Published by AAAS

4 PEOPLE'S CHOICE

In a first, drug treats most cases of cystic fibrosis

In October, scientists celebrated a milestone for gene-based drugs: the approval of an effective treatment for most cases of cystic fibrosis (CF). The treatment, a triple-drug combination called Trikafta, corrects the effects of the most common mutation behind the lung disease. For those who have the mutation—about 90% of all CF patients—it could convert CF from a progressive disease into a more manageable chronic illness. Trikafta is the upshot of 30 years of research since the CF gene, *CFTR*, was discovered.

CF strikes when a child inherits two mutated copies of the gene, and life expectancy for patients born today averages in the mid-40s. Trikafta builds on other CF drugs made by the company Vertex Pharmaceuticals, which target different defects in the CFTR protein. The first, Kalydeco, was leveled at a rare mutation called G551D, which affects about 4% of patients in the United States. In these patients, the CFTR protein fails to open its "gate"

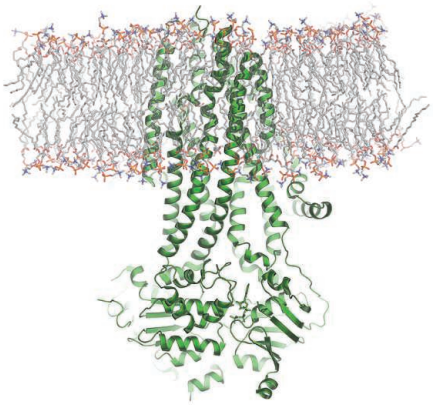

A model of the CFTR protein (green), which is defective in cystic fibrosis, at the cell surface.

and let chloride pass through—which, like other defects in CFTR, leads to a buildup of mucus in the lungs. Kalydeco mended this defect and was approved in 2012. Vertex then combined Kalydeco with another drug aimed at repairing the effects of a different mutation, F508del, which misfolds CFTR and prevents it from reaching the cell surface. But this two-drug formulation, Symdeko, proved less effective than hoped.

Trikafta adds a third drug to the mix to enhance the strategy's effectiveness. The triple combination, which is geared to CF patients who carry at least one copy of F508del, helps CFTR reach the cell membrane and open its gate. In clinical trials the drug boosted lung capacity by 10% to 15% and blunted CF complications.

Questions remain about how early to start the treatment—it's now approved for ages 12 and up but is being tested on younger children—and how to design new drugs for the 10% of patients whose disease isn't targeted by Trikafta.

Amid the excitement looms a shadow, however: Trikafta has a list price of more than $300,000 a year, and presumably must be taken for life. —*Jennifer Couzin-Frankel*

Supplements that improve gut microbes could be a game changer for children like this infant in Bangladesh.

Microbes combat malnourishment

Each year, millions of severely malnourished children fail to recover completely, remaining stunted and sickly even after they are well fed. Ten years of research has pointed to a root cause: Their gut microbes do not mature. This year, an international team built on that research to come up with a low-cost, easy-to-obtain supplement that preferentially stimulates the growth of beneficial gut bacteria. The supplements performed well in a small trial, and larger scale clinical trials are now underway to see how well the supplement works to prevent stunting.

Earlier research determined that malnourished children who fail to recover have gut microbial communities—or microbiomes—characteristic of infants, and that more mature microbiomes are key to responding well to nourishment. The team first pinpointed 15 types of bacteria that characterize a mature gut microbiome. They also identified blood markers, including proteins, that signal a recovery from the effects of malnutrition. They then tested various combinations of food readily found in developing countries to see how the microbiome responded, first in mice, then in pigs, and finally in a small group of malnourished children.

Milk powder and rice, standard components of food aid, did little to foster expansion of the key bacteria, but supplements containing chickpeas, bananas, and soy and peanut flours helped the microbiomes mature. After a short clinical trial, children who received the supplements had more of the blood proteins and metabolites that are markers for normal growth.

More children are being followed for longer periods to see whether these changes translate into recovery from stunting, the final proof that improving the microbiome can help solve this worldwide problem. If it can, and particularly if the treatment can be provided outside a hospital, at home—a recent trend for combatting this problem—"the impact could be huge," says Eric Pamer, a physician scientist at the University of Chicago in Illinois. —*Elizabeth Pennisi*

IMAGES: (TOP TO BOTTOM) FANGYU LIU/JAMES LEE/ROCKEFELLER UNIVERSITY; INTERNATIONAL CENTRE FOR DIARRHOEAL DISEASE RESEARCH, BANGLADESH

Published by AAAS

Artificial intelligence masters multiplayer poker

This year, an artificial intelligence (AI) program beat some of the world's best players in the most popular version of poker, no-limit Texas Hold 'em. The landmark result marks the first time AI has prevailed in a multiplayer contest in which players have only imperfect information about the state of the game.

AI has been trouncing humans in games at a spectacular rate. In 2007, computer scientists developed a program guaranteed not to lose at checkers. In 2016, another team developed an AI program that defeated the best humans at Go, a board game with vastly more configurations than checkers.

Poker presents a stiffer challenge, as players cannot see their opponents' cards and thus have limited information. In 2017, computer scientists developed an AI program unbeatable at a two-player version of Hold 'em—in which each player forms a hand from five cards laid face up on the table and two more each holds privately.

Now, AI has bested world-class players in the full multiplayer game, as computer scientists at Carnegie Mellon University in Pittsburgh, Pennsylvania, announced in August. By playing 1 trillion games against itself, their program, Pluribus, developed a basic strategy for various kinds of situations—say, playing for an inside straight. For each specific hand, it could also think through how the cards would likely play out. In 20,000 hands with six players it outperformed 15 top-level players, as measured by average winnings per hand.

Pluribus played differently from programs for two-player games. Those programs sought out a no-lose strategy, known as a Nash equilibrium, which guarantees that, on average, their opponents would do worse unless they also played with the exact same strategy. With multiple opponents, there is no such guarantee, so Pluribus simply learned what was most effective in a given situation. The program also taught itself to play while running on a single server with 64 processors—whereas the Go-playing program required more than 1200 processors.

AI developers aren't done playing games. In poker there's still room for improvement. Although Pluribus can bluff, it cannot adapt its strategy to exploit an opponent's particular weaknesses. Some more complex games such as contract bridge remain unmastered. Still, the most famous objective in the application of AI to games has fallen to the computers. It may be time humans cashed in their chips. —*Adrian Cho*

ILLUSTRATION: JASON SOLO/THE JACKY WINTER GROUP

Published by AAAS

BREAKDOWNS OF THE YEAR

What went wrong in the world of science in 2019

A burned area of Amazonian forest in Brazil's Pará state on 27 August.

PHOTO: JOAO LAET/AFP VIA GETTY IMAGES

The Amazon ablaze

Forest fires consumed thousands of square kilometers of the Amazon this year, and many blame the policies of Brazil's new president, Jair Bolsonaro, for fanning the flames.

Brazil's National Institute for Space Research (INPE) estimates the number of fires in the Amazon increased by 44% compared with 2018. One factor was an increase in deforestation, to about 9700 square kilometers in the 12 months through July, the largest area since 2007–08, INPE reported in November. Ranchers and farmers cut down and sell valuable trees and then burn the forest to make space for planting crops or raising cattle. Remote sensing indicated that this year's fires tended to be far away from where crops are grown, suggesting ranchers were probably responsible.

Since becoming president in January, Bolsonaro has pushed for agricultural development in the Amazon and cut the budget for environmental protection. After the fires started, Bolsonaro blamed nongovernmental organizations for setting them, and called the deforestation figures "a lie."

When the director of INPE defended the integrity of the agency's analyses, he was fired. The conflagration and Brazil's response drew international opprobrium. The United Nations offered assistance, which Bolsonaro declined, and Germany and Norway stopped donating to the Amazon Fund, which supports forest protection. After the international outcry, Bolsonaro sent in the military to help fight the fires, which dropped off sharply in October. —*Erik Stokstad*

Measles resurgent

Measles came roaring back in the United States this year and continued an upsurge around the world. Poverty, displacement, conflict, and—particularly in the United States and Europe—vaccine misinformation are all playing a role in the resurgence of a virus that killed an estimated 142,300 people in 2018, and for which there is a highly effective vaccine.

In the United States, 1276 measles cases were reported to the U.S. Centers for Disease Control and Prevention through 5 December, the highest tally since 1992. More than 75% of the cases were linked to outbreaks in New York, primarily among unvaccinated people in Orthodox Jewish communities.

The number of cases reported in the World Health Organization's (WHO's) European Region reached 92,000 in the first half of the year, exceeding the tally for all of 2018, previously the worst year this decade.

Globally, the picture was worse. WHO received more than 440,000 confirmed measles case reports through 5 November—25% more than in all of 2018 and more than twice the number in 2017. The real numbers are likely much larger; WHO estimates that fewer than one in 10 cases is reported. Its estimate of actual 2018 cases: 9.8 million.

Several countries were particularly hard hit. A Ukrainian epidemic spawned by political upheaval and vaccine misinformation led to 56,802 case reports through September. In Africa, Madagascar contended with more than 126,000 cases between January and April, before a nationwide emergency immunization campaign dramatically curbed the epidemic. The Democratic Republic of the Congo suffered still higher numbers: It reported 269,079 cases by 2 December, leading to 5430 deaths, mostly in children un-

Published by AAAS

der 5 years old. And in the tiny nation of Samoa, where childhood vaccination rates had dropped to about 30%, an outbreak sickened some 4898 people as of 2 December and killed 71. —*Meredith Wadman*

Bird counts dwindling

A sobering study has documented an almost 30% drop in the number of North American birds since 1970, with common birds such as sparrows and blackbirds declining as well as rarer species. The losses have raised fears that many species could go the way of the passenger pigeon, a species once so abundant that its extinction in the early 1900s seemed unthinkable. Habitat losses and ecosystems under stress from pollution, climate change, and development are among the leading causes.

U.S. and Canadian researchers combined data from annual spring censuses, the Audubon Christmas Bird Count, an international assessment of shorebirds, and aerial studies to look for population changes in 529 species. Thanks to conservation efforts, waterfowl and raptors are thriving. But birds living along shorelines are not doing so well—sanderlings and plovers are down by about one-third—and the number of birds that inhabit grasslands has declined by about 50% over the past 50 years. Even the most familiar birds are in trouble: Nineteen common species have each lost more than 50 million birds since 1970.

All told, North America now has 3 billion fewer birds, but the situation is not hopeless, researchers say. Reversing habitat loss could stabilize populations. And simple steps, such as keeping cats indoors and planting native plants, can help, says a coalition of conservation groups that has come up with policy recommendations and an action plan for citizens. —*Elizabeth Pennisi*

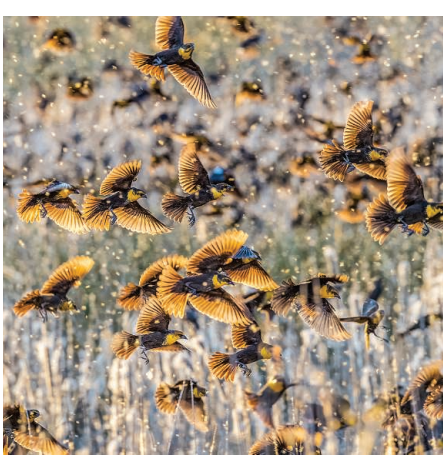

Yellow-headed blackbirds. Even some familiar species, such as blackbirds and starlings, are declining.

PHOTOS: (TOP TO BOTTOM) RON ADAR/SOPA IMAGES/LIGHTROCKET VIA GETTY IMAGES; JACK DYKINGA/NPL/MINDEN PICTURES

Activist Greta Thunberg addressing a rally in New York City demanding political action on climate change.

An eleventh hour climate awakening?

U.S. public acknowledges climate threat while politicians stall

Advocates for stronger U.S. action on climate change took heart this year from signs that public opinion is swinging their way. Numerous polls showed a rising proportion of Americans believes climate change is real, humans are contributing, and government and industry should take steps to address it. But that shift in public opinion has not resulted in political action at the national level—in fact, the Trump administration pulled back several key climate change regulations this year. And with unprecedented wildfires in Australia and North America, coral bleaching in the Pacific Ocean, and a deadly heat wave in Europe making the cost of warming unmistakable, governments' failure to curb global greenhouse gas emissions ignited protests around the world.

A survey by *The Washington Post* and the Kaiser Family Foundation found that almost 80% of Americans now agree that human activity is fueling global warming, and close to 40% call climate change a "crisis," almost double the number willing to use that term 5 years ago. A Pew Research Center survey found a similar shift: Fifty-seven percent of Americans now consider climate change a "major threat" to the United States, up from about 40% in 2013. But surveys also reveal deep divides by age, geography, and political affiliation, with older people, those living in the Midwest and Rocky Mountain regions, and those who identify as conservative less likely than other groups to see climate change as a serious threat requiring action.

Local governments in the United States are responding to public concerns. Although most Democratic politicians have long backed government action on climate change, most Republicans have not. But this year, many Republican officials publicly changed their tune. Florida's Republican governor created a position for a science adviser to help figure out how the state should deal with rising seas and other climate-related challenges. The U.S. Congress, too, saw a glimmer of cross-party cooperation, with lawmakers in both the Senate and the House of Representatives establishing bipartisan caucuses to discuss climate.

Yet the Trump administration has forged ahead with a range of policies, including withdrawing from the Paris climate pact and rolling back emission limits on power plants and automobiles, that experts say will make it more difficult for the United States and the world to curb emissions of greenhouse gases. Overseas, like-minded governments in Australia and Brazil also backed away from efforts to address climate change. And this month at a meeting in Madrid, nations that have signed the Paris pact continued to disagree on how exactly to achieve even the relatively modest commitments they have made, let alone strive for the deeper emissions cuts needed to head off dangerous climate change.

Such political developments, together with the world's continuing appetite for fossil fuels, have cast a pall over efforts to curb warming. Despite the dramatic growth of renewable energy sources such as wind and solar, global emissions of greenhouse gases will keep rising if current energy trends continue, the International Energy Agency (IEA) in Paris concluded last month. To make real progress, IEA Executive Director Fatih Birol said, "We will need to see great political will around the world." —*David Malakoff*

Published by AAAS

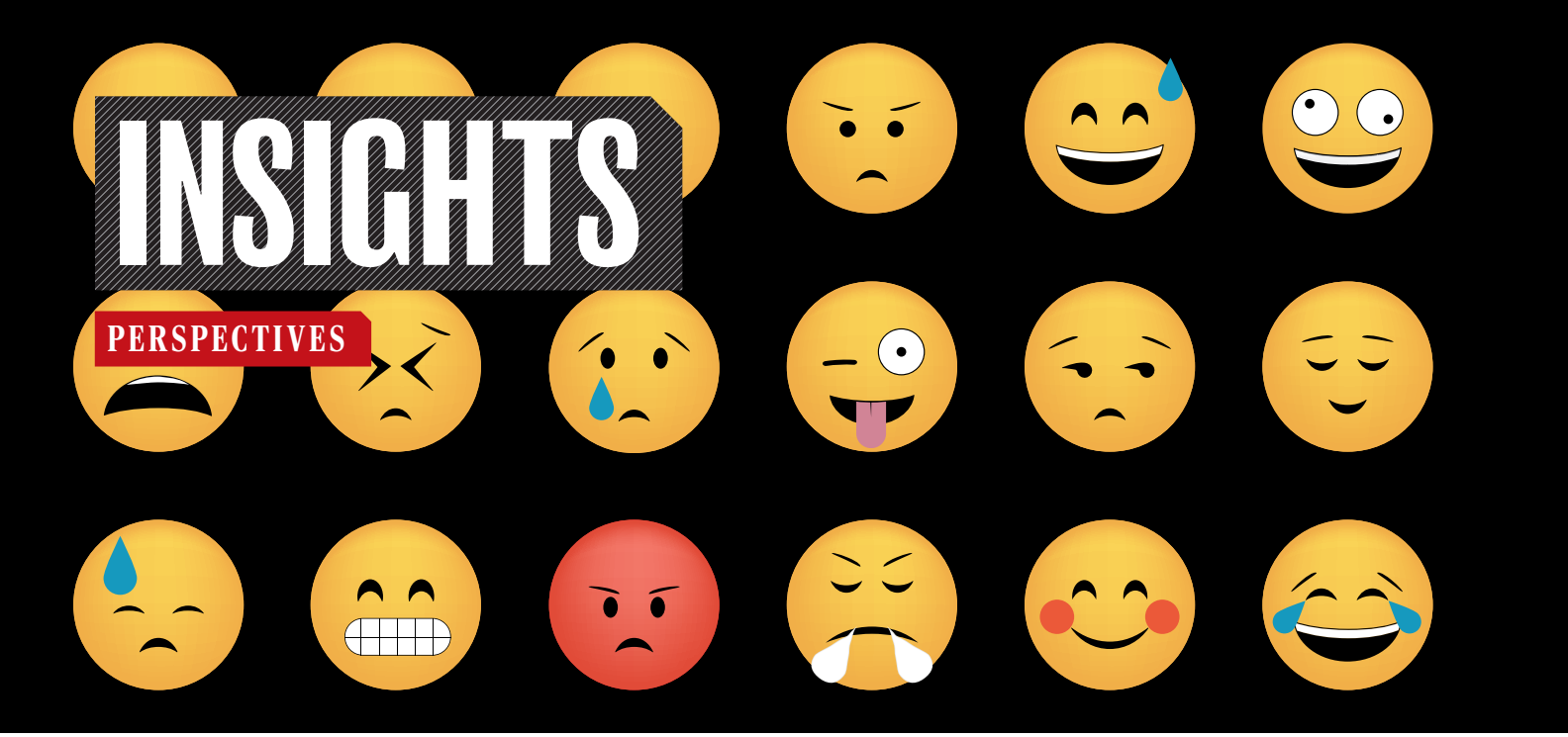

INSIGHTS

PERSPECTIVES

LINGUISTICS

Mapping words reveals emotional diversity

Semantic networks reveal cultural variability in emotion

By **Asifa Majid**

After seeing an elephant mother standing over her dead infant's body, prodding the baby as if to wake it up (*1*), it is hard not to believe that elephants grieve—just as we do. It seems some emotions are so elemental that they are evident even in nonhuman animals. At the same time, some cultures' emotional worlds may appear utterly alien to others (*2*). For example, in Papua New Guinea, Baining hosts feel *awumbuk* when guests leave after having stayed overnight. *Awumbuk*, which has been called a 3-day "social hangover" (*3*), leaves people listless, unable to wake in the morning or to complete mundane tasks. How do we reconcile these disparate observations? Does each culture have its own emotional universe, or is there a bedrock of similarity that unites us all? Centuries of debate have not resolved the issue, but on page 1517, Jackson *et al.* (*4*) present the most ambitious cross-cultural study to date of emotion concepts, mapping semantic networks for more than one-third of the world's languages to reveal substantial variability in how emotion concepts are expressed cross-culturally.

It is difficult to study the subjective, phenomenal aspects of emotions, but language can provide insight into how people conceptualize their inner worlds (*5*). Communicative need and cultural preoccupations lead people to assign words to specific concepts, so when unrelated languages exhibit recurrent patterns despite idiosyncratic differences between cultures, this is indicative of common conceptualizations. Using a database of more than 2000 unique concepts, including 24 emotion concepts, Jackson *et al.* examined the semantics of emotion across 2474 languages, from 20 language families, by establishing how emotion concepts are connected to one another. This builds on a venerable tradition in linguistics where the meaning of a word is determined not only on the basis of what it refers to, but also through the relations between words. Jackson *et al.* relied on data about "colexifications" where a single word is used to refer to multiple concepts. Persian, e.g, does not have distinct words for "grief" and "regret"; instead *ænduh* refers to both. In Dargwa (spoken in the Republic of Dagestan), the term *dard* is used for "grief" and "anxiety." Using network analyses on such colexifications in thousands of languages, Jackson *et al.* show that the semantic structure of emotion concepts varies markedly across language families. They find that the semantics of emotion vary far more than the semantics of color, a domain with known cross-linguistic variation (*6*). The variation is not unbounded, however. Jackson *et al.* find that all languages differentiate emotions primarily by valence and arousal. Moreover, the closer languages are geographically, the more similar their networks.

These findings raise the question of whether emotion semantics are similar among neighbors because of shared communicative or cultural needs. Other work suggests that people from Western individualistic cultures report their ideal affective state as involving high arousal (e.g., "happiness" = being upbeat), but people from Eastern collectivist cultures prefer low-arousal emotions (e.g., "happiness" = being solemn and reserved) (*7*). Such broad differences suggest similar cultural scripts among neighbors. Jackson *et al.* leave open the question of what drives similarities between neighboring languages. They may borrow nifty concepts from their neighbors (e.g., English has borrowed *Schadenfreude* from German) or may inherit a concept from a common ancestor (e.g., English *rue* and German *Reue* for "remorse" are both inherited from proto-Germanic **hrewwō*). Because languages that descended from a common ancestral language (like English and German) are found close together, Jackson *et al.* do not adjudicate between borrowing versus inheritance, but they pave the way for such explorations through phylogenetic methods and computational simulations of historical process (*8*).

Department of Psychology, University of York, York, UK.
Email: asifa.majid@york.ac.uk

ILLUSTRATION: ADAPTED FROM DENISGORELKIN/ISTOCK.COM

Published by AAAS

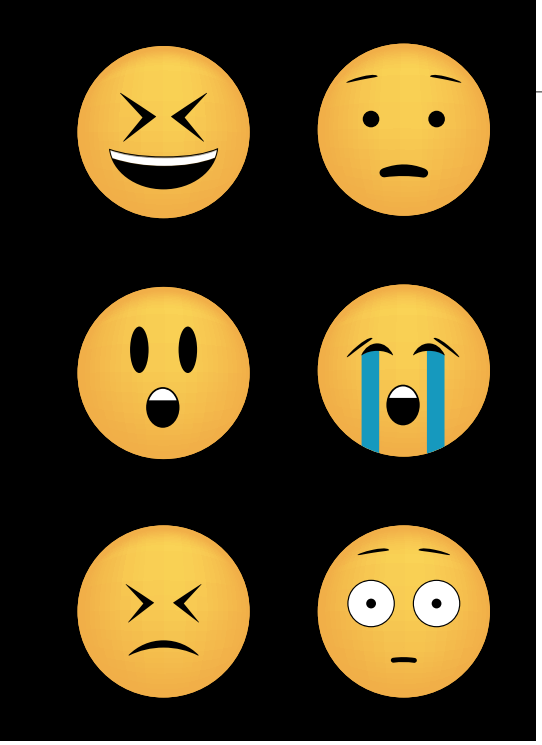

One of the exciting things about the Jackson *et al.* study is that it incorporates data from small languages, with speakers numbering in the thousands, as well as large languages with millions of speakers that are the usual target of cross-cultural study. But it is important to be aware of the limitations of their data. Perhaps the geographical similarities do not reflect shared emotion semantics so much as shared traditions of linguistic description. For example, most small languages are underdescribed, and much of what we know about them comes from lists of words they use. Because field linguists usually work on languages in a particular part of the world, they may use a lingua franca to elicit word lists from multiple languages. This can make such lists prone to areal traditions of nomenclature and analysis, and to the well-known limitations of translation (*9*), especially fraught with potential for semantic slippage and misunderstanding when translating ineffable emotion concepts. Hence, apparent similarity between neighboring languages may be influenced by the methodological and analytic choices of linguists. A challenge for the future is to establish word meanings not just through translation, but also through systematic elicitation methods (*10*).

In the approach taken by Jackson *et al.*, concepts are treated as Platonic ideals: There are things in the world (e.g., "grief" and "regret"), and words that simply refer to these preexisting concepts. Jackson *et al.* show differences in the connectivity between these concepts. But the basic assumption of universal concepts is problematic, because numerous studies find tremendous variation in the concepts themselves (*11*). For example, if a language has a single term that encompasses the continuous color spectrum of hues ranging from green to blue, it seems wrong to say that the language has two concepts "green" and "blue"; instead, it is more parsimonious to posit the unitary concept "grue." Similarly, if a language has a term encompassing "grief" and "regret," as in Persian *ænduh*, one might wonder whether there are really two distinct concepts in Persian rather than a single underlying meaning. This reflects a general debate in which some linguists favor analyses of meaning in terms of polysemy (multiple concepts) and others monosemy (unitary concept). If basic concepts differ as indicated by prior work (*12*), then comparing networks across languages becomes even trickier.

None of this undermines the diversity uncovered by Jackson *et al.* If anything, it suggests that there may be more variation to unpack. Whereas previous studies have focused on close comparison of one or two cultures and a limited selection of emotions, the unprecedented scale of Jackson *et al.*'s study reveals considerable cross-cultural variation. Their work clarifies how people conceptualize emotions through language, although not necessarily how people experience emotions. This leads back to the question of whether different ways of talking about emotions change how people experience emotions. Some evidence suggests that it does not (*12*, *13*); other studies show compelling evidence for such an influence (*14*, *15*). Jackson *et al.*'s important contribution can enable researchers to pinpoint where languages differ in their emotion semantics to guide future empirical inquiry, and then perhaps we will finally be able to answer this most fundamental of questions. ■

REFERENCES AND NOTES

1. I. Douglas-Hamilton, S. Bhalla, G. Wittemyer, F. Vollrath, *Appl. Anim. Behav. Sci.* **100**, 87 (2006).
2. T. Watt Smith, *The Book of Human Emotions: An Encyclopedia of Feeling from Anger to Wanderlust* (Profile, 2015).
3. J. Fajans, *Ethos* **11**, 166 (1983).
4. J. C. Jackson *et al.*, *Science* **366**, 1517 (2019).
5. S. C. Levinson, A. Majid, *Mind Lang.* **29**, 407 (2014).
6. T. Regier, P. Kay, *Trends Cogn. Sci.* **13**, 439 (2009).
7. N. Lim, *Integr. Med. Res.* **5**, 105 (2016).
8. S. C. Levinson, R. D. Gray, *Trends Cogn. Sci.* **16**, 167 (2012).
9. A. Wierzbicka, *Imprisoned in English: The Hazards of English as a Default Language* (Oxford Univ. Press, 2013).
10. A. Majid, in *The Oxford Handbook of Linguistic Fieldwork*, N. Thieberger, Ed. (Oxford Univ. Press, 2012), pp. 54–71.
11. B. C. Malt, A. Majid, *Wiley Interdiscip. Rev. Cogn. Sci.* **4**, 583 (2013).
12. D. A. Sauter, O. LeGuen, D. B. M. Haun, *Emotion* **11**, 1479 (2011).
13. A. Majid, N. Burenhult, M. C. Stensmyr, J. M. de Valk, B. S. Hansson, *Philos. Trans. R. Soc. B* **373**, 20170139 (2018).
14. I. Schweiger Gallo, J.-M. Fernández-Dols, P. M. Gollwitzer, A. Keil, *Front. Psychol.* **8**, (2017).
15. C. M. Doyle, K. A. Lindquist, *J. Exp. Psychol. Gen.* **147**, 62 (2018).

ACKNOWLEDGMENTS

Thanks to L. San Roque, K. Kendrick, and S. Vernes for comments. Supported by a Bank of Sweden Tercentenary Foundation Jubilee Initiative Grant (NHS14-1665:1).

10.1126/science.aba1763

IMMUNOLOGY

Mitochondrial DNA promotes autoimmunity

Stressed mitochondria leak DNA fragments that induce inflammation

By **Mary K. Crow**

The immune system provides essential protection from microbial infection but can damage tissue when its functions are excessive, sustained, or insufficiently regulated. In autoimmune disease, T lymphocytes and autoantibodies (antibodies directed to "self"-antigens) target the immune response to host tissue. But innate immunity, the first response to infection or cell stress, is also important in orchestrating pathologic immune responses in autoimmune diseases. The type I interferon (IFN) family of innate immune cytokines contributes to the aberrant immune functions of systemic lupus erythematosus (SLE) and several other autoimmune diseases (*1*). Self–nucleic acids induce type I IFN in SLE, but the mechanisms are not clear. On page 1531 of this issue, Kim *et al.* (*2*) show that pores formed by oligomerization of the mitochondrial voltage-dependent anion channel (VDAC) allow short mitochondrial DNA (mtDNA) fragments from stressed mitochondria to enter the cytosol, which may then induce type I IFN production.

In SLE, autoantibody-containing immune complexes promote tissue damage and variable symptoms that include rash, arthritis, kidney disease, and cardiovascular disease. White blood cells from SLE patients demonstrate a type I IFN "signature" characterized by increased expression of hundreds of IFN-regulated genes (*1*). Sustained activation of the IFN pathway supports differentiation of T follicular helper cells, development of autoantibody-producing plasma cells, and recruitment of inflammatory cells that produce tissue damage. Candidate cellular pathways that could induce type I IFN in SLE include the endosomal Toll-like receptors (TLRs),

Mary Kirkland Center for Lupus Research, Hospital for Special Surgery, New York, NY 10021, USA.
Email: crowm@hss.edu

Published by AAAS

particularly TLR7, which recognizes single-stranded RNA in lupus immune complexes (*3*), and cytosolic sensors of DNA or RNA that engage the adapter STING (stimulator of interferon genes) (*4*). RNA-containing immune complexes are found in sera from many patients with SLE and have a well-established role in TLR7-dependent production of type I IFN by plasmacytoid dendritic cells, robust producers of the type I IFN-α cytokine (*3*, *5*). The relevance of the cytosolic pathways and their nucleic acid triggers in SLE pathogenesis is less well established.

Conditions of oxidative stress that generate mitochondrial reactive oxygen species (mROS) can cause mtDNA damage and single-stranded breaks, which can lead to mtDNA degradation. The resulting fragments might be a stimulus for type I IFN production (*6*). In contrast to nuclear DNA, mtDNA includes CpG sequences that are less methylated, is packaged into DNA-protein complexes (nucleoids) rather than associated with histones, and may have less robust DNA repair mechanisms. Release of mtDNA might stimulate cytosolic DNA sensors, including cyclic guanosine monophospate (GMP)–adenosine monophosphate (AMP) synthase (cGAS), and activate the downstream kinase TANK-binding kinase 1 (TBK1) and the transcription factor interferon regulatory factor 3 (IRF3) after engaging STING, an inducer of type I IFN production. mtDNA that has been modified by ROS or other cell stressors is a particularly effective inducer of type I IFN (*7*). Thus, mtDNA could be an initiator of SLE by providing a trigger for innate immune system activation. If mtDNA leakage persisted over time, it could amplify established autoimmunity through effects of type I IFN on T and B lymphocytes and neutrophils, inducing clinically important disease flares.

The study by Kim *et al.* identifies a role for mitochondrial stress in inducing oligomerization of VDAC, a molecule in the outer mitochondrial membrane that controls entry and exit of metabolites. The authors demonstrate that interaction of amino-terminal amino acids of VDAC1, one of several VDAC proteins, with mtDNA initiates pore formation. Mitochondria with increased mROS release small fragments of mtDNA into the cytosol through the VDAC pore, triggering induction of type I IFN through a signaling pathway that involves STING (see the figure).

The authors find increased VDAC oligomerization in spleen cells from a mouse model of SLE and in white blood cells from several SLE patients. Administration of an inhibitor of VDAC oligomerization, VBIT-4, to SLE mice reduced accumulation of cytosolic mtDNA, decreased expression of type I IFN-regulated genes, and abrogated features of autoimmune disease, including autoantibody production. Although inhibitors of the VDAC pore might be effective in reducing stimulatory mtDNA, the importance of the VDAC pore for transport of essential metabolites could complicate use of VDAC inhibitors as therapeutics for SLE or other disorders (*8*).

An important aspect of the study of Kim *et al.* is that the model reflects the effect of moderate levels of mitochondrial stress that do not result in cell death. Although a macropore formed by the proteins BAX (Bcl-2 associated X) and BAK (Bcl-2 homologous antagonist/killer) mediates mtDNA release to the cytosol under more extreme conditions, leading to programmed cell death (apoptosis) (*9*), formation of VDAC oligomers may occur under conditions of milder stress, induced by environmental factors, including microbial infection, or host factors that prime mitochondria for sensitivity to endogenous stressors.

Beyond their essential role in energy metabolism, the capacity of mitochondria to interpret external signals through modification of mtDNA and the outer mitochondrial membrane is of considerable interest. The pathogenic bacterium *Streptococcus pyogenes* encodes a protein that promotes transport of mtDNA to the cytosol, triggering production of type I IFN as a mechanism to modulate the immune response (*10*). Of relevance to mechanisms of lupus nephritis, a clinical manifestation of SLE reflecting kidney damage, a genetic variant of apolipoprotein L1 (*APOL1*), which is associated with increased risk of end-stage renal disease in African Americans, encodes isoforms with the capacity to form oligomers that promote opening of mitochondrial pores and induction of type I IFN (*11*). Thus, the study of Kim *et al.* suggests that pores formed by VDAC oligomers could be relevant in additional situations of mitochondrial stress.

In SLE, genetic variability and encounters with environmental stressors may determine the relative contributions of endosomal TLR signaling and sensing of cytosolic DNA in individual patients. The demonstration by Kim *et al.* that transfer of mtDNA to the cytosol occurs under relatively benign conditions of mitochondrial stress suggests that induction of type I IFN through sensing of mtDNA could be applicable to many patients and different environmental triggers. In light of their data, investigating the contribution of mtDNA to innate immune responses in the pathogenesis of SLE and other diseases is warranted. ■

Release of mitochondrial DNA induces interferon production

Moderate amounts of environmental or endogenous stress promote mtDNA (nucleoids) to become fragmented. Interaction of these fragments with VDAC induces its oligomerization to form pores. mtDNA fragments enter the cytosol, where they activate the sensor cGAS and, in turn, STING-mediated induction of type I interferon and inflammation.

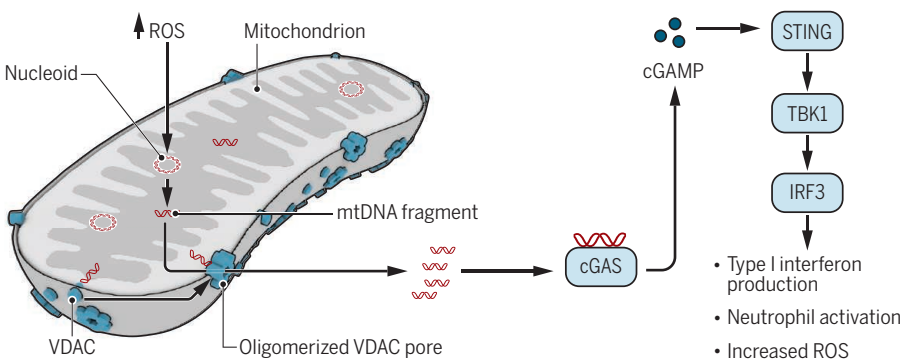

cGAMP, cyclic guanosine monophosphate–adenosine monophosphate; cGAS, cGAMP synthase; IRF3, interferon regulatory factor 3; mtDNA, mitochondrial DNA; ROS, reactive oxygen species; STING, stimulator of interferon genes; TBK1, TANK-binding kinase 1; VDAC, voltage-dependent anion channel.

REFERENCES AND NOTES

1. M. K. Crow *et al.*, *Annu. Rev. Pathol.* **14**, 369 (2019).
2. J. Kim *et al.*, *Science* **366**, 1531 (2019).
3. E. Savarese *et al.*, *Blood* **107**, 3229 (2006).
4. M. Motwani *et al.*, *Nat. Rev. Genet.* **20**, 657 (2019).
5. K. A. Kirou *et al.*, *Arthritis Rheum.* **52**, 1491 (2005).
6. A. P. West, G. S. Shadel, *Nat. Rev. Immunol.* **17**, 363 (2017).
7. N. Gehrke *et al.*, *Immunity* **39**, 482 (2013).
8. C. H. Lipper *et al.*, *Proc. Natl. Acad. Sci. U.S.A.* **116**, 19924 (2019).
9. L. Galluzzi, C. Vanpouille-Box, *Trends Cell Biol.* **28**, 343 (2018).
10. X. Hu *et al.*, *FEBS J.* **286**, 4754 (2019).
11. S. S. Shah *et al.*, *J. Am. Soc. Nephrol.* **30**, 2355 (2019).

10.1126/science.aaz9308

GRAPHIC: VERONICA FALCONIERI/*SCIENCE*

Published by AAAS

Producing adipic acid without the nitrous oxide

Synthesis of nylon monomer from butadiene avoids emission of a potent greenhouse gas

By **Thomas Schaub**[1,2]

Adipic acid is a monomer for nylon polymers such as polyamide 66. As of now, its production by the oxidation of a cyclohexanone–cyclohexanol mixture with nitric acid (*1*) (see the figure) on an annual scale of multimillions of metric tons also produces stoichiometric amounts of the potent greenhouse gas nitrous oxide (N_2O). The double carbonylation of butadiene to adipic acid or its esters could be a viable alternative that would avoid the use of nitric acid and emission of N_2O and would also have a more flexible raw-material base. Several systems for this reaction have been reported in the past decades, mainly from commercial labs, but none have been developed as an industrial process because of insufficient activity, selectivity, or both (*1*, *2*). On page 1514 of this issue, Yang *et al.* (*3*) now report a single-step system for the double carbonylation of butadiene with previously unmatched activity and selectivity.

The selective double carbonylation of butadiene to adipic acid or derivates is difficult because it requires two consecutive and nonselective carbonylations to achieve the desired product with pentenoic acids as intermediates. In most of the earlier reported approaches (*1*, *2*), the reaction was carried out in two steps. Carbonylation of butadiene to 3-pentenoic acid was followed by isomerizing carbonylation of 3-pentenoic acid to adipic acid with homogeneous cobalt, palladium, or rhodium catalysts. The conditions and catalysts for both steps had to be carefully selected because of the many potential unwanted side products, such as isomers or polymers (*3*). The separately optimized reactions were not mutually compatible and could not be developed into an efficient single-step reaction (*2*, *4*, *5*).

Alternative approaches for the double functionalization of butadiene to adipic acid have been developed recently. Mormul *et al.* reported a rhodium-catalyzed double hydroformylation in the presence of glycols to form acetal-protected adipic aldehyde as an intermediate (*6*). The intermediate could then be oxidized to adipic acid. The overall yield of adipic acid of 52%, based on butadiene after oxidation, is not high enough to be economically viable and requires further improvements, despite achieving the difunctionalization to linear intermediate in the hydroformylation step with ~73% yield. Tortajada *et al.* (*7*) recently reported the double carboxylation of butadiene to adipic acid with carbon dioxide (CO_2) using a nickel catalyst that proceeded through the unsaturated diacid as an intermediate, followed by hydrogenation with the same catalyst. This transformation is notable in that it uses CO_2 as a reagent and an earth-abundant metal. However, the yield of adipic acid was only 61%, and in the first step, stoichiometric addition of manganese as a co-reagent was necessary, which prevents the adoption of this system for bulk chemical production.

Given this history, it is notable that Yang *et al.* developed a single-step catalyst system for the double carbonylation of butadiene to adipic acid esters with high activity and selectivity. The chelating phosphine ligand for their palladium catalyst, combined with an acidic cocatalyst like *p*-toluenesulfonic acid, performed the double carbonylation of butadiene to adipic acid esters in one step at moderate conditions [40-bar carbon monoxide (CO) and 120°C]. The yields (up to 95%) and a selectivity for linear products of 97% for the butyl-ester of adipic acid are outstanding, given the high catalyst turnover of >60,000 in a single run. The ester can then be hydrolyzed to obtain adipic acid (*8*).

Despite these impressive results, some issues remain before this reaction can be developed into an industrial process. The elaborate seven-step synthesis of the ligand with an overall yield of <20% will be quite expensive. Its long-term stability under reaction conditions must be evaluated, so a search for simpler effective ligands is warranted. In most homogeneously catalyzed processes, recycling is easier for the precious metals than for ligands, which tend to decompose. High turnover was only achieved at lower yields (64%) and long reaction times (120 hours). Higher catalyst loadings and recycling would be needed in an industrial-scale process. ■

Routes to adipic acid

Industrial synthesis of this nylon monomer emits N_2O, a powerful greenhouse gas. Yang *et al.* report a route from butadiene that could be commercially viable.

Industrial gas synthesis of adipic acid from cyclohexanone and cyclohexanol

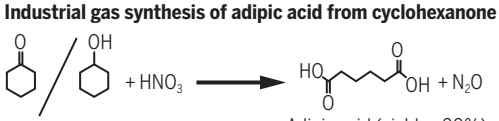

Adipic acid (yields >90%)

Earlier two-step approaches for butadiene carbonylation (*1*, *2*)

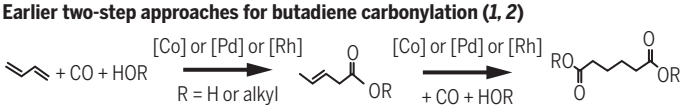

40 to 80% yield

Double hydroformylation of butadiene (*6*)

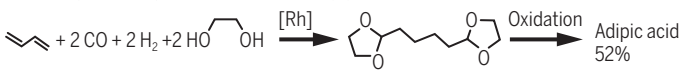

Adipic acid 52%

Double carboxylation of butadiene (*7*)

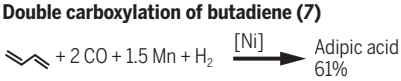

Adipic acid 61%

Single-step double carbonylation by Yang *et al.*

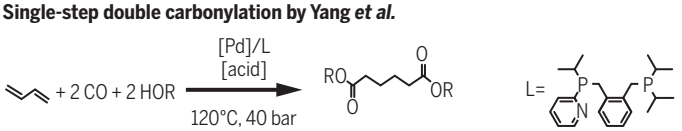

Up to 95% yield at 97% linear selectivity

GRAPHIC: V. ALTOUNIAN/*SCIENCE* FROM T. SCHAUB

[1]BASF SE, Organic Synthesis, Carl-Bosch-Str. 8, 67056 Ludwigshafen, Germany. [2]Catalysis Research Laboratory (CaRLa), Im Neuenheimer Feld 584, 69120 Heidelberg, Germany. Email: thomas.schaub@basf.com

REFERENCES AND NOTES

1. M. T. Musser, in *Ullmann's Encyclopedia of Industrial Chemistry* (Wiley, 2005).
2. W. Bertleff, M. Roeper, X. Sava, in *Ullmann's Encyclopedia of Industrial Chemistry* (Wiley, 2012).
3. J. Yang *et al.*, *Science* **366**, 1514 (2019).
4. E. Drent, W. W. Jager, Patent WO 2000056695 (2000).
5. K. von Nikolaus, Patent DE 2037782 (1970).
6. J. Mormul *et al.*, *ACS Catal.* **6**, 2802 (2016).
7. A. Tortajada, R. Ninokata, R. Martin, *J. Am. Chem. Soc.* **140**, 2050 (2018).
8. W. Gerbert, P. Magnussen, V. Schumacher, W. Praetorius, H. Reitz, U.S. Patent 4310686 (1982).

10.1126/science.aaz6459

Published by AAAS

NEUROIMMUNOLOGY

Bypassing the blood-brain barrier

The meninges membranes surrounding the brain are an immune-blood-brain interface in homeostasis and disease

By **Justin Rustenhoven** and **Jonathan Kipnis**

Brain function requires tight regulation of the cerebral microenvironment, an outcome achieved through specialized brain barriers. The presence of these barriers and the observation that skin grafts transplanted into the brain are poorly rejected (*1*) helped establish the dogma that the central nervous system (CNS) is immune privileged; that is, immune responses are not elicited against antigens originating from the CNS. However, recent studies have identified entry and exit points for immune cells, cytokines, and brain-derived antigens or waste molecules through distinct anatomical routes in the meninges (a triple-layered membrane that surrounds the brain parenchyma). These meningeal "backdoors" might allow for blood-brain barrier (BBB) bypass, providing an interface for peripheral immune system interaction with the CNS, and could play an important role in neuroinflammation and neurodegeneration.

The BBB, a highly selective semipermeable structure segregating peripheral blood from the brain, is characterized by tight junctions between endothelial cells that line the vessels and low expression of leukocyte adhesion molecules (*2*). Thus, although the brain contains resident macrophages (microglia), peripheral immune cells have limited access to the brain parenchyma. A series of classical studies revealed that if an animal is peripherally immunized with an allograft (from an unmatched donor) prior to allograft transplantation into the brain, rejection occurs rapidly (*1*). This suggested that T cells primed in the periphery can gain access to the brain. Thus, although adaptive immune responses in the brain are weak, T cells are not blind to brain-derived antigens.

More recently, the meninges have been recognized as a critical site where immune surveillance of the CNS takes place. The meninges are a triple-layer structure enveloping the brain. Within the two inner layers, called the pia and arachnoid mater (collectively, leptomeninges), flows cerebral spinal fluid (CSF). The outermost dura layer is formed by thick connective tissue, which, unlike the brain and leptomeninges, contains vasculature largely lacking tight junctions between endothelial cells (*3*), allowing extensive leukocyte surveillance (*4*). CSF is produced by specialized epithelial cells of the choroid plexus, fills the brain ventricles, and flows toward the subarachnoid space within the leptomeninges. From the subarachnoid space, CSF enters the Virchow-Robin spaces surrounding large penetrating arteries and flows across astrocyte (a type of stromal cell) projections into the brain parenchyma, where it mixes with the interstitial fluid (ISF). From there, the macromolecule-containing ISF-CSF returns, through perivenular spaces, into the CSF circulation. This "glymphatic" system allows CSF transit through the brain, collecting waste and brain-derived antigens (*5*). Additionally, it provides a route for meningeal immune cell–derived factors, including cytokines, to enter the brain, where they can modulate CNS function (*6*).

CSF volumes must be tightly regulated to avoid hydrocephalus and associated neurological sequelae. The prevailing concept was that CSF drains into dural sinuses, vascular structures carrying venous blood from the brain, through arachnoid granulations (observed only in large animals, including humans), prior to its absorption into the jugular vein. However, whether the dural sinuses drain CSF is unclear and, regardless, such drainage would not result in efficient presentation of CNS-derived antigens to the peripheral immune system. For appropriate immune surveillance and antigen presentation, lymphatic drainage to lymph nodes is required. The brain parenchyma, unlike almost all peripheral tissues, contains no lymphatic network to facilitate waste removal. For decades, it was believed that macromolecules and immune cells are drained along the olfactory nerves, across the cribriform plate, into the nasal mucosa, and thence into draining lymph nodes. If this were the case, however, then molecules inhaled through the nose (including pathogens) would be draining into the same lymph nodes as those receiving brain-derived antigens. Such a scenario is unlikely, especially given recent work demonstrating that lymph drainage from the gut is partitioned into separate lymph nodes, endowing each with a specific function (inflammatory responses or antigen tolerance) (*7*), highlighting the intricate precision of antigen sampling and immune responses within tissues. Why would immune surveillance of the brain, a master organ, be shared with airborne pathogens? It seems more likely that there would be a dedicated system, and indeed a functional CNS-draining lymphatic network housed within the meninges has been characterized (*3*).

Once the CSF exits the brain parenchyma, it is carried across the arachnoid mater into dural spaces, where it is drained through meningeal lymphatic vessels into the deep cervical lymph nodes (dCLNs) situated within the neck, allowing interactions between brain-derived antigens and peripheral T cells. This provides a system of fluid flow that can relay messages from the periphery to the parenchyma and conversely drain parenchymal antigens to the periphery.

Thus, a unified theory of CNS cytokine passage, antigen drainage, and immune surveillance, that is, meningeal bypass, can be envisioned. A cytokine traveling within the peripheral blood is unlikely to cross the BBB, owing to the presence of endothelial cell tight junctions. The cytokine may, however, cross the fenestrated dural vasculature, which lacks tight junctions. From there, the cytokine may traverse the arachnoid mater allowing CSF entrance and subsequently, through glymphatic influx, the brain parenchyma. Although the mechanisms underlying dural-to-CSF flow are unclear, manipulations of dural immune cell populations and specific cytokines alter cognitive functions, including learning and social behaviors, through signaling directly on cytokine receptors expressed on neurons (*6*, *8*). Additionally, CSF reaches the dura (*9*) and small-molecule dyes administered to the skull surface reach the meninges, and subsequently the brain parenchyma (*10*), collectively supporting dural-CSF-brain as a feasible route of cytokine sensing.

In addition to providing a route for molecules to reach the brain independent of the BBB, the meninges also allow the peripheral immune system to sample the brain in a distal site. An antigen that is produced in the CNS will be carried along with the perfusing CSF out of the brain into the subarachnoid space. From there, the antigen eventually drains into the meningeal lymphatic vessels (soluble drainage) or is taken up by meningeal antigen-presenting cells, including migratory dendritic cells present in the dura (*4*), before eventual passage to dCLNs (cellular drainage). Under homeostatic conditions, peripheral T cells, therefore, do not require access to the brain, because they can sample the entire parenchymal antigenic repertoire within the meningeal spaces. Owing to the permeable vasculature, T cells can easily access the dura to interact with local cells pre-

Center for Brain Immunology and Glia (BIG), Department of Neuroscience, University of Virginia, Charlottesville, VA 22908, USA. Email: kipnis@virginia.edu

Published by AAAS

senting CNS-derived antigens (*3*, *9*). Such a scenario would allow T cells to be retained on the basis of their antigenic specificity, or make an immediate exit through nearby dural lymphatics (see the figure).

Collectively, this highlights the dura as a feasible site of CNS immune surveillance and indeed extensive dural immune cell heterogeneity, including T cells, dendritic cells, macrophages, B cells, innate lymphoid cells type 2 (ILC2s), neutrophils, and monocytes, is present under steady-state conditions to sample brain-derived products and rapidly respond to CNS insults (*4*). This proposed meningeal bypass allows brain-specific antigens to be sampled by immune cells, and immune cells to travel within brain borders to modulate CNS function. Thus, does the BBB really bestow immune privilege to the brain? Clearly it limits homeostatic entrance of immune cells, yet this does not confer a lack of peripheral CNS antigen recognition or a contribution from immune cell–derived cytokines. Given the postmitotic nature of parenchymal neurons, the brain is particularly sensitive to inflammatory-mediated cell death. It is therefore conceivable that in the course of its evolution, the CNS "pushed" all of its immune activity to its borders, namely to the meninges, so that neuronal function should not be impeded by infiltrating immune cells. Evolution of the meninges did not alter the close relationship between the brain and the immune system; rather, instead of the two systems interacting and communicating directly, they do so through this distinctive meningeal interface, which could be viewed as an immune organ servicing the brain.

Several recent findings have highlighted how dysfunction in these meningeal influx and efflux systems can facilitate disease progression. Serving as a sink for brain-derived waste, CSF must be effectively drained to maintain cerebral clearance. During aging and Alzheimer's disease, clearance of brain waste, including neurotoxic soluble β-amyloid (Aβ) species, is impaired (*2*), as is the conduit for subsequent CSF drainage, the meningeal lymphatics (*11*). These impairments aggravate Alzheimer's disease pathology, leading to increased amyloid plaque buildup and exacerbation of cognitive dysfunction. Similarly, disruption of meningeal lymphatic drainage worsens Parkinson's disease–like pathology in a mouse model of mutant α-synuclein overexpression (*12*), a pathological protein found in Lewy bodies, which abnormally aggregate within neurons and precipitate cell death. It is plausible that meningeal lymphatic drainage is critical in additional neurodegenerative diseases displaying protein aggregation, including Huntington's disease and tauopathies.

Disrupting lymphatic drainage enhances the severity of certain neurodegenerative diseases but ameliorates neuroinflammatory conditions. Meningeal lymphatic ablation attenuates the severity of inflammation in experimental autoimmune encephalomyelitis (EAE), a mouse model of multiple sclerosis, by limiting T cell trafficking and antigen drainage to dCLNs (*9*). It is likely that similar antigen drainage contributes to additional autoimmune disorders, and perhaps dysfunctional drainage facilitates the aggressiveness of CNS tumors and underlies the lack of appropriate immune rejection.

Recent studies have also highlighted how meningeal entrance pathways facilitate neuroinflammatory responses. During EAE, meningeal T cells traffic across inflamed leptomeningeal vasculature, allowing CNS entrance independent of passage through the BBB (*13*). In aged mice, T cells accumulate within the neurogenic niche and through signaling of the cytokine interferon-γ (IFN-γ) impair adult neurogenesis (*14*). Although the precise entrance route(s) for T cells remains unclear, it is plausible that aging meningeal dysfunction, similar to that observed during inflammatory conditions, allows T cells to enter the CNS.

The identification of vascular channels directly connecting bone marrow of the skull with the surface of the brain has recently been described (*15*). Although their functional homeostatic relevance is unclear, during a stroke these channels allow direct neutrophil migration from skull bone marrow, through the meninges, and into the brain parenchyma, allowing CNS penetration independent of the BBB. Clearly, meningeal routes for brain-immune interactions exist beyond traditional concepts of BBB crossing, and understanding the meninges as an immune-blood-brain interface in homeostasis and disease could provide critical targets for disease-modifying therapeutic interventions. ■

The meninges are an immune-blood-brain interface

The dural meninges are a site for T cell surveillance, cytokine-to-neuron signaling, brain-derived antigen presentation, and drainage. During aging and neurodegenerative diseases, dysfunctional lymphatic vessels impair drainage, contributing to the accumulation of β-amyloid in Alzheimer's disease (AD) and α-synuclein in Parkinson's disease (PD). Immune cell trafficking may be dysregulated in experimental autoimmune encephalomyelitis (EAE) and after stroke.

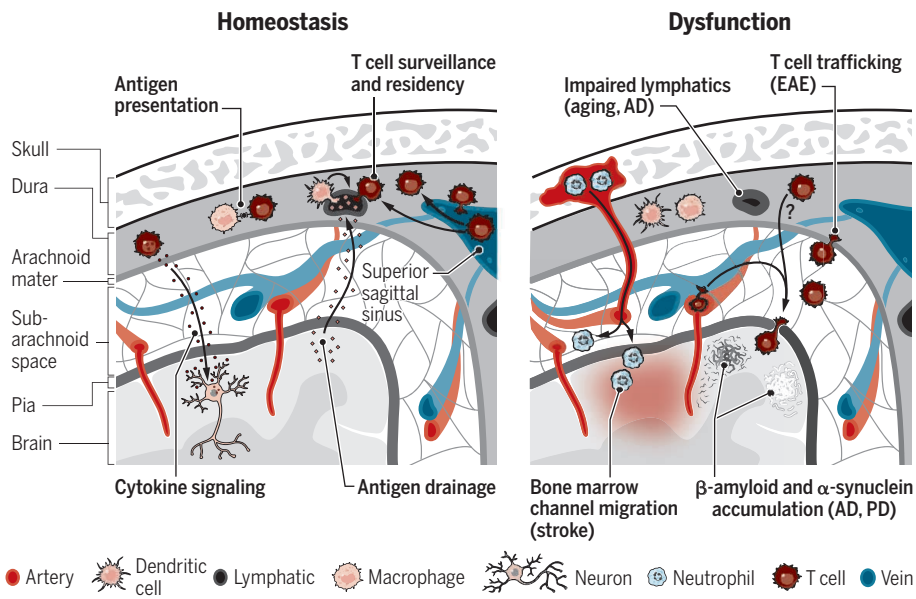

GRAPHIC: A. KITTERMAN/*SCIENCE*

REFERENCES AND NOTES

1. P. B. Medawar, *Br. J. Exp. Pathol.* **29**, 58 (1948).
2. M. D. Sweeney, K. Kisler, A. Montagne, A. W. Toga, B. V. Zlokovic, *Nat. Neurosci.* **21**, 1318 (2018).
3. A. Louveau *et al.*, *Nature* **523**, 337 (2015).
4. H. Van Hove *et al.*, *Nat. Neurosci.* **22**, 1021 (2019).
5. J. J. Iliff *et al.*, *Sci. Transl. Med.* **4**, 147ra111 (2012).
6. A. J. Filiano *et al.*, *Nature* **535**, 425 (2016).
7. D. Esterházy *et al.*, *Nature* **569**, 126 (2019).
8. N. C. Derecki *et al.*, *J. Exp. Med.* **207**, 1067 (2010).
9. A. Louveau *et al.*, *Nat. Neurosci.* **21**, 1380 (2018).
10. T. L. Roth *et al.*, *Nature* **505**, 223 (2014).
11. S. Da Mesquita *et al.*, *Nature* **560**, 185 (2018).
12. W. Zou *et al.*, *Transl. Neurodegener.* **8**, 7 (2019).
13. C. Schläger *et al.*, *Nature* **530**, 349 (2016).
14. B. W. Dulken *et al.*, *Nature* **571**, 205 (2019).
15. F. Herisson *et al.*, *Nat. Neurosci.* **21**, 1209 (2018).

ACKNOWLEDGMENTS

Thanks to S. Smith for help with editing. J.K. is supported by the National Institutes of Health (MH108156, AT010416, and AG034113,). J.K. is an adviser to PureTech Health/Ariya.

10.1126/science.aay0479

Published by AAAS

PHYSICS

Free at last: Bose metal uncaged

A metallic phase disrupts the classic two-state superconductor-insulator picture

By **Philip W. Phillips**[1,2]

Even the particle world is not immune to identity politics. Bosons have been in a bit of an identity crisis, or so it has seemed since 1989 (*1*). Quantum mechanics requires bosons made of two paired electrons to either condense into a superfluid with a well-defined phase with zero electrical resistance or localize in an insulating state with infinite resistance. The direct transition from superconducting to insulating states was widely observed in a range of thin films (*2*–*4*). The most popular model for explaining these observations (*5*) claims that the destruction of superconductivity occurs when the resistance of the thin film exceeds a critical value. For bosons on the brink of localization, electrically insulating behavior is observed if the resistance is greater than the quantum of resistance, $R_q = h/4e^2$, otherwise superconductivity persists, where h is Planck's constant and e is the electric charge. On page 1505 of this issue, Yang *et al.* (*6*) offer a counterexample by establishing that a bosonic metallic phase disrupts the superconductor-insulator transition (SIT) in the high-temperature superconductor $YBa_2Cu_3O_{7-x}$ (YBCO).

Indeed, bosons have been toying with metallicity since 1989 (*2*). However, the older data were dismissed by other researchers as being due to a refrigeration problem. The explanation for the observations was that the bosons were not cooling, instead remaining in suspended animation and conducting. Nonetheless, the metallic states were observed at a frequency that kept hope alive for a true 0 K disruption of the SIT. In the magnetic field–tuned transition in molybdenum germanide (MoGe) (*4*), the resistance flattened at an onset temperature that decreased with increasing field. If the metallicity was due to a heating effect, then the failure to cool the sample would occur at the same temperature, not a temperature determined by the magnetic field (*4*). Similar observations were made on tantalum (*7*) and in single crystals of ion-gated zirconium nitride chloride (ZrNCl) (*8*).

A direct attack on the refrigeration problem came from the experiments that showed that the metallic states in amorphous indium oxides (InO_x) (*3*) and crystalline 2H-phase niobium diselenide (2H-$NbSe_2$) (*9*) were artifacts (*10*) because they vanished by eliminating all sources of electromagnetic radiation. Yang *et al.* used this now-standard electromagnetic radiation–filtering scheme to avoid artifacts and directly address what is carrying the current in the metallic phase.

The experiment utilized a series of high-temperature superconducting YBCO films, which were tuned through the SIT by reactive ion etching. This technique transfers a patterned array of hexagonally plated holes to YBCO. Yang *et al.* observed that the normal-state thin-film resistance increases with increasing etching time. The etching time controls the thickness of the resulting pores' sidewalls, straining the YBCO shell and creating structural defects. The defects increase the resistance of the thin-film sheet. The transition the authors observed is an example of disorder-tuned SIT and similar to the 1989 experiments (*2*).

Yang *et al.* observed three phases with a critical value for the resistance roughly twice the quantum of resistance, R_q (*5*). The metallic phase persisted down to a temperature of 50 mK. To characterize this phase, the authors confirmed previous reports (*11*) of a vanishing Hall resistance. This type of response of the resistance to a magnetic field is an indication of emergent particle-hole symmetry. The ingenuity in the authors' experiments is their measurement of the resistance oscillations as a function of magnetic field. In a typical metal in which electrons are the charge carriers, the oscillations have a period of h/e. Instead, the authors found an $h/2e$ periodicity. This behavior indicates that the charge carriers are two electrons. This experiment thereby proves definitively that bosons are free to roam in a metallic phase, invalidating the standard picture of the two-phase model (*5*).

Hence, the teasing is over. Bosons can exist as a metal. Furthermore, Yang *et al.* observed that the amplitude of the conductance oscillations grows in the superconducting state, remains constant in the metal, and decreases in the insulator. This

A Bose metal

Bosons made of two paired electrons were thought to either condense into a superconducting phase (phase 1, red region) or be electrically insulating (phase 3). New observations show that the paired electrons can behave like a regular metal (phase 2, blue region), located in between the two traditional phases.

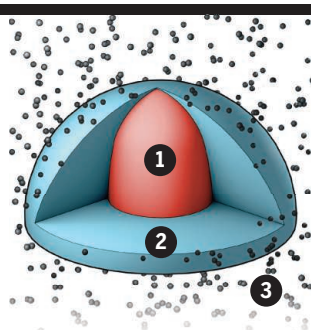

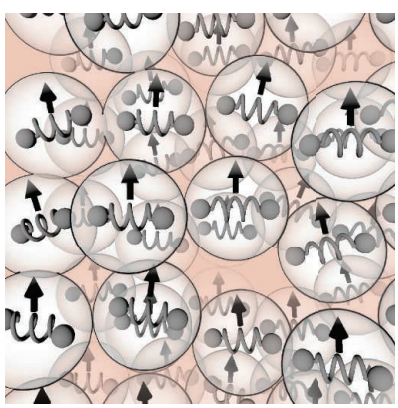

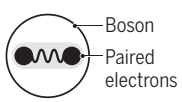

1 Paired electrons are "coherent" (black arrows aligned), and the bosons therefore have the characteristic zero electrical resistance that defines a superconductor.

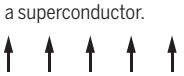

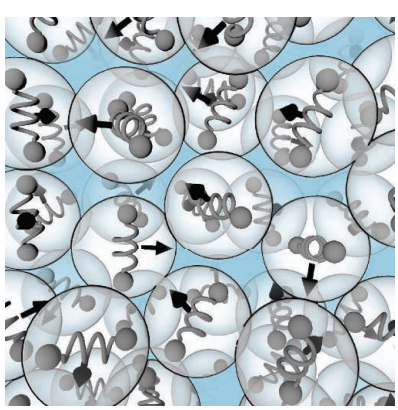

2 At different conditions, the bosons are not "coherent" (black arrows not aligned). This disorder destroys the superconductivity but allows the bosons to move through the material like electrons in a metal.

GRAPHIC: V. ALTOUNIAN/*SCIENCE*

[1]Department of Physics, University of Illinois, 1110 W. Green Street, Urbana, IL 61801, USA. [2]Institute for Condensed Matter Theory, University of Illinois, 1110 W. Green Street, Urbana, IL 61801, USA. Email: dimer@illinois.edu

Published by AAAS

trend is consistent with a divergent phase-coherent length in the superconductor, a finite size in the Bose metal (see the figure), and no phase coherence in the insulator.

The logically correct starting point for understanding the origin of the Bose metal is an array of superconducting islands connected by random tunneling matrix elements. Although adding an underlying normal fermionic metallic matrix to this model can achieve the metallic state (*12*), this is not consistent with the experiments because the charge carriers have charge $2e$ and not e. Because of the disorder, glassy bosonic models are a natural choice. Indeed, state-of-the-art numerical simulations have shown that randomness in superconducting-island models in two dimensions produces a glassy phase with a superfluid stiffness (*13*) that scales with the system size (L) as $L^{-0.39}$ (or $L^{0.27}$ in three dimensions) and hence vanishes in the thermodynamics limit. These glassy models (see the figure) have a nonzero bosonic conductivity (*1*, *14*) with emergent particle-hole symmetry and therefore contain the requisite ingredients needed to explain the disorder-induced Bose metallic state Yang *et al.* report in their experiments.

Experiments similar to those that Yang *et al.* performed should be carried out on the magnetic field–tuned transition to discern if the charge carriers are also $2e$. If the charge carriers are proven to be $2e$, then the Bose metal represents the general exception to the standard paradigm (*5*). In addition, time-resolved measurements could reveal the low-energy excitations of this Bose metal that forms without the fermionic organizing principle of Pauli exclusion. ■

REFERENCES AND NOTES

1. P. Phillips, D. Dalidovich, *Science* **302**, 243 (2003).
2. H. M. Jaeger, D. B. Haviland, B. G. Orr, A. M. Goldman, *Phys. Rev. B Condens. Matter* **40**, 182 (1989).
3. M. A. Paalanen, A. F. Hebard, R. R. Ruel, *Phys. Rev. Lett.* **69**, 1604 (1992).
4. N. Mason, A. Kapitulnik, *Phys. Rev. Lett.* **82**, 5341 (1999).
5. M. P. A. Fisher, *Phys. Rev. Lett.* **65**, 923 (1990).
6. C. Yang *et al.*, *Science* **366**, 1505 (2019).
7. Y. Qin, C. L. Vicente, J. Yoon, *Phys. Rev. B Condens. Matter Mater. Phys.* **73**, 100505 (2006).
8. Y. Saito, Y. Kasahara, J. Ye, Y. Iwasa, T. Nojima, *Science* **350**, 409 (2015).
9. A. W. Tsen *et al.*, *Nat. Phys.* **12**, 208 (2015).
10. I. Tamir *et al.*, arXiv:1804.04648 [cond-mat.supr-con] (12 April 2018).
11. N. P. Breznay, A. Kapitulnik, *Sci. Adv.* **3**, e1700612 (2017).
12. A. Kapitulnik, S. A. Kivelson, B. Spivak, *Rev. Mod. Phys.* **91**, 011002 (2019).
13. H. G. Katzgraber, A. P. Young, *Phys. Rev. B Condens. Matter Mater. Phys.* **66**, 224507 (2002).
14. J. May-Mann, P. W. Phillips, *Phys. Rev. B* **97**, 024508 (2018).

ACKNOWLEDGMENTS

Funding from NSF DMR19-19143 is acknowledged.

10.1126/science.aaz9902

CATALYSIS

Piezoelectricity drives organic synthesis

Ball milling allows for solvent-free mechanoredox catalysis

By **Hesheng Xia**[1] *and* **Zhenhua Wang**[2]

The coupling of mechanical and chemical phenomena on a molecular scale, mechanochemistry, is undergoing an exciting period of rediscovery and renaissance (*1*). Mechanochemistry research can provide deep insight into the rupture mechanism of chemical bonds (*2*). Mechanochemical routes for chemical synthesis can minimize the use of hazardous or undesirable solvents. They also can generate materials along reaction pathways that are inaccessible through thermal or light-activated processes. On page 1500 of this issue, Kubota *et al.* demonstrate that piezoelectric materials can be used as mechanoredox catalysts for organic synthesis (*3*).

Mechanochemical routes include force-induced degradation, activation, catalysis, and initiation. Harsh conditions are needed to cleave the covalent bonds of organic molecules or polymers. These types of extreme conditions are produced by high-energy ball or pan milling, or by ultrasound or hydrodynamic cavitation. These methods can create high shear forces for a mechanochemical reaction but cannot easily be adapted to large-scale synthesis. In the past decade, mechanochemical processes moved toward more mild and tempered methods such as twin-screw extrusion, stirring, compression, and stretching (*4*–*6*). Although these milder techniques are simple to understand, big challenges remain in making them work effectively, as they often depend on new concepts (e.g., weakly bonded mechanophores) or new materials (e.g., metal-organic complexes).

Piezoelectric materials generate charge in response to stress and can convert mechanical energy into chemical transformations with high efficiency. Hence, they may provide an alternative means for mild mechanochemistry. Piezoelectric materials combined with low-power ultrasound have been used to trigger the formation of active species for dye degradation (*7*, *8*) and controlled polymerization (*9*, *10*). Kubota *et al.* used ball milling with the piezoelectric material barium titanate to trigger a single-electron transfer redox reaction. The authors successfully performed mechanoredox activation of various aryl diazonium salts in response to applied mechanical energy for arylation and borylation reactions. The redox reaction was triggered by the mechanical force applied to a mixture of aryl diazonium salt, furan, and barium titanate. During ball milling, the barium titanate particles deform and are transformed into a charge-separated state. This acts as an oxidant and reductant simultaneously. The aryl diazonium salts are reduced into radicals through the single electron transfer reaction for further radical addition synthesis. The charge-separated barium titanate particles efficiently quench the radical addition intermediate (see the figure).

> **"Unlike photoredox arylation and borylation reactions, mechanoredox catalysis reached high yields in much shorter times."**

Only piezoelectric particles such as barium titanate produced good reaction yields, whereas nonpiezoelectric particles produced much lower yields or even no reaction. The authors investigated the effect of substrates comprising electron-deficient, neutral, and electron-rich substituents and found that the former two kinds of substituents gave rise to good yields. The robustness of the approach was further validated by the successful recycling of barium titanate. Unlike photoredox arylation and borylation reactions, mechanoredox catalysis reached high yields in much shorter times. Mechanoredox catalysis also can synthesize polycyclic aromatic hydrocarbons from poorly soluble substrates, as evidenced by the 78% yield for carbon-hydrogen arylation of coronene.

[1]State Key Laboratory of Polymer Materials Engineering, Polymer Research Institute, Sichuan University, Chengdu 610065, China. [2]Institute of Flexible Electronics, Institute of Biomedical Materials and Engineering, Northwestern Polytechnical University, Xi'an 710072, China.
Email: xiahs@scu.edu.cn

Published by AAAS

By contrast, no reaction happens with photoredox catalysis because of the insolubility of coronene. The mechanoredox approach is so effective that a low-tech method—hitting the bag containing reactants more than 200 times with a hammer—produced a 43% yield.

The strategy of using ball milling to drive mechanoredox reactions has several benefits. Reactants and catalysts can be in solid form, avoiding harmful solvents. The ball-milling process is well known and widespread in industry. The piezoelectric catalysts are mature materials with good recyclability and therefore relatively low cost. In contrast, catalysts for photoredox reactions are generally expensive and difficult to recycle because they are often molecularly soluble or uniformly dispersed in media to achieve quantitative excitation. Finally, the wide variety of different piezoelectric materials allows for redox potential adjustment to meet more redox reaction requirements. This should increase the number and types of catalytic reactions to which this method can be applied.

Mechanochemistry has been widely applied in a number of different areas. These include nanoparticle preparation, synthesis of organics and polymers, processing of polymers, recycling of plastics or rubber, electrochemical energy storage, water treatment, drug cocrystal synthesis, metal-organic frameworks, organic semiconductors, graphene exfoliation, cutting of carbon nanotubes, tuning of dynamic covalent chemistry, and self-healing (*6*, *11*–*13*). The authors have successfully opened a new mechanochemical route for robust and sustainable synthesis applicable to a wide range of organic redox reactions. This strategy could be extended into areas such as polymerization, grafting reactions, degradation, recycling, and other radicals-related chemistry. These types of applications will drive efforts to develop more high-efficiency piezoelectric materials to produce a broad array of radical intermediates.

Combining mechanoredox catalysis with transition metal catalysis might allow for controlling the conformation of complex molecules. The mild, scalable, and sustainable mechanosynthesis using ball milling with a piezoelectric material should be an inspiration for rethinking more traditional solution-based catalytic strategies. ■

An example of mechanoredox organic synthesis

Grinding piezoelectric barium titanate ($BaTiO_3$), aryl diazonium salt, and furan with a ball mill allows organic synthesis of aryl furan compounds. The force-induced deformed $BaTiO_3$ particles can act as reductants to produce radicals for further organic reaction, and also as oxidants to quench the radical addition intermediate by single-electron transfer (SET) redox reaction.

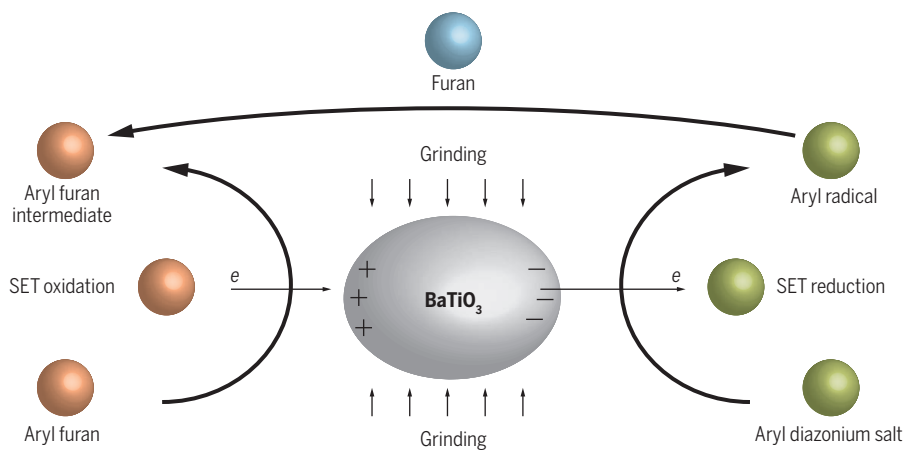

REFERENCES AND NOTES

1. J. L. Do, T. Friščić, *ACS Cent. Sci.* **3**, 13 (2016).
2. S. Akbulatov *et al.*, *Science* **357**, 299 (2017).
3. K. Kubota, Y. Pang, A. Miura, H. Ito, *Science* **366**, 1500 (2019).
4. D. E. Crawford, C. K. G. Miskimmin, A. B. Albadarin, G. Walker, S. L. James, *Green Chem.* **19**, 1507 (2017).
5. H. Yan *et al.*, *Nature* **554**, 505 (2018).
6. N. Willis-Fox, E. Rognin, T. A. Aljohani, R. Daly, *Chem* **4**, 2499 (2018).
7. K.-S. Hong, H. Xu, H. Konishi, X. Li, *J. Phys. Chem. Lett.* **1**, 997 (2010).
8. H. L. You *et al.*, *Electrochem. Commun.* **79**, 55 (2017).
9. H. Mohapatra, M. Kleiman, A. P. Esser-Kahn, *Nat. Chem.* **9**, 135 (2017).
10. Z. Wang *et al.*, *ACS Macro Lett.* **6**, 546 (2017).
11. Z. Chen *et al.*, *Science* **357**, 475 (2017).
12. M. J. Muñoz-Batista, D. Rodriguez-Padron, A. R. Puente-Santiago, R. Luque, *ACS Sustain. Chem. Eng.* **6**, 9530 (2018).
13. A. P. Amrute, Z. Łodziana, H. Schreyer, C. Weidenthaler, F. Schüth, *Science* **366**, 485 (2019).

ACKNOWLEDGMENTS

Supported by National Natural Science Foundation of China grant 51973137.

10.1126/science.aaz9758

CANCER

Targeted drugs ramp up cancer mutability

Drug-induced mutagenesis may accelerate cancer evolution and resistance

By **Marco Gerlinger**

Mutagenesis can drive carcinogenesis and continue during cancer progression, generating genetic intratumor heterogeneity that enables cancer adaptation through Darwinian evolution (*1*). Analyses, such as mutational signature characterization, have revealed specific mutational processes and their temporal activity during carcinogenesis and tumor progression (*2*). Nevertheless, many of the mechanisms that promote genomic instability in cancer are still enigmatic. On page 1473 of this issue, Russo *et al.* (*3*) reveal that drugs targeting oncogenic epidermal growth factor receptor (EGFR) or BRAF signaling increase mutagenesis in colorectal cancer (CRC) cells, which could drive the acquisition of resistance.

Russo *et al.* found that human CRC cell lines that were treated with EGFR or BRAF inhibitors down-regulated the expression of high-fidelity DNA repair proteins and increased that of error-prone DNA repair proteins, which may both increase mutation rates. Using reporter assays, they further showed that the fidelity of DNA mismatch repair (MMR) and homologous recombination (HR) repair systems were impaired and that DNA damage increased during drug treatment. Genetic analysis of cell lines that had been exposed to these inhibitors revealed subclonal mutations in dinucleotide repeats, which are characteristic of defective MMR. In contrast to other cancer mutational processes—such as genetically encoded HR or MMR defects that lead to persistent mutation acquisition or overexpression of the APOBEC (apolipoprotein B mRNA editing enzyme, catalytic polypeptide-like) DNA cytidine deaminases, which generates mutational bursts (*4*)—the mutagenesis program identified by Russo *et al.* was tightly coupled to drug ex-

Translational Oncogenomics Laboratory, The Institute of Cancer Research, 237 Fulham Road, London SW3 6JB, UK. Email: marco.gerlinger@icr.ac.uk

GRAPHIC: N. DESAI/*SCIENCE*

Published by AAAS

posure and ceased after drug removal. This study demonstrates that nongenotoxic targeted oncogene pathway inhibitors can promote a temporally restricted increase in mutability by switching from high-fidelity to error-prone DNA repair.

Adaptive mutagenesis is a mechanism described in bacteria that increases the mutation rate in response to cell stress (*5*). This is triggered by a cell-stress signaling pathway that activates error-prone DNA double-strand break repair and it is accompanied by suppression of MMR. Adaptive mutagenesis increases the probability of generating mutations that enable evolutionary adaptation of unicellular organisms to new environments. On the basis of the pronounced similarities of drug-induced mutagenesis in CRC and adaptive mutagenesis in bacteria, Russo *et al.* explored whether the mammalian target of rapamycin (mTOR) pathway, a major stress signaling pathway in humans, controls drug-induced mutagenesis in cancer cells. mTOR signaling was indeed inactivated by drug treatment, but inhibiting the mTOR pathway alone did not phenocopy the changes in DNA repair protein expression. The trigger of drug-induced mutagenesis in CRC cells is therefore either more complex or different from that in bacteria.

Russo *et al.* speculate that it may nevertheless be the same ancestral stress-induced mutagenesis program found in unicellular organisms that becomes unleashed in cancer. Whether this program could have survived millions of years of evolution from unicellular to multicellular species is unclear. Stress-induced mutagenesis is risky in multicellular organisms because it may trigger cancer in healthy cells, thereby threatening the survival of the individual. Somatic mutagenesis is clearly relevant in humans, for example, in B lymphocytes, in which it contributes to antibody diversity generation. However, this somatic hypermutation program is tightly restricted to immunoglobulin genes, whereas inactivation of high-fidelity DNA repair confers a genome-wide mutator process that can alter oncogenes and tumor suppressor genes. An alternative hypothesis is that the observed changes in DNA repair protein expression in response to signaling pathway inhibition fulfill a physiological function in healthy cells but aggravate mutation generation in cancer cells that have deregulated proliferation and apoptosis. Drug-induced mutagenesis may be a by-product that coincidentally opens opportunities for cancer cells under selective pressure, rather than having specifically evolved as a program that enables cellular adaptation to stress.

The results of Russo *et al.* are important because resistance invariably occurs in CRCs after patients are treated for a few months with EGFR or BRAF inhibitors. These tumors usually contain billions of cancer cells, and the probability that a drug-resistant subclone preexists in a population of this size is high (*6*). By contrast, the acquisition of a resistance mutation in the much smaller number of cells that persist during drug treatment has been considered to be comparably low. Drug-induced mutagenesis may shift this balance, providing a compelling argument that resistance can frequently be acquired during treatment (see the figure).

The contribution of drug-induced mutagenesis to clinically acquired resistance in patients with CRC and other cancer types is now important to assess because this remains unclear for several reasons. Mutational processes differ in the preferred DNA sequence contexts in which they occur and in the genetic variants they generate (*2*). MMR deficiency leads to high rates of deletions in nucleotide repeats and to cytosine-to-thymine base changes. Mutations conferring resistance to EGFR and BRAF inhibitors in CRC are confined to a small number of hotspots in *KRAS*, *NRAS*, *BRAF*, mitogen-activated protein kinase kinase 1 (*MEK1*), or *EGFR* genes (*7*, *8*). Whether these specific mutations can be generated by the drug-induced mutagenesis process is unknown. Moreover, there are additional paths to acquired EGFR and BRAF inhibitor resistance beyond mutations, including gene amplifications and an increase of cancer-associated fibroblasts in the tumor microenvironment that rescue cancer cells by secreting mitogenic growth factors (*9*). Resistance is complicated by the observation that several of these resistance mechanisms can occur in parallel in the same tumor (see the figure). Inhibiting drug-induced mutagenesis to delay resistance evolution will only have clinical impact if this process is the dominant route to resistance in some CRCs.

The DNA repair deficiencies that underlie drug-induced mutagenesis may confer therapeutic vulnerabilities whereby inhibiting another protein or pathway may cause cell death (synthetic lethality). Poly(ADP-ribose) polymerase (PARP) inhibitors are selectively lethal to cancer cells with HR defects due to mutations in the breast cancer 1 (*BRCA1*) and *BRCA2* genes (*10*). Similarly, the Werner syndrome adenosine triphosphate (ATP)–dependent helicase (WRN) has recently been described as a synthetically lethal target in MMR deficient cancers (*11*). Whether drug-induced down-regulation of HR or MMR proteins sensitizes CRC cells to PARP or WRN inhibition is unknown but could be readily tested in the cell line models described by Russo *et al.* Synergies between EGFR inhibition and oxaliplatin chemotherapy have been described (*12*). Oxaliplatin causes DNA double-strand breaks, which may be difficult to repair when HR is repressed by EGFR inhibition. Some drug combinations in routine clinical use may therefore already exploit the described mechanisms for therapeutic benefit. ■

Models of acquired drug resistance

Models of resistance mechanisms to epidermal growth factor receptor (EGFR) inhibitors in colorectal cancer include preexisting resistance, drug-induced mutagenesis, and microenvironment-mediated resistance. Each reveals distinct therapeutic opportunities, but multiple mechanisms may occur within a tumor.

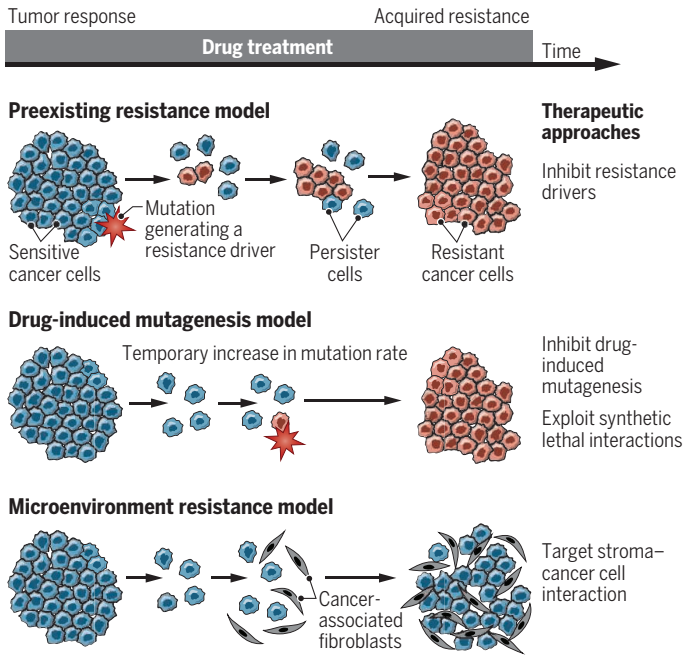

GRAPHIC: KELLIE HOLOSKI/*SCIENCE*

REFERENCES AND NOTES

1. M. Gerlinger *et al.*, *Annu. Rev. Genet.* **48**, 215 (2014).
2. L. B. Alexandrov *et al.*, *Nature* **500**, 415 (2013).
3. M. Russo *et al.*, *Science* **366**, 1473 (2019).
4. M. Petljak *et al.*, *Cell* **176**, 1282 (2019).
5. D. M. Fitzgerald, P. J. Hastings, S. M. Rosenberg, *Annu. Rev. Cancer Biol.* **1**, 119 (2017).
6. L. A. Diaz Jr. *et al.*, *Nature* **486**, 537 (2012).
7. C. Bettegowda *et al.*, *Sci. Transl. Med.* **6**, 224ra24 (2014).
8. L. G. Ahronian *et al.*, *Cancer Discov.* **5**, 358 (2015).
9. A. Woolston *et al.*, *Cancer Cell* **36**, 35 (2019).
10. C. J. Lord, A. Ashworth, *Science* **355**, 1152 (2017).
11. E. M. Chan *et al.*, *Nature* **568**, 551 (2019).
12. D. Balin-Gauthier *et al.*, *Cancer Chemother. Pharmacol.* **57**, 709 (2006).

10.1126/science.aaz9900

Published by AAAS

ORGANIC CHEMISTRY

Peptidic catalysts for macrocycle synthesis

A heptapeptide pulls aldehyde groups of a molecule together for elusive ring-closing reactions

By **Aarón Gutiérrez Collar** and **Tanja Gulder**

Many structurally simplified catalysts have been synthesized that mimic the reactivity and efficiency of enzymes. In this context, the numerous transformations catalyzed by the amino acid proline as a catalytic-site mimic helped drive the field of organocatalysis (*1*). Enzyme activity not only relies on the reactive site but also on the structure of the binding pocket that can orient and twist substrates for reactions. Oligopeptide catalysts, often referred to as foldamers (*2*), can emulate both the reactivity and substrate positioning and folding of enzymes by using the secondary peptide structure such as α-helices or β-turns. On page 1528 of this issue, Girvin *et al.* (*3*) translate enzymatic synthesis of large rings (macrocycles) into a heptapeptide foldamer catalyst that performs an intramolecular aldol condensation (see the figure).

Oligopeptides are short sequences of amino acids that can be designed to self-assemble in a stable secondary structure so that particular side chains can be positioned to become the reactive catalyst sites. The power of this foldamer-template principle has been demonstrated in ample studies from the Miller group, such as the use of chiral peptide catalysts in the site-selective structural modification of the complex natural product erythromycin A by Lewis and Miller (*4*) or by Müller *et al.* for retro aldol reactions of β-hydroxyketones (*5*). Foldamer design can also take advantage of amino acids that bear unnatural side chains to introduce reactive groups beyond those in the enzymatic repertoire and thus extend the scope of addressable transformations compared with those offered by nature.

The synthesis of macrocycles is an example of a very challenging reaction for chemists (*6*) because it is usually disfavored entropically. Although the enzymatic reaction only takes place in a specific region of the enzyme, the entire protein plays an important role. The complex conformation of enzymes forces the linear starting material (such as molecule **2** in the figure) into a certain conformation inside the enzyme-substrate complex. This step mitigates the energetic demand of the intramolecular reaction and favors cyclization over intermolecular processes. However, the structural complexity of proteins that enables this functionality and selectivity also makes enzymes substrate-specific and hampers their broad applicability as ring-closure catalysts.

Girvin *et al.* designed the heptapeptide **1** macrocyclization catalyst to hold the two amine functionalities in place for an intramolecular aldol condensation reaction (see the figure). The foldamer is composed of α and β amino acid residues in an αββ sequence that forms a stable three-dimensional backbone to put the reactive amine moieties in a concise orientation relative to one another. The authors examined the impact of the geometry and the spatial separation of the reactive diad on the transformation and found that the optimal geometry is a helix, with three amino acids per turn and with the catalytically active functionalities separated exactly by one turn. In this case, the amine moieties are optimally aligned for the foldamer to act as a molecular tweezer that pulls together both ends of the dialdehyde **2**.

The use of a pyrrolidine with a primary amine as catalytic residues is crucial for the reaction selectivity. This catalytic diad favors the formation of an electrophilic iminium and a nucleophilic enamine within the same catalytic scaffold **3** and activates substrate **2** for the ring-closing carbon-carbon bond formation. Interestingly, the peptide backbone with two pyrrolidines gives only traces of the cyclic product **4** but is superior in intermolecular crossed aldol condensations (*7*). Girvin *et al.* synthesized macrocycles containing up to 22 ring atoms in excellent yields upon using this enzyme mimic. They implemented the foldamer in the synthesis of the cyclophane natural product robustol **5** and the core structure of nostocyclyne A **6**.

Foldamers can control reactivity and selectivity through structural preorganization of substrates, a feature normally observed only in much larger enzymes. On the basis of this extraordinary concept of foldamer catalysis, transformations showing new selectivities should become available that go beyond aldol reactions. This approach will likely enrich the general synthetic method repertoire and expand the landscape of accessible structural scaffolds. ■

Foldamer-templated macrocyclizations

Girvin *et al.* synthesized a peptide (foldamer) that can catalyze the formation of large rings from linear chains. These reactions have applications in synthesis of natural products. ····· Represents a long molecular chain

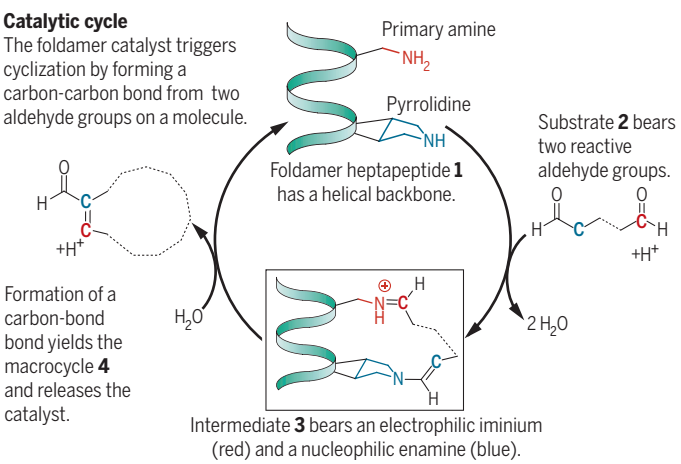

Department of Chemistry and Catalysis Research Center, Technical University Munich, Lichtenbergstrasse 4, 85748 Garching, Germany. Email: tanja.gulder@tum.de

REFERENCES AND NOTES

1. A. Berkessel, H. Gröger, *Asymmetric Organocatalysis* (Wiley-VCH, 2005).
2. G. Guichard, I. Huc, *Chem. Commun.* **47**, 5933 (2011).
3. Z. C. Girvin *et al.*, *Science* **366**, 1528 (2019).
4. C. A. Lewis, S. J. Miller, *Angew. Chem. Int. Ed.* **45**, 5616 (2006).
5. M. M. Müller *et al.*, *Angew. Chem. Int. Ed.* **48**, 922 (2009).
6. T. Gulder, P. S. Baran, *Nat. Prod. Rep.* **29**, 899 (2012).
7. Z. C. Girvin, S. H. Gellman, *J. Am. Chem. Soc.* **140**, 12476 (2018).

ACKNOWLEDGMENTS

T.G. thanks the Emmy-Noether (GU 1134-3) and Heisenberg (GU 1134-4) programs of the German Research Foundation.

10.1126/science.aaz9325

GRAPHIC: N. CARY/*SCIENCE*

Published by AAAS

POLICY FORUM

BIOSCIENCE AND LAW

Biotechnologies nibbling at the legal "human"

Recent advances in the biosciences invite reconsideration of fundamental legal concepts such as the definition of "human"

By **Bartha Maria Knoppers**[1] *and* **Henry T. Greely**[2]

The law has always viewed living human beings—and the tissues, organs, and other body parts derived from them—as special and different from the nonliving, nonhuman. But bioscientific advances are nibbling away at classical legal boundaries that form the bedrock of the normative structures on which societies are based. Recent developments such as in human genetics, neuroscience, and cell and tissue research pose qualitatively different challenges than what has come before, seeming to blur legal distinctions between human beings and other living organisms, between living human beings and dead ones, and between human tissues and cells and nonhuman ones. Although cognizant of the important bioethical and philosophical debates surrounding the issues raised, we focus on how legal systems may respond to these bioscience challenges to traditional binary, legal classifications. Determining whether some "thing" is now some "one" carries with it profound implications for the rights and obligations the law recognizes for "humans." Although it may be tempting to think that these new developments require us to reconsider the time-honored legal definitions of humans, living humans, or human tissue, we suggest that current legal dualisms can be applied in ways that provide adequate flexibility to allow weighing the many issues that surround developments in genetics, neurosciences, and cellular bioengineering and challenge how we legally define what is "human."

Recent advancements in the neurosciences, such as the possible revival of "dead" pig brains, pose issues for our understanding of both cognition-based conceptions of identity and even death itself. In the context of cell and tissue research, the creation of synthetic human entities with embryo-like features (SHEEFs) and human-animal chimeras create penumbras in our accepted legal taxonomies of organisms. CRISPR technologies may lead to likely widely acceptable somatic gene therapies for serious inheritable conditions while also leading to germline editing that affects future "humans," to say nothing of possible frivolous genetic enhancement.

[1]Centre of Genomics and Policy, McGill University, Montreal, Quebec, Canada. [2]Center for Law and the Biosciences, Stanford University, Stanford, California, USA. Email: bartha.knoppers@mcgill.ca

CLASSICAL DUALISMS

The classical dualisms found in legal systems around the world—whether animal versus human, person versus thing ("property"), living versus dead, drug versus device, or enhancement versus therapy—are already in the process of being "retranslated" under specific legislation or by the courts, creating new terms such as human genetic identity or integrity (*1*), common heritage of humanity (*2*), human species, crimes against humanity (*3*), and membership in the human family (*4*). Being "human" is the legal starting point for these concepts. But is the definition of "human" in the legal sense understood? Is it under threat?

As stated in Article 1 of the Universal Declaration of Human Rights, all human beings are "born free and equal in dignity and rights" (*4*). Predicated on the inherent dignity of human beings, human rights and their correlative obligations find their basis in legally recognized personhood. With their framing and internal normative hierarchy, laws provide security and certainty for human interactions in society and in the world. Any proposals for the reclassification of legal and regulatory boundaries surrounding the definition of "human" generally could do well to first understand the complexity and plasticity of the classical dualisms, of the biotechnologies, and of the regulatory ecosystem.

Reference to the inherent dignity of humans as "members of the human family" (*4*) may serve as the legal filter for degrees of protection before birth and after death. The law starts with the position that any living organism born from a person is a natural person from at least the time of birth until the time of death, but things quickly become more complicated.

The special treatment of "humanness" does not apply only in that period or to legal persons. All countries provide some protection for the embryo or fetus through abortion laws, fetal protection laws, limits on embryo research, and other ways. The approaches range from constitutional recognition of legal personhood at conception [for example, (*5*)] to the 14-day rule regarding research on embryos [for example, (*6*)].

Similarly, legal systems use different ways of defining the end of personhood through death. Most jurisdictions declare death, and end rights, when there is either irreversible cessation of cardiopulmonary functions or of all brain functions. But missing persons can, in many jurisdictions, be declared legally dead after a long period when they are not seen. Even after death, the tissues of (former) humans are legally entitled to special treatment; some countries provide distinct treatment to human remains from particular populations, such as with the Native American Graves Protection and Repatriation Act in the United States. Sometimes legal natural persons will lose the benefits of data protection legislation if their data are "anonymized," making them, for that purpose, a kind of "nonperson."

Some are tempted to consider consciousness or self-consciousness, or the likely resumption of either, as a crucial legal criterion for membership in the human family, as a definition of the end of life or possibly of its beginning (*2*).

GENETIC IDENTITY

It could be argued that the human genome defines "human." The definition of the human genome adopted by the United Nations (UN) Educational, Scientific and Cultural Organization (UNESCO) in 1997 was that it "includes both the genetic makeup of humanity as a whole and of the individual genes in their tangible form (genetic material) and genes in their intangible forms (genetic information)." Thus, UNESCO maintained that it is the human genome that "underlies the fundamental unity of all members of the human family as well as the recognition of their inherent dignity and diversity" (*7*). References to human dignity, genetic identity, or genetic integrity are used to prohibit human reproductive cloning (*7*, *8*), human germline intervention (*9*), and eugenics (*8*). For example, human reproductive cloning is deemed to be incompatible with human dignity under the 2005 UN Declaration on Human Cloning (*10*) or even as a crime against the human species (*3*).

Published by AAAS

The vast diversity of human genomes means there is no single "human genome" but billions of them, to say nothing of the billions belonging to the deceased. Their overlap with the genomes of clearly nonhuman organisms creates another problem, as does their vast overlap with, and substantial contribution from, our extinct cousins, Neanderthals and Denisovans. "The human genome" is made still more problematic by the possibility of humans carrying genetic variations never before seen in our species, either from editing or from natural mutation. Genomes change with every human generation. In short, there is no defined "human genome" that can be used as an easy way to determine humanity.

SPECIES IDENTITY

Humans are biological organisms on an evolutionary continuum, in the same biological kingdom as other animals, and science shows that we share the vast majority of the human genome with other clearly nonhuman species. But new research techniques, such as xenotransplantation and human/nonhuman chimeras, challenge the animal-human species divide and that of "human life" with its broad spectrum as opposed to living, natural persons with legally recognized rights and obligations. The creation of chimeric embryos by introducing human stem cells to animal embryos often falls between the gaps of the relevant human and animal legislation (*11*). The status, and rights, of some nonhuman animals with no human cells continues to be contested. A U.S. court recently rejected an effort to extend the writ of habeas corpus to chimpanzees, thus allowing for their continued imprisonment, although not without an interesting separate opinion discussing their "human" qualities (*12*). Merely considering animals "things" in law may be falling out of favor [for example, (*13*)].

NEURO IDENTITY

Is it the brain then that defines "human"? The size and complexity of the human brain distinguishes it from those of other species. However, similar to the case of consciousness, we include individuals with cephalic disorders, including anencephaly, in the human family. Initial legal recognition of brain death allowed the law to keep pace with accepted medical standards. Now, there is evidence of some false positives, in which "noncritical" brain functions continue despite the individual being considered dead. We may have gone from a situation before the adoption of the brain death standards in which it was possible to be biologically dead but legally alive, to one of being biologically alive but legally dead. And what should we do with human neural organoids or large portions of ex vivo human brains that are kept "active"? What about the great apes, dolphins, and other nonhumans with impressive cognitive capacities?

The boundaries between enhancement and therapy, of human and cyborg, also present legal issues. Freedom of conscience and of thought, some of the oldest concepts to be protected through human rights, may need to be reworked in response to neuroenhancements. The right to self-determination may need to be extended and articulated through a right to use, or to refuse, neuroenhancements (*14*).

CELLS AND TISSUES

Whereas regulatory oversight and approvals govern the classification and distribution of drugs and devices and provide transparent public gateways to the market, the demarcations regarding human tissues and cells are increasingly fluid, and public safety is at stake. The United States, Europe, and Japan all take importantly different approaches to medical uses of cell therapies. In order to exercise jurisdiction over and regulate autologous stem cells therapies and their use in rogue clinics, the U.S. Food and Drug Administration classified such cells as "drugs" (*15*). Similar legal contortions will no doubt occur in the future as bioengineered therapies will be considered products or devices, depending on their inclusion of human cells.

Parties the world over also continue to dispute questions of rights in cells or tissues that clearly were once part of a legal person or—in the case of frozen embryos, sperm, or eggs—things that might in the future give rise to a legally recognized person. To date, court decisions hover between classifying such cells and tissues as either property or potential persons, often looking to how the parties themselves understood the cells and tissues. Sometimes, the disputes are determined through the law of persons, seeing the tissues and cells as an extension of the (human) self. Or yet still, destruction of stored cells and tissues may be required under environmental protection law because they are considered to be medical waste.

MOVING FORWARD

Against this movable feast of "human" rights and biological developments, do the classical legal boundaries still matter, and if so, why? Altering the legal meaning of "human" ultimately affects the foundation for all human rights. Between legal classifications of biomedical waste and legal obligations to future generations, both the certainty that law provides in human interaction and the content of the concomitant duties and freedoms it accords are at stake.

"Hominum causa omne jus constitutum est" ("All law is created for the sake of men") is a maxim from Roman law and is the origin of most legal systems the world over. It epitomizes the relationship between "man" and law. Uncertain boundaries can lead to unintended and untoward legal consequences, which only intensify when one considers the effect of judicial decisions. A new classification has the potential to affect and bind all future parties while unsettling the past. Irrespective, classical dualisms continue to serve as frameworks for legal determinations in most specific contexts. Courts, scientists, and physicians continue to be creative in their interpretations of emerging biotechnologies and in the imposition of necessary limits across the dualisms. Regions of the world with different cultural values concerning the beginning or end of life or on the use of tissues and cells still remain subject to the international umbrella filter of "human" rights. Our traditional approaches to this may not be badly out of date, but they need to be applied flexibly. So, what can we suggest as a way forward?

We care about living organisms that are human in their characteristics, but they do not always need to have exactly human characteristics. "Human beings" typically have two arms and two legs, but we recognize as human those without all those limbs, through amputation or congenital condition, as well as people with artificial limbs. Possession of a "human genome" is part of being a legal natural person, but we need to recognize both that a genome is neither in itself sufficient (a human lymphocyte is not a legal person) nor, in exact detail, necessary. Like the body, the genome needs only to be "substantially" human. Unusual or rare variations are not disqualifying in themselves but form part of the decision. The same is true of humans with some tissue from nonhuman organisms or some mechanical implants. It is also true of nonhuman organisms with some human tissues or DNA; a mouse with a human immune system should not be seen as substantially human or a natural legal person. Similarly, some version of "substantially" could be applied to definitions of brain death, not to require some kind of "higher brain death" rule but to avoid complexity when small bits of living brain, either in vivo or in vitro, are used to assert that the legal natural person still lives.

What constitutes "substantially" in these contexts will not be measurable by percentages or similar specific tests but will be a judgment call—like many such legal terms, such as "unreasonable" or "best interests." Using "substantially" will not provide an exact answer but will give the decision-maker (judge, jury, or other) some guidance, just

Published by AAAS

ILLUSTRATION: DAVIDE BONAZZI/SALZMANART

as "beyond a reasonable doubt" says something more than "preponderance of the evidence" when considering the burden of proof and "reckless" means something beyond "negligent" when considering culpability for injuries. For the most part, this should be possible in the interpretation of the meaning of the word "human," without requiring new legislation. As a result, its application may vary from judge to judge and culture to culture while still, as a concept, providing some useful guidance.

The other big question is when we treat molecules, cells, tissues, organs, or bodies as "human" in terms of deserving respect. Again, "substantially" might be a useful part of the definition. Additional consideration may include whether the body part was ever a part of a natural legal person. If a kidney grew in a natural legal person, that argues for it being "human" even if it had a very odd morphology, function, or even genome. A kidney grown totally in a laboratory, even if a fully human kidney, may not deserve respect if it was never inside or "part of" a natural legal person. But a kidney from a pig, genetically modified to function in a human, might not be viewed as "human tissue" while in the pig but be so viewed if it had functioned inside a natural legal person for years.

We have attempted to address the classical legal dualisms defining "human," an approach that may be useful to the law, at least until our cultures arrive at better ways of understanding and approaching these new realities. Rules that include the word "substantially" are never fully satisfying. Nevertheless, in a universe where things blend into each other and living organisms are not cleanly divided into Platonic natural kinds, they may be the best filter we can apply: a malleable term for contextual and proportionate evaluation. "Substantial" is already a term in, inter alia, copyright and data protection law and therefore is an analytic tool the law already possesses. Such rules here will no doubt still lead to close or contested decisions—how to treat a SHEEF for example—but we believe that more frequently they can lead to results that we are (substantially) comfortable with while still preserving the core of our legal dualisms. In practice, our human families do not always meet exact definitions with perfect edges, but we can see substantial connections among them. On the spectrum from living cell to organism to human being, with all their new biotechnological variations, to a natural, legal person (alive or dead), perhaps the concept of membership in the hazily bordered human family can serve as a useful source for the delimitation of the "human." ■

REFERENCES AND NOTES

1. Recommendation 934 (1982) on genetic engineering, Parliamentary Assembly of the Council of Europe, January 1982.
2. UNESCO, *Universal Declaration on Bioethics and Human Rights* (UNESCO, 2005).
3. Article 214-2, Code pénal français, created by Loi no. 2004-800 du 6 août 2004 relative à la bioéthique (1), Republic of France, 6 August 2004.
4. United Nations (UN) General Assembly, Universal Declaration of Human Rights (UN, 1948).
5. Article 1, Constitution of the Republic of El Savador.
6. Assisted Human Reproduction Act 2004, Canada, S.C. 2004, c. 2 (2004).
7. UNESCO, Universal Declaration on the Human Genome and Human Rights (UNESCO, 1997).
8. European Union, Charter of Fundamental Rights of the European Union (2012).
9. Council of Europe, Convention for the Protection of Human Rights and Dignity of the Human Being with regard to the Application of Biology and Medicine: Convention on Human Rights and Biomedicine ("Oviedo Convention") (1997).
10. UN Declaration on Human Cloning (UN Doc A/RES/59/280), resolution adopted by the General Assembly on 8 March 2005.
11. J. J. Koplin, J. Savulescu, *J. Law Biosci.* **6**, 37 (2019).
12. *Nonhuman Rights Project, Inc. v. Lavery*, 54 N.Y.S. 3d 392 (N.Y. App. Div. 2017), motion for leave to appeal denied, 31 N.Y.3d 1054 (2018) (see opinion of Judge Fahey, concurring).
13. The Civil Code of Québec, Article 898.1, CQLR c CCQ-1991, (1991).
14. J.-C. Bublitz, in *Cognitive Enhancement: An Interdisciplinary Perspective*, E. Hildt, A. G. Franke, Eds. (Springer Netherlands, 2013), pp. 233–264.
15. D. Sipp, L. Turner, *Science* **338**, 1296 (2012).

ACKNOWLEDGMENTS

The authors thank M. Beauvais for his invaluable editorial and research assistance. The article was made possible by a grant from the WYNG Foundation. The article is the joint contribution of B.M.K. and H.T.G. It was inspired by an international think tank on the topic (Montreal, 9 to 11 June 2019). The authors declare no competing interests.

10.1126/science.aaz5221

Published by AAAS

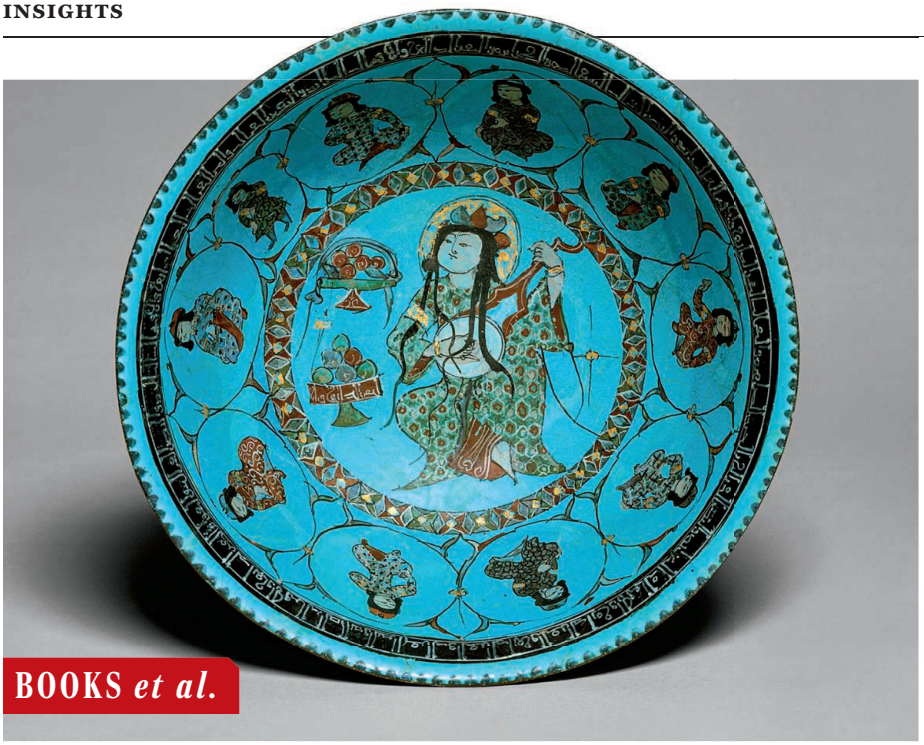

BOOKS *et al.*

A gilded Iranian bowl from the late 12th or early 13th century features an oud player and audience.

ANTHROPOLOGY

More than a merchant's trading route

A vividly illustrated tome traces the cultural impacts of the Silk Road

By **Andrew Robinson**

Between 1271 and 1275, Marco Polo famously explored the overland journey from Europe to Cathay (China). Much later, the route was dubbed "the Silk Road" by German geographer Ferdinand von Richthofen, referencing the goods and ideas ferried between the civilizations of Rome and China along the ancient caravan path.

Today, the route has a much more complicated significance—hence this tome's plural title, *Silk Roads*. The book is a copiously illustrated history with lengthy photo captions and short essays by some 80 scholars, edited by sinologist Susan Whitfield, a longtime scholar of the subject.

Whitfield formerly served as a curator of the Central Asian manuscript collections at the British Library and was the first director of the library's International Dunhuang Project. This collaborative effort seeks to conserve, catalog, and digitize manuscripts, printed texts, paintings, textiles, and artifacts from Dunhuang and various other archaeological sites at the Silk Road's Chinese end.

In her introduction, Whitfield (re)defines the Silk Road as a "system of substantial and persistent overlapping and evolving interregional trade networks across Afro-Eurasia by land and sea from the end of the 1st millennium BC through to the middle of the 2nd millennium CE." Apart from silk, merchants traded in slaves, horses, semiprecious stones, metals, pots, musk, medicines, glass, furs, and fruits—"resulting in movements and exchanges of peoples, ideas, technologies, faiths, languages, scripts, iconographies, stories, music, dance and so on."

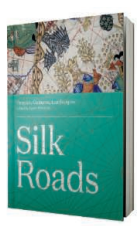

Silk Roads: Peoples, Cultures, Landscapes
Susan Whitfield, editor
University of California Press, 2019. 480 pp.

To take just one example from the nearly 500 illustrations in the book, consider a letter in Sogdian script discovered in an ancient watchtower used for observing caravans near Dunhuang. The letter appears in archaeologist Paul Wordsworth's essay, "Camels and caravanserai: Traversing the desert." It was written on paper in about 313 AD by Miwnay, wife of a Sogdian merchant named Nanai-dhat who traded with northwestern China from his base in Sogdiana. (Sogdiana was an Iranian civilization encompassing territory in present-day Kazakhstan, Tajikistan, and Uzbekistan, centered on the city of Samarkand.) In the letter, Miwnay blames her husband for leaving her destitute in Dunhuang. "I would rather be a dog's or a pig's wife than yours!" she writes angrily. "In a more mildly worded postscript, their daughter Shayn explains that she and Miwnay have been obliged to become servants of the Chinese," notes Nicholas Sims-Williams in the letter's caption.

As this letter implies, studying the Silk Road can be—in Whitfield's word—"daunting." In addition to histories of Central Asia, China, India, Mesopotamia and the Middle East, the eastern Mediterranean, and North Africa (not to mention the earlier Indus civilization, which, surprisingly, was omitted from this book, despite its trading contacts with Mesopotamia), Silk Road scholarship can involve delving into Buddhism, Christianity, Islam, Judaism, Manichaeism, and Zoroastrianism. The book even contains some science of deserts, mountains, rivers, seas, and steppes. "A plethora of unfamiliar names and places can confuse and befuddle. I beg the reader's patience to try not to be distracted by these," Whitfield requests. "Reading one essay or caption may show little, but looking at more will, I hope, start to reveal something of the complex pattern of the Silk Roads."

To orient readers, a detailed map of trade routes ranging from Western Europe to Japan is repeated at the start of each section with freshly labeled page references to the section's essays and captions. But the book lacks even a basic chronology of the Silk Roads and their evolution from the 1st millennium BC to the establishment of the International Dunhuang Project in 1994. The absence of such a time sequence is acutely felt, given that Whitfield's structure deliberately rejects chronology and relies instead on landscape to frame the scholarship, with the book's five sections centering on the steppe, the mountains and highlands, the deserts and oases, the rivers and plains, and the seas and skies.

Despite this crucial omission—and an awkward fragmentation of the short essays by the long image captions—*Silk Roads* is a treasure house of fascinating images and hard-won knowledge. It also provides insight into both human diversity and imperial rivalry over a millennium and a half, at a time when the Silk Road is a region of renewed trade and political conflict with China. ■

The reviewer is the author of *The Story of Writing: Alphabets, Hieroglyphs and Pictograms* (Thames & Hudson, 1995) and *The Indus: Lost Civilizations* (Reaktion Books, 2015).
Email: andrew@andrew-robinson.org

10.1126/science.aba1748

PHOTO: METROPOLITAN MUSEUM OF ART, NEW YORK

Published by AAAS

FOOD SAFETY

The ongoing quest for pure foods

Early adulteration sowed mistrust in the food production system that endures today

By **Deborah Blum**

In 15th-century Europe, the record suggests, authorities took food fakery very seriously. A Nuremberg merchant caught adulterating the spice saffron was burned at the stake, and his confederate was buried alive. Of course, the merchant and his colleague should have been aware of the prohibitions against food tampering by then; they had been in place for centuries. The famed Greek philosopher Plato inscribed rules against adulteration in his book *The Laws*, published in the 4th century BCE.

As Benjamin R. Cohen notes in his thoughtful book *Pure Adulteration*, it is difficult to find a time or a place in history that lacks purveyors of food and drink attempting to cheat their unsuspecting customers. Cohen, a science historian and associate professor at Lafayette College in Easton, Pennsylvania, brings up the age-old problem of adulteration as essential context for his more recent case study of the underlying issues.

As his book's subtitle—*Cheating on Nature in the Age of Manufactured Food*—suggests, Cohen's focus is on the pure food movement of the late 19th and early 20th centuries. His story centers on the scandals and conflicts in the United States during this period that eventually led to the establishment of the federal Food and Drug Act and Meat Inspection Act of 1906. Organizing the book around that battlefield moment allows him to ask a range of provocative and intriguing questions about U.S. food systems. What, for example, does this fight for food purity tell us about the changing nature of the country; its shifting culture, commerce, and politics; and its emerging scientific power?

This was a moment, Cohen points out, in which industry was on the rise, farming was shifting to a bigger business model, and urbanization was starting to outpace rural growth. It was also a moment in which the ability to create an entirely artificial product began to blur our definitions of what constitutes "real food." In response to those pressures, newly empowered researchers led "an effort to take command of patrolling the border between pure and adulterated." To explore that territory, Cohen uses case studies of high-profile examples of adulteration and fakery in the 19th century, including butter, olive oil, lard, and glucose (which was then the common name for products such as corn syrup).

In a chapter titled "Margarine in a Dairy World," Cohen looks at the late-19th-century rise of artificial butter, also known as oleomargarine. At that point, margarine was not the vegetable oil product we know today. It started out as an amalgam of meat fat and other by-products, processed into a creamy spread and dyed yellow to mimic traditional butter. Although manufacturers described it as another natural animal product—sometimes referring to it as "butterine"—critics saw it as industrial-scientific artifice. "Oleomargarine was controversial because its identity was unclear, its origins were murky, and it frustrated stable norms of agricultural activity," Cohen writes.

By contrast, adulterated olive oil—usually mixed with much cheaper cottonseed oil—took advantage of changes in global agricultural practices. Cotton crops were expanding around the world, and growers embraced new uses for the plants' parts and seeds. The cottonseed oil industry, which eventually fostered such lard substitutes as Crisco (shorthand for crystallized cottonseed oil), raised fewer hackles than did the margarine debate, except in the obvious matters of substitution and false advertising.

The starchy sugars of corn and other plants—as opposed to traditional sweeteners such as cane sugar or maple syrup—also came under close scrutiny during this period. Analytical chemists increasingly identified the so-called honeys and syrups of the time as artfully labeled and carefully dyed glucose. In the late 19th century, manufacturers were not required to put ingredient labels on products, so consumers were easily kept in the dark about foods' true composition.

All of this led to a sense, fostered by the research community, that only chemists themselves could counter such chemical chicanery. Cohen devotes the last two chapters of his book to the rise of scientific analysts, notably Harvey Washington Wiley, a U.S. Department of Agriculture chemist who helped pioneer chemical analysis of the food supply and who was a leader in the fight for food safety standards, which culminated in the passage of the Food and Drug Act of 1906.

Although pure food advocates helped establish modern consumer protection in the United States, Cohen argues that their often-bruising political fight also helped establish a mistrust of the food production system that endures today. Adulteration of olive oil and other products has been dramatically reduced but has not disappeared. And in the end, he concludes, the most pertinent question, then as now, may be whom—if anyone—we trust to "patrol that safety-danger border." ■

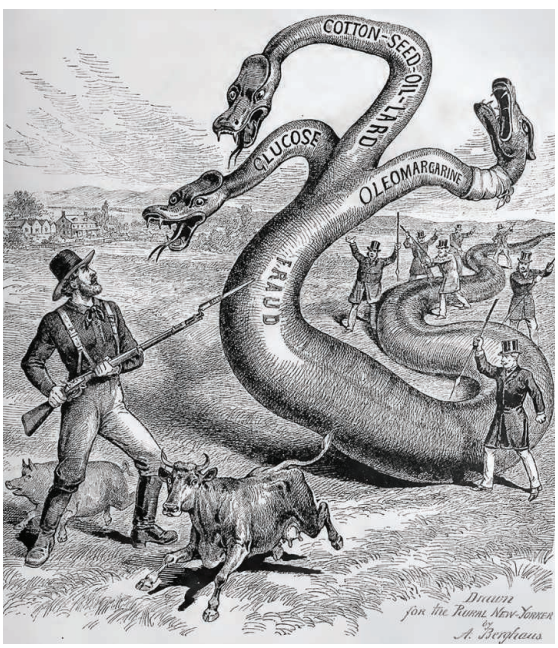

A farmer battles food fraud in an 1890 cartoon.

Pure Adulteration: Cheating on Nature in the Age of Manufactured Food
Benjamin R. Cohen
University of Chicago Press, 2019. 332 pp.

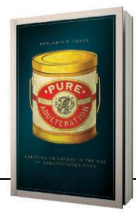

The reviewer is director of the Knight Science Journalism Program, Massachusetts Institute of Technology, Cambridge, MA 02139, USA, and the author of *The Poison Squad: One Chemist's Single-Minded Crusade for Food Safety at the Turn of the Twentieth Century* (Penguin Press, 2018). Email: dlblum@mit.edu

10.1126/science.aaz7902

ILLUSTRATION: UNIVERSITY OF ILLINOIS URBANA-CHAMPAIGN

Published by AAAS

LETTERS

Edited by **Jennifer Sills**

Retraction

The online Research Article "Insular cortex processes aversive somatosensory information and is crucial for threat learning" used optogenetic methods in mice to conclude that insular cortex is involved in auditory cued fear learning (*1*). A reanalysis of the data performed by the authors in October 2019 showed, however, that the mouse behavior data reported in Figs. 1C, 3C, 3F, and 6B, and the corresponding data in supplementary figures, had been manipulated. The reanalysis showed that data points from many individual mice had been moved, with the effect that the difference between optogenetic silencing groups and control groups became larger than in the real data. Thus, in the reanalyzed data, the statistical significance disappears for many datasets of Figs. 1, 3, and 6, and these experiments need to be reestablished in future work. The first author, who performed these measurements, has admitted to having committed the data falsification. No other coauthors were involved in the data manipulation, and thus their data (Figs. 2 and 5 and supplementary figs. S2, S4–S6, S11, and S15–S18) remain valid. Because the data manipulations affect important conclusions of the paper, the authors retract the Research Article. We apologize to the readership of *Science*.

Emmanuelle Berret, Michael Kintscher, Shriya Palchaudhuri, Wei Tang, Denys Osypenko, Olexiy Kochubey, Ralf Schneggenburger*
Laboratory of Synaptic Mechanisms, Brain Mind Institute, School of Life Science, École Polytechnique Fédérale de Lausanne (EPFL), 1015 Lausanne, Switzerland.
*Corresponding author:
Email: ralf.schneggenburger@epfl.ch

REFERENCES AND NOTES

1. E. Berret *et al.*, *Science* **364**, eaaw0474 (2019).

10.1126/science.aba2173

Genome studies reveal flaws in broad consent

In their Research Article "Large-scale GWAS reveals insights into the genetic architecture of same-sex sexual behavior" (30 August, p. eaat7693), A. Ganna *et al.* found that same-sex sexual behavior is influenced by many genes. The study used data and genetic information from a number of sources, including UK Biobank. UK Biobank participants gave broad consent between 2006 and 2010 to the use of their data, health records, and bodily materials for "health-related research purposes" (*1*, *2*). Ganna *et al.*'s study reveals the ethical problems with using broad consent from participants for biobank research.

Is it time to reconsider broad consent models for biobank research?

There are three ways in which studying the genetic architecture of same-sex sexual behavior can be claimed to be health-related. First, it would be health-related if same-sex and/or different-sex behavior were in themselves states of health or illness. However, homosexuality has long been removed from disease classifications, and making such a claim would be normatively problematic in implying that one or both of these behaviors signified disease. Second, the study would be health-related if persons who engage in one of these behaviors are on aggregate more or less likely to experience particular health outcomes. Yet this justification vastly increases the scope of the term "health-related." Any behavior can have a link to health outcomes. For example, voting behavior has such a link (*3*, *4*), but it would be odd to classify a hypothetical study of the genetic architecture of voting behavior as health-related. Third, the study would be health-related if all research that improves our understanding of human biology were health-related. This again leads to a massive expansion of the scope of the term, collapsing the distinction between health-related research and basic molecular biology research.

The understanding of what qualifies as health-related research is likely to change over time, but the restriction on allowable research is governed by the meaning the term had for participants at the time they gave their consent (*5*, *6*). Broad consent was developed at a time when it was difficult to keep in contact with research participants after their initial consent, but keeping that contact is now much easier and cheaper. We should consider implementing more interactive consent models, such as dynamic or meta-consent, that allow participants to vary their consent preferences as the science progresses and societal values change (*7*, *8*).

Søren Holm[1,2]* and Thomas Ploug[3]
[1]Centre for Social Ethics and Policy, Department of Law, University of Manchester, Manchester, UK. [2]Center for Medical Ethics, HELSAM, Faculty of Medicine, University of Oslo, Oslo, Norway. [3]Department of Communication and Psychology, Aalborg University, Aalborg, Denmark.
*Corresponding author.
Email: soren.holm@manchester.ac.uk

REFERENCES AND NOTES

1. UK Biobank, Information Leaflet (2010); www.ukbiobank.ac.uk/wp-content/uploads/2011/06/Participant_information_leaflet.pdf?phpMyAdmin=trmKQlYdjjnQIgJ%2CfAzikMhEnx.
2. UK Biobank, Consent Form (2010); www.ukbiobank.ac.uk/wp-content/uploads/2011/06/Consent_form.pdf.
3. M. Bazargan, T. S. Kang, S. Bazargan, *Int. J. Aging Hum. Dev.* **32**, 181 (1991).

IMAGE: ARTHIMEDES/SHUTTERSTOCK.COM

Published by AAAS

4. P. Söderlund, L. Rapeli, *Polit. Life Sci.* **34**, 28 (2015).
5. N. C. Manson, *J. Med. Ethics* **45**, 291 (2019).
6. T. Ploug, S. Holm, *J. Med. Ethics* **45**, 295 (2019).
7. J. Kaye *et al.*, *Eur. J. Hum. Genet.* **23**, 141 (2015).
8. T. Ploug, S. Holm, *Bioethics* **30**, 721 (2016).

COMPETING INTERESTS

S.H. is a former member of the UK Biobank Ethics and Governance Council.

10.1126/science.aaz3797

Genome studies must account for history

In their Research Article "Large-scale GWAS reveals insights into the genetic architecture of same-sex sexual behavior" (30 August, p. eaat7693), A. Ganna *et al.* found that prevalence of same-sex experience in the UK Biobank population increased four-fold across study participants' birth years, and prevalence in the younger, self-selecting 23andMe consumer population was 6 times that of UK Biobank. The authors treat single nucleotide polymorphisms identified in these populations as ahistorical components of the "architecture of same-sex sexual behavior." We question the generalizability of their findings.

Political context and stigmatization of homosexuality affects whether people engage in and/or report same-sex behavior (*1*, *2*). Historical conditions such as decriminalization of homosexuality in 1967 and legalization of marriage equality in 2013 and 2014 instigated substantial shifts in reporting of same-sex orientations (*3*, *4*). Sampling based on voluntary surveys that limited the cohorts to cis-gender people of white-European descent could exaggerate these dynamics. Furthermore, many sexual minorities are unsampled due to the HIV/AIDS epidemic in the 1980s and 1990s (*5*). Centering the analysis around the variable of birth year and interpreting findings in relation to historical, social, and legal context might alter the study's conclusions (*6*).

Ganna *et al.*'s conjecture that "genetic and sociocultural influences on sexual behavior might interact" does not resolve these concerns. This approach implies that it is acceptable to issue claims of genetic drivers of behaviors and then lay the burden of proof on social scientists to perform post-hoc socio-cultural analysis. Given the epistemic authority of the molecular biosciences and the potential consequences for those with vulnerable social identities, damage caused by these studies is hard to repair. As socio-genomic GWAS studies proliferate, we call for community standards for research design that acknowledge the historical, political, and social context of phenotypes under study.

Sarah S. Richardson,[1,2]* Alexander Borsa,[3] Marion Boulicault,[4] Jonathan Galka,[1] Nayanika Ghosh,[1] Annika Gompers,[2] Nicole E. Noll,[2,5] Meg Perret,[1] Meredith W. Reiches,[6] Juana C. Becerra Sandoval,[1] Heather Shattuck-Heidorn,[7] Joseph Vitti,[8] Brianna Weir,[9] Helen Zhao[10]

[1]Department of the History of Science, Harvard University, Cambridge, MA 02138, USA. [2]Studies of Women, Gender, and Sexuality, Harvard University, Cambridge, MA 02138, USA. [3]Department of Sociomedical Sciences, Columbia University Mailman School of Public Health, New York, NY 10032, USA. [4]Department of Philosophy, Massachusetts Institute of Technology, Cambridge, MA 02139, USA. [5]Department of Psychology, Harvard University, Cambridge, MA 02138, USA. [6]Department of Anthropology, University of Massachusetts Boston, Boston, MA 02125, USA. [7]Women and Gender Studies Program, University of Southern Maine, Portland, ME 04103, USA. [8]Seven Bridges Genomics, Charlestown, MA 02129, USA. [9]Department of Evolutionary and Organismic Biology, Harvard University, Cambridge, MA 02138, USA. [10]Department of Philosophy, Columbia University, New York, NY 10027, USA.
*Corresponding author.
Email: srichard@fas.harvard.edu

REFERENCES AND NOTES

1. M. A. Villarroel *et al.*, *Public Opin. Q.* **70**, 166 (2006).
2. K. B. Coffman, L. C. Coffman, K. M. M. Ericson, *Manage. Sci.* **63**, 3168 (2016).
3. H. Brooks *et al.*, *Br. J. Gen. Pract.* **68**, e187 (2018).
4. B. M. Charlton, H. L. Corliss, D. Spiegelman, K. Williams, S. B. Austin, *Am. J. Public Health* **106**, 2202 (2016).
5. J. M. Twenge, R. A. Sherman, B. E. Wells, *Archives Sex. Behav.* **45**, 1713 (2016).
6. J. N. Rosenquist *et al.*, *Proc. Natl. Acad. Sci. U.S.A.* **112**, 354 (2015).

10.1126/science.aaz6594

Response

Our genome-wide association study (GWAS) on same-sex sexual behavior, which used data from the UK Biobank (*1*), was reviewed and approved by the UK Biobank Access Sub-Committee. We also sought stakeholder input from allies and advocates for the LGBTQIA+ community, as has been done in the past (*2*, *3*). Despite these efforts, Holm and Ploug contend that broad biobank consent is insufficient. They argue that our study only tenuously qualifies as "health-related" and thus stretches the bounds of the participants' consent.

We agree with Holm and Ploug that same- or different-sex sexual behaviors are not states of disease or health; same-sex sexual behavior is a natural part of normal human variation, and we in no way condone othering of members of the LGBTQIA+ community. However, we disagree that our study is related only indirectly to health. Same-sex sexual behavior intersects with health care in a variety of ways. For example, sexual behavior and history are used to guide recommendations of whether to take preexposure prophylaxis medication (*4*). Sexual minorities experience stigma, microaggressions, and prejudice, which have been shown to relate to the higher rates of anxiety and depression (*5*). These connections help contextualize the higher rates of suicidality, mood and anxiety disorders, and alcohol and substance use seen in sexual minorities (*6*–*8*). The genetic correlation analyses in our Research Article add to our understanding about how sexual behavior relates to health outcomes, and publicly available summary statistics from our GWAS may be used by other researchers to better understand genetic and environmental influences on sexual behavior, facilitating a fuller understanding of human health.

Holm and Ploug argue that participants may not have given consent for our study based on the information they had about the potential use of their data. We believe that when broad biobank consent is used, institutional bodies (such as the UK Biobank's Board and its Access Sub-Committee) must take responsibility for approving specific research requests rather than expecting participants to understand all such details for possible research projects. We also point out that participants had more options and information than Holm and Ploug describe. The UK Biobank pamphlet (*9*) emphasizes that participants can skip or select "prefer not to answer" for any question; an additional message underlining this option was presented before the section with sexuality-related questions. The UK Biobank's consent and information forms also explained its intention to "support a diverse range of research" including "the promotion of health throughout society," and it stated that health "is affected by [people's] lifestyle, environment, and genes" (*9*). Given this full context, the genetic study of sexual behavior is both health-related and consistent with the consent of the participants.

Richardson *et al.* discuss the issue of selective sampling and comment that the social and historical context of the participants may affect our findings. We acknowledged both the limits of our samples and the importance of sociocultural context in our Research Article. We agree with Richardson *et al.* that analyzing the data according to birth year and taking into account cultural factors would be fascinating. Indeed, we did attempt some preliminary analyses to evaluate whether this line of inquiry was feasible. Unfortunately, fine-grained analyses stratified by birth year require extremely large

Published by AAAS

samples to detect the relevant effects, and statistical power analyses indicated that the current sample size was insufficient to yield meaningful results (we reported some sensitivity analyses in table S5). As GWAS sample sizes continue to grow, more analyses will become more feasible, and we look forward to contributing to these investigations. We join others (*10*–*12*) in calling for greater diversity in these samples.

Andrea Ganna[1,2,3,4]*, Karin J.H. Verweij[5]*, Michel G. Nivard[6], Robert Maier[1,2,3], Robbee Wedow[1,3,7,8,9,10,11], Alexander S. Busch[12,13,14], Abdel Abdellaoui[5], Shengru Guo[15], J. Fah Sathirapongsasuti[16], 23andMe Research Team[16], Paul Lichtenstein[4], Sebastian Lundström[17], Niklas Långström[4], Adam Auton[16], Kathleen Mullan Harris[18,19], Gary W. Beecham[15], Eden R. Martin[15], Alan R. Sanders[20,21], John R.B. Perry[12]*, Benjamin M. Neale[1,2,3]*, Brendan P. Zietsch[22]*†

[1]Analytic and Translational Genetics Unit, Center for Genomic Medicine, Massachusetts General Hospital, Boston, MA 02114, USA. [2]Program in Medical and Population Genetics, Broad Institute of MIT and Harvard, Cambridge, MA 02142, USA. [3]Stanley Center for Psychiatric Research, Broad Institute of MIT and Harvard, Cambridge, MA 02142, USA. [4]Department of Medical Epidemiology and Biostatistics, Karolinska Institutet, Stockholm, Sweden. [5]Department of Psychiatry, Amsterdam UMC, University of Amsterdam, 1105 AZ, Amsterdam, Netherlands. [6]Department of Biological Psychology, VU University, 1081 BT, Amsterdam, Netherlands. [7]Department of Sociology, Harvard University, Cambridge, MA 02138, USA. [8]Department of Epidemiology, Harvard T.H. Chan School of Public Health, Boston, MA 02115, USA. [9]Department of Sociology, University of Colorado, Boulder, CO 80309–0483, USA. [10]Health and Society Program and Population Program, Institute of Behavioral Science, University of Colorado, Boulder, CO 80309–0483, USA. [11]Institute for Behavioral Genetics, University of Colorado, Boulder, CO 80309–0483, USA. [12]MRC Epidemiology Unit, University of Cambridge School of Clinical Medicine, Institute of Metabolic Science, Cambridge, UK. [13]Department of Growth and Reproduction, Rigshospitalet, University of Copenhagen, Copenhagen, Denmark. [14]International Center for Research and Research Training in Endocrine Disruption of Male Reproduction and Child Health (EDMaRC), Rigshospitalet, Copenhagen, Denmark. [15]Department of Human Genetics, University of Miami, Miami, FL 33136, USA. [16]23andMe, Inc., Sunnyvale, CA 94086, USA. [17]Centre for Ethics, Law, and Mental Health, University of Gothenburg, Gothenburg, Sweden. [18]Carolina Population Center, University of North Carolina at Chapel Hill, Chapel Hill, NC 27516, USA. [19]Department of Sociology, University of North Carolina at Chapel Hill, Chapel Hill, NC 27599, USA. [20]Department of Psychiatry and Behavioral Sciences, NorthShore University HealthSystem Research Institute, Evanston, IL 60201, USA. [21]Department of Psychiatry and Behavioral Neuroscience, University of Chicago, Chicago, IL 60637, USA. [22]Centre for Psychology and Evolution, School of Psychology, University of Queensland, St. Lucia, Brisbane, QLD 4072, Australia.
*Contributed equally.
†Corresponding author.
Email: zietsch@psy.uq.edu.au

REFERENCES AND NOTES

1. C. Bycroft *et al.*, *Nature* **562**, 203 (2018).
2. A. R. Sanders *et al.*, *Sci. Rep.* **7**, 16950 (2017).
3. T. R. Thomas, D. Hofammann, B. G. McKenna, J. J. Michaelson, *bioRxiv* 10.1101/685982 (2019).
4. D. K. Owens *et al.*, *JAMA* **321**, 2203 (2019).
5. L. Timmins, K. A. Rimes, Q. Rahman, *Archiv. Sex. Behav.* 10.1007/s10508-019-01502-2 (2019).
6. M. King *et al.*, *BMC Psychiatr.* **8**, 70 (2008).
7. W. B. Bostwick, C. J. Boyd, T. L. Hughes, S. E. McCabe, *Am. J. Public Health* **100**, 468 (2010).
8. J. Semlyen, M. King, J. Varney, G. Hagger-Johnson, *BMC Psychiatr.* **16**, 67 (2016).
9. UK Biobank (2010); www.ukbiobank.ac.uk/key-documents (see Participant Information Leaflet, Consent Form, and Touchscreen Questionnaire).
10. G. L. Wojcik *et al.*, *Nature* **570**, 514 (2019).
11. M. C. Mills, C. Rahal, *Commun. Biol.* **2**, 9 (2019).
12. A. R. Martin *et al.*, *Am. J. Hum. Genet.* **100**, 635 (2017).

COMPETING INTERESTS

J.F.S. is an employee of MedGenome, Inc. B.M.N. is a member of the scientific advisory board at Deep Genomics and consultant for Camp4 Therapeutics, Takeda Pharmaceutical, and Biogen.

10.1126/science.aaz8941

TECHNICAL COMMENT ABSTRACTS

Comment on "Demographic dynamics of the smallest marine vertebrates fuel coral reef ecosystem functioning"

Jacob E. Allgeier and Timothy J. Cline

Brandl *et al.* (Reports, 21 June 2019, p. 1189) report that cryptobenthic fishes underpin coral reef ecosystem function by contributing ~60% of "consumed fish" biomass and ~20% of production. These results are artifacts of their simulation. Using their data and model, we show that cryptobenthic species contribute less than 4% to fish production, calling into question the extent to which they contribute to the high productivity of coral reefs.

Full text: dx.doi.org/10.1126/science.aay9321

Response to Comment on "Demographic dynamics of the smallest marine vertebrates fuel coral reef ecosystem functioning"

Simon J. Brandl, Renato A. Morais, Jordan M. Casey, Valeriano Parravicini, Luke Tornabene, Christopher H. R. Goatley, Isabelle M. Côté, Carole C. Baldwin, Nina M. D. Schiettekatte, David R. Bellwood

Allgeier and Cline suggest that our model overestimates the contributions of cryptobenthic fishes to coral reef functioning. However, their 20-year model ignores the basic biological limits of population growth. If incorporated, cryptobenthic contributions to consumed fish biomass remain high (20 to 70%). Disturbance cycles and uncertainties surrounding the fate of large fishes on decadal scales further demonstrate the important role of cryptobenthic fishes.

Full text: dx.doi.org/10.1126/science.aaz1301

ERRATA

Erratum for the Report: "The STAT3-Binding Long Noncoding RNA lnc-DC Controls Human Dendritic Cell Differentiation" by P. Wang *et al.*, *Science* 366, eaba5539 (2019). Published online 20 December 2019; 10.1126/science.aba5539

Erratum for the Report: "Aging increases cell-to-cell transcriptional variability upon immune stimulation" by C. P. Martinez-Jimenez *et al.*, *Science* 366, eaba3487 (2019). Published online 20 December 2019; 10.1126/science.aba3487

THE GOLDEN GOOSE AWARD

Congratulations to the 2019 Winners

David Sachar
The Frog Skin that Saved 50 Million Lives

Noel Rose and Ernest Witebsky
Advancing Autoimmunity

Jack Levin and Frederik Bang
The Blood of the Horseshoe Crab

The Golden Goose Award honors federally funded researchers whose work may have seemed odd or obscure when it was conducted but which led to major breakthroughs and significant societal benefit.

Nominations are now being accepted.

www.goldengooseaward.org

AAAS
AMERICAN ASSOCIATION FOR THE ADVANCEMENT OF SCIENCE

Published by AAAS

Cite as: J. E. Allgeier, T. J. Cline, *Science* 10.1126/science.aay9321 (2019).

Comment on "Demographic dynamics of the smallest marine vertebrates fuel coral reef ecosystem functioning"

Jacob E. Allgeier*† and Timothy J. Cline†

Department of Ecology and Evolutionary Biology, University of Michigan, Ann Arbor, MI, USA.

*Corresponding author. Email: jeallg@umich.edu

†The authors contributed equally to this work.

Brandl *et al.* (Reports, 21 June 2019, p. 1189) report that cryptobenthic fishes underpin coral reef ecosystem function by contributing ~60% of "consumed fish" biomass and ~20% of production. These results are artifacts of their simulation. Using their data and model, we show that cryptobenthic species contribute less than 4% to fish production, calling into question the extent to which they contribute to the high productivity of coral reefs.

A long-standing question in coral reef ecology is "How can reefs be so productive while residing in such nutrient-poor environments?" Brandl *et al.* (*1*) estimated the contribution of cryptobenthic fishes, an elusive and underappreciated group, for total coral reef fish production. They provide interesting and novel perspectives on the unique life history characteristics of cryptobenthics, showing that they have disproportionately high reproductive and larval supply rates, but also high mortality, relative to other major reef fishes. On this basis, the authors suggest that cryptobenthics may help to fuel the rapid nutrient- and energy-recycling rates that typify coral reefs (*2*, *3*). Their main finding was that as a result of this high mortality rate, cryptobenthic fishes contribute ~60% of the "consumed fish" biomass in coral reefs (and ~20% of fish production), and thereby represent a large and previously unknown source of energy that supports coral reef fish production.

We applaud the authors for bringing to light these important life history traits, but we argue that their estimates of the contribution of cryptobenthic fish to fish production are an artifact of their analyses. Brandl *et al.* used a numerical simulation of larval supply and growth to calculate the relative production of cryptobenthic species after a single year. In doing so, they neglect the contributions of fish that live more than 1 year, thus vastly overestimating the contributions of cryptobenthic fishes to fish production on coral reefs.

The stated goal of the study was to estimate the extent to which cryptobenthic fish species "promote internal reef fish biomass production" (i.e., secondary production). Instead of focusing on the contribution of cryptobenthics to secondary production, defined as the biomass accumulated by a population per unit time (*4*), Brandl *et al.* focused primarily on quantifying their contribution to "consumed biomass," which they define as all biomass lost to mortality (i.e., all fish that die are consumed) (*1*). Consumed biomass is an inherent component of production, as it represents biomass produced in previous time steps that, once eaten, will not continue to produce biomass. But it is not a good proxy for production. Consider a population with a new cohort of three individual recruits that die over time (Fig. 1A). At time t_1, the contribution to production by all individuals is the same; only the black individual has died and thus contributes 100% to consumed biomass. By t_3, the red individual contributes much more to production because it has not died, but has contributed nothing to consumed biomass. When all fish die, production and consumed biomass are equal. This conceptual figure illustrates two things: (i) Consumption is not a good proxy for production because fish that are not consumed still contribute to secondary production, and (ii) the timing at which estimates are measured is critical to estimates of both production and consumption.

To quantify the importance of cryptobenthic fish to coral reef fish production, Brandl *et al.* used a numerical simulation in which cohorts of 3000 larvae (~65% of which are cryptobenthic species on average) recruit to a reef every day for 365 days [supplementary materials of (*1*)] (Fig. 1B, blue box). Using family-level growth and mortality rates, Brandl *et al.* summed the new biomass produced and the consumed biomass (assuming all fish that die are consumed) of all individuals in their simulation over the first 365 days. Using this model, they found that cryptobenthics represent ~60% of the consumed biomass (i.e., fish that died) and contribute ~20% of total fish production in this first year (with the re-

maining percentages contributed by non-cryptobenthic species).

An important finding of Brandl *et al.* is the high mortality of cryptobenthic fishes, relative to non-cryptobenthic fishes, that occurs in the first year. However, by calculating consumed biomass and production after only 365 days, they ignored all production that occurs from larval recruits that survived past the first year (predominantly non-cryptobenthic fishes). In essence, their model is populating a reef with larval recruits that is otherwise devoid of fish, under the assumption that the recruits are the only fish that can contribute to production. As such, calculating consumed biomass and production after only the first year is tantamount to making this calculation at t_2, assuming that the black and blue fish are cryptobenthics (Fig. 1A)—that is, they represent the majority of larval recruits (*1*). The stated goal of the study was to estimate the contribution of larval recruits to "reef fish biomass production." Without including surviving individuals in their model, the contribution of cryptobenthics to fish production or consumed biomass is overestimated. To avoid these issues, estimating production by recruits requires that cohorts are tracked over longer time horizons, so as to account for differential mortality rates among species (Fig. 1A).

Using the authors' published code and parameters [supplementary materials of (*1*)], we recalculated production and consumed biomass in two ways. First, we tracked 8000 individual cohorts until <1% of individuals remained in each. The average contribution of cryptobenthic fish to total fish production across all cohorts after 2, 3, 10, and 20 years was 3.3%, 2.2%, 1.1%, and 1.0%, respectively (28.4%, 19.0%, 7.7%, and 6.0% for "consumed biomass"; Fig. 2, A and C). Note that extending the simulations by only 1 to 2 years markedly reduces the estimated contribution of cryptobenthics to fish production, thereby demonstrating that the high levels of production from non-cryptobenthic species are not reliant on long-lived, large individuals. Applying a second community-level approach where a new cohort was added per day following Brandl *et al.*, but extending the simulation until <1% of the individuals in the initial cohorts remained (19 to 20 years; Fig. 1B), we found a similar result: Cryptobenthics contribute 1.0% to produced biomass and 6.4% to consumed biomass.

The key mechanism provided by Brandl *et al.* for the importance of cryptobenthic fishes is their high turnover. To calculate turnover, Brandl *et al.* divided the "consumed biomass" by standing biomass, essentially providing a measure of how fast the cohort of cryptobenthics was consumed in the first year—a measure that is circular to their model with implicitly high mortality rates for cryptobenthics. Turnover is typically quantified as production divided by biomass (Brandl *et al.* call this "net turnover"), which provides an important measure of how fast biomass is being replaced via production. In their supplementary materials, Brandl *et al.* themselves show that turnover (i.e., production/biomass) is greater for non-cryptobenthic fish.

We applaud the contribution of this study for highlighting the unique life history characteristics of these poorly understood fishes, and much of the information generated by Brandl *et al.* is important. We also recognize that in many cases Brandl *et al.* use conservative approaches to estimate the contribution of cryptobenthic fish to fish production. But we disagree that cryptobenthic species "underpin reef fish biomass production" as stated by Brandl *et al.*, and we show here that their contribution is likely much lower than the estimates reported by these authors.

REFERENCES

1. S. J. Brandl, L. Tornabene, C. H. R. Goatley, J. M. Casey, R. A. Morais, I. M. Côté, C. C. Baldwin, V. Parravicini, N. M. D. Schiettekatte, D. R. Bellwood, Demographic dynamics of the smallest marine vertebrates fuel coral reef ecosystem functioning. *Science* **364**, 1189–1192 (2019). doi:10.1126/science.aav3384 Medline
2. B. G. Hatcher, Coral reef primary productivity: A beggar's banquet. *Trends Ecol. Evol.* **3**, 106–111 (1988). doi:10.1016/0169-5347(88)90117-6 Medline
3. B. G. Hatcher, Coral reef primary productivity. A hierarchy of pattern and process. *Trends Ecol. Evol.* **5**, 149–155 (1990). doi:10.1016/0169-5347(90)90221-X Medline
4. F. H. Rigler, J. A. Downing, in *A Manual on Methods for the Assessment of Secondary Productivity in Fresh Waters*, J. A. Downing, F. H. Rigler, Eds. (Blackwell, 1984), pp. 19–58.

7 August 2019; accepted 27 November 2019
Published online 20 December 2019
10.1126/science.aay9321

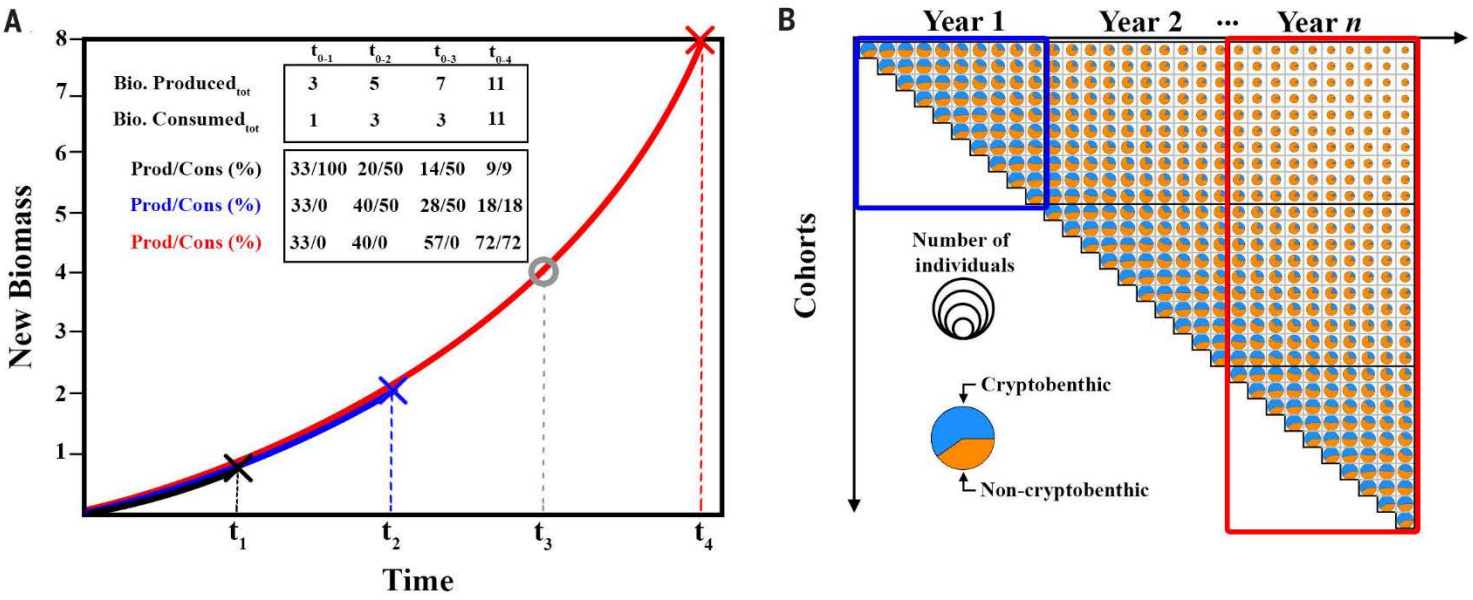

Fig. 1. Conceptual models illustrating the importance of timing for calculating secondary production. (A) Calculating secondary production (i.e., the production of new biomass) following individual cohorts through to death. X indicates when an individual dies; O indicates that it is alive and included in production. The inset shows the total biomass produced and consumed, as well as the percent contributions of each individual to produced and consumed biomass per time step [Prod/Cons (%)]. This illustrates the importance of allowing all individuals to die before calculating production and highlights that considering only those individuals that die at certain time steps is not a useful proxy for production. (B) Calculating secondary production following multiple cohorts until all individuals from the initial cohort die. At each time step, a new cohort enters the system (represented by different rows, with the size of the circle indicating the number of individuals remaining over time). The colored portions of each circle represent the proportion of individuals belonging to cryptobenthic (blue) and non-cryptobenthic (orange) fishes. The proportion of cryptobenthic fishes (blue) diminishes rapidly because of their high mortality rate. Brandl *et al*. (*1*) calculated production for the first year only (blue box). Doing so inflates the production of cryptobenthics because it omits the additional contribution to production by all other cohorts in the community that survive beyond that time period. In essence, their model assumes that the larval recruits are the only fishes on a reef that contribute to production, as if there were no fish present starting at day 0 in their simulation. This has a greater effect on inflating consumed biomass because of the disproportionate amount of cryptobenthic larvae that die shortly after settlement (death is assumed to be by consumption).

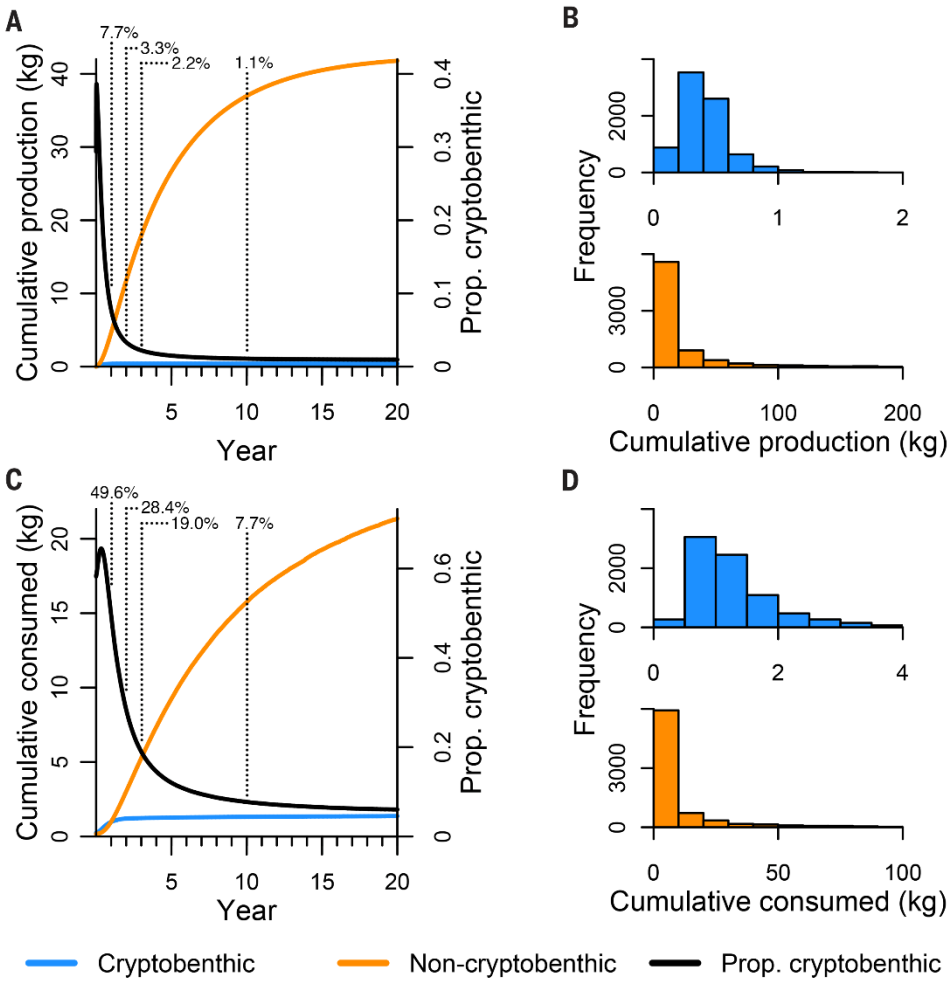

Fig. 2. Production and consumed biomass of cryptobenthic and non-cryptobenthic species using the data and model from Brandl *et al*. carried out to 20 years (<1% of individuals remaining). (**A** and **C**) Average cumulative production (A) and consumption (C) of cryptobenthic (blue) and non-cryptobenthic (orange) species across 8000 stochastic cohorts. Vertical dashed lines represent the percent contribution of cryptobenthic species to production (or consumed biomass) at 1, 3, 5, and 10 years. Brandl *et al*. calculated the mean contribution to consumed biomass and production by averaging proportions, which can only be done when the denominator used to calculate each proportion is the same (not the case here). We calculated proportions by summing the production (or consumed biomass) of cryptobenthic species (black) and dividing by the sum of the total fish production (or consumed biomass) for each time step across all 8000 simulated cohorts. (**B** and **D**) Histograms of the cumulative production (B) and consumption (D) of cryptobenthic species after 20 years for all 8000 simulations. The *x* axis for non-cryptobenthic species is truncated to better show the distribution shape (<1% of simulations are omitted).

Cite as: S. J. Brandl *et al.*, *Science* 10.1126/science.aaz1301 (2019).

Response to Comment on "Demographic dynamics of the smallest marine vertebrates fuel coral reef ecosystem functioning"

Simon J. Brandl[1,2]*, Renato A. Morais[3,4], Jordan M. Casey[5,6,7], Valeriano Parravicini[5,6], Luke Tornabene[8], Christopher H. R. Goatley[9], Isabelle M. Côté[1], Carole C. Baldwin[10], Nina M. D. Schiettekatte[5,6], David R. Bellwood[3,4]

[1]Department of Biological Sciences, Simon Fraser University, Burnaby, BC V5A 1S6, Canada. [2]Tennenbaum Marine Observatories Network, Smithsonian Institution, Edgewater, MD 21037, USA. [3]ARC Centre of Excellence for Coral Reef Studies, James Cook University, Townsville, QLD 4811, Australia. [4]College of Science and Engineering, James Cook University, Townsville, QLD 4811, Australia. [5]PSL Université Paris: EPHE-UPVD-CNRS, USR 3278 CRIOBE, Université de Perpignan, 66860 Perpignan, France. [6]Laboratoire d'Excellence "CORAIL," Perpignan, France. [7]Department of Invertebrate Zoology, National Museum of Natural History, Smithsonian Institution, Washington, DC, USA. [8]School of Aquatic and Fishery Sciences and Burke Museum of Natural History and Culture, University of Washington, Seattle, WA 98105, USA. [9]Function, Evolution and Anatomy Research Lab and Palaeoscience Research Centre, School of Environmental and Rural Science, University of New England, Armidale, NSW 2351, Australia. [10]Department of Vertebrate Zoology, National Museum of Natural History, Smithsonian Institution, Washington, DC, USA.

*Corresponding author. Email: simonjbrandl@gmail.com

Allgeier and Cline suggest that our model overestimates the contributions of cryptobenthic fishes to coral reef functioning. However, their 20-year model ignores the basic biological limits of population growth. If incorporated, cryptobenthic contributions to consumed fish biomass remain high (20 to 70%). Disturbance cycles and uncertainties surrounding the fate of large fishes on decadal scales further demonstrate the important role of cryptobenthic fishes.

In their comment on our study, which highlighted the role of cryptobenthic fishes in coral reef trophic dynamics (*1*), Allgeier and Cline (*2*) question the value of consumed biomass and consumption turnover as components of reef fish productivity and posit that the contributions of cryptobenthic fishes to consumed biomass decrease greatly when our theoretical model is extended to ~20 years, rather than the 365 days used originally. Their comment provides a welcome opportunity to elaborate on the dynamics that underpin the role of cryptobenthic fishes on coral reefs.

We fully agree that consumed biomass is not the same as traditional productivity; rather, it represents the component of production that is transferred to the next trophic level. In fact, we noted that "cryptobenthics appear to make negligible contributions to net productivity and standing fish biomass" when highlighting their role as rapidly replenishing vectors of energy to larger-bodied fishes, a role we quantify as consumed biomass (*1*). Similarly, consumption turnover (our metric) and net turnover [traditionally defined as production/biomass, the P/B ratio (*3*)] quantify distinct aspects of how quickly particles move through the food web. Net turnover describes how quickly newly produced particles are stored as standing biomass, whereas consumption turnover quantifies how rapidly they are passed to larger consumers.

Allgeier and Cline present a series of models to show that (i) at a hypothetical endpoint, when all individuals have died, consumed and produced biomass are equal (this is axiomatic); (ii) without replenishment, cryptobenthic populations rapidly decrease in net produced and consumed biomass [this is also axiomatic, given that small sizes and short lives are the hallmarks of cryptobenthic life history (*4*)]; and (iii) when our model is extended over ~20 years, the contribution of cryptobenthic fishes decreases even when populations are replenished.

Extending short-term simulations of individual growth and mortality to decadal scales introduces a range of unaccounted meta-community, community, and population dynamics and, as such, should be interpreted with caution. Most important, however, Allgeier and Cline's simulations disregard basic size-dependent limits on population growth. After 20 years, the abundance of large reef fishes in Allgeier and Cline's model (~70% of individuals) greatly surpasses that of cryptobenthics (~30%) (Fig. 1A), which sharply contrasts with empirical data. Empirical densities from the three distinct locations in our original paper (*1*) show that

cryptobenthic fishes account for ~66% of individual fishes on reefs [but can, in some cases, account for up to 95% (*5*)], which reflects the positive relationship between body size and self-thinning rates in populations that constrain larger-bodied individuals to lower densities (*6*). This suggests that Allgeier and Cline's simple temporal extension of our model greatly exceeds the ecologically plausible population growth of large reef fish species. The well-documented temporal clustering of large reef fish recruitment (and resulting density-dependent mortality) compared to the continuous settlement, growth, and death of cryptobenthics (*7*) further aggravates this issue. Our paper highlighted the omissions of density dependence and recruitment pulses in our original, short-term model as simplifications that likely reduce the contribution of cryptobenthics to consumed biomass [supplementary materials of (*1*)].

Nonetheless, Allgeier and Cline's comments provide a valuable opportunity to devise a more nuanced model that integrates additional real-world processes. We reran their 20-year simulations with a simple, empirically supported density constraint on large reef fish densities relative to cryptobenthics (based on the proportions detailed above) where recruits experience instantaneous mortality if the population threshold is reached. The extension of the model time frame results in contributions of cryptobenthics to consumed biomass after 2, 3, 10, and 20 years of 43%, 32%, 20%, and 19%, respectively; these proportions are invariably more than three times the estimates of Allgeier and Cline (*2*) (Fig. 1B). Furthermore, Allgeier and Cline misinterpret figure S6E of (*1*) when claiming that large reef fishes have higher net turnover than cryptobenthics (*2*). The figure tracks single cohorts over 365 days, rather than summarizing cumulative contributions that incorporate replenishment. In the extended model, the P/B ratio (i.e., net turnover) of cryptobenthics increases from ~300% to ~390% $year^{-1}$ after 22 years, whereas that of large reef fish declines from 130% to 50% $year^{-1}$ (Fig. 1C).

Although the temporal extension of our model indeed reduces the contribution of cryptobenthics to consumed biomass, even when simple group-specific population thresholds are imposed, ecological dynamics operating on reef fish communities over larger temporal scales cannot be disregarded (Fig. 2). Given sufficient time without disturbance, large-bodied, mature individuals perish and supply a higher contribution to consumed biomass than do cryptobenthics. However, this contribution hinges on spatial and temporal uncertainties. Spatially, in the absence of fishing, most large, mature fishes (e.g., large groupers) will eventually fall prey to large, transient predators [e.g., (*8*)], which transfer energy and nutrients across seascapes (*9*) and represent a net export for reefs. Where fishing occurs, the largest fishes are preferentially caught and consumed (*10*), which again removes energy and nutrients from the reef and diminishes the contribution of large reef fishes to consumed biomass. Temporally, cyclical disturbances (e.g., tropical storms) are likely to alter population dynamics by causing mortality for large individuals [e.g., (*11*)]. Such disturbances occur at much higher frequencies than the 20-year time frame of our model (*12*), thus bringing into question the steady equilibrium of reef fish assemblages in extended simulations.

Overall, through their demonstrated population dynamics, cryptobenthic reef fishes provide a continuously available and predictable daily source of energy and nutrients for predators at local scales despite having a relatively small direct contribution to the traditional metric of secondary production. Over longer time frames and entire seascapes, the contribution of larger, longer-lived species can increase. However, even in the most extreme (and unlikely) scenarios, the daily contributions of cryptobenthic fishes still amount to 20% of consumed fish biomass, and our revised model yields a maximum contribution of 68% after 70 to 80 days. Our original estimate lies firmly within this range. Thus, regardless of the temporal and spatial scales considered, cryptobenthic reef fishes provide a sustained and sustaining resource on coral reefs.

REFERENCES

1. S. J. Brandl, L. Tornabene, C. H. R. Goatley, J. M. Casey, R. A. Morais, I. M. Côté, C. C. Baldwin, V. Parravicini, N. M. D. Schiettekatte, D. R. Bellwood, Demographic dynamics of the smallest marine vertebrates fuel coral reef ecosystem functioning. *Science* **364**, 1189–1192 (2019). doi:10.1126/science.aav3384 Medline
2. J. E. Allgeier, T. J. Cline, Comment on "Demographic dynamics of the smallest marine vertebrates fuel coral reef ecosystem functioning." *Science* **366**, eaay9321 (2019).
3. K. R. Allen, Relation between production and biomass. *J. Fisher. Res. Board Canada* **28**, 1573–1581 (1971). doi:10.1139/f71-236
4. S. J. Brandl, C. H. R. Goatley, D. R. Bellwood, L. Tornabene, The hidden half: Ecology and evolution of cryptobenthic fishes on coral reefs. *Biol. Rev. Camb. Philos. Soc.* **93**, 1846–1873 (2018). doi:10.1111/brv.12423 Medline
5. G. R. Galland, B. Erisman, O. Aburto-Oropeza, P. A. Hastings, Contribution of cryptobenthic fishes to estimating community dynamics of sub-tropical reefs. *Mar. Ecol. Prog. Ser.* **584**, 175–184 (2017). doi:10.3354/meps12364
6. E. P. White, S. K. Ernest, A. J. Kerkhoff, B. J. Enquist, Relationships between body size and abundance in ecology. *Trends Ecol. Evol.* **22**, 323–330 (2007). doi:10.1016/j.tree.2007.03.007 Medline
7. C. D. Lefèvre, K. L. Nash, A. González-Cabello, D. R. Bellwood, Consequences of extreme life history traits on population persistence: Do short-lived gobies face demographic bottlenecks? *Coral Reefs* **35**, 399–409 (2016). doi:10.1007/s00338-016-1406-3
8. J. Mourier, J. Maynard, V. Parravicini, L. Ballesta, E. Clua, M. L. Domeier, S. Planes, Extreme inverted trophic pyramid of reef sharks supported by spawning groupers. *Curr. Biol.* **26**, 2011–2016 (2016). doi:10.1016/j.cub.2016.05.058 Medline
9. D. J. McCauley, H. S. Young, R. B. Dunbar, J. A. Estes, B. X. Semmens, F. Micheli, Assessing the effects of large mobile predators on ecosystem connectivity. *Ecol. Appl.* **22**, 1711–1717 (2012). doi:10.1890/11-1653.1 Medline

10. N. Graham, N. Dulvy, S. Jennings, N. Polunin, Size-spectra as indicators of the effects of fishing on coral reef fish assemblages. *Coral Reefs* **24**, 118–124 (2005). doi:10.1007/s00338-004-0466-y

11. J. A. Khan, C. H. Goatley, S. J. Brandl, S. B. Tebbett, D. R. Bellwood, Shelter use by large reef fishes: Long-term occupancy and the impacts of disturbance. *Coral Reefs* **36**, 1123–1132 (2017). doi:10.1007/s00338-017-1604-7

12. J. H. Connell, T. P. Hughes, C. C. Wallace, A 30-year study of coral abundance, recruitment, and disturbance at several scales in space and time. *Ecol. Monogr.* **67**, 461–488 (1997). doi:10.1890/0012-9615(1997)067[0461:AYSOCA]2.0.CO;2

21 September 2019; accepted 27 November 2019
Published online 20 December 2019
10.1126/science.aaz1301

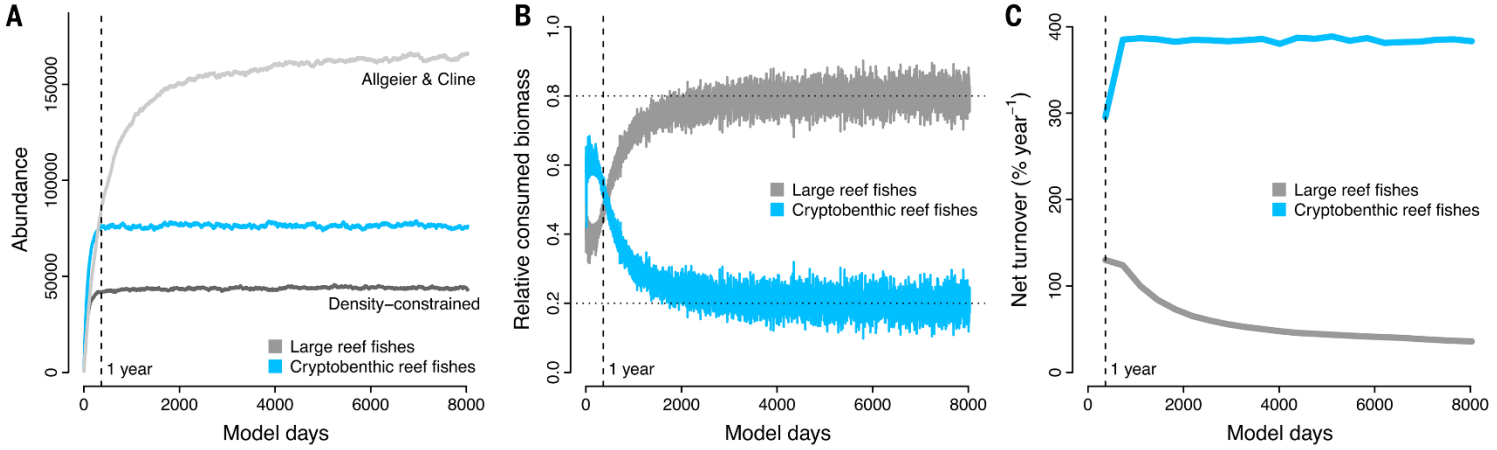

Fig. 1. Contribution of cryptobenthic and large reef fishes to energy and nutrient fluxes over time. (**A**) Abundance of cryptobenthic reef fishes (blue line) and large reef fishes (light gray line) over 8000 days (~22 years). In Allgeier and Cline's simulation, large reef fishes greatly outnumber cryptobenthic individuals (~70% versus 30%), which is at odds with empirical data and ecological theory. The dark gray trajectory shows constrained large reef fish densities based on empirical data from the supplementary materials of (*1*). (**B**) Daily contributions to consumed biomass over ~22 years under the density-constrained simulations. Cryptobenthic reef fishes account for a minimum of ~20% consumed biomass, which is more than three times the estimate of Allgeier and Cline. (**C**) Net turnover of cryptobenthic and large reef fishes, averaged for each year (starting at the end of year 1). Contrary to Allgeier and Cline's interpretation, cumulative cryptobenthic turnover far exceeds that of large reef fishes after 1 year and increases through time.

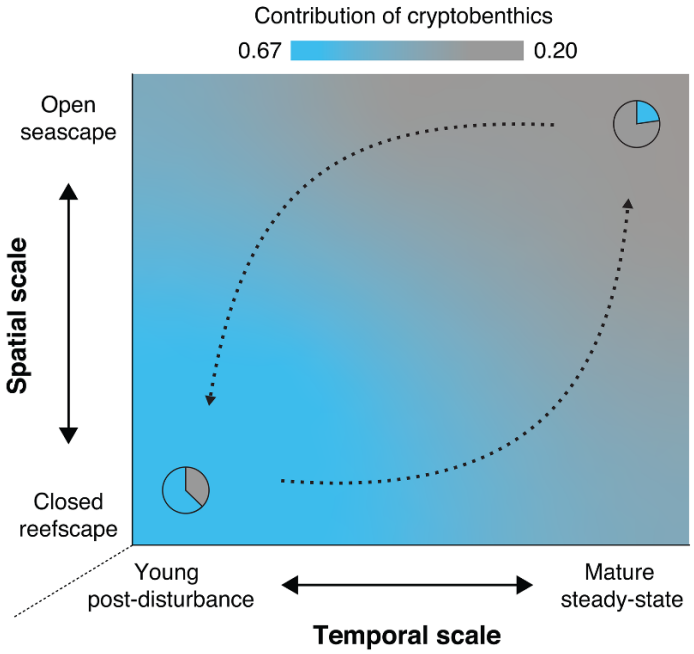

Fig. 2. Conceptual diagram highlighting spatial and temporal factors that determine the trophic contribution of cryptobenthic fishes. Over short time frames (as created by frequent pulse disturbances or fishing pressure) and within a spatially constrained reefscape, cryptobenthics dominate the production of consumed fish biomass. Over longer time frames that result in mature, steady-state fish assemblages and across entire seascapes, the role of larger species may increase, but little is known about the ultimate fate of large-bodied species. Cryptobenthic reef fishes, in contrast, do not die of old age.

AAAS Local Science Engagement Network gets under way

Scientists seek to inform Missouri and Colorado policy-makers and climate solutions for communities

By **Anne Q. Hoy**

The American Association for the Advancement of Science has partnered with pilot initiatives in Missouri and Colorado to integrate scientists with local and state policy-makers, community stakeholders, and the public to leverage scientific evidence and inform efforts to address varied local impacts of climate change.

The AAAS Local Science Engagement Network seeks to forge alliances among diverse and multidisciplinary groups of scientists, civic leaders, academic institutions, decision-makers, and representatives of scientific societies to advance regional responses to the flooding of agricultural lands, impacts of urban heat islands and droughts in Missouri, and premature snow melts, droughts, and suburb-encroaching wildfires in Colorado.

"Instead of focusing on global theoretical concepts of climate change or impacts that are happening in far-flung communities in this country or internationally, we want local scientists to talk about how they can inform local decisions that improve the lives of people sitting in the room," said Dan Barry, director of AAAS's Local Science Engagement Network.

More than a year in the making, the program was initiated by leaders in the scientific community and AAAS members seeking to establish a nationwide plan for supporting networks of scientists to engage with policy-makers and contribute solutions to the range of challenges facing local and state communities.

The climate work of the Local Science Engagement Network is supported by the Grantham Foundation for the Protection of the Environment, Benjamin and Ruth Hammett, Reinier and Nancy Beeuwkes, Rush Holt and Margaret Lancefield, the Atkinson Family Foundation, Gary and Denise David, the estate of Abraham Ringel, and other generous donors.

Going forward, the program aims to set up networks in three additional states, Barry said, to assist communities and state policy-makers in implementing effective solutions to challenges raised by climate change with the help of fact-based and impartial scientific knowledge. The program's current theme may grow into exploring other climate-related impacts, including rural poverty economy and public health concerns, he added.

The pilot network reflects a strategy long recognized by AAAS in expanding scientific engagement with the public, through the articulation of common goals, activities, and structures. Participants in Missouri and Colorado have pledged to take part in civic engagement that elevates the capacity of science through a host of public outreach activities and events.

Communities of scientists also are being assembled by program leaders in each state to serve as an advisory council made up of topical scientific experts willing to participate in policy discussions; share fact-based research drawn from local, regional, and national analyses; and author topical reports. The two pilot programs will collect scientific analyses and reports in electronic libraries to

PHOTO: CAPTAIN DARIN OVERSTREET/U.S. AIR FORCE

Published by AAAS

A Colorado wildfire in 2013 was the state's most destructive.

make such materials more accessible to stakeholders and the public.

"We're hoping that positive solutions, real solutions will take root and that we'll be able to start to engineer a little bit of social change where the value of science is reasserted," said Barry. "Part of the problem we seek to address is that science has been intentionally and unintentionally marginalized as a tool for decision-making in this country."

In Missouri and Colorado, participating scientists will be offered communications training through AAAS Communicating Science workshops that coach participants on fundamental communications techniques and on how best to engage with local and state policy-makers. The workshops, developed by the AAAS Center for Public Engagement with Science and Technology, are tailored to help scientists effectively share information with the public.

Local leaders now being selected in the two states offer a wealth of scientific experience. In Missouri, Rachel Owen, a Ph.D. soil scientist, will become program director of the Missouri Local Science Engagement Network when it launches in January.

The framework for the Missouri Local Science Engagement Network calls on Owen to ensure that the network provides science communications, civic engagement, and effective advocacy from AAAS and other partners and holds regular networking events to facilitate conversations among scientists, policy-makers, and local leaders.

The network plan in Missouri will enable the program to identify the diverse needs of different demographic, economic, and cultural regions in a state that spans from the sparsely populated Ozarks to more populated urban and suburban communities. The plan pledges to engage local stakeholders to ensure that evidence-based perspectives woven into climate solutions apply to diverse communities.

Colorado State Senator Steve Fenberg (left) and Max Boykoff host a climate conversation.

Owen already has received confirmations from seven scientists to serve on the Missouri Local Science Engagement Network's advisory council. So far, the council has begun meeting to discuss everything from policy opportunities to communications and advocacy training. "We're going to try to make it as easy as possible for them to bring science to the conversation," she said.

The initial council members represent a varied group, including university faculty, representatives of the nonprofit The Nature Conservancy, and climate scientists, some of whom are active in Missouri's Climate Action Coalition, a group of elected officials and community leaders throughout Kansas City who work with state policy-makers.

The council also includes Barbara Schaal, a former AAAS president, an evolutionary biologist, and dean and professor at Washington University in St. Louis. Schaal, like many AAAS leaders, has long advocated the need for the science community to engage with policy-makers and the public about the value of science.

In Colorado, Maxwell Boykoff, director of the Center for Science and Technology Policy Research at the University of Colorado Boulder, and Matthew Druckenmiller, a research scientist at the National Snow and Ice Data Center in the Cooperative Institute for Research in Environmental Sciences, also are at work developing the Colorado Local Science Engagement Network set to launch in January.

The Colorado network will produce an annual report to be made up of focused and concise briefing papers on timely policy topics and explore noteworthy scientific advances. The briefs will be authored by a multidisciplinary group of Colorado scientists. Essays written by decision-makers, practitioners, and stakeholders also will be included to provide a mix of perspectives.

The report is intended to ensure that the latest scientific research is made publicly available to inform climate policy decisions facing Colorado lawmakers and to build a diverse network of scientists throughout the state and give communities opportunities to integrate science into policy discussions and decision-making processes.

Boykoff said that community teams will be developed to help frame strategies to more effectively fold science into local policy debates and response proposals, particularly as they relate to addressing climate impacts across the state.

Already, plans are in place to contribute to policy conversations stemming from a climate action plan Boulder adopted 3 years ago. The city plan calls for 80% reductions in greenhouse gas emissions by 2050, 80% reductions of emissions generated by city government operations, and a transformation to 100% renewable electricity by 2030. The plan has led Boulder to adopt a Climate Mobilization Action Plan that places "equity and resilience" at the center of its implementation, Boykoff noted.

"AAAS and the Local Science Engagement Network is going to catalyze all kinds of important connections that need to be made because Boulder is very different than the communities in the state's Western Slope," Boykoff said. "To make those links, we really want to reach beyond the leading actors and engage with folks that might otherwise not be considering too carefully the various science-related challenges that actually impact their everyday lives."

A key objective for Druckenmiller is to establish a network of Colorado scientists who can identify climate change impacts; describe how they affect people, ecosystems, and response plans; and incorporate such information into the annual report.

Challenges facing Colorado are not insignificant, he noted. About 70% of the state's annual water supply comes from snow melt. Yet, warming temperatures and the increasing variability of snow cover require a better scientific understanding of how the state's snowpack and water resources are changing, he said. In addition, the increasing frequency and severity of wildfires are related to fluctuating water resources.

Although the Colorado state legislature's regular session lasts no more than 120 days annually, interim committees continue to work through issues outside of the legislative session. The new initiative aims to put forward a network of scientists to serve as a resource for legislators during that interim period when they are beginning to craft legislation.

The off-session period also is a time when lawmakers visit, talk, and listen to voters. This period, Druckenmiller said, is a perfect time for scientists to not just serve as a significant resource for lawmakers but, importantly, also to reach out to constituents.

"This project is not only about engaging policies," Druckenmiller said. "It gets done by engaging the public."

PHOTO: KATIE WEEMAN/CIRES/UNIVERSITY OF COLORADO BOULDER

Published by AAAS

RESEARCH

IN *SCIENCE* JOURNALS

Edited by **Michael Funk**

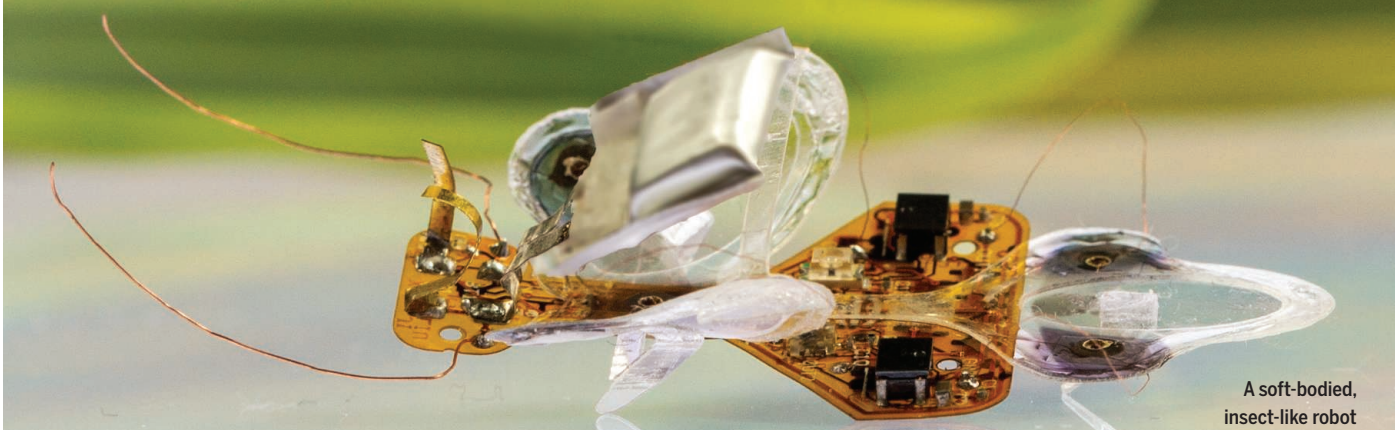

A soft-bodied, insect-like robot

PHOTO: ALBERTO PECONIO

SOFT ROBOTS

Self-contained, sturdy, and small

Many people prefer not to encounter insects, but engineers admire them for their flexibility, multifunctionality, and durability. Ji *et al*. designed insect-scale, lightweight, fast, legged soft robots that move using low-voltage stacked dielectric elastomer actuators (DEAs). The robots, called DEAnsects, do not need to be tethered to a power supply and contain ultralight onboard control electronics for autonomous navigation of a preprinted path. DEAnsects can even survive an impact from a fly swatter and resume motion after a brief pause. —TW

Sci. Robot. **4**, eaaz6451 (2019).

NEURODEVELOPMENT

Hyperexcitable neurons in brain organoids

Individuals with Angelman syndrome experience intellectual disability and seizures throughout their lives. In this condition, ubiquitin-mediated degradation of a key potassium channel is disrupted, allowing for the neuronal excitability and network synchronization that leads to seizure. Sun *et al*. used brain organoid technology to study what happens in human neurons with a mutation in a ubiquitin ligase that is implicated in Angelman syndrome. In these in vitro models and in a mouse model of Angelman syndrome, antagonists for the potassium channel normalized neuronal excitability. —PJH

Science, this issue p. 1486

MECHANOCHEMISTRY

Redox catalysis in a ball mill

Mixing solid reactants in a ball mill is a promising means of avoiding the copious solvent waste associated with most chemical syntheses. Kubota *et al*. now report that adding a piezoelectric catalyst to the mix can promote bond formation through apparent electron transfer cycles (see the Perspective by Xia and Wang). Specifically, barium titanate activates aryl diazonium salts toward borylation and coupling with heterocycles in a manner reminiscent of solution-phase photoredox catalysis. The reactions are insensitive to air and were demonstrated up to gram scale. —JSY

Science, this issue p. 1500; see also p. 1456

EMOTION AND LANGUAGE

The diverse way that languages convey emotion

It is unclear whether emotion terms have the same meaning across cultures. Jackson *et al*. examined nearly 2500 languages to determine the degree of similarity in linguistic networks of 24 emotion terms across cultures (see the Perspective by Majid). There were low levels of similarity, and thus high variability, in the meaning of emotion terms across cultures. Similarity of emotion terms could be predicted on the basis of the geographic proximity of the languages they originate from, their hedonic valence, and the physiological arousal they evoke. —TSR

Science, this issue p. 1517; see also p. 1444

SOLAR CELLS

Optimizing surface passivation

Unproductive charge recombination at surface defects can limit the efficiency of hybrid perovskite solar cells, but these defects can be passivated by the binding of small molecules. Wang *et al*. studied three such small molecules—theophylline, caffeine, and theobromine—that bear both carbonyl and amino groups. For theophylline, hydrogen bonding of the amino hydrogen to surface iodide optimized the carbonyl interaction with a lead antisite defect and improved the efficiency of a perovskite cell from 21 to 22.6%. —PDS

Science, this issue p. 1509

Published by AAAS

IMMUNOLOGY

A different way for γδ T cells to bind

The ligands bound by γδ T cell receptors (TCRs) are less well characterized than those of their αβ TCR cousins, which are antigens presented by major histocompatibility complex (MHC) and related proteins. Le Nours *et al*. identified a phenotypically diverse γδ T cell subset in human tissues that reacts to MHC-related protein 1 (MR1), which presents vitamin B derivatives. A crystal structure of a γδ TCR–MR1–antigen complex revealed that some of these TCRs can bind underneath the MR1 antigen-binding cleft instead of recognizing the presented antigen. This work thus uncovers an additional ligand for γδ T cells and reconceptualizes the nature of T cell antigen recognition. —STS

Science, this issue p. 1522

SUPERFLUIDITY

Following vortices around

When stirred, superfluids react by creating quantized vortices. Studying the dynamics of these vortices, especially in the strongly interacting regime, is technically challenging. Sachkou *et al*. developed a technique for the nondestructive tracking of vortices in thin films of superfluid helium-4. Their system contained a microtoroid optical cavity coated by a thin film of helium-4, in which vortices were created by using laser light. When imaging the subsequent dynamics of the vortices, the researchers found that coherent dynamics strongly dominated over dissipation. —JS

Science, this issue p. 1480

MATERIALS SCIENCE

Probing polycrystals' stress

The way that a polycrystalline material deforms is in part determined by internal stresses between and within crystal grains. Hayashi *et al*. developed an x-ray method for mapping the intragranular stresses in a polycrystalline material. They found surprisingly large stresses, which are important for the fundamental understanding of how these materials will fail. This method will work for other materials and provides important information for multiscale deformation modeling. —BG

Science, this issue p. 1492

CANCER

p53 makes a comeback

One reason that cancer cells are so difficult to kill is that they often lack p53, a key tumor suppressor that promotes apoptosis. To address this problem, Kong *et al*. devised a way to restore *p53* gene expression in tumors by delivering *p53* messenger RNA (mRNA) in nanoparticles. To minimize damage to healthy tissues, the authors used redox-responsive nanoparticles, taking advantage of the relative hypoxia of tumors. The use of mRNA rather than DNA provided an additional safeguard because mRNA acts directly in the cytoplasm, without integrating into host cell DNA and introducing mutations. The researchers tested their approach in multiple models in vitro and in vivo, with promising results. —YN

Sci. Transl. Med. **11**, eaaw1565 (2019).

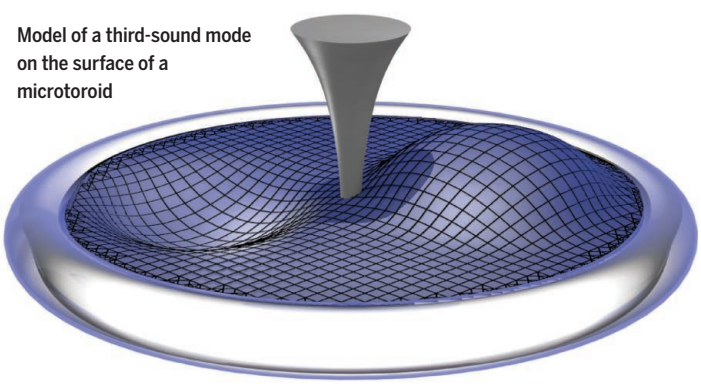

Model of a third-sound mode on the surface of a microtoroid

IN OTHER JOURNALS

Edited by **Caroline Ash** *and* **Jesse Smith**

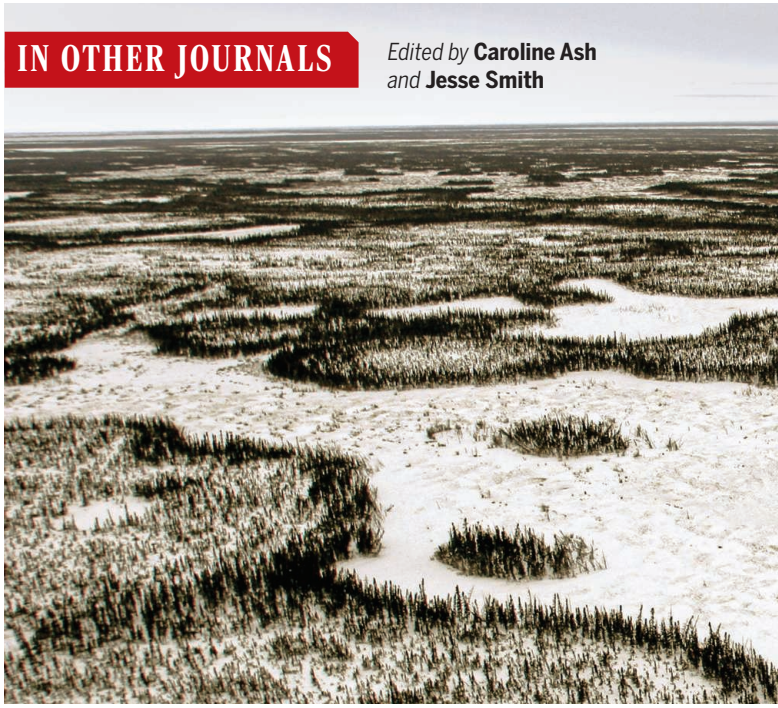

TISSUE REGENERATION

Attending to tendons

For many athletes, an injury to a tendon (the tissue that connects muscle to bone) can be career ending. The regenerative capacity of tendons is limited; even after surgical repair, tendons often do not regain their original mechanical strength because of scar tissue formation. The mechanisms involved in the response to tendon injury are poorly understood. Studying the patellar tendon in mice, Harvey *et al*. found that tendon stem cells and scar tissue progenitor cells reside within the same microenvironmental niche and that the activity of both cell types is stimulated by platelet-derived growth factor receptor α. The shared response to this signaling pathway explains why fibrosis accompanies tendon healing and suggests that therapeutically disentangling the two responses may be difficult. —PAK

Nat. Cell Biol. **12**, 1490 (2019).

SOCIAL PSYCHOLOGY

Repeated fake headlines feel more moral

The repetition of false claims in the news may have downstream effects on information processing. Effron and Raj found that repeatedly viewing a false headline increased approval and reduced perceptions of how unethical it would be to share it with others. Drawing on prior research, the authors hypothesized that repeated exposure increases the extent to which information feels true, even when participants know it is not. This intuitive feeling of truth is then used as an incorrect cue to signal the moral acceptability of sharing. These results suggest that news headlines that repeat false claims may inadvertently improve the moral standing of the speakers of those claims. —TSR

Psychol. Sci. 10.1177/0956797619887896 (2019).

BIOMINERALIZATION

Getting attached early

Carbonate biomineralization in a variety of organisms relies on a crystallization process whereby small calcium carbonate particles directly attach to one another to grow hard parts like shells, spines, and skeletons. Although this mechanism is reasonably widespread today, Gilbert *et al*. wondered how far

CREDITS (FROM LEFT): SACHKOU *ET AL.*; AGEFOTOSTOCK/ALAMY STOCK PHOTO

Published by AAAS

PHOTO: SPORTSPHOTO/ALAMY STOCK PHOTO

Aerial view of the Canadian taiga in northern Manitoba

CLIMATE ECOLOGY

Trees stumped

As global temperatures rise, the distribution of ecological communities will shift, and their composition will change. Other things being equal, tree communities in the northern temperate zone are expected to expand northward. However, this will not be a seamless migration. Solarik *et al*. assessed the factors affecting the potential spread of temperate-zone trees into the boreal forest zone in northeastern North America. They found that substrate conditions, especially decaying wood and conifer needle cover, inhibit germination and establishment of temperate tree seedlings at the temperate-boreal transition. Hence, the northward progress of the temperate forest is likely to be patchy. —AMS

J. Ecol. 10.1111/1365-2745.13311 (2019).

back they could find evidence of a similar process. By studying a characteristic texture that develops from crystallization by particle attachment, they identified this type of mineralization in a wide range of fossils. Particle attachment likely occurred as far back as the Cambrian and developed independently in different species. —BG

Proc. Natl. Acad. Sci. U.S.A. **116**, 17659 (2019).

AGING

Inside the matrix

By performing a screen in human fibroblasts to detect genes that help cells survive the stress of protein misfolding in the endoplasmic reticulum (ER stress), Schinzel *et al*. detected the gene encoding transmembrane protein 2 (TMEM2), which is a cell-surface hyaluronidase active in the extracellular matrix. TMEM2 acted independently of the canonical unfolded-protein response pathways in the ER, instead relying on the cell surface receptor CD44 and stress-activated mitogen-activated protein kinase signaling. Like ER stress, disruptions in the extracellular matrix are seen in aging, and enhanced hyaluronic acid synthesis is thought to be one of the ways that the naked mole-rat, a mammal known for its longevity, is protected from cancer. Thus, such signaling from glycosaminoglycan metabolism may have broad implications in health and disease. —LBR

Cell **179**, 1306 (2019).

ROBOT BEHAVIOR

Dave versus HAL 9000

Cooperation between people depends on a willingness to establish common ground. Zanatto *et al*. asked how the basic rules of human cooperation apply when the other entity is a robot that has as much decision-making range as a human (like HAL 9000 in the film *2001: A Space Odyssey*). In a money-investment game in which cooperativity enhanced gain, just as between two humans, the human-robot pair rewarded cooperativity and punished selfishness. But the human response was tuned according to whether the game was more or less successful than expected and whether the robot was more anthropomorphic or more machinelike. In a benign setting, the machinelike robot elicited more cooperation from the human game players. In a less rewarding setting, the more anthropomorphic robot elicited more cooperation from the human. The authors speculate that in the more hostile environment, people draw more on social attributes to develop cooperation. —PJH

PLOS ONE **14**, e0225028 (2019).

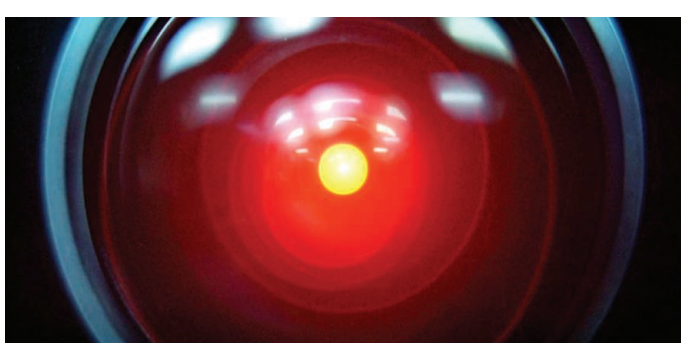

HAL 9000, a nonanthropomorphic robot in the film *2001: A Space Odyssey*

NANOELECTRONICS

A guiding path for graphene circuits

The favorable optical, electronic, and mechanical properties of graphene make it a target material for next-generation opto-electronics. However, that graphene is an atomic layer thick, or several for bilayer and few-layer graphene, can make it challenging to pattern circuits with usual lithographic methods, especially at lateral nanometer scales. Cheng *et al*. show that a carbon nanotube, separated from the graphene by a thin layer of hexagonal boron nitride, creates a one-dimensional conduction path in the graphene that can be controlled by electrostatic gating. Demonstrating that the charged massless quasiparticles, Dirac fermions, can now be confined to an electronic waveguide provides a route to developing a platform for patterning complex graphene circuitry. —ISO

Phys. Rev. Lett. **123**, 216804 (2019).

Published by AAAS

ALSO IN *SCIENCE* JOURNALS

Edited by **Michael Funk**

MOLECULAR BIOLOGY

Biochemical prediction of miRNA targeting

MicroRNAs (miRNAs) regulate most human messenger RNAs and play essential roles in diverse developmental and physiological processes. Correctly predicting the function of each miRNA requires a better understanding of miRNA targeting efficacy. McGeary *et al*. measured binding affinities between six miRNAs and synthetic targets, built a biochemical model of miRNA-mediated repression, and expanded it to all miRNAs using a convolutional neural network. This approach offers insights into miRNA targeting and enables more accurate prediction of intracellular miRNA repression efficacy than previous algorithms. —SYM

Science, this issue p. 1470

TRANSCRIPTOMICS

A blood cell protein-expression atlas

Genome-wide analyses are increasingly providing resources for advances in basic and applied biomedical science. Uhlen *et al*. performed a global expression analysis of human blood cell types and integrated this data with data across all major human tissues and organs in the human protein atlas. This comprehensive compendium allows for classification of all human protein-coding genes with regard to their tissue- and cell-type distribution. —VV

Science, this issue p. 1471

INFECTION

Spying on bacterial signals

Many bacteria produce small molecules for monitoring population density and thus regulating their collective behavior, a process termed quorum sensing. Pathogens like *Pseudomonas aeruginosa*, which complicates cystic fibrosis disease, produce different quorum-sensing ligands at different stages of infection. Moura-Alves *et al*. used experiments in human cells, zebrafish, and mice to show that a host organism can eavesdrop on these bacterial conversations. A host sensor responds differentially to bacterial quorum-sensing molecules to activate or repress different response pathways. The ability to "listen in" on bacterial signaling provides the host with the capacity to fine-tune physiologically costly immune responses. —CA

Science, this issue p. 1472

MITOCHONDRIAL BIOLOGY

VDACs are MOM's ruin

Mitochondrial DNA (mtDNA) is normally kept within the mitochondria. It can be released into the cytosol in response to stress and thus encounter cytosolic DNA sensors, triggering type I interferon responses. During apoptosis, mtDNA release is mediated by macropores in the mitochondrial outer membrane (MOM) created by oligomerization of the proteins BAX and BAK. Kim *et al*. found that during oxidative stress, mtDNA escapes instead through macropores formed by oligomerization of voltage-dependent anion channels (VDACs) (see the Perspective by Crow). In a mouse model of lupus, an inhibitor of VDAC oligomerization diminished mtDNA release and downstream signaling events. This treatment reduced lupus-like symptoms in the model, suggesting a potential therapeutic route for conditions mediated by mtDNA release. —STS

Science, this issue p. 1531; see also p. 1446

CANCER

A cross-kingdom tale of drug resistance

Physicians who treat bacterial infections and those who treat cancer often face a common challenge: the development of drug resistance. It is well known that when bacteria are exposed to antibiotics, they temporarily increase their mutation rate, thus increasing the chance that a descendant antibiotic-resistant cell will arise. Russo *et al*. now provide evidence that cancer cells exploit a similar mechanism to ensure their survival after drug exposure (see the Perspective by Gerlinger). They found that human colorectal cancer cells treated with certain targeted therapies display a transient up-regulation of error-prone DNA polymerases and a reduction in their ability to repair DNA damage. Thus, like bacteria, cancer cells can adapt to therapeutic pressure by enhancing their mutability. —PAK

Science, this issue p. 1473; see also p. 1458

SOLID-STATE PHYSICS

A patterned look into a mysterious phase

A thin superconducting film can become insulating by, for example, exposure to a sufficiently large magnetic field. In between the superconducting and insulating regimes, an intermediate metallic state has been observed whose nature remains unresolved. To study the superconductor–metal insulator transition, C. Yang *et al*. patterned a film of the high-temperature superconductor yttrium barium copper oxide (YBCO) into a network of triangular superconducting islands connected by bridges (see the Perspective by Phillips). The reactive ion-etching process used for patterning reduced the quality of the film in a controlled manner. By increasing the etching time, the film's transport properties could be tuned from superconducting, through metallic, to insulating. The metallic phase exhibited a bosonic character. —JS

Science, this issue p.1505; see also p. 1453

ORGANIC CHEMISTRY

A carbonylation path to a nylon precursor

Adipic acid and its esters are manufactured on a massive scale, primarily to produce nylon. However, the standard route requires large quantities of corrosive nitric acid. J. Yang *et al*. present an efficient alternative route whereby a palladium catalyst adds carbon monoxide to each end of butadiene (see the Perspective by Schaub). Both reactants are available at commodity scale, and the reaction produces no by-products. An optimized bidentate phosphine ligand bearing a pyridine substituent for proton shuttling proved key to attaining the necessary selectivity. —JSY

Science, this issue p. 1514; see also p. 1448

ORGANIC CHEMISTRY

Macrocycles made easy

Macrocycles, which are molecules with large rings of 12 or more atoms, are challenging to produce by intramolecular cyclization because floppy ends tend to join up with another molecule rather than fold back on themselves. Girvin *et al*. identified a foldamer—a short, structured peptide—that can cyclize floppy, dialdehyde substrates through a templated aldol condensation (see the Perspective by Gutiérrez Collar and Gulder). Variation of the residues within the foldamer suggests that its helical structure helps position amine functional groups crucial for catalysis. The authors prepared molecules with a wide range of ring sizes and developed a

Published by AAAS

synthesis for robustol, a macrocycle natural product with a 22-member ring. —MAF

Science, this issue p. 1528; see also p. 1459

NEUROIMMUNOLOGY

Immune surveillance of the brain

The brain is thought to be cut off from the peripheral immune system by the blood-brain barrier, which restricts movement of substances and cells from blood vessels into the brain. However, an emerging view is that the meninges—three distinct layers that surround the brain—orchestrate immune surveillance of the brain and thereby bypass the blood-brain barrier. In a Perspective, Rustenhoven and Kipnis discuss how the meningeal layers modulate immune cell surveillance and removal of waste and how this can go awry in disease. In particular, they discuss how dysfunctional drainage by features of the meninges may promote protein aggregates to build up during neurodegeneration. —GKA

Science, this issue p. 1451

FIBROSIS

Metabolic dysregulation into fibrosis

Excessive fibrosis around alveoli, tiny air sacs that promote gas exchange, prevents the lungs from expanding properly. Yin *et al*. found that the glycolytic enzyme hexokinase 2 (HK2) was abundant in lung fibroblasts from patients with idiopathic pulmonary fibrosis. The profibrotic cytokine transforming growth factor–β (TGF-β) induced HK2 accumulation in mouse and human lung fibroblasts and thus increased glycolysis in these cells. Inhibition of HK2 with the cancer drug lonidamine attenuated the profibrotic actions of TGF-β in fibroblasts and improved lung function in a mouse model of lung fibrosis. These results support a model of HK2-dependent metabolic dysregulation that contributes to lung fibrosis and demonstrates that HK2 is a potential therapeutic target. —AV

Sci. Signal. **12**, eaax4067 (2019).

QUANTUM GASES

Chirality by dissipation

Quantum many-body systems can display exotic dynamics in the presence of dissipation. Dogra *et al*. studied such dynamics in a system consisting of an atomic Bose-Einstein condensate located in an optical cavity and exposed to a standing wave of laser light. Light scattering off the atomic cloud and into the cavity resulted in two distinct, spatially patterned collective modes for the atoms. When the researchers then introduced dissipation to couple the two modes, the system followed a directed circular path through phase space, rotating between the modes. —JS

Science, this issue p. 1496

Published by AAAS

RESEARCH ARTICLE SUMMARY

MOLECULAR BIOLOGY

The biochemical basis of microRNA targeting efficacy

Sean E. McGeary*, Kathy S. Lin*, Charlie Y. Shi, Thy M. Pham, Namita Bisaria, Gina M. Kelley, David P. Bartel†

INTRODUCTION: MicroRNAs (miRNAs) are short RNAs that guide repression of mRNA targets. Each miRNA associates with an Argonaute (AGO) protein to form a complex in which the miRNA recognizes mRNA targets, primarily through pairing to sites that match its extended seed region (miRNA nucleotides 1 to 8) while the AGO protein recruits factors that promote destabilization and translational repression of bound targets. The miRNA targetome is vast, involving most mammalian mRNAs, and miRNA regulatory effects are consequential, with severe developmental or physiological defects often observed after deleting a broadly conserved miRNA (or set of paralogous miRNAs). Deeper understanding of these regulatory roles would be facilitated by a better understanding of miRNA targeting efficacy.

RATIONALE: In principle, targeting efficacy should be a function of the affinity between AGO-miRNA complexes and their target sites, in that greater affinity for a target site would cause increased occupancy at that site and thus increased repression of the target mRNA. However, the set of measured miRNA-target binding affinities has been sparse, and standard thermodynamic models of RNA-RNA pairing poorly predict affinities that have been measured. These limitations have prevented construction of an informative biochemical model of targeting efficacy, such that the best predictive performances have instead relied on indirect, correlative approaches. Here, we adapted RNA bind-n-seq (RBNS) and a convolutional neural network (CNN) to study miRNA-target interactions, thereby obtaining the quantity and diversity of affinity values needed to better understand and predict miRNA targeting efficacy.

RESULTS: Analysis of motifs enriched in RNA sequences bound to the AGO2–miR-1 complex provided unbiased identification of all miR-1 binding sites ≤12 nucleotides (nt) in length, and a newly developed computational procedure simultaneously inferred the relative dissociation constants (K_d values) of all of these sites. Repeating this procedure with AGO2 loaded with five other miRNAs (let-7a, miR-7, miR-124, miR-155, and lsy-6) revealed pronounced miRNA-specific differences in the relative affinities of canonical site types (defined as sites with ≥6-nt contiguous matches to the seed region). The analyses also revealed that each miRNA has a distinct repertoire of noncanonical site types and that dinucleotides flanking both sides of each site influence affinity by as much as 100-fold, primarily because of their impact on site accessibility. Most of the noncanonical sites paired to the seed region but did so with imperfections that reduced affinity to levels below those of the top four canonical sites. Nonetheless, for miR-124 and miR-155, noncanonical sites were identified with affinities approaching that of the top canonical site. These high-affinity noncanonical sites were larger and correspondingly rarer in mRNA sequences, which showed that canonical seed pairing is the most efficient way to achieve high-affinity binding.

ON OUR WEBSITE

Read the full article at http://dx.doi.org/10.1126/science.aav1741

The miRNA-specific differences in site repertoire and relative binding affinities corresponded to differential repression in cells, thereby enabling construction of a biochemical model of miRNA-mediated repression. This biochemical model predicts the occupancy at each site as a function of the K_d measured for the 12-nt sequence encompassing the site. The model outperformed the best correlative model, explaining ~60% of the relevant variation observed after transfecting a miRNA into cells. Although partly attributable to inclusion of noncanonical sites, the improved performance was primarily due to more accurate representation of the effects of canonical sites. Improved performance was extended to miRNAs without RBNS data by building a CNN that was trained with both RBNS-derived K_d values and mRNA-transfection fold-change measurements to predict binding affinity between any miRNA and any 12-nt sequence.

CONCLUSION: We replaced correlative models of targeting efficacy with a principled, biochemical model that explains and predicts about half of the variability attributable to the direct effects of miRNAs on their targets. The success of the model shows that site binding affinity is the major determinant of miRNA-mediated repression. It also shows that although active AGO-miRNA complexes are occupied primarily by canonical sites, noncanonical sites measurably contribute to repression in the cell. Repression efficacy predicted by this model will be available on the TargetScan website to provide improved guidance for placing miRNAs into gene-regulatory networks. ■

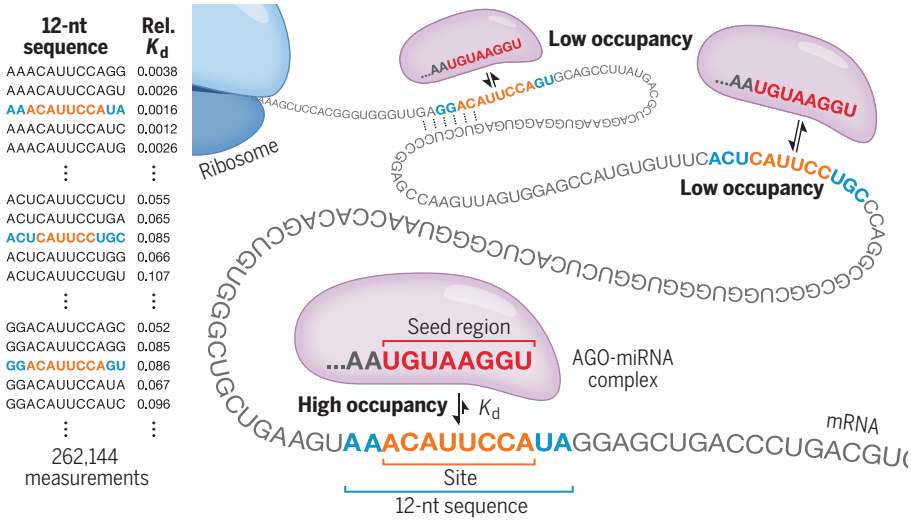

Biochemical modeling of targeting efficacy. RBNS generates relative K_d values for an AGO-miRNA and 262,144 different 12-nt sequences with at least a weak match to the miRNA (left). Values for sites found within an mRNA (colored 12-nt sequences) are used to estimate site occupancy, thereby enabling prediction of mRNA repression. Either a shorter match to the seed region (upper right) or suboptimal flanking nucleotides that promote occlusive mRNA structure (upper middle) can reduce occupancy. Rel. K_d, relative K_d.

The list of author affiliations is available in the full article online.
*These authors contributed equally to this work.
†Corresponding author. Email: dbartel@wi.mit.edu
Cite this article as S. E. McGeary *et al.*, *Science* **366**, eaav1741 (2019). DOI: 10.1126/science.aav1741

IMAGE: A. GODFREY/WHITEHEAD INSTITUTE

RESEARCH ARTICLE

MOLECULAR BIOLOGY

The biochemical basis of microRNA targeting efficacy

Sean E. McGeary[1,2,3]*, Kathy S. Lin[1,2,3,4]*, Charlie Y. Shi[1,2,3], Thy M. Pham[1,2,3], Namita Bisaria[1,2,3], Gina M. Kelley[1,2,3], David P. Bartel[1,2,3,4]†

MicroRNAs (miRNAs) act within Argonaute proteins to guide repression of messenger RNA targets. Although various approaches have provided insight into target recognition, the sparsity of miRNA-target affinity measurements has limited understanding and prediction of targeting efficacy. Here, we adapted RNA bind-n-seq to enable measurement of relative binding affinities between Argonaute-miRNA complexes and all sequences ≤12 nucleotides in length. This approach revealed noncanonical target sites specific to each miRNA, miRNA-specific differences in canonical target-site affinities, and a 100-fold impact of dinucleotides flanking each site. These data enabled construction of a biochemical model of miRNA-mediated repression, which was extended to all miRNA sequences using a convolutional neural network. This model substantially improved prediction of cellular repression, thereby providing a biochemical basis for quantitatively integrating miRNAs into gene-regulatory networks.

MicroRNAs (miRNAs) are ~22–nucleotide (nt) regulatory RNAs that derive from hairpin regions of precursor transcripts (*1*). Each miRNA associates with an Argonaute (AGO) protein to form a silencing complex, in which the miRNA pairs to sites within target transcripts and the AGO protein promotes destabilization and/or translational repression of bound transcripts (*2*). miRNAs are grouped into families on the basis of the sequence of their extended seed (nucleotides 2 to 8 of the miRNA), which is the region of the miRNA most important for target recognition (*3*). The 90 most broadly conserved miRNA families of mammals each have an average of >400 preferentially conserved targets, such that mRNAs from most human genes are conserved targets of at least one miRNA (*4*). Most of these 90 broadly conserved families are required for normal development or physiology, as shown by knockout studies in mice (*1*).

Deeper understanding of these numerous biological functions would be facilitated by a better understanding of miRNA targeting efficacy, with the ultimate goal of correctly predicting the effects of each miRNA on the output of each expressed gene. In principle, targeting efficacy should be a function of the affinity between AGO-miRNA complexes and their target sites, in that greater affinity to a target site would cause increased occupancy at that site and thus increased repression of the target mRNA. Until very recently, binding affinities have been known for only a few target sequences of only three miRNAs (*5*–*11*). In a recent study, high-throughput imaging and cleavage analyses provide extensive binding and slicing data for two of these three miRNAs: let-7a and miR-21 (*12*). Although these measurements provide insight and enable a quantitative model that predicts the efficiency of miR-21–directed slicing in cells (*12*), the sparsity of binding-affinity data still limits insight into how targeting might differ between different miRNAs and prevents construction of an informative biochemical model of targeting efficacy relevant to the vastly more prevalent, nonslicing mode of miRNA-mediated repression.

With insufficient affinity measurements, the most informative models of targeting efficacy rely instead on indirect, correlative approaches. These models focus on mRNAs with canonical 6- to 8-nt sites matching the miRNA seed region (Fig. 1A) and train on features known to correlate with targeting efficacy (including the type of site as well as various features of site context, mRNAs, and miRNAs), by using datasets that monitor mRNA changes that occur after introducing a miRNA (*13*–*16*). Although the correlative model implemented in TargetScan7 performs as well as the best in vivo cross-linking approaches at predicting mRNAs most responsive to miRNA perturbation, it nonetheless explains only a small fraction of the mRNA changes observed upon introducing a miRNA [coefficient of determination (r^2) = 0.14] (*14*). This low value indicates that prediction of targeting efficacy has room for improvement, even when accounting for the fact that experimental noise and secondary effects of inhibiting direct targets place a ceiling on the variability attributable to direct targeting. Therefore, we adapted RNA bind-n-seq (RBNS) (*17*) and a convolutional neural network (CNN) to the study of miRNA-target interactions, with the goal of obtaining the quantity and diversity of affinity measurements needed to better understand and predict miRNA targeting efficacy.

[1]Howard Hughes Medical Institute, Whitehead Institute for Biomedical Research, Cambridge, MA 02142, USA. [2]Whitehead Institute for Biomedical Research, Cambridge, MA 02142, USA. [3]Department of Biology, Massachusetts Institute of Technology, Cambridge, MA 02139, USA. [4]Computational and Systems Biology Program, Massachusetts Institute of Technology, Cambridge, MA 02139, USA.
*These authors contributed equally to this work.
†Corresponding author. Email: dbartel@wi.mit.edu

The site-affinity profile of miR-1

As previously implemented, RBNS provides qualitative relative binding measurements for an RNA-binding protein to a virtually exhaustive list of binding sites (*17*, *18*). A purified RNA-binding protein is incubated with a large library of RNA molecules that each contain a central random-sequence region flanked by constant primer-binding regions. After reaching binding equilibrium, the protein is pulled down and any copurifying RNA molecules are reverse transcribed, amplified, and sequenced. To extend RBNS to AGO-miRNA complexes (Fig. 1B), we purified human AGO2 loaded with miR-1 (*19*) (fig. S1A) and set up five binding reactions, each with a different concentration of AGO2–miR-1 (range of 7.3 to 730 pM, logarithmically spaced) and a constant concentration of an RNA library with a 37-nt random-sequence region (100 nM). We also modified the protein-isolation step of the RBNS protocol, replacing protein pull down with nitrocellulose filter binding, reasoning that the rapid wash step of filter binding would improve retention of low-affinity molecules that would otherwise be lost during the wash steps of a pull down. This modified method was highly reproducible, with high correspondence observed between enrichments for the same 9-nt k-mers (where k-mer is any sequence of length k) in two independent experiments using different preparations of both AGO2–miR-1 and the RNA library (fig. S1B; r^2 = 0.86).

When analyzing our AGO-RBNS results, we first examined enrichment of the canonical miR-1 sites, comparing the frequency of these sites in RNA bound in the 7.3 pM AGO2–miR-1 sample with that of the input library. As expected from the site hierarchy observed in meta-analyses of site conservation and endogenous site efficacy (*3*), the 8mer site (perfect match to miR-1 nucleotides 2 to 8 followed by an A) was most enriched (38-fold), followed by the 7mer-m8 site, then the 7mer-A1 site, and the 6mer site (Fig. 1, A and C). Little if any enrichment was observed for either the 6mer-A1 site or the 6mer-m8 site at this lowest concentration of 7.3 pM AGO2–miR-1 (Fig. 1, A and C), consistent with their weak signal in previous analyses of conservation and efficacy (*4*, *14*, *20*). Enrichment of sites was quite uniform across the random-sequence region, which indicated minimal influence from either the primer-binding sequences or supplementary pairing to the 3′ region of the miRNA (fig. S1D). Although sites with supplementary pairing can have enhanced efficacy and affinity (*3*, *5*, *21*),

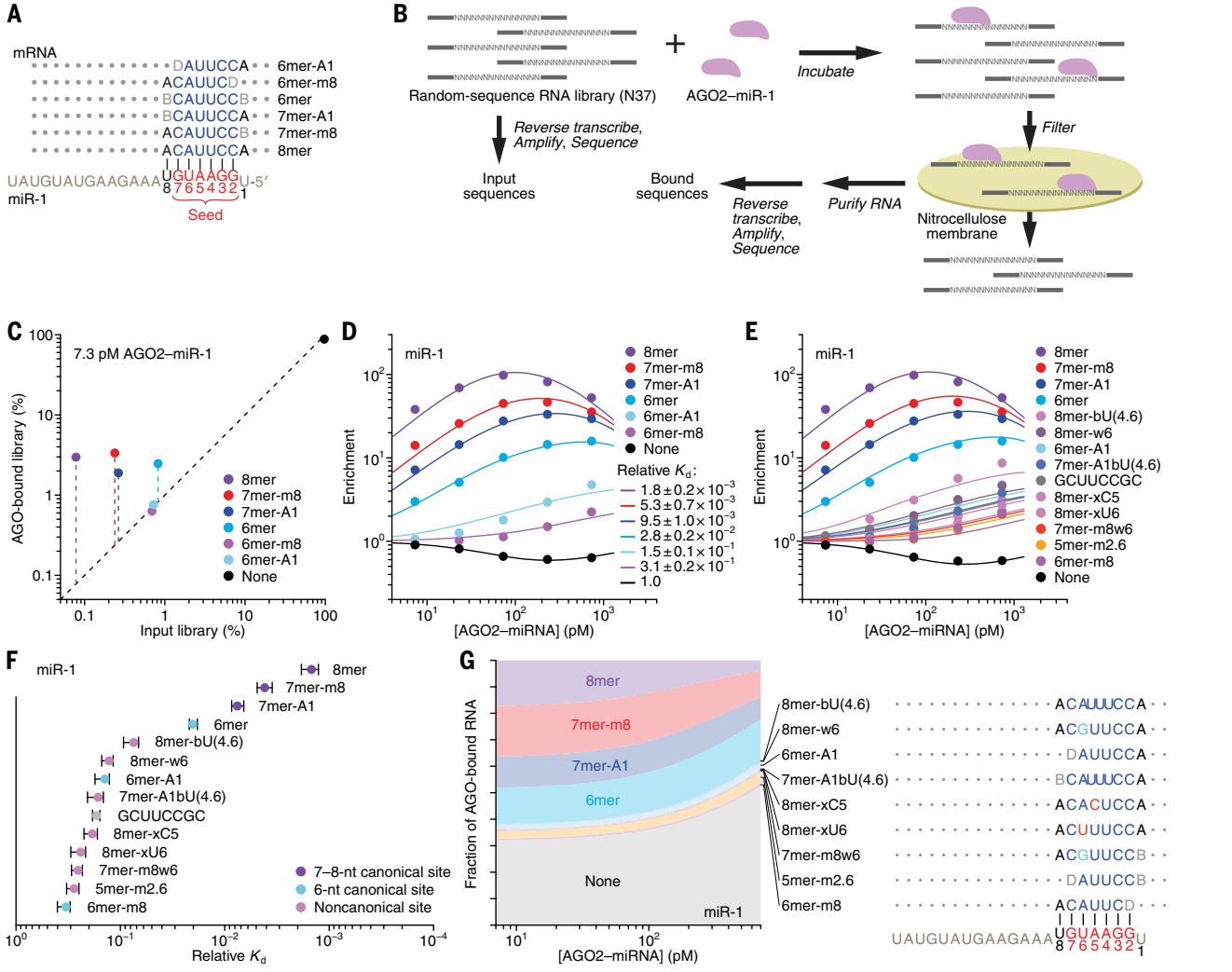

Fig. 1. AGO-RBNS reveals binding affinities of canonical and previously uncharacterized miR-1 target sites. (**A**) Canonical sites of miR-1. These sites have contiguous pairing (blue) to the miRNA seed (red), and some include an additional match to miRNA nucleotide 8 or an A opposite miRNA nucleotide 1 (B represents C, G, or U; D represents A, G, or U). (**B**) AGO-RBNS. Purified AGO2–miR-1 is incubated with excess RNA library molecules that each have a central block of 37 random-sequence positions (N37). After reaching binding equilibrium, the reaction is applied to a nitrocellulose membrane and washed under vacuum to separate library molecules bound to AGO2–miR-1 from those that are unbound. Molecules retained on the filter are purified, reverse transcribed, amplified, and sequenced. These sequences are compared with those generated directly from the input RNA library. (**C**) Enrichment of reads containing canonical miR-1 sites in the 7.3 pM AGO2–miR-1 library. Shown is the abundance of reads containing the indicated site (key) in the bound library plotted as a function of the respective abundance in the input library. Dashed vertical lines depict the enrichment in the bound library; dashed diagonal line shows $y = x$. Reads containing multiple sites were assigned to the site with greatest enrichment. (**D**) AGO-RBNS profile of the canonical miR-1 sites. Plotted is the enrichment of reads with the indicated canonical site (key) observed at each of the five AGO2–miR-1 concentrations of the AGO-RBNS experiment, determined as in (C). Points show the observed values, and lines show the enrichment predicted from the mathematical model fit simultaneously to all of the data. Also shown for each site are K_d values obtained from fitting the model, listing the geometric mean ± the 95% confidence interval determined by resampling the read data, removing data for one AGO–miR-1 concentration and fitting the model to the remaining data, and repeating this procedure 200 times (40 times for each concentration omitted). (**E**) AGO-RBNS profile of the canonical and the newly identified noncanonical miR-1 sites (key). Sites are listed in the order of their K_d values and named and colored based on the most similar canonical site, indicating differences from this site with b (bulge), w (G-U wobble), or x (mismatch) followed by the nucleotide and its position. For example, the 8mer-bU(4.6) resembles a canonical 8mer site but has a bulged U at positions that would normally pair to miRNA nucleotides 4, 5, or 6. Everything else is the same as in (D). (**F**) Relative K_d values for the canonical and the newly identified noncanonical miR-1 sites determined in (E). Sites are classified as either 7- to 8-nt canonical sites (purple), 6-nt canonical sites (cyan), noncanonical sites (pink), or a sequence motif with no clear complementarity to miR-1 (gray). The solid vertical line marks the reference K_d value of 1.0 assigned to reads lacking an annotated site. Error bars indicate 95% confidence interval on the geometric mean, as in (D). (**G**) The proportion of AGO2–miR-1 bound to each site type. Shown are proportions inferred by the mathematical model over a range of AGO2–miR-1 concentrations spanning the five experimental samples, plotted in the order of site affinity (top to bottom), using the same colors as in (E). On the right is the pairing of each noncanonical site, diagrammed as in (A), indicating Watson-Crick pairing (blue), wobble pairing (cyan), mismatched pairing (red), bulged nucleotides (compressed rendering), and terminal noncomplementarity (gray; B represents C, G, or U; D represents A, G, or U; H represents A, C, or U; V represents A, C, or G). The GCUUCCGC motif is omitted because it did not match miR-1 and did not mediate repression by miR-1 (fig. S5B).

the minimal influence of supplementary pairing reflected the rarity of such sites in our library.

Analysis of enrichment of the six canonical sites across all five AGO2–miR-1 concentrations illustrated two hallmarks of this experimental platform (*17*). First, as the concentration increased from 7.3 to 73 pM, enrichment for each of the six site types increased (Fig. 1D), which was attributable to an increase in signal over a constant low background of library molecules isolated even in the absence of AGO2–miR-1. Second, as the AGO2–miR-1 concentration increased beyond 73 pM, 8mer enrichment decreased, and at the highest AGO2–miR-1 concentration, enrichment of the 7mer-m8 and 7mer-A1 sites decreased (Fig. 1D). These waning enrichments indicated the onset of saturation for these high-affinity sites (*17*). These two features, driven by AGO-miRNA–independent background and partial saturation of the higher-affinity sites, respectively, caused differences in enrichment values for different site types to be highly dependent on the AGO2–miR-1 concentration; the lower AGO2–miR-1 concentrations provided greater discrimination between the higher-affinity site types, the higher AGO2–miR-1 concentrations provided greater discrimination between the lower-affinity site types, and no single concentration provided results that quantitatively reflected differences in relative binding affinities.

To account for background binding and ligand saturation, we developed a computational strategy that simultaneously incorporated information from all concentrations of an RBNS experiment to calculate relative K_d values. Underlying this strategy was an equilibrium-binding model that predicts the observed enrichment of each site type across the concentration series as a function of the K_d values for each miRNA site type (including the "no-site" type), as well as the stock concentration of purified AGO2–miR-1 and a constant amount of library recovered as background in all samples. Using this model, we performed maximum likelihood estimation (MLE) to fit the relative K_d values, which explained the observed data well (Fig. 1D). Moreover, these relative K_d values were robustly estimated, as indicated by comparing values obtained using results from only four of the five AGO2–miR-1 concentrations ($r^2 \geq 0.994$ for each of the 10 pairwise comparisons; fig. S1, F and G). These quantitative binding affinities followed the same hierarchy as observed for site enrichment, but the differences in affinities were of greater magnitude (Fig. 1D and fig. S1C).

Up to this point, our analysis was informed by the wealth of previous computational and experimental data showing the importance of a perfect 6- to 8-nt match to the seed region (*3*). However, the ability to calculate the relative K_d of any k-mer of length ≤12 nt (the 12-nt limit imposed by the sparsity of reads with longer k-mers) provided the opportunity for a de novo search for sites, without bias from any previous knowledge. In this search, we (i) calculated the enrichment of all 10-nt k-mers in the bound RNA in the 730 pM AGO2–miR-1 sample, which was the sample with the most sensitivity for detecting low-affinity sites; (ii) determined the extent of complementarity between the 10 most enriched k-mers and the miR-1 sequence; (iii) assigned a site most consistent with the observed k-mers; and (iv) removed all reads containing this newly identified site from both the bound and input libraries. These four steps were iterated until no 10-nt k-mer remained that was enriched ≥10-fold, thereby generating 14 sites for AGO2–miR-1. We then applied our MLE procedure to calculate relative K_d values for this expanded list of sites (Fig. 1, E and F).

This unbiased approach demonstrated that the 8mer, 7mer-m8, 7mer-A1, and 6mer sites to miR-1 were the highest-affinity site types of lengths ≤10 nt. It also identified eight previously uncharacterized sites with binding affinities resembling those of the 6mer-m8 and the 6mer-A1 (Fig. 1F). Comparison of these sites to the sequence of miR-1 revealed that miR-1 can tolerate either a wobble G at position 6 or a bulged U somewhere between positions 4 and 6 and achieve affinity at least 7- to 11-fold above that of the remaining no-site reads and that it can tolerate either a mismatched C at position 5 or a mismatched U at position 6 and achieve affinity four- to fivefold above that of the no-site reads. The GCUUCCGC motif also passed our cutoffs, which was more difficult to explain, because it had contiguous complementarity to positions 2 to 5 of miR-1 flanked by noncomplementary GC dinucleotides on both sides. Nonetheless, among the 1,398,100 possible motifs ≤10 nt, this was the only one that satisfied our criteria yet was difficult to attribute to miRNA pairing.

Our analytical approach and its underlying biochemical model also allowed us to infer the proportion of AGO2–miR-1 bound to each site (Fig. 1G). The 8mer site occupied 3.8 to 17% of the silencing complex over the concentration course, whereas the 7mer-m8, by virtue of its greater abundance, occupied a somewhat greater fraction of the complex. In aggregate, the marginal sites—including the 6mer-A1, 6mer-m8, and seven noncanonical sites—occupied 6.1 to 9.8% of the AGO2–miR-1 complex. Moreover, because of their very high abundance, library molecules with no identified site occupied 32 to 53% of the complex (Fig. 1G). These results support the inference that the summed contributions of background binding and low-affinity sites to intracellular AGO occupancy are of the same order of magnitude as those of canonical sites, suggesting that an individual AGO-miRNA complex spends about half its time associated with a vast repertoire of background and low-affinity sites (*22*, *23*). This phenomenon would help explain why sequences without recognizable sites often cross-link to AGO in cells.

Our results confirmed that AGO2–miR-1 binds the 8mer, 7mer-m8, 7mer-A1, and 6mer sites most effectively and revealed the relative binding affinities and occupancies of these sites. In addition, our results uncovered weak yet specific affinity to the 6mer-A1 and 6mer-m8 sites plus seven noncanonical sites, all with affinities outside the dynamic range of recent high-throughput imaging experiments (*12*). Although alternative binding sites for miRNAs have been proposed on the basis of high-throughput in vivo cross-linking studies (*24*–*28*), our approach provided quantification of the relative strength of these sites without the confounding effects of differential cross-linking efficiencies, potentially enabling their incorporation into a quantitative framework of miRNA targeting.

Distinct canonical and noncanonical binding of different miRNAs

We extended our analysis to five additional miRNAs, including let-7a, miR-7, miR-124, and miR-155 of mammals, chosen for their sequence conservation as well as the availability of data examining their regulatory activities, intracellular binding sites, or in vitro binding affinities (*1*, *5*, *6*, *24*, *25*), and lsy-6 of nematodes, which is thought to bind unusually weakly to its canonical sites (*29*) (Fig. 2 and fig. S2, B and C). In the case of let-7a, previous biochemical analyses have determined the K_d values of some canonical sites (*5*, *6*, *12*), and our values agreed well, which further validated our high-throughput approach (fig. S1H).

The site-affinity profile of let-7a resembled that of miR-1, except the 6mer-m8 and 6mer-A1 sites for let-7a had greater binding affinity than essentially all of the noncanonical sites (Fig. 2A). As with miR-1, the noncanonical sites each paired to the seed region but did so imperfectly, typically with a single wobble, single mismatch, or single-nucleotide bulge, but these imperfections differed from those observed for miR-1 (Figs. 1F and 2A).

The site-affinity profiles of miR-124, miR-155, lsy-6, and miR-7 resembled those of miR-1 and let-7a. All but one included the six canonical sites (with miR-7 missing the 6mer-m8 site), and all contained noncanonical sites with extensive yet imperfect pairing to the miRNA seeds, the imperfections tending to occur at different positions and with different mismatched- or bulged-nucleotide identities for different miRNAs (Fig. 2, B and C, and fig. S2, B and C). In contrast to the noncanonical sites of miR-1 and let-7a, more of the noncanonical sites of the other four miRNAs had affinities interspersed

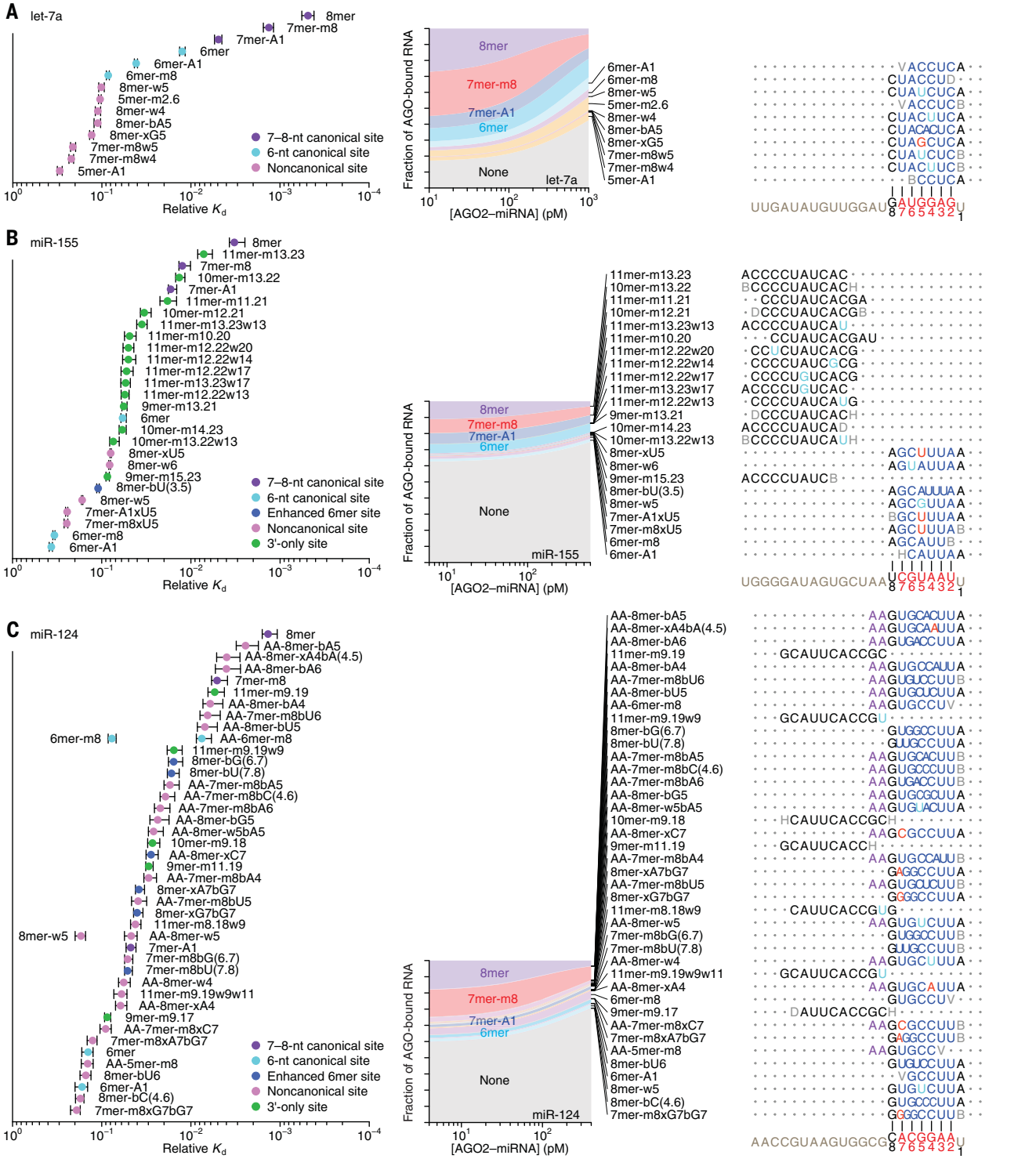

Fig. 2. Distinct canonical and noncanonical binding of different miRNAs. (**A** to **C**) Relative K_d values and proportional occupancy of established and newly identified sites of let-7a (A), miR-155 (B), and miR-124 (C). The two miR-124 sites that were present as a 5′-AA–extended form in addition to an unextended form are shown on the same line (C). Relative K_d values are plotted as in Fig. 1F but in some cases with additional categories, either for 3′-only sites (green) [(B) and (C)] or for 6-nt canonical sites enhanced by either additional wobble-pairing or additional Watson-Crick complementarity separated by a bulged nucleotide (blue) [(B) and (C)]. The proportion of AGO2-miRNA bound to each site type is estimated and shown as in Fig. 1G. These analyses also detected a GCACUUUA motif for let-7a and AACGAGGA motif for miR-155, which were assigned relative K_d values of $7.1 \pm 0.8 \times 10^{-2}$ and $6 \pm 1 \times 10^{-2}$, respectively. These motifs are excluded because each did not match its respective miRNA and did not mediate repression by its respective miRNA (fig. S5B).

with those of the top four canonical sites. Moreover, the profiles for miR-155, miR-124, and lsy-6 also included sites with extended (9- to 11-nt) complementarity to the miRNA 3′ region. These sites had estimated K_d values that were derived from reads with little more than chance complementarity to the miRNA seed, and they had uniform enrichment across the length of the random-sequence region (fig. S1E), which indicated that these sites represented an alternative binding mode dominated by extensive pairing to the 3′ region without involvement of the seed region (Fig. 2, B and C, and fig. S2B). We named them "3′-only sites."

In some respects, the 3′-only sites resembled noncanonical sites known as centered sites, which are reported to function in mammalian cells (*30*). Like 3′-only sites, centered sites have extensive perfect pairing to the miRNA, but for centered sites, this pairing begins at miRNA positions 3 or 4 and extends 11 to 12 nt through the center of the miRNA (*30*). Our unbiased search for sites did not identify centered sites for any of the six miRNAs. We therefore directly queried the region of each miRNA to which extensive noncanonical pairing was favored, determining the affinity of sequences with 11-nt segments of perfect complementarity to the miRNA sequence, scanning from miRNA position 3 to the 3′ end of the miRNA (Fig. 3A). For miR-155, miR-124, and lsy-6, sequences with 11-nt sites that paired to the miRNA 3′ region bound with greater affinity than did those with a canonical 6mer site, whereas for let-7a, miR-1, and miR-7, none of the 11-nt sites conferred stronger binding than did the 6mer. Moreover, for all six miRNAs, the 11-nt sites that satisfied the criteria for annotation as centered sites conferred binding ≤2-fold stronger than that of the 6mer-m8 site, which also starts at position 3 but extends only 6 nt. These results called into question the function of centered sites, although we cannot rule out the possibility that centered sites are recognized by some miRNAs and not others. Indeed, the newly identified 3′-only sites functioned for only miR-155, miR-124, and lsy-6, and even among these, the optimal region of pairing differed, occurring at positions 13 to 23, 9 to 19, and 8 to 18, respectively (Fig. 3A).

When evaluating other types of noncanonical sites proposed to confer widespread repression in mammalian cells (*20*, *24*), we found that all but two bound with affinities difficult to distinguish from background. One of these two was the 5-nt site matching miRNA positions 2 to 6 (5mer-m2.6) (*20*), which was bound by miR-1, let-7a, and miR-7 but not by the other three miRNAs (fig. S3). The other was the pivot site (*24*), which was bound by miR-124 [e.g., 8mer-bG(6.7); Fig. 2C] and lsy-6 [e.g., 8mer-bA (6.7); fig. S2B] but not by the other four miRNAs (fig. S4). Thus, these two previously identified noncanonical site types resembled the newly identified noncanonical sites with extensive yet imperfect pairing to the seed region, in that they function for only a limited number of miRNAs.

In addition to the differences in noncanonical site types observed for each miRNA, we also observed pronounced miRNA-specific differences in the relative affinities of the canonical site types. For example, for miR-155, the affinity of the 7mer-A1 nearly matched that of the 7mer-m8, whereas for miR-124, the affinity of the 7mer-A1 was >9-fold lower than that of the 7mer-m8. These results implied that the relative contributions of the A at target position 1 and the match at target position 8 can substantially differ for different miRNAs. Although prior studies show that AGO proteins remodel the thermodynamic properties of their loaded RNA guides (*5*, *6*), our results show that the sequence of the guide strongly influences the nature of this remodeling, leading to differences in relative affinities across canonical site types and a distinct repertoire of noncanonical site types for each miRNA.

The energetics of canonical binding

With the relative K_d values for the canonical binding sites of six miRNAs in hand, we examined the energetic relationship between the A at target position 1 (A1) and the match at miRNA position 8 (m8), within a framework analogous to a double-mutant cycle (Fig. 3B, left). The apparent binding-energy contributions of the m8 and A1 ($\Delta\Delta G_{m8}$ and $\Delta\Delta G_{A1}$, respectively) were largely independent, as inferred from the relative K_d values of the four site types. That is, for each miRNA, the $\Delta\Delta G_{m8}$ inferred in the presence of the A1 (using the ratio of the 8mer and 7mer-A1 K_d values) resembled that inferred in the absence of the A1 (using the ratio of the 7mer-m8 and 6mer K_d values), and vice versa (Fig. 3B).

The relative K_d values for canonical sites of six miRNAs provided the opportunity to examine the relationship between the predicted free energy of site pairing and measured site affinities. We focused on the 6mer and 7mer-m8 sites because they lack the A1, which does not pair to the miRNA (Fig. 1A) (*8*, *31*). Consistent with the importance of base pairing for site recognition and the known relationship between predicted seed-pairing stability and repression efficacy (*29*), affinity increased with increased predicted pairing stability, although this increase was statistically significant for only the 7mer-m8 site type (Fig. 3C; $p = 0.09$ and 0.005 for the 6mer and 7mer-m8 sites, respectively). However, for both site types, the slope of the relationship was significantly less than expected from $K_d = e^{-\Delta G/RT}$, where ΔG is the change in free energy, R is the universal gas constant, and T is temperature ($p = 0.008$ and 8×10^{-5}, respectively). When considered together with the previous analysis of a miRNA with enhanced seed-pairing stability, these results indicated that in remodeling the thermodynamic properties of the loaded miRNAs, AGO not only enhances the affinity of seed-matched interactions but also dampens the intrinsic differences in seed-pairing stabilities that would otherwise impose much greater inequities between the targeting efficacies of different miRNAs (*6*). Thus, although lsy-6, which has unusually poor predicted seed-pairing stability (*29*), did indeed have the weakest site-binding affinity of the six miRNAs, the difference between its binding affinity and that of the other miRNAs was less than might have been expected.

Correspondence with repression observed in the cell

To evaluate the relevance of our in vitro binding results to intracellular miRNA-mediated repression, we examined the relationship between the relative K_d measurements and the repression of endogenous mRNAs after miRNA transfection into HeLa cells. When examining intracellular repression attributable to 3′UTR (3′ untranslated region) sites of the transfected miRNA, we observed a pronounced relationship between AGO-RBNS–determined K_d values and mRNA fold changes (Fig. 3, D to I; $r^2 = 0.80$ to 0.97). For instance, the different relative affinities of the 7mer-A1 and 7mer-m8 sites, most extremely observed for sites of miR-155 and miR-124, were nearly perfectly mirrored by the relative efficacy of these sites in mediating repression in the cell (Fig. 3, F and G). A similar correspondence between relative K_d values and repression was observed for the noncanonical sites that had both sufficient affinity and sufficient representation in the HeLa transcriptome to be evaluated using this analysis (Fig. 3, D to I). These included the pivot sites for miR-124 and lsy-6 and the bulge-G7–containing sites for miR-7 (Fig. 3, G to I).

Analysis of mRNA changes observed after miRNA transfection was not suitable for measuring efficacy of the highest-affinity noncanonical sites because these sites lacked sufficient representation in endogenous 3′UTRs. Therefore, we implemented a massively parallel reporter assay designed to examine the efficacy of every site type identified by AGO-RBNS, each in 184 different 3′UTR sequence contexts (fig. S5A). This assay showed that 3′-only sites and other high-affinity–but-rare noncanonical site types do mediate repression in cells and that their efficacies tend to track with their affinities (fig. S5B). In sum, we found a strong correspondence between intracellular repression and in vitro binding affinity, regardless of miRNA identity and regardless of whether the target site is canonical or noncanonical or within an endogenous or a reporter mRNA. This result supported a model in which repression is a function of miRNA occupancy, as dictated by

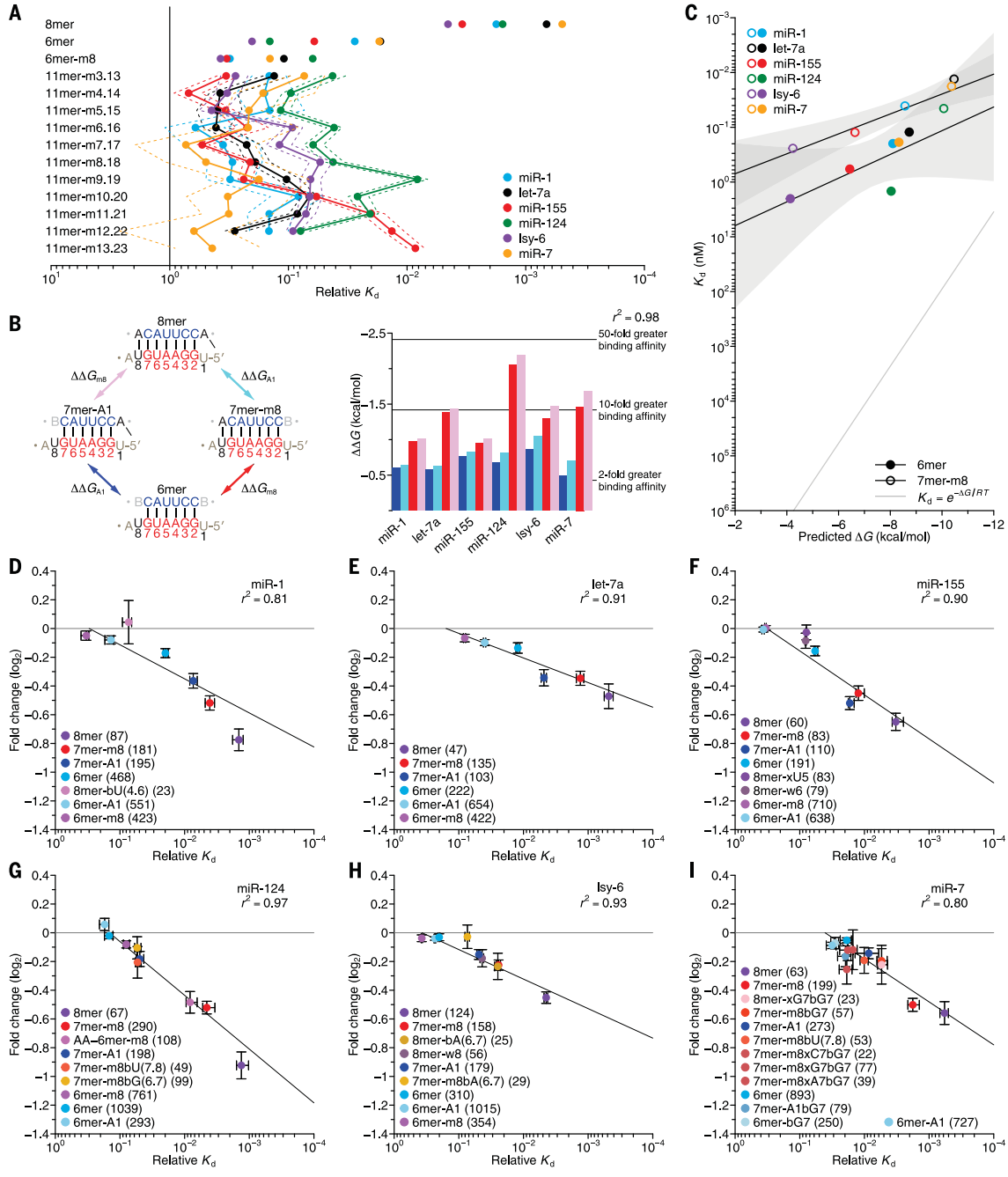

Fig. 3. Additional analyses of binding affinities and the correspondence between binding affinity and repression efficacy. (**A**) Diverse functionality and position dependence of 11-nt 3′-only sites. Relative K_d values for each potential 11-nt 3′-only site are plotted for the indicated miRNAs (key). For reference, values for the 8mer, 6mer, and 6mer-m8 sites are also plotted. The solid vertical line marks the reference K_d value of 1.0, as in Fig. 1F. The solid and dashed lines indicate geometric mean and 95% confidence interval, respectively, determined as in Fig. 1D. (**B**) The independent contributions of the A1 and m8 features. On the left, a double-mutant cycle depicts the affinity differences observed among the four top canonical sites for miR-1, as imparted by the independent contributions of the A1 and m8 features and their potential interaction. On the right, the apparent binding contributions of the A1 ($\Delta\Delta G_{A1}$, blue and cyan) or m8 ($\Delta\Delta G_{m8}$, red and pink) features are plotted, determined from the ratio of relative K_d values of either the 7mer-A1 and the 6mer (blue), the 8mer and the 7mer-m8 (cyan), the 7mer-m8 and the 6mer (red), or the 8mer and the 7mer-A1 (pink) for the indicated AGO2-miRNA complexes. The r^2 reports on the degree of $\Delta\Delta G$ similarity for both the m8 and A1 features using either of the relevant site-type pairs across all six complexes. (**C**) The relationship between the observed relative K_d values and predicted pairing stability of the 6mer (filled circles) and 7mer-m8 (open circles) sites of the indicated AGO-miRNA complex (key), under the assumption that the K_d value for library molecules without a site was 10 nM for all AGO-miRNA complexes. The two black lines are the best fit of the relationship observed for each of the site types (gray regions, 95% confidence interval). The gray line shows the expected relationship with the predicted stabilities given by $K_d = e^{-\Delta G/RT}$. (**D** to **I**) The relationship between repression efficacy and relative K_d values for the indicated sites of miR-1 (D), let-7a (E), miR-155 (F), miR-124 (G), lsy-6 (H), and miR-7 (I). The number of sites of each type in the 3′UTRs is indicated (parentheses). To include information from mRNAs with multiple sites, multiple linear regression was applied to determine the log fold-change attributable to each site type (error bars, 95% confidence interval). The relative K_d values are those of Figs. 1 and 2 and fig. S2 (error bars, 95% confidence interval). Lines show the best fit to the data, determined by least-squares regression, weighting residuals using the 95% confidence intervals of the log fold-change estimates. The r^2 values were calculated using similarly weighted Pearson correlations.

site affinity, and thus miRNA- and site-specific differences in binding affinities explain substantial differences in repression.

The strong influence of flanking dinucleotide sequences

AU-rich nucleotide composition immediately flanking miRNA sites has long been associated with increased site conservation and efficacy in cells (*13*, *31*, *32*), but the mechanistic basis of this phenomenon has not been investigated, presumably because of the sparsity of affinity measurements. The AGO-RBNS data provided the means to overcome this limitation. We first separated the miR-1 8mer site into 256 different 12-nt sites, on the basis of the dinucleotide sequences immediately flanking each side of the 8mer, and determined relative K_d values for each (Fig. 4A). This analysis revealed a ~100-fold range in values, depending on the identities of the flanking dinucleotides, with binding affinity strongly tracking the AU content of the flanking dinucleotides. Extending this analysis across all miR-1 site types (Fig. 4B), as well as to sites to the other five miRNAs (fig. S6, A to E), yielded similar results. The effect of the flanking-dinucleotide context was of such magnitude that it often exceeded the affinity differences observed between miRNA-site types. Indeed, for each miRNA, at least one 6-nt canonical site in its most favorable context had greater affinity than that of the 8mer site in its least favorable context (Fig. 4B and fig. S6, A to E).

To identify general features of the flanking-dinucleotide effect across miRNA sequences and site types, we trained a multiple linear regression model on the complete set of flanking-dinucleotide K_d values corresponding to all six canonical site types of each miRNA, fitting the effects at each of the four positions within the two flanking dinucleotides. The output of the model agreed well with the observed K_d values (Fig. 4C, left; $r^2 = 0.63$), which indicated that the effects of the flanking dinucleotides were largely consistent between miRNAs and between site types of each miRNA. The output of the model also corresponded with the efficacy of intracellular repression, which indicated that these effects on K_d values were consequential in cells (fig. S6F). A and U nucleotides each enhanced affinity, whereas G nucleotides reduced affinity and C nucleotides were intermediate or neutral

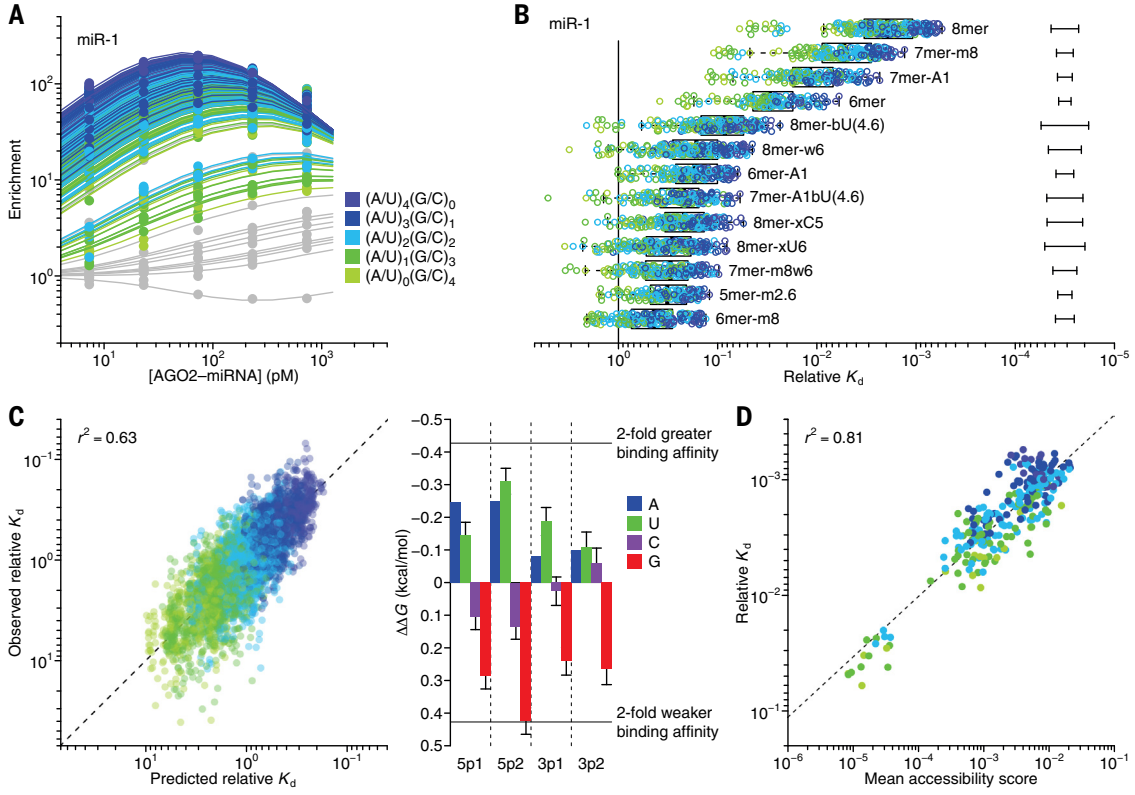

Fig. 4. The influence of flanking dinucleotide sequence context. (**A**) AGO-RBNS profile of miR-1 sites, showing results for the 8mer separated into 256 different 12-nt sites on the basis of the identities of the two dinucleotides immediately flanking the 8mer. For each 12-nt site, the points and line are colored on the basis of the AU content of the flanking dinucleotides (key). For context, results of Fig. 1E are replotted in gray. Everything else is the same as in Fig. 1E. (**B**) Relative K_d values for each miR-1 site identified in Fig. 1F separated into 144 to 256 sites as in (A) on the basis of the identities of the flanking dinucleotides. The points are colored as in (A). Error bars indicate median 95% confidence interval across all K_d values. Everything else is the same as in Fig. 1F. (**C**) Consistency of flanking-dinucleotide effect across miRNA and site type. At the left is a comparison of observed relative K_d values and results of a mathematical model that used multiple linear regression to predict the influence of flanking dinucleotides. Plotted are results for all flanking dinucleotide contexts of all six canonical site types, for all six miRNAs, normalized to the average affinity of each canonical site. Predictions of the model are those observed in a sixfold cross-validation, training on the results for five miRNAs and reporting the predictions for the held-out miRNA. The points for five outliers are not shown. The r^2 quantifies the agreement between the predicted and actual values, considering all points. On the right, the model coefficients (multiplied by $-RT$, where T = 310.15 K) corresponding to each of the four nucleotides of the 5′ (5p) and 3′ (3p) dinucleotides in the 5′-to-3′ direction are plotted (error bars, 95% confidence interval). (**D**) Relationship between the mean structural-accessibility score and the relative K_d for the 256 12-nt sites containing the miR-1 8mer flanked by each of the dinucleotide combinations. Points are colored as in (A). Linear regression (dashed line) and calculation of r^2 were performed using log-transformed values. For an analysis of the relationship between 8mer flanking-dinucleotide K_d and structural accessibility over a range of window lengths and positions relative to the 8mer site, see fig. S6G.

(Fig. 4C, right). Moreover, the identity of the 5′ flanking dinucleotide, which must come into close proximity with the central RNA-binding channel of AGO (*7*), contributed more to binding affinity than did the 3′ flanking sequence (Fig. 4C, right).

One explanation for this hierarchy of flanking nucleotide contributions, with A ≈ U > C > G, is that it inversely reflected the propensity of these nucleotides to stabilize RNA secondary structure that could occlude binding of the silencing complex. To investigate this potential role for structural accessibility in influencing binding, we compared the predicted structural accessibility of 8mer sites in the input and bound libraries of the AGO2–miR-1 experiment, using a score for predicted structural accessibility previously optimized on data examining miRNA-mediated repression (*14*, *33*). This score is based on the predicted probability that the 14-nt segment at target positions 1 to 14 is unpaired. We found that predicted accessibilities of sites in the bound libraries were substantially greater than those for sites in the input library and that the difference was greatest for the samples with the lower AGO2–miR-1 concentrations (fig. S6G), as expected if the accessibility score was predictive of site accessibility and if the most accessible sites were the most preferentially bound.

To build on these results, we examined the relationship between predicted structural accessibility and binding affinity for each of the 256 flanking dinucleotide possibilities. For each input read with a miR-1 8mer site, the accessibility score of that site was calculated. The sites were then differentiated on the basis of their flanking dinucleotides into 256 12-nt sites, and the geometric mean of the structural-accessibility scores of each of these extended sites was compared with the AGO-RBNS–derived relative K_d value (Fig. 4D and fig. S6H). A notable correlation was observed (r^2 = 0.82, $p < 10^{-15}$), with all 16 sites containing a 5′-flanking GG dinucleotide having both unusually poor affinities and unusually low accessibility scores. Moreover, sampling reads from the input library to match the predicted accessibility of sites in the bound library recapitulated the flanking dinucleotide preferences observed in the bound library (fig. S6I, r^2 = 0.79). Taken together, our results demonstrate that local sequence context has a large influence on miRNA-target binding affinity and indicate that this influence results predominantly from the differential propensities of flanking sequences to favor structures that occlude site accessibility.

A biochemical model predictive of miRNA-mediated repression

Inspired by the finding that measured affinities strongly corresponded to the repression observed in cells (Fig. 3, D to I), we set out to build a biochemical framework that predicts the degree to which a miRNA represses each mRNA. Biochemical principles have been used to model miR-21–directed mRNA slicing (*12*). However, previous efforts that used biochemical principles to model aspects of the predominant mode of miRNA-mediated repression, including competition between endogenous target sites (*23*, *34*, *35*) and the influence of miRNAs on reporter gene–expression noise (*36*), were severely limited by the sparsity of the data. Our ability to measure the relative binding affinity of a miRNA to any 12-nt sequence enabled modeling of the quantitative effects of the six miRNAs on each cellular mRNA.

We first reanalyzed all six AGO-RBNS experiments to calculate, for each miRNA, the relative K_d values for all 262,144 12-nt k-mers that contained at least four contiguous nucleotides of the canonical 8mer site (Fig. 5A). These potential binding sites included the canonical sites and most of the noncanonical sites that we had identified, each within a diversity of flanking sequence contexts (Figs. 1F and 2). For each mRNA m and transfected miRNA g, the steady-state occupancy $N_{m,g}$ (i.e., average number of AGO-miRNA complexes loaded with miRNA g bound to mRNA m) was predicted as a function of the K_d values of the potential binding sites contained within the mRNA open reading frame (ORF) and 3′UTR, as well as the concentration of the unbound AGO-miRNA$_g$ complex a_g, which was fit as a single value for each transfected miRNA (Fig. 5B, equation 1). This occupancy value enabled prediction of a biochemically informed expectation of repression, assuming that the added effect of the miRNA on the basal decay rate scaled with the basal rate and $N_{m,g}$ (Fig. 5B, equation 2). To isolate the effects of a transfected miRNA over background, we further offset our prediction of repression by a background-binding term (Fig. 5B, $N_{m,g,\text{background}}$).

The calculation of predicted repression required an estimate of how much a single bound AGO affected the mRNA decay rate (Fig. 5B, b), which was fit as a global value. Additionally, to account for the observation that sites in ORFs are less effective than those in 3′UTRs (*3*), our model included a penalty term for sites in ORFs, which was also fit as a global value (Fig. 5B). Because no appreciable repression was observed from sites in 5′UTRs, our model did not consider these sites.

Our biochemical model was fit against repression observed in HeLa cells transfected with one of five miRNAs with RBNS-derived measurements (let-7a was excluded because of its high endogenous expression in HeLa cells). A strong correspondence was observed when comparing mRNA changes measured upon miRNA transfection with those predicted by the model (fig. S7A, r^2 = 0.30 to 0.37).

The overall performance of our biochemical model (Fig. 5C, r^2 = 0.34) exceeded those of the 30 target-prediction algorithms ($r^2 \leq$ 0.14) that were also tested on changes in mRNA levels observed in response to miRNA transfection (*14*). We reasoned that in addition to our biochemical framework and the use of experimentally measured affinity values, other aspects of our analysis might have contributed to this improvement. For example, the miRNAs chosen for RBNS have high efficacy in transfection experiments, and our RNA-sequencing (RNA-seq) datasets generally had stronger signal over background compared to microarray datasets used to train and test previous target-prediction algorithms. Indeed, when evaluated on the same five datasets, the performance of the latest TargetScan model (TargetScan7) improved from an r^2 of 0.14 to an r^2 of 0.25 (fig. S7B). To explore the possibility that TargetScan7 might also benefit from training on this type of improved data, we generated transfection datasets for 11 additional miRNAs and retrained TargetScan7 on the collection of 16 miRNA-transfection datasets (again omitting the let-7a dataset), putting aside one dataset each time in a 16-fold cross-validation. Training and testing TargetScan on improved datasets further increased the r^2 to 0.28 for the five miRNAs with AGO-RBNS data (Fig. 5D). Nonetheless, the biochemical model still outperformed the retrained TargetScan by >20%, which showed that the use of measured affinity values in a biochemical framework substantially increased prediction performance.

Many features known to correlate with targeting efficacy were captured by our biochemical model. Indeed, the contribution of certain features, such as site type (*3*), predicted seed-pairing stability (*29*), and nucleotide identities at specific miRNA or site positions (*14*), are expected to be represented more accurately in the miRNA-specific K_d values of the 12-nt k-mers than when generalized across miRNAs. However, these K_d values did not fully capture other factors that influence the affinity between miRNAs and their target sites in cells, including the structural accessibility of sites within their larger mRNA contexts and the contribution of supplementary pairing to the miRNA 3′ region, which influences about 5% of sites (*3*). Without sufficient biochemical data quantifying these effects, we approximated their influence using scoring metrics known to correlate with miRNA targeting efficacy (*13*, *14*) and allowed them to modify the K_d values additively in log space (i.e., linearly in free-energy space). Incorporating each of these metrics slightly improved the performance of the biochemical model, as did incorporating a score for the evolutionary conservation of the site (*4*), which helped account for additional unknown or imperfectly captured factors that influence targeting efficacy (fig. S7C).

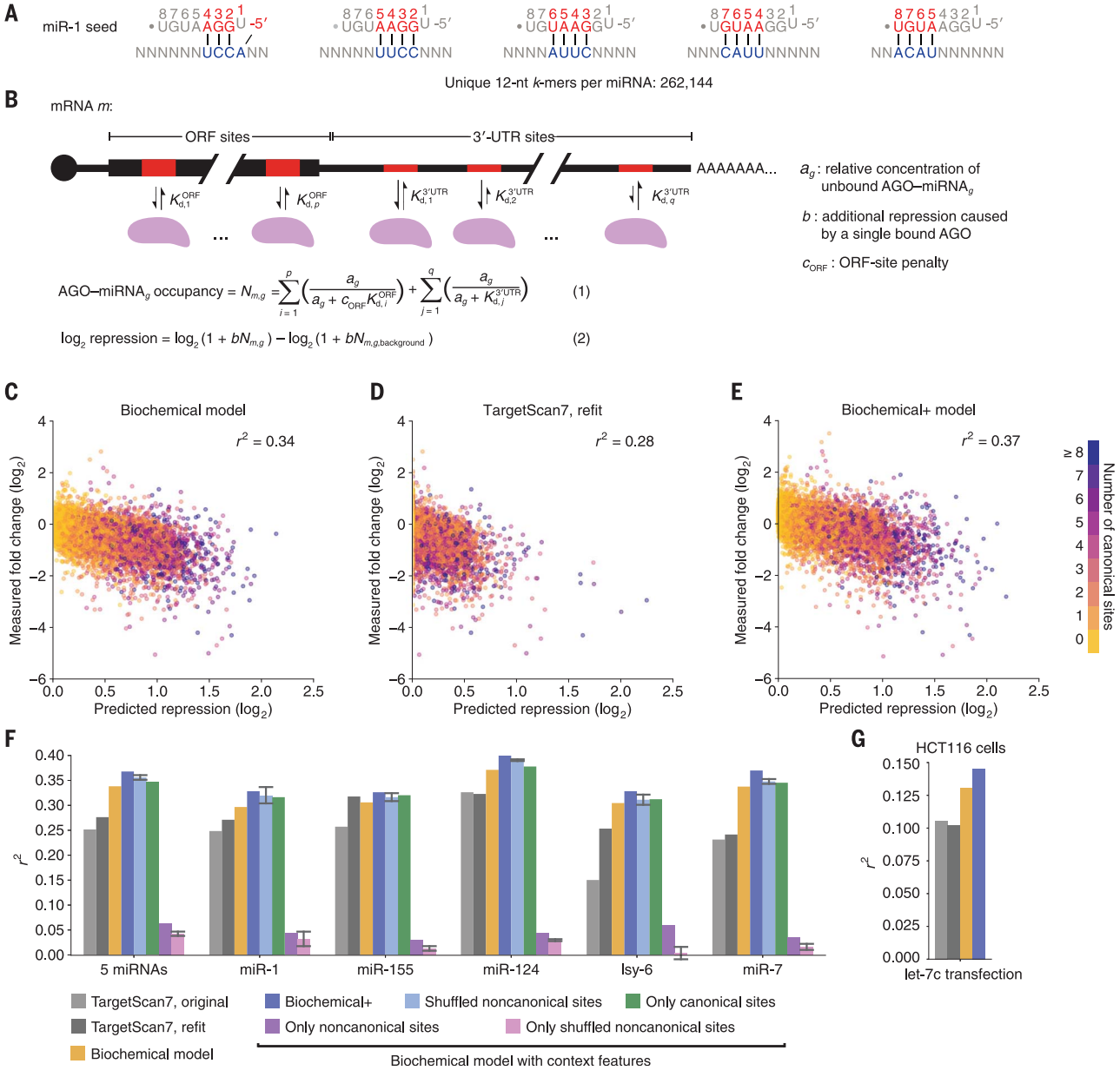

Fig. 5. AGO-RBNS K_d values enable a predictive model of miRNA-mediated repression in cells. (**A**) The 262,144 12-nt *k*-mers with at least four contiguous matches to the extended seed region of miR-1, for which relative K_d values were determined. Relative K_d values were similarly determined for the analogous *k*-mers of the other five miRNAs. (**B**) Biochemical model for estimating miRNA-mediated repression of an mRNA using the relative K_d values of the 12-nt *k*-mers in the mRNA. (**C**) Performance of the biochemical model as evaluated using the combined results of five miRNAs. Plotted is the relationship between mRNA changes observed after transfecting a miRNA and those predicted by the model. Each point represents the mRNA from one gene after transfection of a miRNA and is colored according to the number of canonical sites in the mRNA 3′UTR (key). For easier visual comparison between mRNAs, *y*-axis points for the same mRNA are adjusted by the extrapolated expression level of the mRNA with no transfected miRNA. The Pearson's r^2 between measured and predicted values is for unadjusted values and is reported in the upper right. (**D**). Performance of the retrained TargetScan7 model. Everything else is the same as in (C). (**E**) Performance of the biochemical+ model. Everything else is the same as in (C). (**F**) Model performances and the contribution of cognate noncanonical sites to performance of the biochemical+ model. Results for each model (key) are plotted for individual miRNAs and for all five miRNAs combined (error bars, standard deviation). (**G**) Performances of models tested on mRNA changes observed after transfecting let-7c into HCT116 cells engineered to have reduced endogenous miRNA expression (*37*). This analysis used the average a_g fit for the five miRNAs in (F). Everything else is the same as in (F).

Simultaneously incorporating all three metrics to generate what we call the "biochemical+ model" improved the r^2 by 9% to 0.37 (Fig. 5E).

To examine how well our models generalized to another cell type and to a miRNA family not used for fitting (let-7), we evaluated them on repression data collected after transfecting let-7c into HCT116 (human colon cancer) cells that had been engineered to not express endogenous miRNAs (*37*). Although these data had a considerably lower signal-to-noise ratio, which lowered all r^2 values, our biochemical models substantially outperformed TargetScan7 (Fig. 5G). This improvement extended to predicting repression after

transfecting miR-124 and miR-7 into human embryonic kidney (HEK) 293 cells (*38*) (fig. S8A). Additional analyses showed that the biochemical+ model performed at least as well as in vivo cross-linking immunoprecipitation sequencing (CLIP-seq) approaches in identifying the mRNAs most repressed upon miRNA transfection or most derepressed upon miRNA knockout (*25*, *38*, *39*) (fig. S8, B to D). Furthermore, for individual CLIP clusters enriched in wild type relative to miR-155 knockout, we observed a correlation between the occupancy predicted by our K_d values and the observed enrichment of the cluster [Spearman's rank-order correlation (r_s) = 0.46, $p < 10^{-7}$; fig. S8E], supporting the conclusion that K_d values measured in vitro reflect intracellular AGO binding.

When provided with K_d values for only the 12-nt *k*-mers that contained one of the six canonical sites, the biochemical+ model captured somewhat less variance (Fig. 5F, green bars; r^2 = 0.35), and conversely when provided with K_d values for only the 12-nt *k*-mers lacking a canonical site, the model still retained some predictive power (Fig. 5F, purple bars; r^2 = 0.06, $p < 10^{-15}$, likelihood-ratio test). As a control, we repeated the analysis after replacing the noncanonical sites (and their K_d values) of each miRNA with those of another miRNA, performing this shuffling and reanalysis for all 309 possible shuffle permutations. When using each of these shuffled controls, performance decreased, both when considering all sites (Fig. 5F, light blue bars) and when considering only the noncanonical sites (Fig. 5F, pink bars), as expected if the modest improvement conferred by including noncanonical sites were due, at least in part, to miRNA pairing to those sites. This advantage of cognate over shuffled noncanonical sites was largely maintained when evaluating the results for individual miRNAs (Fig. 5F). Together, our results showed that noncanonical sites can mediate intracellular repression but that their impact is dwarfed by that of canonical sites because high-affinity noncanonical sites are not highly abundant within transcript sequences. Thus, the improved performance over TargetScan achieved by the biochemical model was primarily from more accurate modeling of the effects of canonical sites.

CNN for predicting site K_d values from sequence

Our findings that binding preferences differ substantially between miRNAs and that these differences are not well predicted by existing models of RNA duplex stability in solution posed a major challenge for applying our biochemical framework to other miRNAs. Because performing AGO-RBNS for each of the known miRNAs would be impractical, we attempted to predict miRNA-target affinity from sequence using the six sets of relative K_d values and 16 miRNA-transfection datasets already in hand. Bolstered by recent successful applications of deep learning to predict complex aspects of nucleic acid biology from sequence (*40*–*43*), we chose a CNN for this task.

The overall model had two components. The first was a CNN that predicted relative K_d values for the binding of miRNAs to 12-nt *k*-mers (fig. S9A), and the second was the previously described biochemical model that links intracellular repression with relative K_d values (Fig. 6A). The training process simultaneously tuned both the neural network weights and the parameters of the biochemical model to fit both the relative K_d values and the mRNA repression data, with the goal of building a CNN that accurately predicts the relative K_d values for all 12-nt *k*-mers of a miRNA of any sequence.

For the CNN, we chose to include only the first 10 nucleotides of the miRNA sequence, which includes the position 1 nucleotide, the seed region, and the two downstream nucleotides that could pair to a 12-nt *k*-mer. Because the *k*-mers were not long enough to include sites with 3′ supplementary pairing, we excluded the 3′ region of the miRNA. Pairs of 10-nt truncated miRNA sequences and 12-nt *k*-mers were each parameterized as a 10-by-12-by-16 matrix, with the third dimension representing the 16 possible pairs of nucleotides that could be present at each pair of positions in the miRNA and target. The first layer of the CNN was designed to learn important single-nucleotide interactions, the second layer was designed to learn dinucleotide interactions, and the third layer was designed to learn position-specific information.

The training data for the CNN consisted of more than 1.5 million relative K_d values from six AGO-RBNS experiments and 68,112 mRNA expression estimates derived from 4257 transcripts in 16 miRNA transfection experiments. Five miRNAs had data in both sets. Because some repression was attributable to the passenger strands of the transfected duplexes (fig. S9B), the model considered both strands of each transfected duplex, which allowed the neural network to learn from another 16 AGO-loaded guide sequences.

To test how well the CNN-predicted relative K_d values enabled our approach to be generalized to other miRNAs and another cell type, we generated 12 miRNA-transfection datasets in HEK293FT cells, choosing miRNAs that were not appreciably expressed in HEK293 cells (*44*) and that had not been used in any training (fig. S10). For each miRNA duplex in the test set, the CNN was used to predict relative K_d values for 12-nt *k*-mers to both the miRNA and passenger strands. As observed with the experimentally derived relative K_d values (Fig. 3, D to I), substantial correspondence was observed between CNN-predicted relative K_d values for the six canonical site types of the transfected miRNAs and the mean repression that these site types conferred in cells (Fig. 6B and fig. S11). This correspondence (r^2 = 0.76) substantially exceeded that observed for predictions of RNA-duplex stability in solution (*45*) and predictions derived from cross-linking results (*27*) (Fig. 6C; r^2 = 0.21 and 0.56, respectively). Aside from accurately predicting the relative efficacy of sites to the same miRNA, the CNN was better able to stratify sites of the same type to different miRNAs (e.g., Fig. 6B, purple dots; r^2 = 0.52, p = 0.02). Analysis of other site types suggested that the CNN had some ability to identify effective noncanonical sites for new miRNAs (fig. S11).

When the CNN-predicted K_d values and HeLa-derived global parameters were used as input for the biochemical and biochemical+ models to predict repression of individual mRNAs in HEK293FT cells, the results mirrored those observed when using relative K_d values derived from AGO-RBNS. Median (r^2 = 0.21) and overall performance (r^2 = 0.18) for the test set both exceeded those of TargetScan (r^2 = 0.12 and 0.13, respectively); overall performance improved (r^2 = 0.20) when using the biochemical+ model, implying a 50% improvement over TargetScan, and performance dropped slightly when either shuffling or omitting noncanonical sites (Fig. 6D and fig. S12A; the main exception being the results for miR-190a, for which the performance of the biochemical+ model resembled that of TargetScan when only considering the canonical sites but substantially dropped when also considering noncanonical sites). The overall improvement over TargetScan was maintained when focusing on mRNAs that were expressed in HEK293FT cells but not HeLa cells (Fig. 6D). The CNN-predicted relative K_d values also enabled the biochemical+ model to outperform TargetScan and cross-linking approaches in predicting the effects of deleting or adding a miRNA in other cellular contexts (*46*–*48*) (fig. S12, B to D).

Although our models were improved over previous models, the highest r^2 value achieved by our models for any of our datasets was 0.37 (Fig. 5F and fig. S12A), implying that they explained only a minority of the variability in mRNA fold changes occurring upon introducing a miRNA. However, even perfect prediction of the direct effects of miRNAs was not expected to explain all of the variability; some variability was due to the secondary effects of repressing the primary targets, and some was due to experimental noise. To estimate the maximal r^2 that could be achieved by predicting the primary effects of miRNA targeting, we attempted to quantify and subtract the fraction of the fold-change variability attributable to the other two causes. For each dataset, the

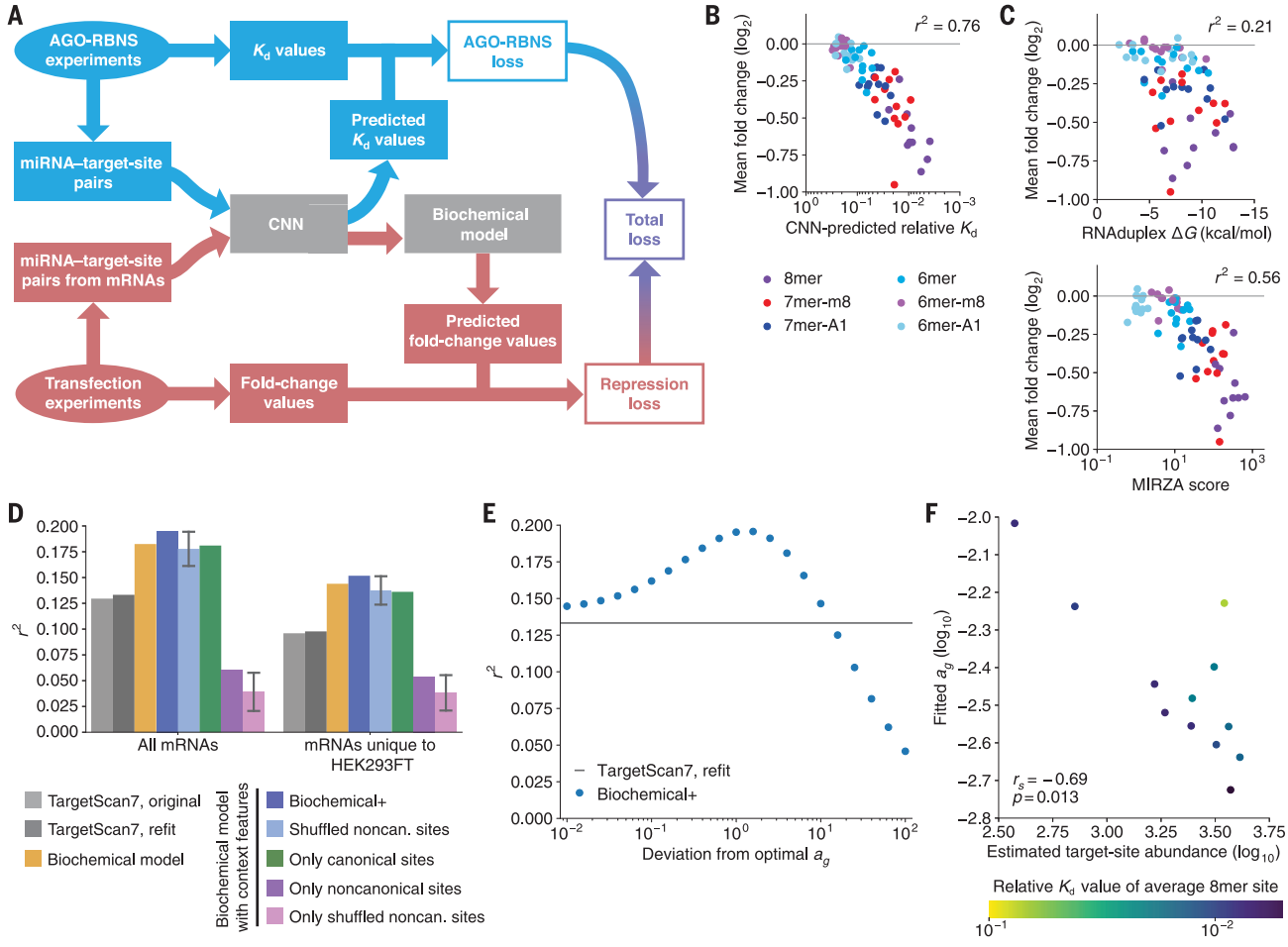

Fig. 6. A CNN for predicting binding affinity from sequence. (**A**) Schematic of overall model architecture for training on RBNS data and transfection data simultaneously. "Loss" refers to squared loss. (**B**) The relationship between repression efficacy and CNN-predicted relative K_d values for the canonical sites for the 12 test miRNAs. Everything else is the same as in Fig. 3, D to I. (**C**) The relationship between repression efficacy and RNAduplex-predicted free-energy values (*45*) (top) or MIRZA scores (*27*) (bottom) for the canonical sites of the 12 test miRNAs. Everything else is the same as in (B). (**D**) Performance of the biochemical and biochemical+ models when provided the CNN-predicted relative K_d values and tested on the 12 datasets examining the effects of transfecting miRNAs into HEK293FT cells. On the left are results obtained when considering all mRNAs, and on the right are results obtained when considering mRNAs expressed in HEK293FT cells but not in HeLa cells. Everything else is the same as in Fig. 5F, except shuffling results were for 250 random permutations rather than all possible permutations. (**E**) Performance of the biochemical+ model on the HEK293FT test set while allowing the a_g values to deviate from the optimal fitted values. (**F**) Relationship between fitted a_g and estimated target-site abundance (*29*) for the guide strands of the 12 duplexes transfected into HEK293FT cells. Points are colored by the average relative K_d value of the 8mer site to each miRNA. The Spearman r_s and p value for the relationship are shown.

fraction attributable to experimental noise was estimated by examining the reproducibility between replicates in our transfection experiments, and the fraction attributable to secondary effects was inferred by assuming that primary miRNA effects only repress mRNAs, whereas secondary effects affect mRNAs in either direction (with effects distributed log normally). After accounting for these other sources of variability, the biochemical+ model provided with experimentally determined affinity values explained ~60% of the variability attributable to direct targeting (fig. S12E, median of five datasets), and when provided with CNN-predicted values, it explained ~50% of the variability attributable to direct targeting (fig. S12F, median of 12 datasets).

Insights into miRNA targeting

The observation that canonical sites are not necessarily those with the highest affinity raises the question of how canonical sites are distinguished from noncanonical ones and whether making such a distinction is useful. Our results show that two criteria readily distinguish canonical sites from noncanonical ones. First, with only one exception, all six canonical site types were identified for each of the six miRNAs (the exception being the 6mer-m8 site for miR-7), whereas the noncanonical site types were typically identified for only one miRNA and never for more than three. Second, the four highest-affinity canonical sites occupied most of the specifically bound AGO2, even for miR-124, which had the largest and highest-affinity repertoire of noncanonical sites (Figs. 1F and 2 and fig. S2, B and C). This greater role for canonical sites was presumably because perfect pairing to the seed region is the most efficient way to bind the silencing complex; to achieve equivalent affinity, the noncanonical sites must be longer and therefore less abundant. The ubiquitous function and more efficient binding of canonical sites explains why these site types have the greatest signal in meta-analyses of site conservation, thereby explaining why they were the first site types to be identified (*31*) and justifying the continued distinction between canonical and noncanonical site types.

The potential role of pairing to miRNA nucleotides 9 and 10 has been controversial.

Although some target-prediction algorithms (such as TargetScan) do not reward pairing to these nucleotides, most algorithms assume that such pairing enhances site affinity. Likewise, although one biochemical study reports that pairing to position 9 reduces site affinity (*6*), another reports that it increases affinity (*12*). We found that extending pairing to nucleotide 9 or 10 neither enhanced nor diminished affinity in the context of seed-matched sites (Fig. 4), whereas extending pairing to nucleotide 9 or 10 enhanced affinity in the context of 3′-only sites (Fig. 2, C and D). These results support the idea that extensive pairing to the miRNA 3′ region unlocks productive pairing to nucleotides 9 to 12, which is otherwise inaccessible (*1*).

The biochemical parameters fit by our model provided additional insights into miRNA targeting. In the framework of our model, the fitted value of 1.8 observed for the parameter b suggested that a typical mRNA bound to an average of one silencing complex will experience a near tripling of its decay rate, which would lead to a ~60% reduction in its abundance. In the concentration regimes of our transfection experiments, this occupancy can be achieved with two to three median 7mer-m8 sites. In addition, our fitted value for the ORF-site penalty suggested that the translation machinery reduces site affinity by 5.5-fold.

Another parameter was a_g, that is, the intracellular concentration of AGO loaded with the transfected miRNA and not bound to a target site. Whereas values of the other parameters could be fit globally in HeLa cells and then used for testing, a_g was fit separately for each miRNA and passenger strand of each transfection experiment. Nonetheless, when a_g values were allowed to deviate from the fitted values, the biochemical+ model still outperformed TargetScan in predicting test-set repression over a 100-fold range of values (Fig. 6E), which indicated that even with rough estimates of miRNA abundances, our modeling framework had an advantage over other predictive methods in new contexts. Information that might be used to more accurately estimate a_g values should come with the determination of these values for more miRNAs in more cellular contexts, together with the observation that, as expected (*29*, *49*), fitted a_g values are higher for miRNAs with lower predicted target abundance and lower general affinity for their targets (Fig. 6F).

Our work replaced the correlative models of targeting efficacy with a principled biochemical model that explains and predicts about half of the variability attributable to the direct effects of miRNAs on their targets, raising the question of how the understanding and prediction of miRNA-mediated repression might be further improved. Acquiring site-affinity profiles for additional miRNAs with diverse sequences will improve the CNN-predicted miRNA-mRNA affinity landscape and further flesh out the two major sources of targeting variability revealed by our study, that is, the widespread differences in site preferences observed for different miRNAs and the substantial influence of local (12-nt) site context. We suspect additional improvement will come with increased ability to predict the other major cause of targeting variability, which is the variability imparted by mRNA features more distant from the site. This variability is captured only partially by the three features added to the biochemical model to generate the biochemical+ model. Perhaps the most promising strategy for accounting for these more distal features will be an unbiased machine-learning approach that uses entire mRNA sequences to predict repression, leveraging substantially expanded repression datasets as well as site-affinity values. In this way, the complete regulatory landscape, as specified by AGO within this essential biological pathway, might ultimately be computationally reconstructed.

Methods summary

AGO2-miRNA complexes were generated by adding synthetic miRNA duplexes to lysate from cells that overexpressed recombinant AGO2, and then these complexes were purified on the basis of affinity to the miRNA seed. RNA libraries were generated by in vitro transcription of synthetic DNA templates. For AGO-RBNS, purified AGO2-miRNA complex was incubated with a large excess of library molecules, and after reaching binding equilibrium, library molecules bound to AGO2-miRNA complex were isolated and prepared for high-throughput sequencing. Examination of k-mers enriched within the bound library sequences identified miRNA target sites, and relative K_d values for each of these sites were simultaneously determined by maximum likelihood estimation, fitting to AGO-RBNS results obtained over a 100-fold range in AGO2-miRNA concentration.

Intracellular miRNA-mediated repression was measured by performing RNA-seq on HeLa cells that had been transfected with a synthetic miRNA duplex. For sites that were sufficiently abundant in endogenous 3′UTRs, efficacy was measured on the basis of their influence on levels of endogenous mRNAs of HeLa cells. Site efficacy was also evaluated using massively parallel reporter assays, which provided information for the rare sites as well as the more abundant ones. The biochemical and biochemical+ models of miRNA-mediated repression were constructed and fit using the measured K_d values, and the repression of endogenous mRNAs was observed after transfecting miRNAs into HeLa cells. The CNN was built using TensorFlow, trained using the measured K_d values and the repression observed in the HeLa transfection experiments, and tested on the repression of endogenous mRNAs observed after transfecting miRNAs into HEK293T cells. Results were also tested on external datasets examining either intracellular binding of miRNAs by CLIP-seq or repression of endogenous mRNAs after miRNAs had been transfected, knocked down, or knocked out. The details of each of these methods are described in the supplementary materials.

REFERENCES AND NOTES

1. D. P. Bartel, Metazoan microRNAs. *Cell* **173**, 20–51 (2018). doi: 10.1016/j.cell.2018.03.006; pmid: 29570994
2. S. Jonas, E. Izaurralde, Towards a molecular understanding of microRNA-mediated gene silencing. *Nat. Rev. Genet.* **16**, 421–433 (2015). doi: 10.1038/nrg3965; pmid: 26077373
3. D. P. Bartel, MicroRNAs: Target recognition and regulatory functions. *Cell* **136**, 215–233 (2009). doi: 10.1016/j.cell.2009.01.002; pmid: 19167326
4. R. C. Friedman, K. K. H. Farh, C. B. Burge, D. P. Bartel, Most mammalian mRNAs are conserved targets of microRNAs. *Genome Res.* **19**, 92–105 (2009). doi: 10.1101/gr.082701.108; pmid: 18955434
5. L. M. Wee, C. F. Flores-Jasso, W. E. Salomon, P. D. Zamore, Argonaute divides its RNA guide into domains with distinct functions and RNA-binding properties. *Cell* **151**, 1055–1067 (2012). doi: 10.1016/j.cell.2012.10.036; pmid: 23178124
6. W. E. Salomon, S. M. Jolly, M. J. Moore, P. D. Zamore, V. Serebrov, Single-molecule imaging reveals that Argonaute reshapes the binding properties of its nucleic acid guides. *Cell* **162**, 84–95 (2015). doi: 10.1016/j.cell.2015.06.029; pmid: 26140592
7. N. T. Schirle, J. Sheu-Gruttadauria, I. J. MacRae, Structural basis for microRNA targeting. *Science* **346**, 608–613 (2014). doi: 10.1126/science.1258040; pmid: 25359968
8. N. T. Schirle, J. Sheu-Gruttadauria, S. D. Chandradoss, C. Joo, I. J. MacRae, Water-mediated recognition of t1-adenosine anchors Argonaute2 to microRNA targets. *eLife* **4**, e07646 (2015). doi: 10.7554/eLife.07646; pmid: 26359634
9. M. H. Jo *et al.*, Human Argonaute 2 has diverse reaction pathways on target RNAs. *Mol. Cell* **59**, 117–124 (2015). doi: 10.1016/j.molcel.2015.04.027; pmid: 26140367
10. S. M. Klum, S. D. Chandradoss, N. T. Schirle, C. Joo, I. J. MacRae, Helix-7 in Argonaute2 shapes the microRNA seed region for rapid target recognition. *EMBO J.* **37**, 75–88 (2018). doi: 10.15252/embj.201796474; pmid: 28939659
11. S. D. Chandradoss, N. T. Schirle, M. Szczepaniak, I. J. MacRae, C. Joo, A dynamic search process underlies microRNA targeting. *Cell* **162**, 96–107 (2015). doi: 10.1016/j.cell.2015.06.032; pmid: 26140593
12. W. R. Becker *et al.*, High-throughput analysis reveals rules for target RNA binding and cleavage by AGO2. *Mol. Cell* **75**, 741–755.e11 (2019). doi: 10.1016/j.molcel.2019.06.012; pmid: 31324449
13. A. Grimson *et al.*, MicroRNA targeting specificity in mammals: Determinants beyond seed pairing. *Mol. Cell* **27**, 91–105 (2007). doi: 10.1016/j.molcel.2007.06.017; pmid: 17612493
14. V. Agarwal, G. W. Bell, J.-W. Nam, D. P. Bartel, Predicting effective microRNA target sites in mammalian mRNAs. *eLife* **4**, e05005 (2015). doi: 10.7554/eLife.05005; pmid: 26267216
15. R. Gumienny, M. Zavolan, Accurate transcriptome-wide prediction of microRNA targets and small interfering RNA off-targets with MIRZA-G. *Nucleic Acids Res.* **43**, 1380–1391 (2015). doi: 10.1093/nar/gkv050; pmid: 25628353
16. M. D. Paraskevopoulou *et al.*, DIANA-microT web server v5.0: Service integration into miRNA functional analysis workflows. *Nucleic Acids Res.* **41**, W169–W173 (2013). doi: 10.1093/nar/gkt393; pmid: 23680784
17. N. Lambert *et al.*, RNA Bind-n-Seq: Quantitative assessment of the sequence and structural binding specificity of RNA binding proteins. *Mol. Cell* **54**, 887–900 (2014). doi: 10.1016/j.molcel.2014.04.016; pmid: 24837674
18. D. Dominguez *et al.*, Sequence, structure, and context preferences of human RNA binding proteins. *Mol. Cell* **70**, 854–867.e9 (2018). doi: 10.1016/j.molcel.2018.05.001; pmid: 29883606
19. C. F. Flores-Jasso, W. E. Salomon, P. D. Zamore, Rapid and specific purification of Argonaute-small RNA complexes from

crude cell lysates. *RNA* **19**, 271–279 (2013). doi: 10.1261/rna.036921.112; pmid: 23249751
20. D. Kim *et al*., General rules for functional microRNA targeting. *Nat. Genet.* **48**, 1517–1526 (2016). doi: 10.1038/ng.3694; pmid: 27776116
21. J. Brennecke, A. Stark, R. B. Russell, S. M. Cohen, Principles of microRNA-target recognition. *PLOS Biol.* **3**, e85 (2005). doi: 10.1371/journal.pbio.0030085; pmid: 15723116
22. R. Denzler, V. Agarwal, J. Stefano, D. P. Bartel, M. Stoffel, Assessing the ceRNA hypothesis with quantitative measurements of miRNA and target abundance. *Mol. Cell* **54**, 766–776 (2014). doi: 10.1016/j.molcel.2014.03.045; pmid: 24793693
23. R. Denzler *et al*., Impact of microRNA levels, target-site complementarity, and cooperativity on competing endogenous RNA-regulated gene expression. *Mol. Cell* **64**, 565–579 (2016). doi: 10.1016/j.molcel.2016.09.027; pmid: 27871486
24. S. W. Chi, G. J. Hannon, R. B. Darnell, An alternative mode of microRNA target recognition. *Nat. Struct. Mol. Biol.* **19**, 321–327 (2012). doi: 10.1038/nsmb.2230; pmid: 22343717
25. G. B. Loeb *et al*., Transcriptome-wide miR-155 binding map reveals widespread noncanonical microRNA targeting. *Mol. Cell* **48**, 760–770 (2012). doi: 10.1016/j.molcel.2012.10.002; pmid: 23142080
26. A. Helwak, G. Kudla, T. Dudnakova, D. Tollervey, Mapping the human miRNA interactome by CLASH reveals frequent noncanonical binding. *Cell* **153**, 654–665 (2013). doi: 10.1016/j.cell.2013.03.043; pmid: 23622248
27. M. Khorshid, J. Hausser, M. Zavolan, E. van Nimwegen, A biophysical miRNA-mRNA interaction model infers canonical and noncanonical targets. *Nat. Methods* **10**, 253–255 (2013). doi: 10.1038/nmeth.2341; pmid: 23334102
28. S. Grosswendt *et al*., Unambiguous identification of miRNA: target site interactions by different types of ligation reactions. *Mol. Cell* **54**, 1042–1054 (2014). doi: 10.1016/j.molcel.2014.03.049; pmid: 24857550
29. D. M. Garcia *et al*., Weak seed-pairing stability and high target-site abundance decrease the proficiency of *lsy*-6 and other microRNAs. *Nat. Struct. Mol. Biol.* **18**, 1139–1146 (2011). doi: 10.1038/nsmb.2115; pmid: 21909094
30. C. Shin *et al*., Expanding the microRNA targeting code: Functional sites with centered pairing. *Mol. Cell* **38**, 789–802 (2010). doi: 10.1016/j.molcel.2010.06.005; pmid: 20620952
31. B. P. Lewis, C. B. Burge, D. P. Bartel, Conserved seed pairing, often flanked by adenosines, indicates that thousands of human genes are microRNA targets. *Cell* **120**, 15–20 (2005). doi: 10.1016/j.cell.2004.12.035; pmid: 15652477
32. C. B. Nielsen *et al*., Determinants of targeting by endogenous and exogenous microRNAs and siRNAs. *RNA* **13**, 1894–1910 (2007). doi: 10.1261/rna.768207; pmid: 17872505
33. H. Tafer *et al*., The impact of target site accessibility on the design of effective siRNAs. *Nat. Biotechnol.* **26**, 578–583 (2008). doi: 10.1038/nbt1404; pmid: 18438400
34. A. D. Bosson, J. R. Zamudio, P. A. Sharp, Endogenous miRNA and target concentrations determine susceptibility to potential ceRNA competition. *Mol. Cell* **56**, 347–359 (2014). doi: 10.1016/j.molcel.2014.09.018; pmid: 25449132
35. M. Jens, N. Rajewsky, Competition between target sites of regulators shapes post-transcriptional gene regulation. *Nat. Rev. Genet.* **16**, 113–126 (2015). doi: 10.1038/nrg3853; pmid: 25488579
36. J. M. Schmiedel *et al*., MicroRNA control of protein expression noise. *Science* **348**, 128–132 (2015). doi: 10.1126/science.aaa1738; pmid: 25838385
37. P. S. Linsley *et al*., Transcripts targeted by the microRNA-16 family cooperatively regulate cell cycle progression. *Mol. Cell. Biol.* **27**, 2240–2252 (2007). doi: 10.1128/MCB.02005-06; pmid: 17242205
38. J. Hausser, M. Landthaler, L. Jaskiewicz, D. Gaidatzis, M. Zavolan, Relative contribution of sequence and structure features to the mRNA binding of Argonaute/EIF2C-miRNA complexes and the degradation of miRNA targets. *Genome Res.* **19**, 2009–2020 (2009). doi: 10.1101/gr.091181.109; pmid: 19767416
39. M. Hafner *et al*., Transcriptome-wide identification of RNA-binding protein and microRNA target sites by PAR-CLIP. *Cell* **141**, 129–141 (2010). doi: 10.1016/j.cell.2010.03.009; pmid: 20371350
40. B. Alipanahi, A. Delong, M. T. Weirauch, B. J. Frey, Predicting the sequence specificities of DNA- and RNA-binding proteins by deep learning. *Nat. Biotechnol.* **33**, 831–838 (2015). doi: 10.1038/nbt.3300; pmid: 26213851
41. R. Tunney *et al*., Accurate design of translational output by a neural network model of ribosome distribution. *Nat. Struct. Mol. Biol.* **25**, 577–582 (2018). doi: 10.1038/s41594-018-0080-2; pmid: 29967537
42. J. T. Cuperus *et al*., Deep learning of the regulatory grammar of yeast 5′ untranslated regions from 500,000 random sequences. *Genome Res.* **27**, 2015–2024 (2017). doi: 10.1101/gr.224964.117; pmid: 29097404
43. K. Jaganathan *et al*., Predicting splicing from primary sequence with deep learning. *Cell* **176**, 535–548.e24 (2019). doi: 10.1016/j.cell.2018.12.015; pmid: 30661751
44. P. Landgraf *et al*., A mammalian microRNA expression atlas based on small RNA library sequencing. *Cell* **129**, 1401–1414 (2007). doi: 10.1016/j.cell.2007.04.040; pmid: 17604727
45. R. Lorenz *et al*., ViennaRNA Package 2.0. *Algorithms Mol. Biol.* **6**, 26–14 (2011). doi: 10.1186/1748-7188-6-26; pmid: 22115189
46. K. Zhang *et al*., A novel class of microRNA-recognition elements that function only within open reading frames. *Nat. Struct. Mol. Biol.* **25**, 1019–1027 (2018). doi: 10.1038/s41594-018-0136-3; pmid: 30297778
47. I. Lipchina *et al*., Genome-wide identification of microRNA targets in human ES cells reveals a role for miR-302 in modulating BMP response. *Genes Dev.* **25**, 2173–2186 (2011). doi: 10.1101/gad.17221311; pmid: 22012620
48. S. W. Eichhorn *et al*., mRNA destabilization is the dominant effect of mammalian microRNAs by the time substantial repression ensues. *Mol. Cell* **56**, 104–115 (2014). doi: 10.1016/j.molcel.2014.08.028; pmid: 25263593
49. A. Arvey, E. Larsson, C. Sander, C. S. Leslie, D. S. Marks, Target mRNA abundance dilutes microRNA and siRNA activity. *Mol. Syst. Biol.* **6**, 363 (2010). doi: 10.1038/msb.2010.24; pmid: 20404830

ACKNOWLEDGMENTS

We thank K. Heindl, T. Eisen, and T. Bepler for helpful discussions; Y. Zhou for providing processed CLIP data from miR-20a overexpression; and members of the Bartel lab for comments on this manuscript. **Funding:** This work was supported by NIH grants GM118135 (D.P.B.) and GM123719 (N.B.). D.P.B. is an investigator of the Howard Hughes Medical Institute. **Author contributions:** S.E.M. developed AGO-RBNS and associated analyses, which he implemented with help from T.M.P. and N.B. K.S.L. devised and implemented the biochemical model and CNN. C.Y.S., G.M.K., and T.M.P. performed transfection and sequencing experiments. C.Y.S. and S.E.M. designed and performed the massively parallel reporter assay. S.E.M., K.S.L., and D.P.B. designed the study and wrote the manuscript with input from other authors. **Competing interests:** The authors declare no competing interests. **Data and materials availability:** Sequencing data are available in the Gene Expression Omnibus (accession number GSE140220), and computational tools are deposited in GitHub (https://github.com/smcgeary/agorbns and https://github.com/kslin/miRNA_models).

SUPPLEMENTARY MATERIALS

science.sciencemag.org/content/366/6472/eaav1741/suppl/DC1
Materials and Methods
Figs. S1 to S12
Tables S1 and S2
References (*50*–*55*)
Data S1 to S3

View/request a protocol for this paper from *Bio-protocol*.

21 August 2018; resubmitted 24 September 2019
Accepted 16 November 2019
Published online 5 December 2019
10.1126/science.aav1741

RESEARCH ARTICLE SUMMARY

TRANSCRIPTOMICS

A genome-wide transcriptomic analysis of protein-coding genes in human blood cells

Mathias Uhlen*, Max J. Karlsson, Wen Zhong, Abdellah Tebani, Christian Pou, Jaromir Mikes, Tadepally Lakshmikanth, Björn Forsström, Fredrik Edfors, Jacob Odeberg, Adil Mardinoglu, Cheng Zhang, Kalle von Feilitzen, Jan Mulder, Evelina Sjöstedt, Andreas Hober, Per Oksvold, Martin Zwahlen, Fredrik Ponten, Cecilia Lindskog, Åsa Sivertsson, Linn Fagerberg†, Petter Brodin†

INTRODUCTION: Blood is the predominant source for molecular analyses in humans, both in clinical and research settings, and is the target for many therapeutic strategies, emphasizing the need for comprehensive molecular maps of the cells constituting human blood. The Human Protein Atlas program (www.proteinatlas.org) is an open-access database that aims to map all human proteins by integrating various omics technologies, including antibody-based imaging. Previously, the Human Protein Atlas included gene expression information from peripheral blood mononuclear cells but not the many subpopulations of blood cells within this cell type. To increase the resolution, we performed an in-depth characterization of the constituent cells in blood to provide a detailed view of the gene expression in individual human blood cells and relate these to the other tissues in the body.

RATIONALE: A quantitative transcriptomics-based expression analysis was performed in 18 canonical immune cell populations (Fig. 1) isolated by flow cytometric sorting. The blood cell expression profiles are presented in combination with expression profiles of tissues, including transcriptomics data from external sources to expand the number of tissue types as well as brain regions included in the database. A genome-wide classification of the protein-coding genes has been performed in terms of expression specificity and distribution, both in blood cells and tissues.

ON OUR WEBSITE

Read the full article at http://dx.doi.org/10.1126/science.aax9198

RESULTS: We present an atlas of the expression of all protein-coding genes in human blood cells, integrated with a classification of the specificity and distribution of all protein-coding genes in all major tissues and organs in the human body. A genome-wide analysis of blood cell RNA expression profiles allowed the identification of genes with elevated expression in various immune cells, confirming well-known protein markers, but also identified novel targets for in-depth analysis. There are 1448 protein-coding genes that have enriched expression in a single immune cell type. It will be interesting to study the corresponding proteins further to explore the biological functions linked to the respective cell phenotypes. A network plot of all cell type–enriched and group-enriched genes (Fig. 1B) reveals that many of the cell type–enriched genes are in neutrophils, eosinophils, and plasmacytoid dendritic cells, while many of the elevated genes in T and B cells are group-enriched across subpopulations of these lymphocytes. To illustrate the usefulness of this resource, we show the cellular distribution of genes known to cause primary immunodeficiencies in humans and find that many of these genes are expressed in cells not currently implicated in these diseases, illustrating how this global atlas can help us better understand the function of specific genes across cells and tissues in humans.

CONCLUSION: In this study, we have performed a genome-wide transcriptomic analysis of protein-coding genes in sorted blood immune cell populations to characterize the expression levels of each individual gene across all cell types. All data are presented in an interactive, open-access Blood Atlas as part of the Human Protein Atlas and are integrated with expression profiles across all major tissues to provide spatial classification of all protein-coding genes. This allows for a genome-wide exploration of the expression profiles across human immune cell populations and all major human tissues and organs. ■

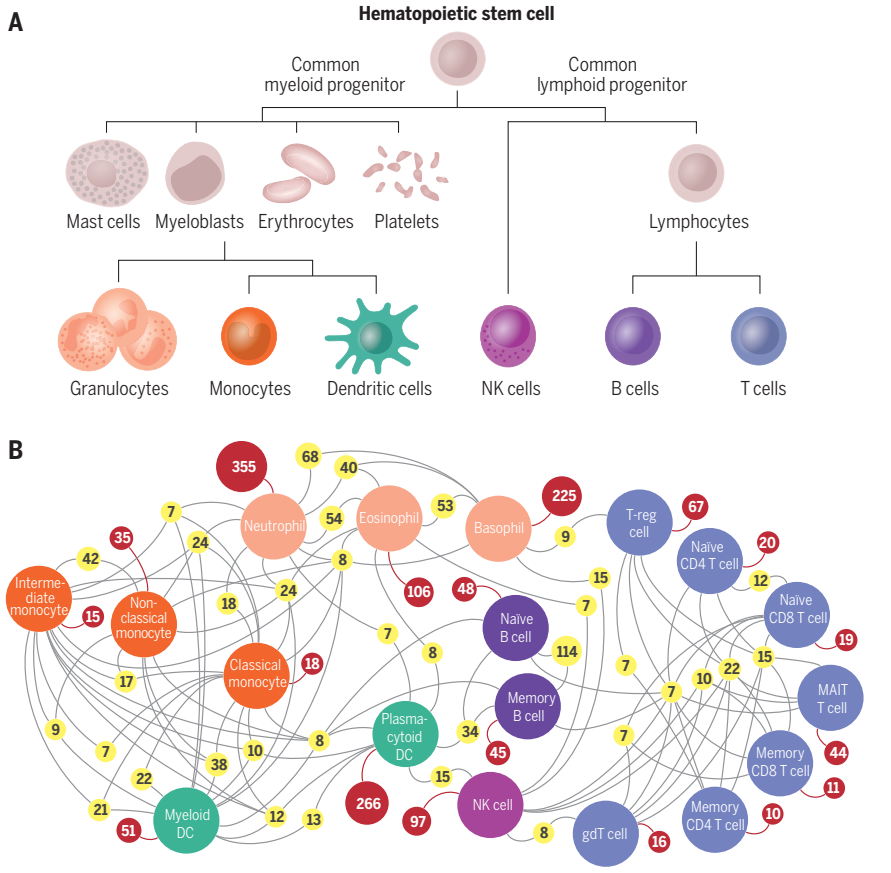

Fig. 1. Outline of the analysis of human single blood cell types. (**A**) A schematic view of the hematopoietic differentiation. This study analyzes the cell types shown in the bottom row. NK, natural killer. (**B**) Network plot showing the number of cell type– (red) and group-enriched (yellow) genes in the 18 cell types. The network is limited to nodes with a minimum of seven genes. DC, dendritic cell; T-reg, regulatory T cell; gdT cell, gamma delta T cell; MAIT, mucosal associated invariant.

The list of author affiliations is available in the full article online.
*Corresponding author. Email: mathias.uhlen@scilifelab.se
†These authors contributed equally to this work.
Cite this article as M. Uhlen *et al.*, *Science* **366**, eaax9198 (2019). DOI: 10.1126/science.aax9198

RESEARCH ARTICLE

TRANSCRIPTOMICS

A genome-wide transcriptomic analysis of protein-coding genes in human blood cells

Mathias Uhlen[1,2,3]*, Max J. Karlsson[1], Wen Zhong[1], Abdellah Tebani[1], Christian Pou[4], Jaromir Mikes[4], Tadepally Lakshmikanth[4], Björn Forsström[1], Fredrik Edfors[1], Jacob Odeberg[1,5], Adil Mardinoglu[1,6], Cheng Zhang[1], Kalle von Feilitzen[1], Jan Mulder[2], Evelina Sjöstedt[2], Andreas Hober[1], Per Oksvold[1], Martin Zwahlen[1], Fredrik Ponten[7], Cecilia Lindskog[7], Åsa Sivertsson[1], Linn Fagerberg[1]†, Petter Brodin[4,8]†

Blood is the predominant source for molecular analyses in humans, both in clinical and research settings. It is the target for many therapeutic strategies, emphasizing the need for comprehensive molecular maps of the cells constituting human blood. In this study, we performed a genome-wide transcriptomic analysis of protein-coding genes in sorted blood immune cell populations to characterize the expression levels of each individual gene across the blood cell types. All data are presented in an interactive, open-access Blood Atlas as part of the Human Protein Atlas and are integrated with expression profiles across all major tissues to provide spatial classification of all protein-coding genes. This allows for a genome-wide exploration of the expression profiles across human immune cell populations and all major human tissues and organs.

Resolving the molecular details of proteome variation in the different cells, tissues, and organs of the human body may considerably increase our knowledge of human biology and disease. Several efforts to map the molecular components of the human body in a comprehensive manner have been initiated, including efforts to generate experimental data such as the Human Cell Atlas (*1*), the Human Biomolecular Atlas Program (HuBMAP) (*2*), the Biohub (*3*), the Genotype-Tissue Expression (GTEx) project (*4*), the Functional Annotation of the Mammalian Genome (FANTOM) project (*5*), and the Allen Brain Atlas (*6*), involving many alternative technologies, including single-cell genomics (*7*), in situ analysis (*8*), transcriptomics (*9*), proteomics (*10*), and antibody-based profiling (*11*). In addition, several knowledge resources have been created to annotate, assemble, and integrate data from such sources, such as UniProt (*12*), ELIXIR (*13*), ArrayExpress (*14*), Peptide Atlas (*15*), and ImmPort (*16*). The combined efforts of these resources have the potential to allow a systematic knowledge base of the molecular components of human life that will aid a systems biology understanding of human biology and diseases.

A complement to these efforts is the Human Protein Atlas program (*17*), which is exploring the human proteome using gene-centric and genome-wide antibody-based profiling on tissue microarrays. This allows for spatial pathology-based annotation of protein expression that is performed in combination with deep sequencing transcriptomics profiling of the same tissue types. The aim is to map all human proteins in cells, tissues, and organs using integration of various omics technologies, including antibody-based imaging, mass spectrometry–based proteomics, and transcriptomics. The earlier version of the Human Protein Atlas consists of three separate parts, each focusing on a particular aspect of the genome-wide analysis of human proteins: the Tissue Atlas (*17*), showing the distribution of proteins across all major tissues and organs in the human body; the Cell Atlas (*18*), showing the subcellular localization of proteins in single cells; and the Pathology Atlas (*19*), showing the impact of different protein levels in tumor tissue on the survival of cancer patients. However,

[1]Science for Life Laboratory, KTH–Royal Institute of Technology, Stockholm, Sweden. [2]Department of Neuroscience, Karolinska Institute, Stockholm, Sweden. [3]Novo Nordisk Foundation Center for Biosustainability, Technical University of Denmark, Kongens Lyngby, Denmark. [4]Science for Life Laboratory, Department of Women's and Children's Health, Karolinska Institutet, Stockholm, Sweden. [5]Coagulation Unit, Department of Hematology, Karolinska University Hospital, Stockholm, Sweden. [6]Centre for Host-Microbiome Interactions, Faculty of Dentistry, Oral and Craniofacial Sciences, King's College London, London, UK. [7]Department of Immunology, Genetics and Pathology, Rudbeck Laboratory, Uppsala University, Uppsala, Sweden. [8]Unit of Pediatric Rheumatology, Karolinska University Hospital, Stockholm, Sweden.
***Corresponding author. Email: mathias.uhlen@scilifelab.se**
†These authors contributed equally to this work.

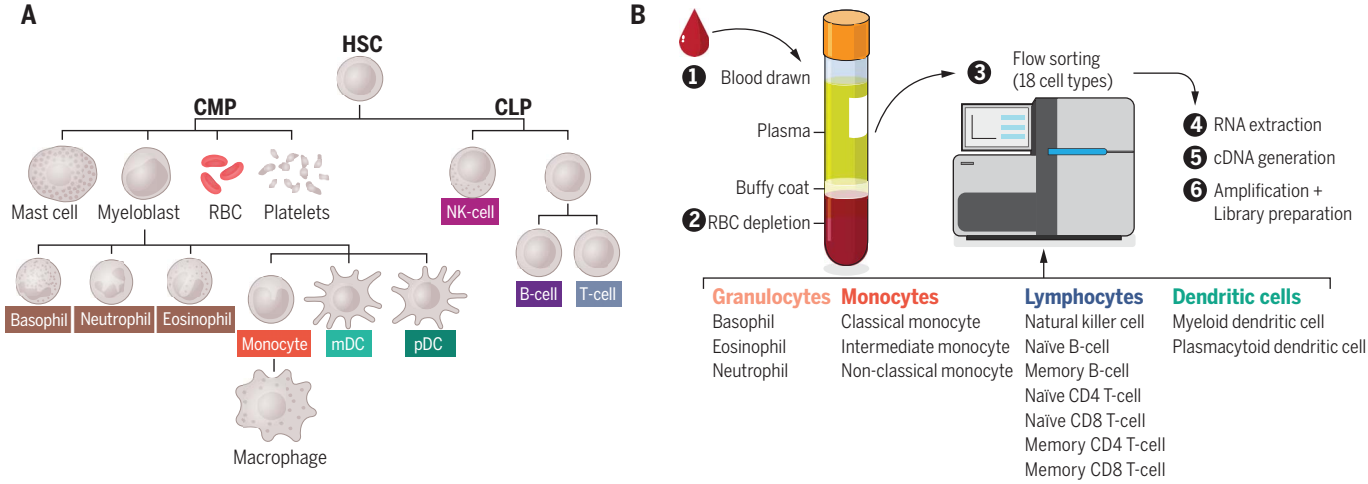

Fig. 1. Outline of the analysis of human single blood cell types. (**A**) A schematic view of the hematopoietic differentiation with the cell types analyzed in this study highlighted. HSC, hematopoietic stemcell; CMP, common myeloid progenitor; CLP, common lymphoid progenitor; RBC, red blood cell; mDC, myeloid dendritic cell; pDC, plasmacytoid dendritic cell. (**B**) A schematic view of the experimental procedure to analyze the transcript expression levels in human single cell types. The 18 cell types listed include seven subsets of T cells, two variants of B cells, three different monocytic cell types, and the three known forms of granulocytes.

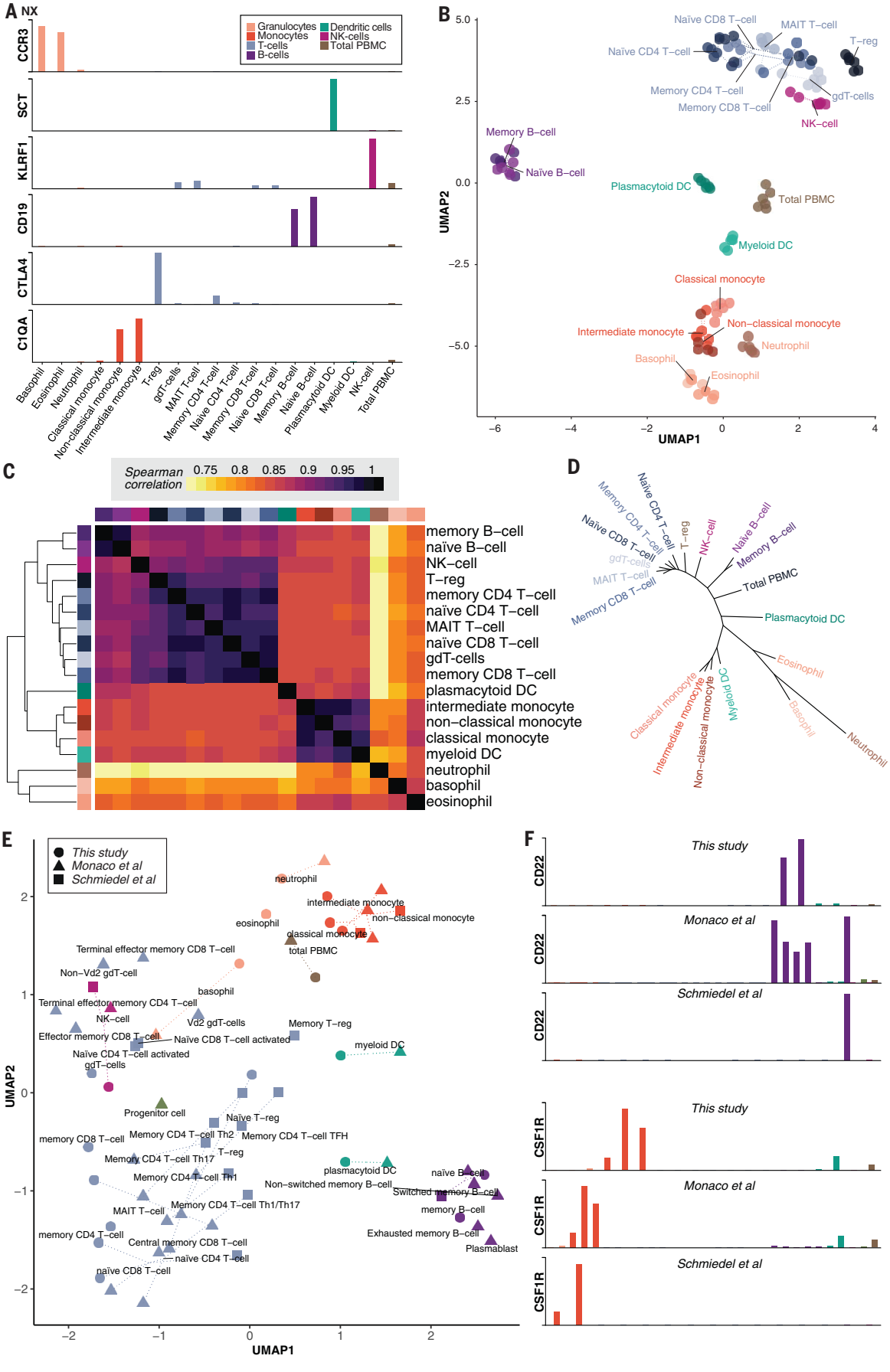

Fig. 2. The expression profiles of the protein-coding genes in human single blood cell types. (**A**) Examples of expression profiles for six genes enriched in one of the cell lineages (see www.proteinatlas.org for details). (**B**) A UMAP analysis of the relationship between the global expression patterns in all the 109 blood cell samples analyzed here. (**C**) A heatmap showing the pairwise Spearman correlation between the global expression profiles for the 18 analyzed cell types. (**D**) Transcriptomics-derived hematopoietic tree showing the similarities in global expression patterns between different human blood cell types. (**E**) UMAP analysis showing the relationship between all the blood cell samples from three different sources. Cell types overlapping between two or all three datasets are connected by dotted lines. (**F**) Comparison of expression profiles for the three datasets, as exemplified for the genes *CD22* and *CSF1R* (see www.proteinatlas.org for details).

there is a lack of data regarding protein expression levels in human blood cells. Given that blood is the most commonly used material for molecular analyses in clinical labs and in research, characterizing the constituents of blood and updating the Human Protein Atlas with a more fine-grained view of the immune cells in blood will be of importance.

In this study, we performed a quantitative expression analysis of 18 canonical immune cell populations, as well as total peripheral blood mononuclear cells (PBMCs) from human blood separated by flow cytometric sorting. The data are integrated with recent transcriptomics efforts involving flow sorting of blood cells, including the analysis in 15 blood cell types by Schmiedel *et al.* (*20*) and 29 blood cell types as well as total PBMCs by Monaco *et al.* (*21*). We presented the expression profiles in specific cell populations and combined the new single-cell blood data with the data from the Tissue Atlas (*17*) by incorporating transcriptomics data from the GTEx (*4*) and the FANTOM5 (*5*) projects. Moreover, we expanded the set of normal tissue samples by adding tissues such as retina and tongue, as well as extensive data covering the different regions of the brain. A genome-wide classification of the protein-coding genes with regard to tissue and cell distribution as well as specificity has been performed using between-sample normalized data (*22*, *23*). The results are presented in an interactive database (www.proteinatlas.org) that can serve as a reference for researchers interested in spatial expression profiles of human blood cells in relation to the body-wide profiles in all major tissues and organs.

Transcriptome analysis of isolated human immune cell populations

We used flow cytometric sorting to allow whole-genome transcriptome analysis of the major blood cell types from human blood (Fig. 1A). Whole blood was collected from six healthy individuals, and 18 immune cell types were separated by flow cytometric sorting, as outlined in Fig. 1B. The cell types recovered included naïve and memory B cells, CD4 and CD8 T cell populations, natural killer (NK) cells, three monocyte subsets, neutrophils, eosinophils, and basophils, as well as plasmacytoid and myeloid dendritic cells. These can be classified into six different blood cell lineages consisting of granulocytes, monocytes, T cells, B cells, dendritic cells, and NK cells. The sorted cells were immediately processed using RNA extraction and cDNA generation followed by deep mRNA sequencing. The RNA expression levels were determined for all protein-coding genes (n = 19,670) across the 18 immune cell populations and visualized in a newly created Blood Atlas, launched here as an extended edition of the open-access Human Protein Atlas (www.proteinatlas.org/blood).

In the Blood Atlas, the expression levels for each of the 19,670 genes are displayed for the 18 cell types and PBMC as exemplified in Fig. 2A. The first example is the G-coupled C-C motif chemokine receptor 3 (CCR3), involved in allergic reactions, showing distinct expression in basophil and eosinophils, with much lower levels in neutrophils. Next, the secretin propeptide (SCT), previously described (*24*) as being produced in the gastrointestinal tract (duodenum and colon), is here found to also be expressed in the human plasmacytoid dendritic cells. The killer cell lectin like receptor F1 (KLRF1), known to stimulate cytotoxicity and cytokine release in NK cells (*25*), is an example of an NK cell enriched gene, but the data also show expression in gamma delta T (gdT) cells and mucosal-associated T invariant (MAIT) cells. The purity of our sorting is verified by known marker expression patterns, such as the canonical cell surface receptor CD19, exclusively expressed in B cells, and the cytotoxic T lymphocyte–associated protein 4 (CTLA4), expressed on regulatory T cells (T_{regs}). The complement C1q A chain (C1QA) of the complement system is instead enriched in monocytes, and the profiling shows high expression in intermediate and nonclassical monocytes but no expression in classical monocytes. In addition to the sorted single cell type populations, the mixed PBMCs were collected from the individuals, as described before (*26*), and the transcriptome determined.

Global expression profiles for the blood cell types

The relationships between all blood cell samples on the basis of their global expression profiles were analyzed using different algorithms, including principal components analysis (PCA) (*27*) and uniform manifold approximation and projection (UMAP) (*28*), and the UMAP results for all samples for all cell types are shown in Fig. 2B. The samples from the different cell types showed similar global expression profiles with the multitude of different B cell and T cell types clustering together. A heatmap based on pairwise Spearman correlation of the expression profiles of the 18 cell types (Fig. 2C) showed that cells of similar origin have similar overall expression profiles, with the three granulocyte cell types having the most distinct expression profiles. All lymphocytes form a separate cluster, including all seven T cells clustering together with the NK cells, and naïve and mature B cells clustering together. The monocytes are most closely related to the myeloid dendritic cells and the plasmacytoid dendritic cells. To analyze the similarities between the cell types of different origins in more detail, we constructed a transcriptomics-derived hematopoietic tree (Fig. 2D) to further illustrate the relation in global expression profiles between the different single blood cell types.

The transcript expression profiles from the recent studies by Schmiedel *et al.* (*20*) and Monaco *et al.* (*21*), having partially overlapping data for 13 and 27 blood cell types, respectively, are also included in the Blood Atlas. UMAP results for all cell types from the three different data sources are shown in Fig. 2E, confirming the distinct expression profiles between various types of blood cells. A summary of the genome-wide expression levels from all three datasets is visualized for all protein-coding genes in the Blood Atlas resource online (Fig. 2F). More in-depth analyses are needed to establish whether the differences seen are due to differential activation states based on sample handling, differences in sample handling and cell sorting, or whether they reflect biological differences among cohorts, representing individuals from Europe (this study), the United States (*20*), and Asia (*21*).

Genome-wide transcriptomics profiles across all major organs and tissues

With the new data covering the blood cell expression profiles as well as an expanded set of normal tissue types, the body-wide tissue profiling performed earlier (*29*) was revised. Because the brain regions were only superficially covered in the earlier analysis, we also decided to include more brain regions using publicly available data from the GTEx (*4*) and FANTOM (*5*) consortia to allow for more in-depth coverage of the different regions of the human brain. Altogether, 1710 samples from selected human brain regions were added to the classification covering 23 human subregions and summarized into 12 main structures of the brain (Fig. 3A). The detailed analysis of the protein expression in these brain structures will be described elsewhere, but here the expression profiles were used in the body-wide tissue classification of all genes. In addition, the five tissues dominated by immune cells (thymus, appendix, spleen, lymph node, and tonsil) were summarized into "lymphoid tissues," and the four highly related tissues from the gut (duodenum, small intestine, colon, and rectum) were summarized into "intestine," as outlined in Fig. 3A. Some additional tissues, including lactating breast, vagina, retina, ductus deferens, and tongue, were also added to the comparative analysis. The expression data for the 18 blood cell types as well as PBMC described above were summarized into "blood." A body-wide classification based on the genome-wide expression profiles of the protein-coding genes was performed with 171 different cells, tissues, and organs, which are summarized into 37 tissue types.

The transcriptomics data was normalized by applying two different strategies with the main objective to allow (i) within-sample comparisons and (ii) between-sample comparisons, respectively, as outlined in fig. S1. For the within-sample comparisons, the fraction of transcripts corresponding to a particular gene

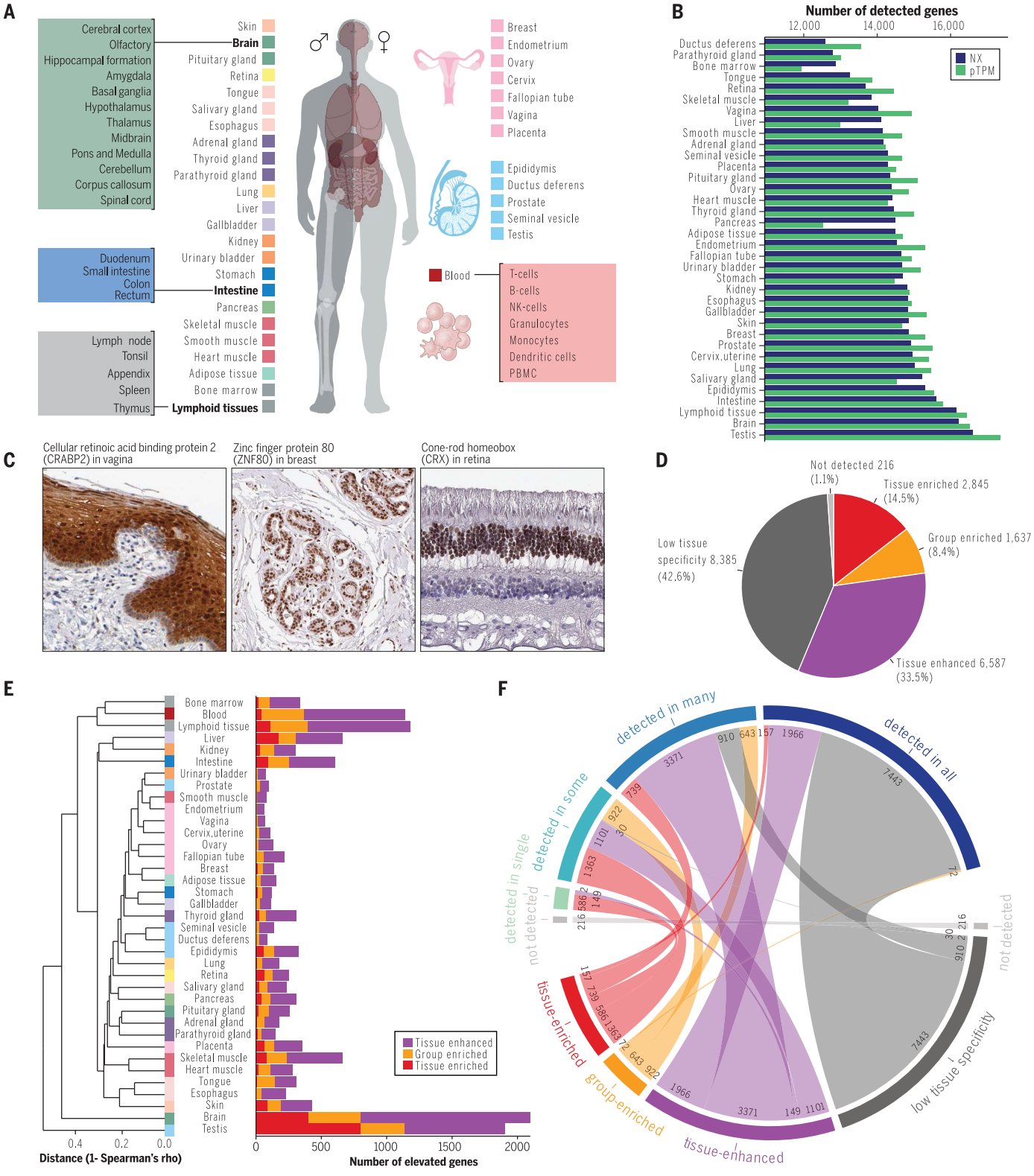

Fig. 3. Classification of the human global gene expression profiles across all major tissues and organs and the immune cell types. (**A**) Schematic view of all human tissues and organs analyzed. (**B**) The number of detected genes in selected tissues based on pTPM and NX values, respectively. (**C**) Three examples of tissues introduced in this study. (**D**) Pie chart showing the number of genes classified according to the specificity categories. (**E**) (Left) A dendrogram based on the correlation of global expression profiles across all tissues and organs, including blood. (Right) Barplot displaying the number of elevated genes for each tissue type. (**F**) Chord diagram showing the relationship between the distribution classification and the specificity classification. Each link represents the number of genes with the linked distribution category and specificity category.

is used. We focus on the protein-coding transcripts and the fraction of transcripts per million of total transcripts from protein-coding genes (pTPM) calculated for each individual gene in every sample. The pTPM value is visualized on the Blood Atlas page of the Human Protein Atlas across the samples for each of the genes. The pTPM values can be considered as the within-sample normalized data from the deep sequencing, in which noncoding RNA has been excluded from the analysis. The pTPM values can be used to investigate the abundance of a particular gene, gene family, or gene class relative to all other transcripts in a particular cell, tissue, or organ.

The second normalization strategy is carried out to allow for comparisons across samples and to avoid batch effects caused by sampling, technology platforms, or the difference in transcriptome size between different types of tissues, as exemplified by pancreas and salivary gland, where a small number of genes are very highly expressed (*22*, *23*). This is particularly important when tissue samples based on different transcriptomic technology platforms have been used, as described for the tissue analysis where RNA sequencing data from multiple sources as well as cap analysis of gene expression data from the FANTOM5 program have been combined. Here, we used a normalization based on trimmed mean of M values (TMM) (*30*), Pareto scaling (*31*), and the Limma R package (*32*) to calculate a normalized expression value (NX) for each gene in every sample. In the Human Protein Atlas, the NX value for each gene is visualized in parallel with the pTPM value for all tissues and cell types. The objective of using the NX value is to facilitate the analysis of differences in expression of genes between cells, tissues, and organs and to allow for a specificity classification based on the genome-wide expression of all genes across the human blood cells, tissues, and organs.

The number of detected genes in the different tissues and organs was investigated using both the within-sample normalization (pTPM) and the between-sample normalization (NX), in both cases using a cutoff value of 1, as described previously (*17*). In Fig. 3B and fig. S2, the results for selected tissues are shown, and the analysis demonstrated a similar number of detected genes for most samples, with some notable exceptions, including tissues with a small fraction of highly abundant transcripts, such as bone marrow (hemoglobin), pancreas (digestive enzymes), liver (albumin), and salivary gland (digestive proteins).

The revised tissue classification of all human genes

The extended data allowed us to refine the classification for the putative protein-coding genes on the basis of their expression across all 37 cells, tissues, and organs. Some examples of genes detected in the recently added tissues are shown in Fig. 3C. The first example, CRABP2 in vagina, plays a role in the vitamin A signaling pathway, with tissue-enhanced expression in squamous mucosa and with nuclear and cytoplasmic positivity in suprabasal squamous epithelia. Another example is breast with ZNF80, a protein with unknown function that here shows nuclear positivity with tissue enhanced expression in blood and breast tissue. Also shown is retinal epithelium with cone-rod homeobox protein (CRX), showing nuclear positivity in the cone-and-rod photoreceptor layer.

All 19,670 genes were classified according to a strategy based on scoring both tissue specificity and tissue distribution (tables S1 and S2; full list of results in data S1). Of all protein-coding genes, 56% (n = 11,069) showed elevated expression in at least one of the analyzed tissues, and these were further subdivided into (i) tissue-enriched genes with at least fourfold higher expression levels (based on NX values) in one tissue type as compared with any other analyzed tissue; (ii) group-enriched genes with enriched expression in a small number of tissues (2 to 5); and (iii) tissue-enhanced genes with only moderately elevated expression (table S1). 2845 genes (14%) of the protein-coding genes were found to be enriched in one of the analyzed tissues (Fig. 3D), and only 216 genes were not detected in any of the analyzed tissues. Our classification shows the number of tissue-enriched genes for each tissue type, as well as the number of genes enriched in different groups of tissues (Fig. 3E). The largest number of tissue-enriched genes are found in the testes, as shown in our previous results (*17*); however, the largest number of elevated genes is now found in the brain, most likely owing to the inclusion of many more brain regions as compared with earlier versions of the atlas. Whereas the specificity classification showed us the enrichment of genes, the distribution classification showed us the fraction of tissues where the gene is expressed. Only 737 genes (4%) are restricted to a single tissue, while almost half of the protein-coding genes are expressed in all tissues (n = 9638) (fig. S3).

The global expression profiles were investigated using the between-sample normalized values (NX) using PCA (fig. S4), UMAP (fig. S5), and hierarchical clustering based on genome-wide correlation between the cells, organs, and tissue types (fig. S6). The resulting dendrogram (Fig. 3E) shows that testis and brain have the most distinct expression profiles compared with all other tissues, and that blood is most highly correlated with lymphoid tissues and bone marrow. The overall results corresponded well with the origin and function of each tissue, as exemplified by many of the female tissues clustering together and the close connectivity of the two tissues composed of striated muscle (cardiac and skeletal muscle).

In Fig. 3F and table S3, a summary of all 19,670 genes with regard to both tissue specificity and distribution classification is shown with the genome-wide relationship of the two classification schemes introduced, showing that only 586 genes are "tissue specific," meaning they are tissue-enriched and, at the same time, only detected in a single tissue (this list is available at www.proteinatlas.org). Relatively few genes (n = 1637) were found to be group-enriched, and this lower number compared with earlier results (*17*) is most likely explained by the fact that some tissues have now been grouped together, such as lymphoid tissues, intestine, and brain. 43% (n = 8385) of the genes were classified as "low tissue specificity," and most of these are found in the "detected in all" category. All 19,670 protein-coding genes in humans have now been analyzed with respect to their tissue specificity and distribution across all major organs, tissues, and blood cells in the human body, and the results are available in the Human Protein Atlas.

Transcriptome usage in different cells and tissues

An analysis of the transcriptome allowed us to determine the fraction of transcripts corresponding to different genes in each analyzed cell type and tissue. Here, we report the transcriptome usage for some representative blood cell types and tissues on the basis of within-sample normalized pTPM values (Fig. 4A and fig. S7A) and between-sample NX normalized values (Fig. 4B and fig. S7B). These are further stratified according to genes coding for secreted, membrane-bound, and intracellular proteins. It is notable that, for pancreas and salivary gland, as much as 80 and 50%, respectively, of the transcripts (based on pTPM) encode for secreted proteins. This demonstrates the extreme specialization of these "secretory cell factories" for production of extracellular proteins, with a few genes dominating the transcriptome load. The most abundant proteins in pancreas code for digestive enzymes, such as lipases (PNLIP, CLPS), proteases (PRSS1, CELA3A), and peptidases (CPA1, CPB1). The most abundant proteins in salivary gland are a protein with essentially unknown function (submaxillary gland androgen regulatory protein 3B, SMR3B) and statherin (STATH), which prevents the precipitation of calcium phosphate in saliva, maintaining a high calcium level in saliva that is necessary for remineralization of tooth enamel. The second- and fourth-most abundant proteins in salivary gland are antimicrobial peptides (HTN3 and HTN1). Similarly, the liver has a large fraction of secreted proteins with the most abundant being albumin (ALB), haptoglobin (HP), and apolipoprotein A2 (APOA2).

In contrast, >60% of all pTPM values for cardiac muscle code for membrane proteins, mainly consisting of mitochondrial proteins,

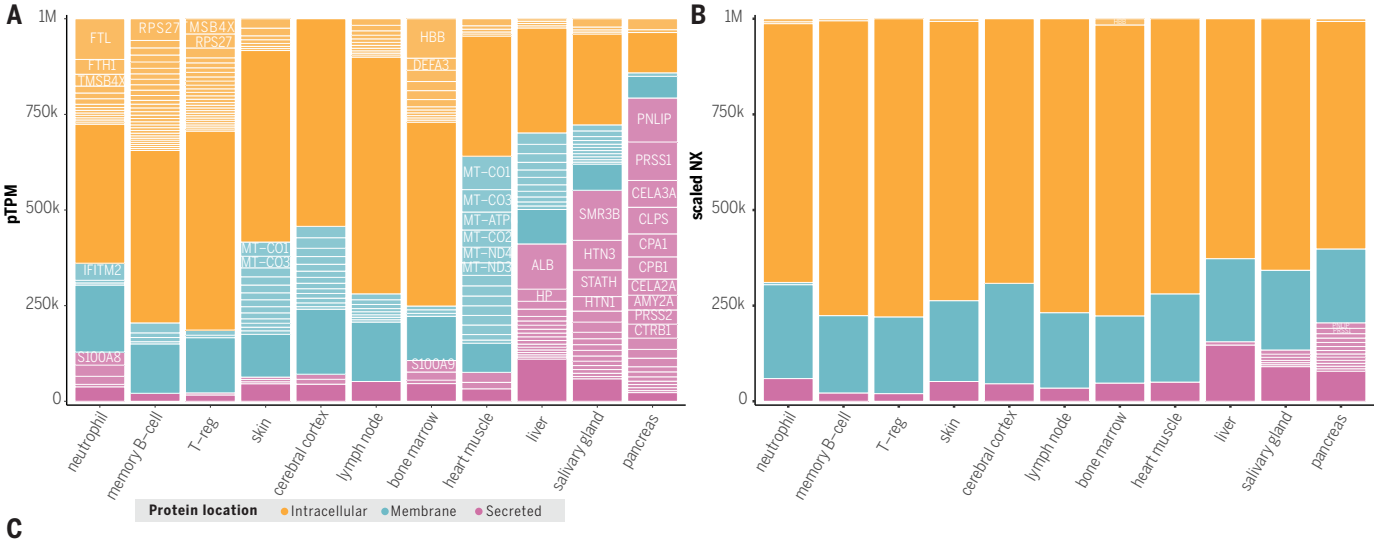

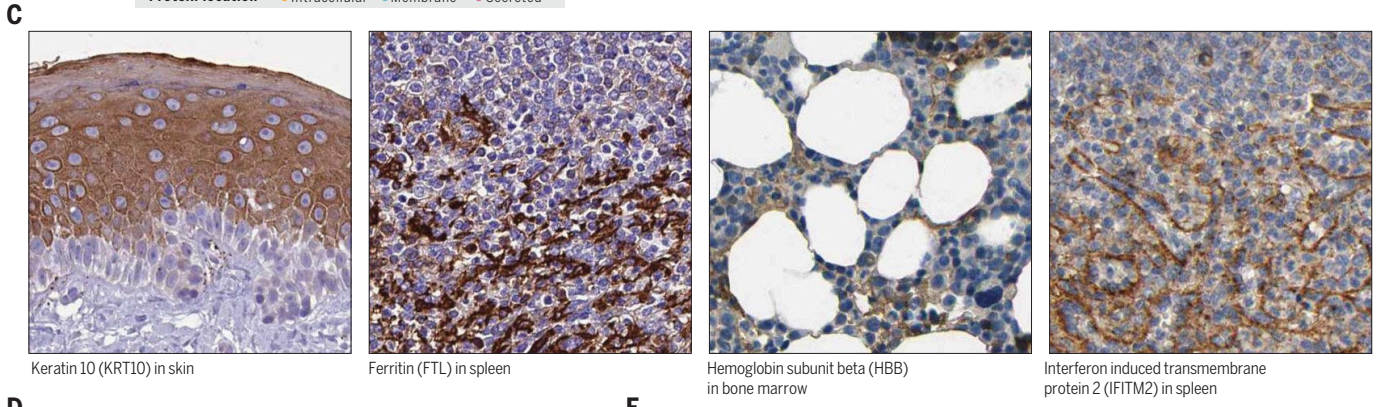

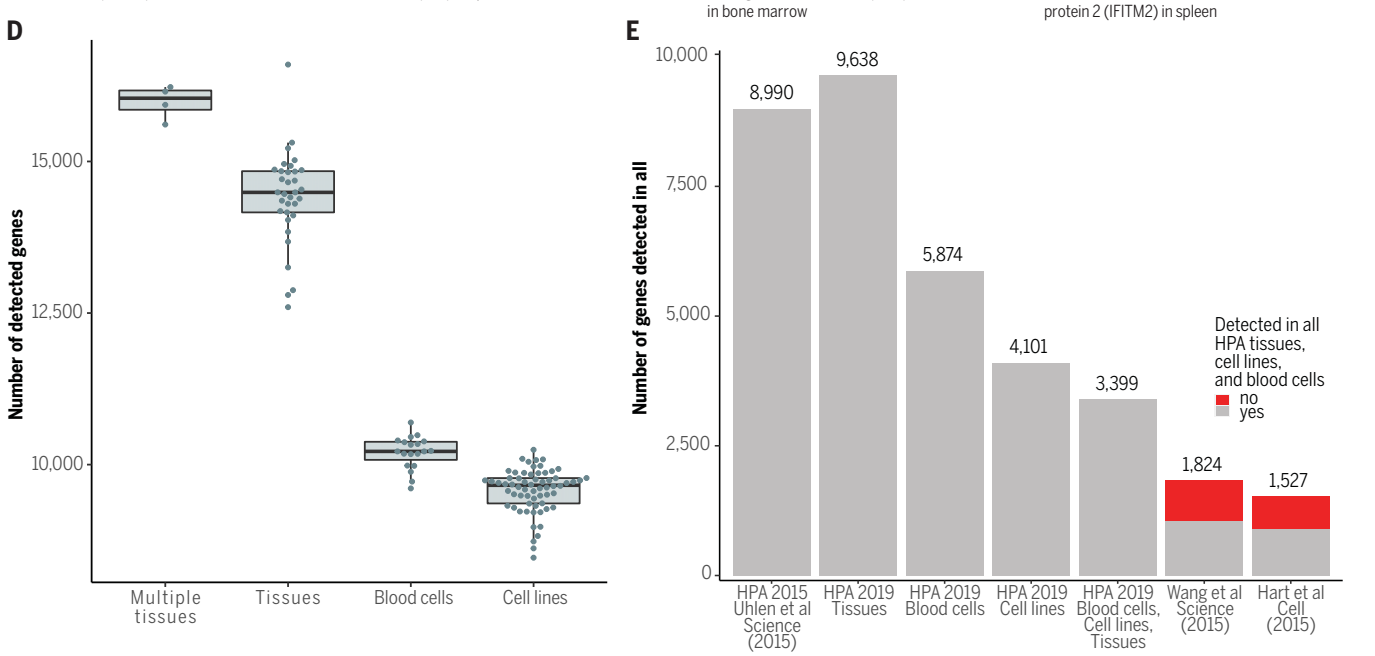

Fig. 4. Analysis of the global expression profiles in the various tissues. (**A**) The transcriptional load based on pTPM in some selected cells and tissues stratified according to protein location: secreted, membrane-bound, or intracellular. The genes with most abundant transcripts are labeled. (**B**) Same as (A), but based on the between-sample normalized NX values scaled to a sum of one million. (**C**) Immunohistochemistry (IHC) images from the Human Protein Atlas for four examples of the most abundant genes in some selected tissues. (**D**) Boxplot showing the distribution of the number of detected genes for the combined groups of tissue types (brain, blood, intestine, and lymphoid tissues), all single tissue types, the 18 blood cell types, and cell lines (*18*). (**E**) The number of genes expressed in all samples is shown based on the earlier analysis (*17*), and in all tissues, the immune cell types reported here as well as for 60 cell lines. Also shown is the number of genes when including all these three sample types. We also compare the number of genes identified as "essential" using CRISPR knock-out strategies (*33*, *34*) and highlight the number of genes not "detected in all" for all samples covering the cell lines, tissues, and blood cells.

which is not unexpected given the extreme requirement of energy in the cardiac muscle. For most tissues and for all the single blood cells, the intracellular proteins instead constitute most of the transcriptome load, as exemplified by bone marrow with hemoglobin (HBB) and the skin with keratin (KRT10) (Fig. 4C) as the most abundant transcript, respectively. In the blood cells, there are fewer genes with a dominant abundance, although the most abundant transcript in neutrophils is the gene encoding the intracellular protein ferritin light chain (FTL), a subunit of ferritin, the major protein responsible for intracellular iron storage. A notable example of a gene with abundant transcripts, but with almost no known functional information, is the interferon-induced transmembrane protein 2 (IFITM2), which is highly expressed in neutrophils and here is shown in spleen. The transcriptome maps demonstrate the high specialization of each tissue with a large portion of the transcript burden devoted to functions of relevance for the corresponding cells in respective tissue type.

Number of detected genes and the "housekeeping" genes

An analysis of the number of detected genes in the various samples (Fig. 4D) shows that ~16,000 genes are detected in the four combined groups of multiple tissue types (blood, brain, intestine, and lymphoid tissues), while the analysis of single tissues shows a slightly smaller number of genes (~14,000 on average) —with the exception of testis, in which 16,598 genes are detected. This is in contrast to the much smaller number of detected genes when analyzing cell lines (~9500 genes per cell line) and single blood cell types (~10,000 genes). The fact that more genes are detected in tissues as compared with the single cell type analysis is not unexpected, as it reflects the presence of a multitude of different cell types present in composite tissues. The observation that a slightly smaller number of genes are detected in the cell lines as compared with the single blood cells is interesting, and it is tempting to speculate that this is due to the in vitro specialization of the cell lines.

Almost half (49%) of the protein-coding genes (n = 9638) were detected in all analyzed tissues (Fig. 4E), and these genes include known "housekeeping" genes encoding mitochondrial proteins, and proteins involved in overall cell structure, translation, transcription, and replication. An analysis of the human cell lines shows that 4101 genes are detected in all samples. Similarly, the analysis of the 18 single blood cell types shows that 5874 genes are ubiquitously detected across all immune cells. If the tissues, cell lines, and single blood cell types are combined, the number of protein-coding genes detected in all samples is decreased to 3399 (Fig. 4E). This is still a much larger number when compared with the determination of essential genes using genome-wide CRISPR-Cas9 knock outs (*33*, *34*), which identified 1824 and 1527 genes with unconditional importance for cell survival, respectively. This suggests that many genes are present in all cells but that they perform redundant functions in cell lines. Altogether, we identified genes that are both essential in genome-wide knock-out screens and here detected in all blood cells, cell lines, tissues, and organs. This list of genes (available at www.proteinatlas.org) contains many well-known housekeeping genes involved in replication, translation, and cellular processes, and more in-depth studies are needed to explore the function of the genes detected in all tissues and yet not identified as essential by the knock-out screen.

It is reassuring that the number of "missing genes," i.e., those not detected in any tissue or cell type, is now reduced to 216, which is only ~1% of the total number of predicted protein-coding genes. We therefore revised (*35*) the number of genes for which evidence at protein level is present by combining our antibody-based data with the manual annotation of literature by the UniProt consortium (*36*) and the results from mass spectrometry–based proteogenomics analyses (*37*). The analysis showed that there are 17,660 protein-coding genes with proteins identified from at least one of the three efforts and 15,155 genes with experimental evidence from at least two of the efforts (fig. S8; see www.proteinatlas.org/humanproteome/proteinevidence for details). Furthermore, there are 1794 additional genes with evidence only at the RNA level, and these genes are obvious targets for more comprehensive functional protein studies. It is notable that chromosome 11 has many more missing genes than the other chromosomes, likely owing to its high number of olfactory genes. A summary of the supporting data in a chromosome-centric manner is shown in the new version of the Human Protein Atlas launched as part of this publication.

Classification of cell type–specific expression profiles in human blood immune cells

We next performed a genome-wide analysis with regard to expression profiles in the blood cells for the identification of proteins with an elevated expression in immune cells. This was performed both on the cell type level (n = 18 cell types) and on cell lineage level in which the various cell types were combined into six groups, including T cells, B cells, and granulocytes (see full list of results in data S1). The number of genes in each of the five specificity categories is shown in Fig. 5A, with 1448 genes classified as cell type–enriched in one of the cell types and 5934 (30%) of all protein-coding genes elevated in at least one of the human blood cell types. Many genes (n = 3797) were not detected in any of the blood cells, while 9939 showed low specificity for expression in blood cells. The cell type distribution (fig. S9) showed that only 1713 genes were detected in a single cell type, while 5934 were detected in all 18 cell types. The relationship of the two classification schemes is compared in fig. S10 and table S4, showing that 889 genes are cell type–enriched and detected in a single cell type. These genes are of interest for further study to explore the biological functions linked to the respective different cell phenotypes. A heatmap showing the transcript expression profiles for all 1448 immune cell type–enriched genes shows that most are found in neutrophils, basophils, and plasmacytoid dendritic cells (Fig. 5B), while the group-enriched genes are more evenly distributed across the 18 cell types.

A network plot of all cell type–enriched and group-enriched genes (Fig. 5C) reveals a cluster of genes enriched in T cells and another cluster enriched in myeloid cells. Many genes (n = 114) are also shared between the two types of B cell populations (mature and naïve). In Fig. 5D, the number of elevated genes in the different blood cell types, clustered on the basis of the expression profiles, is shown, again highlighting the many cell type–enriched genes in neutrophils, eosinophils, and plasmacytoid dendritic cells, while many of the elevated genes in T and B cells are group-enriched across subpopulations of these lymphocytes. In fig. S11, all group-enriched and tissue-enriched genes are visualized and the relationship of sharing enriched expression between the cell types can be observed.

The extensive data generated here also allowed us to investigate the relationship between (body-wide) tissue expression and the expression in the single blood cell types. In Fig. 5E, a summary of all individual genes is shown with classification based on distribution in all tissues and blood cell types, respectively, and a summary of the genes that are enriched both on tissue level and blood cell level can be found in fig. S15. Some, but not a majority, of the genes expressed in a single or several blood cell types are shown to be predominately expressed in blood cells even when all major tissues and organs are considered. It is notable that many of the genes detected in all tissues are only detected in some of the blood cell types, suggesting that they are not necessary for cell survival.

Enriched genes among the blood immune cell types

Using our definition of cell population enrichment and cell group enrichment of genes, we analyzed the enriched genes among the 18 immune cell populations. Figure 6A shows the top five genes most enriched for each cell population, colored by their predicted protein location either in the membrane, secreted, or intracellular. Notable examples (Fig. 6B) include

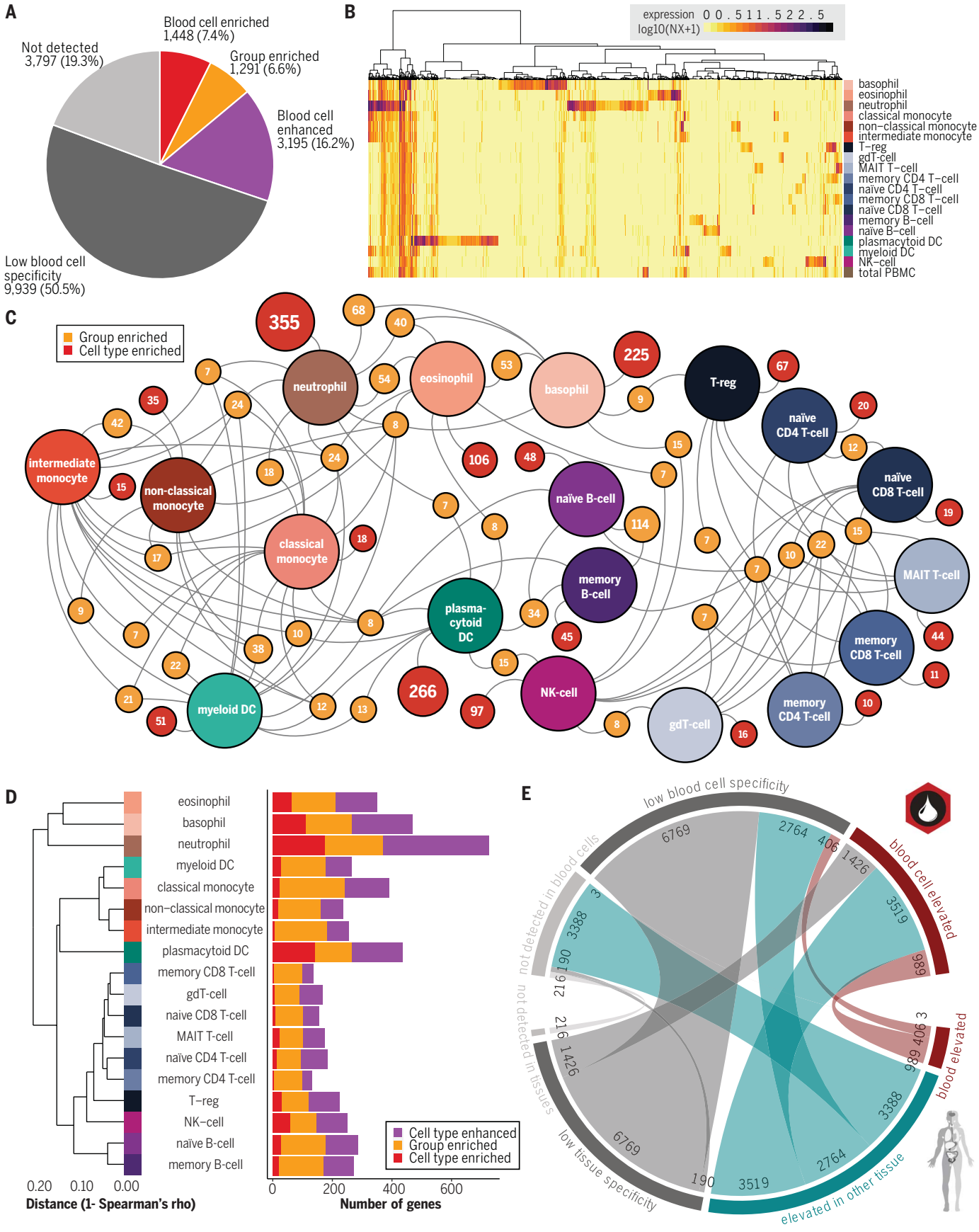
A
Blood cell enriched
1,448 (7.4%)
Not detected
3,797 (19.3%)
Group enriched
1,291 (6.6%)
Blood cell
enhanced
3,195 (16.2%)
Low blood cell
specificity
9,939 (50.5%)
B
expression 0 0 . 5 1 1 . 5 2 2 . 5
log10(NX+1)
basophil
eosinophil
neutrophil
classical monocyte
non−classical monocyte
intermediate monocyte
T−reg
gdT-cell
MAIT T−cell
memory CD4 T−cell
naïve CD4 T−cell
memory CD8 T−cell
naïve CD8 T−cell
memory B−cell
naïve B−cell
plasmacytoid DC
myeloid DC
NK−cell
total PBMC
C
Group enriched
Cell type enriched
neutrophil
eosinophil
basophil
T-reg
naïve CD4 T-cell
naïve CD8 T-cell
intermediate monocyte
non-classical monocyte
classical monocyte
naïve B-cell
memory B-cell
plasma-cytoid DC
MAIT T-cell
memory CD8 T-cell
myeloid DC
NK-cell
gdT-cell
memory CD4 T-cell
D
eosinophil
basophil
neutrophil
myeloid DC
classical monocyte
non−classical monocyte
intermediate monocyte
plasmacytoid DC
memory CD8 T-cell
gdT-cell
naive CD8 T-cell
MAIT T-cell
naïve CD4 T-cell
memory CD4 T-cell
T−reg
NK−cell
naïve B-cell
memory B-cell
0.20 0.10 0.00
Distance (1- Spearman's rho)
0 200 400 600
Number of genes
Cell type enhanced
Group enriched
Cell type enriched
E
low blood cell specificity
blood cell elevated
blood elevated
elevated in other tissue
low tissue specificity
not detected in tissues
not detected in blood cells
6769
2764
406
1426
3519
689
3
3388
190
216

Fig. 5. Cell type–specific classification of the human blood cells. (**A**) The number of genes classified according to cell type specificity. (**B**) A heatmap showing the expression of all the cell type–enriched genes across the 18 cell types. Heatmaps for the other specificity categories can be found in figs. S12 to S15. (**C**) Network plot showing the number of cell type– and group-enriched genes in the 18 cell types. The network is limited to nodes with a minimum number of seven genes. (**D**) (Left) A dendrogram based on the correlation of global expression profiles across the 18 cell types. (Right) Barplot displaying the number of elevated genes for each cell type. (**E**) The relationship of all human protein-coding genes with regard to single blood cell type specificity and whole-body tissue and organ specificity.

catalase (CAT), a gene encoding a key antioxidant enzyme converting the toxic reactive oxygen species hydrogen peroxide to water and oxygen and believed to be expressed broadly in the peroxisome of most cells (*38*). Our data indicated a strongly enriched expression level of CAT in eosinophils, which is much higher than the expression in any other immune cell population. This finding warrants more mechanistic analyses of CAT in eosinophils. Another notable finding is the chemokine receptor CXCR6, which is more highly expressed by MAIT cells than any other cell population, suggesting a particular importance of this receptor and its ligand, the chemokine CXCL16, in regulating MAIT cell trafficking. MAIT cells are a population of T cells that has gained a lot of interest in recent years for its role in antibacterial defense, particularly on mucosal sites, through its recognition of molecules derived from the bacterial and fungal riboflavin biosynthesis pathway (*39*). These cells have been shown to express multiple trafficking receptors, and their circulation between blood and tissues has been debated.

Another example is the granzyme B (*GZMB*) gene, a well-known serine protease secreted in granules by cytotoxic T cells and NK cells and necessary for target cell apoptosis (*40*). We found that GZMB expression is strongly enriched in plasmacytoid dendritic cells (pDCs). GZMB expression in pDCs has been reported previously (*40*), but according to our data, GZMB expression in pDCs is about fivefold higher than in any other cell type, which suggests an important function of granzyme B in pDCs (*41*). It is of interest that the population of pDCs also exhibits elevated levels of several other genes (*AXL*, *PPP1R14A*, *SIGLEC6*, *ITM2C*, and *DAB2*) suggested to be specific for a low abundant subgroup of DCs called AS DC with negative GZMB expression, recently described by Villani *et al.* (*42*). Because GZMB variants have been associated with the autoimmune disease vitiligo (*43*), pDCs could potentially play an unappreciated role in the pathogenesis of this condition. To confirm this elevated expression in pDC at the protein level, blood immune cells were analyzed by mass cytometry, and the results confirm higher protein levels of granzyme B in the cytoplasm of pDCs as compared with NK cells and $CD8^+$ T cells (Fig. 6C). The GZMB expression levels examined by mass cytometry could not distinguish the proposed AS DC subgroup within the pDC population.

We also complemented our classification strategy by performing a large number of differential expression analyses based on DESeq2 (*44*) to identify genes with variable expression when comparing two cell lineages or two cell populations (fig. S17). The comparison between cell lineages B and T cells show many genes with differential expression, including well-known B cell markers, such as CD19, CD22, and CD79, but also several genes not previously described as elevated in B cells, such as Ras associated domain family member 6 (RASSF6) and the zinc finger protein 860 (ZNF860). Similarly, genes identified as T cell markers include well-known genes, such as *CD3*, *CD6*, inducible T-cell costimulatory (*ICOS*), and thymocyte selection associated (*THEMIS*), but also other genes not yet identified as T cell elevated, such as Ras guanyl releasing protein 1 (*RASGRP1*) and fibroblast growth factor binding protein 2 (*FGFBP2*). All significantly differentially expressed genes for each DESeq2 analysis are available as a separate list (data S2).

Cellular expression of genes causing inborn errors of immunity

In a recent listing of primary immunodeficiency diseases (PID), 354 diseases were listed as consequences of monogenic defects in genes associated with the immune system (*45*) involving 224 known genes. The mechanism of disease is often incompletely understood, and we reasoned that an analysis of cellular expression of identified genes could help generate better hypotheses for further mechanistic investigation. We analyzed the NX levels of 224 PID genes across the 18 sorted immune cell populations, as well as some selected tissue profiles, and identified seven clusters with shared cellular and tissue distribution (Fig. 6D and figs. S18 and S19). A first group (cluster A) consists of 11 proteins restricted to T cells and NK cells, such as CD3 and the signaling intermediates ZAP70 and LCK (Fig. 6E). A second group (cluster B) consists of a subgroup of 15 genes present in all blood cells, but with much lower expression in the other tissues. Cluster C consists of genes ubiquitously expressed across all analyzed tissues and immune cell types. Cluster D consists of 34 proteins mainly originating from the liver and involves known plasma proteins such as complement factors C5, C8, and C9. Cluster E consists of proteins mainly expressed in particular cell lineages, such a B cell–restricted proteins, CD19, and CD79A. Cluster F consists of genes with elevated expression in monocytes and dendritic cells, and cluster G has relatively high expression in lymphoid tissues and bone marrow but low expression in the mature immune cell type in circulation. Several examples of interesting expression patterns can be observed, including the *CEBPE* gene (cluster E) causing specific granule deficiency 1 (SG1) (*46*) that has high expression in eosinophils. This condition has been considered a neutrophil-granule deficiency associated with recurrent pyogenic infections, but our cell type expression pattern indicates that CEBPE is mostly expressed by eosinophils and not at all by neutrophils. It is possible that during neutrophil development, or upon stimulation, CEBPE might also be expressed in neutrophils, but our results suggested that eosinophil deficiency should also be considered in SG1. This use case illustrates the usefulness of the updated human protein atlas as novel genes are identified as possible causes of immunodeficiencies and other diseases in human patients.

Discussion

Here, we present an atlas of the expression of all protein-coding genes in human blood cells, and this data has been integrated with an analysis of the tissue specificity of all genes covering all major tissues and organs in the human body. An interactive Blood Atlas resource is presented as part of the Human Protein Atlas, including expression data from other sources, such as blood cell transcriptomics from Monaco *et al.* (*21*) and Schmiedel *et al.* (*20*). The resource described here enables comparative analysis with other sources of data, such as single-cell genomics, proteomics, and antibody-based measurements, to allow comprehensive molecular profiles of the individual human blood cell types. In addition, the Tissue Atlas (*17*) was complemented with transcript expression data for brain and other normal tissue types from GTEx (*4*) and FANTOM5 (*5*). A normalization strategy has been introduced which has allowed integration of the various diverse datasets to produce a consensus classification across the cells, tissues, and organs. This has enabled the analysis of the cell type–specific expression across the blood immune cell types as well as the various tissues and organs. A revised classification of all protein-coding genes is presented with regard to both cell and tissue distribution.

The tissue expression profiles described earlier (*17*) are supported, but the inclusion of the comprehensive single cell type analysis of human blood, together with inclusion of more brain regions and specialized tissue, has changed some of the patterns of tissue specificity. The

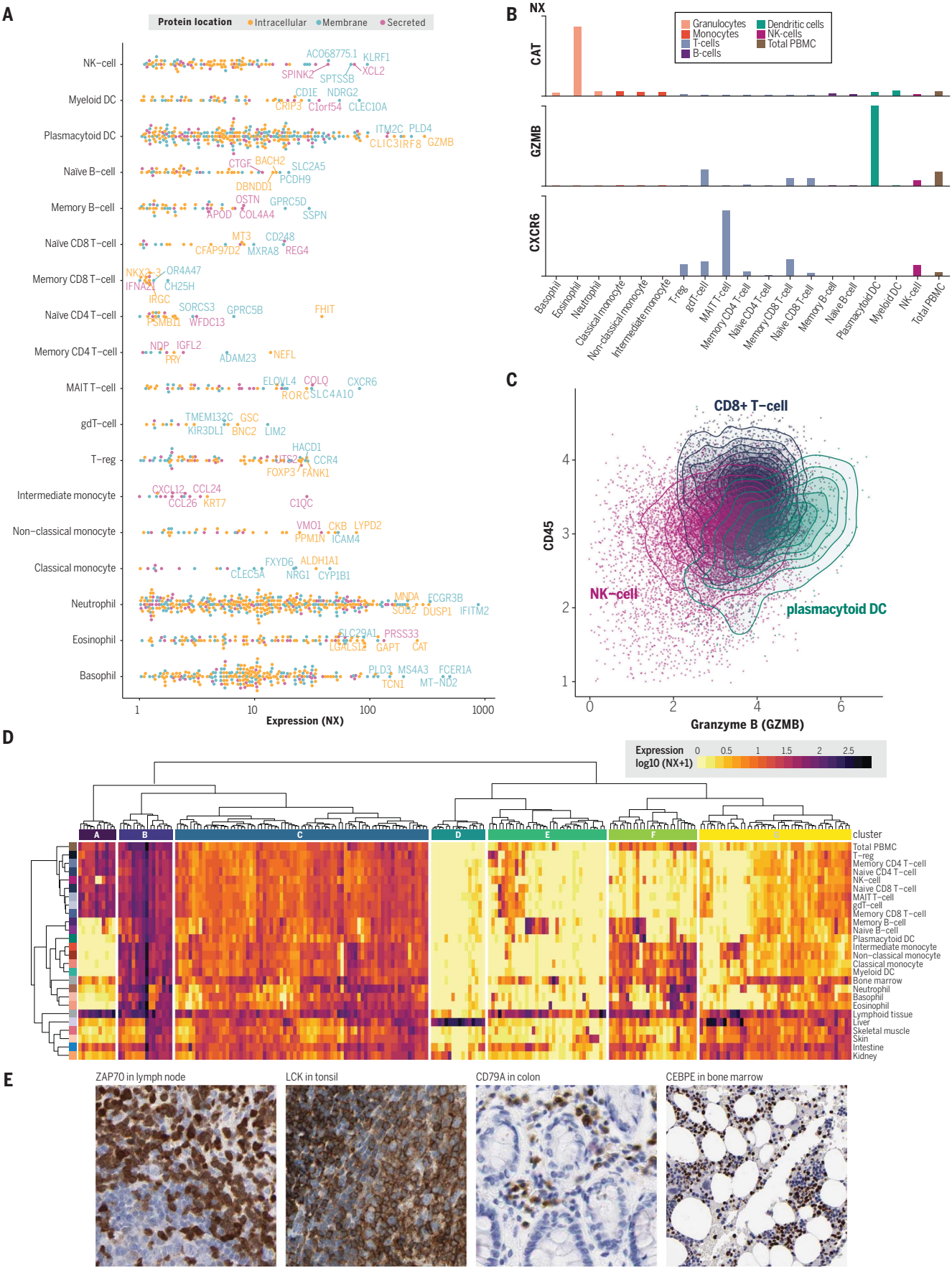
A
Protein location
Intracellular
Membrane
Secreted
NK–cell
Myeloid DC
Plasmacytoid DC
Naïve B–cell
Memory B–cell
Naïve CD8 T–cell
Memory CD8 T–cell
Naïve CD4 T–cell
Memory CD4 T–cell
MAIT T–cell
gdT–cell
T–reg
Intermediate monocyte
Non–classical monocyte
Classical monocyte
Neutrophil
Eosinophil
Basophil
Expression (NX)
B
NX
CAT
GZMB
CXCR6
Granulocytes
Monocytes
T–cells
B–cells
Dendritic cells
NK–cells
Total PBMC
C
CD8+ T–cell
NK–cell
plasmacytoid DC
CD45
Granzyme B (GZMB)
D
Expression log10 (NX+1)
cluster
Total PBMC
T–reg
Memory CD4 T–cell
Naive CD4 T–cell
NK–cell
Naive CD8 T–cell
MAIT T–cell
gdT–cell
Memory CD8 T–cell
Memory B–cell
Naive B–cell
Plasmacytoid DC
Intermediate monocyte
Non–classical monocyte
Classical monocyte
Myeloid DC
Bone marrow
Neutrophil
Basophil
Eosinophil
Lymphoid tissue
Liver
Skeletal muscle
Skin
Intestine
Kidney
E
ZAP70 in lymph node
LCK in tonsil
CD79A in colon
CEBPE in bone marrow

Fig. 6. The relationship between blood cell type–specific genes and tissue-specific genes and analysis of genes causing inborn errors of immunity. (**A**) The expression levels of all cell type–enriched genes, with the five most abundant genes named. (**B**) The expression profiles of some selected genes. (**C**) The results of flow sorting (CyTOF) using antibodies toward GZMB and CD45. (**D**) A heatmap showing the expression of 224 genes known to cause human inborn errors of immunity and their expression across all major tissues in the human body. A similar heatmap containing the gene names can be found in fig. S18, and separate heatmaps of each major disease type in all blood cells and tissues can be found in fig. S19. (**E**) IHC images from the Human Protein Atlas for four of the genes causing inborn errors.

brain now has the highest number of elevated genes, while testis still has most enriched genes, defined as an expression fourfold higher than that of any other tissue. The inclusion of more cells and tissues has also allowed us to provide evidence for many more genes, and the total number of missing genes with no protein or RNA evidence is now only ~200. For blood cells, a comprehensive list of all proteins showing an enriched expression in the various cell types is presented, confirming well-known protein markers but also identifying interesting targets for in-depth analysis both to study the basic biology of blood cells and to develop new targets for immune-based diagnostics and therapies. The examples presented here illustrate the potential of the Blood Atlas, and its determination of cell type gene enrichment, for the generation of hypotheses from previously unknown differences in cell population expression of important genes in the immune system.

This newly created resource elucidates the gene expression of individual immune cell populations to allow a better understanding of diseases involving the immune system. The emerging technology of single-cell genomics (*42*, *47*) will in the future be a good complement to such studies to identify low abundant cell subpopulations previously not described. Here, we also highlighted the cell type–specific expression of 224 genes associated with primary immunodeficiencies in humans, and we find cell type–specific expression patterns of relevance for their respective clinical phenotype. A large fraction of these genes is expressed in a large number of cell types, enforcing the need to take a holistic, body-wide approach to identify genes of importance for human biology and diseases. To facilitate such studies, we have launched an interactive, open-access Blood Atlas with all the data integrated as part of the Human Protein Atlas, allowing for genome-wide exploration of the protein-coding genes expressed across immune cell populations and in relation to spatial expression patterns in all major human tissues and organs.

REFERENCES AND NOTES

1. A. Regev *et al*., The Human Cell Atlas. *eLife* **6**, e27041 (2017). doi: 10.7554/eLife.27041; pmid: 29206104
2. J. M. Smith, R. M. Conroy, The NIH Common Fund Human Biomolecular Atlas Program, (HuBMAP): Building a Framework for Mapping the Human Body. *FASEB J.* **32**, 818.2 (2018).
3. J. Kaiser, Chan Zuckerberg Biohub funds first crop of 47 investigators. *Science* 10.1126/science.aal0719 (2017). doi: 10.1126/science.aal0719
4. J. Lonsdale *et al*., The Genotype-Tissue Expression (GTEx) project. *Nat. Genet.* **45**, 580–585 (2013). doi: 10.1038/ng.2653; pmid: 23715323
5. H. Kawaji, T. Kasukawa, A. Forrest, P. Carninci, Y. Hayashizaki, The FANTOM5 collection, a data series underpinning mammalian transcriptome atlases in diverse cell types. *Sci. Data* **4**, 170113 (2017). doi: 10.1038/sdata.2017.113; pmid: 28850107
6. M. J. Hawrylycz *et al*., An anatomically comprehensive atlas of the adult human brain transcriptome. *Nature* **489**, 391–399 (2012). doi: 10.1038/nature11405; pmid: 22996553
7. T. Kalisky, S. R. Quake, Single-cell genomics. *Nat. Methods* **8**, 311–314 (2011). doi: 10.1038/nmeth0411-311; pmid: 21451520
8. P. L. Ståhl *et al*., Visualization and analysis of gene expression in tissue sections by spatial transcriptomics. *Science* **353**, 78–82 (2016). doi: 10.1126/science.aaf2403; pmid: 27365449
9. A. Mortazavi, B. A. Williams, K. McCue, L. Schaeffer, B. Wold, Mapping and quantifying mammalian transcriptomes by RNA-Seq. *Nat. Methods* **5**, 621–628 (2008). doi: 10.1038/nmeth.1226; pmid: 18516045
10. M. Wilhelm *et al*., Mass-spectrometry-based draft of the human proteome. *Nature* **509**, 582–587 (2014). doi: 10.1038/nature13319; pmid: 24870543
11. M. Uhlén *et al*., Towards a knowledge-based Human Protein Atlas. *Nat. Biotechnol.* **28**, 1248–1250 (2010). doi: 10.1038/nbt1210-1248; pmid: 21139605
12. A. Bairoch *et al*., The universal protein resource (UniProt). *Nucleic Acids Res.* **33**, D154–D159 (2005). doi: 10.1093/nar/gki070; pmid: 15608167
13. L. C. Crosswell, J. M. Thornton, ELIXIR: A distributed infrastructure for European biological data. *Trends Biotechnol.* **30**, 241–242 (2012). doi: 10.1016/j.tibtech.2012.02.002; pmid: 22417641
14. A. Brazma *et al*., ArrayExpress—A public repository for microarray gene expression data at the EBI. *Nucleic Acids Res.* **31**, 68–71 (2003). doi: 10.1093/nar/gkg091; pmid: 12519949
15. F. Desiere *et al*., The PeptideAtlas project. *Nucleic Acids Res.* **34**, D655–D658 (2006). doi: 10.1093/nar/gkj040; pmid: 16381952
16. S. Bhattacharya *et al*., ImmPort, toward repurposing of open access immunological assay data for translational and clinical research. *Sci. Data* **5**, 180015 (2018). doi: 10.1038/sdata.2018.15; pmid: 29485622
17. M. Uhlén *et al*., Tissue-based map of the human proteome. *Science* **347**, 1260419 (2015). doi: 10.1126/science.1260419; pmid: 25613900
18. P. J. Thul *et al*., A subcellular map of the human proteome. *Science* **356**, eaal3321 (2017). doi: 10.1126/science.aal3321; pmid: 28495876
19. M. Uhlén *et al*., A pathology atlas of the human cancer transcriptome. *Science* **357**, eaan2507 (2017). doi: 10.1126/science.aan2507; pmid: 28818916
20. B. J. Schmiedel *et al*., Impact of genetic polymorphisms on human immune cell gene expression. *Cell* **175**, 1701–1715.e16 (2018). doi: 10.1016/j.cell.2018.10.022; pmid: 30449622
21. G. Monaco *et al*., RNA-seq signatures normalized by mRNA abundance allow absolute deconvolution of human immune cell types. *Cell Reports* **26**, 1627–1640.e7 (2019). doi: 10.1016/j.celrep.2019.01.041; pmid: 30726743
22. J. Lovén *et al*., Revisiting global gene expression analysis. *Cell* **151**, 476–482 (2012). doi: 10.1016/j.cell.2012.10.012; pmid: 23101621
23. J. E. Coate, J. J. Doyle, Variation in transcriptome size: Are we getting the message? *Chromosoma* **124**, 27–43 (2015). doi: 10.1007/s00412-014-0496-3; pmid: 25421950
24. A. S. Kopin, M. B. Wheeler, A. B. Leiter, Secretin: Structure of the precursor and tissue distribution of the mRNA. *Proc. Natl. Acad. Sci. U.S.A.* **87**, 2299–2303 (1990). doi: 10.1073/pnas.87.6.2299; pmid: 2315322
25. S. Kuttruff *et al*., NKp80 defines and stimulates a reactive subset of CD8 T cells. *Blood* **113**, 358–369 (2009). doi: 10.1182/blood-2008-03-145615; pmid: 18922855
26. P. Brodin *et al*., Variation in the human immune system is largely driven by non-heritable influences. *Cell* **160**, 37–47 (2015). doi: 10.1016/j.cell.2014.12.020; pmid: 25594173
27. H. Wold, "Estimation of principal components and related models by iterative least squares" in *Multivariate Analysis*, P. R. Krishnajah, Ed. (Academic Press, 1966), pp. 391–420.
28. L. McInnes, J. Healy, J. Melville, UMAP: Uniform Manifold Approximation and Projection for Dimension Reduction. arXiv:1802.03426 [stat.ML] (9 February 2018).
29. M. Uhlén, Mapping the human proteome using antibodies. *Mol. Cell. Proteomics* **6**, 1455–1456 (2007). pmid: 17703056
30. M. D. Robinson, A. Oshlack, A scaling normalization method for differential expression analysis of RNA-seq data. *Genome Biol.* **11**, R25 (2010). doi: 10.1186/gb-2010-11-3-r25; pmid: 20196867
31. R. A. van den Berg, H. C. J. Hoefsloot, J. A. Westerhuis, A. K. Smilde, M. J. van der Werf, Centering, scaling, and transformations: Improving the biological information content of metabolomics data. *BMC Genomics* **7**, 142 (2006). doi: 10.1186/1471-2164-7-142; pmid: 16762068
32. M. E. Ritchie *et al*., *limma* powers differential expression analyses for RNA-sequencing and microarray studies. *Nucleic Acids Res.* **43**, e47 (2015). doi: 10.1093/nar/gkv007; pmid: 25605792
33. T. Hart *et al*., High-resolution CRISPR screens reveal fitness genes and genotype-specific cancer liabilities. *Cell* **163**, 1515–1526 (2015). doi: 10.1016/j.cell.2015.11.015; pmid: 26627737
34. T. Wang *et al*., Identification and characterization of essential genes in the human genome. *Science* **350**, 1096–1101 (2015). doi: 10.1126/science.aac7041; pmid: 26472758
35. L. Fagerberg *et al*., Contribution of antibody-based protein profiling to the human Chromosome-centric Proteome Project (C-HPP). *J. Proteome Res.* **12**, 2439–2448 (2013). doi: 10.1021/pr300924j; pmid: 23276153
36. M. Magrane; UniProt Consortium, UniProt Knowledgebase: A hub of integrated protein data. *Database* **2011**, bar009 (2011). pmid: 21447597
37. P. Gaudet *et al*., The neXtProt knowledgebase on human proteins: 2017 update. *Nucleic Acids Res.* **45**, D177–D182 (2017). doi: 10.1093/nar/gkw1062; pmid: 27899619
38. P. Chelikani, I. Fita, P. C. Loewen, Diversity of structures and properties among catalases. *Cell. Mol. Life Sci.* **61**, 192–208 (2004). doi: 10.1007/s00018-003-3206-5; pmid: 14745498
39. R. J. Napier, E. J. Adams, M. C. Gold, D. M. Lewinsohn, The role of mucosal associated invariant T cells in antimicrobial immunity. *Front. Immunol.* **6**, 344 (2015). doi: 10.3389/fimmu.2015.00344; pmid: 26217338
40. M.-C. Rissoan *et al*., Subtractive hybridization reveals the expression of immunoglobulin-like transcript 7, Eph-B1, granzyme B, and 3 novel transcripts in human plasmacytoid dendritic cells. *Blood* **100**, 3295–3303 (2002). doi: 10.1182/blood-2002-02-0638; pmid: 12384430
41. C. Chauvin, R. Josien, Dendritic cells as killers: Mechanistic aspects and potential roles. *J. Immunol.* **181**, 11–16 (2008). doi: 10.4049/jimmunol.181.1.11; pmid: 18566364
42. A.-C. Villani *et al*., Single-cell RNA-seq reveals new types of human blood dendritic cells, monocytes, and progenitors. *Science* **356**, eaah4573 (2017). doi: 10.1126/science.aah4573; pmid: 28428369
43. Y. Jin *et al*., Genome-wide association studies of autoimmune vitiligo identify 23 new risk loci and highlight key pathways and regulatory variants. *Nat. Genet.* **48**, 1418–1424 (2016). doi: 10.1038/ng.3680; pmid: 27723757
44. M. I. Love, W. Huber, S. Anders, Moderated estimation of fold change and dispersion for RNA-seq data with DESeq2. *Genome Biol.* **15**, 550 (2014). doi: 10.1186/s13059-014-0550-8; pmid: 25516281
45. P. W. Sullivan, V. H. Ghushchyan, G. Globe, M. Schatz, Oral corticosteroid exposure and adverse effects in asthmatic patients. *J. Allergy Clin. Immunol.* **141**, 110–116.e7 (2018). doi: 10.1016/j.jaci.2017.04.009; pmid: 28456623
46. Online Mendelian Inheritance in Man, OMIM, McKusick-Nathans Institute of Genetic Medicine, Johns Hopkins University (2018); https://omim.org/.

47. V. S. Patil *et al*., Precursors of human CD4$^+$ cytotoxic T lymphocytes identified by single-cell transcriptome analysis. *Sci. Immunol.* **3**, eaan8664 (2018). doi: 10.1126/sciimmunol.aan8664; pmid: 29352091

ACKNOWLEDGMENTS

We thank the nurses at the Coagulation Unit, Karolinska University Hospital, for their assistance in handling donors and sampling. We acknowledge the entire staff of the Human Protein Atlas program and the Science for Life Laboratory for their valuable contributions. **Funding:** Funding was provided by the Knut and Alice Wallenberg Foundation (WCPR), the Erling Persson Foundation (KCAP), and the Novo Nordisk Foundation (CFB). Support from the National Genomics Infrastructure in Stockholm is acknowledged, with funding from Science for Life Laboratory, the Knut and Alice Wallenberg Foundation, the Swedish Research Council, and SNIC/Uppsala Multidisciplinary Center for Advanced Computational Science. **Author contributions:** M.U. and L.F. conceived of and designed the study. C.P., J.Mi., T.L., and P.B. performed the single cell sorting and analysis. B.F., F.E., and J.O. collected the clinical samples. M.U., Å.S., A.M., C.L., E.S., J.Mi., B.F., F.E., F.P., A.H., W.Z., M.J.K., J.Mu., A.T., C.Z., and L.F. performed the data analysis. K.v.F., P.O., and M.Z. provided the infrastructure for the data. M.U. drafted the manuscript. M.U., L.F., P.B., M.J.K., and Å.S. revised the manuscript. All authors discussed the results and contributed to the final manuscript. **Competing interests:** No competing interests. **Data and materials availability:** All raw flow cytometry data are available at FlowRepository (http://flowrepository.org/) under ID FR-FCM-Z28R. Sequencing data used in the study are available without restriction at the Human Protein Atlas portal (www.proteinatlas.org/about/download). All custom code used for normalization and categorization can be downloaded from Github (https://github.com/human-protein-atlas/BloodAtlas).

SUPPLEMENTARY MATERIALS

science.sciencemag.org/content/366/6472/eaax9198/suppl/DC1
Materials and Methods
Figs. S1 to S21
Tables S1 to S4
References (*48*–*61*)
Data S1 to S3
View/request a protocol for this paper from *Bio-protocol*.

10 May 2019; accepted 6 November 2019
10.1126/science.aax9198

RESEARCH ARTICLE SUMMARY

INFECTION

Host monitoring of quorum sensing during *Pseudomonas aeruginosa* infection

Pedro Moura-Alves*, Andreas Puyskens, Anne Stinn, Marion Klemm, Ute Guhlich-Bornhof, Anca Dorhoi, Jens Furkert, Annika Kreuchwig, Jonas Protze, Laura Lozza, Gang Pei, Philippe Saikali, Carolina Perdomo, Hans J. Mollenkopf, Robert Hurwitz, Frank Kirschhoefer, Gerald Brenner-Weiss, January Weiner 3rd, Hartmut Oschkinat, Michael Kolbe, Gerd Krause, Stefan H. E. Kaufmann*

INTRODUCTION: The interaction between a bacterial pathogen and its host can be viewed as an "arms race" in which each participant continuously responds to the evolving strategies of the other partner. A mechanism allowing bacteria to rapidly adapt to such changing circumstances is provided by density-dependent cell-to-cell communication known as quorum sensing (QS). QS involves a hierarchy of signaling molecules, which in pathogenic bacteria is associated with biofilm formation and virulence regulation. Notably, some QS molecules are detected by the host, and these can provoke specific immune responses. However, the receptors and their signaling pathways that the host uses to eavesdrop on bacteria remain poorly understood.

RATIONALE: We hypothesized that if a host sensor can detect and differentiate between bacterial QS molecules and their expression patterns, it will allow hosts to customize their immune responses according to the stage and state of infection. We recently showed that the aryl hydrocarbon receptor (AhR) directly recognizes pigmented bacterial virulence factors, such as the phenazines produced by *Pseudomonas aeruginosa*, which are downstream products of QS. Upon binding phenazines, the AhR elicits diverse immune responses that coordinate host resistance to infection. As a result of its capacity to sense a broad array of ligands, we postulated that the host AhR is well positioned to spy on bacterial communications, continuously monitor bacterial infection dynamics, and thereby signal to the host to tune immune responses according to the state of infection.

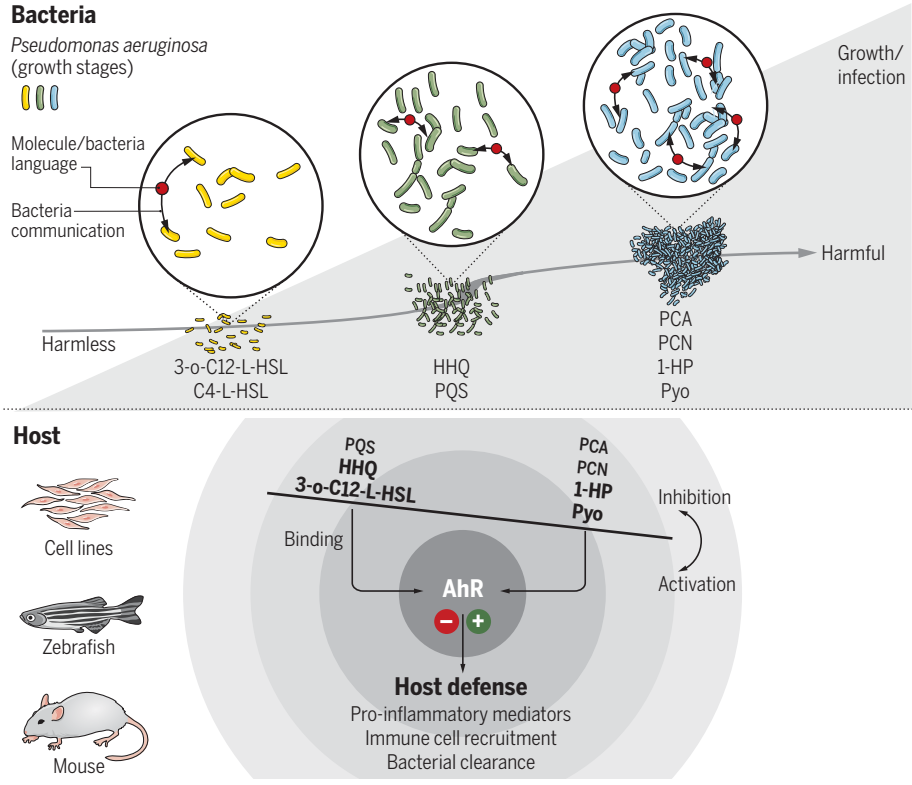

Bacterial communication under the radar of the host aryl hydrocarbon receptor (AhR). The AhR spies on bacterial communication and translates the bacterial signaling vocabulary into the most appropriate host defenses. The expression of bacterial quorum-sensing molecules, such as homoserine lactones, quinolones, and phenazines, varies according to community density and state of infection. The AhR can detect the type and quantity of quorum-sensing molecules and hence the state of infection, and thus tunes host defenses.

RESULTS: Our results demonstrated that infected hosts show differential modulation of host AhR signaling over the course of *P. aeruginosa* infection in zebrafish, mice, and human cells. AhR signaling depended on the relative abundances of several classes of *P. aeruginosa* QS molecules, including homoserine lactones (e.g., *N*-3-oxo-dodecanoyl-homoserine lactone), quinolones (e.g., 4-hydroxy-2-heptylquinoline), and phenazines (e.g., pyocyanin). In vitro and in vivo studies showed that the AhR not only detects *P. aeruginosa* QS molecules in a qualitative way but also quantifies their relative abundances. Quantitative assessment enables the host to sense bacterial community densities that may have distinct gene expression programs and infection dynamics, and thereby to regulate the scale and intensity of host defense mechanisms, which can range from induction of inflammatory mediators to immune cell recruitment and bacterial clearance.

ON OUR WEBSITE

Read the full article at http://dx.doi.org/10.1126/science.aaw1629

CONCLUSION: Our findings emphasize a crucial role for host AhR as master regulator of host defense responses, capable of tuning immunity according to the stage of infection and disease. By inhibiting profuse and inessential immune responses, the host can counteract some of the detrimental effects of infection and avoid collateral damage. We propose that host surveillance of bacterial communication allows not only a trade-off between energy expenditure and efficient defense in the host, but also a trade-off between energy expenditure and virulence in the pathogen.

QS is not restricted to *P. aeruginosa*, and we postulate that monitoring of bacterial QS by hosts may be a widespread phenomenon. Different therapeutic strategies to manipulate *P. aeruginosa* QS have been attempted, including adaptive treatment regimens for cystic fibrosis patients, who suffer severely from this pathogen. A better understanding of the cross-talk between host AhR and bacterial QS could pave the way to specific host-directed therapies to treat infectious diseases, tailored not only to the type of infection but also to the specific stage of disease. ■

The list of author affiliations is available in the full article online.
*Corresponding author. Email: pedro.mouraalves@ludwig.ox.ac.uk (P.M.-A.); kaufmann@mpiib-berlin.mpg.de (S.H.E.K.)
Cite this article as P. Moura-Alves *et al.*, *Science* **366**, eaaw1629 (2019). DOI: 10.1126/science.aaw1629

RESEARCH ARTICLE

INFECTION

Host monitoring of quorum sensing during *Pseudomonas aeruginosa* infection

Pedro Moura-Alves[1,2]*, Andreas Puyskens[1], Anne Stinn[1,3,4,5], Marion Klemm[1], Ute Guhlich-Bornhof[1], Anca Dorhoi[1,6,7], Jens Furkert[8], Annika Kreuchwig[8], Jonas Protze[8], Laura Lozza[1,9], Gang Pei[1], Philippe Saikali[1], Carolina Perdomo[1], Hans J. Mollenkopf[10], Robert Hurwitz[11], Frank Kirschhoefer[12], Gerald Brenner-Weiss[11], January Weiner 3rd[1]†, Hartmut Oschkinat[8], Michael Kolbe[3,4,5], Gerd Krause[8], Stefan H. E. Kaufmann[1,13]*

Pseudomonas aeruginosa rapidly adapts to altered conditions by quorum sensing (QS), a communication system that it uses to collectively modify its behavior through the production, release, and detection of signaling molecules. QS molecules can also be sensed by hosts, although the respective receptors and signaling pathways are poorly understood. We describe a pattern of regulation in the host by the aryl hydrocarbon receptor (AhR) that is critically dependent on qualitative and quantitative sensing of *P. aeruginosa* quorum. QS molecules bind to AhR and distinctly modulate its activity. This is mirrored upon infection with *P. aeruginosa* collected from diverse growth stages and with QS mutants. We propose that by spying on bacterial quorum, AhR acts as a major sensor of infection dynamics, capable of orchestrating host defense according to the status quo of infection.

Pseudomonas aeruginosa is a resourceful and ubiquitous Gram-negative bacterium that causes infectious diseases in a broad spectrum of organisms, including plants, animals, and humans (*1*). Its prevalence in burn victims, cystic fibrosis (CF) patients, and immunocompromised individuals (such as AIDS patients) is commonly associated with a poor, often fatal outcome (*2*). *P. aeruginosa* is also a major cause of nosocomial infections, such as bacterial pneumonia, urinary tract infection, and surgical-wound contamination (*1*). Because of its profound antibiotic resistance, therapy of *P. aeruginosa* is extremely difficult (*1*). Moreover, this pathogen possesses a wide range of mechanisms to adapt to different and sometimes harsh environments, further aggravating its eradication, even by antibiotic treatment (*1*).

One such important and unifying mechanism is the capacity of *P. aeruginosa* to perform quorum sensing (QS) (*1*, *3*, *4*). QS is a cell-to-cell signaling mechanism used by different bacteria to coordinate their activities in response to changes in community density. This coordination depends on chemical communication using different diffusible molecules, so-called autoinducers, and their receptors (Fig. 1A) (*3*, *4*). In *P. aeruginosa*, QS regulates the production of a vast set of virulence factors, such as extracellular proteases and phenazines, and is crucial for colonization and infection, regulating diverse mechanisms such as biofilm formation and antimicrobial resistance (*1*, *3*–*5*). Differences in *P. aeruginosa* virulence and transition from acute to chronic infection have been linked to changes in autoinducer levels and in the expression of QS-regulated genes (*1*, *3*, *6*–*8*). Consequently, QS constitutes an obvious target in the current search for novel treatment options for *P. aeruginosa* infections (*3*, *4*, *9*). Changes in the expression of autoinducers and QS-regulated genes may have an impact not only on bacterial community dynamics, but also on the host response during infection. It was previously reported that different QS-regulated molecules, such as homoserine lactones (HSLs), quinolones, and phenazines, can interact with host cells, thereby influencing a broad range of responses including immunomodulation (*9*). Thus far, the host receptors and signaling pathways, as well as the mechanisms involved in monitoring infection dynamics, are incompletely understood.

Recently, we demonstrated that the aryl hydrocarbon receptor (AhR), a highly conserved ligand-dependent transcription factor, directly recognizes *P. aeruginosa* phenazines and thereby plays an important role in infection control (*10*). AhR binds to phenazines, mediates their degradation, and regulates the expression of several host genes including detoxifying enzymes, chemokines, and cytokines. Accordingly, resistance of AhR-deficient ($AhR^{-/-}$) mice to *P. aeruginosa* is diminished (*10*). Taking into consideration the vast set of ligands that AhR is able to detect and the numerous biological roles it can exert, we hypothesized that AhR monitors the course of bacterial infection and disease by sensing different bacterial QS molecules expressed at various stages of infection (Fig. 1A), and thereby orchestrates the most appropriate immune response against different stages of infection.

AhR senses bacterial QS molecules in vitro

Using luciferase AhR reporter cells (*10*), we infected THP-1 macrophages (THP-1 AhR reporter) and A549 alveolar type II pneumocytes (A549 AhR reporter) with *P. aeruginosa* laboratory wild-type UCBPP-PA14 (PA14 WT) and green fluorescent protein–labeled (PA14 WT-GFP) strains collected from distinct stages of bacterial growth (early log, $OD_{600} < 0.3$; mid-log, $0.5 < OD_{600} < 0.8$; late log, $OD_{600} > 1$). AhR was more profoundly activated by bacteria from later growth phases (Fig. 1B and fig. S1A), whereas multiplicity of infection (MOI; fig. S1B) and percentage of infected cells remained comparable over the different growth stages (fig. S1, C and D). Similar results were obtained with filtered bacterial supernatants from PA14 WT strains (Fig. 1C and fig. S1E), pointing to different AhR signaling by distinct *P. aeruginosa* molecules. A comparable phenotype was observed using supernatants from PAO1, a different commonly used *P. aeruginosa* laboratory strain (fig. S1F). Among the obvious candidates are the *P. aeruginosa* phenazines, previously identified as AhR ligands (*10*). Consistently, increasing concentrations of the *P. aeruginosa* phenazine pyocyanin (Pyo) were detected in PA14 supernatants along bacterial growth stages (fig. S1, G and H), correlating with the observed AhR activation (Fig. 1, B and C, and fig. S1, A and E).

Phenazines are among the QS-regulated molecules expressed by *P. aeruginosa*, with Pyo providing a terminal signal of QS (*3*, *4*, *11*, *12*). *P. aeruginosa* QS is regulated by four tightly controlled pathways, namely Las, Rhl, Pqs, and Iqs (Fig. 1A) (*3*, *4*, *12*). These pathways are tightly interconnected and their cognate autoinducer molecules are capable of activating a distinct downstream transcriptional

[1]Department of Immunology, Max Planck Institute for Infection Biology, 10117 Berlin, Germany. [2]Ludwig Institute for Cancer Research, Nuffield Department of Clinical Medicine, University of Oxford, Oxford OX3 7DQ, UK. [3]Structural Systems Biology, Max Planck Institute for Infection Biology, 10117 Berlin, Germany. [4]Department of Structural Infection Biology, Centre for Structural Systems Biology, Helmholtz Centre for Infection Research (HZI), 22607 Hamburg, Germany. [5]Faculty of Mathematics, Informatics and Natural Sciences, University of Hamburg, 20148 Hamburg, Germany. [6]Institute of Immunology, Friedrich-Loeffler Institut, Greifswald–Insel Riems, Germany. [7]Faculty of Mathematics and Natural Sciences, University of Greifswald, Greifswald, Germany. [8]Leibniz-Forschungsinstitut für Molekulare Pharmakologie (FMP), 13125 Berlin, Germany. [9]Epiontis GmbH–Precision for Medicine, 12489 Berlin, Germany. [10]Microarray Core Facility, Max Planck Institute for Infection Biology, Department of Immunology, 10117 Berlin, Germany. [11]Protein Purification Core Facility, Max Planck Institute for Infection Biology, 10117 Berlin, Germany. [12]Institute of Functional Interfaces, Karlsruhe Institute of Technology, Karlsruhe, Germany. [13]Hagler Institute for Advanced Study at Texas A&M University, College Station, TX 77843, USA.
†Present address: Core Unit of Bioinformatics, Berlin Institute of Health, 10117 Berlin, Germany.
*Corresponding author. Email: pedro.mouraalves@ludwig.ox.ac.uk (P.M.-A.); kaufmann@mpiib-berlin.mpg.de (S.H.E.K.)

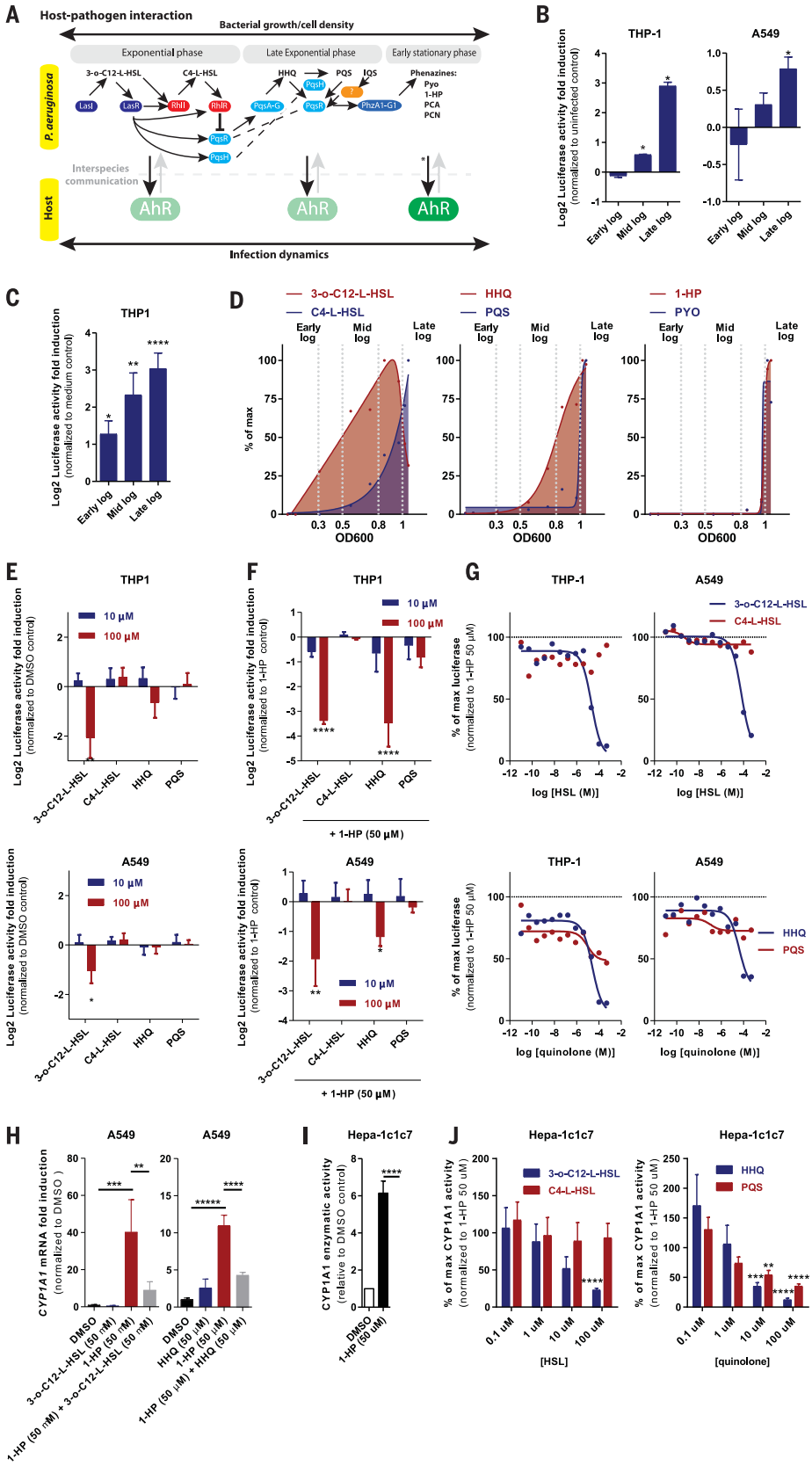

Fig. 1. AhR modulation by *P. aeruginosa*. (**A**) Scheme of AhR sensing of *P. aeruginosa* QS molecules during infection. In this depiction of the *P. aeruginosa* signaling cascade during different bacterial growth stages. QS molecules are shown in black and proteins in colored circles, with different colors corresponding to each QS molecule. The black arrow with asterisk indicates a known interaction between *P. aeruginosa* phenazines and host AhR. (**B**) Luciferase activity of AhR reporter THP-1 (monocytic) and A549 (pneumocytic) cells upon 24 hours of infection with *P. aeruginosa* PA14 WT strain grown in lysogeny broth (LB) medium, at a multiplicity of infection (MOI) of 50 (pooled data from $n = 3$ independent experiments). (**C**) Luciferase activity of AhR reporter THP-1 and A549 cells upon 24 hours of stimulation with *P. aeruginosa* filtered supernatants (1:25 diluted), collected from different bacterial growth phases (pooled data from $n = 4$ independent experiments). (**D**) Expression of QS molecules in supernatants of PA14 WT, detected by HPLC. Data are from one representative experiment of two independent experiments. (**E**) Luciferase activity of AhR reporter THP-1 and A549 cells upon 4 hours of stimulation with different concentrations of *P. aeruginosa* homoserine lactones (3-o-C12-L-HSL or C4-L-HSL) and quinolones (HHQ or PQS) in the absence of *P. aeruginosa* 1-HP; pooled data from $n = 6$ (THP-1) or $n = 4$ (A549) independent experiments. (**F** and **G**) Same as (E) but in the presence of *P. aeruginosa* 1-HP; pooled data from $n = 3$ (THP-1) or $n = 4$ (A549) independent experiments (F); $n = 3$ (THP-1), $n = 9$ (A549, top), or $n = 3$ (A549, bottom) independent experiments (G). (**H**) *CYP1A1* gene expression upon 24 hours of stimulation of A549 cells with QS molecules. Data are from one representative experiment of at least three independent experiments ($n = 3$ biological replicates). (**I** and **J**) CYP1A1 enzymatic activity after 24 hours of stimulation of Hepa-1c1c7 cells with 50 µM 1-HP alone (I) or in the presence or absence of other QS molecules (J). Data are pooled from $n = 7$ or $n = 4$ independent experiments, respectively. Pyo, pyocyanin; 1-HP, 1-hydroxyphenazine; PCA, phenazine-1-carboxylic acid; PCN, phenazine carboxamide, 3-o-C12-L-HSL, *N*-(3-oxodecanoyl)-L-homoserine lactone; C4-L-HSL, *N*-butyril-L-homoserine lactone; HHQ, 4-hydroxy-2-heptylquinoline; PQS, 2-heptyl-3,4-dihydroxyquinoline; IQS, 2-(2-hydroxylphenyl)-thiazole-4-carbaldehyde. Data are means ± SEM [(B), (C), (E), (F), (G), (I)] or means ± SD (H). $^*P < 0.05$, $^{**}P < 0.01$, $^{***}P < 0.001$, $^{****}P < 0.0001$ [one-way analysis of variance (ANOVA) in (B), (C), (E), (F), (H), (J); two-tailed Student *t* test in (I)].

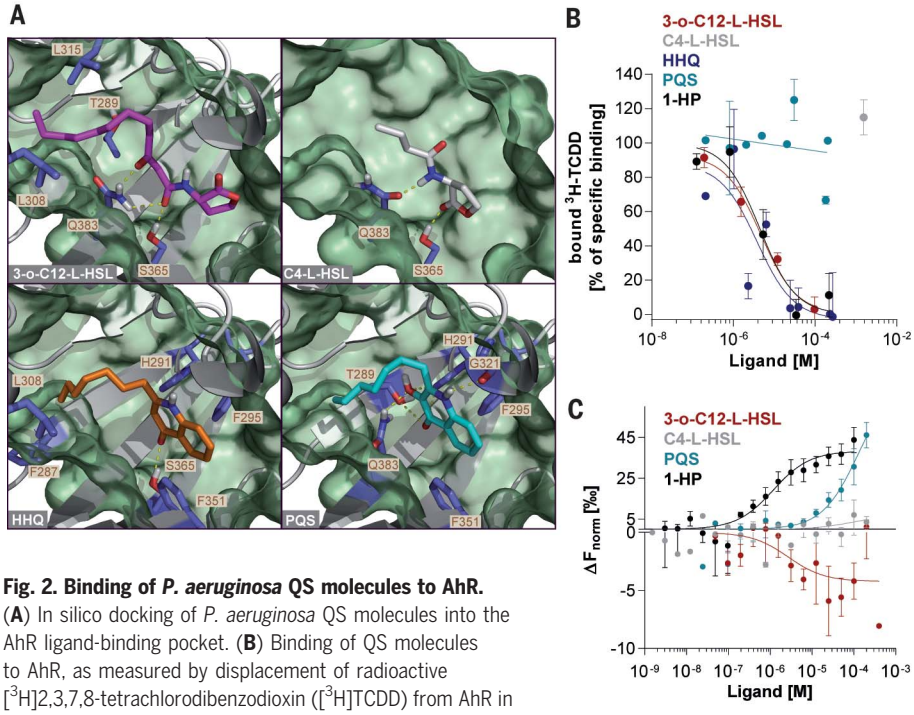

Fig. 2. Binding of *P. aeruginosa* QS molecules to AhR. (**A**) In silico docking of *P. aeruginosa* QS molecules into the AhR ligand-binding pocket. (**B**) Binding of QS molecules to AhR, as measured by displacement of radioactive [^{3}H]2,3,7,8-tetrachlorodibenzodioxin ([^{3}H]TCDD) from AhR in wild-type mouse liver cytosol. K_d values: 3-o-C12-L-HSL, 4.67 μM; HHQ, 3.77 μM; 1-HP, 4.48 μM. Data are pooled from n = 3 (3-o-C12-L-HSL), n = 2 (C-4-L-HSL), n = 4 (HHQ), n = 2 (PQS), or n = 3 (1-HP) independent experiments. (**C**) Binding of QS molecules to AhR, as measured by microscale thermophoresis assay. K_d values: 3-o-C12-L-HSL, 2.69 μM; PQS, 130 μM; 1-HP, 1.18 μM. Data are pooled from n = 4 (3-o-C12-L-HSL), n = 3 (C4-L-HSL), n = 4 (PQS), or n = 4 (1-HP) independent experiments.

pathway (Fig. 1A). In brief, *N*-3-oxo-dodecanoyl-homoserine lactone (3-o-C12-L-HSL) and *N*-butanoyl-homoserine lactone (C4-L-HSL) are produced in a sequential manner via Las and Rhl systems, and activate the receptors LasR and RhlR, respectively (*3*, *4*, *12*). A third pathway, Pqs, leads to the synthesis of the *Pseudomonas* quinolone signaling molecule 2-heptyl-3-hydroxy-4-quinolone (PQS) and its precursor 4-hydroxy-2-heptylquinoline (HHQ), which signal via the receptor PqsR (*3*, *4*, *12*). Recently, the Iqs pathway was discovered; however, the mechanisms by which 2-(2-hydroxyphenyl)-thiazole-4-carbaldehyde (IQS) and its receptor are produced are less well understood (*1*, *3*).

Using high-performance liquid chromatography (HPLC), we confirmed a sequential autoinducer abundance in the supernatants of PA14 (Fig. 1D). Considering the distinct expression profiles of the QS molecules 3-o-C12-L-HSL, C4-L-HSL, HHQ, and PQS, we determined their ability to modulate canonical AhR signaling. Stimulation of THP-1 and A549 AhR reporter cells with the different *P. aeruginosa* QS molecules resulted in differential modulation of AhR signaling (Fig. 1E). 3-o-C12-L-HSL and HHQ potently inhibited AhR activation by the known *Pseudomonas* AhR ligand 1-hydroxyphenazine (1-HP) (*10*) in a dose-dependent manner (Fig. 1, F and G). Several QS molecules have been reported to induce apoptosis in host cells, depending on the concentration, cell type, and exposure time (*13*, *14*). No major differences in cell viability were detected for the majority of the conditions tested here, as measured by lactate dehydrogenase (LDH) release (fig. S2A). An exception occurred after 24 hours of stimulation of THP-1 cells with high concentrations of 3-o-C12-L-HSL (fig. S2A). These results are in agreement with previous studies showing that epithelial cells, such as A549, are more resistant to 3-o-C12-L-HSL–induced apoptosis than macrophages (*13*, *14*). All experiments with THP-1 cells in the presence of 3-o-C12-L-HSL were performed at earlier time points, when no differences in cell viability were detected. Yet we decided to further exclude a possible relationship between apoptosis-related effects and AhR modulation in this cell type. As shown in fig. S2, B to E, no relationship was observed, and we decided to focus on A549 cells in following experiments.

Previous studies showed that concentrations of QS molecules in *P. aeruginosa*, such as 3-o-C12-L-HSL, can vary profoundly according to growth status, type of culture [planktonic cultures (1 to 5 μM) or biofilms (up to 600 μM)], and sample type (sputum or murine infection samples) (*15*–*18*). Notably, high concentrations of these molecules have been detected in biofilms of CF patients' lungs, and thus in close contact with the epithelium (*18*). Consequently, we decided to use 50 μM of the different QS molecules in subsequent studies.

A hallmark of AhR activity is the transcriptional induction of genes that encode detoxifying enzymes, such as CYP1A1 and CYP1B1, and the AhR repressor (AhRR) (*19*). As previously reported (*10*), stimulation of A549 cells with 1-HP induces mRNA expression of these genes (Fig. 1H and fig. S3A). Intriguingly, 3-o-C12-L-HSL and HHQ inhibited 1-HP–induced gene expression (Fig. 1F and fig. S3A). Because CYP1A1 is involved in tryptophan metabolism, alterations in its expression and activity can influence AhR activation (*20*, *21*). We took advantage of an established model using mouse liver cells (Hepa-1c1c7), which express copious levels of CYP1A1 and are therefore best suited to detect its expression and enzymatic activity (*22*). Similar to other cell types, AhR activation in hepatocytes was induced by 1-HP, as measured by increased luciferase activity in an AhR reporter cell line, and led to an increase in CYP1A1 enzymatic activity, as measured by the ethoxyresorufin-*O*-deethylase (EROD) assay (Fig. 1I and fig. S3, B and C). Intriguingly, 3-o-C12-L-HSL, HHQ, and PQS inhibited 1-HP–induced AhR activation and CYP1A1 enzymatic activity in these cells, whereas C4-L-HSL did not (Fig. 1J and fig. S3, B and C). In sum, QS molecules, including HSLs, quinolones, and phenazines, modulated AhR activity in both a stimulatory and an inhibitory direction.

QS molecules are not only expressed by *P. aeruginosa*; several other Gram-negative bacteria also produce HSLs, with subtle modifications, mostly in the carbon side chain (*3*, *4*) (table S1). Because the crystal structure of AhR has not yet been solved, it is challenging to predict ligands that bind to AhR. Taking advantage of the AhR-modulatory properties of a vast number of HSLs and their tested analogs (fig. S4, A to C), we optimized an existing in silico model (*10*) to interrogate whether and how these QS molecules from *P. aeruginosa* can be accommodated in the AhR-binding pocket (Fig. 2A). The ligands were divided by impact on agonistic or competitive behavior and sorted according to increasing molecular mechanics generalized Born surface area (MM-GBSA) binding energies (ΔG^{Bind}). This revealed 3-o-C12-L-HSL as the strongest binder and C4-L-HSL as the weakest binder in this study (fig. S4D). In this model, all residues previously found to interact with the bona fide AhR ligand 2,3,7,8-tetrachlorodibenzodioxin (TCDD) by mutagenesis experiments (*23*, *24*) are predicted to be involved in forming the binding pocket. The key residues, Thr^{289}, His^{291}, Phe^{295}, Ser^{365}, and Gln^{383}, form hydrogen bonds with most of the ligands investigated here (fig. S4, D and E). Furthermore, and in agreement with data retrieved from ligand-selective modulation of

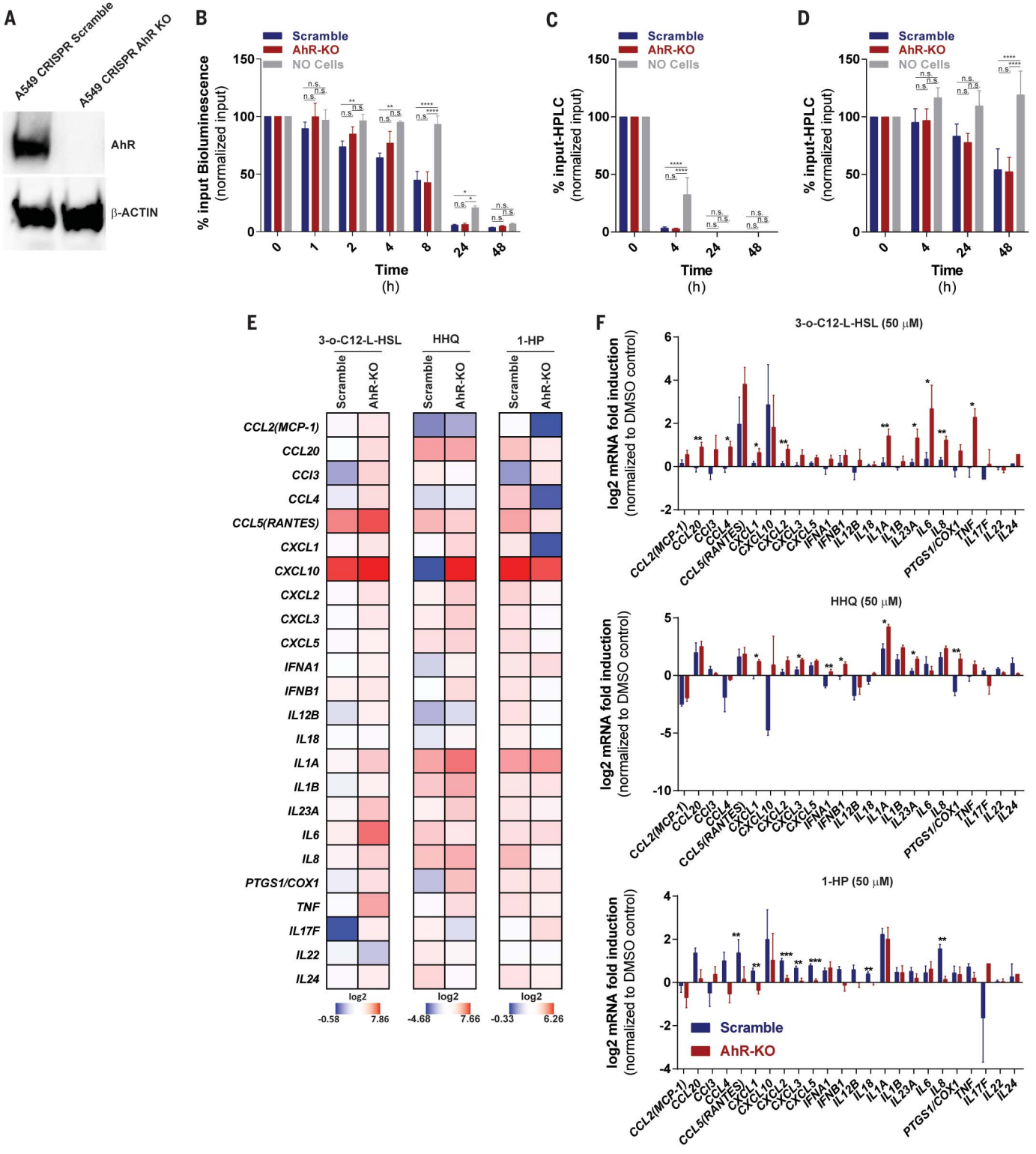

Fig. 3. AhR-dependent responses. (**A**) Western blot detection of AhR protein expression in A549 CRISPR scramble control and CRISPR AhR-KO cells. (**B** and **C**) Degradation of 3-o-C12-L-HSL measured in the supernatants of stimulated A549 CRISPR cells compared to control without cells. Expression of 3-o-C12-L-HSL was detected by bacterial PA14-R3 bioluminescence reporter assay (data pooled from n = 3 independent experiments) (B) or HPLC (data pooled from n = 3 independent experiments) (C). (**D**) Degradation of HHQ measured and detected as in (C) (data pooled from n = 4 independent experiments). (**E** and **F**) Gene expression analysis of different cytokines and chemokines in A549 CRISPR cells upon 24 hours of stimulation with *P. aeruginosa* QS molecules. Data are pooled from 3-o-C12-L-HSL (n = 6), HHQ (n = 5), or 1-HP (n = 7) independent experiments. Data are means ± SEM [(B), (C), (D), (F)]. *P < 0.05, **P < 0.01, ***P < 0.001, ****P < 0.0001 [two-way ANOVA in (B), two-tailed Student t test in (F)]; n.s., not significant.

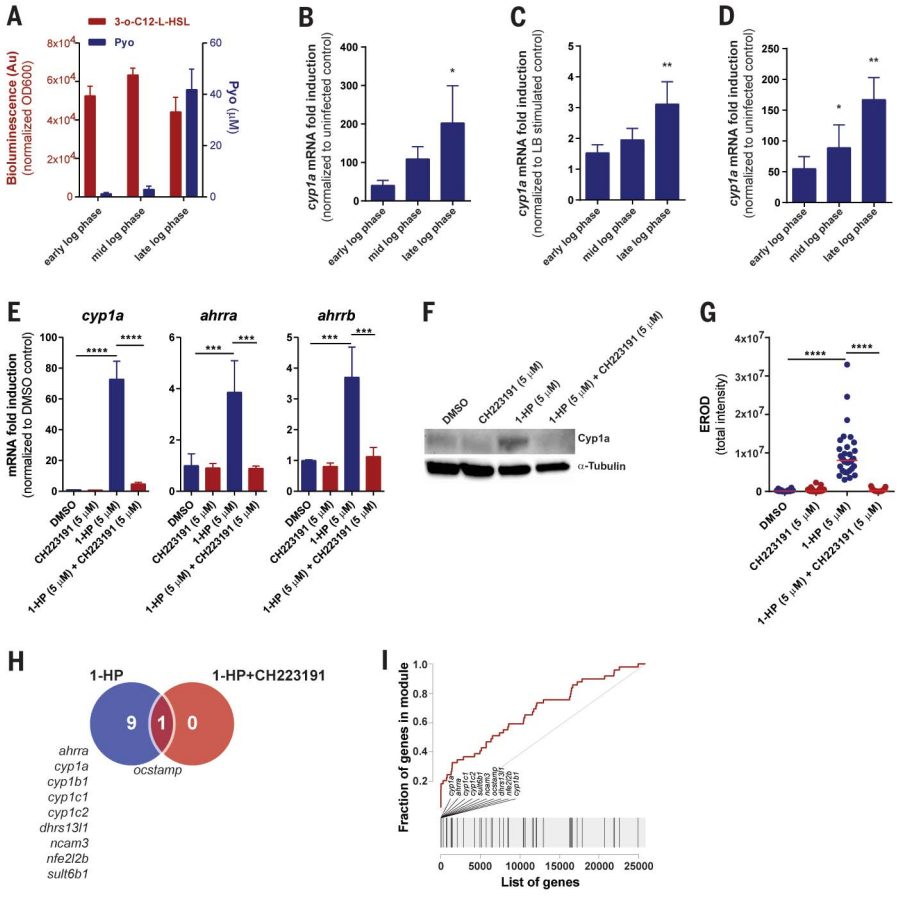

Fig. 4. AhR activation by *P. aeruginosa* QS molecules in zebrafish larvae. (**A**) Expression of 3-o-C12-L-HSL and Pyo in supernatants of PA14 WT, collected at different growth phases in LB medium; 3-o-C12-L-HSL determined by PA14-R3 bioluminescence reporter assay and Pyo concentrations evaluated by spectrophotometry (data pooled from n = 9 independent experiments). (**B** to **D**) *cyp1a* expression in 2-dpf zebrafish larvae infected by immersion with PA14 WT [(B) and (D)] or exposed to bacterial supernatants for 5 hours (C) (data pooled from n = 7 independent experiments). In (B), zebrafish were infected with different bacterial loads collected from various phases of PA14 WT growth, according to the defined final OD_{600} in E3 medium (adjusted to early log-OD_{600} = 0.2, mid log-OD_{600} = 0.7, late log-OD_{600} = 1; data pooled from n = 3 independent experiments). In (D), zebrafish were infected with 1×10^9 CFU/ml, with PA14 WT collected from various phases of bacterial growth (data pooled from n = 7 independent experiments). (**E**) Gene expression analysis of *cyp1a*, *ahrra*, and *ahrrb* transcripts from zebrafish larvae (2 dpf) treated (red) or untreated (blue) for 2 hours with 5 μM CH223191 (AhR inhibitor) followed by a further 4 hours of exposure to 5 μM 1-HP or DMSO vehicle control. One representative experiment of at least three independent experiments is shown. Triplicates of 12 larvae are depicted at each data point. (**F**) Cyp1a protein expression detected by Western blot analysis in 2-dpf zebrafish larvae treated for 24 hours with DMSO, 5 μM 1-HP, 5 μM CH223191, or both 1-HP and CH223191. (**G**) Cyp1a enzymatic activity expressed as total intensity of resorufin (EROD assay) detected per 2-dpf larva treated (red) or not (blue) for 2 hours with 5 μM CH223191 followed by a further 4 hours of exposure to 5 μM 1-HP or DMSO vehicle control (each dot represents one larva; data are median values). One representative experiment of at least three independent experiments is shown. (**H** and **I**) Microarray analysis of 2-dpf larvae preexposed to DMSO or 5 μM CH223191 for 2 hours, followed by 4 hours of exposure to 5 μM 1-HP or DMSO, in the presence or absence of 5 μM CH223191. Data are pooled from n = 5 independent experiments. (H) Venn diagram depicting the differentially expressed genes; (I) AhR gene enrichment curve. Data are means ± SEM [(A) to (D)] or means ± SD (E). *P < 0.05, **P < 0.01, ***P < 0.001, ****P < 0.0001 (one-way ANOVA).

AhR ligand binding, AhR complexes with bound competitors showed additional hydrophobic interactions with Phe^{287}, Leu^{308}, and Leu^{315} (fig. S4, D and E) (*25*). 1-HP is predicted to contact Phe^{324} via interactions of the aromatic rings (fig. S4E). This residue is known to mediate agonist/antagonist switching upon mutation (Phe^{324} → Ala/Leu) and converts agonists such as 3-methylcholanthrene (3-MC) or β-naphthoflavone (BNF) into antagonists (*25*). Predictions were validated by ligand-binding studies (*10*) that confirmed the binding of 3-o-C12-L-HSL and HHQ, with dissociation constant (K_d) values of 4.67 μM and 3.77 μM, respectively (Fig. 2B and fig. S4F). In addition, we developed a complementary method to detect AhR binding of different ligands, including TCDD (*26*), using purified AhR and aryl hydrocarbon receptor nuclear translocator (ARNT) proteins in a microscale thermophoresis (MST) assay (fig. S4G). This approach also demonstrated AhR binding to QS molecules including 3-o-C12-L-HSL, PQS, and 1-HP, but not to C4-L-HSL (Fig. 2C). (HHQ binding could not be analyzed by MST because of its intrinsic fluorescence properties, which interfere with the assay.) Together, these findings show that various QS molecules other than phenazines bind to AhR and modulate its activity; hence, this pathway is appropriate as a potential target for sensing bacterial infection dynamics in the host.

AhR QS ligand interactions were further defined using an A549 AhR CRISPR knockout (KO) cell line (Fig. 3A and fig. S5A). Induction of AhR-dependent genes was detected upon 1-HP stimulation of CRISPR scramble control, and was absent in the AhR-KO cells (fig. S5B). In contrast, and as previously shown in wild-type A549 cells, 3-o-C12-L-HSL and HHQ caused AhR inhibition (fig. S5, B and C). Major functions of AhR include xenobiotic metabolism, toxin degradation, and excretion (*26*). Previously, we demonstrated that AhR mediates the degradation of bacterial molecules such as *P. aeruginosa* phenazines and *Mycobacterium tuberculosis* naphthoquinone phthiocol (*10*). Using an established *P. aeruginosa* 3-o-C12-L-HSL luminescence reporter strain (PA14-R3) (*27*) to detect 3-o-C12-L-HSL levels (fig. S5D), we evaluated its degradation profile upon exposure to AhR-proficient and AhR-deficient cells (fig. S5E). Bioluminescence emitted by the bacterial reporter cells decreased in a time-dependent manner, indicating reduced abundance of 3-o-C12-L-HSL (Fig. 3B). In contrast, no differences were detected between scramble control and AhR-KO cells (Fig. 3B). These results were confirmed by HPLC (Fig. 3C). A similar approach was used to determine the metabolism of HHQ (fig. S5E), using the PAO1 *pqsA* CTX-lux::*pqsA* reporter strain (fig. S5F) (*28*) and HPLC. Surprisingly, no degradation of HHQ was observed with any of the methods when exposing cells to 50 μM HHQ (fig. S5, G and H). However, when cells were exposed to a lower concentration of HHQ (0.5 μM), diminished levels of HHQ were detected at late time points, although no differences between AhR-proficient and AhR-deficient cells were observed (Fig. 3D).

Together, under the conditions tested, our results argue against an involvement of AhR in the degradation of *P. aeruginosa* 3-o-C12-L-HSL or HHQ. In addition to its role in xenobiotic metabolism, AhR participates in the

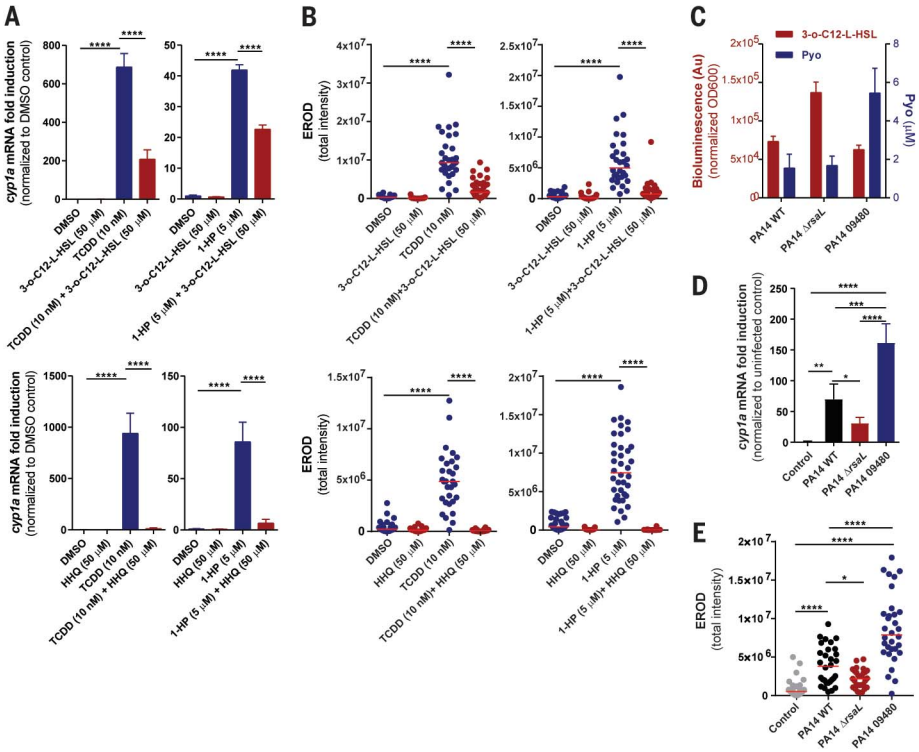

Fig. 5. AhR modulation by *P. aeruginosa* QS molecules in zebrafish larvae. (**A** and **B**) *cyp1a* gene expression (A) and Cyp1a enzymatic activity (B) upon 4 hours of exposure of 2-dpf larvae to diverse *P. aeruginosa* QS molecules or TCDD. One representative experiment of at least three independent experiments is shown. In (A), triplicates of 12 larvae are depicted at each data point. In (B), each dot represents one larva; data are median values. (**C**) Expression of 3-o-C12-L-HSL (determined by PA14-R3 bioluminescence reporter assay) and Pyo (evaluated by spectrophotometry) in the supernatants of different PA14 strains collected at mid-log growth phase; pooled data from $n = 6$ independent experiments. (**D** and **E**) Infection of 2-dpf zebrafish larvae by immersion for 5 hours with 1×10^9 CFU/ml of different *P. aeruginosa* strains collected at mid-log growth phase. (D) *cyp1a* gene expression; triplicates of 12 larvae are depicted at each data point. (E) Cyp1a enzymatic activity. Each dot represents one larva; data are median values. Data are from one representative experiment of at least three independent experiments. Data are means ± SD [(A) and (D)] or means ± SEM (C). $^*P < 0.05$, $^{**}P < 0.01$, $^{***}P < 0.001$, $^{****}P < 0.0001$ (one-way ANOVA).

regulation of different immune mediators (*10*, *19*, *26*, *29*). Accordingly, we evaluated whether AhR regulates cytokine and chemokine expression upon exposure to different QS molecules. Different bacterial ligands induced different gene expression patterns (Fig. 3, E and F). It was previously reported that infection with *P. aeruginosa*, or exposure to 3-o-C12-L-HSL, leads to *IL-6* and *IL-8* expression (*30*, *31*). Consistently, among the genes induced by 3-o-C12-L-HSL, *IL-6* and *IL-8* were highly induced in the AhR-KO cells as compared to scramble control. Elevated induction of IL-8 was also observed upon exposure of AhR-KO cells to HHQ, whereas 1-HP stimulation led to reduced induction. A similar profile was observed for *CXCL1*, *CXCL2*, and *CXCL3* (Fig. 3, E and F). These results emphasize differential AhR modulation of host responses, where sensing the different levels of QS molecules expressed along the infection process can differentially regulate the composition of multiple cytokines and chemokines. Thus, sensing of QS molecules by AhR shapes immunity to infection.

AhR senses bacterial QS molecules in vivo

As mentioned above, AhR is conserved among different species (including human, mouse, and zebrafish) and few amino acid positions differ in the ligand-binding site of AhR proteins (fig. S6A). However, subtle amino acid differences have been reported to affect binding to specific ligands (*26*). For example, the human Val^{381}, corresponding to Ala in mouse and zebrafish, is implicated in species-related differences regarding binding affinity to TCDD; specifically, mouse AhR has higher binding affinity to TCDD than does human AhR (*26*, *32*). Consistently, using our in silico modeling, higher TCDD binding affinities of mouse and zebrafish AhR were detected relative to human AhR (fig. S6B). A similar approach was chosen for the *P. aeruginosa* QS molecules, and MM-GBSA ΔG^{Bind} values were calculated starting from the same ligand docking pose as obtained for the human AhR (fig. S6C). Strikingly, no species-specific differences were predicted to occur, further pointing to a conserved mechanism of sensing of *P. aeruginosa* infection.

The zebrafish (*Danio rerio*) has become a powerful model in developmental biology and genetics, and more recently in toxicology and immunology (*33*–*36*). The AhR pathway is conserved in zebrafish and has also been shown to be involved in xenobiotic metabolism (*36*). As a result of genome-wide duplication events, teleosts express various co-orthologs of mammalian genes, although not all are functional. Zebrafish express three AhR isoforms (*ahr1a*, *ahr1b*, and *ahr2*), and AhR2 is the primary isoform for recognition of toxic ligands such as TCDD (*36*). Upon ligand activation, AhR2 drives the expression of hallmark genes such as *cyp1a*, *ahrra*, and *ahrrb* (*36*).

It was previously reported that static immersion of zebrafish larvae in a bacterial suspension, including *P. aeruginosa*, increases *cyp1a* expression (*37*, *38*). Similar results were obtained from microarray analysis of larvae at 2 days post-fertilization (2 dpf) infected with PA14 WT for 5 or 24 hours (fig. S7A and tables S2 and S3). Moreover, in addition to *cyp1a*, increased expression of additional AhR-related genes such as *ahrra* and *cyp1c1* was

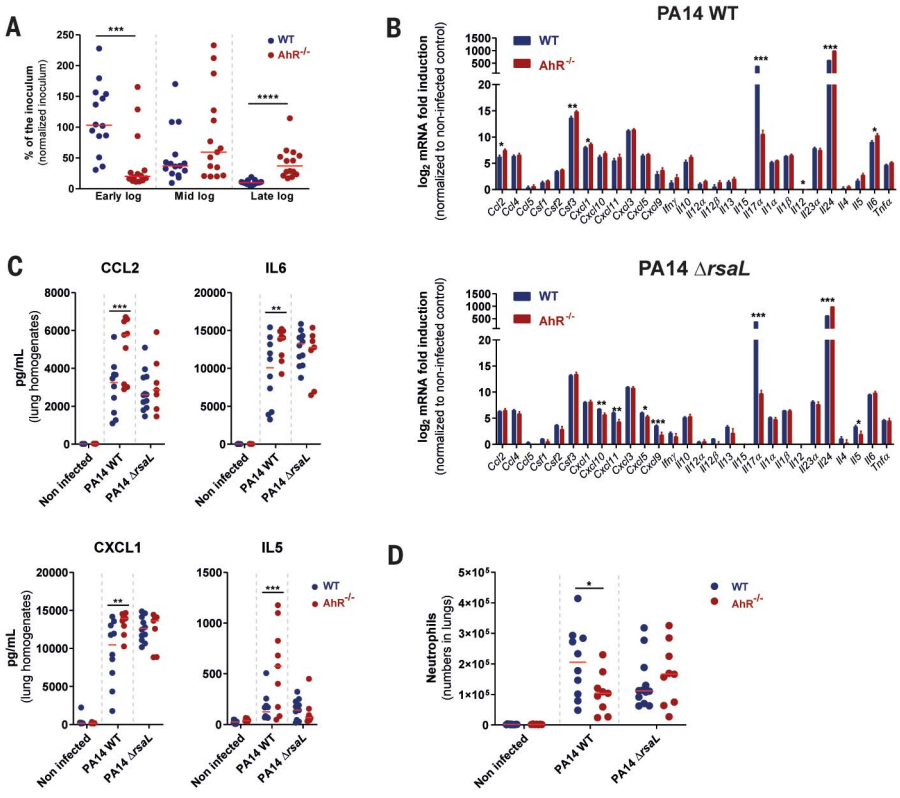

Fig. 6. AhR-mediated responses upon *P. aeruginosa* infection in mice. (**A**) Bacterial clearance in the lungs of WT and AhR-knockout ($AhR^{-/-}$) mice after 8 hours of infection with *P. aeruginosa* PA14 09480 (2×10^6 CFU administered per mouse). Bacterial growth phases: early log, $OD_{600} < 0.3$; mid-log, $0.5 < OD_{600} < 0.8$; late log, $OD_{600} > 1$. Each dot represents one mouse (data pooled from $n = 2$ independent experiments; median values are shown). (**B** to **D**) Infection of WT and $AhR^{-/-}$ mice for 8 hours with PA14 WT or PA14 Δ*rsaL* strains (data pooled from $n = 2$ independent experiments). (B) Gene expression analysis of different cytokines and chemokines in the lungs of infected mice, compared to the respective noninfected mouse strain (WT, $n = 8$ mice; $AhR^{-/-}$, $n = 6$ mice). Data are means ± SEM. (C) Cytokine and chemokine median protein levels in lung homogenates after infection. Each dot represents one mouse (data pooled from $n = 2$ independent experiments). (D) Neutrophil numbers (medians) in the lungs of infected and non-infected mice. Each dot represents one mouse (data pooled from $n = 2$ independent experiments). $^*P < 0.05$, $^{**}P < 0.01$, $^{***}P < 0.001$, $^{****}P < 0.0001$ [Mann-Whitney U test in (A) and (D); two-tailed Student *t* test in (B); two-way ANOVA in (C)].

observed (*36*). Therefore, we evaluated whether we could recapitulate our in vitro findings using this in vivo model organism. Here, 5 hours of exposure of 2-dpf larvae to PA14 WT collected from different phases of bacterial growth with distinct expression patterns of QS molecules (e.g., 3-o-C12-L-HSL and Pyo; Fig. 4A) resulted in distinct AhR activation, as measured by *cyp1a* mRNA expression (Fig. 4B). To mimic the course of infection, we collected bacteria from different growth phases, and washed and further resuspended them in E3 medium to a final optical density (OD) similar to the point of collection (i.e., early log, $OD_{600} = 0.2$; mid-log, $OD_{600} = 0.7$; late log, $OD_{600} = 1$). Exposure of larvae to these bacterial suspensions led to increasing *cyp1a* expression along the growth phase (Fig. 4B). Still, this could be the result of higher expression of QS molecules and/or increasing bacterial density. To exclude the latter option, we exposed zebrafish larvae to bacterial supernatants after filtration and dilution in E3 medium (1:25 ratio) or to similar bacterial numbers collected from the different growth stages. Exposure of 2-dpf larvae to filtered supernatants or to infection by immersion resulted in elevated *cyp1a* expression toward late stages of bacterial growth (Fig. 4, C and D). These results are in agreement with our in vitro findings (Fig. 1, B and C, and fig. S1, A and E), thereby confirming that *P. aeruginosa* molecules expressed during diverse growth phases modulate AhR differentially.

Next, we verified in the zebrafish model our in vitro findings that *P. aeruginosa* expresses QS molecules that either activate or inhibit the canonical AhR pathway. We previously demonstrated that *P. aeruginosa* phenazines (e.g., 1-HP) activate the AhR pathway in human and mouse (*10*). Here, exposure of 2-dpf zebrafish larvae to TCDD induced the expression of AhR-dependent genes (*36*) (fig. S7B). AhR dependency was confirmed by reduced gene expression in the presence of the AhR inhibitor CH223191 (*39*) (fig. S7, B and C). Similarly, we observed AhR modulation upon exposure to the *P. aeruginosa* phenazine 1-HP at the transcriptional level (Fig. 4E) and Cyp1a protein expression in response to 1-HP (Fig. 4F). To determine whether increased Cyp1a expression translates into enhanced enzymatic activity, we measured its activity in vivo in a semi–high-throughput assay (fig. S7, D and E). An increment in fluorescence, as readout of increased Cyp1a enzymatic activity, was detected upon exposure to 1-HP or TCDD and was inhibited by CH223191 (Fig. 4G and fig. S7, E and F). AhR was the major sensor of *P. aeruginosa* phenazines in vivo, because microarray analysis of larvae exposed to 1-HP in the presence or absence of the AhR inhibitor revealed that AhR-dependent genes (*36*) were among the top 10 1-HP–induced genes and that their induction was reverted by the CH223191 inhibitor (Fig. 4, H and I, fig. S7G, and table S4). Not all of the differentially 1-HP–induced genes had been previously shown to be transcriptionally regulated by AhR in zebrafish. Therefore, we performed an in silico analysis to identify xenobiotic responsive elements (XREs) in their promotor regions (*40*). We identified putative XREs in the promoter regions of all evaluated genes (fig. S7H).

Given that our in vitro studies demonstrated that *P. aeruginosa* also expresses QS molecules that inhibit the AhR pathway, we exposed larvae in vivo to 3-o-C12-L-HSL or HHQ in the presence or absence of 1-HP. Simultaneous exposure to 3-o-C12-L-HSL or HHQ together with 1-HP reduced induction of AhR-related genes by 1-HP (Fig. 5A and fig. S8, A to D). Moreover, Cyp1a enzymatic activity was diminished when zebrafish larvae were co-exposed to 3-o-C12-L-HSL, HHQ, and PQS together with 1-HP, whereas C4-L-HSL did not affect 1-HP–induced activation (Fig. 5B and fig. S8B). Remarkably, 3-o-C12-L-HSL and HHQ even inhibited AhR activation by TCDD (Fig. 5, A and B, and fig. S8, A and B). Microarray analysis further confirmed that 3-o-C12-L-HSL inhibited AhR activation by 1-HP (table S5). None of the ligands induced toxicity in zebrafish larvae under the conditions tested (fig. S8E). Overall, our results demonstrate that zebrafish AhR recognizes diverse *P. aeruginosa* QS molecules.

Taking advantage of *P. aeruginosa* mutants producing dissimilar levels of distinct QS molecules, we tested whether AhR is differentially modulated in vivo in response to bacteria expressing different QS molecules. We used the mutant PA14 Δ*rsaL* and PA14 09480 *P. aeruginosa* strains, which overproduce 3-o-C12-L-HSL (*27*, *41*) or phenazines (*10*), respectively. No differences in bacterial growth

or in the sequential expression of QS molecules were observed among these strains (fig. S9, A and B), whereas the levels of 3-o-C12-L-HSL and phenazines differed as previously documented (fig. S9C). Consistent with earlier studies (*41*), Pyo levels were also elevated in the PA14 Δ*rsaL* relative to PA14 WT (fig. S9C). Therefore, we focused on bacteria collected from one distinct growth phase (mid-log phase) with consistent differences in the levels of 3-o-C12-L-HSL and Pyo (Fig. 5C). Static immersion of larvae to similar bacterial numbers [1 × 10^9 colony-forming units (CFU)/ml; fig. S10A] led to distinct Cyp1a expression and activity (Fig. 5, D and E), apparently related to the proportions of the AhR activators and inhibitors (Fig. 5C and fig. S10B). Relative to PA14 WT, higher expression of phenazines (PA14 09480) increased Cyp1a activity, whereas higher expression of 3-o-C12-L-HSL (PA14 Δ*rsaL*) decreased Cyp1a activity (Fig. 5E). We conclude that AhR recognition of these molecules, whose expressions are tightly regulated in *P. aeruginosa*, allows for quantitative sensing of the course of infection.

Recognition of phenazines by AhR is important for clearance of *P. aeruginosa* (*10*). Infection of wild-type and $AhR^{-/-}$ mice with a Pyo-overexpressing strain (PA14 09480) (*10*) (figs. S9C and S11A) confirmed the importance of AhR in bacterial clearance in responses to these molecules (Fig. 6A). Intriguingly, infection with bacteria from earlier stages of growth, not expressing phenazines (fig. S11A), had detrimental consequences mediated by AhR (Fig. 6A). These results further illustrate that distinct *P. aeruginosa* molecules expressed at different growth stages modulate AhR signaling differentially. To evaluate the impact of AhR sensing of QS molecules expressed at early stages, focusing on the AhR inhibitor 3-o-C12-L-HSL identified here, we infected mice with the *P. aeruginosa* strain (PA14 Δ*rsaL*). We focused on bacteria from mid-log growth phase to exclude differences in lung CFUs between the two mouse strains (WT and $AhR^{-/-}$) after 8 hours of infection (fig. S11, B and C). Differential expression of various cytokines and chemokines depended not only on the mouse strain, but also on the *P. aeruginosa* strain (Fig. 6, B and C, and fig. S11D). These in vivo results are consistent with our in vitro experiments (Fig. 3, E and F), where AhR differentially regulated the expression of distinct cytokines and chemokines, depending on the presence of distinct QS molecules. Previously we reported a critical role of AhR in the recruitment of neutrophils to the lungs of *P. aeruginosa*–infected mice (*10*). Likewise, lower numbers of neutrophils were detected in the lungs of $AhR^{-/-}$ mice upon infection with PA14 WT (Fig. 6D). Strikingly, these differences were lost when infecting mice with PA14 Δ*rsaL*, where we observed comparable numbers of neutrophils in the lungs of wild-type and $AhR^{-/-}$ mice (Fig. 6D).

In sum, these results reveal differential modulation of AhR during the course of infection, depending on the relative abundances of distinct QS molecules. Taken together, our data show that AhR not only detects *P. aeruginosa* QS molecules in a qualitative way, but also quantifies their relative levels. This quantitative assessment endows the host with the capacity to sense bacterial community densities, and consequently infection dynamics. Thus, our findings emphasize a crucial role of AhR as master regulator of host defense responses, capable of tuning immunity according to the stage of infection and disease and hence to their threat to the host.

Discussion

Recently we showed that AhR, by binding bacterial pigmented virulence factors such as *P. aeruginosa* phenazines, regulates host resistance to infection (*10*). Our present findings show that in addition to phenazines, AhR recognizes QS molecules comprising different chemical entities including homoserine lactones and quinolones. In contrast to phenazines, the QS cognates 3-o-C12-L-HSL and HHQ inhibit the canonical AhR signaling by competing and antagonizing the effects of known AhR activators, such as *P. aeruginosa* 1-HP (*10*) or the bona fide AhR ligand TCDD (*19*, *42*). Strikingly, AhR sensing of QS molecules is not restricted to a particular cell type or a specific in vitro model: (i) Mammalian macrophages, hepatocytes, and epithelial cells responded in a similar fashion, and in all cases subtle alterations in the ratios of bacterial ligands influenced the outcome of AhR activation and its downstream responses, such as cytokine and chemokine expression. (ii) These results are reciprocated in vivo using zebrafish, where exposure of larvae to different concentrations of *P. aeruginosa* QS molecules modulated AhR activation and elicited downstream responses. (iii) Exposure of zebrafish larvae to different *P. aeruginosa* mutants producing distinct QS molecules at different abundances at a given point of infection resulted in a specific AhR activation profile. (iv) Complementing these findings, an experimental mouse infection model with *P. aeruginosa* strains expressing variable levels of QS molecules revealed that AhR regulates bacterial elimination upon sensing bacterial quorum. In sum, AhR resembles a "processing hub" that integrates the information linked to the abundance of different QS molecules, both activators and inhibitors, thereby mobilizing the most appropriate host defense mechanisms at a given stage of infection.

QS is used by certain bacteria to coordinate their gene expression in response to changes in their population density or their stage of infection (*1*, *3*, *4*). Accordingly, direct correlation between different QS molecules and severity of infection has been observed (*7*). In *P. aeruginosa*, QS regulates different virulence and adaptation mechanisms and is therefore crucial for coordinated colonization of a new environment (*1*, *3*, *4*, *12*). Differences in *P. aeruginosa* virulence and transition from acute to chronic infection have been linked to altered expression of QS molecules and their regulated genes (*1*, *6*, *8*). For instance, the expression of phenazines plays a critical role in biofilm formation and development (*7*, *43*), and *P. aeruginosa* QS mutants producing thinner and less developed biofilms, are more sensitive to antibiotics and eradication (*1*, *5*, *44*). Furthermore, high concentrations of *P. aeruginosa* phenazines are detected in the sputum of CF patients, who are severely affected by this pathogen (*2*, *7*). Therefore, depending on its metabolic state, mirrored by a distinct composition of QS molecules, the bacteria may pose different threats to the host, and the host needs to adapt its response accordingly. Interestingly, inter– and intra–*P. aeruginosa* species differences in virulence and expression of secreted molecules have been reported to occur, not only among clinical isolates but also among laboratory strains (e.g., between PAO1 sublines or between PA14 and PAO1). For example, expression levels of Pyo, rhamnolipids, PQS, exopolysaccharides, and elastase have been reported to differ between PA14 and PAO1 or among diverse PAO1 sublines (*45*–*48*). It is tempting to speculate that as a result of its capacity to detect different levels of *P. aeruginosa* QS molecules, including Pyo or PQS, AhR is also well suited to detect strain-related differences during the course of infection, and consequently regulate host responses accordingly. However, further studies are needed to evaluate this hypothesis.

Interactions of *P. aeruginosa* QS molecules with different host receptors and signaling pathways have been reported (*9*). For example, 3-o-C12-L-HSL has been found to be sensed by the Ras GTPase-activating–like protein IQGAP1 or the peroxisome proliferator–activated receptors (PPAR β/δ/γ) (*9*, *49*, *50*). Additionally, *P. aeruginosa* HSLs (e.g., 3-o-C12-L-HSL) and quinolones (HHQ and PQS) modulate different host signaling pathways involving NF-κB or PPAR (*9*, *50*–*52*). Curiously, interactions between AhR and the indicated signaling pathways (e.g., NF-κB and PPAR) have been described (*19*), but their interplay and elicited responses upon *P. aeruginosa* infection remain unknown and should be the focus of future studies. Nonetheless, the capacity of AhR to bind and recognize three distinct types of QS molecules (HSLs, quinolones, and phenazines), as well as its capacity to monitor and integrate their relative expression levels, supports the identification of this

receptor as a major host sensor of bacterial quorum and infection dynamics. It is tempting to speculate that host AhR and bacterial QS systems can actively spy on each other by recognizing similar molecules, even beyond the QS molecules described here. Recently, Ismail *et al.* (*53*) described how host epithelia can produce QS-like molecules, including an autoinducer-2 mimic, enabling it to interfere with bacterial QS circuits. However, the host AhR can sense *P. aeruginosa* QS molecules and has vast ligand-binding properties, so we cannot exclude the possibility that it senses and modulates the expression of different host molecules (such as host QS-like molecules) that may be involved in this host-bacteria interkingdom cross-talk during infection (Fig. 1A, gray arrows).

Given that AhR acts as a host sensor that monitors different QS molecules and their expression profiles along the course of infection and disease, the host can tune immune defense according to the stage and density of the bacterial community and the threat of infection. This mechanism would be particularly apt for nosocomial pathogens, which can be tolerated by the immunocompetent host at low density but become harmful once a threshold of tolerability has been exceeded. In this way, cost of energy for defense would be focused on the harmful trait only, with the harmless trait being ignored. Because *P. aeruginosa* is an opportunistic pathogen, defense mobilization is avoided at low bacterial densities, which can be tolerated, and it kicks in only with increasing population densities, which can harm the host. We propose that by spying on interbacterial communication, AhR is capable of sensing the status quo of the *P. aeruginosa* community during infection, allowing the host to mobilize the most appropriate defense mechanism according to the severity of threat.

REFERENCES AND NOTES

1. M. F. Moradali, S. Ghods, B. H. Rehm, *Pseudomonas aeruginosa* Lifestyle: A Paradigm for Adaptation, Survival, and Persistence. *Front. Cell. Infect. Microbiol.* **7**, 39 (2017). doi: 10.3389/fcimb.2017.00039; pmid: 28261568
2. J. C. Davies, Pseudomonas aeruginosa in cystic fibrosis: Pathogenesis and persistence. *Paediatr. Respir. Rev.* **3**, 128–134 (2002). doi: 10.1016/S1526-0550(02)00003-3; pmid: 12297059
3. K. Papenfort, B. L. Bassler, Quorum sensing signal-response systems in Gram-negative bacteria. *Nat. Rev. Microbiol.* **14**, 576–588 (2016). doi: 10.1038/nrmicro.2016.89; pmid: 27510864
4. C. M. Waters, B. L. Bassler, Quorum sensing: Cell-to-cell communication in bacteria. *Annu. Rev. Cell Dev. Biol.* **21**, 319–346 (2005). doi: 10.1146/annurev.cellbio.21.012704.131001; pmid: 16212498
5. P. C. Shih, C. T. Huang, Effects of quorum-sensing deficiency on Pseudomonas aeruginosa biofilm formation and antibiotic resistance. *J. Antimicrob. Chemother.* **49**, 309–314 (2002). doi: 10.1093/jac/49.2.309; pmid: 11815572
6. C. Winstanley, J. L. Fothergill, The role of quorum sensing in chronic cystic fibrosis Pseudomonas aeruginosa infections. *FEMS Microbiol. Lett.* **290**, 1–9 (2009). doi: 10.1111/j.1574-6968.2008.01394.x; pmid: 19016870
7. B. Rada, T. L. Leto, Pyocyanin effects on respiratory epithelium: Relevance in Pseudomonas aeruginosa airway infections. *Trends Microbiol.* **21**, 73–81 (2013). doi: 10.1016/j.tim.2012.10.004; pmid: 23140890
8. H. L. Barr *et al.*, Pseudomonas aeruginosa quorum sensing molecules correlate with clinical status in cystic fibrosis. *Eur. Respir. J.* **46**, 1046–1054 (2015). doi: 10.1183/09031936.00225214; pmid: 26022946
9. Y. C. Liu, K. G. Chan, C. Y. Chang, Modulation of Host Biology by Pseudomonas aeruginosa Quorum Sensing Signal Molecules: Messengers or Traitors. *Front. Microbiol.* **6**, 1226 (2015). doi: 10.3389/fmicb.2015.01226; pmid: 26617576
10. P. Moura-Alves *et al.*, AhR sensing of bacterial pigments regulates antibacterial defence. *Nature* **512**, 387–392 (2014). doi: 10.1038/nature13684; pmid: 25119038
11. L. E. Dietrich, A. Price-Whelan, A. Petersen, M. Whiteley, D. K. Newman, The phenazine pyocyanin is a terminal signalling factor in the quorum sensing network of Pseudomonas aeruginosa. *Mol. Microbiol.* **61**, 1308–1321 (2006). doi: 10.1111/j.1365-2958.2006.05306.x; pmid: 16879411
12. P. Nadal Jimenez *et al.*, The multiple signaling systems regulating virulence in Pseudomonas aeruginosa. *Microbiol. Mol. Biol. Rev.* **76**, 46–65 (2012). doi: 10.1128/MMBR.05007-11; pmid: 22390972
13. A. Crabbé *et al.*, Alveolar epithelium protects macrophages from quorum sensing-induced cytotoxicity in a three-dimensional co-culture model. *Cell. Microbiol.* **13**, 469–481 (2011). doi: 10.1111/j.1462-5822.2010.01548.x; pmid: 21054742
14. K. Tateda *et al.*, The Pseudomonas aeruginosa autoinducer N-3-oxododecanoyl homoserine lactone accelerates apoptosis in macrophages and neutrophils. *Infect. Immun.* **71**, 5785–5793 (2003). doi: 10.1128/IAI.71.10.5785-5793.2003; pmid: 14500500
15. J. P. Pearson *et al.*, Structure of the autoinducer required for expression of Pseudomonas aeruginosa virulence genes. *Proc. Natl. Acad. Sci. U.S.A.* **91**, 197–201 (1994). doi: 10.1073/pnas.91.1.197; pmid: 8278364
16. T. S. Charlton *et al.*, A novel and sensitive method for the quantification of N-3-oxoacyl homoserine lactones using gas chromatography-mass spectrometry: Application to a model bacterial biofilm. *Environ. Microbiol.* **2**, 530–541 (2000). doi: 10.1046/j.1462-2920.2000.00136.x; pmid: 11233161
17. D. L. Erickson *et al.*, Pseudomonas aeruginosa quorum-sensing systems may control virulence factor expression in the lungs of patients with cystic fibrosis. *Infect. Immun.* **70**, 1783–1790 (2002). doi: 10.1128/IAI.70.4.1783-1790.2002; pmid: 11895939
18. P. K. Singh *et al.*, Quorum-sensing signals indicate that cystic fibrosis lungs are infected with bacterial biofilms. *Nature* **407**, 762–764 (2000). doi: 10.1038/35037627; pmid: 11048725
19. B. Stockinger, P. Di Meglio, M. Gialitakis, J. H. Duarte, The aryl hydrocarbon receptor: Multitasking in the immune system. *Annu. Rev. Immunol.* **32**, 403–432 (2014). doi: 10.1146/annurev-immunol-032713-120245; pmid: 24655296
20. C. Schiering *et al.*, Feedback control of AHR signalling regulates intestinal immunity. *Nature* **542**, 242–245 (2017). doi: 10.1038/nature21080; pmid: 28146477
21. E. Wincent *et al.*, Inhibition of cytochrome P4501-dependent clearance of the endogenous agonist FICZ as a mechanism for activation of the aryl hydrocarbon receptor. *Proc. Natl. Acad. Sci. U.S.A.* **109**, 4479–4484 (2012). doi: 10.1073/pnas.1118467109; pmid: 22392998
22. C. J. Sinal, J. R. Bend, Aryl hydrocarbon receptor-dependent induction of cyp1a1 by bilirubin in mouse hepatoma hepa 1c1c7 cells. *Mol. Pharmacol.* **52**, 590–599 (1997). doi: 10.1124/mol.52.4.590; pmid: 9380021
23. A. Pandini, M. S. Denison, Y. Song, A. A. Soshilov, L. Bonati, Structural and functional characterization of the aryl hydrocarbon receptor ligand binding domain by homology modeling and mutational analysis. *Biochemistry* **46**, 696–708 (2007). doi: 10.1021/bi061460t; pmid: 17223691
24. A. Pandini *et al.*, Detection of the TCDD binding-fingerprint within the Ah receptor ligand binding domain by structurally driven mutagenesis and functional analysis. *Biochemistry* **48**, 5972–5983 (2009). doi: 10.1021/bi900259z; pmid: 19456125
25. A. A. Soshilov, M. S. Denison, Ligand promiscuity of aryl hydrocarbon receptor agonists and antagonists revealed by site-directed mutagenesis. *Mol. Cell. Biol.* **34**, 1707–1719 (2014). doi: 10.1128/MCB.01183-13; pmid: 24591650
26. R. Pohjanvirta, *The AH Receptor in Biology and Toxicology* (Wiley, 2011).
27. F. Massai *et al.*, A multitask biosensor for micro-volumetric detection of N-3-oxo-dodecanoyl-homoserine lactone quorum sensing signal. *Biosens. Bioelectron.* **26**, 3444–3449 (2011). doi: 10.1016/j.bios.2011.01.022; pmid: 21324665
28. M. Fletcher, M. Cámara, D. A. Barrett, P. Williams, Biosensors for qualitative and semiquantitative analysis of quorum sensing signal molecules. *Methods Mol. Biol.* **1149**, 245–254 (2014). doi: 10.1007/978-1-4939-0473-0_20; pmid: 24818910
29. C. Esser, A. Rannug, The aryl hydrocarbon receptor in barrier organ physiology, immunology, and toxicology. *Pharmacol. Rev.* **67**, 259–279 (2015). doi: 10.1124/pr.114.009001; pmid: 25657351
30. M. L. Mayer, J. A. Sheridan, C. J. Blohmke, S. E. Turvey, R. E. Hancock, The Pseudomonas aeruginosa autoinducer 3O-C12 homoserine lactone provokes hyperinflammatory responses from cystic fibrosis airway epithelial cells. *PLOS ONE* **6**, e16246 (2011). doi: 10.1371/journal.pone.0016246; pmid: 21305014
31. R. S. Smith *et al.*, IL-8 production in human lung fibroblasts and epithelial cells activated by the Pseudomonas autoinducer N-3-oxododecanoyl homoserine lactone is transcriptionally regulated by NF-κB and activator protein-2. *J. Immunol.* **167**, 366–374 (2001). doi: 10.4049/jimmunol.167.1.366; pmid: 11418672
32. P. Ramadoss, G. H. Perdew, Use of 2-azido-3-[^{125}I]iodo-7,8-dibromodibenzo-*p*-dioxin as a probe to determine the relative ligand affinity of human versus mouse aryl hydrocarbon receptor in cultured cells. *Mol. Pharmacol.* **66**, 129–136 (2004). doi: 10.1124/mol.66.1.129; pmid: 15213304
33. A. Planchart *et al.*, Advancing toxicology research using in vivo high throughput toxicology with small fish models. *ALTEX* **33**, 435–452 (2016). pmid: 27328013
34. S. A. Renshaw, N. S. Trede, A model 450 million years in the making: Zebrafish and vertebrate immunity. *Dis. Model. Mech.* **5**, 38–47 (2012). doi: 10.1242/dmm.007138; pmid: 22228790
35. A. H. Meijer, H. P. Spaink, Host-pathogen interactions made transparent with the zebrafish model. *Curr. Drug Targets* **12**, 1000–1017 (2011). doi: 10.2174/138945011795677809; pmid: 21366518
36. T. C. King-Heiden *et al.*, Reproductive and developmental toxicity of dioxin in fish. *Mol. Cell. Endocrinol.* **354**, 121–138 (2012). doi: 10.1016/j.mce.2011.09.027; pmid: 21958697
37. J. J. van Soest *et al.*, Comparison of static immersion and intravenous injection systems for exposure of zebrafish embryos to the natural pathogen Edwardsiella tarda. *BMC Immunol.* **12**, 58 (2011). doi: 10.1186/1471-2172-12-58; pmid: 22003892
38. F. Díaz-Pascual, J. Ortíz-Severín, M. A. Varas, M. L. Allende, F. P. Chávez, *In vivo* Host-Pathogen Interaction as Revealed by Global Proteomic Profiling of Zebrafish Larvae. *Front. Cell. Infect. Microbiol.* **7**, 334 (2017). doi: 10.3389/fcimb.2017.00334; pmid: 28791256
39. B. Zhao, D. E. Degroot, A. Hayashi, G. He, M. S. Denison, CH223191 is a ligand-selective antagonist of the Ah (Dioxin) receptor. *Toxicol. Sci.* **117**, 393–403 (2010). doi: 10.1093/toxsci/kfq217; pmid: 20634293
40. M. E. Jönsson, A. Kubota, A. R. Timme-Laragy, B. Woodin, J. J. Stegeman, Ahr2-dependence of PCB126 effects on the swim bladder in relation to expression of CYP1 and cox-2 genes in developing zebrafish. *Toxicol. Appl. Pharmacol.* **265**, 166–174 (2012). doi: 10.1016/j.taap.2012.09.023; pmid: 23036320
41. M. T. Cabeen, Stationary phase-specific virulence factor overproduction by a lasR mutant of Pseudomonas aeruginosa. *PLOS ONE* **9**, e88743 (2014). doi: 10.1371/journal.pone.0088743; pmid: 24533146
42. P. K. Mandal, Dioxin: A review of its environmental effects and its aryl hydrocarbon receptor biology. *J. Comp. Physiol. B* **175**, 221–230 (2005). doi: 10.1007/s00360-005-0483-3; pmid: 15900503
43. I. Ramos, L. E. Dietrich, A. Price-Whelan, D. K. Newman, Phenazines affect biofilm formation by Pseudomonas aeruginosa in similar ways at various scales. *Res. Microbiol.* **161**, 187–191 (2010). doi: 10.1016/j.resmic.2010.01.003; pmid: 20123017
44. L. K. Nelson, G. H. D'Amours, K. M. Sproule-Willoughby, D. W. Morck, H. Ceri, Pseudomonas aeruginosa las and rhl quorum-sensing systems are important for infection and inflammation in a rat prostatitis model. *Microbiology* **155**, 2612–2619 (2009). doi: 10.1099/mic.0.028464-0; pmid: 19460822
45. J. Klockgether *et al.*, Genome diversity of Pseudomonas aeruginosa PAO1 laboratory strains. *J. Bacteriol.* **192**, 1113–1121 (2010). doi: 10.1128/JB.01515-09; pmid: 20023018

46. L. Wiehlmann *et al*., Population structure of Pseudomonas aeruginosa. *Proc. Natl. Acad. Sci. U.S.A.* **104**, 8101–8106 (2007). doi: 10.1073/pnas.0609213104; pmid: 17468398
47. C. E. Chandler *et al*., Genomic and Phenotypic Diversity among Ten Laboratory Isolates of *Pseudomonas aeruginosa* PAO1. *J. Bacteriol.* **201**, e00595-18 (2019). doi: 10.1128/JB.00595-18; pmid: 30530517
48. S. Chugani *et al*., Strain-dependent diversity in the Pseudomonas aeruginosa quorum-sensing regulon. *Proc. Natl. Acad. Sci. U.S.A.* **109**, E2823–E2831 (2012). doi: 10.1073/pnas.1214128109; pmid: 22988113
49. T. Karlsson, M. V. Turkina, O. Yakymenko, K. E. Magnusson, E. Vikström, The Pseudomonas aeruginosa N-acylhomoserine lactone quorum sensing molecules target IQGAP1 and modulate epithelial cell migration. *PLOS Pathog.* **8**, e1002953 (2012). doi: 10.1371/journal.ppat.1002953; pmid: 23071436
50. A. Jahoor *et al*., Peroxisome proliferator-activated receptors mediate host cell proinflammatory responses to Pseudomonas aeruginosa autoinducer. *J. Bacteriol.* **190**, 4408–4415 (2008). doi: 10.1128/JB.01444-07; pmid: 18178738
51. V. V. Kravchenko *et al*., Modulation of gene expression via disruption of NF-κB signaling by a bacterial small molecule. *Science* **321**, 259–263 (2008). doi: 10.1126/science.1156499; pmid: 18566250
52. K. Kim *et al*., HHQ and PQS, two Pseudomonas aeruginosa quorum-sensing molecules, down-regulate the innate immune responses through the nuclear factor-κB pathway. *Immunology* **129**, 578–588 (2010). doi: 10.1111/j.1365-2567.2009.03160.x; pmid: 20102415
53. A. S. Ismail, J. S. Valastyan, B. L. Bassler, A Host-Produced Autoinducer-2 Mimic Activates Bacterial Quorum Sensing. *Cell Host Microbe* **19**, 470–480 (2016). doi: 10.1016/j.chom.2016.02.020; pmid: 26996306

ACKNOWLEDGMENTS

We thank B. Stockinger (Francis Crick Institute) for the *AhR*$^{-/-}$ mice; C. Grabher (Karlsruhe Institute of Technology) and D. Panakova (Max Delbruck Center) for the zebrafish AB WT strain; L. Leoni (University Roma Tre) for *P. aeruginosa* strains PA14 Δ*rsaL* and PA14-R3; B. Tuemmler (Medizinische Hochschule Hannover) for PA14 WT and PA14 09480; F. Ausubel (Harvard Medical School/Massachusetts General Hospital) for PA14-GFP; P. Williams (University of Nottingham) for PAO1 WT, PAO1 *pqsA*, and CTX-lux::*pqsA*; U. Klemm for mouse breedings; N. Fielko, J. Otto, A. Fadeev (Max Planck Institute for Infection Biology), and M. Simões (Max Delbruck Center) for zebrafish breedings; and A. Diehl (Leibniz-Institut für Molekulare Pharmakologie) for technical help to prepare mouse liver lysates. Special thanks to A. Meijer and V. Torraca (University of Leiden) for support in setting up a zebrafish facility, zebrafish handling, and experimental design. **Funding:** Supported by the European Research Council under the Horizon 2020 program of the European Commission, grant 311371 (A.S. and M.K.B.), the Helmholtz BioInterfaces in Technology and Medicine (BIFTM) program of Karlsruhe Institute of Technology (F.K. and G.B.W.), and the Max Planck Society. **Author contributions:** P.M.-A. and S.H.E.K. conceived and designed the study and wrote the manuscript; P.M.-A. designed and performed experiments and data analysis; A.P., G.P., U.G., and M.K. provided technical help for in vitro and in vivo experiments; A.D., P.S., and C.P. performed mouse infection experiments; L.L. performed and analyzed Fluidigm experiments; M.K.B., A.S., and J.F. performed binding studies; R.H., F.K., and G.B.W. performed and analyzed HPLC experiments; A.K., J.P., G.K., and H.O. performed virtual docking studies; and H.J.M. and J.W. performed and analyzed microarray experiments. All authors commented on the paper. **Competing interests:** Authors declare no competing interests. **Data and materials availability:** All data are available in the main text or the supplementary materials. Data are deposited in GEO under accession number GSE121101.

SUPPLEMENTARY MATERIALS

science.sciencemag.org/content/366/6472/eaaw1629/suppl/DC1
Materials and Methods
Figs. S1 to S11
Tables S1 to S11
References (*54*–*85*)

View/request a protocol for this paper from *Bio-protocol*.

23 November 2018; resubmitted 25 July 2019
Accepted 13 November 2019
10.1126/science.aaw1629

RESEARCH ARTICLE

CANCER

Adaptive mutability of colorectal cancers in response to targeted therapies

Mariangela Russo[1,2]*, Giovanni Crisafulli[1,2], Alberto Sogari[1,2], Nicole M. Reilly[3], Sabrina Arena[1,2], Simona Lamba[1], Alice Bartolini[1], Vito Amodio[1,2], Alessandro Magrì[1,2], Luca Novara[1], Ivana Sarotto[1], Zachary D. Nagel[4], Cortt G. Piett[4], Alessio Amatu[5,6], Andrea Sartore-Bianchi[5,6], Salvatore Siena[5,6], Andrea Bertotti[1,2], Livio Trusolino[1,2], Mattia Corigliano[7,8], Marco Gherardi[7,8], Marco Cosentino Lagomarsino[7,8], Federica Di Nicolantonio[1,2], Alberto Bardelli[1,2]*

The emergence of drug resistance limits the efficacy of targeted therapies in human tumors. The prevalent view is that resistance is a fait accompli: when treatment is initiated, cancers already contain drug-resistant mutant cells. Bacteria exposed to antibiotics transiently increase their mutation rates (adaptive mutability), thus improving the likelihood of survival. We investigated whether human colorectal cancer (CRC) cells likewise exploit adaptive mutability to evade therapeutic pressure. We found that epidermal growth factor receptor (EGFR)/BRAF inhibition down-regulates mismatch repair (MMR) and homologous recombination DNA-repair genes and concomitantly up-regulates error-prone polymerases in drug-tolerant (persister) cells. MMR proteins were also down-regulated in patient-derived xenografts and tumor specimens during therapy. EGFR/BRAF inhibition induced DNA damage, increased mutability, and triggered microsatellite instability. Thus, like unicellular organisms, tumor cells evade therapeutic pressures by enhancing mutability.

More than 75 years ago, Luria and Delbrück demonstrated that bacterial resistance to phage viruses was due to random mutations that spontaneously occurred in the absence of selection (*1*). Resistance to targeted therapies in human tumors is also widely thought to be due to mutations that exist before treatment (*2*). The conventional view is that relapses occur because drug-resistant mutant subclones are present in any detectable metastatic lesion before the initiation of therapy. According to this view, resistance is a fait accompli, and the time to recurrence is merely the interval required for preexisting drug-resistant (mutant) cells to repopulate the lesion (*3*).

Here, we explore the hypothesis that resistance to targeted therapies can also be fostered by a transient increase in genomic instability during treatment, leading to de novo mutagenesis. A similar process has been shown to increase the emergence of microbial strains resistant to antibiotics (*4*, *5*). In a stable microenvironment, the mutation rate of microorganisms is usually low, which precludes the accumulation of deleterious mutations. However, several mechanisms of stress-induced genetic instability and increased mutability, known as stress-induced mutagenesis (SIM), have been described in bacteria and yeast (*6*–*12*).

Bacterial persister cells can survive lethal stress conditions imposed by antibiotics through a reduction in growth rate. A subsequent reduction in the efficiency of DNA mismatch repair (MMR) (*4*, *9*, *13*) and a shift to error-prone DNA polymerases increases the rate at which adaptive mutations occur in the surviving population (*4*, *9*, *14*, *15*). Selection then allows the growth of mutant subpopulations capable of replicating under stressful conditions. Once the stressed population has adapted to the new conditions, the hypermutator status is counterselected to avoid the accumulation of deleterious mutations and to prevent the continuous increase of mutational load (*9*, *16*–*20*). Together, these processes boost genetic diversity, foster adaptability to new microenvironments, and contribute to the development of resistance (*9*, *12*, *18*, *19*).

In the setting of cancer, the emergence of a drug-tolerant persister population is often observed when oncogene-dependent tumor cells are challenged with targeted agents (*21*). Persister cancer cells survive exposure to targeted therapies through poorly understood mechanisms (*21*) and represent a reservoir from which genetically divergent, drug-resistant derivatives eventually emerge (*22*, *23*). Recent work showed that drug-resistant mutant cancer cells can originate not only from rare, preexisting mutant clones, but also from drug-tolerant subpopulations (*24*). The probability that the latter resistance mechanism occurs would be greatly increased if the genetic diversity of tumor cells were enhanced during treatment. Accordingly, we hypothesized that during the persister state, tumor cells, like unicellular organisms, alter DNA-repair and DNA-replication mechanisms to enhance adaptive mutability.

Targeted therapy–induced down-regulation of MMR and HR proficiency of CRC cells

To test our hypothesis, we studied the response of microsatellite-stable (MSS) human colorectal cancer (CRC) cell lines to the anti-EGFR (epidermal growth factor receptor) antibody cetuximab, which is approved, together with panitumumab, for the treatment of patients with metastatic CRC whose tumors lack *RAS* and *BRAF* mutations (*25*), or with the BRAF inhibitor dabrafenib (DAB) as combinatorial treatment, which has shown promising activity in patients with CRC harboring *BRAF* mutations (*26*). We selected human CRC cell lines that are *RAS* and *BRAF* wild-type and sensitive to EGFR blockade (DiFi cells, fig. S1A) or that carry the oncogenic *BRAF* p.V600E mutation and are sensitive to concomitant EGFR and BRAF inhibition (WiDr cells, fig. S1A). Treatment with targeted agents led to G_1 cell-cycle arrest (fig. S1B). However, a small number of drug-tolerant persister cells survived several weeks after treatment initiation (fig. S1, C and D). Indeed, when drug pressure was removed, these cells rapidly resumed growth and again showed sensitivity to targeted therapy, thus demonstrating that persisters are only transiently and reversibly resistant to the treatment (fig. S1, E and F). By contrast, prolonged treatment led to the generation of permanently resistant cells, which did not reacquire sensitivity after the removal of drug pressure (fig. S1, E and F).

We next assessed whether CRC cells modulate the expression of DNA-repair genes upon drug treatment. Transcriptional profiles revealed decreased expression of the MMR genes *MLH1*, *MSH2*, and *MSH6*, as well as of homologous recombination (HR) effectors such as *BRCA2* and *RAD51* (Fig. 1A and fig. S1, G and H). Expression of *EXO1*, a gene coding for an exonuclease that participates in mismatch and double-strand break (DSB) repair, was also affected (Fig. 1A and fig. S1, G and H). A time-dependent down-regulation of MMR and HR proteins was also observed (Fig. 1B and fig. S2, A and B). Comparable results were obtained in another cetuximab-sensitive human CRC cell line, NCIH508 (fig. S3, A to C), and in

[1]Candiolo Cancer Institute, FPO–IRCCS, Candiolo (TO) 10060, Italy. [2]Department of Oncology, University of Torino, Candiolo (TO) 10060, Italy. [3]Fondazione Piemontese per la Ricerca sul Cancro ONLUS, Candiolo (TO) 10060, Italy. [4]Department of Environmental Health, JBL Center for Radiation Sciences, Harvard T.H. Chan School of Public Health, Boston, MA 02115, USA. [5]Niguarda Cancer Center, Grande Ospedale Metropolitano Niguarda, 20162 Milan, Italy. [6]Department of Oncology and Hemato-Oncology, Università degli Studi di Milano, 20133 Milan, Italy. [7]IFOM-FIRC Institute of Molecular Oncology, 20139 Milan, Italy. [8]Department of Physics, Università degli Studi di Milano, and I.N.F.N., 20133 Milan, Italy.
*Corresponding author. Email: alberto.bardelli@unito.it (A.B.); mariangela.russo@unito.it (M.R.)

BRAF-mutant HT29 cells that were derived from the same patient from whom the WiDr cell line originated (fig. S3, D and E). Furthermore, we confirmed that down-regulation or loss of DNA-repair components is maintained in persister cells (fig. S4, A to D). Therapy-induced modulation of DNA-repair gene expression was transient and expression levels returned to normal upon removal of treatment (fig. S5A). Cancer cells that had previously developed permanent resistance to targeted agents did not modulate the expression of DNA-repair genes in response to drugs (fig. S5, B and C).

To ascertain whether targeted therapies affect DNA-repair competence in CRC cells, we used fluorescence-based multiplex host-cell reactivation (FM-HCR) assays (*27*). CRC cells were transfected with a G:G mismatch-containing plasmid to determine the impact of drug treatment on MMR capacity. An MMR-deficient (MMRd) human CRC cell line (LIM1215) was used as a positive control for MMR loss. We found that in CRC cells treated with targeted agents, MMR proficiency (MMRp) was significantly reduced (Fig. 1C and fig. S6A).

We next evaluated cellular HR capability by using the two-step, plasmid-based pDRGFP/pCBASce-I assay (*28*). Upon stable expression of the pDRGFP plasmid, we measured the generation of a green fluorescent signal upon DSBs induced by Sce-I expression. This assay showed that both DiFi and WiDr cells had a marked reduction in HR proficiency upon treatment with targeted therapies (Fig. 1D and fig. S6B).

MMR proteins are down-regulated in samples of CRC residual disease after targeted treatment

To determine whether the cell-based findings extend to patient-derived tumor samples, we exploited our CRC biobank of molecularly and therapeutically annotated patient-derived xenograft (PDX) models (*29*, *30*). We selected six MSS PDX models with wild-type *KRAS*, *NRAS*, and *BRAF* in which EGFR inhibition by cetuximab led to tumor regression to a variable extent, paralleling the clinical scenario (Fig. 2A). Immunohistochemistry analysis unveiled areas with down-regulation of MLH1 and/or MSH2 in all neoplastic samples obtained when tumors were at the point of maximum response to cetuximab but still contained residual persisters (Fig. 2, B and C, and fig. S7, A to D), as compared with placebo-treated controls.

We next investigated whether down-regulation of DNA-repair proteins also occurs in clinical specimens from two CRC patients who achieved an objective partial response upon treatment with FOLFOX (folinic acid, 5-fluorouracil, and oxaliplatin) plus panitumumab. In both instances, tumor specimens were longitudinally collected at diagnosis and at maximal therapeutic response, when a limited number of tumor cells persist despite treatment. MLH1 and MSH2 were down-regulated in tumor samples obtained at response compared with pretreatment specimens, confirming the clinical relevance of our findings (Fig. 2D).

Induction of DNA damage and error-prone DNA polymerases in CRC cells treated with targeted therapies

In addition to reduced DNA-repair ability, we found that targeted therapies triggered a switch from high-fidelity to low-fidelity DNA polymerases. DNA polymerases usually

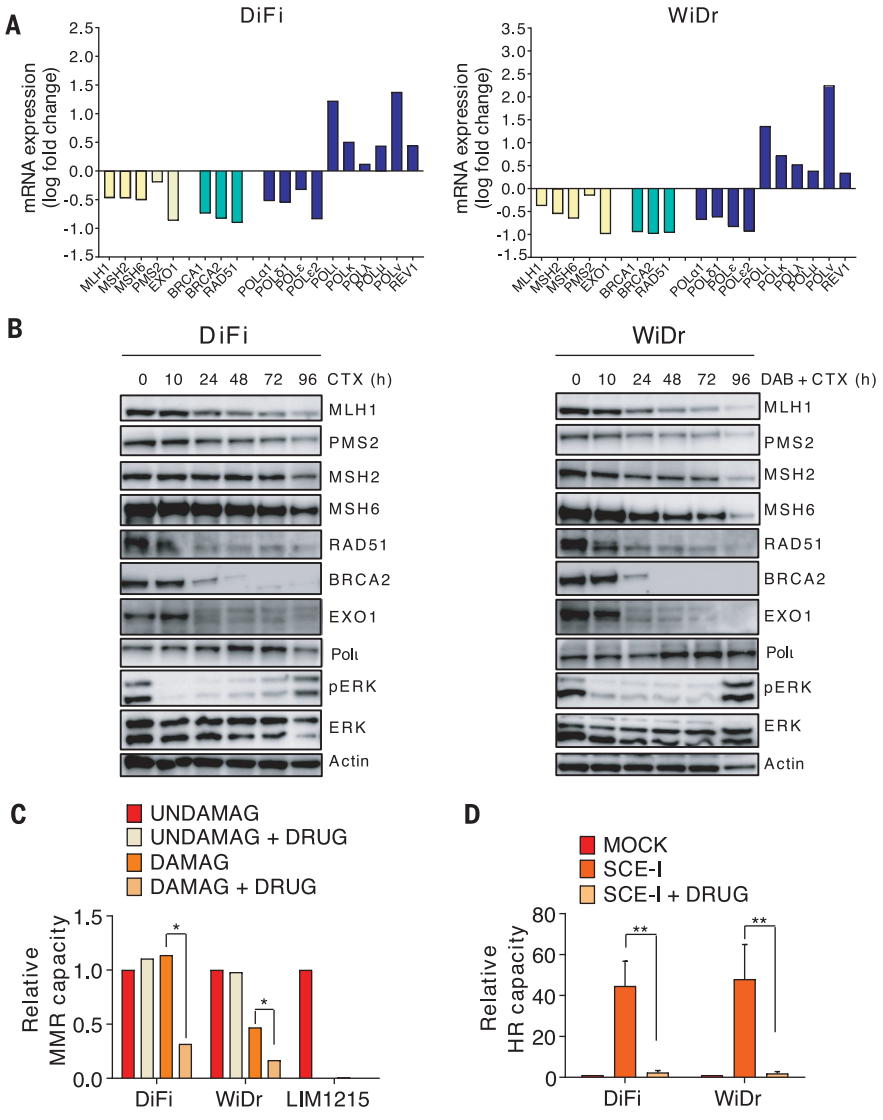

Fig. 1. CRC cells modulate DNA-repair effectors in response to targeted agents. (**A**) CRC cells were treated with cetuximab alone (DiFi) or in combination with the BRAF inhibitor DAB (WiDr) for 96 hours and RNA-sequencing analysis was performed. MMR (yellow), HR (green), and DNA polymerase (blue) genes are reported. Results represent means of two independent experiments. (**B**) CRC cells were treated and analyzed at the indicated time points by Western blot. CTX, cetuximab; pERK, phosphorylated extracellular signal–regulated kinase. (**C**) CRC cells were transfected with G:C undamaged (UNDAMAG) plasmid or with G:G mismatch-damaged (DAMAG) plasmid. Where indicated (DRUG), cells were treated with targeted therapies for 50-60 hours and analyzed by flow cytometry. A mock transfection was used as a control. Quantification of MMR capacity of each cell line relative to control is reported in the bar graph. LIM1215, MMR-deficient CRC cells, were used as a positive control for MMR loss. Results represent means of two independent experiments. *$p < 0.05$ (Student's t test). (**D**) pDRGFP-stably expressing CRC cells were transfected with the pCBASce-I plasmid and then either left in the absence of drug or treated with targeted therapies for 50-60 hours and analyzed by flow cytometry. A mock transfection was used as a control. Quantification of HR capacity of each cell line relative to mock is reported in the bar graph. Results represent means ± SD ($n = 3$). **$p < 0.01$ (Student's t test).

involved in accurate DNA replication, such as POLδ and POLε, were down-regulated, whereas DNA polymerases characterized by poor accuracy, low processivity, and absence of proofreading capacity (i.e., error-prone polymerases) were induced (Fig. 1A and fig. S4A). These included Polι, Polκ, and Rev1 (which belong to the Y family of polymerases, orthologous to the bacterial stress–induced polymerases Pol IV and Pol V), as well as Polλ and Polμ (*31*) (Fig. 1, A and B, and figs. S1, G and H; S2B; S3, B to C and E; and S4, A and D). Error-prone polymerases replace canonical high-fidelity polymerases that stall when encountering a DNA lesion and facilitate DNA replication across DNA damage sites in a manner that introduces errors into the genome (*15*, *16*, *20*); this may lead to base

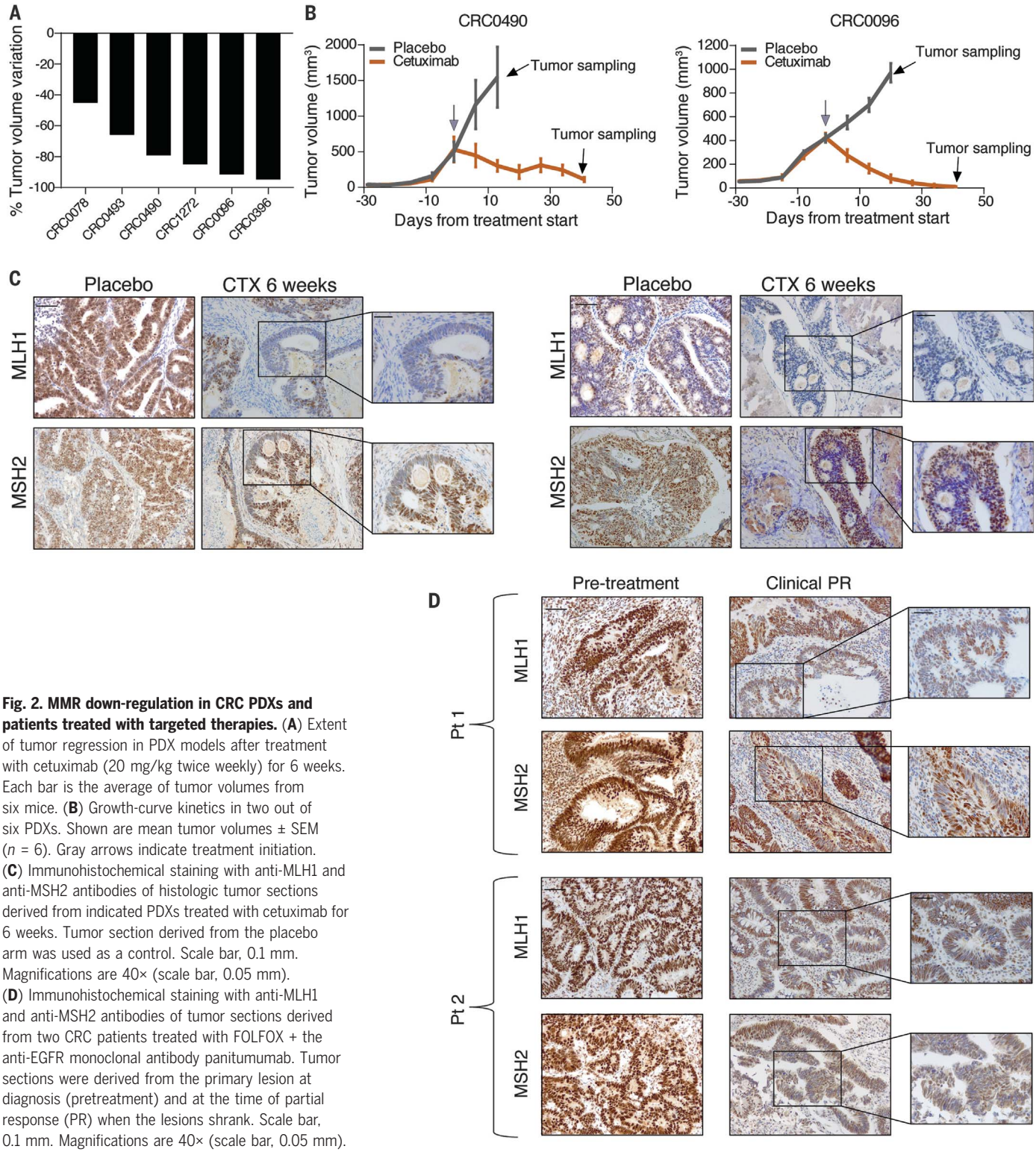

Fig. 2. MMR down-regulation in CRC PDXs and patients treated with targeted therapies. (**A**) Extent of tumor regression in PDX models after treatment with cetuximab (20 mg/kg twice weekly) for 6 weeks. Each bar is the average of tumor volumes from six mice. (**B**) Growth-curve kinetics in two out of six PDXs. Shown are mean tumor volumes ± SEM (n = 6). Gray arrows indicate treatment initiation. (**C**) Immunohistochemical staining with anti-MLH1 and anti-MSH2 antibodies of histologic tumor sections derived from indicated PDXs treated with cetuximab for 6 weeks. Tumor section derived from the placebo arm was used as a control. Scale bar, 0.1 mm. Magnifications are 40× (scale bar, 0.05 mm). (**D**) Immunohistochemical staining with anti-MLH1 and anti-MSH2 antibodies of tumor sections derived from two CRC patients treated with FOLFOX + the anti-EGFR monoclonal antibody panitumumab. Tumor sections were derived from the primary lesion at diagnosis (pretreatment) and at the time of partial response (PR) when the lesions shrank. Scale bar, 0.1 mm. Magnifications are 40× (scale bar, 0.05 mm).

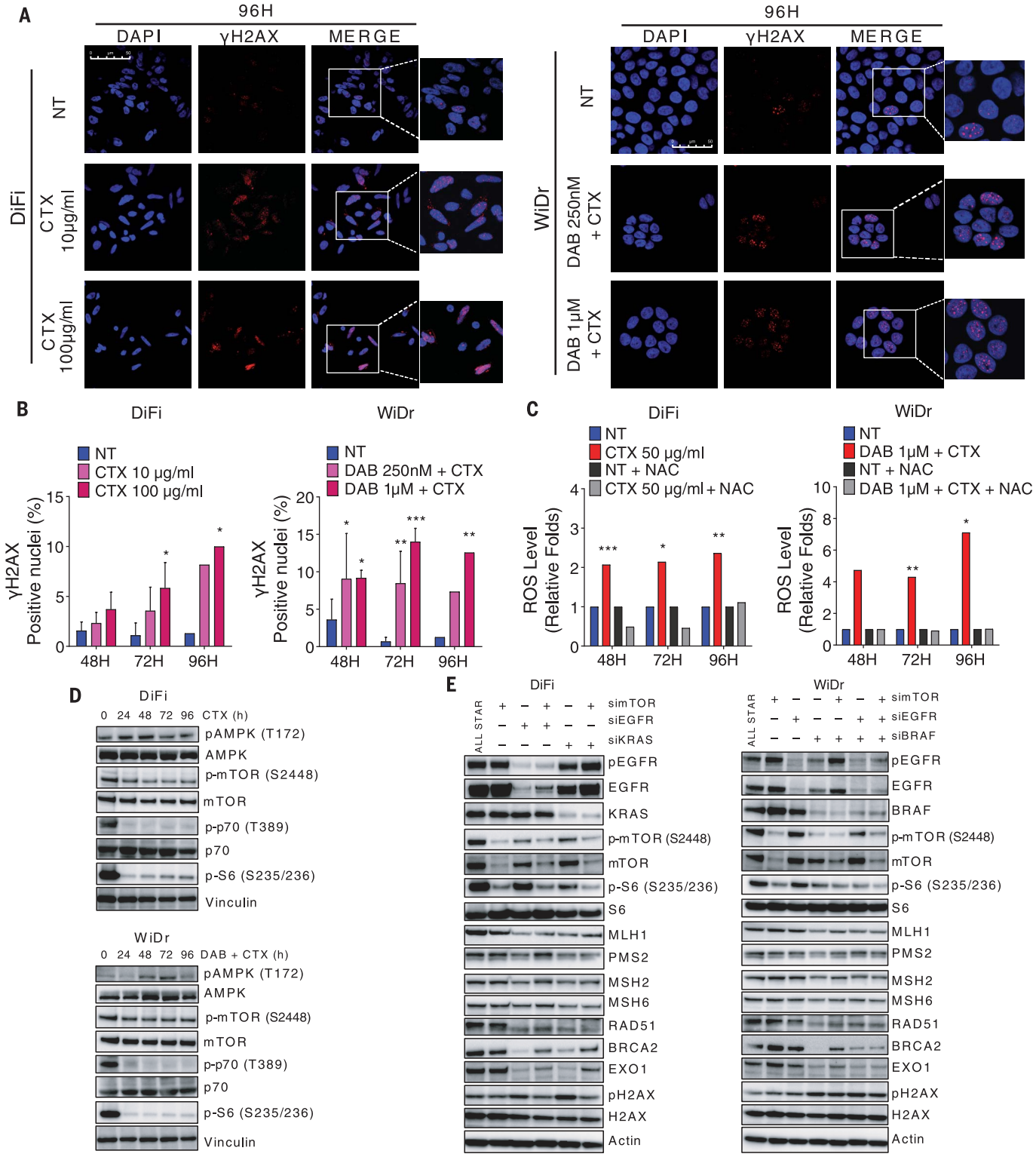

Fig. 3. Targeted therapies trigger a stress response, increase ROS levels, and induce DNA damage in CRC cells. (**A**) CRC cells were treated as reported and fixed and stained with anti-γH2AX antibody at the indicated time points. Vehicle-treated cells (NT) were used as controls. Nuclei are stained with DAPI (blue) and anti-γH2AX antibody (red). Scale bar, 50 μm. Representative images for each condition are shown. (**B**) Quantification of nuclear γH2AX foci in DiFi (left panel) and WiDr (right panel) cells. Results represent means ± SD (n = 3 for 48 and 72 hours; n = 2 for 96 hours). *p < 0.05; **p < 0.01; ***p < 0.001 (two-way ANOVA). (**C**) CRC cells were treated as indicated and ROS levels were measured. NAC was used as a control to rescue ROS production. Results represent means of two independent experiments. *p < 0.05; **p < 0.01; ***p < 0.001 (Student's t test). (**D**) CRC cells were treated with targeted therapies and analyzed by Western blot at the indicated time points. pAMPK, phosphorylated adenosine monophosphate kinase. (**E**) Wild-type DiFi (left panel) and *BRAF*-mutated WiDr (right panel) cells were transfected with the indicated siRNA or combination of siRNAs for 72 hours and analyzed by Western blot. ALL STAR, nontargeting siRNA.

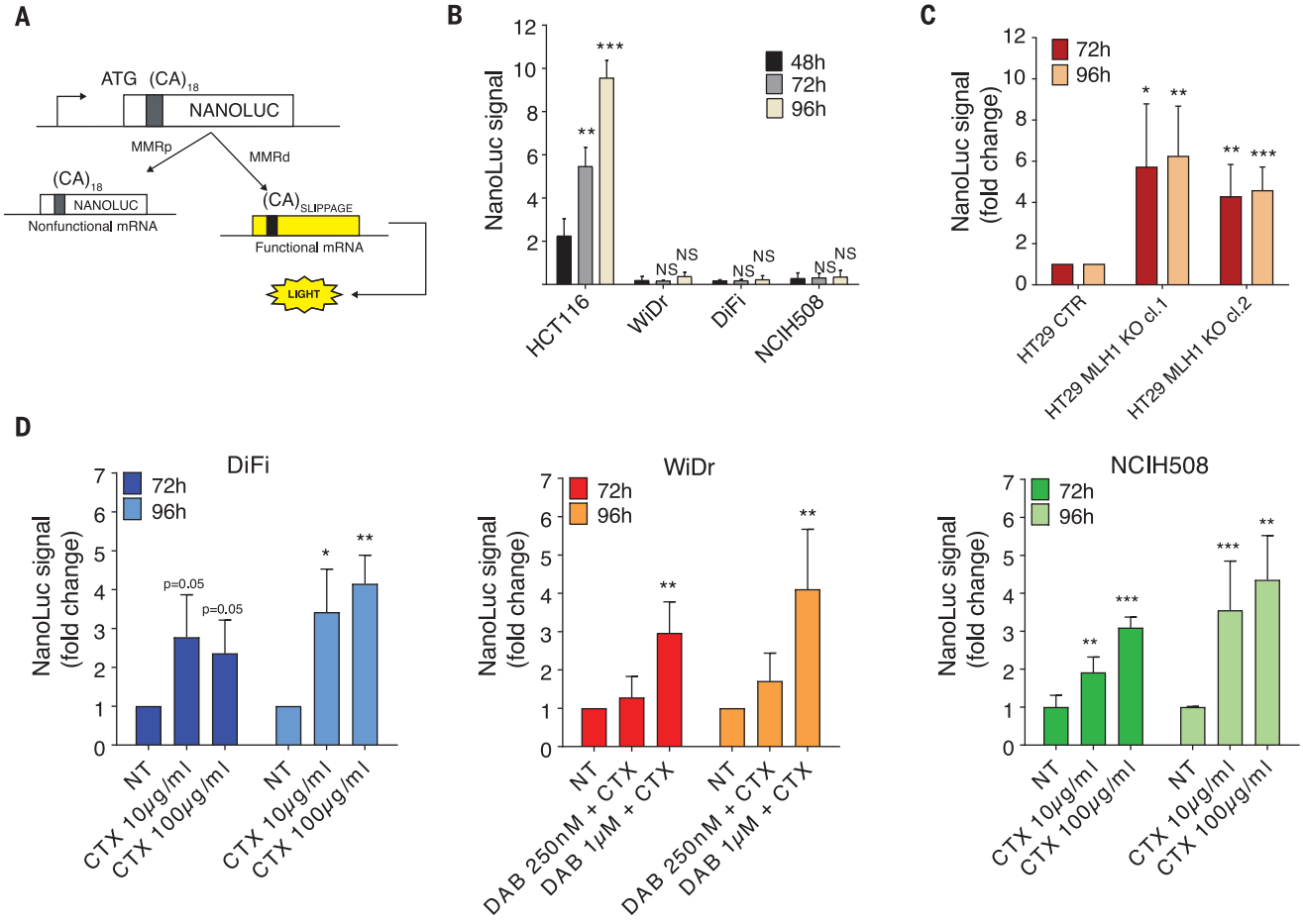

Fig. 4. Treatment with targeted therapies promotes mutagenesis in CRC cells. (**A**) Schematic representation of the CA-NanoLuc reporter assay. (**B**) MMRd HCT116 and MMRp DiFi, WiDr, and NCIH508 CRC cells were transduced with the NanoLuc lentivirus. At the indicated time points, NanoLuc signal was evaluated and normalized to cell viability. Results represent means ± SD (n = 3). $^{**}p < 0.01$; $^{***}p < 0.001$ (Student's t test). NS, not a statistically significant difference. (**C**) NanoLuc signal in HT29 *MLH1*-KO clones (cl. 1 and cl. 2). NanoLuc signal was evaluated after 72 and 96 hours of growth in standard conditions and normalized to cell viability. NanoLuc signal from *MLH1* KO clones was then compared with signal detected in *MLH1* wild-type cells (CTR). Results represent means ± SD (n = 4). $^{*}p < 0.05$; $^{**}p < 0.01$; $^{***}p < 0.001$ (Student's t test). (**D**) DiFi, WiDr, and NCIH508 CRC cells were treated as indicated. NanoLuc signal was normalized to cell viability. NanoLuc signal from treated cells was then compared with signal detected in untreated (NT) cells. Results represent means ± SD (n = 3). $^{*}p < 0.05$; $^{**}p < 0.01$; $^{***}p < 0.001$ (Student's t test).

mispairings, incorporation of aberrant DNA primer ends, and increased mutagenesis rate (*32*, *33*).

We therefore investigated whether treatment with targeted therapies leads to genomic damage in cancer cells and if error-prone–mediated repair of DNA damage is favored when CRC cells encounter the hostile environment imposed by targeted therapies. Indeed, quantification of phosphorylation of H2AX at Ser^{139} (γH2AX), a common marker of DNA damage (*34*), revealed a dose- and time-dependent increase in the number of foci-positive nuclei upon drug treatment (Fig. 3, A and B, and fig. S8, A and B), whereas no further increase was observed in permanently resistant cells upon drug treatment (fig. S8, C and D). In addition, we observed a dose- and time-dependent increase in the number of 53BP1-positive nuclei upon EGFR and BRAF blockade (fig. S9, A and B). In direct opposition to BRCA1, 53BP1 promotes nonhomologous end joining–mediated DSB repair while preventing HR through restriction of end resection (*35*). These data suggest that targeted therapies trigger a switch from high-fidelity to error-prone–mediated repair of DNA damage, thereby potentially increasing the occurrence of mutations conferring drug resistance.

We next explored the possible causes of the DNA damage observed upon the administration of targeted therapies. Although several chemotherapeutic agents directly generate DNA damage, drugs interfering with oncogenic signaling (such as EGFR or BRAF inhibitors) are not directly genotoxic. However, it has been shown that certain targeted therapies, such as ABL and BRAF inhibitors, increase the levels of reactive oxygen species (ROS) in cancer cells (*36*, *37*), potentially contributing to DNA damage during treatment. ROS levels significantly increased when CRC cells were exposed to EGFR and BRAF inhibitors (Fig. 3C). By contrast, ROS levels were not increased in permanently drug-resistant (adapted) cells upon drug treatment (fig. S9C).

The drug-induced increase in ROS levels was abrogated when targeted therapies were administered in the presence of the antioxidant *N*-acetyl-L-cysteine (NAC) (Fig. 3C). NAC administration partially reduced the number of γH2AX foci-positive nuclei upon EGFR and BRAF blockade (fig. S10, A and B). However, cotreatment with NAC did not prevent or rescue down-regulation of DNA-repair genes (fig. S10C). The addition of NAC delayed onset of relapse to targeted therapies when administered

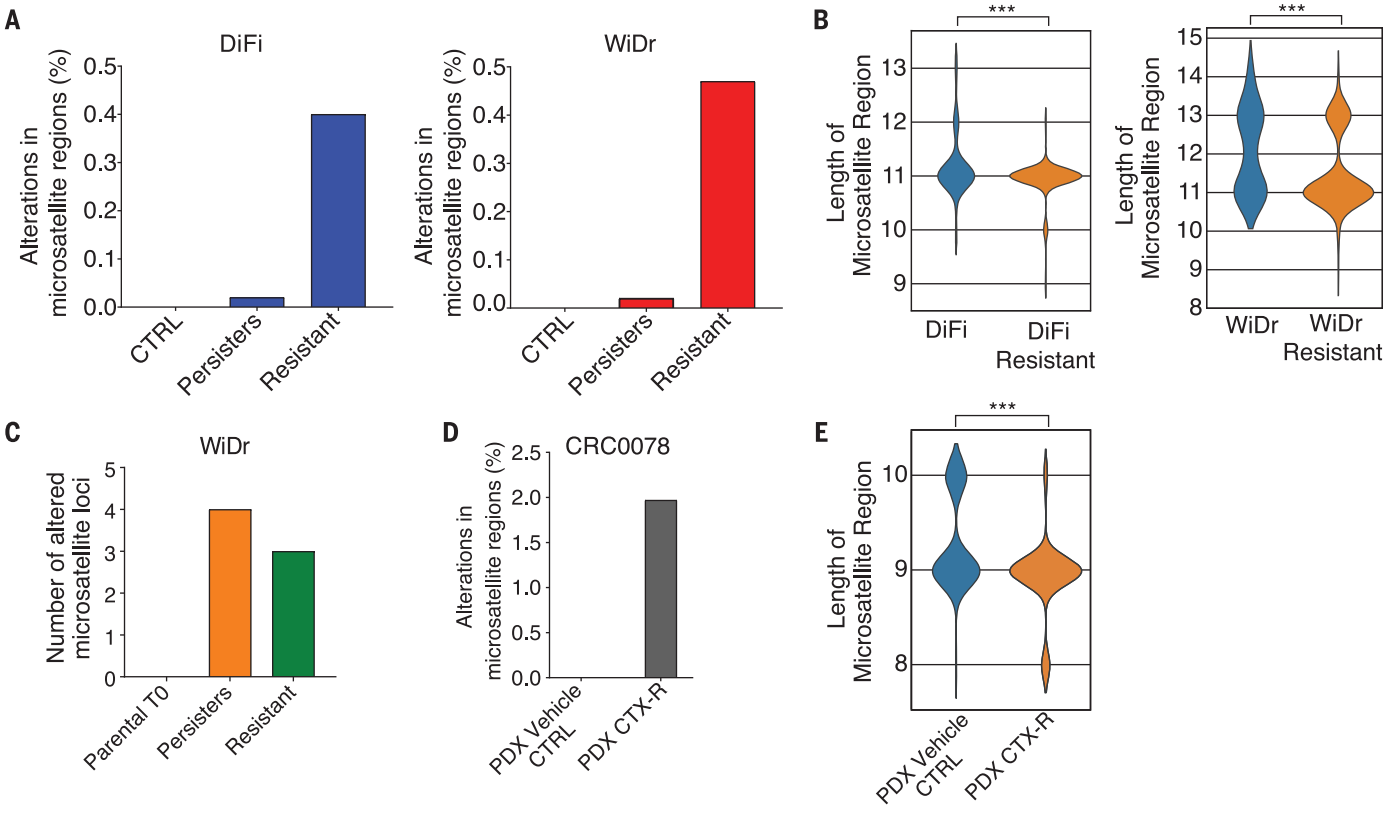

Fig. 5. Adaptive mutability leads to genetic instability in CRC cells in response to therapy-induced stress. (**A**) Percentage of unstable microsatellite regions in DiFi and WiDr persister and resistant cells compared with their parental counterpart (CTRL). (**B**) Length distribution of one representative microsatellite region for drug-resistant DiFi and WiDr cell lines. ***$p < 0.001$ (χ^2 test). (**C**) Number of unstable microsatellite sites detected by NGS-based high-depth capture panel in WiDr cells (parental) treated with cetuximab + DAB for 14 days (persisters) and at resistance. (**D**) DNA was collected from one vehicle-treated and one cetuximab-resistant PDX. Percentage of unstable microsatellite regions of the tumor collected from the cetuximab-resistant mouse (PDX CTX-R) compared with the vehicle-treated (CTRL) mouse is reported. (**E**) Length distribution of one representative microsatellite region. ***$p < 0.001$ (χ^2 test).

together with mitogen-activated protein kinase (MAPK) pathway inhibitors (fig. S10, D and E) (*38*, *39*).

Interfering with oncogenic dependencies initiates a stress response in CRCs

To elucidate the mechanistic basis of therapy-induced mutagenesis in cancer cells, we tested whether the adaptive mutability that we observed in response to targeted therapies was simply a secondary response to G_1 cell-cycle arrest or DNA damage or if it represented an active stress response. We found that thymidine-mediated cell-cycle stress (fig. S11, A to C) or direct DNA damage with the alkylating agent oxaliplatin (fig. S11, D to F) instead promoted the up-regulation of the MMR- and HR-repair systems (fig. S11, C and F), and G_1 cell-cycle arrest by nutrient starvation did not lead to modulation of DNA-repair gene expression (fig. S11, G to I). In bacterial cells, both the DNA damage–activated SOS response and the general stress response appear to be required to induce adaptive mutagenesis (*14*). We therefore examined the modulation of the kinase mammalian target of rapamycin (mTOR), which is a master regulator of mammalian cellular stress response (*40*). Indeed, the mTOR effectors pS6K–p70K were down-regulated with kinetics comparable to that of MMR and HR regulation upon EGFR and BRAF pharmacological blockade (Fig. 3D). However, silencing of mTOR did not affect the expression of DNA-repair proteins or γH2AX (Fig. 3E). It is therefore plausible that down-regulation of mTOR contributes to stress-induced mutagenesis of cancer cells but is not sufficient to activate this phenotype.

The exquisite sensitivity of DiFi and WiDr cells to EGFR and BRAF blockade reflects cell-specific oncogenic alterations. The *EGFR* locus is amplified in DiFi cells (*2*); the WiDr cells carry the *BRAF* p.V600E oncogenic mutation, but they also become dependent on feedback activation of EGFR when treated with BRAF inhibitors (*41*). We therefore investigated whether interfering with the oncogenic dependency of cancer cells could directly initiate the drug-induced stress phenotype. Indeed, small interfering RNA (siRNA)–mediated knockdown of *EGFR* or *KRAS* in DiFi cells and of *BRAF* (±*EGFR*) in WiDr cells led to reduced expression of DNA-repair proteins, triggered DNA damage and mTOR down-regulation (Fig. 3E), and increased ROS levels (fig. S12). These results exclude the possibility that drug-induced down-regulation of DNA-repair pathways could be due to a nonspecific (off-target) effect of the anti-EGFR antibody cetuximab or the BRAF inhibitor dabrafenib.

Targeted therapies induce adaptive mutability in CRC cells

Next, we tested whether the stress response induced by targeted therapies translated into increased mutagenesis in CRC cells. We used a reporter assay in which a dinucleotide CA-repeat microsatellite drives the NanoLuc enzyme coding sequence out of frame (Fig. 4A). Random mutations that introduce frameshifts in this region, in the absence of a functional MMR, would restore the NanoLuc open reading frame, leading to bioluminescence. Analogous approaches have previously been used to measure MMR defects in cancer cells (*42*–*44*).

To validate the assay, we first introduced the CA-NanoLuc vector into a MMRd human CRC cell line (HCT116) and three MMRp human CRC cell lines (DiFi, WiDr, and NCIH508). The NanoLuc signal was significantly higher in MMRd cells after 48 hours of standard growth conditions (Fig. 4B). This difference was further increased when HCT116 cells were kept in culture for several days, whereas the signal in the MMRp lines remained low (Fig. 4B), indicating that the CA-NanoLuc assay effectively detects MMR deficiency in cancer cells.

We next used the CA-NanoLuc system to measure the impact of ectopic inactivation of MMR in CRC cells. To this end, we used CRISPR-CAS9 to inactivate the *MLH1* gene in the HT29 human CRC cell line. After the isolation of two independent *MLH1* knockout (KO) clones (fig. S13, A and B), they were transduced with the CA-NanoLuc vector. *MLH1* KO clones exhibited higher levels of NanoLuc signal as expected, confirming that the assay can detect inactivation of DNA MMR (Fig. 4C). Next, drug-dependent (transient) MMR down-regulation was evaluated. EGFR and BRAF inhibition led to time-dependent increases of bioluminescence (Fig. 4D), paralleling the down-regulation of DNA-repair effectors and the up-regulation of low-fidelity polymerases. We further found that permanently resistant derivatives no longer exhibited adaptive mutability in response to targeted therapies (fig. S14).

Genomic alterations in CRC cells upon treatment with targeted therapies

To determine whether molecular evidence of adaptive mutability was present in the genome of CRC cells treated with EGFR and BRAF inhibitors, we analyzed whole-exome sequencing (WES) data from DiFi and WiDr parental, persister, and drug-resistant derivative cells. The overall mutational burden (i.e., the number of mutations per megabase) of persisters and the drug-resistant cell population was only marginally affected (fig. S15, A and B). As a control, we assessed whether MMR permanent inactivation induced by *MLH1* KO affected the mutational burden of HT29 CRC cells and found that it was only marginally affected (fig. S16A).

Given these results, we changed our approach. Because treatment with targeted therapies led to a transient MMR-deficient phenotype, we reasoned that MMR status could be more easily detected by examining microsatellite regions, where DNA replication slippage errors occur frequently and are ineffectively repaired in the absence of MMR. Indeed, WES analysis unveiled alterations in microsatellite regions of HT29 in which the *MLH1* gene was genetically knocked out (fig. S16, B and C). We also detected increased genetic instability in the microsatellite regions of CRC cells made resistant to targeted agents (Fig. 5, A and B), as shown by a shift in the length of microsatellite regions, highlighting the impact of targeted therapies on the DNA-repair process and mutagenicity. To detect the occurrence of microsatellite alterations in nonclonal cell populations, we utilized a high-depth capture panel that detects hotspot somatic variants and shifts in the length of microsatellite regions. Indeed, such high-sensitivity analysis unveiled a significant shift in the length of microsatellite regions in both persister and drug-resistant cells (Fig. 5C and fig. S17).

We next assessed the impact of targeted therapies on the genomic landscape of PDXs by studying a PDX model (CRC0078) (Fig. 2A and fig. S7D) that was continuously treated with cetuximab until it developed resistance (fig. S18). WES analysis of the cetuximab-resistant tumor tissue revealed alterations in microsatellite genomic regions that were not present in the PDX tumor collected from the corresponding untreated mouse (Fig. 5, D and E). Overall, these results indicate that CRC cells and a CRC PDX model exposed to targeted therapies experience loss of replication fidelity in regions of nucleotide repeats.

Discussion

The development of resistance has emerged as a major limitation of targeted therapies directed against oncoproteins such as EGFR, BRAF, and ABL (*25*).

In this study, we tested the hypothesis that cancer cells treated with targeted therapies activate stress-induced mutagenic mechanisms. We found that persister (drug-tolerant) cancer cells that survive EGFR and/or BRAF inhibition exhibit DNA damage, down-regulate mismatch and HR repair proteins, switch from high-fidelity to error-prone–mediated repair of DNA damage, and transiently increase their mutagenic ability.

Stress-induced mutagenesis is a characteristic trait of unicellular organisms to transiently accelerate genetic diversity in a fraction of the population when encountering a hostile environment. (*16*). Indeed, we found that therapy-induced modulation of DNA repair in cancer cells is also transitory and reverts back once a mutational landscape able to restore the ability to grow in the presence of the drug is achieved. We postulate that in cells of multicellular organisms, stress-induced mutagenesis is not operational. However, in cancer cells that have lost tissue-imposed homeostasis—and in many ways operate like unicellular organisms—this ancestral program is still available and is unleashed by oncoprotein-targeted drugs. A similar process has also been observed in cancer cells undergoing hypoxia-driven stress (*7*, *45*, *46*).

The analysis of mutational signatures has emerged as a valuable tool with which to document the mutational processes operative in cells (*47*). In future studies, it will be interesting to establish whether specific mutational signatures emerge under targeted therapies. Resolving such processes, which we postulate occur transiently in small cell subpopulations, is likely to require extensive genomic comparisons of multiple clones and independent data points.

These results may have clinical implications. The knowledge that cancer cells under therapeutic stress down-regulate key effectors of the DNA-repair machinery, such as MMR and HR, exposes a vulnerability that could be clinically exploited. For example, it will be important to assess whether down-regulation of HR proteins confers sensitivity to poly-ADP-ribose polymerases (PARP) inhibitors as observed in HR-deficient cancers (*48*–*50*). Moreover, pharmacological or genetic interference could be deployed to curb the cellular mechanisms that initiate drug-driven adaptive mutagenesis with the goal of reducing the generation of new variants during treatment. This strategy could potentially increase and prolong the clinical efficacy of targeted therapies.

REFERENCES AND NOTES

1. S. E. Luria, M. Delbrück, *Genetics* **28**, 491–511 (1943).
2. S. Misale *et al.*, *Nature* **486**, 532–536 (2012).
3. L. A. Diaz Jr. *et al.*, *Nature* **486**, 537–540 (2012).
4. A. Gutierrez *et al.*, *Nat. Commun.* **4**, 1610 (2013).
5. H. Long *et al.*, *Proc. Natl. Acad. Sci. U.S.A.* **113**, E2498–E2505 (2016).
6. I. Bjedov *et al.*, *Science* **300**, 1404–1409 (2003).
7. D. M. Fitzgerald, P. J. Hastings, S. M. Rosenberg, *Annu. Rev. Cancer Biol.* **1**, 119–140 (2017).
8. P. L. Foster, *Crit. Rev. Biochem. Mol. Biol.* **42**, 373–397 (2007).
9. R. S. Galhardo, P. J. Hastings, S. M. Rosenberg, *Crit. Rev. Biochem. Mol. Biol.* **42**, 399–435 (2007).
10. E. Shor, C. A. Fox, J. R. Broach, *PLOS Genet.* **9**, e1003680 (2013).
11. E. Heidenreich, *Crit. Rev. Biochem. Mol. Biol.* **42**, 285–311 (2007).
12. D. M. Fitzgerald, S. M. Rosenberg, *PLOS Genet.* **15**, e1007995 (2019).
13. G. P. Rodriguez *et al.*, *Proc. Natl. Acad. Sci. U.S.A.* **109**, 6153–6158 (2012).
14. R. G. Ponder, N. C. Fonville, S. M. Rosenberg, *Mol. Cell* **19**, 791–804 (2005).
15. G. J. McKenzie, S. M. Rosenberg, *Curr. Opin. Microbiol.* **4**, 586–594 (2001).
16. P. L. Foster, *BioEssays* **22**, 1067–1074 (2000).
17. F. Taddei *et al.*, *Nature* **387**, 700–702 (1997).
18. J. Torkelson *et al.*, *EMBO J.* **16**, 3303–3311 (1997).
19. W. A. Rosche, P. L. Foster, *Proc. Natl. Acad. Sci. U.S.A.* **96**, 6862–6867 (1999).
20. G. J. McKenzie, R. S. Harris, P. L. Lee, S. M. Rosenberg, *Proc. Natl. Acad. Sci. U.S.A.* **97**, 6646–6651 (2000).
21. S. V. Sharma *et al.*, *Cell* **141**, 69–80 (2010).
22. G. R. Oxnard, *Nat. Med.* **22**, 232–234 (2016).
23. M. Ramirez *et al.*, *Nat. Commun.* **7**, 10690 (2016).
24. A. N. Hata *et al.*, *Nat. Med.* **22**, 262–269 (2016).
25. S. Misale, F. Di Nicolantonio, A. Sartore-Bianchi, S. Siena, A. Bardelli, *Cancer Discov.* **4**, 1269–1280 (2014).
26. S. Kopetz *et al.*, *N. Engl. J. Med.* **381**, 1632–1643 (2019).
27. Z. D. Nagel *et al.*, *Proc. Natl. Acad. Sci. U.S.A.* **111**, E1823–E1832 (2014).
28. A. J. Pierce, R. D. Johnson, L. H. Thompson, M. Jasin, *Genes Dev.* **13**, 2633–2638 (1999).
29. A. Bertotti *et al.*, *Nature* **526**, 263–267 (2015).
30. C. Isella *et al.*, *Nat. Commun.* **8**, 15107 (2017).
31. A. J. Rattray, J. N. Strathern, *Annu. Rev. Genet.* **37**, 31–66 (2003).

32. V. M. Krutiakov, *Mol. Biol. (Mosk.)* **40**, 3–11 (2006).
33. M. F. Goodman, *Annu. Rev. Biochem.* **71**, 17–50 (2002).
34. L. J. Mah, A. El-Osta, T. C. Karagiannis, *Leukemia* **24**, 679–686 (2010).
35. S. Panier, S. J. Boulton, *Nat. Rev. Mol. Cell Biol.* **15**, 7–18 (2014).
36. G. Cesi, G. Walbrecq, A. Zimmer, S. Kreis, C. Haan, *Mol. Cancer* **16**, 102 (2017).
37. M. Koptyra *et al*., *Blood* **108**, 319–327 (2006).
38. M. L. Sagristá, A. E. García, M. A. De Madariaga, M. Mora, *Free Radic. Res.* **36**, 329–340 (2002).
39. E. D. Chan, D. W. Riches, C. W. White, *Am. J. Respir. Cell Mol. Biol.* **24**, 627–632 (2001).
40. R. A. Saxton, D. M. Sabatini, *Cell* **168**, 960–976 (2017).
41. A. Prahallad *et al*., *Nature* **483**, 100–103 (2012).
42. J. Shen *et al*., *Nat. Med.* **24**, 556–562 (2018).
43. N. Chatterjee, Y. Lin, B. A. Santillan, P. Yotnda, J. H. Wilson, *Proc. Natl. Acad. Sci. U.S.A.* **112**, 3764–3769 (2015).
44. R. Parsons *et al*., *Cell* **75**, 1227–1236 (1993).
45. V. T. Mihaylova *et al*., *Mol. Cell. Biol.* **23**, 3265–3273 (2003).
46. R. S. Bindra, P. M. Glazer, *Cancer Lett.* **252**, 93–103 (2007).
47. M. Petljak *et al*., *Cell* **176**, 1282–1294.e20 (2019).
48. L. Li, H. Wang, E. S. Yang, C. L. Arteaga, F. Xia, *Cancer Res.* **68**, 9141–9146 (2008).
49. S. Nowsheen *et al*., *PLOS ONE* **6**, e24148 (2011).
50. J. Mateo *et al*., *Ann. Oncol.* **30**, 1437–1447 (2019).

ACKNOWLEDGMENTS

We thank members of Molecular Oncology Laboratory at Candiolo Cancer Institute for critically reading the manuscript, A. Cassingena and F. Sassi for their help with experiments, and G. McKenzie for the NanoLuc plasmid design. **Funding:** This research was supported by Fondazione AIRC under the 5 per Mille 2018 ID 21091 Program (P.I. A. Bardelli, G.L. S. Siena, G.L. A. Bertotti, G.L. L. Trusolino, G.L. F. Di Nicolantonio); AIRC 2010 Special Program Molecular Clinical Oncology 5 per Mille, Project No. 9970 Extension Program (A. Bardelli); AIRC IG no. 16788 (A. Bardelli); AIRC IG 2018–ID 21923 project (P.I. A. Bardelli); H2020 grant agreement no. 635342-2 MoTriColor (A. Bardelli); Ministero Salute, Ricerca Corrente 2019 RC2019 (A. Bardelli); H2020 grant agreement no. 754923 COLOSSUS (L.T.). A. Bardelli has also received research funding from PhoreMost and NeoPhore. **Author contributions:** M.R. and A. Bardelli conceived the study. M.R., A.S., N.M.R., S.A., S.L., V.A., A.M. M.C., M.G., and M.C.L. conducted the experiments and analyzed data. G.C. performed NGS and bioinformatics analysis. A. Bartolini performed NGS panel-based experiments. L.N. performed RNAseq bioinformatics analysis. Z.D.N. and C.G.P. provided plasmids harboring DNA damage. A. Bertotti and L.T. analyzed and provided PDX material. I.S. performed and analyzed IHC data; A.A., A.S.-B., and S.S. provided patient samples. F.D.N. analyzed data. M.R. and A. Bardelli wrote the manuscript. A. Bardelli supervised the study. **Competing interests:** L.T. is a paid consultant for Eli Lilly, AstraZeneca, and Merck KGaA. Z.D.N. is an inventor on a patent (U.S. 9,938,587) covering methods and kits for determining DNA-repair capacity. A. Bardelli is a member of the scientific advisory board of NeoPhore and a shareholder of NeoPhore and PhoreMost. The other authors declare no competing interests. **Data and materials availability:** The FM-HCR reporter plasmids are available from Z.D.N. under a material transfer agreement. The pDRGFP and the pCBASce-I plasmids are available from AddGene under a material transfer agreement. The NanoLuc-expressing plasmid is available from PhoreMost, Ltd. (Cambridge, UK) under a material transfer agreement. The HT29 empty and *MLH1* KO cells are available from A. Bardelli (UNITO) under a material transfer agreement. RNA-sequencing and DNA-sequencing data have been deposited in ENA (from EBI; no. PRJEB28674).

SUPPLEMENTARY MATERIALS

science.sciencemag.org/content/366/6472/1473/suppl/DC1
Materials and Methods
Figs. S1 to S18
Tables S1 and S2
References (*51*–*61*)

View/request a protocol for this paper from *Bio-protocol*.

21 September 2018; resubmitted 24 July 2019
Accepted 26 October 2019
Published online 7 November 2019
10.1126/science.aav4474

SUPERFLUIDITY

Coherent vortex dynamics in a strongly interacting superfluid on a silicon chip

Yauhen P. Sachkou[1]*, Christopher G. Baker[1]*, Glen I. Harris[1]*, Oliver R. Stockdale[2], Stefan Forstner[1], Matthew T. Reeves[2], Xin He[1], David L. McAuslan[1], Ashton S. Bradley[3], Matthew J. Davis[1,2], Warwick P. Bowen[1]†

Quantized vortices are fundamental to the two-dimensional dynamics of superfluids, from quantum turbulence to phase transitions. However, surface effects have prevented direct observations of coherent two-dimensional vortex dynamics in strongly interacting systems. Here, we overcome this challenge by confining a thin film of superfluid helium at microscale on the atomically smooth surface of a silicon chip. An on-chip optical microcavity allows laser initiation of clusters of quasi–two-dimensional vortices and nondestructive observation of their decay in a single shot. Coherent dynamics dominate, with thermal vortex diffusion suppressed by five orders of magnitude. This establishes an on-chip platform with which to study emergent phenomena in strongly interacting superfluids and to develop quantum technologies such as precision inertial sensors.

Strongly interacting many-body quantum systems exhibit rich behaviors of significance to areas ranging from superconductivity (*1*) to quantum computation (*2*, *3*), astrophysics (*4*–*6*), and even string theory (*7*). The first example of such a behavior, superfluidity, was discovered >80 years ago in cryogenically cooled liquid helium-4. It was found to persist even in very thin two-dimensional films, for which the well-known Mermin–Wagner theorem precludes condensation into a superfluid phase in the thermodynamic limit [see, e.g., discussion in (*8*)]. This apparent contradiction was resolved by Berezinskii, Kosterlitz, and Thouless (BKT), who predicted that quantized vortices allow a topological phase transition into superfluidity (*9*, *10*). It is now recognized that quantized vortices dominate much of the two-dimensional dynamics of out-of-equilibrium superfluids even outside the regime of BKT superfluidity, including quantum turbulence (*11*) and anomalous hydrodynamics (*12*).

Recently, laser control and imaging of vortices in ultracold gases (*13*, *14*) and semiconductor exciton-polariton systems (*15*, *16*) have provided rich capabilities to study superfluid dynamics including, for example, the formation of collective quasi–two-dimensional vortex dipoles with negative temperature and large-scale order (*17*, *18*) as predicted by Lars Onsager 70 years ago (*19*). However, these experiments are generally limited to the regime of weak interactions, where the Gross–Pitaevskii equation provides a microscopic model of the dynamics of the superfluid. The regime of strong interactions can be reached by tuning the atomic scattering length in ultracold gases (*20*–*23*), although three-body losses can limit the system lifetime (*20*). Superfluid helium, by contrast, exists naturally in this state, which offers the possibility of studying many-vortex dynamics over a much greater range of length and time scales (*24*). The strongly interacting regime is relevant for astrophysical superfluid phenomena such as pulsar glitches (*6*) and superfluidity of the quark-gluon plasma in the early universe (*5*) and is highly challenging to treat theoretically (*25*, *26*). The vortex dynamics in this regime are typically predicted using phenomenological vortex models. However, questions such as whether the vortices have inertia (*27*, *28*), what is the precise nature of the forces they experience from the normal component of the fluid (*29*), and how to treat dissipation given the nonlocal nature of the vortex flow fields (*8*, *30*) all remain to be conclusively answered. Moreover, point-vortex modeling offers limited insight into the processes of vortex creation and annihilation, which are crucial to understanding the dynamics of topological phase transitions.

Here, we report the observation of coherent dynamics of quasi–two-dimensional vortices in a strongly interacting superfluid. We achieve this by developing a microscale photonic platform to initialize vortex clusters in a few-nanometer-thick film of helium-4 on a silicon chip, confine them, and image their spatial distribution over time. Our experiments characterize vortex distributions through their interactions with resonant superfluid surface waves, taking advantage of ultraprecise sensing methods from cavity optomechanics (*31*–*33*). Microscale confinement greatly enhances the interactions and enables resolution of the dynamics of few-vortex clusters in a single shot and tracked over many minutes as they interact, dissipate energy, and annihilate. We find that evaporative heating occurs, where the annihilation of low-energy vortices draws energy out of a background flow, causing a net increase in free-vortex kinetic energy as the system evolves.

Our experiments yield a vortex diffusivity five orders of magnitude lower than has been observed previously for unpinned vortices in superfluid helium films (*34*). This verifies that the diffusivity can become exceptionally small when operating at temperatures far below the superfluid transition temperature, as conjectured from extrapolation of 30-year-old experimental observations (*8*, *34*). Therefore, the system operates well within the regime of coherent vortex dynamics, with the time scale for dissipation found to exceed the coherent evolution time by more than five orders of magnitude. The on-chip system reported here provides a platform with which to explore the dynamics of phase transitions and quantum turbulence in strongly interacting superfluids and to study how such fluids evolve toward thermal equilibrium and dissipate energy.

Nonequilibrium vortex clusters can be generated with laser light

Figure 1A shows a schematic of our experimental apparatus. A microscale optical ring cavity with laser-reflowed atomically smooth surface, conventionally known as a microtoroid (*35*), is placed inside a sealed sample chamber within a closed-cycle ^{3}He cryostat. The microtoroid confines light in whispering gallery mode resonances, which are excited through an optical nanofiber. The microtoroid is fabricated from silica, has a radius of R = 30 μm, and is suspended above a silicon chip by a pedestal that narrows to a radius of r_p ~ 1 μm where it contacts the bottom surface of the microtoroid (Fig. 1A, inset). The sample chamber is filled with ^{4}He gas at room temperature. The pressure is chosen so that the gas condenses directly into an unsaturated superfluid film at ~1 K. This film coats the inside of the chamber, including the optical microcavity (*31*, *36*). Vortices and superfluid surface waves can coexist in the superfluid film and are geometrically confined to the surface of the microtoroid.

Our experiments operate with a superfluid film thickness of d ~ 7.5 nm and a temperature of T ~ 500 mK, well below the superfluid transition. In these conditions, the thickness far exceeds the superfluid healing length, such that the system is outside the regime of BKT superfluidity. However, from the hydrodynamic perspective, the system is quasi–two-dimensional because both the lowest-energy vertically propagating phonon modes and the lowest-energy Kelvin modes of vortices have

[1]Australian Research Council Centre of Excellence for Engineered Quantum Systems, School of Mathematics and Physics, University of Queensland, St. Lucia, Queensland 4072, Australia. [2]Australian Research Council Centre of Excellence in Future Low-Energy Electronics Technologies, School of Mathematics and Physics, University of Queensland, St. Lucia, Queensland 4072, Australia. [3]Department of Physics, Centre for Quantum Science, and Dodd-Walls Centre for Photonic and Quantum Technologies, University of Otago, Dunedin 9016, New Zealand.
*These authors contributed equally to this work.
†Corresponding author. Email: w.bowen@uq.edu.au

energies comparable to the thermal energy, so only a few of these modes are expected to be thermally excited [see section 1.1 of (*37*)].

We find experimentally that vortex clusters can be optically initialized on the surface of the microtoroid in several ways, including pulsing the intensity of the injected laser to induce superfluid flow through the "fountain effect" (*36*) and optomechanical driving of low-frequency surface waves by dynamical backaction (*31*). Both of these techniques induce flow that exceeds the superfluid critical velocity at the interface between the pedestal and the microtoroid. This triggers the generation of vortex pairs on the bottom surface of the microtoroid in close proximity to the pedestal (Fig. 1B). In the presence of a circular boundary, an ensemble of vortex pairs evolves into a metastable state characterized at high energies by a large-scale negative-temperature Onsager vortex dipole (*17*, *19*) [see section 3.2 of (*37*)]. In our case, the microtoroid pedestal introduces a deep potential to which vortices can pin [see section 7 of (*37*)], qualitatively modifying the physics. Vortices of one sign become pinned, creating a macroscopic circulation, whereas vortices of the opposite sign evolve into a free-orbiting metastable cluster similar to the case without a pinning site [see section 3.2 of (*37*)].

The time scale within which a metastable state is reached can be estimated from the characteristic turnover time for internal rearrangement of the free-vortex cluster, $\tau \sim r_c^2/N\kappa$, where N is the number of free vortices, r_c is the radius of the cluster, and $\kappa = h/m_{He}$ is the circulation quantum, with m_{He} being the mass of a helium atom and h Planck's constant (*38*) [see section 3.2 of (*37*)]. Considering the case of two free vortices separated by the disk radius provides an upper bound to the turnover time of $\tau \lesssim 5$ ms. This is substantially faster than both the dissipation of the system and the temporal resolution of our measurements, which are ~1 min and 1 s, respectively. Consequently, the vortex cluster can be well approximated to exist in a metastable state throughout its evolution, with this state modified continuously by dissipation and in discrete steps by vortex annihilation events.

Each possible metastable state is uniquely characterized by the number of free vortices, kinetic energy, and angular momentum. Performing point-vortex simulations, we determine the possible metastable vortex distributions as a function of these three parameters [see section 3.2 of (*37*)]. In their metastable state, the free vortices exist in an orbiting horseshoe-shaped cluster separated from the origin, which, together with the macroscopic circulation, forms a vortex dipole. Figure 1C illustrates how the distribution of the cluster evolves as a consequence of changes in vortex number, kinetic energy, and angular momentum.

Interactions with third-sound allow vortex imaging

The interaction between light and vortices is extremely weak in superfluid helium because of its exceedingly low refractive index and the Angström scale of the vortex cores. This precludes direct optical imaging techniques. Furthermore, the tracer particles used to image vortex dynamics in bulk three-dimensional helium (*24*) are too large to be applied in thin films. Instead, in our experiments, the vortex dynamics are tracked through their influence on resonant superfluid third-sound waves that are also confined to the bottom surface of the microtoroid (Fig. 2A). Third-sound waves are surface waves analogous to shallow-water waves but with a restoring force provided by the van der Waals interaction with the substrate rather than gravity [see, e.g., (*39*)]. They also exist on the top surface of the microtoroid but in this case are isolated from the vortices because of their physical separation [see section 2 of (*37*)]. We monitor the thermal excitations of third-sound modes in real time through their effect on the height of the superfluid film in the optical evanescent field of the microtoroid (*31*). This manifests as fluctuations of the phase of light confined inside the cavity, which are resolved through balanced homodyne detection implemented within a fiber interferometer (Fig. 1A). Frequency analysis of the output photocurrent reveals resonances with frequencies that are in good agreement with expectations for third-sound modes confined to a circular geometry [see sections 1 and 2 of (*37*)]. The resonances are Bessel modes, characterized by their radial m and azimuthal n mode numbers (*41*).

The vortex flow field causes Doppler shifts of the frequencies of the third-sound modes,

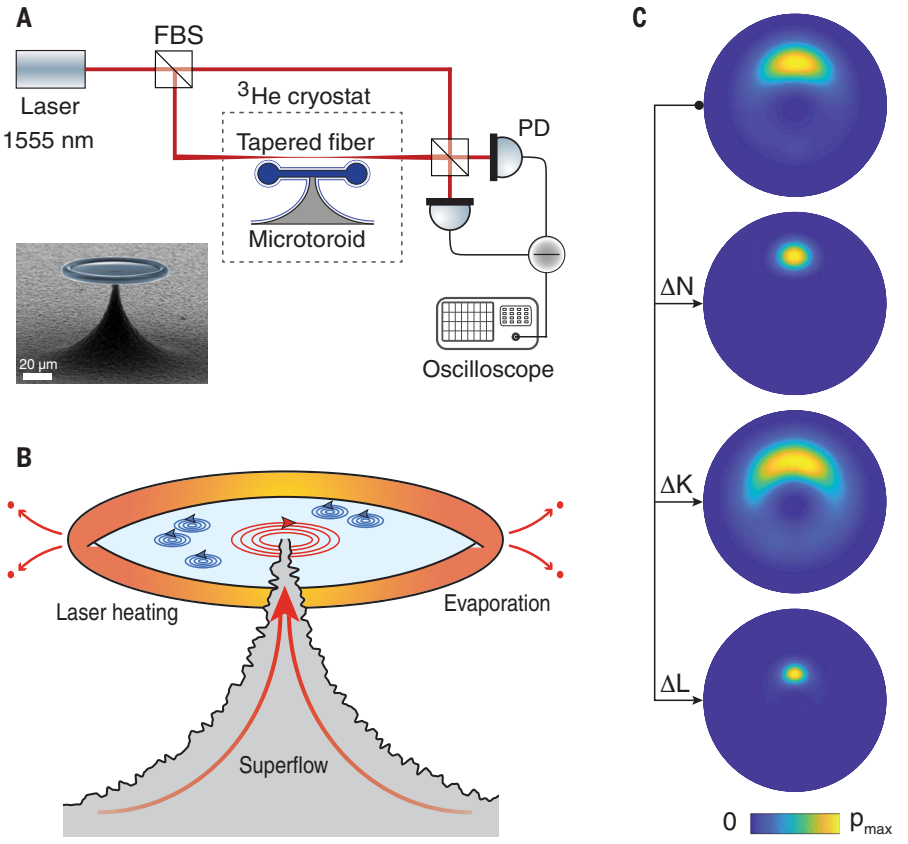

Fig. 1. Laser initialization of vortex clusters. (**A**) Experimental setup. A balanced homodyne detection scheme is implemented within a fiber interferometer. FBS, fiber beam splitter; PD, photodetector. Inset shows a scanning electron microscope image of the microtoroidal optical cavity used in the experiments. Scale bar, 20 μm. (**B**) Sketch of the vortex generation process. Laser heating of the microtoroid perimeter causes superfluid evaporation, followed by superflow (*36*). The flow exceeds the superfluid critical velocity at the top of the microtoroid pedestal, seeding the generation of vortex pairs. (**C**) Exemplar simulated metastable distributions showing the effects of vortex annihilation and of changes in total kinetic energy K and angular momentum L. The color map indicates the free-vortex probability density, with a maximum of $p_{max} = \{0.035, 0.075, 0.023, 0.12\}$ μm^{-2}, respectively, for the top to bottom metastable states. Top metastable state: $\{N,K,L\} = \{10, 0.43$ aJ, 120 ag μm^2 s$^{-1}\}$; second to top: $N \rightarrow 9$; second to bottom: $K \rightarrow 0.41$ aJ; and bottom: $L \rightarrow 44$ ag μm^2 s^{-1}.

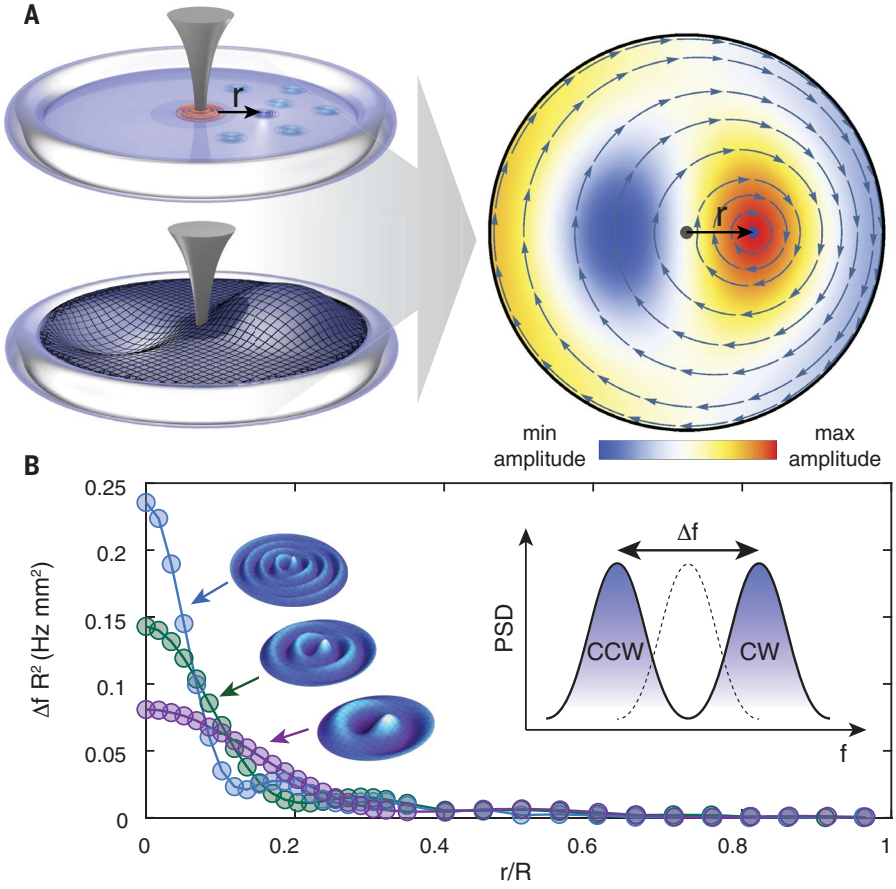

Fig. 2. Interactions between vortices and third-sound on a disk. (**A**) Top left: Free vortices (blue) and pinned circulation (red) on the bottom surface of the microtoroid. Bottom left: A third-sound mode on the same surface. The vortices and third-sound couple due to the superposition of their flow fields, shown on the right for the case of a single vortex (blue dot) offset from the disk origin by distance *r*. Here, the surface color represents the third-sound mode amplitude profile and the blue lines are vortex streamlines. Confinement within the same microscale domain enhances both the interaction rate between vortices and third-sound and the resulting frequency splitting between counterpropagating third-sound modes. (**B**) Normalized splitting per vortex for third-sound modes (*m*,*n*) = (1,3), (1,5), and (1,8) calculated by finite-element modeling using the techniques detailed in (*40*) and outlined in section 2.1 of (*32*), with their respective spatial profiles. The inset schematically depicts the vortex-induced splitting Δf between clockwise and counterclockwise third-sound modes in the presence of a clockwise vortex, which would be observed as a function of frequency *f* in the power spectral density (PSD) of the optically measured superfluid motion.

lifting the degeneracy between clockwise and counterclockwise waves (Fig. 2). The magnitude of the frequency splitting induced by a vortex scales inversely with the area in which it is confined (*39*, *40*). As such, the microscale confinement provided by our microtoroid allows greatly enhanced resolution compared with previous experiments (*39*, *42*). The splitting also depends both on the position of the vortex and on the spatial profile of the third-sound mode, as shown for several modes in Fig. 2B. Despite the strong interactions between helium atoms, the phase coherence and incompressibility of the superfluid combine to ensure linearity. Therefore, the total flow field of a vortex cluster is given by the linear superposition of the flow of each constituent vortex. The total splitting between counter-rotating third-sound modes is then equal to the sum of the splittings generated by each vortex and by the macroscopic circulation pinned to the pedestal. We exploit this linearity, combined with the vortex position–dependent interaction and simultaneous measurements of splitting on several third-sound modes, to characterize the spatial distribution of vortex clusters in a manner analogous to experiments that use multiple cantilever eigenmodes to image the distribution of deposited nanoparticles (*43*).

Vortex clusters evolve coherently

To determine the instantaneous metastable vortex distribution from a single continuous measurement, we generate a nonequilibrium vortex cluster by optically initiating supercritical flow. We then simultaneously measure the frequency splittings induced on the (*m*,*n*) = (1,3), (1,4), (1,5), (1,7), and (1,8) third-sound modes as the cluster evolves over time, anticipating vortex-dipole decay as illustrated in Fig. 3A. As a representative example, Fig. 3B shows the observed power spectral density and frequency splitting of the (1,7) third-sound mode at the start of the measurement run, just after the vortex cluster has been initialized [see section 2 of (*37*) for the initial power spectral densities of all modes]. Using the vortex position–dependent splitting function $\Delta f(r)$ (Fig. 2B), the frequency shifts expected on each of the third-sound modes are computed for all possible metastable distributions and compared with the observed shifts. This allows us to ascertain both the metastable state that most closely matches the observed frequency shifts at a given time, as well as the range of metastable states for which the shifts are statistically indistinguishable.

As shown for the initial metastable vortex distribution in Fig. 3C (colored circular points), we find excellent agreement between the observed frequency splittings and those obtained with the best-fit metastable distribution. Moreover, although the measurements only loosely constrain the angular momentum [see section 4.2 of (*37*)], we find that the statistical uncertainty in the number of free vortices and kinetic energy is relatively small. The free vortex number in the initial vortex dipole is statistically constrained to a value of either 16 or 17. For the case of 16 vortices, the total kinetic energy and angular momentum are constrained to $K = 0.8^{+0.2}_{-0.02}$ aJ and $L = 0.2^{+0.3}_{-0.07}$ fg μm² s⁻¹, respectively, whereas for 17 vortices, they are constrained to $K = 0.8^{+0.1}_{-0.03}$ aJ and $L = 0.3^{+0.05}_{-0.2}$ fg μm² s⁻¹. We are also able to determine the dipole separation, which in the case of 17 vortices is found to be $7.3^{+1.2}_{-0.8}$ μm.

Continuously monitoring the superfluid third-sound modes reveals that their splittings decay over a time scale on the order of minutes (Fig. 3C). The observed splittings are well characterized by a metastable vortex dipole throughout this entire decay process. By contrast, they are inconsistent with other vortex dynamics models such as expansion of a single-sign vortex cluster caused by either vortex-vortex interactions or diffusive hopping between pinning sites on the surface of the microtoroid [see section 4 of (*37*)].

The kinetic energy and free-vortex number of the metastable state are shown as a function of time for a single shot in Fig. 4, A and B (blue curves). The total kinetic energy of the dipole decays continuously with time as a consequence of weak dissipation. This decay occurs over a period of ~1 min, comparable to previous nonspatially resolved measurements of the decay of a persistent current (*44*). In our

experiments, the decay is accompanied by a reduction in the number of free vortices as vortex-vortex interactions and dissipation drive vortices into the center of the disk, where they can annihilate with quanta of circulation of opposite sign pinned to the pedestal. These dynamics are supported by point-vortex simulations (Fig. 4, C and D), which show good quantitative agreement with only the mutual friction coefficient α as a fitting parameter. The agreement between experiment and theory indicates that within experimental uncertainties, the vortex dynamics are consistent with a simple point vortex model including local phenomenological dissipation and without the need to introduce surface pinning sites, inertia to the vortex cores (*27*, *28*), or an Iordanskii force between vortices and the normal component of the fluid (*29*).

The mutual friction coefficient quantifies the ratio of coherent to dissipative time scales in the superfluid dynamics and in our system is expected to be determined by a combination of temperature-dependent phonon- and ripplon-scattering processes, as well as surface roughness effects. From the fit, it is found to be $\alpha \sim 2 \times 10^{-6}$ [see section 3.3 of (*37*)]. A second experiment under similar conditions but with an initial free-vortex number of $N = 33^{+2}_{-1}$ is broadly consistent, yielding $\alpha \sim 3 \times 10^{-6}$ [see section 5 of (*37*)]. These values are similar to both measurements (*45*, *46*) and theoretical predictions [see section 3.4 of (*37*)] for bulk superfluid helium, suggesting that surface effects are small despite the quasi–two-dimensional geometry. It has generally been thought that fast dissipative processes would preclude the observation of coherent dynamics in superfluid helium films. However, the mutual friction coefficient obtained here shows that this is not the case in general, with coherent dynamics dominating by more than five orders of magnitude. This is competitive with the best ultracold atom experiments, which typically achieve $\alpha \sim 6 \times 10^{-4}$ (*17*).

Nonequilibrium vortex dynamics is observed in a single shot

The pinning of vortices on the microtoroid pedestal results in a macroscopic circulation, as discussed above. The kinetic energy associated with the free vortex cluster is given by $K_{free} = K - K_{pinned}$, where $K_{pinned} = \rho d(N\kappa)^2 \ln(R/r_p)/4\pi$, the kinetic energy of the macroscopic circulation alone, with $\rho = 145$ kg/m^3 being the density of superfluid helium. K_{free} is shown for both our experimental data and simulations by the red curves in Fig. 4, A and C. During the first minute of evolution, it is negative and, notably, increases with time. The dynamics are characterized by steps up in energy during vortex annihilation events interspersed with a continuous dissipative decay.

The negativity of the free-vortex energy can be understood by considering the interference between the flow fields of a free vortex and the macroscopic circulation. Although the high flow velocity near the core of a free vortex introduces kinetic energy, the vortex flow field also cancels a component of the background flow. For a sufficiently large circulation, this cancellation effect dominates, leading to an overall negative energy cost to introducing the vortex cluster [see section 7.2 of (*37*)].

The increase in free-vortex energy over time can be explained by considering the process of vortex annihilation in a macroscopic background flow. To annihilate, a free vortex must reach the pedestal, where its contribution to the total kinetic energy is at a minimum. To do this, it gives up kinetic energy to the remaining free vortices. This process of removing low-energy vortices has been described as evaporative heating (*18*), in analogy to evaporative cooling of ultracold atomic ensembles. However, whereas standard evaporative heating can explain a per-vortex increase in kinetic energy, its effect is to reduce the net free-vortex kinetic energy (*18*). The physics is modified here by the presence of a macroscopic background flow. The annihilation of a free vortex with a pinned circulation quanta cancels a component of this flow, reducing its kinetic energy while leaving the total kinetic

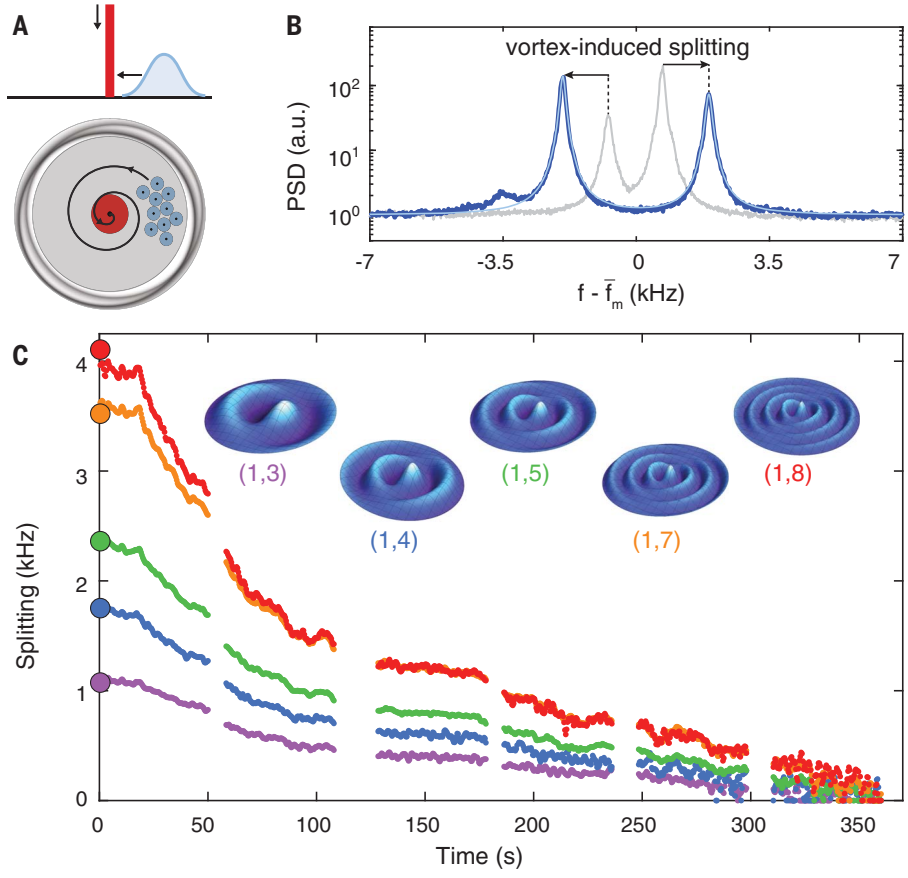

Fig. 3. Temporal dynamics of third-sound splitting. (**A**) Vortex-dipole decay process. Red indicates quantized circulation around the pedestal reduces due to annihilation events. Light blue indicates orbiting free-vortex cluster spirals toward the origin due to dissipation. Dissipation is exaggerated for clarity. (**B**) Experimental splitting observed in the PSD of the (*m*,*n*) = (1,7) third-sound mode pair immediately after vortex-dipole initialization. Gray spectra are the third-sound mode pair without vortices. The residual splitting in these unperturbed spectra is caused by irregularities in the circularity of the microtoroid that break the degeneracy between standing-wave Bessel modes (*31*) and is accounted for in data processing [see section 1.3 of (*37*)]. *f* is the frequency of superfluid motion; $\bar{f}_m$ is the mean resonance frequency of third-sound mode pair. (**C**) Temporal decay of splitting of the (*m*,*n*) = (1,8), (1,7), (1,5), (1,4), and (1,3) third-sound modes (top to bottom traces, respectively). These specific modes were chosen because of the high signal-to-noise ratio of their PSDs. The raw data were recorded on a high-bandwidth, high-memory-depth oscilloscope. Six continuous measurements were taken, separated by ~10-s data-saving periods. Colored circles at the start of each trace show the theoretical splitting of each third-sound mode pair for the best-fit initial vortex metastable distribution. Insets show spatial amplitude profiles of each third-sound mode.

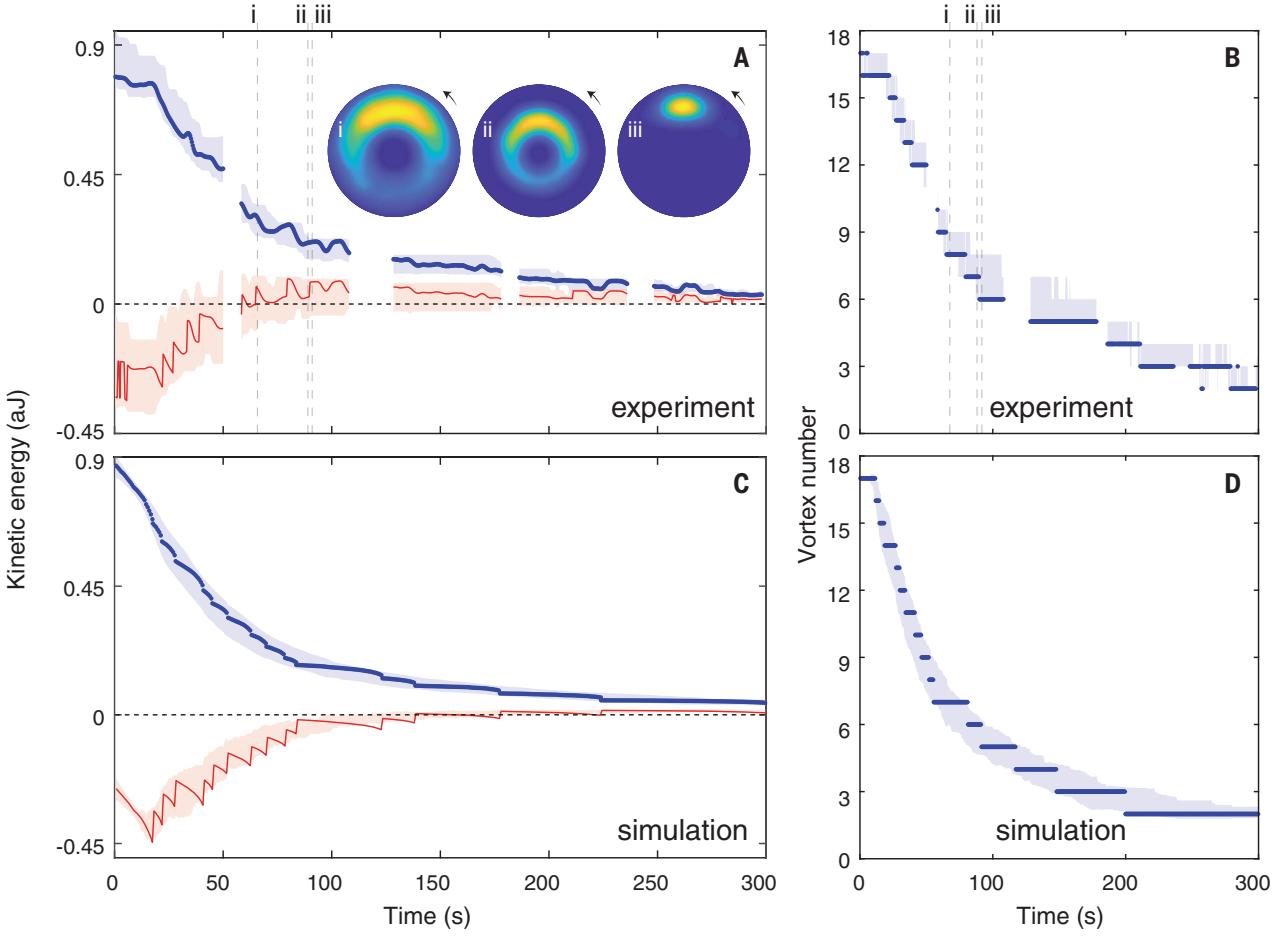

Fig. 4. Single-shot evolution of vortex-cluster metastable states. (**A**) Evolution of total kinetic energy (blue curve) and free-vortex cluster kinetic energy (red curve). Insets show metastable vortex probability densities at times indicated by the vertical dashed lines. These probability densities have the same color scale as those in Fig. 1C, with p_{max} = {0.0087, 0.015, 0.032} μm^{-2}, respectively, from left to right. The second and third metastable distributions are taken, respectively, just before and just after the 7-to-6 annihilation event. The angular momentum of each distribution is chosen, within the uncertainty window of the fit, to maximize the entropy of the state and therefore represents the most statistically likely of the experimentally plausible distributions. (**B**) Experimentally determined decay of the vortex number. Vertical dashed lines correspond to times in (A). Note that although these data display steps in the vortex number, this is a feature of our analysis that minimizes the root-mean-square uncertainty only over discrete vortex number. Our experiments approach single-vortex resolution; however, the continuous variation of vortex-induced splitting with time precludes direct unambiguous observation of individual steps in the splitting that result from creation or annihilation (*40*). (**C** and **D**) Point-vortex simulations of the system evolution [see section 3.3 of (*37*) for implementation]. (C) Evolution of the total (blue curve) and free-vortex (red curve) kinetic energies. (D) Evolution of the free-vortex number. In all traces, the shaded area corresponds to a 1-SD uncertainty.

energy essentially unchanged, as can be seen by the lack of discrete steps in the blue curves of Fig. 4, A and C. Therefore, annihilation events increase the kinetic energy of the free-vortex cluster by drawing energy out of the background flow. This pushes the cluster outward to a higher separation, as illustrated by the metastable states just before and after an annihilation event, as shown in insets ii and iii, respectively, in Fig. 4A.

In addition to allowing the observation of evaporative heating in a single continuous shot, our experiments allow the diffusivity D of vortices to be established in a regime for superfluid helium films, where it was previously inaccessible. The vortex diffusivity plays an important role in dynamic corrections to the BKT transition (*10*) and in the dissipation of persistent flow (*47*). This has motivated substantial research efforts to quantify it both near the BKT transition and outside the regime of BKT superfluidity (*8*, *34*, *44*). However, achieving a high signal-to-noise ratio has generally proved challenging (*8*), and surface pinning is known to have a major influence on measurement outcomes (*34*, *48*). By contrast, our experiments are not dominated by surface pinning [see section 6 of (*37*)] and achieve near-single-vortex resolution. From them, we obtain a value of $D = k_B T\alpha/\rho d\kappa \sim 100\ nm^2\ s^{-1}$, where k_B is the Boltzmann constant. This is five orders of magnitude below previous measurements for which the vortex dynamics are not dominated by pinning (*34*), verifying the extrapolation from 30-year-old experimental observations that the diffusivity could become exceedingly small outside the BKT regime at low temperatures (*8*). Future experiments varying the temperature, film thickness, and surface properties may further elucidate the details of dissipation in thin superfluid helium films.

Concluding perspectives

The experiments reported here were enabled by the use of microscale confinement, which greatly enhances the interactions between vortices, between third-sound and vortices, and between third-sound and light. Interactions with strong pinning sites have previously prevented the observation of coherent vortex

dynamics in superfluid helium films (*42*). In our experiments, vortex-vortex interactions dominate because of the increased confinement and atomically smooth surface of the device. The smoothness of the surface results in a conservative upper bound to the vortex unpinning velocity of 0.2 cm/s [see section S6 of (*37*)], three orders of magnitude lower than previous experiments (*42*). As such, vortex-vortex interactions dominate even for the smallest possible clusters containing only two vortices. Furthermore, a four-order-of-magnitude enhancement in the interaction strength between vortices and third-sound compared with earlier experiments (*39*, *42*) allows resolution approaching the single-vortex level. Together, these capabilities provide a tool for future study of the rich dynamics of quasi–two-dimensional vortices in strongly interacting superfluids on a silicon chip. Vortex dynamics in the regime of BKT superfluidity may also be accessible by operating with thinner films.

The ability to nondestructively track vortex dynamics in a single shot opens the prospect to explore out-of-equilibrium dynamics and stochastic noise-driven processes that are challenging to study with other techniques (*16*, *49*). It also promises to resolve contentious aspects of vortex dynamics in strongly interacting superfluids, such as dissipation and diffusion models (*8*, *30*), vortex inertia (*27*, *28*), and the Iordanskii force (*29*). Furthermore, whereas the experiments reported here were performed with a relatively small number of vortices, the Angström scale of the vortex core in helium-4 will enable future research on the dynamics of ensembles of thousands of vortices, a regime well outside current capabilities with cold atom and exciton-polariton superfluids (*38*). This could allow emergent phenomena in two-dimensional turbulence, such as turbulent cascades (*38*) and anomalous hydrodynamics (*12*), to be explored.

REFERENCES AND NOTES

1. D. Mitra *et al*., *Nat. Phys.* **14**, 173–177 (2017).
2. C. Gross, I. Bloch, *Science* **357**, 995–1001 (2017).
3. A. D. King *et al*., *Nature* **560**, 456–460 (2018).
4. N. Chamel, *J. Astrophys. Astron.* **38**, 43 (2017).
5. STAR Collaboration, *Nature* **548**, 62–65 (2017).
6. P. W. Anderson, N. Itoh, *Nature* **256**, 25–27 (1975).
7. P. K. Kovtun, D. T. Son, A. O. Starinets, *Phys. Rev. Lett.* **94**, 111601 (2005).
8. P. W. Adams, W. I. Glaberson, *Phys. Rev. B* **35**, 4633–4652 (1987).
9. J. M. Kosterlitz, D. J. Thouless, *J. Phys. Chem.* **5**, L124–L126 (1972).
10. D. J. Bishop, J. D. Reppy, *Phys. Rev. Lett.* **40**, 1727–1730 (1978).
11. T. W. Neely *et al*., *Phys. Rev. Lett.* **111**, 235301 (2013).
12. P. Wiegmann, A. G. Abanov, *Phys. Rev. Lett.* **113**, 034501 (2014).
13. D. V. Freilich, D. M. Bianchi, A. M. Kaufman, T. K. Langin, D. S. Hall, *Science* **329**, 1182–1185 (2010).
14. S. Donadello *et al*., *Phys. Rev. Lett.* **113**, 065302 (2014).
15. A. Amo *et al*., *Science* **332**, 1167–1170 (2011).
16. E. Estrecho *et al*., *Nat. Commun.* **9**, 2944 (2018).
17. G. Gauthier *et al*., *Science* **364**, 1264–1267 (2019).
18. S. P. Johnstone *et al*., *Science* **364**, 1267–1271 (2019).
19. L. Onsager, *Nuovo Cim.* **6** (S2), 279–287 (1949).
20. P. Makotyn, C. E. Klauss, D. L. Goldberger, E. A. Cornell, D. S. Jin, *Nat. Phys.* **10**, 116–119 (2014).
21. M. W. Zwierlein, J. R. Abo-Shaeer, A. Schirotzek, C. H. Schunck, W. Ketterle, *Nature* **435**, 1047–1051 (2005).
22. C. Eigen *et al*., *Nature* **563**, 221–224 (2018).
23. B. Ko, J. W. Park, Y. Shin, *Nat. Phys.* (2019).
24. E. Fonda, D. P. Meichle, N. T. Ouellette, S. Hormoz, D. P. Lathrop, *Proc. Natl. Acad. Sci. U.S.A.* **111** (Suppl 1), 4707–4710 (2014).
25. H. Hu, B. C. Mulkerin, U. Toniolo, L. He, X.-J. Liu, *Phys. Rev. Lett.* **122**, 070401 (2019).
26. F. Ancilotto *et al*., *Int. Rev. Phys. Chem.* **36**, 621–707 (2017).
27. D. J. Thouless, J. R. Anglin, *Phys. Rev. Lett.* **99**, 105301 (2007).
28. T. Simula, *Phys. Rev. A* **97**, 023609 (2018).
29. E. B. Sonin, *Phys. Rev. B* **55**, 485–501 (1997).
30. L. Thompson, P. C. E. Stamp, *Phys. Rev. Lett.* **108**, 184501 (2012).
31. G. I. Harris *et al*., *Nat. Phys.* **12**, 788–793 (2016).
32. A. Kashkanova *et al*., *Nat. Phys.* **13**, 74–79 (2016).
33. A. Noury *et al*., *Phys. Rev. Lett.* **122**, 165301 (2019).
34. K. A. Gillis, S. M. Volz, J. M. Mochel, *Phys. Rev. B* **40**, 6684–6694 (1989).
35. D. K. Armani, T. J. Kippenberg, S. M. Spillane, K. J. Vahala, *Nature* **421**, 925–928 (2003).
36. D. L. McAuslan *et al*., *Phys. Rev. X* **6**, 021012 (2016).
37. Materials and methods are available as supplementary materials.
38. M. T. Reeves, T. P. Billam, X. Yu, A. S. Bradley, *Phys. Rev. Lett.* **119**, 184502 (2017).
39. F. M. Ellis, H. Luo, *Phys. Rev. B* **39**, 2703–2706 (1989).
40. S. Forstner *et al*., *New J. Phys.* **21**, 053029 (2019).
41. C. G. Baker *et al*., *New J. Phys.* **18**, 123025 (2016).
42. F. M. Ellis, L. Li, *Phys. Rev. Lett.* **71**, 1577–1580 (1993).
43. M. S. Hanay *et al*., *Nat. Nanotechnol.* **10**, 339–344 (2015).
44. D. T. Ekholm, R. B. Hallock, *Phys. Rev. Lett.* **42**, 449–452 (1979).
45. A. I. Golov, P. M. Walmsley, *J. Low Temp. Phys.* **156**, 51–70 (2009).
46. E. Kozik, B. Svistunov, *Phys. Rev. Lett.* **100**, 195302 (2008).
47. L. Yu, *Phys. Rev. B* **25**, 198–215 (1982).
48. G. Agnolet, D. F. McQueeney, J. D. Reppy, *Phys. Rev. B* **39**, 8934–8958 (1989).
49. S. Serafini *et al*., *Phys. Rev. X* **7**, 021031 (2017).
50. Y. P. Sachkou *et al*., Experimental and simulation datasets for: Coherent vortex dynamics in a strongly-interacting superfluid on a silicon chip, Version 1.0, Zenodo (2019); https://doi.org/10.5281/zenodo.3524827.
51. Y. P. Sachkou *et al*., Data processing and simulation scripts for: Coherent vortex dynamics in a strongly-interacting superfluid on a silicon chip, Version 1.0, Zenodo (2019); https://doi.org/10.5281/zenodo.3524872.

ACKNOWLEDGMENTS

We thank X. Yu, M. Cawte, Y. Sfendla, A. Sadawsky, A. Doherty, P. Warszawski, and M. Woolley for insightful discussions. Device fabrication was performed in part at the Queensland node of the Australian National Fabrication Facility. **Funding:** This work was funded by the U.S. Army Research Office through grant no. W911NF17-1-0310. It was also partially supported by the Australian Research Council Centre of Excellence for Engineered Quantum Systems (EQUS, project no. CE170100009) and the Australian Research Council Centre of Excellence in Future Low-Energy Electronics Technologies (FLEET, project no. CE170100039). W.P.B. acknowledges Australian Research Council Future Fellowship FT140100650. C.G.B. acknowledges a Fellowship from the University of Queensland (UQFEL1833877) and a Discovery Early Career Researcher Award from the Australian Research Council (DE190100318). **Author contributions:** Y.P.S., C.G.B., G.I.H., D.L.M., and X.H. performed the experiments. G.I.H., D.L.M., and W.P.B. designed the experiments. Y.P.S., C.G.B., S.F., O.R.S., M.T.R., M.J.D., and W.P.B. analyzed and interpreted the data. O.R.S., M.T.R., M.J.D., and A.S.B. performed the point vortex simulations. Y.P.S., C.G.B., G.I.H., and W.P.B. wrote the paper with contributions from the other authors. W.P.B. provided overall leadership for the project. **Competing interests:** The authors declare no competing interests. **Data and materials availability:** All data presented in this work and data processing and simulation scripts can be found at Zenodo (*50*, *51*).

SUPPLEMENTARY MATERIALS

science.sciencemag.org/content/366/6472/1480/suppl/DC1
Materials and Methods
Supplementary Text
Figs. S1 to S16
Table S1
References (*52*–*80*)

6 February 2019; accepted 6 November 2019
10.1126/science.aaw9229

NEURODEVELOPMENT

Potassium channel dysfunction in human neuronal models of Angelman syndrome

Alfred Xuyang Sun[1,2]*†, Qiang Yuan[3,4]*, Masahiro Fukuda[4], Weonjin Yu[4], Haidun Yan[5], Grace Gui Yin Lim[1], Mui Hoon Nai[6], Giuseppe Alessandro D'Agostino[7], Hoang-Dai Tran[2], Yoko Itahana[8], Danlei Wang[1]‡, Hidayat Lokman[4], Koji Itahana[8], Stephanie Wai Lin Lim[4], Jiong Tang[9], Ya Yin Chang[1], Menglan Zhang[4], Stuart A. Cook[7], Owen J. L. Rackham[7], Chwee Teck Lim[6], Eng King Tan[1,4], Huck Hui Ng[2], Kah Leong Lim[1,10,11], Yong-Hui Jiang[5]§, Hyunsoo Shawn Je[4,10]†

Disruptions in the ubiquitin protein ligase E3A (*UBE3A*) gene cause Angelman syndrome (AS). Whereas AS model mice have associated synaptic dysfunction and altered plasticity with abnormal behavior, whether similar or other mechanisms contribute to network hyperactivity and epilepsy susceptibility in AS patients remains unclear. Using human neurons and brain organoids, we demonstrate that UBE3A suppresses neuronal hyperexcitability via ubiquitin-mediated degradation of calcium- and voltage-dependent big potassium (BK) channels. We provide evidence that augmented BK channel activity manifests as increased intrinsic excitability in individual neurons and subsequent network synchronization. BK antagonists normalized neuronal excitability in both human and mouse neurons and ameliorated seizure susceptibility in an AS mouse model. Our findings suggest that BK channelopathy underlies epilepsy in AS and support the use of human cells to model human developmental diseases.

Angelman syndrome (AS) is a neurodevelopmental disorder characterized by delayed development, intellectual disability, and seizures (*1*). Approximately 90% of AS cases are caused by a loss-of-function mutation of the ubiquitin protein ligase E3A (*UBE3A*) gene, which encodes a HECT E3 ubiquitin ligase (*2*). Loss of the UBE3A protein could result in accumulation of AS-relevant substrate proteins and contribute to disease pathogenesis (*3*). Studies using an AS mouse model have demonstrated impaired synaptic connectivity, an imbalance between network excitation and inhibition, and delayed neurodevelopmental processes (*4*–*8*). Studies using neurons differentiated from AS patient–derived induced pluripotent stem cells (iPSCs) have suggested disrupted maturation (*9*, *10*), but neither the pathological mechanisms underlying seizures in AS nor the biological substrate(s) of UBE3A has been established.

[1]National Neuroscience Institute, 11 Jalan Tan Tock Seng, Singapore 308433, Singapore. [2]Genome Institute of Singapore, 60 Biopolis Street, Singapore 138672, Singapore. [3]Graduate School for Integrative Sciences and Engineering, National University of Singapore, 28 Medical Drive, Singapore 117456, Singapore. [4]Signature Program in Neuroscience and Behavioral Disorders, Duke-NUS Medical School, 8 College Road, Singapore 169857, Singapore. [5]Department of Neurobiology, Duke University School of Medicine, Durham, NC 27710, USA. [6]Department of Biomedical Engineering, National University of Singapore, Singapore 117576, Singapore. [7]Program in Cardiovascular and Metabolic Disorders, Duke-NUS Medical School, 8 College Road, Singapore 169857, Singapore. [8]Program in Cancer and Stem Cell Biology, Duke-NUS Medical School, 8 College Road, 169857, Singapore. [9]Singapore Bioimaging Consortium, Agency for Science Technology and Research (A*STAR), Singapore 138667, Singapore. [10]Department of Physiology, Yong Loo Lin School of Medicine, National University of Singapore, Singapore 117597, Singapore. [11]Lee Kong Chian School of Medicine, Nanyang Technological University, 11 Mandalay Road, Singapore 308232, Singapore.
*These authors contributed equally to this work.
†Corresponding author. Email: sunxya@gis.a-star.edu.sg (A.X.S.); shawn.je@duke-nus.edu.sg (H.S.J.)
‡Present address: Department of Neurobiology and Anatomy, University of Utah, Salt Lake City, UT 84112, USA. §Present address: Department of Genetics, Yale University School of Medicine, New Haven, CT 06520, USA.

Altered excitability and fAHP in UBE3A-null human neurons

To understand the cellular and functional consequences of the loss of UBE3A in human neurons, we used the CRISPR-Cas9 system to generate *UBE3A* knockout (KO) cells in the human embryonic stem cell line (hESC) H9 (Fig. 1A). One clone (KO) harbored a homozygous 5-bp deletion in exon 6 that resulted in a frame shift and early translational termination (Fig. 1A). This clone lacked the UBE3A protein (Fig. 1A). We found no off-target effects from CRISPR-Cas9 on the top 10 predicted off-target sites of our single guide RNA sequence (table S1). *UBE3A* KO hESCs were karyotypically normal (fig. S1A), expressed key pluripotency markers, and proliferated normally (fig. S1, B and C).

Next, we induced neuronal differentiation from these isogenic hESCs by ectopically expressing *Ngn2* (*11*). This protocol generates homogenous populations of electrically mature cortical neurons in a time frame shorter than that achieved with morphogen-guided differentiation protocols (*12*). Both *UBE3A* wild-type (WT) and KO hESCs were converted to neurons with similar efficiency (fig. S2A). At 35 days post-induction, we observed morphologically mature neurons with dendritic arborizations decorated with synaptic markers (Fig. 1B). There were no significant differences between WT and KO neurons in terms of dendritic complexity or the number of morphological synapses (Fig. 1, C and D). This lack of morphological alterations in KO neurons prompted us to investigate functional changes using whole-cell patch clamp recordings. By injecting stepped currents into neurons to trigger action potentials (APs), we observed that currents higher than 300 pA resulted in increased AP firing frequencies in KO neurons (Fig. 1, E to G). There were no differences in membrane capacitance, input resistance, AP threshold, and AP amplitudes between WT and KO neurons (fig. S2, B to E). Therefore, we monitored changes in voltage-gated sodium (V-Na^+) and potassium (V-K^+) channels, which are essential for AP generation (*13*). Current–voltage curves induced by stepped depolarization were indistinguishable between WT and KO neurons (fig. S2F). However, when we examined the fast components of after-hyperpolarization (fAHPs) (fig. S2G), which can affect neuronal excitability in a bidirectional manner (*14*–*16*), we observed that fAHPs were significantly augmented in *UBE3A* KO neurons [WT: −8.6 ± 1.5 mV (mean ± SEM); KO: −14.8 ± 1.1 mV; $P = 0.0014$] (Fig. 1, H and I). The changes in AP firing and fAHP observed in KO neurons were restored by the ectopic expression of WT UBE3A (fig. S2, H to L), confirming that the lack of UBE3A was responsible for these functional changes. To verify that these differences are not specific to this particular hESC line (H9), we generated independent pairs of isogenic *UBE3A* WT and KO clones in another hESC line (H1) (fig. S2M) and were able to reproduce similar functional changes (fig. S2, N to S). In humans, AS is associated with loss of the maternal *UBE3A* allele, and this could not be recapitulated in our homozygous KO clones. Thus, we sought to determine whether neurons from AS patient–derived iPSCs exhibit a similar increase in excitability with augmented fAHP. To this end, we generated neurons from an AS iPSC line that carried a microdeletion in chromosome 15q11.2-q13.1 (which includes the *UBE3A* gene) and confirmed that the UBE3A protein was not observed in induced neurons (Fig. 1J). The introduction of WT UBE3A into these AS iPSC–derived neurons similarly rescued functional changes in AP firing and fAHPs (Fig. 1, K to N). Taken together, our results established that the loss of UBE3A in human neurons results in altered neuronal excitability associated with enhanced fAHP.

BK augmentation underlies increased fAHP

fAHPs are primarily mediated by calcium- and voltage-dependent big potassium (BK) channels in neurons (*17*). To determine whether the enhanced fAHPs observed in KO neurons resulted from increased BK channel activity, we pharmacologically isolated BK currents (fig. S3A). Compared with WT-derived neurons, *UBE3A* KO neurons exhibited larger BK currents (Fig. 2A

and fig. S3B). Although a previous report indicated that SK2 (small-conductance Ca^{2+}-activated K^+ channel 2) is a substrate of UBE3A (*18*), we did not observe any significant difference in SK2-mediated medium AHPs (fig. S3, C and D). The higher BK currents observed in KO neurons might simply be due to increased BK protein expression. Indeed, Western blot analyses showed that the level of the obligatory subunit of BK (BKα) was higher in KO neurons (fig. S3, E and F). We independently confirmed this finding by employing single-molecule, atomic force microscopy (AFM) to assess the densities of BK proteins on cellular membranes by analyzing the physical interactions between BK proteins and BK-specific antibodies conjugated to the AFM tip (Fig. 2B and fig. S4) (*19*). Sequential AFM force mapping was conducted by spatially moving the functionalized tip on the soma membranes of neurons. Figure 2C shows an example of a heatmap in which each colored block indicates the presence of BK channels at that location. The results revealed that the BK channel density was higher on the membranes of KO cells (Fig. 2, C and D). If increased BK levels lead to enhanced fAHP and elevated excitability in KO neurons, we hypothesized that treatment with a BK antagonist would normalize these differences. Indeed, application of BK antagonists (either 5 μM paxilline or 100 nM IBTX) (Fig. 2, E to H, and fig. S5, A to C), but not of an SK antagonist, apamin (200 nM) (fig. S5D),

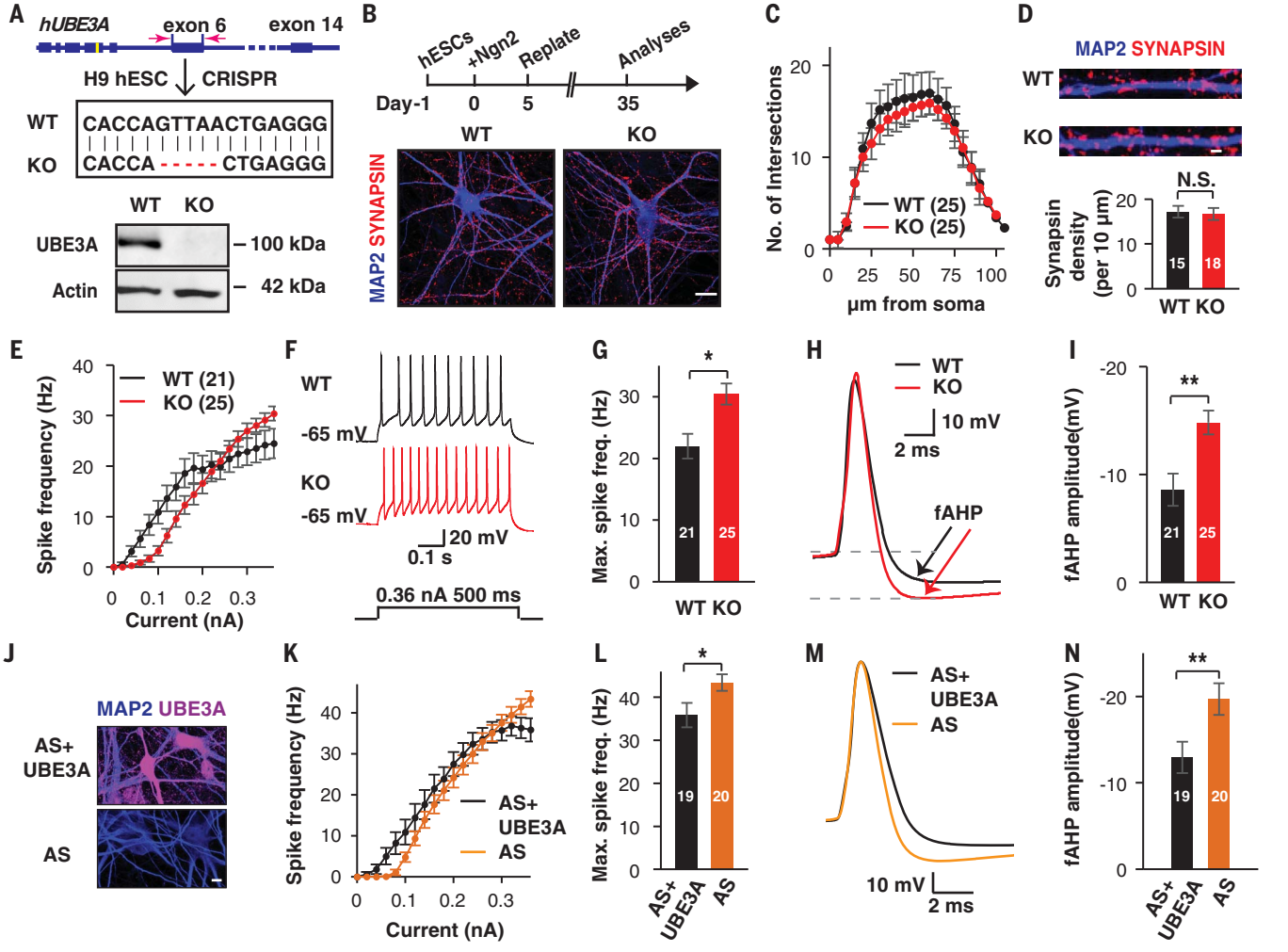

Fig. 1. Altered functional properties of UBE3A-deficient human neurons. (**A** to **D**) Generation of human induced neurons from WT and *UBE3A* KO hESCs. (A) Schematic illustrating the CRISPR-Cas9-mediated gene editing approach used to knock out *UBE3A* in hESCs (top) and immunoblot showing the absence of UBE3A protein in *UBE3A* KO hESCs (bottom). (B) Schematic illustrating the protocol used to generate the human neurons used in this study (top) and representative morphological images of day-35 WT and KO neurons immunostained for MAP2 (blue) and synapsin (magenta) (bottom). Scale bar, 20 μm. (C) Sholl analysis of WT and KO induced neurons at day 35. (D) Representative images and quantification of synaptic puncta densities, calculated from neurons immunostained for synapsin. Scale bar, 1 μm. (**E** to **I**) Altered excitability in KO neurons (H9 derived). (E) Frequency–current (*F-I*) curves showing spike frequency versus current injections in WT and KO induced neurons. (F and G) Representative traces and quantification of maximal spike frequencies by current injection in induced WT and KO neurons. (H and I) Representative traces and quantification of spike fAHP amplitudes of induced WT and KO neurons. (**J** to **N**) Induced neurons derived from AS iPSCs showed reproduced excitability and fAHP changes. (J) Immunostaining for UBE3A in AS neurons, with and without ectopic expression of *UBE3A*. Scale bar, 10 μm. (K) *F-I* curves showing spike frequencies versus current injection in induced neurons derived from AS iPSCs. (L) Quantification of maximal spike frequencies in the current injections. (M and N) Representative traces and amplitude quantification of spike fAHP. Data represent means ± SEM. The two-tailed unpaired Student's *t* test was used for all analyses. The numerals in all bars indicate the number of analyzed neurons. $^{**}P < 0.01$; $^{*}P < 0.05$; N.S., not significant.

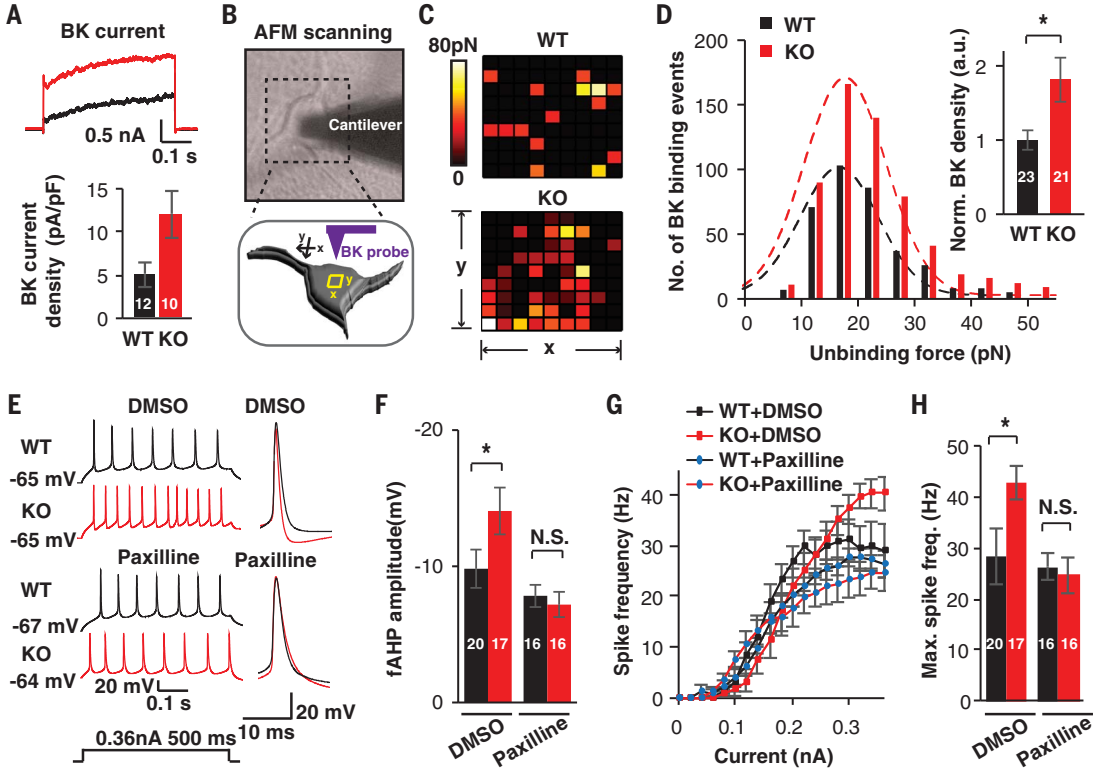

Fig. 2. *UBE3A* deletions increase BK channel function in human neurons. (**A**) Representative traces and quantification of BK currents isolated from WT and KO neurons treated with paxilline (5 μM). (**B**) Diagrams illustrating the detection of BK channels using a functionalized probe with AFM. (**C**) Representative heatmaps of specific BK probe binding events. Force–distance curves (10 data points by 10 data points) were obtained over 1-μm^2 areas. Colors indicate the measured force of specific binding events. (**D**) Unbinding force distribution and BK channel density on the surface of WT and KO neurons. (**E** to **H**) Pharmacological rescue by the BK antagonist paxilline. (E and F) Representative traces and quantification of fAHP with and without paxilline (5 μM). DMSO, dimethyl sulfoxide. (G and H) *F-I* curves showing spike frequencies versus current injections and related quantification in induced neurons. Data represent means ± SEM. In all bars, the values indicate the number of analyzed neurons. The two-tailed unpaired Student's *t* test was used. *$P < 0.05$; N.S., not significant.

normalized the differences in fAHP amplitude and AP firing frequency between KO and WT neurons, demonstrating that BK channels mediate the augmented fAHP observed in KO neurons.

UBE3A mediates ubiquitination and proteasomal degradation of BK

Next, we sought to determine how the loss of UBE3A led to BK augmentation. As UBE3A is an E3 ligase, we hypothesized that BK is one of the substrates of UBE3A-mediated ubiquitination and proteasomal degradation (*3*). To test this hypothesis, we first performed in vitro coimmunoprecipitation (IP) in heterologous cells and confirmed that there is an interaction between UBE3A and BK (fig. S6A). Second, when FLAG-tagged BK was coexpressed with hemagglutinin (HA)–tagged ubiquitin, we observed more BK ubiquitination when WT UBE3A was present than when a catalytically dead mutant (MT; C885A) was used (fig. S6B). BK ubiquitination by UBE3A was further confirmed in an in vitro ubiquitination assay using recombinant proteins (fig. S6C) and by assessing endogenous BK ubiquitination using mouse cortical neurons derived from either WT or *Ube3a*$^{m-/p+}$ mice (fig. S6, D and E). Furthermore, coexpressing BK cDNA with increasing amounts of UBE3A cDNA resulted in a corresponding decline in the BK protein level, and this decrease in the BK level was abolished by the proteasome inhibitor MG312 (fig. S6, F to H). Collectively, these data demonstrate that BK is one of the targeted substrates of UBE3A-mediated ubiquitination and proteasomal degradation. A small subset of people with AS do not carry genetic deletions in *UBE3A* but instead possess missense mutations in *UBE3A* (*2*). Ectopically expressing AS-associated *UBE3A* missense mutants (Glu^{550}→Leu, Leu^{502}→Pro) (*20*), but not an autism-associated mutant (Thr^{485}→Ala) (*21*), failed to down-regulate BK protein levels (fig. S6I), indicating that increased neuronal BK levels may also be a pathophysiological phenotype in AS patients with missense mutations in *UBE3A*. Although our data thus far suggest that UBE3A affects BK protein abundance via its E3 ligase activity, UBE3A could regulate BK levels via transcriptional modulation (*22*). However, quantitative real-time reverse transcription polymerase chain reaction (PCR) analysis revealed that there was no significant difference in BKα subunit expression between WT and KO neurons (fig. S7A). To identify which transcripts are altered by UBE3A deficiency at the genome-wide level, we performed mRNA sequencing on WT and KO neurons (fig. S7, B to D, and tables S2 to S4). Differential expression analysis showed a slight perturbation in the transcriptome overall: in total, 129 differentially expressed genes (adjusted $P < 0.05$) (figs. S7D and S8A and table S2) were identified, and all of these genes showed minor changes, as indicated by the small range of $\log_2$(fold change) values. Consistent with our quantitative PCR results, we found no significant differences in the expression levels of BK channel genes (fig. S8B and table S2). Taken together, our results support the notion that, in human neurons, UBE3A primarily regulates BK levels via a posttranslational mechanism.

A BK antagonist restores neuronal excitability and network activity in 3D organoids

One advantage of using our single-step neuronal induction protocol instead of morphogen-guided differentiation protocols is that our protocol can produce electrically mature neurons (*11*). However, neurons obtained using this protocol do not follow a normal developmental trajectory, in that they bypass the progenitor stage, raising the question of whether these functional deficits are relevant to AS disease progression. To address this issue, we generated three-dimensional (3D) cortical organoids and used this system to investigate functional changes in UBE3A-deficient neurons that follow a normal developmental maturation

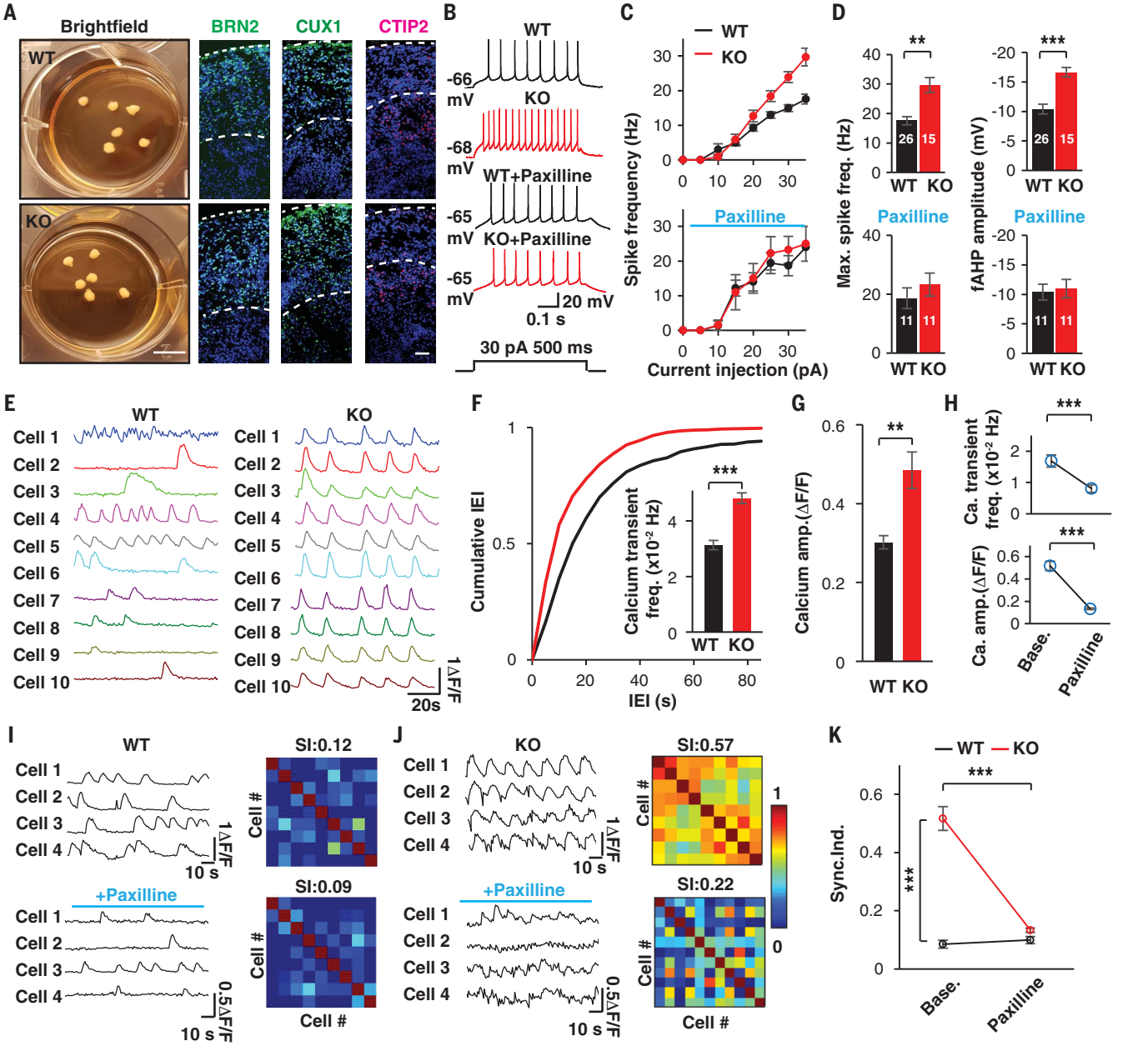

Fig. 3. Altered functional properties of neurons and enhanced network activity in UBE3A-deficient organoids. (**A**) Bright-field images of organoids and immunostaining of cortical layer markers in WT and KO organoids at day 120. Scale bars, 5 mm (bright-field images) or 50 μm (immunostaining). (**B** to **D**) Altered electrophysiological properties in neurons from KO organoids, as illustrated with representative traces (B), *F-I* curves evoked by current injection (C), and quantifications (D), with and without paxilline (10 μM). a.u., arbitrary units. (**E** to **K**) Two-photon (2P) live calcium imaging of WT and KO organoids. (E) Calcium transient traces extracted from individual neurons of WT and KO organoids. (F) Cumulative distribution of interevent intervals (IEI) in time bins for calcium transients recorded in WT and KO organoids. The inserted bar graph shows the quantification. *n* = 131 and 236 neurons from *N* = 12 and 17 organoids, respectively, for WT and KO organoids. (G) Quantification of the amplitudes of calcium transients recorded in WT and KO organoids. (H) Quantification of the frequencies and amplitudes of calcium transients before and after paxilline treatment (10 μM). *N* = 10 and 11 organoids for WT and KO, respectively. (I and J) Representative traces of calcium transients in individual neurons (left) and correlation heatmaps (right) obtained from WT (I) and KO (J) organoids. SI, synchronization index. (K) Summary of the synchronization index recorded in WT and KO organoids upon paxilline treatment (10 μM). *N* = 10 and 11 organoids for WT and KO, respectively. Data represent means ± SEM. Numerals in bars indicate the number of analyzed neurons. The two-tailed paired Student's *t* test was used for analysis of data in (H) and (K); the two-tailed unpaired Student's *t* test was used for analysis of data in all other panels. $^{**}P < 0.01$; $^{***}P < 0.001$.

sequence (*23*). These brain organoids have been shown to better recapitulate the developmental timelines of human brains (*24*). After 20 days of differentiation, both WT and KO cells produced spheroids that were indistinguishable in size. They were similarly composed of polarized, proliferating neuroepithelial cells that expressed canonical neuronal progenitor markers, including PAX6, SOX2, and NESTIN (fig. S9, A and B). These brain organoids continued to grow over the next 100 days to ~1 to 2 mm (Fig. 3A). After 120 days, immunostaining revealed the presence of a substantial number of NeuN-positive ($NeuN^+$) neurons. Consistent with previous reports, multiple

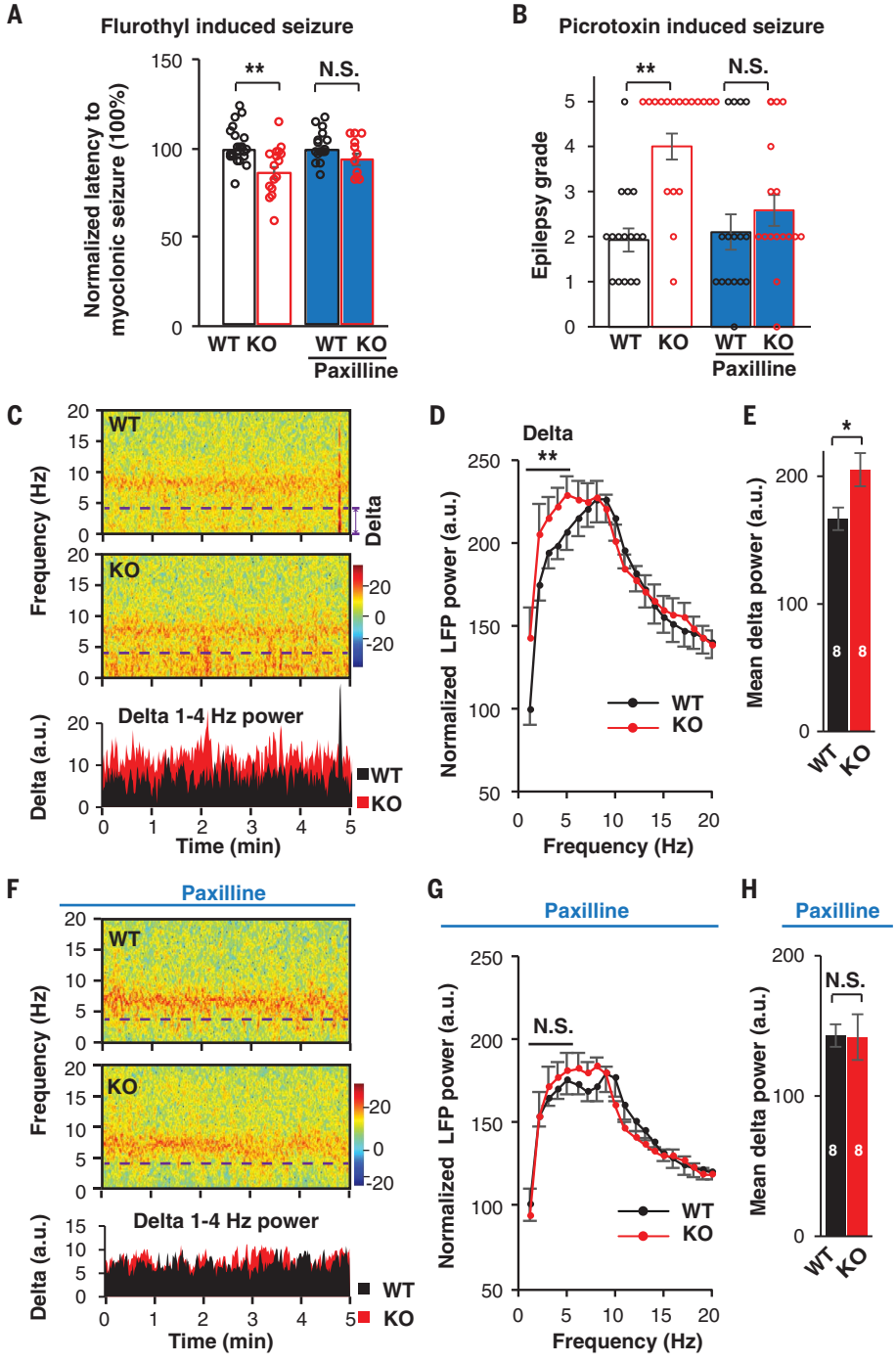

Fig. 4. BK modulation ameliorates seizure susceptibility in a mouse model of AS. (**A**) Latency to myoclonic seizure induced by flurothyl in WT and KO (*Ube3a*$^{m-/p+}$) mice. WT without paxilline, *N* = 23; KO without paxilline, *N* = 17; WT with paxilline, *N* = 16; KO with paxilline, *N* = 12. (**B**) Epilepsy grade induced by picrotoxin in WT and KO mice. WT without paxilline, *N* = 16; KO without paxilline, *N* = 18; WT with paxilline, *N* = 16; KO with paxilline, *N* = 16. (**C**) Samples of spectrogram and averaged delta power data for LFP from BIC of WT and KO mice with sound stimuli. Delta rhythmicity below the dashed line was averaged for analysis. (**D**) Summary of power spectral density (PSD) of LFP recorded from BIC of WT and KO mice with sound stimuli. *N* = 8 mice from two batches. Normalization was performed to remove the baseline difference due to batch effect. A two-way analysis of variance (ANOVA) with the Bonferroni post hoc test was used for frequencies of 1 to 4 Hz to analyze differences between WT and KO mice. (**E**) Mean delta (1 to 4 Hz) power of WT and KO mice LFPs. *N* = 8 mice from two batches. (**F**) Sample spectrogram and averaged delta power of LFPs in BIC of WT and KO mice with paxilline treatment (0.35 mg/kg; four times, at 1-hour intervals). (**G**) Summary of PSD of LFPs in BIC recorded in WT and KO mice with paxilline treatment. Two-way ANOVA with the Bonferroni post hoc test was used for frequencies of 1 to 4 Hz to analyze differences between WT and KO mice. (**H**) Mean delta power (1 to 4 Hz) of WT and KO mice LFPs with paxilline treatment. *N* = 8 mice from two batches. Numerals in bars indicate the number of animals analyzed. Data represent means ± SEM. The two-tailed unpaired Student's *t* test was used to analyze data for all panels except for (D) and (G). **P* < 0.05; ***P* < 0.01; N.S., not significant.

cortical layer markers were also observed, including BRN2/CTIP2/CUX1, and these segregated the neurons into upper and deep layers (Fig. 3A). Quantification analyses showed that there was no significant difference in the number of NeuN$^+$ neurons or the expression of the cortical layer markers between WT and KO organoids (fig. S9C). We detected a few γ-aminobutyric acid–positive (GABA$^+$) neurons, indicating the presence of inhibitory neurons, within the organoids. Glial fibrillary acidic protein–positive cells, which are indicative of mature astrocytes, were also observed in both WT and KO organoids (fig. S9D). Collectively, these data demonstrated that both the WT and KO organoids contain similar compositions of mature cortical cell types when grown in long-term cultures.

Next, we performed whole-cell patch-clamp recordings to evaluate the intrinsic properties of neurons in WT and KO organoids after 120 to 150 days in culture. Similar to the results obtained in 2D-induced neurons, pyramidal-shaped neurons within *UBE3A* KO organoids exhibited augmented excitability and elevated fAHPs (Fig. 3, B to D), whereas other electrophysiological properties remained the same, indicating that the overall developmental maturation is similar between WT and KO organoids (fig. S10, A to C). Immunoblots of BK proteins confirmed that BK levels were higher in KO organoids (fig. S10D). Paxilline treatment normalized the augmented neuronal excitability and fAHP changes observed in neurons of KO organoids (Fig. 3, B to D). We obtained similar results with cortical organoids

generated from AS iPSCs (fig. S10, E to G). Thus, our recordings performed in long-term cultured 3D human cortical organoids reproduced the phenotypes observed in 2D human neurons.

Because 3D organoids are capable of assembling more sophisticated neuronal networks than can be achieved in 2D neuronal cultures, we sought to use calcium (Ca^{2+}) imaging to monitor differences in neuronal network dynamics in large populations of cells in WT and KO cortical organoids. Incubating cortical organoids with Fluo-4AM (2 μM) resulted in labeled cells located up to 170 μm from the surface (movie S1). In WT organoids, bath application of TTX (2 μM) abolished spontaneous calcium transients (fig. S10H and movie S2). Whereas neurons in day-120 to day-150 WT organoids displayed prominent spontaneous Ca^{2+} transients, at the network level synchronization of transients was rare, and most neurons fired in a stochastic manner (Fig. 3E and movie S3) (*25*). In contrast, neurons in *UBE3A* KO organoids exhibited more frequent firing with augmented dynamic ranges of Fluo-4 fluorescence, and neurons in some KO organoids seemed to discharge regularly and synchronously (Fig. 3, E to G, and movie S3). Soma calcium transients were correlated with intrinsic neuronal activity, as indicated by the finding that the intensity of somatic Fluo-4 fluorescence gradually increased along with graded electrical train stimulations in individual neurons (fig. S10I), demonstrating that regular fluorescence fluctuations were related to intrinsic neuronal bursting, as shown in previous reports (*26*, *27*). In addition, perforated patch recordings revealed that neurons exhibit spontaneous burst firing in *UBE3A* KO organoids (fig. S10J). Paxilline treatment completely converted spontaneous burst firing into single AP firing in these neurons (fig. S10, J and K) and decreased both the frequencies and the amplitudes of calcium transients in the organoids (Fig. 3H), suggesting that augmented BK activity promoted burst firing in individual neurons and subsequent hyperactivity in the entire network. Finally, we investigated network-level synchronization in cortical organoids. We found that KO organoids and AS iPSC–derived organoids exhibited higher levels of synchronization and that this effect was abolished by treatment with paxilline (Fig. 3, I to K, and movies S3 and S4). Taken together, our data suggest that aberrant intrinsic firing of UBE3A-null neurons collectively elicits network-level hyperactivity and synchronization that resemble the seizure activity observed in AS patients (*28*).

A BK antagonist ameliorates epileptic susceptibility in a mouse model of AS

Our data thus far demonstrate that changes in intrinsic excitability are mediated by augmented BK channel activities in neurons derived from both isogenic *UBE3A* KO hESCs and AS iPSCs. Because none of these phenotypes had been previously reported in AS mouse models, we sought to determine whether they are also present in neurons obtained from mice with a maternal *Ube3*a deletion ($Ube3a^{m-/p+}$) (fig. S11A), which has been shown to recapitulate many of the symptoms associated with AS in humans (*29*). At postnatal day 28, the BK currents were significantly larger in hippocampal neurons obtained from $Ube3a^{m-/p+}$ mice than in those obtained from WT mice (fig. S11B). Similar to human neurons, changes in excitability and comparatively higher fAHP were observed in neurons obtained from $Ube3a^{m-/p+}$ mice (fig. S11, C and D) (fAHP; WT: −4.4 ± 1.4 mV, n = 26; $Ube3a^{m-/p+}$: −6.4 ± 1.2 mV, n = 29; $p <$ 0.001). Paxilline normalized these changes (fig. S11, C and D). These results indicate the presence of evolutionally conserved BK augmentation in mouse neurons that lack Ube3a, and they prompted us to test whether the enhanced seizure susceptibility observed in $Ube3a^{m-/p+}$ mice (*7*) could be normalized upon BK antagonist treatment. First, we exposed mice to the putative GABA type A receptor ($GABA_AR$) antagonist flurothyl (100 μl/min), and we observed that $Ube3a^{m-/p+}$ mice exhibited a significant reduction in the latency to myoclonic seizure, and this effect could be normalized by paxilline pretreatment [0.35 mg/kg, intraperitoneal (i.p.) injection] (Fig. 4A). Similarly, another $GABA_AR$ antagonist, picrotoxin (3 mg/kg, i.p.), induced a grade 1 to 2 seizure phenotype based on Racine's scale (*30*) in WT mice, whereas the same treatment induced a much more severe seizure phenotype (grade 5) in $Ube3a^{m-/p+}$ mice (Fig. 4B). Paxilline pretreatment was able to normalize the seizure grade of $Ube3a^{m-/p+}$ mice to a level comparable to that observed in WT mice (Fig. 4B). Next, to investigate the AS-like electroencephalogram (EEG) abnormalities observed in these mice, we recorded resting-state local field potentials (LFPs), which are analogous to intracortical EEG changes, in freely moving mice (fig. S12A) (*31*). As previously reported, compared to the WT mice, $Ube3a^{m-/p+}$ mice exhibited a strong trend toward total spectral power being increased in the delta rhythmicity (1 to 4 Hz) (Fig. 4, C to E, P = 0.0044) (*31*). We also observed increased power in other bands, including theta (4 to 8 Hz), beta (12 to 30 Hz), and gamma (30 to 80 Hz) bands, in $Ube3a^{m-/p+}$ mice, but these differences were not statistically significant (fig. S12B). Because increased delta rhythmicity has been linked to seizure susceptibility of $Ube3a^{m-/p+}$ mice (*7*), we sought to determine whether paxilline treatment could normalize the delta rhythmicity. Indeed, paxilline treatment normalized the enhancement observed in the delta band in $Ube3a^{m-/p+}$ mice (P = 0.85) (Fig. 4, F to H). Taken together, we conclude that BK augmentation similar to that observed in human *UBE3A* KO neurons is observed in neurons of $Ube3a^{m-/p+}$ mice, and paxilline treatment ameliorates the seizure threshold as well as the high delta oscillation observed in these mice.

Outlook

By characterizing the functional properties of 2D human neurons and 3D cortical organoids derived from *UBE3A* KO hESCs and AS iPSCs, we demonstrated an evolutionally conserved channelopathy that contributes to network dysfunction and hyperactivity in AS. Our results suggest that BK channels are substrates for UBE3A and that BK might thus be a therapeutic target for treatment of patients with AS.

REFERENCES AND NOTES

1. K. Buiting, C. Williams, B. Horsthemke, *Nat. Rev. Neurol.* **12**, 584–593 (2016).
2. A. M. Mabb, M. C. Judson, M. J. Zylka, B. D. Philpot, *Trends Neurosci.* **34**, 293–303 (2011).
3. G. L. Sell, S. S. Margolis, *Front. Neurosci.* **9**, 322 (2015).
4. Y. H. Jiang *et al.*, *Neuron* **21**, 799–811 (1998).
5. M. L. Wallace, A. C. Burette, R. J. Weinberg, B. D. Philpot, *Neuron* **74**, 793–800 (2012).
6. M. L. Wallace, G. M. van Woerden, Y. Elgersma, S. L. Smith, B. D. Philpot, *J. Neurophysiol.* **118**, 634–646 (2017).
7. M. C. Judson *et al.*, *Neuron* **90**, 56–69 (2016).
8. M. C. Judson *et al.*, *J. Neurosci.* **37**, 7347–7361 (2017).
9. S. J. Chamberlain *et al.*, *Proc. Natl. Acad. Sci. U.S.A.* **107**, 17668–17673 (2010).
10. J. J. Fink *et al.*, *Nat. Commun.* **8**, 15038 (2017).
11. Y. Zhang *et al.*, *Neuron* **78**, 785–798 (2013).
12. F. Yi *et al.*, *Science* **352**, aaf2669 (2016).
13. B. P. Bean, *Nat. Rev. Neurosci.* **8**, 451–465 (2007).
14. N. Gu, K. Vervaeke, J. F. Storm, *J. Physiol.* **580**, 859–882 (2007).
15. J. R. Montgomery, A. L. Meredith, *Proc. Natl. Acad. Sci. U.S.A.* **109**, 18997–19002 (2012).
16. T. Kimm, Z. M. Khaliq, B. P. Bean, *J. Neurosci.* **35**, 16404–16417 (2015).
17. J. F. Storm, *J. Physiol.* **385**, 733–759 (1987).
18. J. Sun *et al.*, *Cell Rep.* **12**, 449–461 (2015).
19. J. L. Maciaszek, H. Soh, R. S. Walikonis, A. V. Tzingounis, G. Lykotrafitis, *J. Neurosci.* **32**, 11435–11440 (2012).
20. B. Sadikovic *et al.*, *Hum. Mutat.* **35**, 1407–1417 (2014).
21. J. J. Yi *et al.*, *J. Biol. Chem.* **292**, 12503–12515 (2017).
22. S. Ramamoorthy, Z. Nawaz, *Nucl. Recept. Signal.* **6**, e006 (2008).
23. A. M. Paşca *et al.*, *Nat. Methods* **12**, 671–678 (2015).
24. I. Kelava, M. A. Lancaster, *Cell Stem Cell* **18**, 736–748 (2016).
25. P. Kirwan *et al.*, *Development* **142**, 3178–3187 (2015).
26. J. N. Kerr, D. Greenberg, F. Helmchen, *Proc. Natl. Acad. Sci. U.S.A.* **102**, 14063–14068 (2005).
27. V. Emiliani, A. E. Cohen, K. Deisseroth, M. Häusser, *J. Neurosci.* **35**, 13917–13926 (2015).
28. K. Pelc, S. G. Boyd, G. Cheron, B. Dan, *Seizure* **17**, 211–217 (2008).
29. Y. Jiang, T. F. Tsai, J. Bressler, A. L. Beaudet, *Curr. Opin. Genet. Dev.* **8**, 334–342 (1998).
30. R. J. Racine, *Electroencephalogr. Clin. Neurophysiol.* **32**, 281–294 (1972).
31. M. S. Sidorov *et al.*, *J. Neurodev. Disord.* **9**, 17 (2017).

ACKNOWLEDGMENTS

We thank E. Chua and N. Meenubharathi for their assistance in cell culture, molecular cloning, and Western blotting and N. Harmston for help with RNA sequencing (RNA-seq) data processing. We thank C. Yong (ZJU) for sharing the BK plasmid. We thank G. Augustine, J. Lee, and W.-K. Ho for valuable discussions. We thank S.T. Li (SJTU) for help with animal epilepsy experiments. We thank the Advanced Bioimaging Core of Duke-NUS/SingHealth for their technical support with multiphoton microscopy.
Funding: This work was supported by the Singapore Ministry of Education (MOE) Academic Research Fund (MOE2014-T2-2-071 to H.S.J.), a National Medical Research Council Collaborative

Research Grant (NMRC/OFIRG/0050/2017 to A.X.S. and H.S.J.), a KHOO Bridge funding (Duke-NUS-KBrFA/2017/0004 to H.S.J.), a Duke-NUS Signature Research Program block grant (to H.S.J. and K.I.), a Khoo Postdoctoral Fellowship Award (Duke-NUS-KPFA/2016/0007 to M.F.), the National Parkinson's Disease Translational Clinical Research Program fund (NMRC/TCR/013-NNI/2014 to E.K.T.), a Singapore Translational Research Investigator Award (NMRC/STaR/014/2013 to E.K.T.), and an NMRC Young Investigator Research Grant (NMRC/OFYIRG/0022/2016) to O.J.L.R. **Author contributions:** A.X.S., cell culture, biochemistry, and molecular biology experiments. Q.Y., electrophysiology, biochemistry, and molecular biology experiments and behavioral tests. M.F., organoid Ca^{2+} imaging. W.Y., organoid electrophysiology. H.Y. and Y.-H.J., mouse electrophysiology. G.G.Y.L. and K.L.L., ubiquitin assays. M.H.N. and C.T.L., AFM. G.A.D., S.A.C., and O.J.L.R., RNA-seq. H.-D.T., CRISPR-Cas9 genome editing. Y.I. and K.I., co-IP and biochemistry. D.W. and H.L., cell culture and gene expression. S.W.L.L., cell culture and biochemistry. J.T., biochemistry. Y.Y.C and M.Z., imaging. E.K.T. and H.H.N., research support and data discussion. A.X.S., Q.Y., and H.S.J. conceived and designed the study and wrote the manuscript, with input from all members. **Competing interests:** The authors declare no competing interests. **Data and materials availability:** RNA sequencing raw data and counts were deposited in the Gene Expression Omnibus with accession number GSE120225.

SUPPLEMENTARY MATERIALS

science.sciencemag.org/content/366/6472/1486/suppl/DC1
Materials and Methods
Figs. S1 to S13
Tables S1 to S5
References (*32*–*47*)
Movies S1 to S4

View/request a protocol for this paper from *Bio-protocol*.

26 September 2018; resubmitted 29 September 2019
Accepted 13 November 2019
10.1126/science.aav5386

REPORT

MATERIALS SCIENCE

Intragranular three-dimensional stress tensor fields in plastically deformed polycrystals

Yujiro Hayashi*, Daigo Setoyama, Yoshiharu Hirose, Tomoyuki Yoshida, Hidehiko Kimura

The failure of polycrystalline materials used in infrastructure and transportation can be catastrophic. Multiscale modeling, which requires multiscale measurements of internal stress fields, is the key to predicting the deformation and failure of alloys. We determined the three-dimensional intragranular stress tensor fields in plastically deformed bulk steel using a high-energy x-ray microbeam. We observed intragranular local stresses that deviated greatly from the grain-averaged stresses and exceeded the macroscopic tensile strength. Even under deformation smaller than the uniform elongation, the intragranular stress fields were in highly triaxial stress states, which cannot be determined from the grain-averaged stresses. The ability to determine intragranular stress tensor fields can facilitate the understanding and prediction of the deformation and failure of materials through multiscale modeling.

Polycrystalline materials such as steel are ubiquitous in infrastructure and transportation industries. The failure of such materials caused by the accumulation of deformation can be catastrophic. Plastic deformation of single crystals is predictable because the stress tensors acting along slip planes can be determined from macroscopic loads. For polycrystalline materials, multiscale modeling is required to predict the deformation of a huge number of grains and multiscale microstructures (*1*). Establishing a multiscale model requires nondestructive, multiscale, observational data for the three-dimensional (3D) fields of the stresses and plastic strains in bulk polycrystals and their evolution produced by plastic deformation (*2*). Nondestructive, multiscale 3D observations of the plastic strains and microstructures in bulk polycrystals have become possible using a variety of synchrotron-based x-ray diffraction and imaging techniques, including x-ray computed tomography (CT) (*3*), scanning x-ray diffraction CT (*4*), scanning Laue diffraction microscopy (*5*), diffraction contrast tomography (DCT) (*6*), 3D x-ray diffraction microscopy (3DXRD) (*7*–*11*), scanning 3DXRD (*12*), differential-aperture x-ray microscopy (DAXM) (*13*–*15*), dark-field x-ray microscopy (DFXM) (*16*), and Bragg coherent diffraction imaging (*17*, *18*). Nevertheless, advances in 3D multiscale measurements of the stress tensors in bulk polycrystals are still needed because stresses cause only small changes in the scattering directions of diffracted x-rays compared with the changes caused by plastic strain–induced crystallographic rotations.

Toyota Central R&D Laboratories, Nagakute, Aichi 480-1192, Japan.
*Corresponding author. Email: y-hayashi@mosk.tytlabs.co.jp

Generally, 3DXRD allows for grain-resolved 3D measurements of stress tensors for embedded grains in bulk polycrystals using synchrotron-based, high-energy x-rays. Grain-averaged stress tensors, called type II stresses, are obtained by determining the lattice parameters of individual grains from multiple diffraction spots per grain (*19*). 3DXRD-based type II stress evaluation is a useful method for materials science (*20*, *21*), modeling (*22*, *23*), and engineering (*24*–*26*). One example is the study from Sedmak *et al.*, which determined the macroscopic (type I) stress tensor fields in a tensioned polycrystalline alloy using the type II stress tensors they measured to verify martensite transformation models (*20*). Their work also showed the deviation of type II stresses from the type I stress fields. Abdolvand *et al.* used type II stresses that they measured to verify crystal plasticity models and found a valid model for predicting type II stresses based on the orientations of neighboring grains (*23*). However, 3DXRD cannot be used to measure intragranular local stress tensors, called type III stresses. The measurement of these stresses, which reveal the stress tensor fields in individual grains, is the key to verifying state-of-the-art multiscale models.

Using DAXM allows for the nondestructive measurement of type III stresses by scanning a focused polychromatic x-ray beam and detecting multiple Laue diffraction spots per grain (*27*). However, DAXM is limited to the measurement of near-surface grains because the polychromatic x-ray illumination of numerous grains causes massive overlap of diffraction spots. DFXM imaging of type III elastic strain fields in embedded single grains in bulk polycrystals can be accomplished by magnifying individual diffraction spots (*28*). However, determining a type III stress tensor is challenging because the six tensor components must be calculated by detecting multiple diffraction spots per grain. Additionally, stress tensor measurement in grains with plastic strains is difficult because small changes in the x-ray scattering directions caused by shear stress components become buried in the more dominant changes caused by crystallographic rotations.

Obtaining 3D type III stress measurements for nondeformed bulk polycrystals requires scanning 3DXRD, where the intragranular local lattice parameters in deeply embedded grains are determined from multiple diffraction spots per grain, detected using a focused monochromatic high-energy x-ray beam (*29*). The six stress tensor components in nondeformed polycrystals with small intragranular misorientations are obtained by determining six lattice parameters (*19*). The six stress tensor components are derived using the differences in the lattice parameters between strained and unstrained grains. However, type III stress measurement for plastically deformed bulk alloys is still difficult because the six lattice parameters of strained grains cannot be accurately determined because of large, intragranular misorientations.

We overcame this obstacle by determining elastic strains directly from the difference in lattice spacing between strained and unstrained grains, without needing to accurately determine the six lattice parameters of strained grains. We determined six stress tensor components from the elastic strains in various directions, which we obtained by detecting multiple diffraction spots per grain. Our analysis using the multiple diffraction spots also allows us to measure intragranular local stresses. The difference in the position of a diffraction spot caused by an intragranular local stress is small because the focused x-ray beam penetrates the grain. The sensitivity to the local stress is increased by penetrating the region with the local stress from various directions and detecting multiple diffraction spots. We also detected non-overlapping diffraction spots from plastically deformed, millimeter-sized bulk steel with a large number of grains using a conical slit. Thus, we achieved the 3D visualization of the difference between type II and type III stress tensor fields (Fig. 1) (*30*). Although we still need to overcome some remaining limitations, such as intragranular averaging and artifacts for quantitative reconstruction (*30*), this demonstration reveals the existence of type III stress tensor fields with complex distributions and type III stresses that deviated greatly from type II stresses. These stresses are important for materials modeling.

We conducted the scanning 3DXRD measurements at beamline BL33XU (*31*) of SPring-8 for low-carbon steel with a mean grain size of 20 μm, a yield strength of σ_{YS} = 230 MPa, a

tensile strength of σ_{TS} = 330 MPa, a uniform elongation of 10.5%, and a total elongation of 25% (figs. S2 and S3). We illuminated a low-carbon steel sample with a 1 μm–by–1 μm x-ray microbeam. We detected diffracted beams through the conical slit as diffraction spots on an area detector (Fig. 1B). We continuously acquired diffraction images every 0.6° for 180° with an exposure time of 38 ms while we rotated the sample around its z axis. We conducted this scan at an interval of 1.2 μm in the y direction for 20 min. We repeated the 2D scan at an interval of 1.2 μm in the z direction for 12 hours. We mapped the orientations of αFe and elastic strains for 37^3 voxels with a voxel size of 1.2 μm by 1.2 μm by 1.2 μm using a cluster computer from 3.5×10^5 diffraction images acquired by the 3D scan. This task took 1 week to complete.

The sample was elongated by 5.1% in the z direction (Fig. 1A). After stress relaxation from 302 to 290 MPa, we obtained the 3D maps of the elastic strains. The average of the type III longitudinal elastic strains, ε_{zz}, after the 5.1% elongation agreed with the macroscopic strain of 1×10^{-3} at the macroscopic elastic limit. The averages of the type III transverse elastic strains, ε_{xx} and ε_{yy}, were -2×10^{-4} and -3×10^{-4}, respectively, and they were consistent with the Poisson effect. Though the intragranular averaging remains, we observed type III strains of up to 2×10^{-3} (Fig. 2A). We estimated the lower limits of the spatial resolutions to be two and four voxels for the type III longitudinal and transverse strains, respectively, using a reconstruction simulation (*30*). Similar high intragranular local elastic strains have been found using high–angular resolution electron backscatter diffraction (HR-EBSD) (*32*). The HR-EBSD method can detect higher local elastic strains (*33*) because of its higher spatial resolution compared with that of scanning 3DXRD. However, HR-EBSD is limited to surface strain measurements.

We converted the elastic strain tensors into stress tensors using the elastic stiffness constants of αFe and the grain orientations, thereby obtaining the 3D type III stress tensor fields (2D, see fig. S40 and movie S3; 3D, see fig. S42 and movie S4). We then compared the type II and type III stress tensors (Fig. 2B). The type III longitudinal stresses (σ_z) reached 500 MPa beyond σ_{TS}, whereas the type II σ_z did not exceed σ_{TS}. The type I σ_z (average for all voxels) was 240 MPa, which approximately agrees with the applied load. Even though no loads were applied in the transverse directions (x and y), we observed type III transverse stresses (σ_x and σ_y) comparable to σ_{TS}. These high type III stresses were not observed before the 5.1% elongation (2D, see fig. S36 and movie S1; 3D, see fig. S38 and movie S2).

In continuum mechanics and failure theories, many stress criteria have been proposed

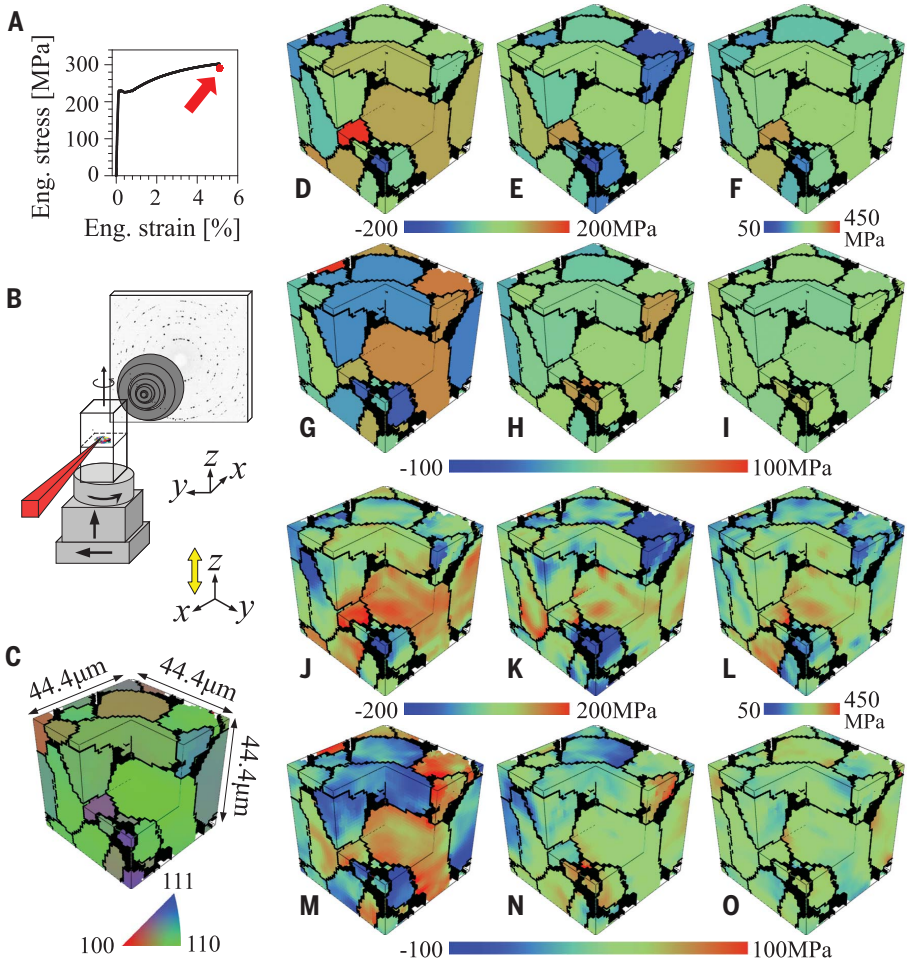

Fig. 1. 3D type II and type III stress tensor fields in plastically deformed bulk steel. (**A**) In situ stress–strain curve. After 5.1% elongation, the scanning 3DXRD measurement was conducted under an applied tensile load of 290 MPa, indicated by the red arrow and red dot. The tensile direction was parallel to the z direction. Eng., engineering. (**B**) Schematic diagram of scanning 3DXRD setup with a conical slit. (**C**) 3D orientation map. Orientation is represented by the inverse pole figure for the tensile direction. (**D** to **I**) 3D grain-averaged (type II) maps of (D) σ_x, (E) σ_y, (F) σ_z, (G) τ_{xy}, (H) τ_{yz}, and (I) τ_{zx}, where σ_x is a normal stress in the x direction and τ_{xy} is a shear stress on the plane normal to the x axis acting in the y direction. (**J** to **O**) 3D intragranular (type III) fields of (J) σ_x, (K) σ_y, (L) σ_z, (M) τ_{xy}, (N) τ_{yz}, and (O) τ_{zx}.

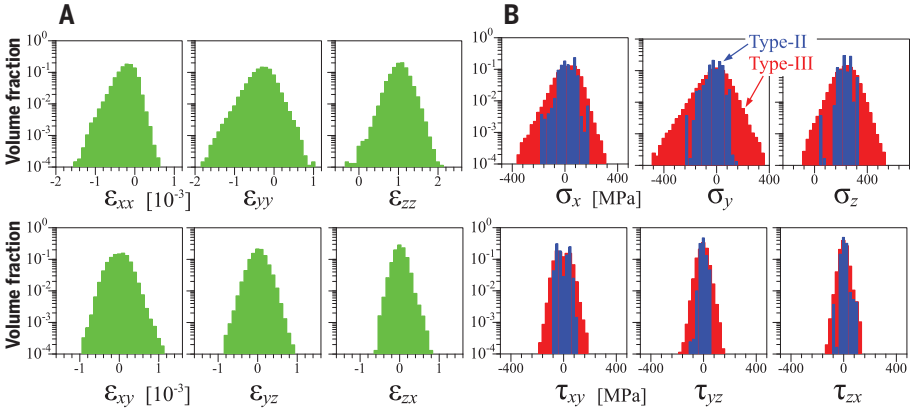

Fig. 2. Statistical comparison of type II and type III stress tensors. (**A**) Histograms of the volume fractions of elastic strain tensors with a bin width of 1×10^{-4}. (**B**) Histograms of the volume fractions of type II and type III stress tensors with a bin width of 25 MPa.

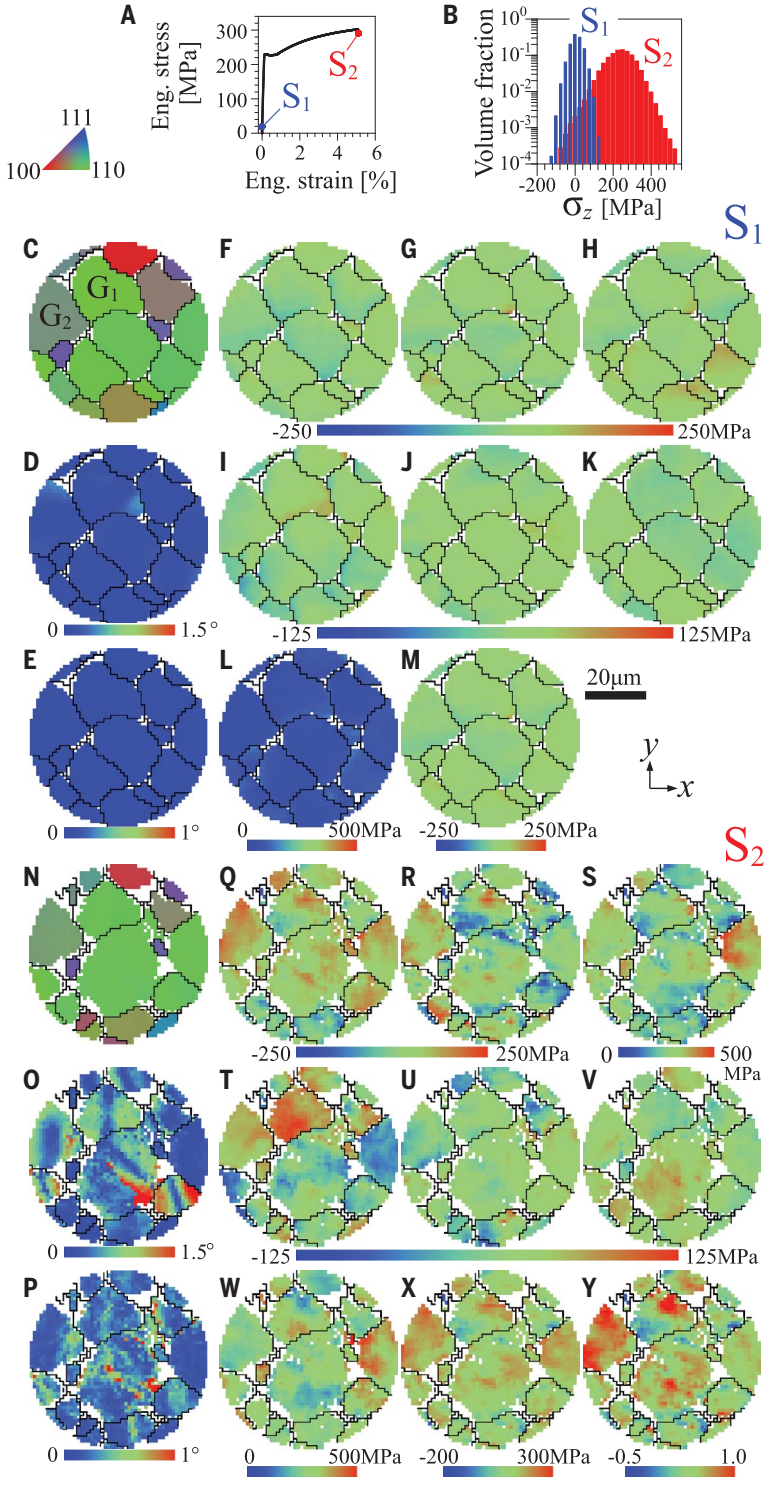

Fig. 3. Type III stress tensor fields obtained before and after plastic deformation. (**A**) In situ stress–strain curve. Orientation maps and stress tensor fields were obtained at S_1 and S_2 (stress–strain states 1 and 2). (**B**) Histograms of the volume fractions of σ_z with a bin width of 25 MPa at S_1 and S_2. Histograms for the other strain and stress components are shown in figs. S44 and S45. 2D maps (z = 4.8 μm) of (**C**) orientation, (**D**) intragranular misorientation (IGM), and (**E**) kernel-averaged misorientation (KAM) obtained at S_1, where KAM was evaluated in individual grains. (**F** to **K**) 2D fields of (F) σ_x, (G) σ_y, (H) σ_z, (I) τ_{xy}, (J) τ_{yz}, and (K) τ_{zx} obtained at S_1. (**L** and **M**) 2D maps of (L) σ_e and (M) σ_m obtained at S_1, where σ_e is the equivalent stress and σ_m is the mean stress. (**N** to **P**) 2D maps of (N) orientation, (O) IGM, and (P) KAM obtained at S_2. (**Q** to **V**) 2D fields of (Q) σ_x, (R) σ_y, (S) σ_z, (T) τ_{xy}, (U) τ_{yz}, and (V) τ_{zx} obtained at S_2. (**W** to **Y**) 2D maps of (W) σ_e, (X) σ_m, and (Y) σ_m/σ_e obtained at S_2, where σ_m/σ_e is the stress triaxiality.

for predicting yielding and failure in ductile alloys. The von Mises (or equivalent) stress, σ_e, calculated using six stress tensor components, is most commonly used to predict yielding. An important stress component, or factor, for predicting ductile failure is hydrostatic (or mean) stress, σ_m, or stress triaxiality, σ_m/σ_e (*34*). High σ_m/σ_e limits plastic deformation and leads to the growth and coalescence of voids that originate at inclusions. We produced maps of σ_e, σ_m, and σ_m/σ_e in the *xy* plane from the type III stress tensors obtained before and after 5.1% elongation (2D, see Fig. 3, figs. S37 and S41, and movie S5; 3D, see figs. S39 and S43 and movie S6). Even under the small 5.1% elongation, the highest type III σ_m/σ_e was approximately three times as high as the average (0.35) and the macroscopic σ_m/σ_e (0.33) for uniaxial uniform elongation (fig. S45). This raises the question of how low-carbon steel can endure such high stress triaxiality until the total elongation at fracture. In general, plastic strain is coupled with stress triaxiality as a failure criterion. Although plastic strain cannot be directly derived, the increase in misorientation implies the production of plastic strain, because plastic deformation in low-carbon steel is caused by the slipping of crystal planes, which leads to local crystallographic rotations. We observed deformation-induced local misorientations, as shown in the kernel-averaged misorientation (KAM) maps obtained before and after the 5.1% elongation (Fig. 3, E and P), where KAM was evaluated in individual grains. We found that the positions of high KAM do not necessarily agree with those of high stress triaxiality, as shown in grains G_1 and G_2 (Fig. 3, P and Y). We speculate that low-carbon steel can endure high local stress triaxiality under the 5.1% elongation because of the nonuniform distribution of plastic strain, where the small local plastic strain in the high-triaxiality region is compensated by the large plastic strain in the adjacent region. The local plastic strain grows with further elongation and eventually reaches the plastic failure strain in high-triaxiality regions.

In addition to high type III σ_m/σ_e, we observed the coexistence of high and low σ_m/σ_e in single grains, which resulted in moderate type II σ_m/σ_e, as shown in G_1 (Fig. 3Y). We compared some type III and type II stresses as a function of position in the *xy* plane (Fig. 4). In G_1, the type III σ_z ranges from 20 ± 100 to 470 ± 170 MPa, and the type II σ_z is 280 MPa (Fig. 4D), where the measurement errors of the type III stresses were evaluated from the deviations of forces from equilibrium (*30*). The type III σ_z reaches 520 ± 160 MPa inside G_1 (Fig. 4E) and 560 ± 100 MPa near the grain boundary in grain G_3 (Fig. 4H). In G_3, the type III σ_x and σ_y range from 10 ± 93 to 390 ± 94 MPa and from 10 ± 130 to 430 ± 140 MPa,

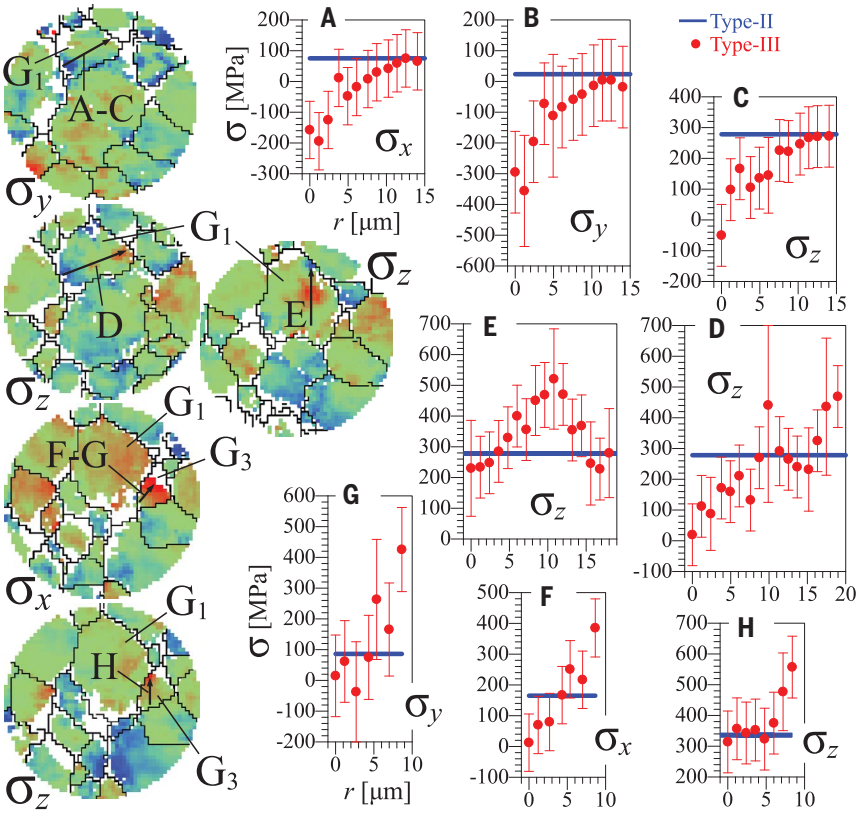

Fig. 4. Type III stresses that deviated markedly from type II stresses as a function of position. Type III (**A**) σ_x and (**B**) σ_y at z = 1.2 μm and σ_z at (**C**) z = 1.2 μm, (**D**) z = 6.0 μm, and (**E**) z = 12.0 μm, as a function of position in grain G_1. Type III (**F**) σ_x and (**G**) σ_y at z = 18.0 μm and (**H**) σ_z at z = 20.4 μm, as a function of position in grain G_3. The type III stresses were extracted from the unsmoothed stress maps shown in fig. S29 and movie S7. Type II stresses are represented by solid lines, which are independent of position in each grain. Error bars indicate the measurement errors of the type III stresses, evaluated from the deviations of forces from equilibrium.

respectively, and the type II σ_x and σ_y are 170 and 90 MPa, respectively (Fig. 4, F and G). The type III σ_x and σ_y reach compressive maximum values of −190 ± 93 and −360 ± 180 MPa, respectively, near the boundary in G_1 (Fig. 4, A and B).

The macroscopic σ_{YS} increases with decreasing grain size and satisfies the Hall-Petch equation as a function of grain size. The Hall-Petch equation for low-carbon steel predicts that σ_{YS} will increase from 234 MPa for a grain size of 20 μm to 700 MPa for a grain size of 1 μm. The strong dependence of σ_{YS} on grain size means that the plastic deformation resistance (pinning of dislocation propagation) is localized near grain boundaries. Therefore, local regions with high strength, including inclusions inside grains, may exist even in coarse-grained steel. Although the reconstruction became difficult for voxels near grain boundaries, the number of voxels with σ_z > 450 MPa was 0.3% of the total number of reconstructed voxels after plastic deformation. This means that 5% elongated, coarse-grained low-carbon steel with a grain size of 20 μm contains tensile longitudinal stress corresponding to the σ_{YS} of fine-grained low-carbon steel with a grain size of 3 μm at a volume ratio of at least 0.3%.

We achieved intragranular 3D stress tensor measurements for plastically deformed bulk polycrystalline materials by overcoming grain averaging. Although the intragranular averaging of stress fields remains, we determined 3D stress tensor fields with complex distributions in individual grains for elongated bulk steel. The intragranular stresses we observed deviated by a value as high as the yield strength from the grain-averaged stresses. The stress fields were in highly triaxial stress states under plastic deformation smaller than the uniform elongation. The ability to nondestructively map intragranular 3D stress tensors voxel by voxel for multiple grains will facilitate the development of materials modeling for predicting the observed evolution of local stresses, stress triaxiality, and plastic strains as yielding and failure criteria. Advancement in multiscale materials modeling, which connects material responses at the nanoscale to the macroscopic mechanical behavior, is crucial for the quantitative prediction of key properties concerning the plastic deformation, creep, fatigue, and fracture of engineering alloys.

REFERENCES AND NOTES

1. R. Pippan, P. Gumbsch, Eds., *Multiscale Modelling of Plasticity and Fracture by Means of Dislocation Mechanic* (Springer, 2010).
2. R. Suter, *Science* **356**, 704–705 (2017).
3. E. Maire, P. J. Withers, *Int. Mater. Rev.* **59**, 1–43 (2014).
4. P. Bleuet *et al.*, *Nat. Mater.* **7**, 468–472 (2008).
5. F. Hofmann *et al.*, *Nat. Commun.* **4**, 2774 (2013).
6. A. King, G. Johnson, D. Engelberg, W. Ludwig, J. Marrow, *Science* **321**, 382–385 (2008).
7. L. Margulies, G. Winther, H. F. Poulsen, *Science* **291**, 2392–2394 (2001).
8. S. Schmidt *et al.*, *Science* **305**, 229–232 (2004).
9. B. Jakobsen *et al.*, *Science* **312**, 889–892 (2006).
10. H. F. Poulsen, *Three-Dimensional X-ray Diffraction Microscopy: Mapping Polycrystals and Their Dynamics* (Springer, 2004).
11. H. F. Poulsen, *J. Appl. Cryst.* **45**, 1084–1097 (2012).
12. Y. Hayashi, Y. Hirose, Y. Seno, *J. Appl. Cryst.* **48**, 1094–1101 (2015).
13. B. C. Larson, W. Yang, G. E. Ice, J. D. Budai, J. Z. Tischler, *Nature* **415**, 887–890 (2002).
14. L. E. Levine *et al.*, *Nat. Mater.* **5**, 619–622 (2006).
15. G. E. Ice, J. D. Budai, J. W. Pang, *Science* **334**, 1234–1239 (2011).
16. H. Simons *et al.*, *Nat. Commun.* **6**, 6098 (2015).
17. A. Yau, W. Cha, M. W. Kanan, G. B. Stephenson, A. Ulvestad, *Science* **356**, 739–742 (2017).
18. M. J. Cherukara *et al.*, *Nat. Commun.* **9**, 3776 (2018).
19. J. Oddershede *et al.*, *J. Appl. Cryst.* **43**, 539–549 (2010).
20. P. Sedmák *et al.*, *Science* **353**, 559–562 (2016).
21. L. Renversade, A. Borbély, *J. Appl. Cryst.* **50**, 1144–1157 (2017).
22. T. Turner *et al.*, *Metall. Mater. Trans. A* **48**, 627–647 (2017).
23. H. Abdolvand, J. Wright, A. J. Wilkinson, *Nat. Commun.* **9**, 171 (2018).
24. J. Oddershede *et al.*, *Acta Mater.* **60**, 3570–3580 (2012).
25. J. C. Schuren *et al.*, *Curr. Opin. Solid State Mater. Sci.* **19**, 235–244 (2015).
26. D. Naragani *et al.*, *Acta Mater.* **137**, 71–84 (2017).
27. Y. Guo *et al.*, *Acta Mater.* **96**, 229–236 (2015).
28. H. Simons *et al.*, *Nat. Mater.* **17**, 814–819 (2018).
29. Y. Hayashi, D. Setoyama, Y. Seno, *Mater. Sci. Forum* **905**, 157–164 (2017).
30. Materials and methods are available as supplementary materials.
31. T. Nonaka *et al.*, *AIP Conf. Proc.* **1741**, 030043 (2016).
32. A. J. Wilkinson, G. Meaden, D. J. Dingley, *Mater. Sci. Technol.* **22**, 1271–1278 (2006).
33. M. Ojima, Y. Adachi, S. Suzuki, Y. Tomota, *Acta Mater.* **59**, 4177–4185 (2011).
34. G. Mirone, *Eng. Fract. Mech.* **74**, 1203–1221 (2007).

ACKNOWLEDGMENTS

The authors thank H. Ohashi and H. Yumoto for the x-ray optics design, Y. Seno and Y. Takatani for assistance in the experiments, and

T. Ohsuna for comments on the manuscript. **Funding:** This research received no specific grants from any funding agency. **Author contributions:** Y.Ha., D.S., and Y.Hi. designed the research. Y.Ha. and T.Y. performed the experiments. Y.Ha. and H.K. wrote the manuscript. All authors discussed the results and commented on the manuscript. **Competing interests:** The authors declare no conflicts of interest. **Data and materials availability:** Raw data were generated at SPring-8. The derived data are available from https://github.com/Scanning3DXRDpublish/2017B7002.

SUPPLEMENTARY MATERIALS

science.sciencemag.org/content/366/6472/1492/suppl/DC1
Materials and Methods
Supplementary Text
Figs. S1 to S45
References (*35*–*89*)
Movies S1 to S8

4 May 2019; accepted 13 November 2019
10.1126/science.aax9167

QUANTUM GASES

Dissipation-induced structural instability and chiral dynamics in a quantum gas

Nishant Dogra*, Manuele Landini†, Katrin Kroeger, Lorenz Hruby, Tobias Donner‡, Tilman Esslinger

Dissipative and unitary processes define the evolution of a many-body system. Their interplay gives rise to dynamical phase transitions and can lead to instabilities. In this study, we observe a nonstationary state of chiral nature in a synthetic many-body system with independently controllable unitary and dissipative couplings. Our experiment is based on a spinor Bose gas interacting with an optical resonator. Orthogonal quadratures of the resonator field coherently couple the Bose-Einstein condensate to two different atomic spatial modes, whereas the dispersive effect of the resonator losses mediates a dissipative coupling between these modes. In a regime of dominant dissipative coupling, we observe the chiral evolution and relate it to a positional instability.

In a many-body system, unitary processes generally give rise to coherent evolution, whereas dissipative processes lead to stationary states (*1*). The interplay of these two types of processes in a driven-dissipative setting can influence a many-body system in profound ways. Examples are dissipative phase transitions (*2*–*9*), the emergence of new universality classes (*10*, *11*), dissipation-induced topological effects (*12*), complex dynamics (*13*), and the splitting of multicritical points (*14*). In this study, we observe a phenomenon in which chiral nonstationary dynamics emerges if the energy scales of dissipative and unitary processes are similar. In our experiment, we use a quantum gas to create a driven many-body system with controllable unitary and dissipative couplings. This allows us to explore the system's macroscopic behavior at the boundary between stationary and nonstationary states. We gain a conceptual understanding of the observed dynamics by considering dissipation as a structure-dependent force, analogous to mechanical nonconservative positional forces (*15*–*17*). In addition, our observations permit us to draw connections to limit cycles (*18*, *19*).

Our experiment consists of a spinor Bose-Einstein condensate (BEC) of two different Zeeman states that is coherently coupled to two different spatial atomic configurations (*20*): One coupling induces a density mode (DM) in which the density of the gas shows a checkerboard modulation, whereas the other coupling favors a spin mode (SM) in which the gas instead develops a checkerboard modulation of the spin degree of freedom (unit cells are shown in Fig. 1A). These coherent couplings are mediated via photons scattered by the atomic system from a standing-wave transverse pump laser field into a high-finesse optical cavity mode (Fig. 1B). The DM and the SM interact with orthogonal quadratures of the cavity mode. We engineer a dissipative coupling in this system, exploiting the finite cavity decay rate κ and the associated phase shift of the intracavity field across the cavity resonance: The light field scattered from the pump into the cavity acquires a phase shift ϕ_κ that effectively mixes the orthogonal quadratures, giving rise to a dissipative coupling between the DM and the SM (Fig. 1, A and B).

The strengths λ_D and λ_S of the coherent couplings between the BEC and the DM or the SM, respectively, are tuned by the lattice depth V_{TP} and polarization angle φ of the transverse pump (*20*). These couplings soften the effective excitation frequencies ω_D and ω_S of both modes, such that at a critical lattice depth the frequency of the more strongly coupled mode vanishes. This mode can then be macroscopically occupied, and the system undergoes a self-organization phase transition (*21*), breaking a spatial Z(2) symmetry. Simultaneously, the corresponding quadrature of the cavity mode is coherently populated, which we detect with a heterodyne detection system analyzing the light field leaking from the cavity (*22*).

The cavity-induced phase shift ϕ_κ and hence the dissipative coupling strength K^2 between

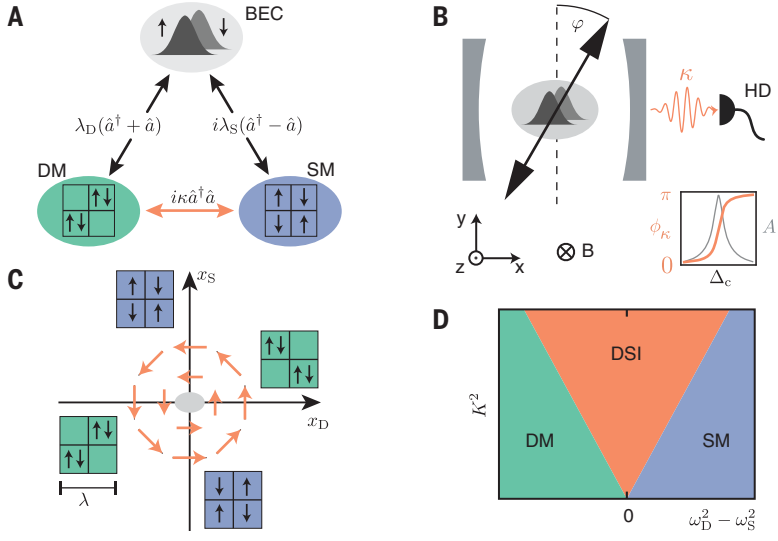

Fig. 1. Engineered dissipative coupling. (**A**) A spinor BEC containing a mixture of two Zeeman states (depicted by up and down arrows) is coherently coupled with rates λ_D and λ_S to a DM and an SM, respectively, via the two quadratures of a cavity field with annihilation operator $\hat{a}$. A dissipative coupling (orange arrow) between DM and SM is induced by the phase response of the cavity. Occupation of the DM (SM) leads to a density (spin) modulation, displayed as atoms occupying the same (opposite) checkerboard lattice sites of an exemplary green (blue) two-by-two square unit cell of dimensions λ by λ, where λ is the wavelength of the transverse pump field (see below). (**B**) The spinor BEC is coupled with a cavity mode and irradiated by a standing-wave transverse pump in the *z* direction with linear polarization (black arrow) at angle φ with respect to the *y* direction. The magnetic field B is oriented along the *z* direction. Light leaking out of the cavity at decay rate κ is analyzed via a heterodyne detector (HD). (Inset) Phase ϕ_κ and amplitude *A* response of the cavity as a function of detuning Δ_c. (**C**) Dissipation acts like a chiral force (orange); here, x_D (x_S) represents the amplitude of the density (spin) modulation. (**D**) Schematic representation of three different regimes as a function of dissipative coupling strength K^2 and detuning between the frequencies ω_D and ω_S of the DM and SM, respectively. The green (blue) region represents the DM (SM) being dominantly coupled to the spinor BEC.

Institute for Quantum Electronics, ETH Zurich, CH-8093 Zurich, Switzerland.
*Present address: Cavendish Laboratory, University of Cambridge, Cambridge CB3 0HE, UK. †Present address: Institut für Experimentalphysik und Zentrum für Quantenphysik, Universität Innsbruck, 6020 Innsbruck, Austria.
‡Corresponding author. Email: donner@phys.ethz.ch

the two modes can be controlled by the detuning Δ_c between the cavity resonance and the frequency of the transverse pump (*23*). The effect of this dissipative coupling can be understood in the x_D-x_S plane, where x_D and x_S represent the amplitudes of the density and spin modulation [see below and (*23*)] caused by the occupation of DM and SM, respectively (Fig. 1C). In this plane, the dissipative coupling acts as a force field that favors a rotation of the system's state around the origin: If the DM and the SM are degenerate, even an infinitesimally small dissipative coupling leads to a dissipation-induced structural instability (DSI) in which the system rotates with fixed chirality between the different atomic modes. The strength of the resulting force field increases with the strength of the dissipative coupling, such that the instability occurs also for increasingly nondegenerate modes, as qualitatively shown by the broadening of the DSI region in the schematic in Fig. 1D.

We prepare the ^{87}Rb spinor BEC with $N = (23 \pm 2) \times 10^3$ atoms in each of the different Zeeman states $|F = 1, m_F = \pm 1\rangle$, where F and m_F denote the total angular momentum and the corresponding magnetic quantum number, respectively. We linearly ramp up the lattice depth of the transverse pump in 50 ms and analyze the cavity output with our heterodyne setup. In Fig. 2, A and B, we show the mean photon number n_{ph} and phase ϕ (modulo 2π)

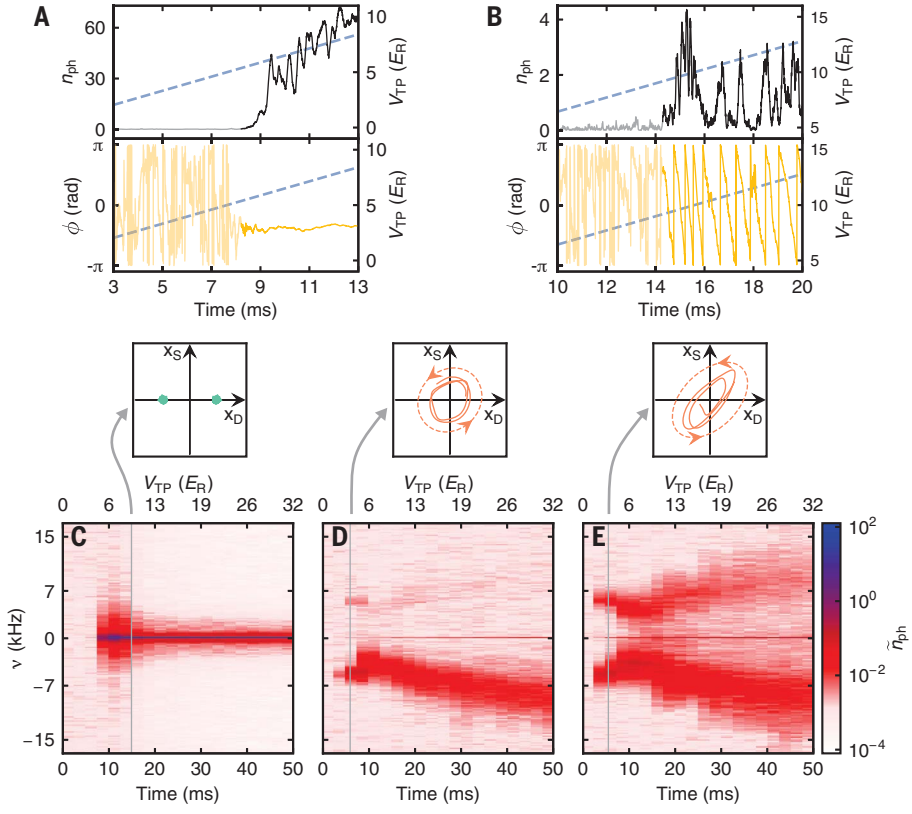

Fig. 2. Detection of the DSI. (**A** and **B**) Time evolution of the mean number of photons n_{ph} (black) in the cavity and the corresponding phase φ modulo 2π (orange) for (A) $\varphi = 58.3(1.0)°$, $\tilde{\Delta}_c/2\pi = -5.5(1)$MHz and (B) $\varphi = 63.3(1.0)°$, $\tilde{\Delta}_c/2\pi = -5.5(1)$MHz. The detuning $\tilde{\Delta}_c$ includes the effect of the atomic dispersive shift on the detuning Δ_c (*23*). The linear ramp of the lattice depth V_{TP} of the transverse pump is shown as dashed blue line. Gray and light orange lines correspond to zero occupation of the cavity. (**C** to **E**) Spectrograms showing the mean number of photons $\tilde{n}_{ph}$ as a function of frequency ν and time for (C) $\varphi = 58.3(1.0)°$, $\tilde{\Delta}_c/2\pi = -5.4(2)$ MHz; (D) $\varphi = 63.3(1.0)°$, $\tilde{\Delta}_c/2\pi = -2.5(2)$ MHz; and (E) $\varphi = 58.3(1.0)°$, $\tilde{\Delta}_c/2\pi = -2.4(2)$ MHz. A window size of 5 ms is used to construct the spectrograms, and each data set is averaged over 20 experimental realizations. Frequency ν is defined relative to the transverse pump. Corresponding insets show the evolution of the atomic state in the x_D-x_S plane extracted from the spectrograms in a duration of 500 μs at the position of the gray lines. In the inset to (C), we plot the data and its mirror about x_S to illustrate the Z(2) symmetry breaking of the self-organization phase transition. Dashed lines in the insets to (D) and (E) are the qualitative predictions of the noninteracting theory for vanishing gain (Eq. 3). All insets are rescaled with respect to each other and the theoretical lines for better visibility. Linecuts through spectrograms for similar data are presented in (*23*).

of the intracavity light field for two different sets of parameters. We find two qualitatively different behaviors: Above a critical pump power, the cavity field has a nonzero amplitude and either a well-defined (Fig. 2A) or a monotonically changing phase (modulo 2π; Fig. 2B). A well-defined phase indicates that only one quadrature of the cavity field is excited, corresponding to either the SM or the DM being populated, which is determined by the prevailing coherent coupling. In contrast, a monotonically changing phase is observed when the dissipative coupling is dominant and signals that the system is continuously evolving through the different spatial modes linked with the two quadratures of the cavity field.

The many-body Hamiltonian of the system is given by

$$\hat{H} = -\hbar\Delta_c\hat{a}^\dagger\hat{a} + \hbar\omega_0(\hat{J}_{z,+} + \hat{J}_{z,-}) + \frac{\hbar}{\sqrt{N}}\left[\lambda_D(\hat{a}^\dagger + \hat{a})(\hat{J}_{x,+} + \hat{J}_{x,-}) - i\lambda_S(\hat{a}^\dagger - \hat{a})(\hat{J}_{x,+} - \hat{J}_{x,-})\right] \quad (1)$$

where $\hat{a}(\hat{a}^\dagger)$ is the annihilation (creation) operator corresponding to the y-polarized cavity mode in the frame of the transverse pump frequency. The atomic system is represented by an ensemble of N effective "spins" in each of the two Zeeman states (labeled with ±), with $\hat{J}_{x,\pm}, \hat{J}_{y,\pm}$, and $\hat{J}_{z\pm}$ being the corresponding angular momentum operators. This pseudo-spin is constructed from the macroscopically occupied zero momentum state $|0\rangle$ of the BEC and an excited state $|k\rangle$ with a symmetric superposition of four momentum states $|p_x = \pm\hbar k,\ p_z = \pm\hbar k\rangle$, which represent one recoil momentum $\hbar k$ each in the cavity and the transverse pump direction (*21*). The wave number of the transverse laser field with wavelength λ is given by $k = 2\pi/\lambda$. For zero lattice depth V_{TP} of the transverse pump, the energy difference between the states $|0\rangle$ and $|k\rangle$ is $\hbar\omega_0 = 2E_R = \hbar^2k^2/m$, where m is the mass of a ^{87}Rb atom and $\hbar$ is Planck's constant divided by 2π. The first two terms in Eq. 1 describe the energies of the bare photonic and atomic modes, respectively, whereas the third term captures the couplings of the DM and the SM to the respective quadratures of the cavity field (*23*). In this framework, the amplitudes of the DM and the SM are given by $x_D = \frac{1}{N}(\langle\hat{J}_{x,+}\rangle + \langle\hat{J}_{x,-}\rangle)$ and $x_S = \frac{1}{N}(\langle\hat{J}_{x,+}\rangle - \langle\hat{J}_{x,-}\rangle)$, respectively.

The damping of the cavity mode can be modeled by a decay term $-\kappa\hat{a}^\dagger$ in the equation of motion of the operator $\hat{a}^\dagger$. It causes a phase shift $\phi_\kappa = \tan^{-1}(-\kappa/\Delta_c)$ of the field scattered into the cavity by the atomic system. We adiabatically eliminate the cavity field and write the linearized equations of motion near the ground state of the noninteracting

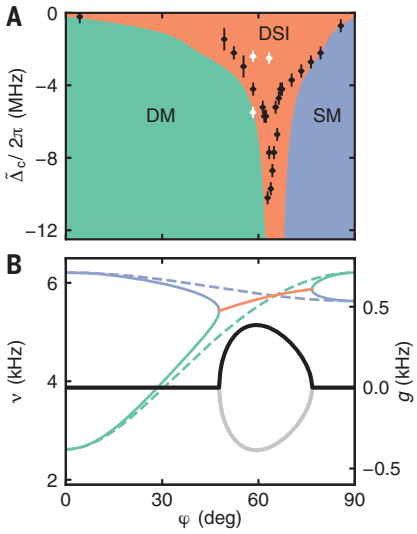

Fig. 3. Boundary of the instability-dominated regime. (**A**) Critical detuning, including the dispersive shift (*23*), for the onset of the dissipation-induced instability as a function of polarization angle φ. The black data points indicate the smallest detuning, where the strength of the sidebands becomes larger than the signal at the transverse pump frequency in the spectrograms for a fixed lattice depth of $21E_R$. The white diamonds indicate the parameters for the spectrograms shown in Fig. 2, C to E. Error bars are given by the discretized detuning interval in which the transition was detected. The polarization angle determination has an error of 1°. The green and blue regions correspond to DM and SM being respectively more strongly coupled to the spinor BEC. In the orange region, the system is dominated by the dissipation-induced instability. The boundary between different regions is obtained from a noninteracting theory [see main text and (*23*)]. (**B**) Green and blue solid (dashed) lines show the frequency ν of the two eigenmodes of the system as a function of the polarization angle in the presence (absence) of dissipative coupling. Without dissipation, the two modes are the DM (green) and the SM (blue). Dissipation leads to level attraction between the two modes and hence changes their frequencies. In the instability-dominated regime, the two modes are synchronized (orange). Correspondingly, the gains *g* of the amplified mode (black) and the damped mode (gray) are plotted. The lines are drawn for $\tilde{\Delta}_c/2\pi = -2.7$MHz or $\Delta_c/2\pi = -4$MHz and $V_{TP} = 1.5E_R$.

spinor BEC for the average amplitudes x_D and x_S (*23*)

$$\frac{d^2}{dt^2}\begin{pmatrix} x_D \\ x_S \end{pmatrix} = \begin{pmatrix} -\omega_D^2 & -K^2 \\ K^2 & -\omega_S^2 \end{pmatrix}\begin{pmatrix} x_D \\ x_S \end{pmatrix} \quad (2)$$

where $\omega_D^2 - \omega_S^2 \propto \sin\delta\phi$ with $\delta\phi = 2\tan^{-1}(\lambda_S/\lambda_D) - \pi/2$ is a measure of the relative coupling strength of the BEC to the SM and the DM. The strength of the dissipative coupling $K^2 \propto V_{TP}\sin^2\phi_\kappa\cos\delta\phi$ can thus be enhanced by either increasing the cavity-induced phase shift or making the two modes degenerate. This dissipative coupling generates a chiral force orthogonal to the current position vector of the system in the x_D-x_S plane (Fig. 1C) and provides an example of a positional force (*17*, *24*). Such positional forces are known in mechanical systems such as a rotating shaft subject to friction caused by an incompressible viscous fluid in a bearing. The incompressibility of the fluid leads to unequal frictional forces on opposite sides of the shaft, resulting in a positional force orthogonal to the direction of the displacement (*15*, *16*). These positional forces represent the only possible linear mechanical forces besides conservative trapping forces, centripetal forces, and frictional forces (*23*). In our system, when the two atomic modes are degenerate, this positional force cannot be counteracted by the restoring harmonic force pointing toward the origin, thus leading to a dissipation-induced structural or positional instability (*17*, *24*, *25*).

Mode degeneracy (i.e., $\lambda_D = \lambda_S$ such that $\delta\phi = 0$) is reached at the critical polarization angle $\varphi_c = 65.1°$ for the chosen wavelength of the transverse pump of λ = 784.7 nm. To explain our observations, we analyze the solutions of Eq. 2 and the corresponding intracavity light field for polarization angles close to φ_c—that is, for a small $\delta\phi$ (*23*)

$$[x_D^c, x_S^c] = A\left[\cos\omega t, \sin\left(\omega t + \frac{\Delta_c}{\kappa}\delta\phi\right)\right]e^{gt}$$

$$\langle \hat{a}^\dagger \rangle \propto (x_D^c - ix_S^c) - \frac{\delta\phi}{2}(x_D^c + ix_S^c)$$
$$\propto A\left[e^{-i\omega t} - \frac{\delta\phi}{2}\left(1 + i\frac{\Delta_c}{\kappa}\right)e^{i\omega t}\right]e^{gt} \quad (3)$$

In the limit $\delta\phi = 0$, this time-dependent solution implies that the system is rotating in the x_D-x_S plane with fixed chirality at frequency ω and amplification rate *g* (additionally, *t* is time and A is the amplitude at t=0) (*23*). Microscopically, this rotation is associated with the atomic spins moving from one λ-periodic spatial pattern to another (Fig. 1C). Because the two atomic modes are connected to different quadratures of the cavity, the phase of the cavity field evolves monotonically, as observed in Fig. 2B and shown in Eq. 3.

The frequency spectrum of the light leaking from the cavity is also accessible with our heterodyne setup (*22*). Figure 2, C to E, shows spectrograms for three different sets of parameters of data similar to Fig. 2, A and B, but averaged over 20 repetitions. Figure 2C shows a spectrogram where the signal is located at zero frequency (ν = 0). It corresponds to the frequency of the transverse pump and is identical to the observation of a constant time phase of the cavity field, as shown in Fig. 2A. We identify this as the formation of a static checkerboard density pattern that coherently scatters the pump field into the cavity (*20*, *23*). The corresponding steady state of the system is displayed in the inset to Fig. 2C.

In contrast, Figs. 2, D and E, depict red (ν < 0) and blue (ν > 0) detuned sidebands with the peak frequency being a function of the lattice depth of the transverse pump. Observation of only a red sideband, as in Fig. 2D, is equivalent to a linearly running phase. For small lattice depths ($V_{TP} < 6E_R$), the sideband frequency is expected to be close to the root mean square ω_e of the two mode frequencies—that is, $\omega \approx \omega_e = \sqrt{(\omega_D^2 + \omega_S^2)/2}$. Evolution at this intermediate frequency reflects a synchronization process (*26*) between the two spatial modes arising from the dissipative coupling. For large lattice depths, the sideband frequency depends on the dissipative coupling strength: $\omega \approx K^2/2|\omega_e|$ (*23*). In this limit, the two mode frequencies become imaginary, corresponding to the self-organization phase transition in the absence of dissipative coupling.

The relative strength *R* of the blue with respect to the red sideband increases toward 1 as φ deviates from the critical angle φ_c. The presence of the blue sideband is connected to nonzero $\delta\phi$ (Eq. 3) and leads to an elliptical evolution in the x_D-x_S plane. The relative strength *R*, and hence the ellipticity of the chiral solution, can be influenced via Δ_c or $|\delta\phi|$. Microscopically, the blue sideband is connected to the motion of a different number of atoms in each Zeeman state. The insets to Fig. 2, D and E, show data of the time-varying trajectory of the system together with solutions obtained from Eq. 2 for *g* = 0, illustrating the nonstationary chiral state. When preparing the system in the DSI at a fixed lattice depth, we observe a narrow red sideband that persists over tens of milliseconds (*23*), corresponding to a uniform circular motion in the x_D-x_S plane. This observation hints at the presence of a limit cycle in our system (*18*, *19*).

Our mean-field description of the system in terms of a positional instability does not describe all aspects of the observed dynamics. For example, the number of photons in the case of the DSI (Fig. 2, D and E) is much smaller than during self-organization (Fig. 2C), although the instability is associated with a finite amplification rate *g*. Even the limit cycle–like behavior persisted for a long time without much increase in the corresponding amplitude. Moreover, there is a finite lattice depth threshold for the onset of the DSI (Fig. 2B), although *g* is positive for infinitesimal lattice depths. We attribute this, as well as the observed pulsing behavior in the number of photons (Fig. 2B), to collisional interactions between the atoms (*23*). Such a behavior of collisional interactions can possibly be modeled as an atomic

dissipation channel that competes with the cavity-induced instability. Similar competitions between multiple heat baths are predicted to give rise to dissipative frustration (*27*, *28*).

We experimentally map out the boundary of the DSI region by ramping up the transverse pump lattice to $25E_R$ in 50 ms for various polarization angles φ and detunings Δ_c (Fig. 3A). For a given polarization angle, we define the onset of the DSI by the minimum detuning where the strength of the sidebands exceeds the signal at the transverse pump frequency. We theoretically obtain the boundary of the DSI (orange region in Fig. 3A) from Eq. 2 as $|\omega_D^2 - \omega_S^2| = 2K^2$, which results in a critical detuning $\Delta_{c,b} = -\kappa/\tan|\delta\phi|$. A study of the extent of the DSI as a function of polarization angle and transverse pump lattice depth is presented in (*23*).

Physically, the boundary of the DSI can be understood as the onset of synchronization between DM and SM. Such a synchronization process is the result of a dissipation-induced level attraction, a hallmark of non-Hermitian systems (*29*, *30*). Figure 3B shows the frequencies of the DM and SM in the absence (dashed lines) and presence (solid lines) of dissipation. In the vicinity of the critical angle, this level attraction leads to the emergence of two degenerate modes with opposite chirality. Whereas one of these modes is damped, the other is amplified, which gives rise to the DSI. Similar forms of level attraction leading to instability are observed in optomechanical systems (*31*) and, in general, in non-Hermitian photonic systems, where they can be associated with parity–time symmetry-breaking phase transitions (*30*) and exceptional points (*32*, *33*). We have experimentally studied a many-body system in which both coherent and dissipative couplings are independently tunable. Our observation of a dissipation-induced instability represents a form of quantum many-body dynamics that shares characteristics with but is distinct from limit cycles (*18*, *19*, *34*) and time crystals (*35*, *36*).

REFERENCES AND NOTES

1. H.-P. Breuer, F. Petruccione, *The Theory of Open Quantum Systems* (Oxford Univ. Press, 2002).
2. N. Syassen *et al*., *Science* **320**, 1329–1331 (2008).
3. G. Barontini *et al*., *Phys. Rev. Lett.* **110**, 035302 (2013).
4. F. Brennecke *et al*., *Proc. Natl. Acad. Sci. U.S.A.* **110**, 11763–11767 (2013).
5. R. Labouvie, B. Santra, S. Heun, H. Ott, *Phys. Rev. Lett.* **116**, 235302 (2016).
6. T. Tomita, S. Nakajima, I. Danshita, Y. Takasu, Y. Takahashi, *Sci. Adv.* **3**, e1701513 (2017).
7. I. Carusotto, C. Ciuti, *Rev. Mod. Phys.* **85**, 299–366 (2013).
8. T. Fink, A. Schade, S. Höfling, C. Schneider, A. Imamoglu, *Nat. Phys.* **14**, 365–369 (2018).
9. J. T. Young, A. V. Gorshkov, M. Foss-Feig, M. F. Maghrebi, arXiv:1903.02569 [cond-mat.quant-gas] (6 March 2019).
10. S. Diehl, A. Tomadin, A. Micheli, R. Fazio, P. Zoller, *Phys. Rev. Lett.* **105**, 015702 (2010).
11. D. Nagy, G. Szirmai, P. Domokos, *Phys. Rev. A* **84**, 043637 (2011).
12. S. Diehl, E. Rico, M. A. Baranov, P. Zoller, *Nat. Phys.* **7**, 971–977 (2011).
13. B. Buča, J. Tindall, D. Jaksch, *Nat. Commun.* **10**, 1730 (2019).
14. M. Soriente, T. Donner, R. Chitra, O. Zilberberg, *Phys. Rev. Lett.* **120**, 183603 (2018).
15. B. L. Newkirk, H. Taylor, *Gen. Electr. Rev.* **28**, 559–568 (1925).
16. P. L. Kapitsa, *Zh. Tekh. Fiz.* **9**, 124–147 (1939).
17. D. R. Merkin, *Introduction to the Theory of Stability* (Springer, 1996).
18. F. Piazza, H. Ritsch, *Phys. Rev. Lett.* **115**, 163601 (2015).
19. E. I. Rodríguez Chiacchio, A. Nunnenkamp, *Phys. Rev. Lett.* **122**, 193605 (2019).
20. M. Landini *et al*., *Phys. Rev. Lett.* **120**, 223602 (2018).
21. K. Baumann, C. Guerlin, F. Brennecke, T. Esslinger, *Nature* **464**, 1301–1306 (2010).
22. R. Landig, F. Brennecke, R. Mottl, T. Donner, T. Esslinger, *Nat. Commun.* **6**, 7046 (2015).
23. Supplementary materials.
24. R. Krechetnikov, J. E. Marsden, *Rev. Mod. Phys.* **79**, 519–553 (2007).
25. S. H. Crandall, in "Rotordynamic Instability Problems in High-Performance Turbomachinery" (NASA Conference Publications 2133, NASA, 1982), vol. 2250, pp. 274–283.
26. A. Pikovsky, M. Rosenblum, J. Kurths, *Synchronization: A Universal Concept in Nonlinear Science* (Cambridge Univ. Press, 2003).
27. H. Kohler, F. Sols, *New J. Phys.* **8**, 149 (2006).
28. D. Maile, S. Andergassen, W. Belzig, G. Rastelli, *Phys. Rev. B* **97**, 155427 (2018).
29. I. Rotter, *J. Phys. A Math. Theor.* **42**, 153001 (2009).
30. R. El-Ganainy *et al*., *Nat. Phys.* **14**, 11–19 (2018).
31. N. R. Bernier, L. D. Tóth, A. K. Feofanov, T. J. Kippenberg, *Phys. Rev. A* **98**, 023841 (2018).
32. W. D. Heiss, *J. Phys. A Math. Theor.* **45**, 444016 (2012).
33. M.-A. Miri, A. Alù, *Science* **363**, eaar7709 (2019).
34. M. Gutzwiller, *Chaos in Classical and Quantum Mechanics* (Springer, 1990).
35. J. Zhang *et al*., *Nature* **543**, 217–220 (2017).
36. S. Choi *et al*., *Nature* **543**, 221–225 (2017).
37. N. Dogra, M. Landini, K. Kroeger, L. Hruby, T. Donner, T. Esslinger, "Dissipation Induced Structural Instability and Chiral Dynamics in a Quantum Gas," ETH Zurich Research Collection (2019); https://doi.org/10.3929/ethz-b-000366051.

ACKNOWLEDGMENTS

We thank B. Buca, E. Rodriguez Chiacchio, F. Ferri, D. Jaksch, A. Nunnenkamp, and J. Tindall for discussions. **Funding:** We acknowledge funding from SNF [project nos. 182650 and 175329 (NAQUAS QuantERA) and NCCR QSIT], EU Horizon 2020 [ERC Advanced Grant TransQ (project no. 742579)], and SBFI (QUIC, contract no. 15.0019). **Author contributions:** N.D., M.L., K.K., and L.H. prepared the experiment and collected the data; N.D., M.L., and K.K. evaluated the data; N.D. and M.L. developed the theory; T.D. and T.E. supervised the project; and all authors contributed to discussions and writing of the manuscript. **Competing interests:** The authors declare no competing interests. **Data and materials availability:** Data and scripts are available in the ETH Zurich Research Collection repository (*37*).

SUPPLEMENTARY MATERIALS

science.sciencemag.org/content/366/6472/1496/suppl/DC1
Materials and Methods
Supplementary Text
Figs. S1 to S5
References (*38*–*41*)

20 December 2018; accepted 6 November 2019
10.1126/science.aaw4465

MECHANOCHEMISTRY

Redox reactions of small organic molecules using ball milling and piezoelectric materials

Koji Kubota[1,2]*, Yadong Pang[2], Akira Miura[2], Hajime Ito[1,2]*

Over the past decade, photoredox catalysis has harnessed light energy to accelerate bond-forming reactions. We postulated that a complementary method for the redox-activation of small organic molecules in response to applied mechanical energy could be developed through the piezoelectric effect. Here, we report that agitation of piezoelectric materials via ball milling reduces aryl diazonium salts. This mechanoredox system can be applied to arylation and borylation reactions under mechanochemical conditions.

Visible light photoredox catalysis represents a recent key development in contemporary organic synthesis (*1*–*5*). In these transformations, the photoexcited catalyst can act as a potent single-electron oxidant, transferring an electron to an acceptor, after which single-electron oxidation of a donor affords the product under concomitant regeneration of the ground-state catalyst (Fig. 1A). The broad success of photoredox catalysis hinges on the susceptibility of the coupling partners to redox activation and ensuing bond-forming reactions with high levels of efficiency and selectivity.

There has also been substantial parallel progress in mechanochemical organic transformations using ball milling (*6*–*18*). Since the term mechanochemistry was introduced by Ostwald in 1887, mechanochemical synthesis has been extensively exploited in materials science (*6*–*8*), polymer chemistry (*9*), and inorganic synthesis (*8*), but its application to organic synthesis is more recent (*10*–*18*). Advantages of mechanochemical synthesis using ball milling include the avoidance of potentially harmful organic solvents and external heating, shorter reaction times, and simpler operational handling. Additionally, mechanochemical reactions are particularly useful for substrates that are poorly soluble in common organic solvents.

Inspired by the unique profile of photoredox systems based on light irradiation and the utility of ball milling in mechanochemistry, we hypothesized that redox activation of small organic molecules could be achieved through a mechanistically distinct approach using mechanical energy (*19*–*22*). Specifically, we envisioned that the agitation of piezoelectric materials (*23*–*35*) via ball milling could generate temporarily highly polarized particles. These particles might act as strong reductants to transfer electrons to small organic molecules, followed by oxidative quenching of a donor, thereby inducing the selective formation of bonds in a manner analogous to photoredox catalysis (Fig. 1B). Such a mechanoredox approach could potentially represent a powerful and attractive strategy to reduce the environmental impact of chemical processes; photoredox approaches, similarly to other conventional organic reactions, often require complicated reaction setups, substantial amounts of dry and degassed organic solvents, and an inert gas atmosphere (*1*–*5*).

For a proof-of-concept study, we selected commercially available, inexpensive, and easy-to-handle $BaTiO_3$ nanoparticles as the piezoelectric material (Fig. 1B). This choice was motivated by pioneering studies, in which ultrasonic agitation of $BaTiO_3$ produces a suitable electrochemical potential to overcome the water splitting potential (1.23 V) (*28*, *29*) and reduce a *N*,*N*,*N*′,*N*′,*N*″,*N*″-hexamethyl[tris(aminoethyl)amine] (Me_6TREN)–ligated $CuBr_2$ complex, which has a reduction potential of −0.30 V [versus saturated calomel electrode (SCE)] (*29*, *36*). These studies suggested that mechanical agitation of $BaTiO_3$ in a ball mill could generate an electrochemical potential suitable for

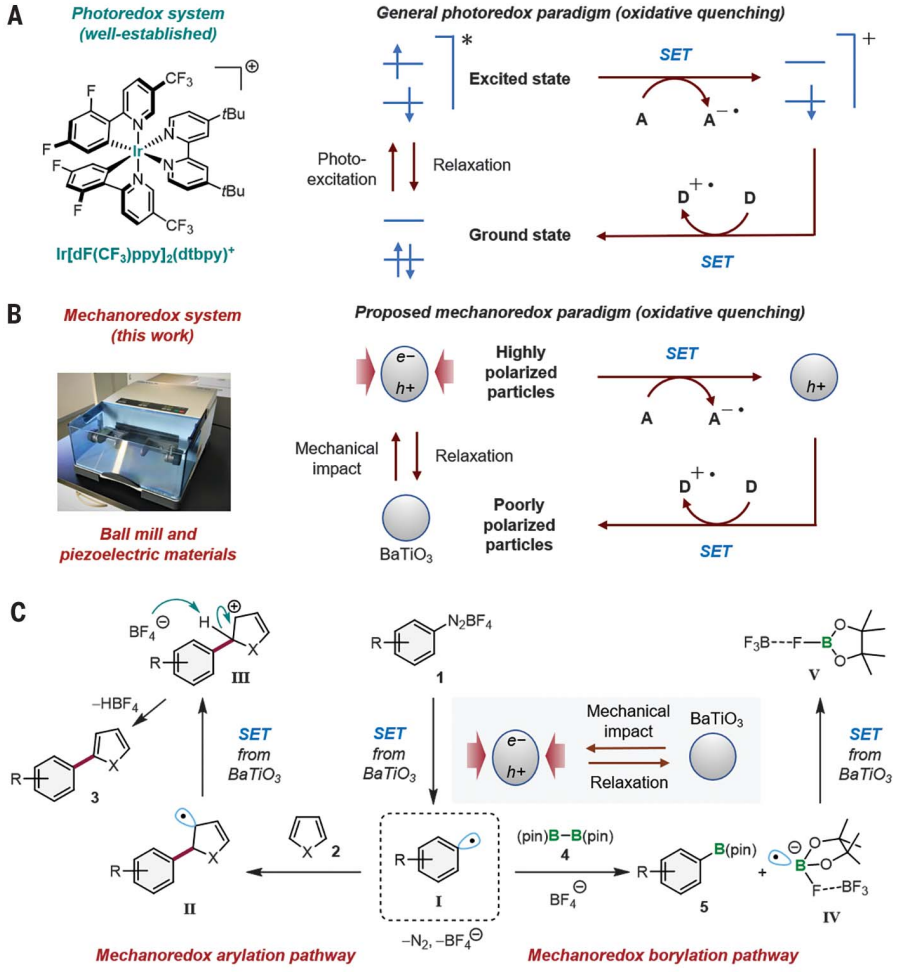

Fig. 1. Working hypothesis for a mechanoredox system for the activation of small organic molecules in organic synthesis. (**A**) A commonly employed photoredox catalyst and a generic photoredox oxidative quenching cycle. A, acceptor; D, donor. (**B**) Proposed mechanoredox paradigm using a ball mill and a piezoelectric material. (**C**) Proposed mechanism for the mechanoredox arylation and borylation using $BaTiO_3$ and ball milling. *t*Bu, tertiary butyl; ppy, (2-pyridinyl)phenyl; dtbpy, 4,4′-di-tert-butyl-2,2′-bipyridine; pin, pinacolato; R, substituent.

[1]Institute for Chemical Reaction Design and Discovery (WPI-ICReDD), Hokkaido University, Sapporo, Hokkaido 060-8628, Japan. [2]Division of Applied Chemistry, Graduate School of Engineering, Hokkaido University, Sapporo, Hokkaido 060-8628, Japan.
*Corresponding author. Email: hajito@eng.hokudai.ac.jp (H.I.); kbt@eng.hokudai.ac.jp (K.K.)

the activation of redox-active, small organic molecules in organic synthesis.

The photoredox systems that activate aryl diazonium salts for coupling with heteroarenes (*37*) or borylation (*38*) have been reported by König and Yan, respectively. The key step in these transformations is the photochemical reduction of aryl diazonium salts to aryl radical species. Andrieux and Pinson have reported a reduction potential of −0.16 V (versus SCE) for phenyl diazonium tetrafluoroborate (*39*), which was within range for feasible redox activation using $BaTiO_3$. In our postulated mechanism (Fig. 1C), the agitation of $BaTiO_3$ via ball milling generates a temporary electrochemical potential in response to mechanical impact. According to the aforementioned inorganic studies (*28*, *29*), the temporary polarization should be sufficiently persistent to reduce an aryl diazonium salt (**1**) via a single-electron transfer (SET) mechanism analogous to the photoredox reaction, to furnish the corresponding aryl radical **I**. The addition of **I** to heteroarene **2** would afford radical addition intermediate **II**, which would be subsequently oxidized by the hole in the agitated $BaTiO_3$ to form carbocation intermediate **III** (*37*). Finally, deprotonation of **III** would lead to arylation product **3**. In the borylation (*38*), the generated radical **I** reacts with bis(pinacolate) diboron (**4**), to cleave the B–B bond, resulting in the formation of the boryl substitution product **5** as well as radical anion intermediate **IV**. Subsequently, oxidation of **IV** by the agitated $BaTiO_3$ could form F–B(pin) (**V**) as a by-product.

To explore this mechanistic hypothesis, we first attempted the proposed mechanoredox C–H arylation with **1a** and furan (**2a**) in the presence of commercially available $BaTiO_3$, using a Retch MM400 mixer mill (1.5-ml stainless steel milling jar with 5-mm diameter stainless steel ball) (Fig. 2A). The corresponding arylation product (**3a**) was obtained in 40% yield after milling at 20 Hz for 1 hour under air. The reaction did not proceed in the absence of $BaTiO_3$, suggesting that the mechanical energy provided by ball milling generated the piezoelectric potential to reduce **1a**. In contrast, even when ultrasound irradiation was applied to the mixture with $BaTiO_3$ in dimethyl sulfoxide (DMSO) under a nitrogen atmosphere, the formation of the product was not observed. A small amount of **3a** was obtained when the reaction was carried out in the presence of $SrTiO_3$, which exhibits piezoelectric properties upon applying in-plain strain (*40*). When using non-piezoelectric ceramic materials, such as TiO_2, $BaCO_3$, or Al_2O_3, the reaction did not proceed, which suggests that piezoelectric materials are essential for this arylation reaction. We found that conducting the reaction at higher ball-milling frequency (30 Hz) substantially improved the yield (81%).

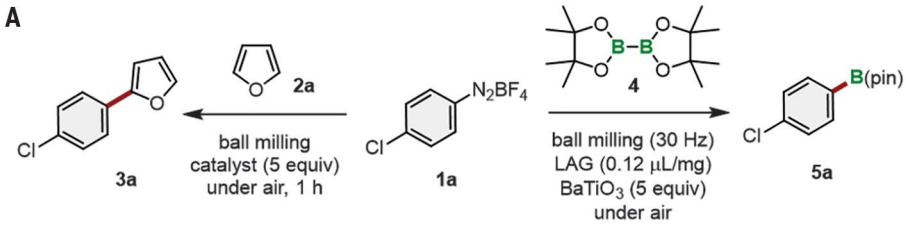

Optimization for mechanoredox arylation

catalyst	milling frequency (Hz)	NMR yield of **3a** (%)
$BaTiO_3$	20	40
none	20	<1
$BaTiO_3$	–	<1*
$SrTiO_3$	20	3
TiO_2	20	<1
$BaCO_3$	20	<1
Al_2O_3	20	<1
$BaTiO_3$	**30**	**81**
$LiNbO_3$	30	24
ZnO	30	15

*In DMSO with ultrasound under N_2.

Optimization for mechanoredox borylation

LAG	time (h)	NMR yield of **5a** (%)
none	1	21
MeCN	1	54
DMF	1	37
DMSO	1	13
toluene	1	11
hexane	1	15
MeCN	1.5	62
MeCN	**3**	**89**
MeCN	3	<1*

*Reaction was carried out without $BaTiO_3$.

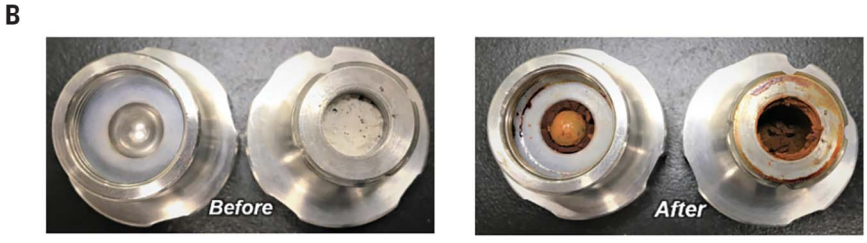

Fig. 2. Mechanoredox arylation and borylation using mechanical force. (**A**) Optimization of the mechanoredox arylation and borylation reactions. (**B**) Reaction mixture of the mechanoredox arylation of **2a** after grinding in a ball mill. A stainless steel milling jar (1.5 ml) and a stainless steel ball (diameter, 5 mm) were used. See supplementary materials for details. equiv, equivalent; h, hour.

This result is consistent with our hypothesis that the required piezoelectric potential is generated by mechanical force provided by the ball milling of $BaTiO_3$. Using other piezoelectric materials, such as $LiNbO_3$ and ZnO, also afforded **3a**, albeit in lower yield (24% and 15%, respectively). Using a bigger jar (5.0 ml) and ball (7.5 mm) provided **3a** in high yield (82%, table S2). Product **3a** was isolated by filtration of the obtained crude solid mixture (Fig. 2B), followed by column chromatography on silica gel.

We then investigated the possibility of mechanoredox borylation using the same setup (Fig. 2A). We found that the borylation of **1a** with **4** in the presence of $BaTiO_3$ afforded the desired arylboronate (**5a**) in 21% yield. Next, we attempted to improve the reactivity by using liquid-assisted grinding (LAG), in which a substoichiometric amount of liquid is added (*41*). In all LAG reactions, the ratio of liquid additive (microliters) to reactant (milligrams) was 0.12. Use of acetonitrile (MeCN) as the LAG additive improved the yield of **5a**, whereas other common solvents, such as *N*,*N*-dimethylformamide (DMF), DMSO, toluene, or hexane, led to little or no improvement. We also found that prolonging the reaction time led to a higher yield of **3a** (89%) when MeCN was used as the LAG additive. Using a bigger jar (5.0 ml) and ball (7.5 mm) did not substantially affect the transformation (86%, table S3). The reaction without $BaTiO_3$ did not proceed, supporting our mechanistic hypothesis. Compared with the analogous photoredox reaction, the present mechanoredox borylation exhibited much faster reaction kinetics and a better product yield (*38*).

Subsequently, we explored the scope of the mechanoredox arylation reaction with various aryl diazonium salts using a 5-ml stainless steel milling jar with a 7.5-mm diameter stainless steel ball (Fig. 3A). Electron-deficient aryl diazonium salts (**1a** to **1h**) were converted into the desired products (**3a** to **3h**) in good yield under the optimized conditions. Simple aromatic substrates (**1i** to **1k**) also reacted to give the corresponding products (**3i** to **3k**) in good

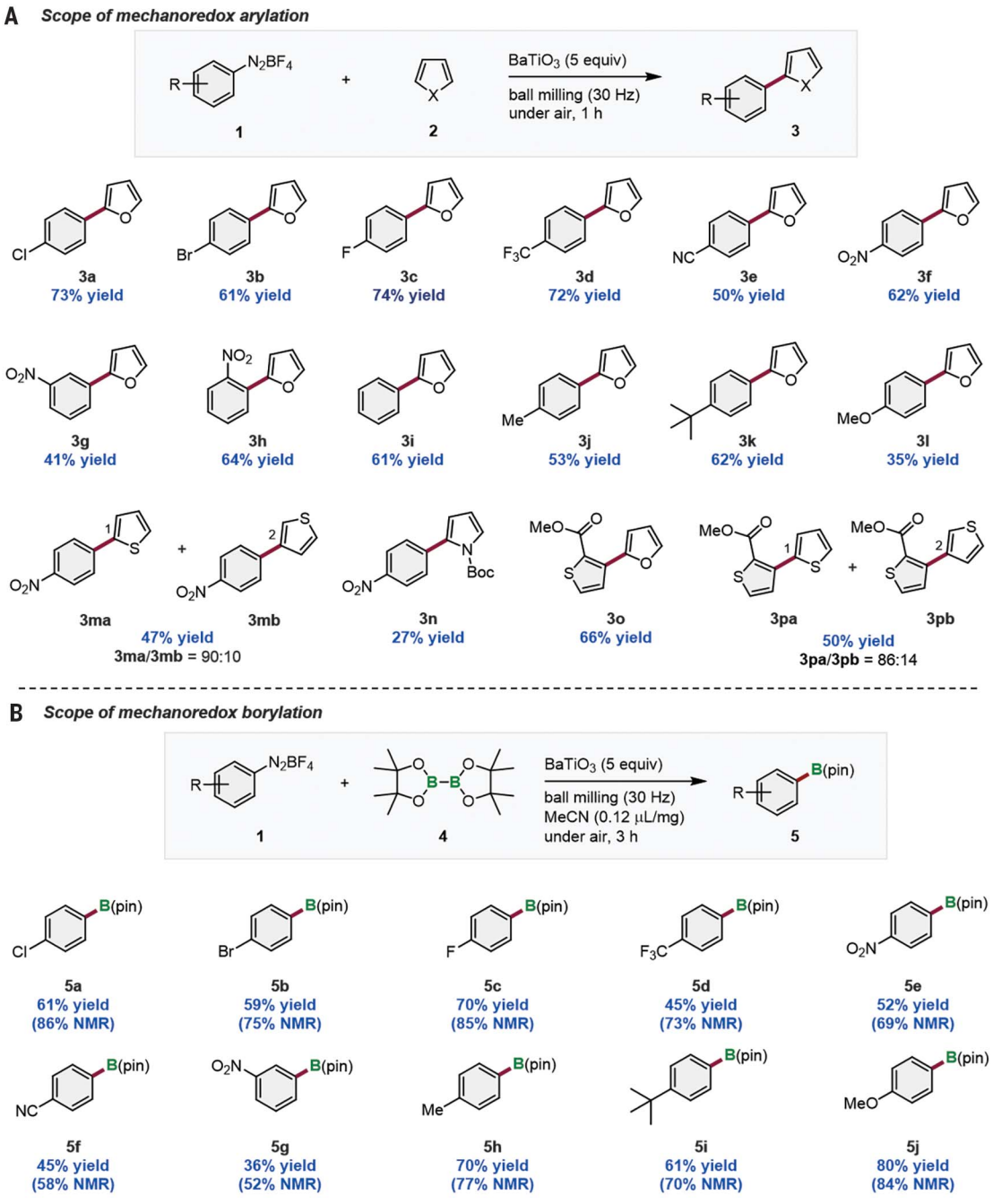

Fig. 3. Scope of the mechanoredox arylation and borylation reactions using aryl diazonium salts. Data for each entry (in bold) are reported as isolated yield percentages. Proton NMR integrated yields are shown in parentheses. (**A**) Substrate scope of the mechanoredox arylation of heteroaromatic compounds. (**B**) Substrate scope of the mechanoredox borylation of aryl diazonium salts. Reactions were performed at 0.3 mmol scale using a stainless steel milling jar (5 ml) and stainless steel ball (diameter, 7.5 mm). Arylation conditions: **1** (0.3 mmol), **2** (4.5 mmol), and $BaTiO_3$ (1.5 mmol). Borylation conditions: **1** (0.3 mmol), **4** (0.3 mmol), $BaTiO_3$ (1.5 mmol), and MeCN (0.12 μL/mg). See supplementary materials for details. Me, methyl; Boc, tertiary butoxycarbonyl.

yield. However, in the case of an electron-rich, methoxy-substituted diazonium salt (**1l**), the product (**3l**) was obtained in relatively low yield. This was probably due to the relatively high reduction potential of **1l**. Other heteroarenes, namely, thiophene and pyrrole, successfully reacted to form the desired products (**3m** and **3n**). Arylation reactions using thienyl diazonium salts afforded the corresponding heterobiaryls (**3o** and **3p**), which are typical structural motifs for organic semiconductors (*42*). Minor regioisomers (**3mb** and **3pb**) were observed as competing products in the reactions with thiophene, whereas the photoredox system developed by König and co-workers, using eosin Y, produced **3ma** and **3pa** as single isomers (*37*). We also confirmed that the developed mechanoredox borylation conditions were applicable to a variety of aryl diazonium salts (Fig. 3B).

To demonstrate the practical utility of this protocol, we investigated a gram-scale synthesis of heterobiaryls under the developed mechanoredox conditions, as well as the recycling of $BaTiO_3$ (Fig. 4, A and B). The mechanoredox C–H arylation of furan (**2a**) with **1o** was carried out on an 8-mmol scale in a 25-ml stainless steel ball-milling jar with one 15-mm diameter stainless steel ball, affording **3o** in 71% yield (Fig. 4A). After separation from the crude reaction mixture and washing, $BaTiO_3$ could be reused for the mechanoredox arylation of furan (**2a**) under the same reaction conditions at least three times before the yield of **3k** declined substantially (Fig. 4B).

Direct C–H arylation of polycyclic aromatic hydrocarbons (PAHs) has attracted considerable interest (*43*, *44*) on account of their role in organic light-emitting diodes, organic photovoltaics,

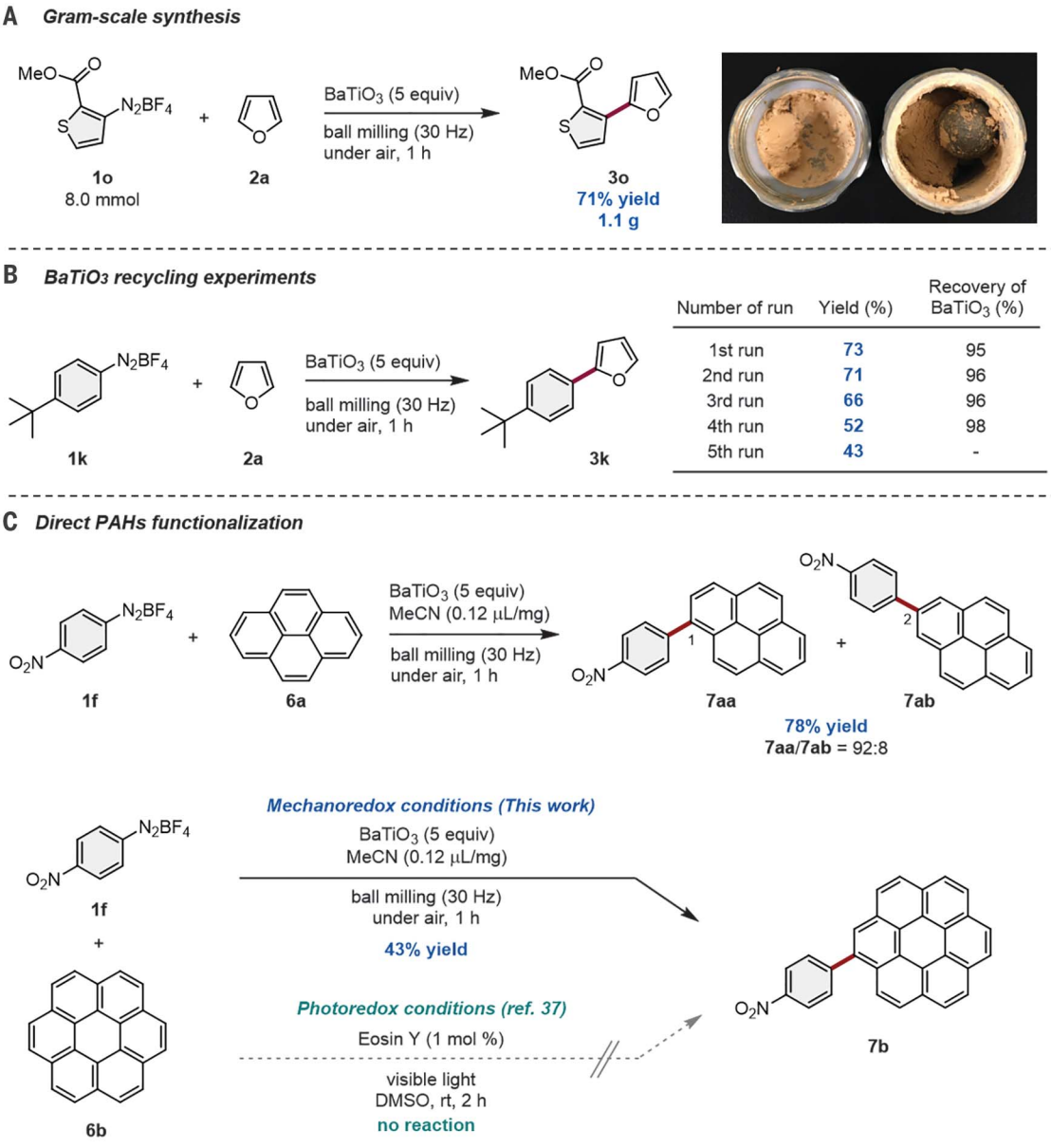

Fig. 4. Exploration of a gram-scale synthesis, catalyst recycling, and the arylation of polyaromatic hydrocarbon compounds. (**A**) Mechanoredox arylation of **2a** with **1o** on the gram scale using a 25-ml ball-milling jar (pictured on the right). (**B**) $BaTiO_3$ recycling experiments using **1k** and **2a**. (**C**) Mechanoredox arylation of the polyaromatic hydrocarbons **6** with **1f**. See supplementary materials for details. rt, room temperature.

organic semiconductors, and organic thin-film transistors. With this in mind, we conducted a preliminary investigation of the feasibility of the C–H arylation of PAHs using our mechanoredox approach (Fig. 4C). The reaction of **1f** with pyrene (**6a**) in the presence of $BaTiO_3$ and a small amount of MeCN as the LAG additive afforded the desired C–H arylation product (**7aa**) in good yield with high regioselectivity (**7aa**:**7ab** = 92:8). Furthermore, coronene (**6b**) was also arylated in moderate yield under the mechanoredox conditions. When the arylation of coronene (**6b**) was attempted via König's photoredox procedure using eosin Y, no reaction occurred (*37*). This was probably due to the low solubility of coronene (**6b**) in the polar solvents required for such photoredox reactions. These results demonstrate the promising potential of the mechanoredox arylation as an operationally simple and mild route to synthesize functionalized PAHs from poorly soluble substrates that are incompatible with photoredox conditions.

We postulated that the mechanoredox C–H arylation and borylation were proceeding via SET events, in which an aryl radical is generated through piezoelectric reduction (Fig. 1C); this assumption is supported by the results of preliminary mechanistic investigations (Fig. 5). When 2,2,6,6-tetramethylpiperidinoxyl (TEMPO) (**8**) was treated with aryl diazonium salt **1a** in the absence of furan (**2a**), the TEMPO-trapped intermediate **9** was obtained (Fig. 5A). Furthermore, the addition of TEMPO (**8**) to a reaction mixture containing **1a**, furan (**2a**), and $BaTiO_3$ halted the arylation process, and the TEMPO-trapped intermediates **9** and **10** were detected (Fig. 5A). Compound **10** might have been formed through the reaction of TEMPO (**8**) with the intermediate **II** (Fig. 1C), followed by oxidative aromatization by $BaTiO_3$ or atmospheric oxygen. Overall, the identified compounds suggest that the mechanoredox activation with $BaTiO_3$ proceeds via a radical pathway.

We used a scanning electron microscopy (SEM) analysis to confirm that the mechanical stimulus provided by ball milling is transferred onto the $BaTiO_3$ particles under the applied conditions (Fig. 5B) (*24*). The SEM image of commercially available $BaTiO_3$ powder shows

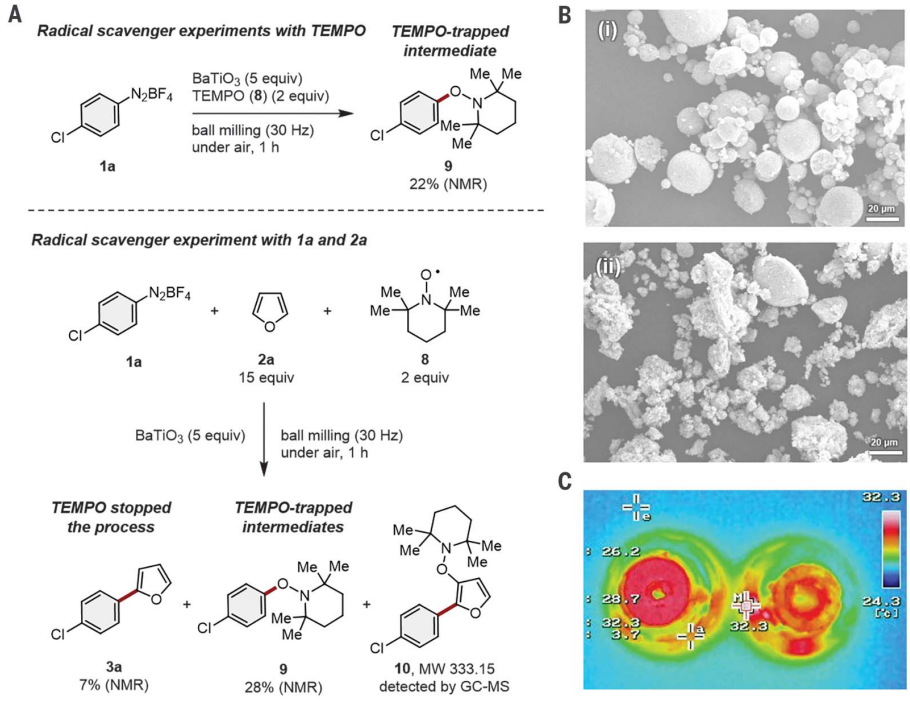

Fig. 5. Mechanistic studies. (**A**) Radical scavenger experiments. (**B**) SEM images of $BaTiO_3$ particles (i) before and (ii) after ball milling (30 Hz; 60 min). (**C**) Thermographic image of the milling jar after the mechanoredox arylation of **2a** with **1a**. See supplementary materials for details. GC-MS, gas chromatography–mass spectrometry.

a regular shape of the $BaTiO_3$ particles before the reaction (approximate size, <75 μm) [Fig. 5B (i)]. Subsequently, the powder was subjected for 60 min to ball milling at 30 Hz and then analyzed by SEM. The resulting image clearly shows a pronounced distortion of the shape and a decrease in the size of the $BaTiO_3$ particles [Fig. 5B (ii)]. These results suggest that the mechanical stimulus provided by ball milling is efficiently transferred onto the $BaTiO_3$ particles, which would result in the generation of localized electrochemical potentials on the surface of the $BaTiO_3$ particles that can be used for the activation of the aryl diazonium salts.

To investigate whether the friction during ball milling generates a thermal effect, the temperature inside the milling jar during the mechanoredox arylation of **2a** with **1a** was measured using thermography immediately after opening the jar (Fig. 5C). The crude mixtures were prepared under optimized conditions. The obtained image showed that the temperature after arylation in the ball mill was around 30°C, which discounts the possibility of thermal activation of the aryldiazonium salts generating aryl radical species by the heat provided from ball milling.

To demonstrate the robustness of the mechanoredox transformations, we conducted the borylation of **1k** with $BaTiO_3$ in air using a hammer (fig. S8 and movie S1). First, the reaction mixture was prepared by gentle grinding in a mortar. Subsequently, the mixture was wrapped in a piece of a weighing paper and placed in a zipper-locking plastic bag, followed by striking with a hammer over 200 times. Even under these crude conditions, the mechanoredox borylation product **5i** was obtained in 43% yield, as assessed by nuclear magnetic resonance (NMR) integration.

The present mechanoredox reactions can be carried out on gram scale without the use of large amounts of dry and degassed organic solvents in air, and the reactions do not require special operating conditions. This operational simplicity suggests that the present approach may complement existing photoredox transformations in a practical and environmentally friendly manner. Beyond the immediate benefits of this protocol, our strategy could be applicable to light-sensitive or light-absorbing substrates that cannot be subjected to conventional photoredox systems.

REFERENCES AND NOTES

1. C. Stephenson, T. Yoon, D. W. C. MacMillan, *Visible Light Photocatalysis in Organic Chemistry* (Wiley, ed. 1, 2018).
2. C. K. Prier, D. A. Rankic, D. W. C. MacMillan, *Chem. Rev.* **113**, 5322–5363 (2013).
3. N. A. Romero, D. A. Nicewicz, *Chem. Rev.* **116**, 10075–10166 (2016).
4. C.-S. Wang, P. H. Dixneuf, J.-F. Soulé, *Chem. Rev.* **118**, 7532–7585 (2018).
5. K. L. Skubi, T. R. Blum, T. P. Yoon, *Chem. Rev.* **116**, 10035–10074 (2016).
6. T. Friščić, *J. Mater. Chem.* **20**, 7599–7605 (2010).
7. S.-E. Zhu, F. Li, G.-W. Wang, *Chem. Soc. Rev.* **42**, 7535–7570 (2013).
8. P. Baláž, *Mechanochemistry in Nanoscience and Minerals Engineering* (Springer, 2008).
9. R. Boulatov, Ed., *Polymer Mechanochemistry* (Springer, 2015).
10. S. L. James *et al.*, *Chem. Soc. Rev.* **41**, 413–447 (2012).
11. G.-W. Wang, *Chem. Soc. Rev.* **42**, 7668–7700 (2013).
12. J.-L. Do, T. Friščić, *ACS Cent. Sci.* **3**, 13–19 (2017).
13. J. G. Hernández, C. Bolm, *J. Org. Chem.* **82**, 4007–4019 (2017).
14. D. Tan, T. Friščić, *Eur. J. Org. Chem.* **2018**, 18–33 (2018).
15. J. L. Howard, Q. Cao, D. L. Browne, *Chem. Sci.* **9**, 3080–3094 (2018).
16. J. Andersen, J. Mack, *Green Chem.* **20**, 1435–1443 (2018).
17. C. Bolm, J. G. Hernández, *Angew. Chem. Int. Ed.* **58**, 3285–3299 (2019).
18. F. Gomollón-Bel, *Chem. Int.* **41**, 12–17 (2019).
19. J. C. Robertson, M. L. Coote, A. C. Bissember, *Nat. Rev. Chem.* **3**, 290–304 (2019).
20. J. Liang, J. M. Fernández, *J. Am. Chem. Soc.* **133**, 3528–3534 (2011).
21. P. Dopieralski *et al.*, *Nat. Chem.* **5**, 685–691 (2013).
22. H. Yan *et al.*, *Nature* **554**, 505–510 (2018).
23. S. Ikeda *et al.*, *Phys. Chem. Chem. Phys.* **1**, 4485–4491 (1999).
24. M. Hara *et al.*, *Appl. Catal. A Gen.* **190**, 35–42 (2000).
25. Z. L. Wang, J. Song, *Science* **312**, 242–246 (2006).
26. X. Wang, J. Song, J. Liu, Z. L. Wang, *Science* **316**, 102–105 (2007).
27. Y. Qin, X. Wang, Z. L. Wang, *Nature* **451**, 809–813 (2008).
28. K.-S. Hong, H. Xu, H. Konishi, X. Li, *J. Phys. Chem. Lett.* **1**, 997–1002 (2010).
29. H. Mohapatra, M. Kleiman, A. P. Esser-Kahn, *Nat. Chem.* **9**, 135–139 (2017).
30. M. B. Starr, J. Shi, X. Wang, *Angew. Chem. Int. Ed.* **51**, 5962–5966 (2012).
31. M. B. Starr, X. Wang, *Sci. Rep.* **3**, 2160 (2013).
32. H. Lin *et al.*, *Appl. Phys. Lett.* **104**, 162907 (2014).
33. W. Lv *et al.*, *J. Chem. Technol. Biotechnol.* **92**, 152–156 (2017).
34. M. B. Starr, X. Wang, *Nano Energy* **14**, 296–311 (2015).
35. Z. Wang *et al.*, *ACS Macro Lett.* **8**, 161–165 (2019).
36. K. Matyjaszewski, *Macromolecules* **45**, 4015–4039 (2012).
37. D. P. Hari, P. Schroll, B. König, *J. Am. Chem. Soc.* **134**, 2958–2961 (2012).
38. J. Yu, L. Zhang, G. Yan, *Adv. Synth. Catal.* **354**, 2625–2628 (2012).
39. C. P. Andrieux, J. Pinson, *J. Am. Chem. Soc.* **125**, 14801–14806 (2003).
40. J. H. Haeni *et al.*, *Nature* **430**, 758–761 (2004).
41. T. Friščić, S. L. Childs, S. A. A. Rizvi, W. Jones, *CrystEngComm* **11**, 418–426 (2009).
42. M. E. Cinar, T. Ozturk, *Chem. Rev.* **115**, 3036–3140 (2015).
43. Y. Segawa, H. Ito, K. Itami, *Nat. Rev. Mater.* **1**, 15002 (2016).
44. Y. Segawa, T. Maekawa, K. Itami, *Angew. Chem. Int. Ed.* **54**, 66–81 (2015).

ACKNOWLEDGMENTS

Funding: This work was supported by the Japan Society for the Promotion of Science (JSPS) through KAKENHI grants 18H03907, 17H06370, and 19K15547; by the JST CREST grant number JPMJCR19R1; and by the Institute for Chemical Reaction Design and Discovery (ICReDD), which was established by the World Premier International Research Initiative (WPI), MEXT, Japan. Y.P. thanks the Otsuka Toshimi Scholarship Foundation for a scholarship. We thank D. F. Toste and T. Shimada for advice on the preparation of this manuscript. We thank Nippon Chemical Industrial Co., Ltd. for the gift of piezoelectric materials. **Author contributions:** H.I. came up with the original idea; K.K. and H.I. directed the project; K.K. and H.I. designed the experiments; K.K. and Y.P. performed the experiments; A.M. prepared ceramic materials used in this study; and K.K. and H.I. wrote the manuscript with feedback from the other authors. **Competing interests:** H.I. and K.K. are inventors on patent application JP, 2019-163323 submitted by Hokkaido University that covers mechanoredox reactions using piezoelectric materials and manufacturing methods using the reaction setup with the ball mill. The authors declare no other competing interests. **Data and materials availability:** All data are available in the supplementary materials.

SUPPLEMENTARY MATERIALS

science.sciencemag.org/content/366/6472/1500/suppl/DC1
Materials and Methods
Figs. S1 to S9
Tables S1 to S5
NMR Spectra
References (*45*–*58*)
Movie S1

22 July 2019; accepted 30 October 2019
10.1126/science.aay8224

SOLID-STATE PHYSICS

Intermediate bosonic metallic state in the superconductor-insulator transition

Chao Yang[1]*, Yi Liu[2,3]*, Yang Wang[1], Liu Feng[1], Qianmei He[1], Jian Sun[2,3], Yue Tang[2,3], Chunchun Wu[1], Jie Xiong[1]†, Wanli Zhang[1], Xi Lin[2,3,4,5], Hong Yao[3,6,7], Haiwen Liu[8], Gustavo Fernandes[9], Jimmy Xu[9,10], James M. Valles Jr.[10]†, Jian Wang[2,3,4,5,7]†, Yanrong Li[1]

Whether a metallic ground state exists in a two-dimensional system beyond Anderson localization remains an unresolved question. We studied how quantum phase coherence evolves across superconductor–metal–insulator transitions through magnetoconductance quantum oscillations in nanopatterned high-temperature superconducting films. We tuned the degree of phase coherence by varying the etching time of our films. Between the superconducting and insulating regimes, we detected a robust intervening anomalous metallic state characterized by saturating resistance and oscillation amplitude at low temperatures. Our measurements suggest that the anomalous metallic state is bosonic and that the saturation of phase coherence plays a prominent role in its formation.

The scaling theory of localization predicts that metallic states are absent at zero temperature in two-dimensional (2D) disordered systems because of quantum interference (*1*, *2*). Consistently, when electrons form Cooper pairs in 2D disordered systems, the ground state should be a superconductor or an insulator. Nevertheless, approaching zero temperature, an anomalous metallic state has been experimentally observed (*3*–*15*) that shows a residual resistance far below the quantum resistance at low temperatures. The existence and origin of this unexpected metallic state are intensely debated (*16*–*25*).

The resistance saturation as a characteristic of an anomalous metallic state in 2D superconductors (*3*–*15*) has been experimentally observed in the ultralow temperature regime. However, extrinsic effects such as noise and carrier overheating may also disrupt phase coherence in superconductors, which casts doubt on the existence of 2D metallic ground states in superconducting systems (*26*). The phase coherence could be key to understanding the 2D metallic state. If the phase coherence length of electrons saturates at low temperatures, owing to the weakening of constructive quantum interference, the diffusion should not be absolutely prohibited, resulting in a possible metallic state in a low-dimensional electron system (*27*–*29*). Thus, it is crucial to investigate the phase coherence of Cooper pairs in the anomalous metallic state of 2D superconductors.

Here, we present a systematic study of Cooper pair phase coherence through the superconductor–anomalous metal phase transition followed by the anomalous metal-insulator phase transition in high-temperature (T_c) superconductor (HTS) films patterned with an array of holes.

We used reactive ion etching (RIE) to etch a high-quality, 12-nm-thick $YBa_2Cu_3O_{7-x}$ (YBCO) thin film through a contact mask with a triangular array of holes (fig. S1). Each mask is an anodized aluminum oxide (AAO) membrane formed on and then separated from an aluminum base (Fig. 1A). The approach offers the advantages of minimal molecular residuals and processing contamination (*30*–*32*).

The RIE transfers the pattern, which has ~70-nm-diameter holes with center-to-center hole spacing of ~103 nm, onto the HTS film (Fig. 1B). In the process, the ion bombardment impacts the sidewalls of the resultant pores to create a less crystalline and strained YBCO shell, which becomes thicker with increasing etching time (*32*, *33*). This was confirmed in a detailed high-resolution transmission electron microscopy (HRTEM) analysis, which showed a high density of structural defects around the nanopatterned holes (*34*). Thus, the normal state resistance grows with increasing etching time (fig. S2). We deduced from the transport data presented below that this process forms superconducting islands at the nodes of the triangular pore lattice connected to three links. The islands shrink, and the links become more resistive, with increasing etching time (Fig. 1C). The behavior of the measured $R_S(T)$ curves, where R_S is the sheet resistance and T is the temperature, of the nanopatterned YBCO thin films is consistent with a quantum phase transition (QPT) (Fig. 1D). The YBCO thin film subjected to the minimal RIE time remains superconducting (Fig. 1D). The superconducting onset critical temperature T_c^{onset} is defined as the temperature at which the sheet resistance $R_S(T)$ curve deviates from the linear extrapolation of the normal state (Fig. 1D and fig. S3), and the normal state sheet resistance is defined as $R_N = R_S(T_c^{onset})$. With increasing etching time, the superconducting transition region becomes wider, and the zero-resistance state fades away. We define this state as the anomalous metal (AM) state because there is a plateau of residual resistance at lower temperatures. The sheet resistance of a representative film (AM1) is shown in Fig. 1D. For films with the normal resistance larger than the critical value $R_S \approx 13$ kilohms, $R_S(T)$ has a positive slope ($dR_S/dT > 0$) below T_c^{onset} that turns negative ($dR_S/dT > 0$) at lower temperatures, indicating an insulating transition; we define this as a transitional state (TS). A typical TS curve is marked in Fig. 1D. The samples with more etching exhibit a more pronounced insulating upturn emerging at higher temperatures. With further etching, $R_S(T)$ increases monotonically ($dR_S/dT > 0$) toward infinity at zero temperature, indicating an insulating property over the whole temperature range. An example labeled as INS (insulating state) is shown in Fig. 1D. More details of electrical transport of all films can be found in fig. S3.

The characteristics of the anomalous metal state in HTS films with an array of nanopores are shown in Fig. 2. The Arrhenius plot of the anomalous metallic–state films and superconducting films are presented in Fig. 2A. For superconducting films, the resistance below T_c^{onset} drops to zero within the measurement resolution. For metallic-state films, in the low-temperature regime, the resistance drops and saturates to a finite value that can be up to five orders of magnitude smaller than that of the normal-state resistance. In the smallest saturating resistance film, the saturation of resistance starts at ~5 K, which is much higher than that of conventional superconductors (*4*–*8*, *10*–*15*). To exclude external noise effects, we measured a metallic-state film using well-filtered electrical leads in a dilution refrigerator cryostat down to 50 mK (Fig. 2B). The current-voltage relation (*I-V*) curves are linear below 100 nA, indicating that the measurements are in the ohmic regime (Fig. 2B, inset). The resistance saturation remains almost the same with or

[1]State Key Laboratory of Electronic Thin Films and Integrated Devices, University of Electronic Science and Technology of China, Chengdu 610054, China. [2]International Center for Quantum Materials, School of Physics, Peking University, Beijing 100871, China. [3]Collaborative Innovation Center of Quantum Matter, Beijing 100871, China. [4]CAS Center for Excellence in Topological Quantum Computation, University of Chinese Academy of Sciences, Beijing 100190, China. [5]Beijing Academy of Quantum Information Sciences, Beijing 100193, China. [6]Institute for Advanced Study, Tsinghua University, Beijing 100084, China. [7]State Key Laboratory of Low Dimensional Quantum Physics, Tsinghua University, Beijing 100084, China. [8]Center for Advanced Quantum Studies, Department of Physics, Beijing Normal University, Beijing 100875, China. [9]School of Engineering, Brown University, 182 Hope Street, Providence, RI 02912, USA. [10]Department of Physics, Brown University, 182 Hope Street, Providence, RI 02912, USA.
*These authors contributed equally to this work.
†Corresponding author. E-mail: jianwangphysics@pku.edu.cn (J.W.); james_valles_jr@brown.edu (J.M.V.); jiexiong@uestc.edu.cn (J.X.)

without the resistor-capacitor (RC) filters, demonstrating that the metallic state is intrinsic.

To further explore the nature of the anomalous metallic state, the Hall resistance (R_{xy}) and longitudinal resistance (R_{xx}) were measured simultaneously. Below T_c^{onset}, the slopes of $R_{xy}(H)$ curves, where H is the magnetic field strength, are largely suppressed and drop to zero with decreasing temperature for a representative metallic-state film (Fig. 2C, inset). Shown in Fig. 2C is the temperature dependence of R_{xy}, which becomes zero within the measurement resolution at a relatively high temperature of ~50 K, whereas R_{xx} is still finite. The absence of Hall resistance at low temperatures reveals the emergence of particle-hole symmetry in the anomalous metal. Furthermore, a giant positive longitudinal magnetoresistance is simultaneously observed as another important feature of this anomalous metallic state (Fig. 2D) (*13*). The observed zero Hall resistance and giant positive magnetoresistance can be further confirmed in another representative anomalous metallic–state film (AM10) (fig. S4).

Below T_c^{onset}, the perpendicular magnetoconductance of all the YBCO nanopore thin

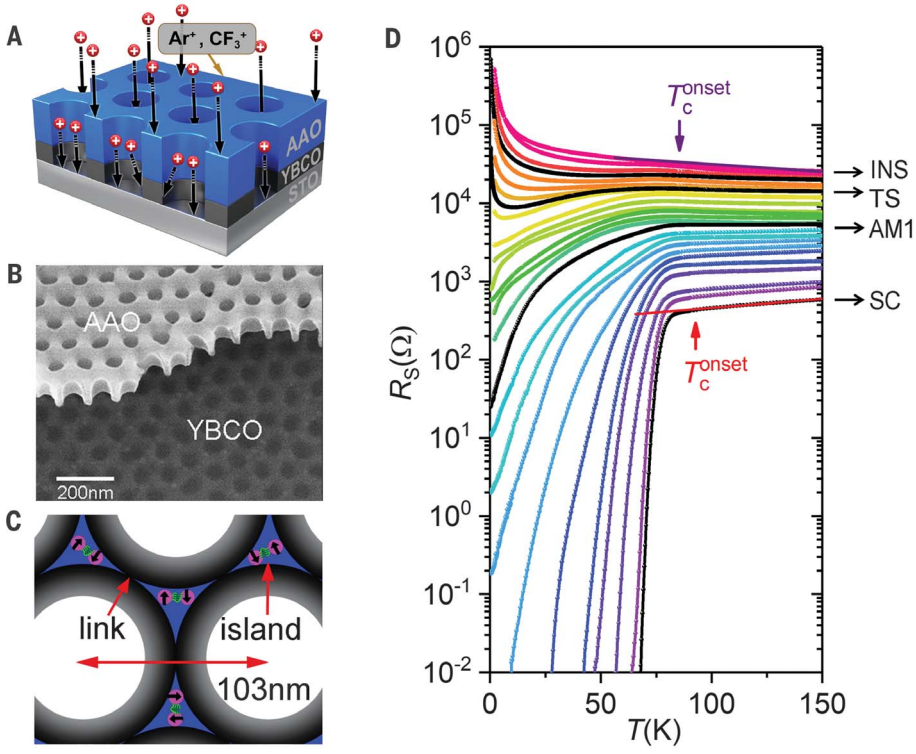

Fig. 1. Superconductor–anomalous metal–insulator transition in nanopore-modulated YBCO thin films. (**A**) Illustration of the fabricating process of nanopore-modulated YBCO thin films by means of reactive ion etching patterned by AAO (*41*). (**B**) Scanning electron microscopy image of etched nanopore YBCO films along with the AAO pattern. (**C**) Illustration of etched nanopore YBCO films. The gray halos indicate the parts weakened by the ion bombardment and etching; blue triangles indicate the superconducting islands. Cooper pairs are indicated with purple sphere pairs. (**D**) Temperature dependence of resistance for the etched nanopore YBCO films for different etching times, which increase from the bottom to the top curve, ranging from 20 to 160 s. The nanopore YBCO films undergo a QPT by tuning the etching time. The resistance of four representative films marked as superconducting (SC), anomalous metallic (AM1), transitional (TS), and insulating (INS) are shown in black.

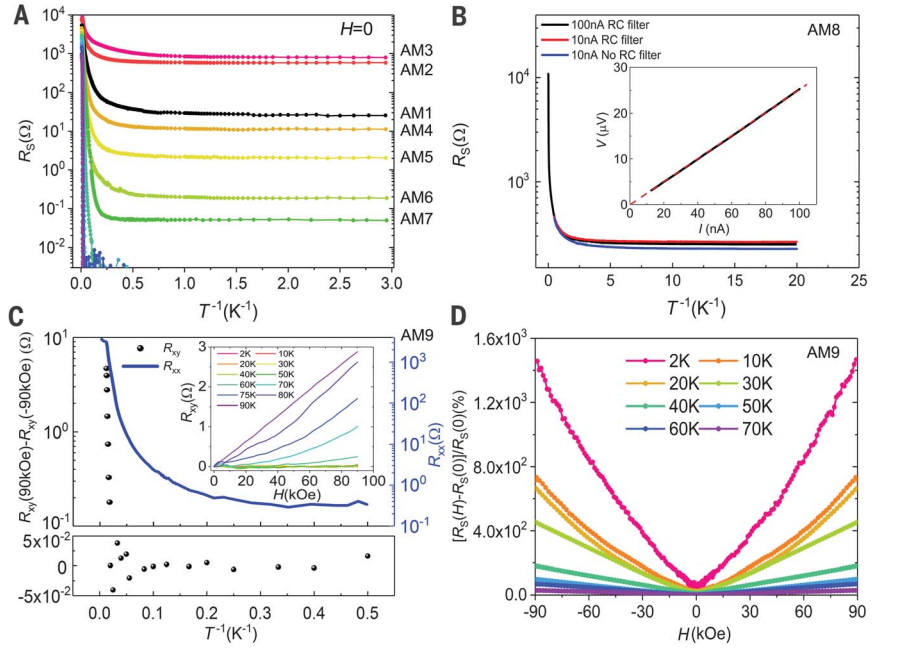

Fig. 2. The characteristics of anomalous metallic states. (**A**) Arrhenius plot of all the anomalous metallic–state films (AM1-AM7) and superconducting films. (**B**) Arrhenius plot of longitudinal resistance (R_{xx}) down to 50 mK, with and without filters of an anomalous metallic–state film (AM8). (Inset) *I-V* curve of the anomalous metallic–state film. The good linearity below 100 nA indicates that the measurements are within the ohmic region. (**C**) Arrhenius plot of Hall resistance (R_{xy}) and longitudinal resistance (R_{xx}) of a representative anomalous metallic–state film (AM9). The Hall resistance (R_{xy}) goes to zero at ~50 K. (Inset) Hall resistance (R_{xy}) of a representative anomalous metallic–state film. (**D**) Giant positive magnetoresistance of a representative anomalous metallic–state film (AM9).

films in Fig. 1D oscillates at low fields (Fig. 3, A to C) for three representative films. We present the data as the negative change of magnetoconductance $-\Delta G = G_0 - G(H)$, where G_0 is the conductance at zero magnetic field. The magnetoconductance of all films is symmetric, and the magnetoconductance oscillations appear on a monotonically rising background (full data are shown in fig. S5). Up to four magnetoconductance oscillations were detected with a constant period of $H_0 \sim 2.25$ kOe. This period is consistent with one superconducting flux quantum $\Phi_0 = h/2e$ threading an area of one unit cell of the nanopattern (around 9200 nm^2), where h is Planck's constant and e is the electron charge. The appearance of the charge $2e$ quantum oscillations just below T_c^{onset} demonstrate that Cooper pairs participate in the transport in all the states through the superconductor–metal–insulator transitions.

To highlight the temperature dependence of the oscillations, we define the magnetoconductance oscillation amplitude as $G_{osc} = |G(1/2H_0) - G_0|$ after subtracting the rising background (fig. S6). The temperature dependence of G_{osc} is shown in Fig. 3D on a logarithm scale for the films that exhibit superconducting, anomalous metallic, and insulating states. For the films in the superconducting state, the oscillation amplitude monotonically grows to a giant value beyond our measurement limit with decreasing temperature. By contrast, the oscillation amplitude saturates in the anomalous metallic region below 5 K (Fig. 3D), which is reminiscent of the residual resistance plateau of the anomalous metallic state at low temperatures (Fig. 2A). For insulating films (INS films), G_{osc} peaks and then drops with decreasing temperature. With increasing disorder, G_{osc} varies by at least nine orders of magnitude from the superconducting films to most insulating films in the zero-temperature limit, whereas the normal resistance only changes by two orders of magnitude. This finding demonstrates that the Cooper pair coherence can be controlled over a wide range by tuning the link resistance of nanopatterned YBCO films.

The electrical transport and the magnetoconductance oscillations in YBCO nanopore thin films can be qualitatively understood by modeling them as resistively shunted Josephson junction arrays. With increasing etching time, the link resistances grow, and the superconducting islands shrink (*35*), which drives the system through a superconductor–anomalous metal–insulator transition. For all films, T_c^{onset} varies by no more than 15% from the superconducting film to the insulating film, which indicates that the strength of local superconducting pairing remains stable through the QPT, whereas Cooper pair phase coherence can be tuned by increasing the link resistance.

The magnetoconductance oscillations originate from Cooper pair quantum interference effects in the multiply connected geometry imposed by the array structure (*36*, *37*). These effects enter through the Josephson coupling energy between nodes of the array, as given by $E_J = -J\cos(\phi_i - \phi_j - A_{ij})$, where $\phi_i - \phi_j$ is the gauge invariant phase difference of the order parameter between islands i and j, and $A_{ij} = 2e/\hbar\int_j^i \boldsymbol{A}\cdot\boldsymbol{dl}$ is the line integral of the vector potential between neighboring nodes ($\hbar$ is Planck's constant h divided by 2π). J is proportional to the order parameter amplitude on the islands. Josephson coupling energy E_J oscillates with increasing magnetic field because of the requirement that the line integral of the phase around a closed loop be a multiple of 2π. The dimensions of the array unit dictate the period of the oscillations. The magnetoconductance oscillates on the superconducting side because E_J is the barrier to thermally activated vortex motion (*37*); on the insulating and anomalous metal side, the magnetoconductance oscillates because E_J is proportional to the Cooper pair tunneling rate.

We now discuss the evolution of the temperature dependence of the oscillations across the QPT within this array model. For all the YBCO films, the oscillations appear just below T_c^{onset}, indicating that local phase coherence develops as soon as the amplitude of the order parameter forms on the islands. At lower temperatures, the oscillation amplitude is approximately proportional to the phase coherence as the growth of the order

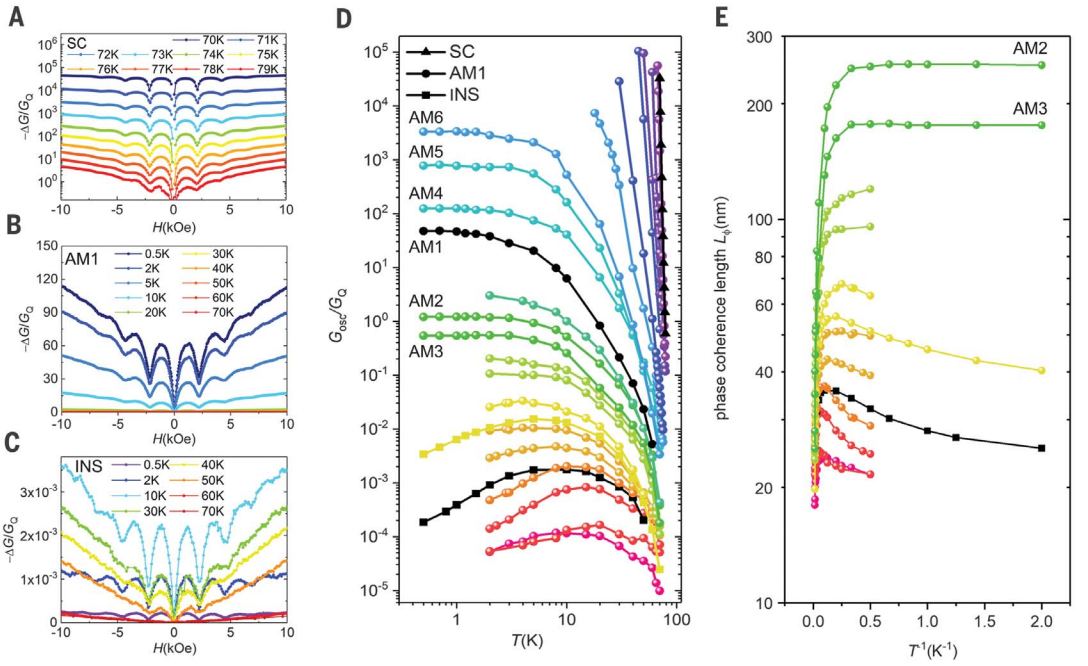

Fig. 3. The evolution of Cooper pairs coherence through the QPT. (**A** to **C**) Perpendicular negative change of magnetoconductance $-\Delta G/G_Q$ of three representative YBCO nanopore films at various temperatures. Shown are the data from a (A) superconducting-state film (SC), (B) anomalous metallic–state film (AM1), and (C) insulating-state film (INS). Up to four magnetoconductance oscillations are detected with a constant period of $H_0 \sim 2.25$ kOe, corresponding to one superconducting flux quantum per unit cell of the nanopattern. (**D**) Temperature dependence of magnetoconductance oscillations amplitude of all the YBCO films on a logarithmic scale. For the anomalous metallic–state films, G_{osc} saturates with decreasing temperature at ~5 K. By contrast, G_{osc} diverges at low temperatures for superconducting–state films, and G_{osc} peaks and drops at low temperatures for insulating–state film. Three representative YBCO films are shown in black. (**E**) Deduced phase coherence length of insulating and some metallic-state films with G_{osc} smaller or comparable with quantum conductance. In the anomalous metallic regime, the phase coherence length L_ϕ saturates at lower temperatures; in the insulating regime, the phase coherence length L_ϕ decreases with decreasing temperature.

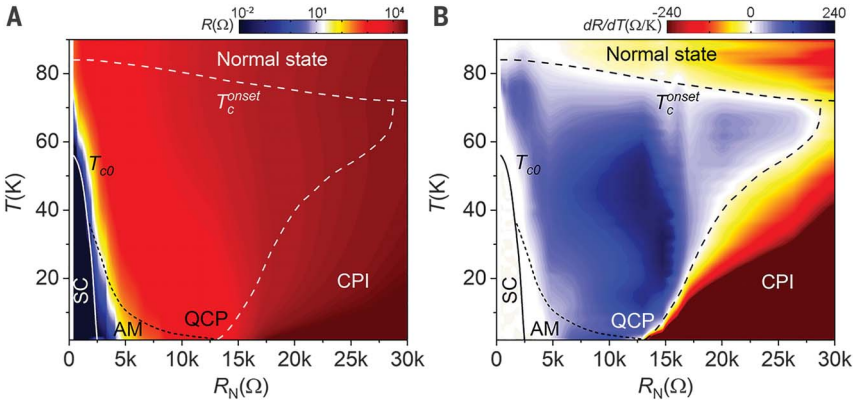

Fig. 4. Phase diagram of disorder tuned QPT in nanopatterned high-temperature superconductors. (**A** and **B**) Color-scaled maps of the (A) resistance and (B) differential resistance as a function of temperature and the normal-state resistance. The normal state and other states are separated by T_c^{onset} (top dashed line). Below T_c^{onset}, with increasing the normal-state resistance, the system is initially in the SC phase (zero resistance state within the instrument resolution), then AM phase (residual resistance plateau at low temperatures), and last, CPI phase (Cooper pair localized insulator). When approaching zero temperature, with increasing normal resistance, the system evolves from AM to CPI, separated by a quantum critical point around R_N ~ 13 kilohms.

parameter on the islands ceases. For superconducting films, the oscillation amplitude monotonically grows beyond our measurement range with decreasing temperature, indicating that the phase coherence length diverges in the zero-temperature limit. By contrast, the oscillation amplitude of the anomalous metallic–state films saturates below ~5 K after a steep growth. The saturating temperature dependence of the oscillation amplitude is consistent with that of the resistance, indicating that phase coherence saturation should be crucial to the formation of the anomalous metallic state. For the insulating films, as the link resistance rises beyond $R_Q = h/4e^2$ with decreasing temperature, the inter-island capacitance and self-capacitances of the islands can produce a Coulomb blockade to Cooper pair transport (*38*). Thus, G_{osc} and the phase coherence length decrease as the Cooper pairs become localized. In order to quantify phase coherence through the QPT, we estimated the phase coherence length L_ϕ by using the formula $G_{osc} = \frac{4e^2}{h}\left(\frac{L_\phi}{\pi r}\right)^{1.5}\exp\left(-\frac{\pi r}{L_\phi}\right)$ for quasi-particle quantum interference (*29*, *39*), where r is half of the center-to-center hole spacing ~50 nm. The above formula can only be applied to insulating or some metallic-state films with relatively large residual resistance when G_{osc} is smaller or comparable with quantum conductance. The temperature dependence of L_ϕ are presented in Fig. 3E, indicating a saturation of quantum coherence for anomalous metallic states in the low-temperature regime. The magnetoconductance oscillation amplitude observed in the anomalous metallic states with small residual resistance is giant and much larger than the quantum conductance, which is difficult to explain by using only quasi-particle quantum interference, leaving this an open question for further investigation.

The phase diagrams of resistance and differential resistance as a function of temperature and normal resistance R_N in Fig. 4 provide a summary of the results. We use R_N as the tuning parameter because it is directly related to the etching time (fig. S2) and increases with increasing disorder in the nanopatterned films (*35*). The normal state and other states are separated by T_c^{onset}. At the boundary from $dR_s/dT > 0$ to $dR_s/dT = 0$, the array resistance drops below T_c^{onset} to zero (SC) or a plateau of residual resistance (AM) at the lowest temperatures, as shown in the bottom-left part of the phase diagram (Fig. 4). The short dashed line in Fig. 4 represents the crossover between the AM state and the region where resistance drops rapidly. Below T_c^{onset}, the onset of insulating behavior is visible in the lower right region in Fig. 4, where dR_s/dT is negative. We label this region as the Cooper pair insulator (CPI). Approaching zero temperature, with increasing R_N, there is a regime where dR_s/dT changes from zero to a negative value, which can be interpreted as the critical regime of a quantum phase transition. The phase diagram shows the evolution of an anomalous metallic state to a Cooper pair insulating state separated by a QCP around R_N ~ 13 kilohms.

To date, the nature of the anomalous metallic state in 2D systems remains a mystery. Candidate theories invoke coupling to a dissipative bath (*16*–*18*), a Bose metal phase (*19*–*21*), order parameter fluctuations (*22*–*24*), and a composite Fermi liquid phase (*25*). In our HTS system, this anomalous metallic state is clearly a bosonic state demonstrated by the $h/2e$ periodic quantum oscillations and zero Hall resistance, which appears to rule out the scenarios that are based on charge e carriers. The phase coherence saturation is argued to be the key to understanding the low-dimensional metallic state at low temperatures (*27*–*29*, *40*). Investigations of Cooper pair phase coherence may be the right approach for revealing the nature of this anomalous metallic state. Furthermore, our work on this HTS also paves the way for investigations on the anomalous state of matter by using finite frequency probes, such as terahertz spectroscopy, that are more difficult to apply at dilution refrigerator temperatures.

REFERENCES AND NOTES

1. E. Abrahams, P. W. Anderson, D. C. Licciardello, T. V. Ramakrishnan, *Phys. Rev. Lett.* **42**, 673–676 (1979).
2. B. L. Altshuler, A. G. Aronov, in *Electron–Electron Interactions in Disordered Systems* A. L. Efros, M. Pollak, Eds. (North-Holland, 1985).
3. H. M. Jaeger, D. B. Haviland, B. G. Orr, A. M. Goldman, *Phys. Rev. B* **40**, 182–196 (1989).
4. D. Ephron, A. Yazdani, A. Kapitulnik, M. R. Beasley, *Phys. Rev. Lett.* **76**, 1529–1532 (1996).
5. N. Mason, A. Kapitulnik, *Phys. Rev. Lett.* **82**, 5341–5344 (1999).
6. C. Christiansen, L. M. Hernandez, A. M. Goldman, *Phys. Rev. Lett.* **88**, 037004 (2002).
7. S. Eley, S. Gopalakrishnan, P. M. Goldbart, N. Mason, *Nat. Phys.* **8**, 59–62 (2012).
8. W. Liu *et al.*, *Phys. Rev. Lett.* **111**, 067003 (2013).
9. J. Garcia-Barriocanal *et al.*, *Phys. Rev. B* **87**, 024509 (2013).
10. Z. Han *et al.*, *Nat. Phys.* **10**, 380–386 (2014).
11. Y. Saito, Y. Kasahara, J. Ye, Y. Iwasa, T. Nojima, *Science* **350**, 409–413 (2015).
12. N. P. Breznay, A. Kapitulnik, *Sci. Adv.* **3**, e1700612 (2017).
13. A. Kapitulnik, S. A. Kivelson, B. Spivak, *Rev. Mod. Phys.* **91**, 011002 (2019).
14. C. G. L. Bøttcher *et al.*, *Nat. Phys.* **14**, 1138–1144 (2018).
15. Z. Chen *et al.*, *Nat. Commun.* **9**, 4008 (2018).
16. E. Shimshoni, A. Auerbach, A. Kapitulnik, *Phys. Rev. Lett.* **80**, 3352–3355 (1998).
17. A. Kapitulnik, N. Mason, S. A. Kivelson, S. Chakravarty, *Phys. Rev. B* **63**, 125322 (2001).
18. V. M. Galitski, G. Refael, M. P. A. Fisher, T. Senthil, *Phys. Rev. Lett.* **95**, 077002 (2005).
19. D. H. Lee, S. Kivelson, S. C. Zhang, *Phys. Rev. Lett.* **67**, 3302–3305 (1991).
20. D. Das, S. Doniach, *Phys. Rev. B* **60**, 1261–1275 (1999).
21. P. Phillips, D. Dalidovich, *Science* **302**, 243–247 (2003).
22. M. Feigel'man, A. Larkin, *Chem. Phys.* **235**, 107–114 (1998).
23. B. Spivak, A. Zyuzin, M. Hruska, *Phys. Rev. B* **64**, 132502 (2001).
24. B. Spivak, P. Oreto, S. A. Kivelson, *Phys. Rev. B* **77**, 214523 (2008).
25. M. Mulligan, S. Raghu, *Phys. Rev. B* **93**, 205116 (2016).
26. I. Tamir *et al.*, *Sci. Adv.* **5**, eaau3826 (2019).
27. P. Mohanty, E. M. Q. Jariwala, R. A. Webb, *Phys. Rev. Lett.* **78**, 3366–3369 (1997).
28. J. J. Lin, J. P. Bird, *J. Phys. Condens. Matter* **14**, 201 (2002).
29. F. Pierre *et al.*, *Phys. Rev. B* **68**, 085413 (2003).
30. J. Liang, H. Chik, A. Yin, J. Xu, *J. Appl. Phys.* **91**, 2544–2546 (2002).
31. H. Chik, J. M. Xu, *Mater. Sci. Eng. Rep.* **43**, 103–138 (2004).
32. S. G. Cloutier, P. A. Kossyrev, J. Xu, *Nat. Mater.* **4**, 887–891 (2005).
33. S. A. Cybart *et al.*, *Nat. Nanotechnol.* **10**, 598–602 (2015).
34. S. G. Cloutier, C. H. Hsu, P. A. Kossyrev, J. Xu, *Adv. Mater.* **18**, 841–844 (2006).
35. J. M. Valles Jr. *et al.*, *Phys. Rev. B* **39**, 11599–11602 (1989).

36. M. D. Stewart Jr., A. Yin, J. M. Xu, J. M. Valles Jr., *Science* **318**, 1273–1275 (2007).
37. I. Sochnikov, A. Shaulov, Y. Yeshurun, G. Logvenov, I. Bozović, *Nat. Nanotechnol.* **5**, 516–519 (2010).
38. Y. Takahide, H. Miyazaki, A. Kanda, Y. Ootuka, *J. Phys. Soc. Jpn.* **72**, 96–99 (2003).
39. E. Akkermans, G. Montambaux, *Mesoscopic Physics of Electrons and Photons* (Cambridge Univ. Press, 2007).
40. S. Washburn, R. A. Webb, *Adv. Phys.* **35**, 375–422 (1986).
41. Materials and methods are available as supplementary materials.
42. C. Yang *et al.*, Raw data for "Intermediate bosonic metallic state in the superconductor-insulator transition". Zenodo (2019); doi:10.5281/zenodo.3517821.

ACKNOWLEDGMENTS

We thank S. A. Kivelson, J. M. Kosterlitz, D. Oller, D. He, J. H. Kim, D. J. Lee, K. Liu, J. Qi, Yudong Liu, Q. Li, Yanzhao Liu, and Y. Xing for the fruitful discussions. **Funding:** This work was supported by the National Natural Science Foundation of China (grants 11888101, 51722204, 11774008, 91421110, 11474175, 11674028, and 11825404), the National Key Research and Development Program of China (grants 2018YFA0305604, 2015CB358600, 2017YFA0303300, 2016YFA0301001, and 2017YFA0304600), Fundamental Research Funds for the Central Universities (ZYGX2016Z004), the Strategic Priority Research Program of Chinese Academy of Sciences (grant XDB28000000), the Open Research Fund Program of the State Key Laboratory of Low-Dimensional Quantum Physics, Tsinghua University (grant KF201703), Beijing Natural Science Foundation (Z180010), Beijing Municipal Science and Technology Commission (Z181100004218001), and China Postdoctoral Science Foundation (grant 2019M650290). **Author contributions:** J.W., J.X., and J.M.V. conceived and instructed the research; C.Y. and Y.Liu performed the transport measurements, with the assistance of Y.W., Q.H., C.W., J.S., Y.T., X.L., and J.W.; C.Y., L.F., J.X., W.Z., and Y.Li fabricated the samples with the instruction from J.M.X. and G.F.; H.L. and H.Y. gave the theoretical analysis; C.Y., Y.Liu, J.W., J.X., and J.M.V. analyzed the data, with the contribution of H.L.; C.Y., Y.Liu, J.W., J.X., J.M.X., and J.M.V. wrote the manuscript, with input from all authors. **Competing interests:** The authors declare no competing interests. **Data and materials availability:** All experimental data shown in the main text and in the supplementary materials are accessible at the Zenodo repository (*42*).

SUPPLEMENTARY MATERIALS

science.sciencemag.org/content/366/6472/1505/suppl/DC1
Materials and Methods
Supplementary Text
Figs. S1 to S7

4 April 2019; accepted 1 November 2019
Published online 14 November 2019
10.1126/science.aax5798

SOLAR CELLS

Constructive molecular configurations for surface-defect passivation of perovskite photovoltaics

Rui Wang[1]*, Jingjing Xue[1]*†, Kai-Li Wang[2]*, Zhao-Kui Wang[1,2]†, Yanqi Luo[3], David Fenning[3], Guangwei Xu[1], Selbi Nuryyeva[1,4], Tianyi Huang[1], Yepin Zhao[1], Jonathan Lee Yang[5], Jiahui Zhu[1], Minhuan Wang[1], Shaun Tan[1], Ilhan Yavuz[6]†, Kendall N. Houk[4]†, Yang Yang[1,7]†

Surface trap–mediated nonradiative charge recombination is a major limit to achieving high-efficiency metal-halide perovskite photovoltaics. The ionic character of perovskite lattice has enabled molecular defect passivation approaches through interaction between functional groups and defects. However, a lack of in-depth understanding of how the molecular configuration influences the passivation effectiveness is a challenge to rational molecule design. Here, the chemical environment of a functional group that is activated for defect passivation was systematically investigated with theophylline, caffeine, and theobromine. When N-H and C=O were in an optimal configuration in the molecule, hydrogen-bond formation between N-H and I (iodine) assisted the primary C=O binding with the antisite Pb (lead) defect to maximize surface-defect binding. A stabilized power conversion efficiency of 22.6% of photovoltaic device was demonstrated with theophylline treatment.

Defect passivation to reduce unproductive charge recombination is an effective strategy to increase the power conversion efficiency (PCE) of polycrystalline metal-halide perovskite thin-film photovoltaics (PVs) (*1*–*6*). The ionic nature of the perovskite lattice enables molecular passivation through coordinate binding based on Lewis acid-base chemistry (*7*–*10*). Organic molecules containing various functional groups, such as carbonyl groups, can passivate defects (*11*–*17*). The selection of molecules with optimal binding configurations for defect passivation would benefit from molecular design rules.

We demonstrate high efficiencies for $(FAPbI_3)_x(MAPbBr_3)_{1-x}$ (where FA is formamidinium and MA is methylammonium; x is 0.92 in the precursor) perovskite PV devices through defect identification followed by rational design and comprehensive investigation of the chemical environment around the active functional group for defect passivation (*18*). In high-quality perovskite polycrystalline thin films that have monolayered grains (*19*–*21*), interior defects of perovskite are negligible compared with the surface defects. We used density functional theory (DFT) calculations to compare the formation energies of selected native defects on the perovskite surface. Particularly taken into consideration were Pb- and I-involving point defects, Pb vacancy (V_{Pb}), I vacancy (V_I), and Pb-I antisite (Pb_I and I_{Pb}, corresponding to I site substitution by Pb and Pb site substitution by I, respectively) because the band edges of perovskite were reported to be composed of Pb and I orbitals (*22*, *23*).

As confirmed by x-ray photoelectron spectroscopy (XPS), the surface of the as-fabricated perovskite thin film synthesized by a two-step method was Pb-rich (fig. S1), and we focused on the (100) surface with PbI_2 termination in a Pb-rich condition. The types of surface defects studied and their corresponding top-layer view of atomic structures are shown in Fig. 1A. Using the Dispersion Correction 3 (DFT-D3) method, we calculated the defect formation energies (DFEs) (table S1) of V_{Pb}, V_I, Pb_I, and I_{Pb} on the surface to be 3.20, 0.51, 0.57, and 3.15 eV, respectively. Compared with the values reported in bulk perovskite, V_{Pb}, V_I, and I_{Pb} defects show similar DFEs (*24*), whereas the Pb_I antisite defect exhibited particularly lower formation energy than that in the bulk. Thus, the Pb_I antisite defect should form more readily and predominate on the surface. We did not consider V_I further despite its DFE being as low as that of Pb_I, because the interaction of molecules with the V_I turned out to be not energy favorable (fig. S2).

On the basis of these results, we focused on the interaction between the surface Pb_I antisite defect and candidate molecules for defect passivation. A set of small molecules sharing the identical functional groups but with strategically varying chemical structure were investigated, namely theophylline, caffeine, and theobromine, interacting with the defects (Fig. 1B). These molecules are found in natural

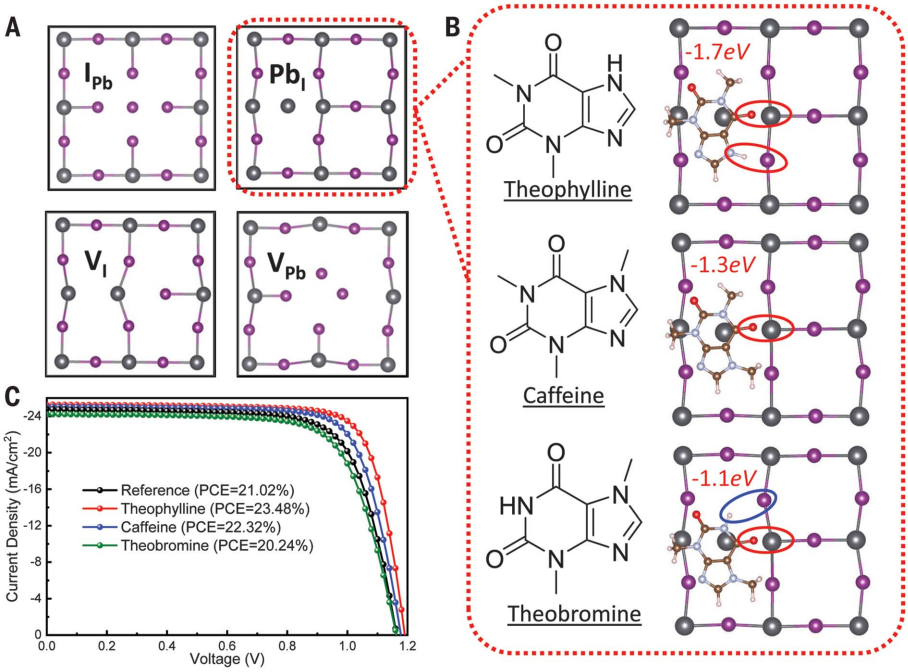

Fig. 1. Surface-defect identification and constructive configuration of the C=O group in three different chemical environments. (**A**) Top view of the various types of surface defects. (**B**) Theoretical models of perovskite with molecular surface passivation of Pb_I antisite with theophylline, caffeine, and theobromine. (**C**) *J-V* curves of perovskite solar cells with or without small-molecules treatment under reverse scan direction.

[1]Department of Materials Science and Engineering and California NanoSystems Institute, University of California Los Angeles, CA 90095, USA. [2]Institute of Functional Nano & Soft Materials (FUNSOM), Jiangsu Key Laboratory for Carbon-Based Functional Materials & Devices, Soochow University, Suzhou 215123, China. [3]Department of Nanoengineering, University of California, San Diego, La Jolla, CA 92093, USA. [4]Department of Chemistry and Biochemistry, University of California Los Angeles, CA 90095, USA. [5]College of Chemistry, University of California Berkeley, CA 94720, USA. [6]Department of Physics, Marmara University, Ziverbey, Istanbul 34722, Turkey. [7]School of Engineering, Westlake University, Hangzhou 310024, China.
*These authors contributed equally to this work.
†Corresponding author. Email: jjxue@ucla.edu (J.X.); zkwang@suda.edu.cn (Z.-K.W.); ilhan.yavuz@marmara.edu.tr (I.Y.); houk@chem.ucla.edu (K.N.H.); yangy@ucla.edu (Y.Y.)

products (tea, coffee, and chocolate, respectively) and are readily accessible. In these molecules, the conjugated structure as well as the dipoles induced by the hetero atoms tend to increase the intermolecular interaction. This renders them nonvolatile in nature, which is key to the investigation of their interactions with defects in perovskite and long-term stability of the devices. The xanthine core also helps maintain the coplanarity of the carbonyl group and the N–H. Unlike other small molecules with flexible alkyl chains, this rigidity allows us to define the configuration and distance between the carbonyl group and N–H when they are interacting with the defects, as a result of which the constructive molecular configuration for defect passivation can be unraveled.

We incorporated theophylline onto the surface of perovskite thin film using a post-treatment method, and a PCE enhancement from 21.02% (stabilized 20.36%) to 23.48% (stabilized 22.64%) was observed in the PV devices with ITO/SnO_2/perovskite/Spiro-OMeTAD/Ag structure under reverse scan direction [where ITO is indium tin oxide, SnO_2 is tin oxide, and Spiro-OMeTAD is 2,2′7,7′-tetrakis-(*N*,*N*-di-*p*-methoxyphenyl amine)-9,9′-spirobifluorene]. Current density-voltage (*J-V*) curves of the PV devices with and without theophylline treatment are compared in Fig. 1C and table S2. The control device showed an open-circuit voltage (V_{OC}) of 1.164 V, a short-circuit current (J_{SC}) of 24.78 mA cm^{-2}, and a fill factor (FF) of 72.88%, whereas the target device showed a V_{OC} of 1.191 V, a J_{SC} of 25.24 mA cm^{-2}, and an FF of 78.11%. The enhancement in the V_{OC} was attributed to the surface passivation by theophylline through the Lewis base-acid interaction between C=O group and the antisite Pb. As shown in the surface structure model of perovskite with theophylline (Fig. 1B), the C=O group on theophylline strongly interacted with the antisite Pb. The neighboring N–H on the imidazole ring also interacted with the I of PbI_6^{2-} octahedron through a hydrogen bond (H-bond), which strengthened the absorption of theophylline onto the Pb_I defect, resulting in an interaction energy (E_{int}, defined as $E_{molecule\text{-}perovskite} - E_{perovskite} - E_{molecule}$) as strong as −1.7 eV.

This observation suggested that the neighboring H-bond between the xanthine molecule and the PbI_6^{2-} octahedron can contribute to the defect passivation. A methyl group was added to the N on the imidazole ring of theophylline (resulting in caffeine) to eliminate the effect from H-bonding between the N–H and I, leaving just the interaction with surface Pb_I defects (Fig. 1B). The missing H-bond between N–H and PbI_6^{2-} octahedron resulted in a weakened interaction and a less favorable E_{int} of −1.3 eV. Compared with the theophylline-treated device, a caffeine-treated perovskite PV device had a lower PCE of 22.32% along with a lower V_{OC} of 1.178 V, J_{SC} of 25.04 mA cm^{-2}, and FF of 75.76%.

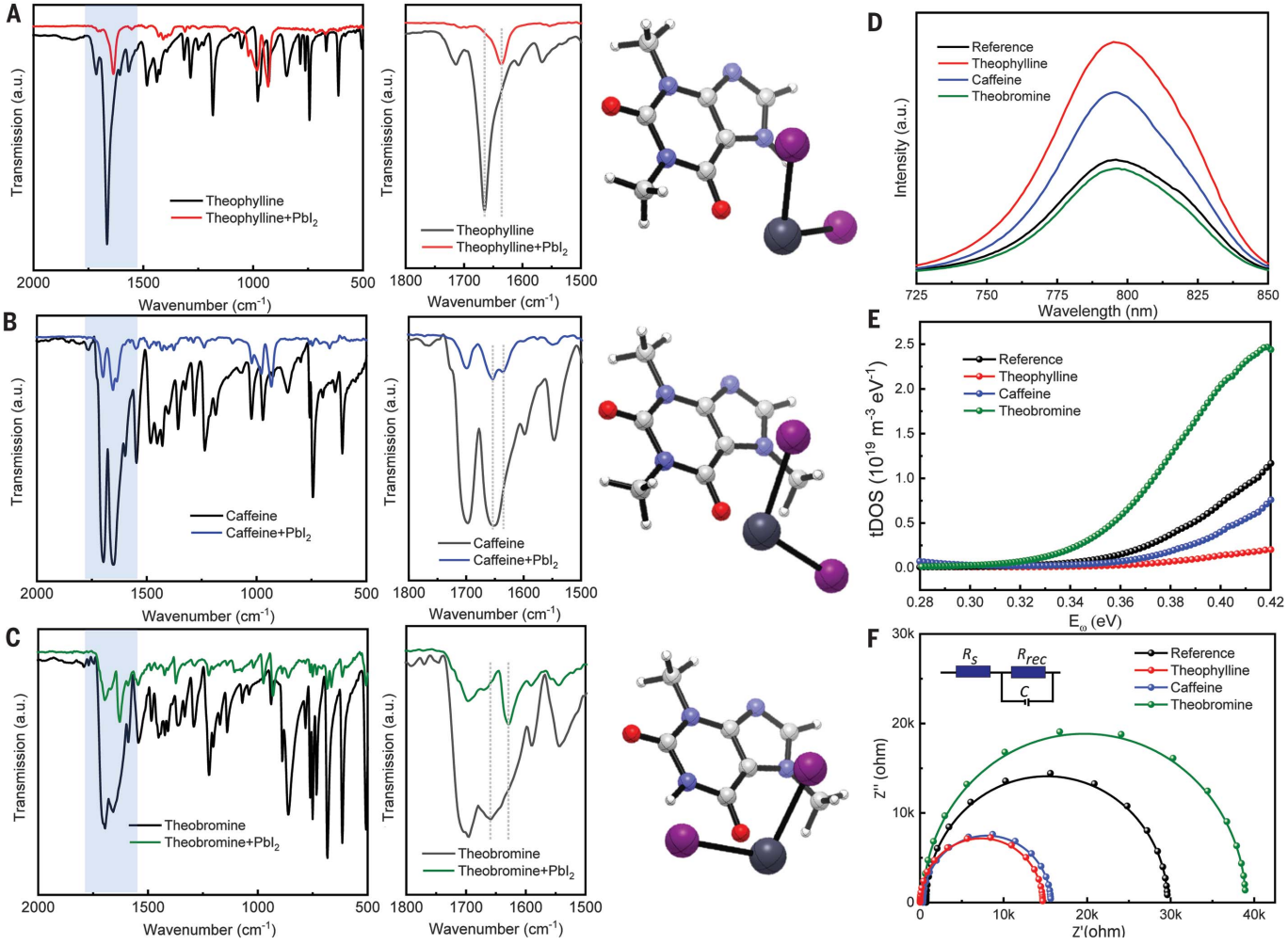

Fig. 2. Investigation of the interactions between surface defects and the small molecules. FTIR spectra of (**A**) pure theophylline and theophylline-PbI_2 films, (**B**) pure caffeine and caffeine-PbI_2 films, and (**C**) pure theobromine and theobromine-PbI_2 films. (**D**) PL spectra of perovskite films without and with small-molecules treatment. (**E**) *t*DOS in perovskite solar cells with or without small-molecules treatment. (**F**) Nyquist plots of perovskite solar cells with or without small-molecules treatment measured in the dark and at corresponding open-circuit voltages. a.u., arbitrary units; *C*, junction capacitance; R_{rec}, recombination resistance; R_s, Series Resistance.

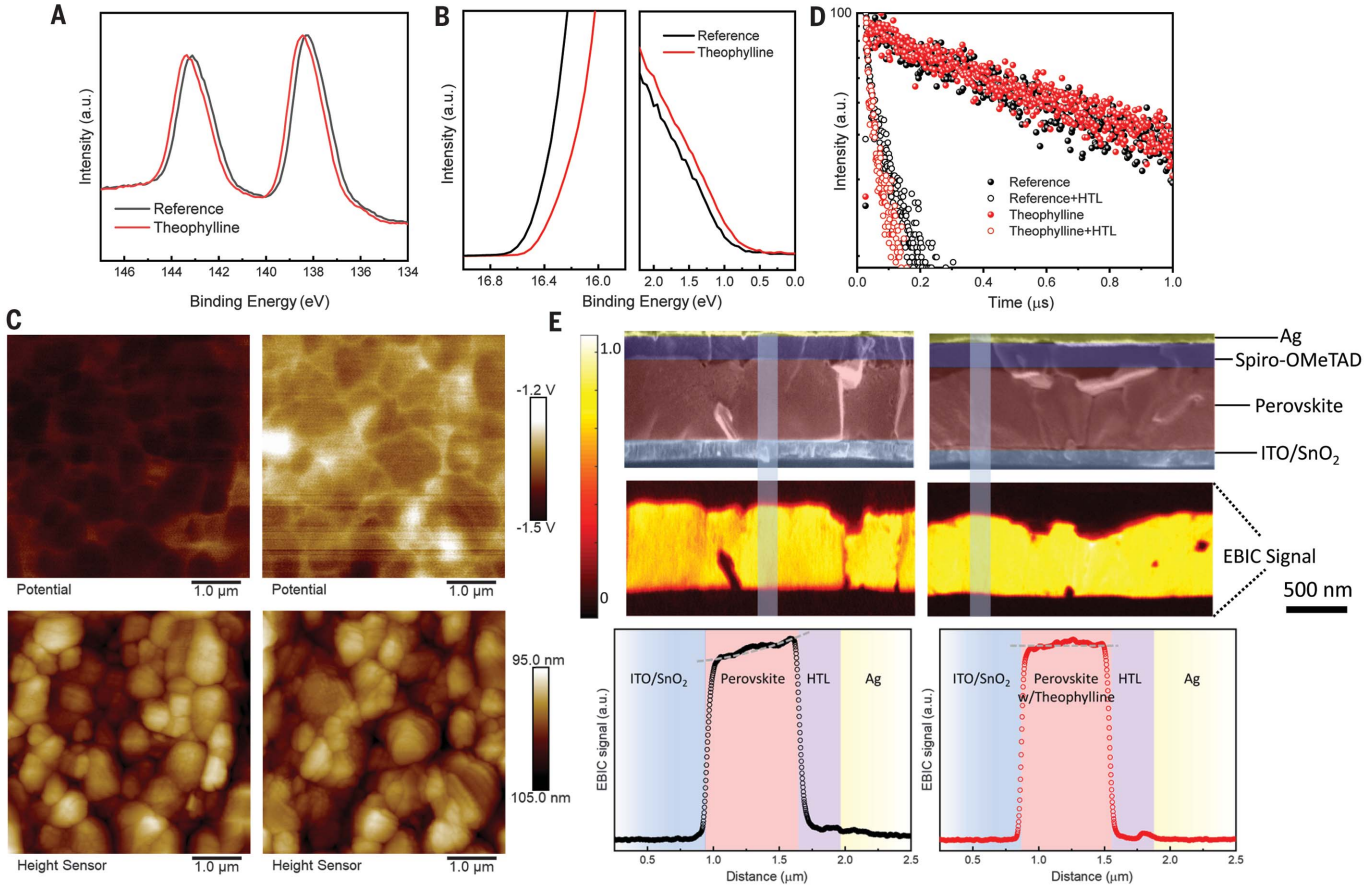

Fig. 3. Characterization of perovskite films and interfaces with theophylline treatment. (**A**) XPS data for Pb 4f 7/2 and Pb 4f 5/2 core-level spectra in perovskite films with or without theophylline treatment. (**B**) UPS spectra of perovskite films with or without theophylline treatment. (**C**) AFM and KPFM images of perovskite films with (right) or without (left) theophylline treatment. (**D**) Time-resolved PL spectra of perovskite films before and after depositing Spiro-OMeTAD without and with theophylline treatment. (**E**) Cross-section SEM images and the corresponding EBIC images and line profile of the perovskite solar cells with (right) or without (left) theophylline treatment.

When the N–H group was located next to the C=O group on the same six-membered ring, producing a shorter distance between the C=O and the N–H, in theobromine, the spatially effective interaction between the N–H and I was disabled as C=O was bound to antisite Pb, resulting in an even weaker E_{int} of −1.1 eV (Fig. 1B). Although C=O and N–H are both present on the molecule, the lack of appropriate coordination of I to the molecule led to a spatially destructive molecular configuration. The theobromine-treated devices showed a decrease in PCE to 20.24% with a lower V_{OC} of 1.163 V, J_{SC} of 24.27 mA cm^{-2}, and FF of 71.58% compared with the reference device. This result emphasizes the importance of the constructive configuration of N–H and C=O groups that enable the cooperative multisite interaction and synergistic passivation effect.

We studied the variation in the C=O and the PbI_2-terminated perovskite surface interaction with different molecular configurations using Fourier-transform infrared spectroscopy (FTIR). The C=O in pure theophylline showed a typical stretching vibration mode at 1660 cm^{-1} that it shifted to 1630 cm^{-1} upon binding to PbI_2 (Fig. 2A). The downward shift of 30 cm^{-1} of the C=O stretching vibration frequency resulted from the electron delocalization in C=O when a Lewis base-acid adduct was formed, demonstrating a strong interaction between PbI_2 and C=O in theophylline. The atomic distance between the O in C=O and the Pb in PbI_2, on the basis of theoretical modeling, was as low as 2.28 Å.

When the H atom was replaced by a methyl group on the N of imidazole to eliminate the effect of an H bond, the vibration frequency of C=O in caffeine shifted only 10 cm^{-1} upon addition of PbI_2, indicating a weakened interaction between the C=O and PbI_2 (Fig. 2B). The atomic distance between the corresponding O and Pb also increased to 2.32 Å. In the case of theobromine, when the N–H was in a closer position to C=O, the interaction between the molecule and PbI_2 became comparable to that in theophylline, as evidenced by the large shift of C=O stretching vibration frequency from 1655 to 1620 cm^{-1} and the short distance between O and Pb (Fig. 2C). However, this strong interaction was enabled by the free rotation of PbI_2, which resulted in a different configuration than that in theophylline and caffeine. Hence, when the configuration of PbI_2 was fixed and had a 90° angle between Pb and I atom, like that on perovskite surface (the PbI_6^{2-} octahedron), the N–H was in a position that led to an unfavorable interaction with I. This configuration would cause either weakened interaction between the molecule and the perovskite surface or distorted PbI_6^{2-} octahedron, resulting in the ineffectiveness of defect passivation and perhaps causing even more defects through lattice distortion (fig. S3).

The surface passivation effects of the three molecules with different configuration were further studied by photoluminescence (PL). The PL intensity increased noticeably with the treatment by theophylline (Fig. 2D), implying the suppressed nonradiative charge-recombination sites from defects (*15*). With

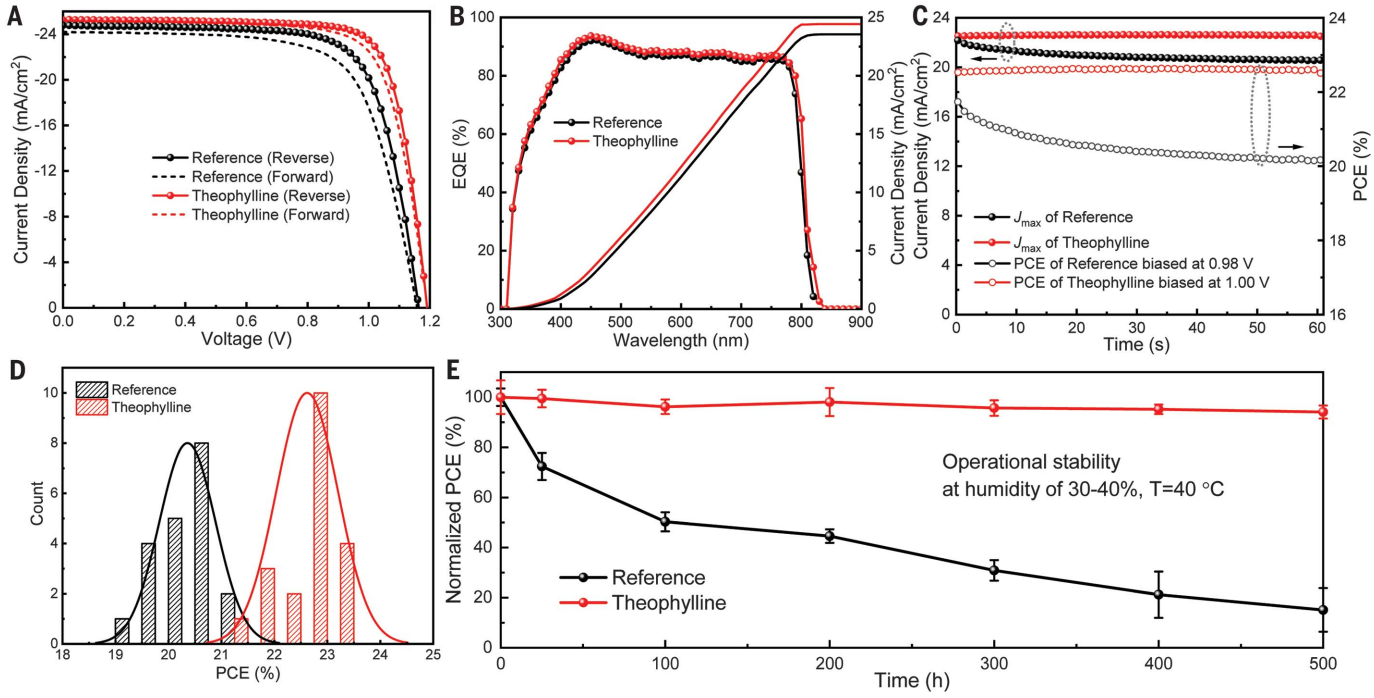

Fig. 4. Enhanced photovoltaic performance and long-term stability of perovskite solar cells with theophylline treatment. (**A**) *J-V* curves of perovskite solar cells with or without theophylline treatment. (**B**) EQE curves of perovskite solar cells with or without theophylline treatment. (**C**) Stabilized maximum power output and the photocurrent density at maximum power point as a function of time for the best-performing perovskite solar cells with or without theophylline treatment, as shown in (A), recorded under simulated 1-sun AM1.5G illumination. (**D**) PCE distribution of perovskite solar cells with or without theophylline treatment. (**E**) Evolution of the PCEs measured from the encapsulated perovskite solar cells with or without theophylline treatment exposed to continuous light (90 ± 10 mW cm^{-2}) under open-circuit condition.

the caffeine treatment, enhanced PL intensity was also observed, but not as strong as that with the theophylline, suggesting a less effective passivation effect. For theobromine, however, a decrease in PL intensity was observed compared with the reference material, which can be attributed to the destructive molecular configuration of the passivation agents causing more charge recombination sites.

The trap density of states (*t*DOS) of the as-fabricated devices were also deduced from the angular frequency-dependent capacitance. As shown in Fig. 2E, the *t*DOS as a function of the defect energy demonstrated a reduction in trap states for theophylline- and caffeine-treated perovskite compared with the reference device. By contrast, theobromine treatment induced more trap states, consistent with the decrease in PCE. The change in *t*DOS with different surface treatments was also confirmed by theoretical modeling (fig. S4). In addition, electrochemical impedance spectroscopy (EIS) characterization was performed to demonstrate the carrier transport processes under illumination at the interface. The middle frequency zone of the EIS semicircle should be dominated by junction capacitance and recombination resistance related to the interfaces between transport materials and perovskite. According to Fig. 2F, the device with theophylline surface treatment has the smallest impedance, signifying a substantially suppressed charge recombination at the interface, which originated from the reduced surface-defect states. A larger impedance was observed in caffeine-treated device, and an even larger impedance was measured in theobromine-treated device.

Further characterizations were performed to better understand the perovskite interface with theophylline. High-resolution XPS patterns of the Pb 4f for the theophylline-treated film showed two main peaks located at 138.48 and 143.38 eV, corresponding to the Pb 4f 7/2 and Pb 4f 5/2, respectively (Fig. 3A), whereas the reference film showed two main peaks at 138.27 and 143.13 eV. The peaks from Pb 4f shifted to higher binding energies in the film with theophylline surface treatment, indicating the interaction between the theophylline and the Pb on perovskite surface. We used ultraviolet photoelectron spectroscopy (UPS) to measure the surface band structure with and without the theophylline surface treatment. The work function was determined to be −4.77 and −4.96 eV with the valance band maximum of −5.66 and −5.73 eV for reference and theophylline, respectively (Fig. 3B). This difference indicated a less *n*-type surface after theophylline treatment, which could improve the hole extraction in devices.

Atomic force microscopy (AFM) combined with Kelvin probe force microscopy (KPFM) was further applied to probe the effect of theophylline on the surface morphology and surface potential. The theophylline-treated surface exhibited a higher electronic chemical potential than that of reference film, while keeping the surface morphology unchanged (Fig. 3C). The transient PL of the perovskite films with hole-transporting layer (HTL) was compared in Fig. 3D to delineate the carrier dynamics of the devices. The perovskite film with theophylline treatment showed a slightly longer carrier lifetime than the reference film, whereas a faster decay profile was observed when adding the HTL on top of the perovskite film. This result demonstrated a better hole extraction with theophylline treatment (*20*), most likely arising from lesser recombination sites at the interface and the slightly shallower work function of the perovskite film with theophylline.

The improved carrier dynamics originating from the effective surface passivation by theophylline was further characterized by cross-sectional electron-beam–induced current (EBIC) measurement. In EBIC measurement,

the electron-beam–excited carriers were collected on the basis of the collection probability CP (x, L_d), where x is the distance between junction and incident beam position, and L_d is the diffusion length of the carriers (fig. S5). The device with theophylline treatment exhibited higher EBIC current compared with the reference device (Fig. 3E). The average intensity extracted from these EBIC maps demonstrated a general increase in the EBIC signal after treatment with theophylline (fig. S6), indicating an enhanced carrier collection efficiency (*25*). Specifically, in Fig. 3E, a representative EBIC line profile of the reference device showed a current decay from the HTL-perovskite to the SnO_2-perovskite interface. The decay indicates that carrier collection was limited by the hole-diffusion length as the beam position moved away from the HTL-perovskite interface. By contrast, the device with theophylline treatment displays minimal decay in the perovskite layer in the EBIC line profile. This difference suggests that a longer diffusion length of holes was present in theophylline-treated sample and balanced electron and that hole charge transport and collection was achieved, which is likely the result of fewer surface recombination sites (Fig. 3E).

Further assessment of the performance of the PV devices based on the theophylline surface passivation was performed. The devices showed a negligible hysteresis (4.1%) (Fig. 4A) because of the balanced charge collection originating from the effective surface passivation, whereas the reference device showed a large hysteresis (up to 7.6%) (table S3). External quantum efficiency (EQE) spectra of the devices were compared in Fig. 4B. An integrated J_{SC} of 24.42 mA cm^{-2} from the target device matched well with the value measured from the *J-V* scan (<5% discrepancy), whereas the control device showed an integrated J_{SC} of 23.56 mA cm^{-2}. A stabilized PCE of 22.64% was achieved with the target device when biased at 1.00 V, whereas that of the control device was 20.36% when biased at 0.98 V (Fig. 4C). The histogram of PV efficiencies for 40 devices is shown in Fig. 4D (the detailed parameters are shown in table S2), which confirms good reproducibility of the performance improvement with theophylline (11.1% improvement in an average PCE from 20.36 ± 0.53% to 22.61 ± 0.58% with the incorporation of the theophylline).

The changes in PCE of the encapsulated devices at a relative humidity of 30 to 40% and temperature of 40°C were tracked over time to test the long-term operational stability (Fig. 4E). The reference device (initial PCE 19.34%) degraded by more than 80% in 500 hours, whereas the target device maintained >90% of its initial efficiency (21.32%) during this time. Also, as shown in fig. S7, the shelf stability of the device based on theophylline treatment was noticeably enhanced, maintaining >95% of its original PCE (22.78%) when stored under ambient conditions with 20 to 30% humidity at 25°C for 60 days. By contrast, the reference device lost >35% of its initial efficiency (20.67%). The strong interaction between the theophylline and the surface defects likely suppressed deleterious ion migration (*26*–*28*).

REFERENCES AND NOTES

1. J. Tong *et al*., *Science* **364**, 475–479 (2019).
2. H. Tan *et al*., *Science* **355**, 722–726 (2017).
3. X. Zheng *et al*., *Nat. Energy* **2**, 17102 (2017).
4. J. J. Yoo *et al*., *Energy Environ. Sci.* **12**, 2192–2199 (2019).
5. Q. Jiang *et al*., *Nat. Photonics* **13**, 460–466 (2019).
6. N. Li *et al*., *Nat. Energy* **4**, 408–415 (2019).
7. J. S. Manser, J. A. Christians, P. V. Kamat, *Chem. Rev.* **116**, 12956–13008 (2016).
8. H. Zhang *et al*., *ACS Appl. Mater. Interfaces* **10**, 42436–42443 (2018).
9. J. W. Lee, H. S. Kim, N. G. Park, *Acc. Chem. Res.* **49**, 311–319 (2016).
10. Y. Zong *et al*., *Chem* **4**, 1404–1415 (2018).
11. D. Bi *et al*., *Nat. Energy* **1**, 16142 (2016).
12. B. Chen, P. N. Rudd, S. Yang, Y. Yuan, J. Huang, *Chem. Soc. Rev.* **48**, 3842–3867 (2019).
13. T. Wu *et al*., *Adv. Energy Mater.* **9**, 1803766 (2019).
14. T. Niu *et al*., *Adv. Mater.* **30**, e1706576 (2018).
15. R. Wang *et al*., *Joule* **3**, 1464–1477 (2019).
16. W. Xu *et al*., *Nat. Photonics* **13**, 418–424 (2019).
17. H. Zhang, M. K. Nazeeruddin, W. C. H. Choy, *Adv. Mater.* **31**, e1805702 (2019).
18. W. J. Yin, T. Shi, Y. Yan, *Appl. Phys. Lett.* **104**, 063903 (2014).
19. W. S. Yang *et al*., *Science* **356**, 1376–1379 (2017).
20. N. J. Jeon *et al*., *Nat. Energy* **3**, 682–689 (2018).
21. E. H. Jung *et al*., *Nature* **567**, 511–515 (2019).
22. M. A. Green, A. Ho-Baillie, H. J. Snaith, *Nat. Photonics* **8**, 506–514 (2014).
23. Z. Xiao, Z. Song, Y. Yan, *Adv. Mater.* **31**, e1803792 (2019).
24. N. Liu, C. Yam, *Phys. Chem. Chem. Phys.* **20**, 6800–6804 (2018).
25. E. Edri *et al*., *Nat. Commun.* **5**, 3461 (2014).
26. R. Wang *et al*., *Adv. Funct. Mater.* **29**, 1808843 (2019).
27. J. A. Christians *et al*., *Nat. Energy* **3**, 68–74 (2018).
28. Y. Hou *et al*., *Science* **358**, 1192–1197 (2017).

ACKNOWLEDGEMENTS

Funding: Y.Y. acknowledges the Office of Naval Research (ONR) (N00014-17-1-2,484) for their financial support. Part of this material is based upon work supported by the U.S. Department of Energy's Office of Energy Efficiency and Renewable Energy (EERE) under the Solar Energy Technologies Office Award Number DE- EE0008751. Z.-K.W. acknowledges the Natural Science Foundation of China (no. 91733301). This project was also supported by the Collaborative Innovation Center of Suzhou Nano Science and Technology. Y.L. and D.F. are grateful for the financial support of a California Energy Commission Advance Breakthrough award (EPC-16-050). This work was performed in part at the San Diego Nanotechnology Infrastructure (SDNI) of UCSD supported by the National Science Foundation (grant ECCS-1542148). Part of the computations were performed in the SIMULAB of Marmara University, Physics Department and in the UHEM cluster of Turkey. K.N.H. and S.N. are grateful to the National Science Foundation (CHE-1764328) for financial support of this research. Computer time was provided by the UCLA Institute for Digital Research and Education (IDRE).
Author contributions: R.W., J.X., and Y.Y. conceived the idea for the study. R.W. and J.X. fabricated the solar cell devices and designed the experiments. K.-L.W. performed the film and device characterizations under the supervision of Z.-K.W. Y.L. and D.F. performed the EBIC measurement. G.X. carried out the *t*DOS measurement. S.N., I.Y., and K.N.H. performed the DFT calculation. T.H. carried out the TPC and TPV measurement. Y.Z., J.L.Y., J.Z., M.W., and S.T. assisted with the device fabrication and characterizations. R.W., J.X., and Y.Y. wrote the manuscript. All authors discussed the results and commented on the manuscript. Y.Y. supervised the project. **Competing interests:** None declared.
Data and materials availability: All (other) data needed to evaluate the conclusions in the paper are present in the paper or the supplementary materials.

SUPPLEMENTARY MATERIALS

science.sciencemag.org/content/366/6472/1509/suppl/DC1
Materials and Methods
Supplementary Text
Figs. S1 to S13
Tables S1 to S3
References (*29*–*41*)

1 August 2019; accepted 8 November 2019
10.1126/science.aay9698

ORGANIC CHEMISTRY

Direct synthesis of adipic acid esters via palladium-catalyzed carbonylation of 1,3-dienes

Ji Yang[1], Jiawang Liu[1], Helfried Neumann[1], Robert Franke[2,3], Ralf Jackstell[1], Matthias Beller[1]*

The direct carbonylation of 1,3-butadiene offers the potential for a more cost-efficient and environmentally benign route to industrially important adipic acid derivatives. However, owing to the complex reaction network of regioisomeric carbonylation and isomerization pathways, a selective practical catalyst for this process has thus far proven elusive. Here, we report the design of a pyridyl-substituted bidentate phosphine ligand (HeMaRaphos) that, upon coordination to palladium, catalyzes adipate diester formation from 1,3-butadiene, carbon monoxide, and butanol with 97% selectivity and 100% atom-economy under industrially viable and scalable conditions (turnover number > 60,000). This catalyst system also affords access to a variety of other di- and triesters from 1,2- and 1,3-dienes.

Carbonylation reactions are among the most important applications of industrial catalysis (*1*–*5*): Using carbon monoxide (CO) as a highly versatile C1 building block with olefins, more than 10 million metric tons of various carbonyl compounds (aldehydes, acids, and esters) are produced annually for numerous consumer products. CO is a central intermediate in the chemical industry that can be easily produced either from fossil-based resources (coal or gas) or from renewables (CO_2 or biowaste). Despite the initial discovery of homogeneously catalyzed carbonylation processes nearly 80 years ago (*6*–*15*), several unattained objectives remain, perhaps most saliently the direct dicarbonylation of 1,3-dienes. This reaction would enable more environmentally benign, atom-economical production of adipate esters, the building blocks of polyamides and polyesters currently produced on a multimillion–metric ton scale (*16*, *17*). More specifically, adipate diesters are used for plasticizers, perfumes, lubricants, solvents, several active pharmaceutical ingredients, and, with respect to scale, most importantly for the production of nylons. Now, the main industrial route to produce adipate diesters involves oxidation of a mixture of cyclohexanol and cyclohexanone by an excess of nitric acid, followed by esterification with the corresponding alcohols (*18*–*20*). This process requires special equipment owing to the acid's corrosiveness and produces stoichiometric amounts of nitrous oxide (N_2O) (*21*), which is a major scavenger of stratospheric ozone and has nearly 300 times the atmospheric heat-trapping capacity of CO_2 (*22*).

Over several decades, numerous companies all over the world, including BASF, Dupont, Shell, Dow, Kuraray, and Sinopec, investigated the prospect of accessing adipate esters via butadiene dicarbonylation. However, despite extensive explorations, no such industrially viable transformation was developed (*23*–*38*). Some pilot tests were implemented (*23*–*36*), but those processes all involved multistep reactions with insufficient selectivity (~60 to 80%) for the desired linear diester.

Here, we present a palladium-catalyzed dicarbonylation of 1,3-butadiene that provides dialkyl adipates in ≥95% yield and ≥97% selectivity. Key to success was the ligand design. Recently, we developed bidentate phosphine ligands for palladium-catalyzed alkoxycarbonylation reactions in which basic pyridyl substituents on phosphorus proved essential for high activity (*39*). On the basis of that work and our long-standing interest in carbonylation reactions (*40*), we proceeded to investigate the dicarbonylation reaction of 1,3-butadiene with butanol as a model for the direct synthesis of adipate diesters.

As shown in Fig. 1, there are multiple challenges associated with this catalytic process: (i) The catalyst must promote two different carbonylation reactions on the diene substrate (which could not be achieved previously); (ii) the linear dicarbonylation product must be

[1]Leibniz-Institut für Katalyse e.V. an der Universität Rostock, Albert-Einstein Str. 29a, D-18059 Rostock, Germany. [2]Evonik Performance Materials GmbH, Paul-Baumann-Str. 1, 45772 Marl, Germany. [3]Theoretical Chemistry, Ruhr-University Bochum, 44780 Bochum, Germany.
*Corresponding author. Email: matthias.beller@catalysis.de

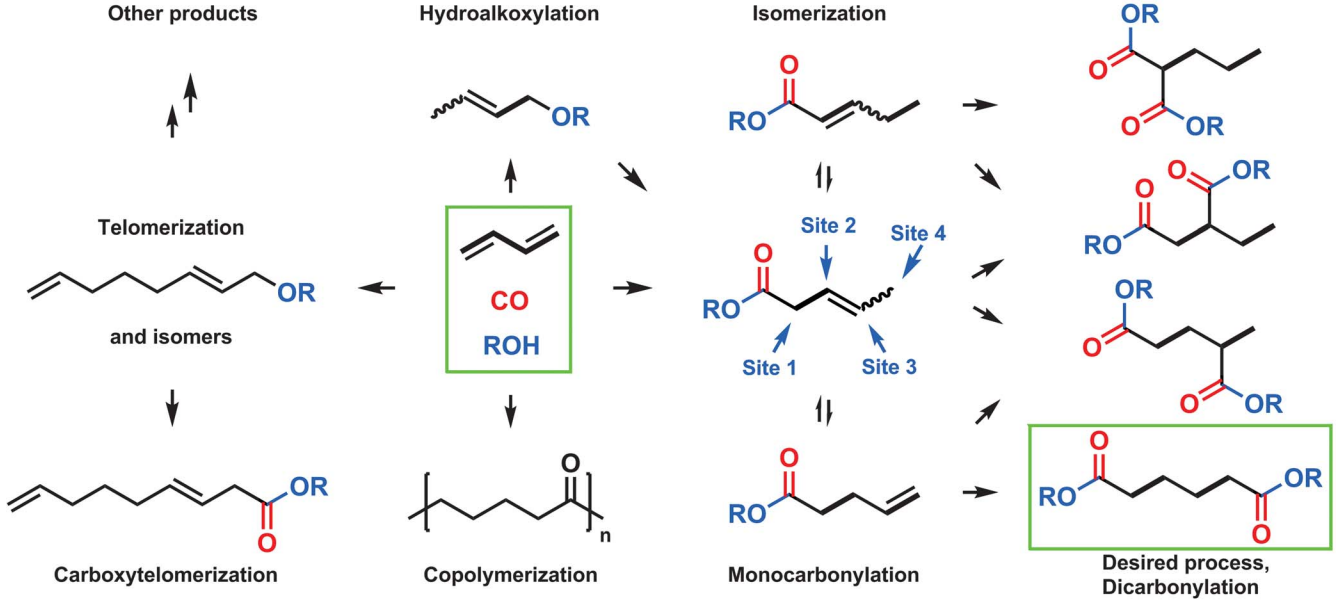

Fig. 1. Reaction network involved in synthesis of adipates from 1,3-butadienes. The green outlines indicate the starting materials (1,3-butadiene, carbon monoxide, and alcohol) and desired product adipic diester.

formed selectively, despite the fact that isomerization of the initially formed monocarbonylated intermediate to the terminal olefin is thermodynamically particularly unfavorable; and (iii) other side reactions such as telomerization (*41*), hydroalkoxylation, and (co)polymerization must be suppressed.

We sought to realize the selective dicarbonylation of 1,3-butadiene by using base-modified derivatives of the 1,2-bis[(di-*tert*-butylphosphino) methyl]benzene ligand (**L1**, dtbpx), which is used for the bulk production of methyl methacrylate (*42*). Initial optimization studies with this ligand (Fig. 2) showed slight activity but good selectivity to give the linear di-*n*-butyl adipate **4a** at 120°C and 40 bar CO with *p*-toluenesulfonic acid as a cocatalyst. To improve the catalyst performance, dtbpx derivatives **L2** and **L3** were tested. However, no increase of activity was observed. According to our hypothesis above, the incorporation of suitable basic groups on this specific ligand backbone should increase the activity of the corresponding palladium catalyst system in alkoxycarbonylation reactions. Indeed, using **L4** considerably increased activity and yield of diesters (77%) but at the expense of insufficient selectivity (48%). Considering the appropriate reactivity of **L4** and the suitable selectivity of **L1**, we designed the ligand **L5** (HeMaRaphos), which combines the two structural fragments of **L1** and **L4**: The bulky and electron-rich di-*tert*-butylphosphino fragment could promote fast isomerization of carbon-carbon double bonds (*43*–*45*) while the *tert*-butyl-2-pyridyl phosphino group facilitated formation of the active palladium hydride complex and accelerated the final alcoholysis step. Mixing **L5** and Pd(0) bis(dibenzylideneacetone) [$Pd(dba)_2$] in the presence of HCl resulted in the formation of a bright yellow palladium complex, which was suitable for x-ray crystallography (fig. S1). Although no coordination of the pyridine-N atom to the palladium center was observed in solid state, the durability of the catalyst in solution might be enhanced by such hemilabile binding. To our delight, the dicarbonylation of 1,3-butadiene proceeded in the presence of HeMaRaphos and Pd(II) trifluoroacetate [$Pd(TFA)_2$] to adipate diester with a yield of 85% and a linear selectivity of 97%. We benchmark the distinct behavior of **L5** in comparison with more than 70 other ligands, including well-known mono- and bidentate phosphines, in table S1.

To understand the performance of the palladium catalyst with HeMaRaphos, we conducted kinetic monitoring experiments (fig. S3). In the first half hour, formation of the active palladium hydride complex was observed in the in situ mixture of $Pd(TFA)_2$, **L5**, and *p*-toluenesulfonic acid (PTSA). Then, alkoxycarbonylation occurred to selectively produce *n*-butyl pent-3-enoate **3a**. This intermediate continuously accumulated to reach a maximum yield of about 50% after 90 min. Stopping the reaction at this time allowed isolation of **3a** from the reaction mixture. Meanwhile, the active catalyst also promoted olefin isomerization. The terminal olefin *n*-butyl pent-4-enoate **3c** could not be detected, which we attribute to its fast conversion into the linear adipate diester.

Next, detailed optimization studies on the effect of palladium precursor, acid, temperature, and pressure were performed to further improve the practicality of the process (tables S2 to S7). In particular, excellent catalyst turnover numbers (>60,000) were obtained using the presynthesized Pd(II)-HeMaRaphos complex under optimal conditions (table S9). Scaled-up reactions of 1,3-butadiene with methanol and *n*-butanol were then carried out at low catalyst loading [<0.5 mole % (mol %)] (table S8). The resulting esters were smoothly obtained in 88 to 95% yield and >97% linear selectivity. As an example, a reaction without additional solvent could be performed on a >200-g scale with a Pd loading of only 0.05 mol % (fig. S2 and table S8).

Beyond the specific importance of the dicarbonylation of 1,3-butadiene in the chemical industry, this methodology also offers

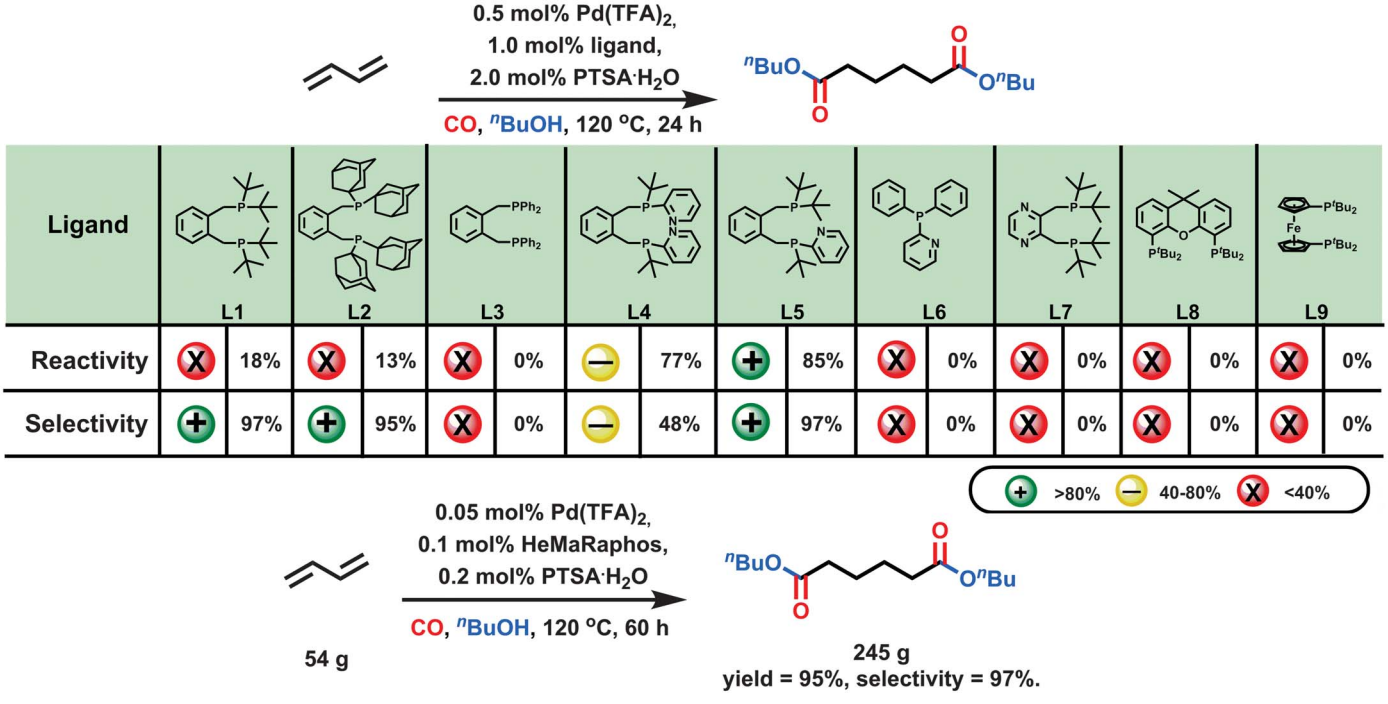

Fig. 2. Ligand optimization for palladium-catalyzed dicarbonylation of 1,3-butadiene. Reaction conditions for ligand optimization: butadiene (1.0 mmol, solution in toluene), $Pd(TFA)_2$ (0.005 mmol, 0.5 mol %), ligand (0.01 mmol, 1.0 mol %), PTSA•H_2O (2.0 mol %), ^{n}BuOH (2.0 ml), CO (40 bar), 120°C, and 24 hours; the ratio of products and yields were determined by gas chromatography analysis with mesitylene as the internal standard. Reactivity represents the yield of the diester. Selectivity represents the ratio of linear diester to all diesters. ^{n}Bu, *n*-butyl; ^{t}Bu, *tert*-butyl.

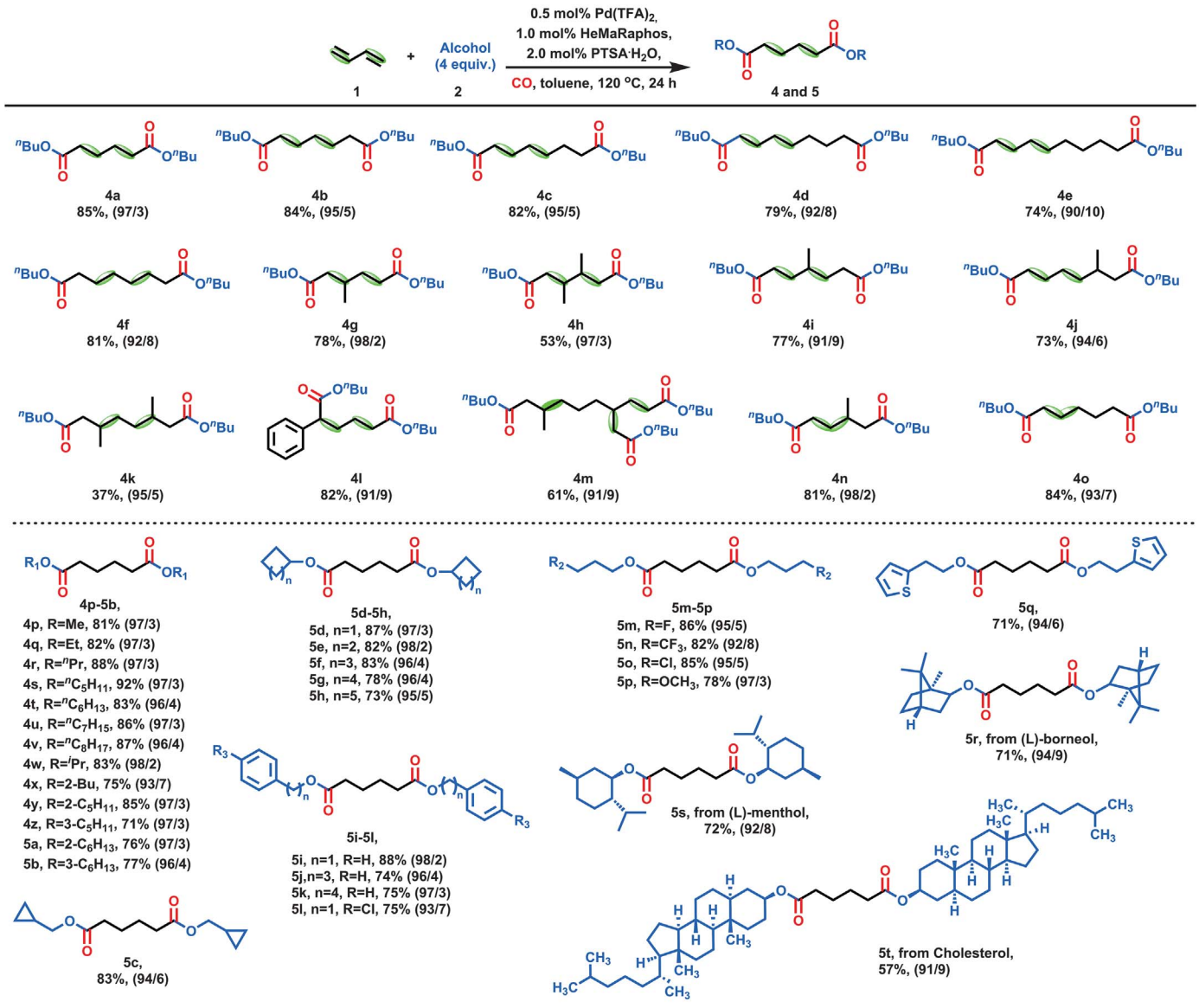

Fig. 3. Palladium-catalyzed dicarbonylation of 1,2- and 1,3-dienes. Me, methyl; Et, ethyl; ^{n}Pr, *n*-propyl; ^{i}Pr, isopropyl.

prospects for valorization of other dienes for fine chemical production (*46*–*48*). To showcase the generality of the catalyst system, 15 different dienes and more than 30 alcohols were converted in high yield and selectivity to the corresponding diesters (Fig. 3). For example, several linear conjugated dienes **1a** to **1f** showed excellent reactivity and regioselectivity. Even for internal conjugated double bonds (**1f**), isomerization reactions led preferentially to the terminal products. Increased steric hindrance on the carbon chain, including a tetra-substituted conjugated diene, influenced the reactivity; however, the regioselectivity to the corresponding linear diesters remained very high (**1g** to **1k**). 1-Phenyl–substituted 1,3-diene **1l**, for which the regioselectivity might be more difficult to control, afforded excellent 1,4-site selectivity. Using myrcene **1m** as an exemplary inexpensive, widely available natural diterpene, tri-alkoxycarbonylation was achieved smoothly. In addition to conjugated 1,3-dienes, 1,2-dienes **1n** and **1o** were converted to the corresponding linear diesters with similar activity and regioselectivity.

Numerous aliphatic alcohols (products **4p** to **4z** and **5a** to **5h**) were also tolerated by the catalyst system and gave diesters in high yields and selectivity (>93%). Various functional groups (products **5m** to **5p**)—including electron-withdrawing fluorine, chlorine, and trifluoromethyl, as well as electron-donating methoxy—were compatible. Furthermore, a heterocyclic derivative (**5q**) and hydroxylated natural products [(L)-menthol, (L)-borneol, and cholesterol] yielded the desired products with high regioselectivity.

REFERENCES AND NOTES

1. W. Bertleff, M. Roeper, X. Sava, in *Ullmann's Encyclopedia of Industrial Chemistry* (Wiley-VCH, 2007).
2. R. Franke, D. Selent, A. Börner, *Chem. Rev.* **112**, 5675–5732 (2012).
3. J.-B. Peng, H.-Q. Geng, X.-F. Wu, *Chem* **5**, 526–552 (2019).
4. D. U. Nielsen, X.-M. Hu, K. Daasbjerg, T. Skrydstrup, *Nat. Catal.* **1**, 244–254 (2018).
5. H. Alper, *J. Organomet. Chem.* **300**, 1–6 (1986).
6. R. Otto, German Patent 849548 (1938).
7. H. Adkins, G. Krsek, *J. Am. Chem. Soc.* **71**, 3051–3055 (1949).
8. M. E. Piotti, H. Alper, *J. Am. Chem. Soc.* **118**, 111–116 (1996).
9. P. B. Webb *et al*., *J. Am. Chem. Soc.* **125**, 15577–15588 (2003).

10. R. A. Periana, O. Mironov, D. Taube, G. Bhalla, C. J. Jones, *Science* **301**, 814–818 (2003).
11. Q. Liu *et al*., *Angew. Chem. Int. Ed.* **49**, 3371–3374 (2010).
12. D. Willcox *et al*., *Science* **354**, 851–857 (2016).
13. X. Ren *et al*., *Angew. Chem. Int. Ed.* **56**, 310–313 (2017).
14. J. Y. Wang, A. E. Strom, J. F. Hartwig, *J. Am. Chem. Soc.* **140**, 7979–7993 (2018).
15. C. You *et al*., *J. Am. Chem. Soc.* **140**, 4977–4981 (2018).
16. E. M. Aizenshtein, *Fibre Chem.* **42**, 341–349 (2011).
17. M. T. Musser, in *Ullmann's Encyclopedia of Industrial Chemistry* (Wiley-VCH, 2000).
18. A. Castellan, J. C. J. Bart, S. Cavallaro, *Catal. Today* **9**, 237–254 (1991).
19. K. Sato, M. Aoki, R. Noyori, *Science* **281**, 1646–1647 (1998).
20. K. C. Hwang, A. Sagadevan, *Science* **346**, 1495–1498 (2014).
21. M. H. Thiemens, W. C. Trogler, *Science* **251**, 932–934 (1991).
22. P. Forster *et al*., in *Climate Change 2007: The Physical Science Basis. Contribution of Working Group I to the Fourth Assessment Report of the Intergovernmental Panel on Climate Change*, S. Solomon, D. Qin, Eds. (Cambridge Univ. Press, 2007), pp. 130–234.
23. J. B. Zachry, C. L. Aldridge, U.S. Patent 3161672 (1964).
24. K. N. Von, U.S. Patent 3876695 A (1975).
25. Y. Isogai, M. Hosokawa, T. Ookawa, N. Wakui, T. Watanabe, Japanese Patent 5788147 A (1982).
26. C. K. Hsu, F. Dobinson, U.S. Patent 4575562 A (1986).
27. R. Maerkl *et al*., U.S. Patent 4777284 A (1988).
28. E. Drent, J. Van Gogh, U.S. Patent 4861912 A (1989).
29. T. Omatsu, Y. Tokito, Japanese Patent 04208247 A (1992).
30. E. M. Atadan, H. S. Bruner, U.S. Patent 5292944 A (1994).
31. A. Matsuda, T. Fujii, Japanese Patent 06192175 A (1994).
32. P. Denis, C. Patois, R. Perron, European Patent 0648731 A1 (1995).
33. O. E. Sielcken, H. Hovenkamp, Patent WO 9506027 A1 (1995).
34. A. D. Poole, J. G. Sunley, UK Patent 2327420 A (1999).
35. E. Drent, W. W. Jager, Patent WO 00056695 A1 (2000).
36. O. E. Sielcken *et al*., Patent WO 0121569 A1 (2001).
37. J. Mormul *et al*., *ACS Catal.* **6**, 2802–2810 (2016).
38. A. Tortajada, R. Ninokata, R. Martin, *J. Am. Chem. Soc.* **140**, 2050–2053 (2018).
39. K. Dong *et al*., *Nat. Commun.* **8**, 14117–14127 (2017).
40. X. Fang, H. Li, R. Jackstell, M. Beller, *Angew. Chem. Int. Ed.* **53**, 9030–9034 (2014).
41. R. Jackstell *et al*., *Angew. Chem. Int. Ed.* **41**, 986–989 (2002).
42. W. Clegg *et al*., *Chem. Commun.* **1999**, 1877–1878 (1999).
43. Y. Liu, K. Dong, M. Beller, S. Mecking, *ACS Catal.* **8**, 9232–9237 (2018).
44. P. B. Webb, T. E. Kunene, D. J. Cole-Hamilton, *Green Chem.* **7**, 373–379 (2005).
45. J. Liu, J. Yang, F. Ferretti, R. Jackstell, M. Beller, *Angew. Chem. Int. Ed.* **58**, 4690–4694 (2019).
46. N. Herrmann, D. Vogelsang, A. Behr, T. Seidensticker, *ChemCatChem* **10**, 5342–5365 (2018).
47. J. Tsuji, *Acc. Chem. Res.* **6**, 8–15 (1973).
48. J. R. Zbieg, E. Yamaguchi, E. L. McInturff, M. J. Krische, *Science* **336**, 324–327 (2012).

ACKNOWLEDGMENTS

We thank the analytical staff of the Leibniz-Institute for Catalysis, Rostock, for their excellent service. **Funding:** We gratefully acknowledge the support of Federal Ministry of Education and Research (BMBF), the State of Mecklenburg-Vorpommern, Evonik Industries, and the European Research Council. J.Y. thanks China CSC Scholarship for financial support (201704910879). **Author contributions:** J.Y. and J. L. contributed equally. J.Y., M.B., R.F., and R.J. planned the project. J.Y., H.N., and M.B. developed and prepared the catalysts. J.Y., J.L., and R.J. designed and performed all the experiments. J.Y., M.B., and R.F. wrote the paper. **Competing interests:** A patent has been filed on the catalyst system under EP3121184 A2. **Data and materials availability:** X-ray data are available free of charge from the Cambridge Crystallographic Data Centre under CCDC 1941490; all other data are in the supplementary materials.

SUPPLEMENTARY MATERIALS

science.sciencemag.org/content/366/6472/1514/suppl/DC1
Materials and Methods
Figs. S1 to S4
Tables S1 to S9
NMR and HRMS Spectra
References (*49*–*52*)

14 August 2019; accepted 7 November 2019
10.1126/science.aaz1293

EMOTION AND LANGUAGE

Emotion semantics show both cultural variation and universal structure

Joshua Conrad Jackson[1]*, Joseph Watts[2,3,4,5]†, Teague R. Henry[1]†, Johann-Mattis List[2], Robert Forkel[2], Peter J. Mucha[6,7], Simon J. Greenhill[2,8], Russell D. Gray[2,9], Kristen A. Lindquist[1]*

Many human languages have words for emotions such as "anger" and "fear," yet it is not clear whether these emotions have similar meanings across languages, or why their meanings might vary. We estimate emotion semantics across a sample of 2474 spoken languages using "colexification"—a phenomenon in which languages name semantically related concepts with the same word. Analyses show significant variation in networks of emotion concept colexification, which is predicted by the geographic proximity of language families. We also find evidence of universal structure in emotion colexification networks, with all families differentiating emotions primarily on the basis of hedonic valence and physiological activation. Our findings contribute to debates about universality and diversity in how humans understand and experience emotion.

Many human languages have rich vocabularies devoted to communicating emotions. Although not all emotion words are common—the German word *Sehnsucht* refers to a strong desire for an alternative life and has no direct translation in English—there are many words that appear to name similar emotional states across the world's spoken languages. Translation dictionaries, for example, suggest that the English word *love* can be equated with the Turkish word *sevgi* and the Hungarian word *szerelem*. But does this mean that the concept of "love" is the same in English, Turkish, and Hungarian? Here, we explore this question by examining the meaning of emotion concepts in a sample of 2474 languages from 20 major language families. Using a new method from comparative linguistics, we examine sources of variation and structure in emotion semantics across this global sample of languages.

Early theories of emotion, drawing from Darwin (*1*), suggested that there are a discrete number of universal emotions from which all other emotions are derived (*2*–*4*). Many of these theories claimed that, just as there are primary colors (e.g., yellow, red), there may be primary emotions (e.g., anger, sadness) that evolved in mammalian brains (*4*). In turn, many languages may develop words for primary emotion concepts such as "anger" and "sadness" because these concepts name experiences derived from universal biological structures that are shared by all humans (*2*–*4*). These theories do allow for cultural and linguistic variation in emotion, but tend not to model or predict this variation.

There is a growing recognition, however, that emotions can vary systematically in their meaning and experience across culture and language (*5*–*7*). Constructionist models of emotion in particular claim that concepts such as "anger" and "sadness" do not derive from dedicated brain structures (*8*), but occur when humans make socially learned inferences about the meaning of basic physiological processes linked to maintaining the body's homeostasis (*9*, *10*). The meaning of emotion concepts (i.e., "emotion semantics") should thus draw from both culturally evolved conceptualizations as well as biologically evolved physiology.

If cultural evolutionary processes shape the meaning of emotion concepts, the historical relationships between language groups should predict which languages have the most similar emotion semantics. Language groups in closer geographic proximity are the most likely to engage in borrowing (the sharing of concepts, norms, etc.) and also tend to share more recent common ancestors than geographically distant groups (*11*). We thus hypothesize that emotion semantics are associated with a language group's geographic location: Language groups in close geographic proximity may have more similar emotion semantics than distant groups. Although cultural variation in emotion is plausible under many models of emotion, a link between geographic distance and emotion semantics would support constructionism's claim that emotions are conceptualized using social learning.

Biologically evolved physiology should provide universal structure to emotion semantics, but the exact sources of this structure are not clear. Constructionist models of emotion emphasize the roles of valence—the hedonic pleasantness versus unpleasantness of emotions—and activation—the physiological arousal associated with experiencing emotions (*8*–*10*). According to these models, valence and activation reflect basic neurophysiological processes that signal when the body shifts away from homeostasis (*9*), and the universal importance of these processes may lead all languages to differentiate emotions primarily on the basis of their degree of valence and activation. Other accounts, however, suggest that factors such as dominance, certainty, sociality, and approach-avoidance may also represent universal dimensions of variance in emotion semantics (*12*–*15*).

Predictions about the influence of culture and biology on emotion have long been examined and debated, yet findings from past studies are mixed. An early study found that human subjects from remote Papua New Guinea matched posed facial expressions to emotional situations at similar rates to North Americans (*16*), whereas recent field studies among other small-scale societies have found considerably more cultural variability in people's conceptualization of emotion (*17*). These mixed results may be due to methodological limitations of past research. Owing to logistical challenges, the vast majority of cross-cultural studies have been two-group comparisons (*17*), and the few multigroup studies on emotion have sampled predominantly from industrial and globalized nations (*18*, *19*). Moreover, human subject–based studies seldom present emotions as they naturally occur, instead using posed facial expressions, fictional vignettes, and exaggerated vocalizations as test stimuli. Finally, human subject–based studies may be susceptible to demand characteristics and researcher bias: Studies with imposed training phases and forced choice paradigms have found evidence for universal recognition of emotion (*16*), whereas studies with fewer constraints have found more cultural variability (*17*).

As an alternative to human subjects–based research, analyses of naturally occurring language can have high ecological validity and do not rely on human subject recruitment. Language may be an imprecise metric of experience, but analyzing how people use words can reveal how they experience emotions as similar or different. Several linguistic studies have conducted these analyses by qualitatively comparing the meaning of emotion words by searching for semantic primitives that have similar meanings across many languages (*20*). Yet few studies have quantitatively compared the meaning of emotion words because the field lacks metrics that quantify the semantic

[1]Department of Psychology and Neuroscience, University of North Carolina at Chapel Hill, Chapel Hill, NC, USA. [2]Department of Linguistic and Cultural Evolution, Max Planck Institute for the Science of Human History, Jena, Germany. [3]Religion Programme, University of Otago, Dunedin, New Zealand. [4]Center for Research on Evolution, Belief, and Behaviour, University of Otago, Dunedin, New Zealand. [5]Social and Evolutionary Neuroscience Research Group, Department of Experimental Psychology, University of Oxford, Oxford, UK. [6]Carolina Center for Interdisciplinary Applied Mathematics, Department of Mathematics, University of North Carolina at Chapel Hill, Chapel Hill, NC, USA. [7]Department of Applied Physical Sciences, University of North Carolina at Chapel Hill, Chapel Hill, NC, USA. [8]ARC Centre of Excellence for the Dynamics of Language, ANU College of Asia and the Pacific, Australian National University, Canberra, Australia. [9]School of Psychology, University of Auckland, Auckland, New Zealand.
***Corresponding author. Email: joshcj@live.unc.edu (J.C.J.); kristen.lindquist@unc.edu (K.A.L.)** †These authors contributed equally to this work.

distance between words such as the English *love* and the Turkish *sevgi* (*21*).

To overcome this challenge, we take a new quantitative approach to estimate variability and structure in emotion semantics. Our approach examines cases of colexification, instances in which multiple concepts are coexpressed by the same word form within a language. Colexifications are useful for addressing questions about semantic structure because they often arise when two concepts are perceived as conceptually similar (*22*, *23*) (see fig. S5). Persian, for instance, uses the word-form *ænduh* to express both the concepts of "grief" and "regret," whereas the Sirkhi dialect of Dargwa uses the word-form *dard* to express both the concepts of "grief" and "anxiety." Persian speakers may therefore understand "grief" as an emotion more similar to "regret," whereas Dargwa speakers may understand "grief" as more similar to "anxiety."

Past research has used colexification patterns across languages to examine the semantic structure of non-emotion concepts. Youn and colleagues coded dictionaries from 81 languages to show that concepts such as "sun," "river," "mountain," and "hill" had universal patterns of colexification that reflected concepts' material and functional properties (*21*). For instance, languages were more likely to colexify concepts such as "water" and "sea," than concepts such as "sun" and "water," implying that speakers of these languages viewed "water" and "sea" as semantically similar concepts and "sun" and "water" as distinct. We use a similar approach to estimate the variation and structure of emotion semantics across language families.

To gather a high-powered sample, we computationally aggregated colexifications into a database of cross-linguistic colexifications (CLICS) featuring 2474 languages and 2439 distinct concepts—including 24 emotion concepts. We then used a random walk probability procedure to generate colexification networks (*24*). In these networks, nodes represented emotion concepts, and edges represented colexifications between these concepts, weighted by the number of languages that possessed a particular colexification. We used this procedure to construct a network for all languages in our database, and then for 20 individual language families whose colexification networks had a significant level of modularity ($ps < 0.001$). Although nodes in each language family network were labeled with the same emotion concepts ("anger"), comparing patterns of colexification across language families allowed us to test whether these nodes actually showed universal semantic equivalence or whether their patterns of association reflected semantic variation (see supplementary text for more details).

A key step in these network comparisons involved identifying communities: clusters of emotion concepts that are more tightly colexified with one another than with emotion concepts outside of the community. For each network, we computed community structure using the Cluster Optimal algorithm (*25*). Figure 1 displays the global colexification network and the five largest language family–specific networks, and fig. S1 displays the remaining language families. Family-specific colexification networks allowed us to estimate global variability in emotion semantics and to predict variation and structure in emotion semantics across language families.

We estimated global variation in emotion semantics by comparing the community structures of language family networks. We quantified agreement in community structure using adjusted Rand indices (ARIs), which indicate the similarity of two networks' community structures (*26*). Negative ARI values indicate that two networks' community partitions vary more than would be expected by chance, ARI values of 0 indicate that two networks' community partitions vary at a level that would be expected at chance, and ARI values approaching 1 reflect high agreement in community structure between two networks. The distribution of raw ARIs indicated high variability

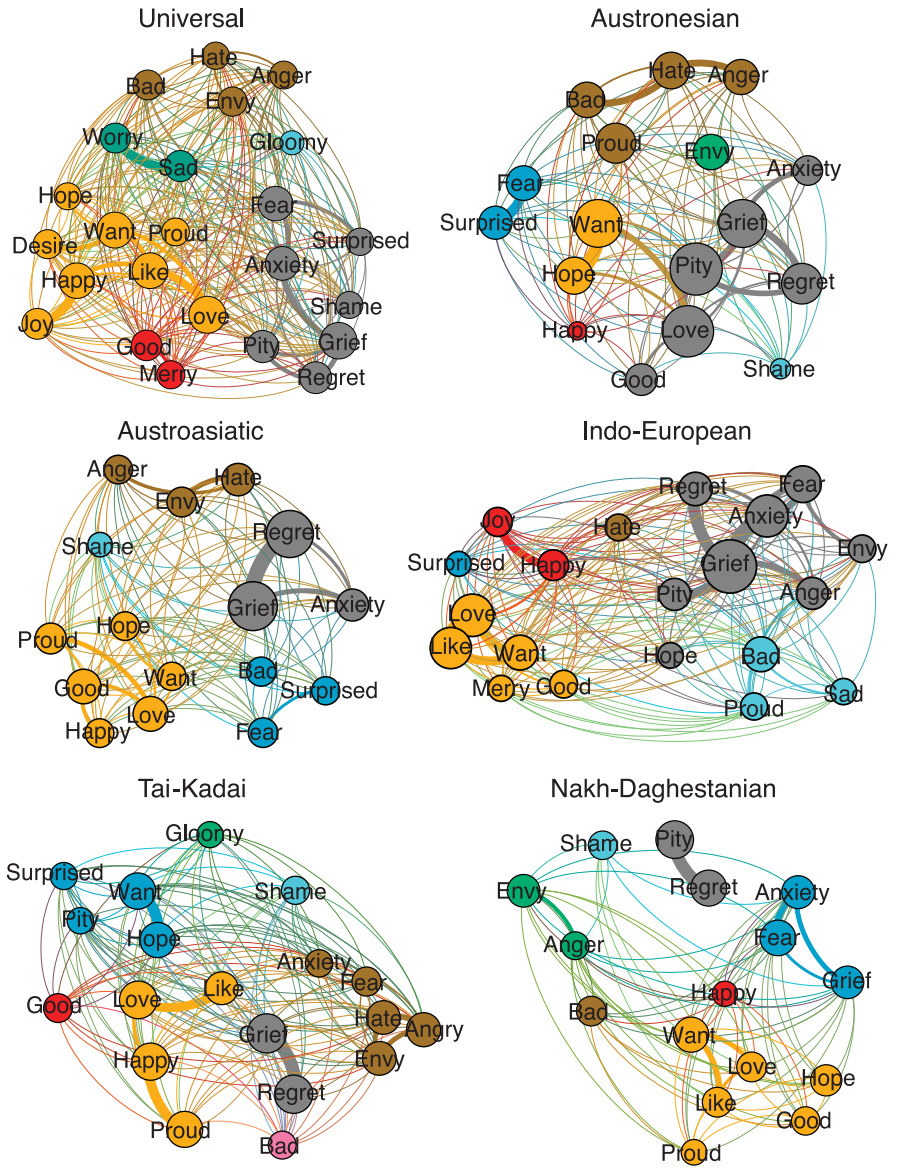

Fig. 1. Colexification of emotion concepts across all languages (top left) and the largest language families. Nodes are emotion concepts, and node size represents the number of colexifications involving the concept. Edges represent colexifications, and edge thickness represents the number of colexifications between two emotion concepts. Node color designates community.

in community structure across language families, with a mean ARI of 0.09 (SD = 0.11). Because ARIs can be artificially low in networks with few edges owing to isolated nodes, we also examined the ARI values for a thresholded set of community comparisons. Through a series of permutation tests, we identified pairs of communities that were more similar than would be expected by chance and then thresholded our sample to only include these permutation-robust community comparisons. With this more conservative set of comparisons, the mean ARI was 0.22 (SD = 0.09), still reflecting high variability in emotion semantics across language families.

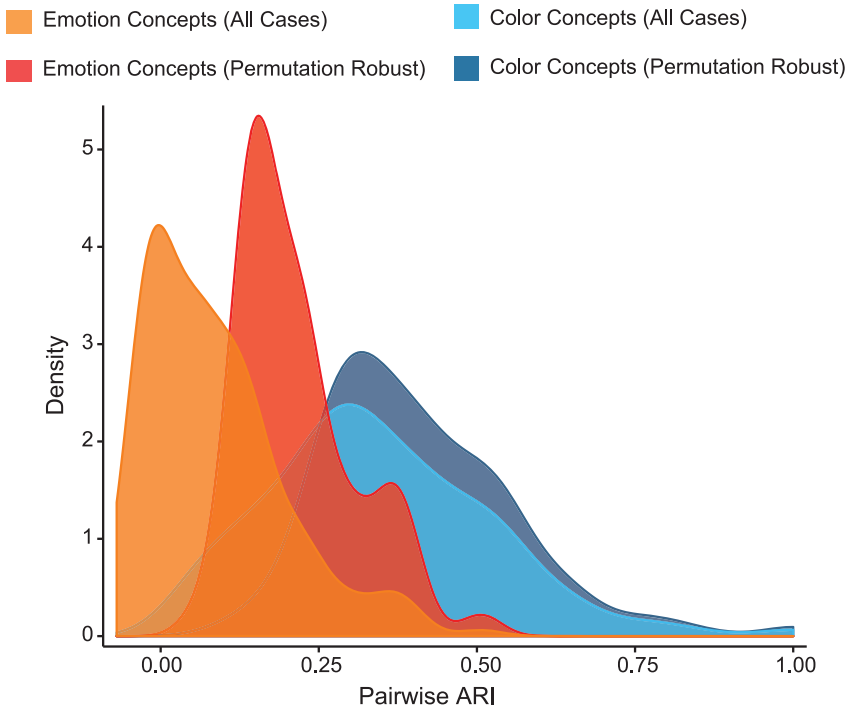

Fig. 2. The distributions of all pairwise language family ARI values for emotion concepts (in orange) and color concepts (in light blue), and the distributions of permutation-robust ARI values for emotion concepts (in red) and color concepts (in dark blue). Emotion concepts had significantly lower ARI values than color concepts, showing more semantic variability.

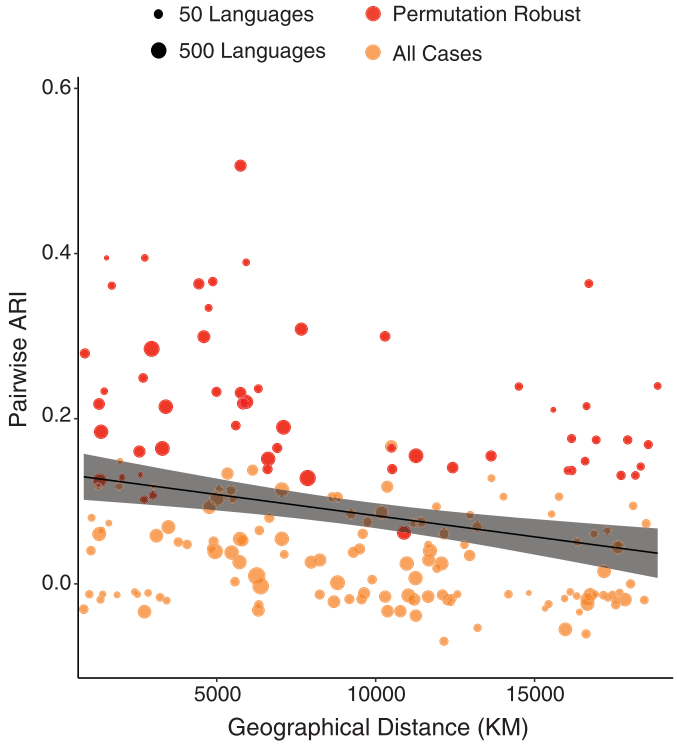

Fig. 3. The relationship between geographic proximity and pairwise ARI values. Point size illustrates the number of languages in a comparison. In the key, the nodes denoting point size are not colored because they apply to both red and orange points. The red points display the permutation-robust ARI values (r = −0.29), and the orange points display the remaining ARI values (r = −0.26). The regression line is fitted to all cases, and the shading represents standard error.

To test whether variation in emotion colexification patterns merely arose from methodological factors, such as the way that concepts were glossed in our database, we next compared the ARI values from our emotion concept comparisons to ARI values for colexification networks involving color concepts. Color concepts have also been studied cross-linguistically (*27*) and are frequently compared to emotion concepts (*4*), making them an appropriate sample of comparison concepts. In the full sample of comparisons, color concepts had a mean ARI of 0.35 (SD = 0.17), significantly higher than the full sample of emotion concept comparisons, $t(390) = 18.51$, $p < 0.001$. In the permutation-robust sample of comparisons, color concepts had a mean ARI of 0.41 (SD = 0.15), again showing more universality than the permutation-robust sample of emotion concept comparisons, $t(158) = 11.44$, $p < 0.001$ (Fig. 2). This difference also replicated when equating the number of color and emotion concepts, $t(334) = 15.52$, $p < 0.001$ (see materials and methods for more details). Emotion semantics thus vary widely across language families, and their variation is significantly greater than variation in color semantics.

Our next analysis investigated whether geographic proximity predicted the pattern of variation in emotion semantics across language families. We tested this hypothesis by correlating the geographic proximity of language families (via the latitude and longitude coordinates of their languages) with their pairwise ARI values. As predicted, language families with higher pairwise ARI values were in closer geographic proximity, both in the full sample of our ARI comparisons, $r(188) = -0.26$, $p < 0.001$, and in the smaller permutation-robust sample, $r(55) = -0.29$, $p = 0.03$ (Fig. 3). These associations suggest that emotion semantics do not vary randomly; their variation is tied to the cultural evolutionary relationship between language families.

Finally, we tested whether any psychophysiological dimensions could predict the semantic structure of emotion across language families. We examined the explanatory power of six dimensions (valence, activation, dominance, certainty, approach-avoidance, and sociality) by testing whether they predicted the community membership of emotion concepts across colexification networks. Using ratings of 200 online participants (90 female, 110 male; $M_{age} = 34.11$, $SD_{age} = 10.52$), we first classified our emotion concepts on these dimensions using a 1-10 Likert-type scale. We also classified a set of five "neutral" concepts

(ordinary, nondescript, indifferent, neutral, and impartial). Using a multilevel structural equation model in which participants' ratings of emotion concepts on these dimensions predicted the community membership of emotion concepts, we were then able to test how well each dimension differentiated emotion communities from our set of neutral words. If a dimension was highly predictive, the model's Akaike information criteria (AIC) fit would show a large decrement when the dimension was removed from the model. By contrast, removing nonpredictive dimensions would have less of an impact on the model's AIC fit. We ran this analysis for all language families except the Nuclear Macro-Je, for which models did not converge because only a single community contained multiple emotion concepts.

The results of this leave-one-out analysis revealed higher predictive power for valence and activation than for other dimensions (Fig. 4). Valence was the most predictive dimension, with the highest AIC fit decrements (M_{AIC} = 323.50) for the all-family network and for 13 of the 19 language families in our analysis. Activation was the most predictive dimension for the remaining six language families (M_{AIC} = 208.76). Approach (M_{AIC} = 35.82), certainty (M_{AIC} = 30.26), dominance (M_{AIC} = 26.18), and sociality (M_{AIC} = 7.41) had far less predictive power than valence and activation, and comparing the distributions of fit decrements across language families revealed that both

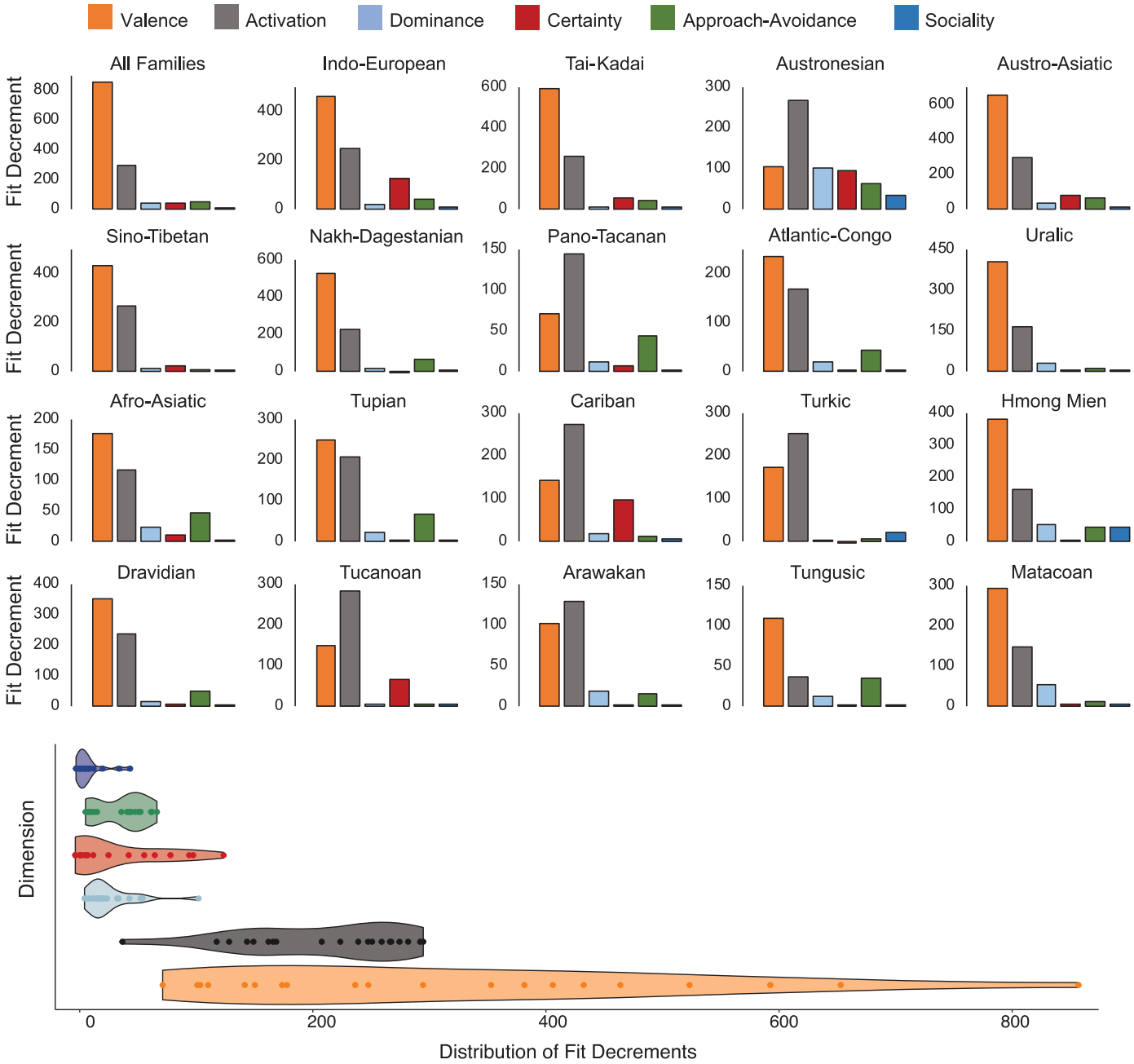

Fig. 4. Results from a leave-one-out analysis examining relative decrements in model fit following the removal of each dimension. The top panel represents the AIC fit decrements associated with removing dimensions from a predictive model of emotion community membership. Higher decrements indicate that the dimension was more predictive. The bottom panel shows the distribution of AIC fit decrements for each dimension. Valence and activation had significantly higher average decrements than other dimensions.

valence ($ps < 0.001$) and activation ($ps < 0.001$) had significantly higher decrements (i.e., explained more variance) than these other dimensions, and that valence had a higher average fit decrement than activation, $t(19) = 2.70$, $p = 0.01$. These findings suggest that languages around the world primarily differentiate emotions on the basis of valence and activation (see materials and methods for further analyses and discussion).

Our findings reveal wide variation in emotion semantics across 20 of the world's language families. Emotion concepts had different patterns of association in different language families. For example, "anxiety" was closely related to "fear" among Tai-Kadai languages, but was more related to "grief" and "regret" amongst Austroasiatic languages. By contrast, "anger" was related to "envy" among Nakh-Daghestanian languages, but was more related to "hate," "bad," and "proud" among Austronesian languages. We interpret these findings to mean that emotion words vary in meaning across languages, even if they are often equated in translation dictionaries. The supplementary materials contain an extended discussion of why other technical and sampling artifacts are unlikely to account for the variation that we observed in emotion semantics.

Geography partly explained variation in emotion semantics, such that geographically closer language families tended to colexify emotion concepts in more similar ways than distant language families. Geographically proximal societies often have more opportunities for contact through trade, conquest, and migration and share more recent common ancestry than distant groups (*11*). This suggests that historical patterns of contact and common ancestry may have shaped cross-cultural variation in how people conceptualize emotions. We encourage future research to examine the specific vertical and horizontal transmission processes that give rise to geographic variation in emotion semantics.

Despite this variation, we find evidence for a common underlying structure in the meaning of emotion concepts across languages. Valence and physiological activation—which are linked to neurophysiological systems that maintain homeostasis (*9*)—served as universal constraints to variability in emotion semantics. Positively and negatively valenced emotions seldom belonged to the same colexification communities, although there were notable exceptions to this pattern. For example, some Austronesian languages colexified the concepts of "pity" and "love," which implies that these languages may conceptualize "pity" as a more positive (or "love" as a more negative) concept than other languages. The ability of valence and activation to consistently predict structure in emotion semantics across language families suggests that these are common psychophysiological dimensions shared by all humans.

Questions about the meaning of human emotions are age-old, and debate about the nature of emotion persists in scientific literature. The colexification approach that we take here provides a new method and a set of metrics to answer these questions by creating vast networks of how people use words to name experiences. Analyzing these networks sheds light on the cultural and biological evolutionary mechanisms underlying how emotions are ascribed meaning in languages around the world. Although debates about the relationship between language and conscious experience are notoriously difficult to resolve (*28*), our findings also raise the intriguing possibility that emotion experiences vary systematically across cultural groups. More broadly, our study shows the value of combining large comparative linguistic databases with quantitative network methods. Analyzing the diverse ways that people use language promises to yield insights into human cognition on an unprecedented scale.

REFERENCES AND NOTES

1. C. Darwin, *Expression of the Emotions in Man and Animals* (Univ. of Chicago Press, Chicago, 1965 [1872]).
2. P. Ekman, *Cogn. Emotion* **6**, 169–200 (1992).
3. S. S. Tomkins, R. McCarter, *Percept. Mot. Skills* **18**, 119–158 (1964).
4. R. Plutchik, *Am. Sci.* **89**, 344–350 (2001).
5. R. E. Jack, O. G. B. Garrod, H. Yu, R. Caldara, P. G. Schyns, *Proc. Natl. Acad. Sci. U.S.A.* **109**, 7241–7244 (2012).
6. B. Mesquita, M. Boiger, J. De Leersnyder, *Curr. Opin. Psychol.* **8**, 31–36 (2016).
7. C. Heyes, *Behav. Brain Sci.* **42**, e169 (2019).
8. K. A. Lindquist, T. D. Wager, H. Kober, E. Bliss-Moreau, L. F. Barrett, *Behav. Brain Sci.* **35**, 121–143 (2012).
9. L. F. Barrett, *Soc. Cogn. Affect. Neurosci.* **12**, 1–23 (2017).
10. J. A. Russell, *Psychol. Rev.* **110**, 145–172 (2003).
11. E. A. Eff, *Struct. Dyn.* **3**, 208–222 (2008).
12. J. R. Fontaine, K. R. Scherer, E. B. Roesch, P. C. Ellsworth, *Psychol. Sci.* **18**, 1050–1057 (2007).
13. M. Kossowska, M. Bukowski, A. Van Hiel, *Pers. Individ. Dif.* **45**, 744–749 (2008).
14. A. S. Cowen, D. Keltner, *Proc. Natl. Acad. Sci. U.S.A.* **114**, E7900–E7909 (2017).
15. A. A. Marsh, N. Ambady, R. E. Kleck, *Emotion* **5**, 119–124 (2005).
16. P. Ekman, W. V. Friesen, *J. Pers. Soc. Psychol.* **17**, 124–129 (1971).
17. M. Gendron, C. Crivelli, L. F. Barrett, *Curr. Dir. Psychol. Sci.* **27**, 211–219 (2018).
18. K. R. Scherer, R. Banse, H. G. Wallbott, *J. Cross Cult. Psychol.* **32**, 76–92 (2001).
19. D. Matsumoto, S. H. Yoo, S. Nakagawa; 37 member of the Multinational Study of Cultural Display Rules, *J. Pers. Soc. Psychol.* **94**, 925–937 (2008).
20. A. Wierzbicka, *Cogn. Sci.* **16**, 539–581 (1992).
21. H. Youn *et al.*, *Proc. Natl. Acad. Sci. U.S.A.* **113**, 1766–1771 (2016).
22. A. François, "Semantic maps and the typology of colexification: Intertwining polysemous networks across languages" in *From Polysemy to Semantic Change: Towards a Typology of Lexical Semantic Associations* (John Benjamin, Philadelphia, PA, 2008), pp. 163–215.
23. J. M. List *et al.*, *Linguist. Typol.* **22**, 277–306 (2018).
24. P. Pons, M. Latapy, Computing communities in large networks using random walks, in *International Symposium on Computer and Information Sciences* (Springer, 2005), 284–293.
25. U. Brandes *et al.*, *IEEE Trans. Knowl. Data Eng.* **20**, 172–188 (2008).
26. D. Steinley, *Psychol. Methods* **9**, 386–396 (2004).
27. B. Berlin, P. Kay, *Basic Color Terms: Their Universality and Evolution* (Univ. of California Press, Berkeley, CA, 1991).
28. F. Jackson, *Philos. Q.* **32**, 127–136 (1982).

ACKNOWLEDGMENTS

We acknowledge the many linguists who provided the word lists necessary to detect and analyze colexifications across languages. We also acknowledge the feedback of our editor and six anonymous reviewers; K. Gray, K. Payne, E. McCormick, J. Leshin, and N. Caluori; and the research assistance of R. Drabble, I. Khismatova, and A. Veeragandham. **Funding:** This study was supported by a National Science Foundation Graduate Research Fellowship and a Thomas S. and Caroline H. Royster Fellowship to J.C.J.. The compilation of the CLICS data and software used in this study was funded by the Max Planck Society (as part of the CLLD project, https://clld.org), the Max Planck Institute for the Science of Human History and the Royal Society of New Zealand (Marsden Fund grant 13-UOA-121 and GlottoBank project, https://glottobank.org), the DFG research fellowship grant 261553824 and the ERC Starting Grant 715618 (both awarded to J.M.L.), and the ARC's Discovery Project DE 120101954 and the ARC Center of Excellence CE140100041 (both awarded to S.J.G.). J.W. is supported by funds from the Templeton Religious Trust (TRT0153). No funding agency was involved in the conceptualization, design, data collection, analysis, decision to publish, or preparation of this manuscript, and the views expressed in this manuscript do not necessarily reflect the views of our funding agencies. **Author contributions:** J.C.J., J.W., and K.L. conceptualized and designed the study. J.C.J., J.W., T.H., J.M.L., and P.J.M. acquired and analyzed the data. J.M.L., R.F., and S.J.G. contributed software and data used in our analyses. J.C. J., J.W., T.H., P.J.M., and K.L. interpreted the analysis. J.C.J., J.W., K.L., J.M.L., and R.D.G. wrote the manuscript. All authors approved the submitted manuscript. **Competing interests:** The authors have no competing interests to declare. **Data and materials availability:** All data, scripts, and materials are available at https://osf.io/d9tr5/.

SUPPLEMENTARY MATERIALS

science.sciencemag.org/content/366/6472/1517/suppl/DC1
Materials and Methods
Supplementary Text
Figs. S1 to S5
Tables S1 to S6
References (*29*–*62*)

27 January 2019; accepted 20 November 2019
10.1126/science.aaw8160

IMMUNOLOGY

A class of γδ T cell receptors recognize the underside of the antigen-presenting molecule MR1

Jérôme Le Nours[1,2]*, Nicholas A. Gherardin[3,4]*, Sri H. Ramarathinam[1], Wael Awad[1], Florian Wiede[1,5], Benjamin S. Gully[1,2], Yogesh Khandokar[1], T. Praveena[1], Jacinta M. Wubben[1], Jarrod J. Sandow[6,7], Andrew I. Webb[6,7], Anouk von Borstel[1,2], Michael T. Rice[1,2], Samuel J. Redmond[3], Rebecca Seneviratna[3], Maria L. Sandoval-Romero[1], Shihan Li[3,4], Michael N. T. Souter[3], Sidonia B. G. Eckle[3], Alexandra J. Corbett[3], Hugh H. Reid[1,2], Ligong Liu[8,9], David P. Fairlie[8,9], Edward M. Giles[10], Glen P. Westall[11,12], Richard W. Tothill[13,14], Martin S. Davey[1,2], Richard Berry[1,2], Tony Tiganis[1,5], James McCluskey[3], Daniel G. Pellicci[3,4]†, Anthony W. Purcell[1], Adam P. Uldrich[3,4], Dale I. Godfrey[3,4]‡§, Jamie Rossjohn[1,2,15]‡§

T cell receptors (TCRs) recognize antigens presented by major histocompatibility complex (MHC) and MHC class I–like molecules. We describe a diverse population of human γδ T cells isolated from peripheral blood and tissues that exhibit autoreactivity to the monomorphic MHC-related protein 1 (MR1). The crystal structure of a γδTCR–MR1–antigen complex starkly contrasts with all other TCR–MHC and TCR–MHC-I-like complex structures. Namely, the γδTCR binds underneath the MR1 antigen-binding cleft, where contacts are dominated by the MR1 α3 domain. A similar pattern of reactivity was observed for diverse MR1-restricted γδTCRs from multiple individuals. Accordingly, we simultaneously report MR1 as a ligand for human γδ T cells and redefine the parameters for TCR recognition.

Alpha beta T cell receptors (αβTCRs) recognize antigens presented by major histocompatibility complex (MHC) and MHC class I–like molecules, including CD1 and MHC-related protein 1 (MR1) (*1*). A paradigm in T cell–mediated immunity is TCR binding atop the antigen-binding cleft of these molecules. However, knowledge of the range of physiological ligands that γδ T cells recognize is very limited. MR1 presents vitamin B precursors and by-products to a highly abundant innate-like T cell subset in humans called mucosal-associated invariant T (MAIT) cells (*2*, *3*). Whether the γδ T cell lineage also encompasses MR1-reactive T cells is unknown.

We detected MR1-tetramer$^+$ γδ T cells among human peripheral blood mononuclear cells (PBMCs) (Fig. 1A). These cells ranged from <0.001 to 0.1% of CD3$^+$ T cells (Fig. 1B), and from <0.1 to 5% of γδ T cells (Fig. 1C). MR1–5-OP-RU tetramer$^+$ γδ T cells [5-OP-RU, 5-(2-oxopropylideneamino)-6-D-ribitylaminouracil] were mostly CD4$^-$CD8α$^-$ or CD8α$^+$ with variable CD161 expression. Thus, they resembled other cells of the γδ T cell lineage (Fig. 1, D to G). Next, we magnetically enriched total γδTCR$^+$ cells from healthy human blood and screened these with MR1 tetramers (Fig. 1, H to J). The staining profiles were variable, with some donors exhibiting defined populations with high- or low-intensity staining (donors 5 and 6, respectively). However, the majority of donors displayed more-diffuse staining patterns (like donor 7). These were similar in frequency to CD1d-reactive γδ T cells (Fig. 1, H to J). We also assessed tissue samples from healthy subjects (fig. S1). Similar to blood, subpopulations of γδ T cells stained with MR1 tetramers in liver, stomach, lung, and duodenum (fig. S1). Notably, a newly diagnosed Celiac disease patient had an enrichment of Vδ1$^+$ γδ T cells that stained with MR1–5-OP-RU tetramers but not MR1–6-FP tetramers (fig. S2). In a tumor infiltrate from a Merkel cell carcinoma patient, γδ T cells were highly enriched (fig. S3). TCR sequencing of this population revealed clonally expanded cells, including 20% with a Vδ1-Vγ3$^+$ TCR, which, upon transduction into human embryonic kidney 293T (HEK293T) cells, exhibited antigen-independent MR1 reactivity (fig. S3). Thus, MR1-restricted γδ T cells are present in the blood and tissues of healthy subjects and may be enriched in association with some diseases.

Next, total Vδ2$^-$ γδ T cells were magnetically enriched from healthy donor PBMC samples (fig. S4) (*4*). Although there were some antigen-related modulations in MR1-tetramer staining intensity of some populations, most of the MR1 tetramer$^+$ γδ T cells were stained regardless of the type of antigen loaded. Thus, there appears to be an inherent autoreactivity toward MR1 by most PBMC-derived MR1-restricted γδ T cells (Fig. 1K). We then determined which γδTCR genes were used by these cells (table S1). Analysis of 76 TCR δ-chains revealed that most (72%) used *TRDV1*. The remainder, aside from one *TRDV5*$^+$ clone, expressed *TRDV3* (Fig. 2A). MR1-restricted γδ T cells used all functional *TRGV* genes including *TRGV2*, *3*, *4*, *5*, *8*, and *9* (Fig. 2A). The *TRDV1*$^+$ and *TRDV3*$^+$ TCRs predominantly paired with *TRGV8*. The unusual "clustered" staining profile was due to different clonal populations exhibiting variable staining intensities (fig. S5). Thus, MR1-restricted γδ T cells can use diverse γδTCR genes to bind to MR1.

To test antigen reactivity, some MR1-restricted γδTCRs were transfected into HEK293T cells. All of these TCRs bound human MR1 tetramers loaded with 5-OP-RU or with Ac-6-FP, although some (G19 and G82.C8.2) stained more brightly with MR1–5-OP-RU tetramer (Fig. 2B). Only some of these TCRs bound to mouse MR1–Ac-6-FP tetramer (Fig. 2B). However, all of these TCRs recognized the empty form of human MR1 (MR1–K43A) (Fig. 2C). Thus, MR1 autoreactivity appears to be a driving force for γδTCR recognition of MR1, but with some potential for antigenic modulation.

We investigated MR1-dependent signaling through the γδTCRs on TCR-transduced Jurkat-76 cell lines. Four of these lines were activated (marked by the up-regulation of CD69) in response to MR1-transduced cell lines (Fig. 2D). The other four TCRs (G7, G19, G82.C7.1, and G83.C5) failed to trigger CD69 up-regulation despite clear binding to MR1 tetramers. We then determined whether these TCRs signaled in response to MR1, as measured by mitogen-activated protein kinase 1 and 2 (ERK1/2) phosphorylation (Fig. 2E). A significant response was observed for all but one of the γδTCR$^+$ cell lines tested. Thus, MR1-restricted γδTCRs are capable of activating T cells upon MR1 recognition, with the magnitude of signaling and activation varying between different γδTCRs.

We purified recombinant soluble forms of the G7, G19, and G21 γδTCRs and measured the affinity of their interaction with MR1 bound to 6-FP, Ac-6-FP, and 5-OP-RU using surface plasmon resonance (SPR) (fig. S6).

[1]Infection and Immunity Program and Department of Biochemistry and Molecular Biology, Biomedicine Discovery Institute, Monash University, Clayton, Victoria 3800, Australia. [2]Australian Research Council Centre of Excellence in Advanced Molecular Imaging, Monash University, Clayton, Victoria 3800, Australia. [3]Department of Microbiology and Immunology, Peter Doherty Institute for Infection and Immunity, University of Melbourne, Melbourne, Victoria 3000, Australia. [4]Australian Research Council Centre of Excellence in Advanced Molecular Imaging, University of Melbourne, Melbourne, Victoria 3010, Australia. [5]Peter MacCallum Cancer Centre, Melbourne, Victoria 3000, Australia. [6]The Walter and Eliza Hall Institute of Medical Research, Parkville, Victoria 3052, Australia. [7]Department of Medical Biology, University of Melbourne, Parkville, Victoria 3052, Australia. [8]Institute for Molecular Bioscience, The University of Queensland, Brisbane, Queensland 4072, Australia. [9]Australian Research Council Centre of Excellence in Advanced Molecular Imaging, University of Queensland, Brisbane, Queensland 4072, Australia. [10]Department of Paediatrics, Monash University, and Centre for Innate Immunity and Infectious Disease, Hudson Institute of Medicine, Clayton, Victoria 3168, Australia. [11]Lung Transplant Service, Alfred Hospital, Melbourne, Victoria 3004, Australia. [12]Department of Medicine, Monash University, Clayton, Victoria 3800, Australia. [13]Department of Clinical Pathology and Centre for Cancer Research, University of Melbourne, Parkville, Victoria 3052, Australia. [14]The Sir Peter MacCallum Department of Oncology, University of Melbourne, Parkville, Victoria 3000, Australia. [15]Institute of Infection and Immunity, Cardiff University School of Medicine, Heath Park, Cardiff CF14 4XN, UK.
*These authors contributed equally to this work. †Present address: Murdoch Children's Research Institute, Parkville, Victoria 3052, Australia. ‡These authors contributed equally to this work.
§Corresponding author. Email: jamie.rossjohn@monash.edu (J.R.); godfrey@unimelb.edu.au (D.I.G.)

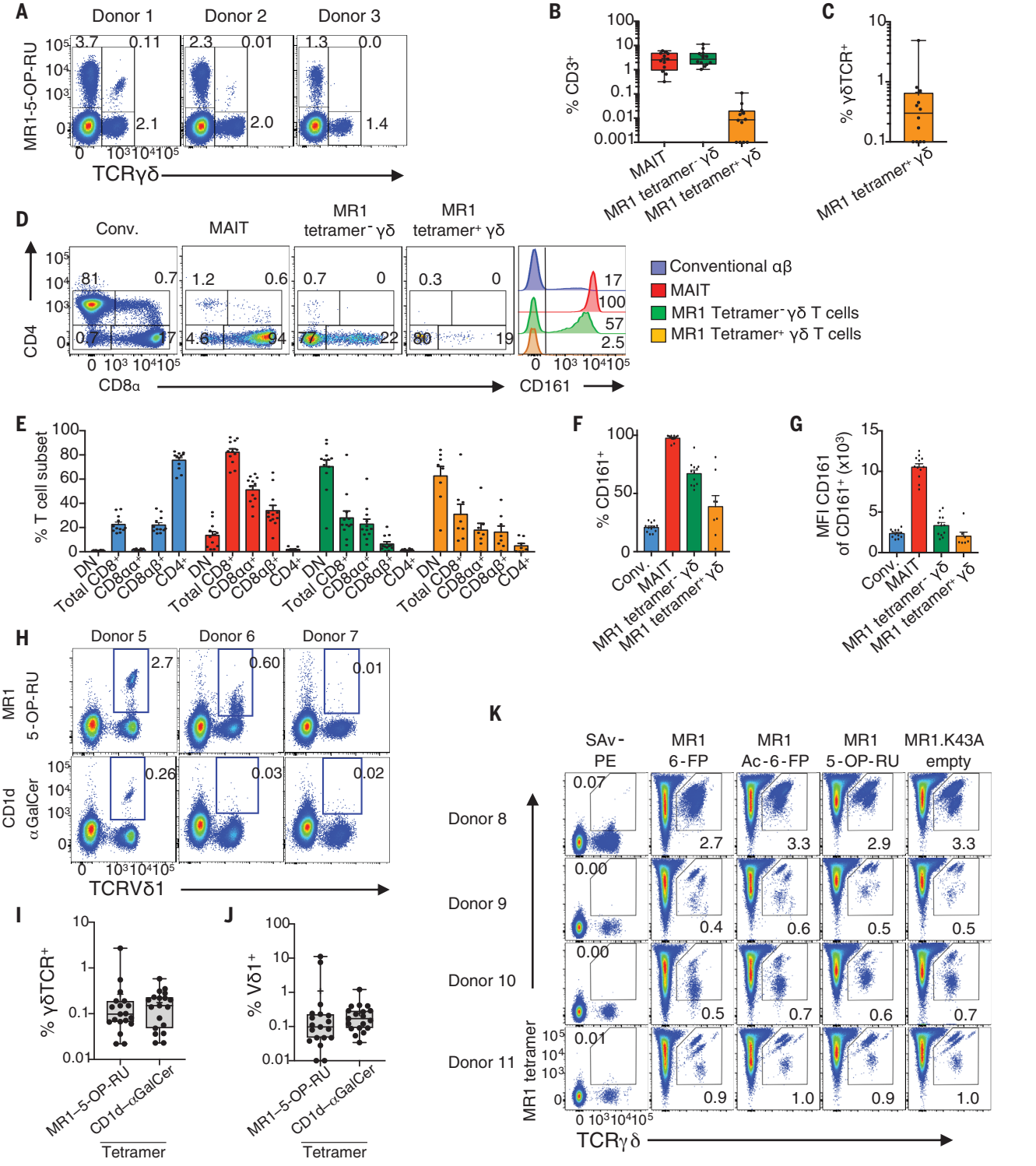

Fig. 1. Identification and characterization of MR1-restricted γδ T cells. (**A**) Flow cytometry dot plots showing MR1 tetramer$^+$ γδ T cells in PBMCs (gated on CD3$^+$ CD19$^-$CD14$^-$ cells). (**B**) Percentage of MAIT cells (red), MR1 tetramer$^-$ γδ T cells (green), and MR1 tetramer$^+$ γδ T cells (orange) of total T cells or (**C**) percentage of γδ T cells in PBMC (n = 12 PBMC samples). Points on x axis are <0.001% (B) or <0.1% (C) (n = 12 donors). Whiskers denote minimum and maximum points. (**D**) Flow cytometry dot plots showing CD4, CD8, and CD161 expression on conventional T cells, MAIT cells, MR1 tetramer$^-$, and MR1 tetramer$^+$ γδ T cells from a representative donor. (**E** to **G**) Cumulative data showing CD4 and CD8 distribution (E), CD161 expression (F), and CD161 mean fluorescence intensity (MFI) on CD161$^+$ cells (G) for T cell subsets (n = 12). Error bars denote SEM. DN, double negative (CD4$^-$CD8$^-$); Conv., conventional. (**H**) Flow cytometry dot plots showing MR1–5-OP-RU and CD1d-αGalCer-tetramer staining of Vδ1$^+$ γδ T cells enriched from three representative PBMC samples. (**I** and **J**) Percentage of MR1–5-OP-RU or CD1d–αGalCer-tetramer$^+$ cells of total γδ T cells (I) or Vδ1$^+$ T cells (J) (n = 7 donors). Whiskers denote minimum and maximum points. (**K**) Flow cytometry dot plots showing MR1-tetramer staining of enriched and expanded TRAV1-2$^-$ MR1–Ac-6-FP tetramer$^+$ cells from four PBMC samples. SAv-PE, streptavidin-phycoerythrin.

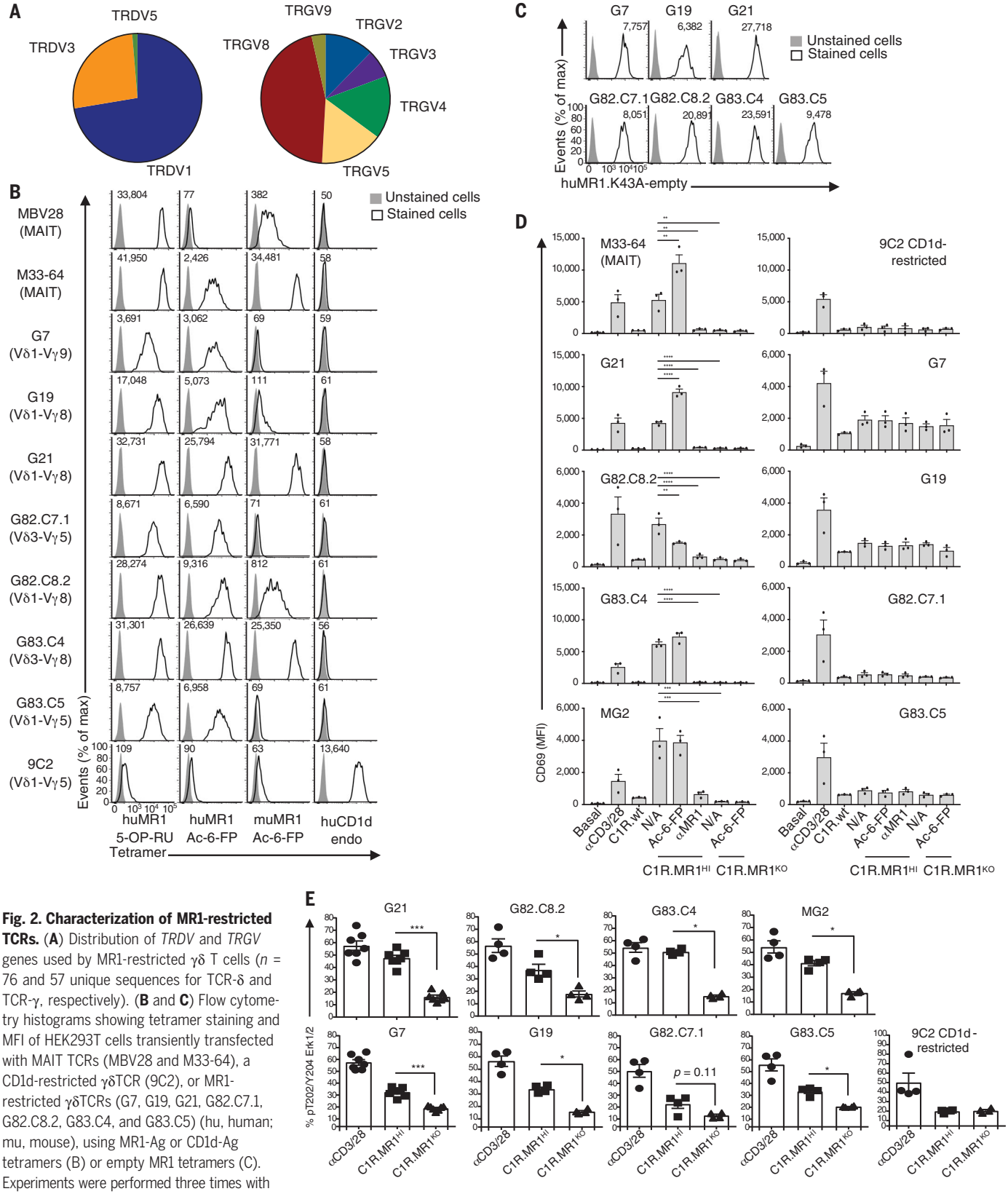

Fig. 2. Characterization of MR1-restricted TCRs. (**A**) Distribution of *TRDV* and *TRGV* genes used by MR1-restricted γδ T cells (n = 76 and 57 unique sequences for TCR-δ and TCR-γ, respectively). (**B** and **C**) Flow cytometry histograms showing tetramer staining and MFI of HEK293T cells transiently transfected with MAIT TCRs (MBV28 and M33-64), a CD1d-restricted γδTCR (9C2), or MR1-restricted γδTCRs (G7, G19, G21, G82.C7.1, G82.C8.2, G83.C4, and G83.C5) (hu, human; mu, mouse), using MR1-Ag or CD1d-Ag tetramers (B) or empty MR1 tetramers (C). Experiments were performed three times with similar results. (**D**) CD69 expression (mean of MFI) on Jurkat76 cells transduced with TCRs as in (B), after coculture with wild-type, $MR1^{HI}$, or $MR1^{KO}$ C1R APC cell lines in the presence of absence of Ac-6-FP or Ac-6-FP plus anti-MR1. Basal indicates Jurkat76 cells alone. Error bars denote mean ± SEM. Each data point is from an independent experiment and represents mean of two technical replicate wells. Statistical analyses performed were paired Student's t tests with Bonferroni correction for multiple hypothesis testing. (**E**) Detection of ERK1/2 phosphorylation (pERK1/2) in Jurkat76 cell lines described in (C), after coculture with $MR1^{HI}$ or $MR1^{KO}$ C1R cell lines analyzed by flow cytometry. Data shows means ± SEM for (n = 7 separate experiments for G7 and G21; n = 4 for remaining cell lines). Statistical analysis was performed using the Mann-Whitney U test.

All three γδTCRs recognized MR1–5-OP-RU with moderate affinity (fig. S6, A to C). The G7 and G21 γδTCRs interacted with MR1–6-FP and Ac-6-FP with similar affinity to that of MR1–5-OP-RU (fig. S6, A and B), whereas G19 bound with weaker affinity to MR1–6-FP when compared with that of MR1–5-OP-RU (fig. S6C). Thus, γδTCRs may exhibit MR1 autoreactivity, but with some potential to be modulated by MR1-bound antigen.

We determined the crystal structure of the G7 γδTCR–MR1–5-OP-RU ternary complex (table S2). Here, the G7 γδTCR adopted a highly distinct and unusual docking strategy in that it bound to the α3 domain of MR1 (Fig. 3A and fig. S7), sharply contrasting the docking mode adopted by the MAIT TCR above the MR1-antigen binding cleft (Fig. 3B). The G7 γδTCR sat underneath the MR1 antigen-binding cleft, where the Vγ chain was orientated toward the plane of the membrane and the Vδ chain pointed toward the cleft. Given the highly unusual G7 γδTCR–MR1 docking topology observed in the crystal lattice, we investigated the docking topology in solution, using solution phase hydrogen–deuterium exchange mass spectrometry (figs. S8 to S10) and small-angle X-ray scattering (SAXs) (fig. S11). These complementary approaches (see supplementary text and tables S3 and S4) fully validated the observed docking mode.

The γδTCR–MR1 total buried surface area (BSA) upon complexation was 2030 Å^2. Within this γδTCR–MR1 footprint, the BSA of the G7 TCR was 1050 Å^2, to which the TCR δ and γ chains contributed 84 and 16% BSA to the γδTCR–MR1 interaction, respectively (Fig. 3C). The TCR γ chain mainly contacted the base of the α3 domain (BSA: ~190 Å^2) (Fig. 3C and

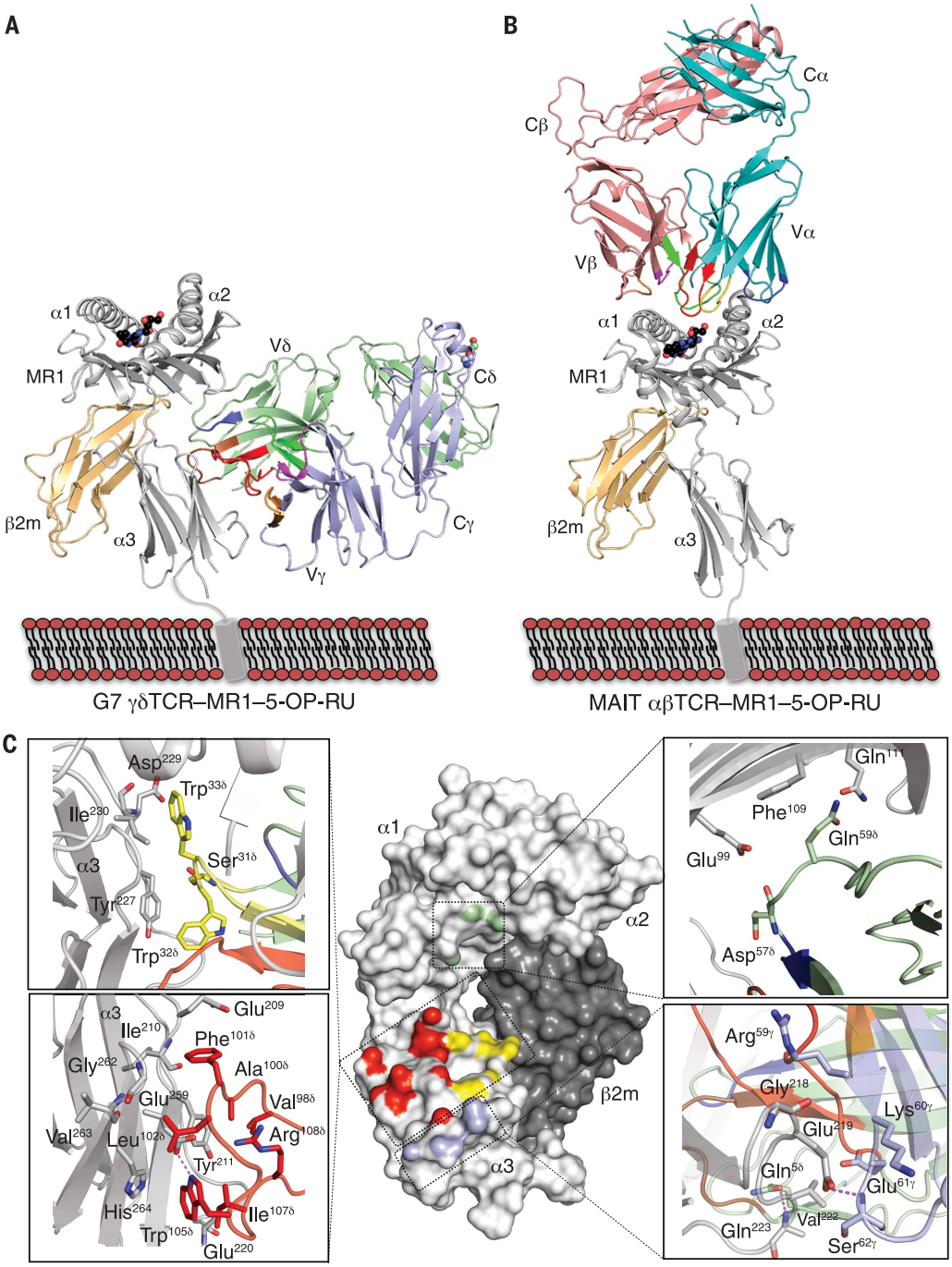

Fig. 3. Overview of the G7 γδTCR–MR1–5-OP-RU complex and molecular interactions. (**A**) Cartoon representation of the G7 γδTCR–MR1–5-OP-RU ternary complex: huMR1, gray; β2m, light orange; γ9 chain, light blue; δ1 chain, pale green; CDR1γ, magenta; CDR2γ, orange; CDR3γ, green; CDR1δ, brown; CDR2δ, blue; and CDR3δ, red. C termini of γδTCR are shown as spheres. (**B**) Cartoon representation of the MAIT αβTCR–MR1–5-OP-RU ternary complex (PDB ID: 4NQC): MR1, gray; β2m, light orange; α-chain, teal; β-chain, salmon; CDR1α, yellow; CDR2α, blue; CDR3α, red; CDR1β, magenta; CDR2β, orange; CDR3β, green. (**C**) Molecular interactions of MR1 with CDR1δ, framework δ chain, CDR3δ, and framework γ chain. MR1, light gray; CDR1δ, yellow; CDR3δ, red; framework δ chain, pale green; framework γ chain, light blue. For clarity, only hydrogen bonds are shown as red dashed lines. Footprint of the G7 γδTCR on the surface of MR1 (color coding as above).

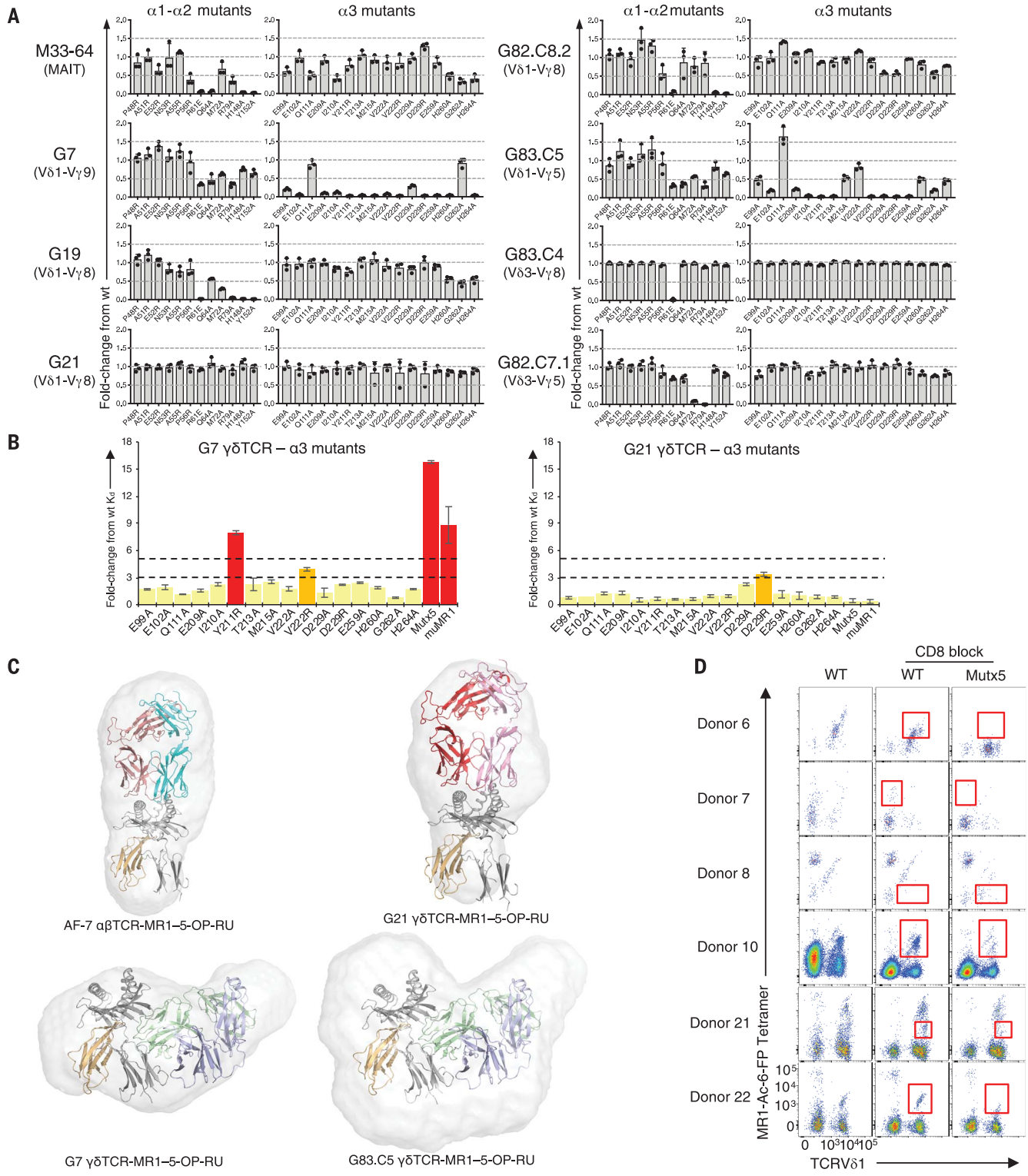

Fig. 4. Generality of α3-docking MR1-restricted γδTCRs. (**A**) Intensity of tetramer staining of HEK293T cells transfected to express MR1-restricted γδTCRs and a MAIT TCR and stained with a panel of α3 and α1-α2 domain MR1 mutant tetramers. Error bars denote SEM of three independent experiments. (**B**) Histograms of the affinity measurements of the G7 and G21 γδTCRs for the α3-domain MR1 mutants depicting the equilibrium dissociation constant (K_d) fold difference between the wild-type MR1 K_d and the corresponding mutants K_d (yellow bars: less than threefold difference; orange bars: threefold to fivefold difference; red bars: greater than fivefold difference). Error bars represent SEM from two independent experiments, each measurement in duplicate. (**C**) SAXs envelopes for the AF-7 αβTCR, G7 γδTCR, G21 γδTCR, and G83.C5 γδTCR bound to MR1 (also see fig. S11). (**D**) Flow cytometry showing wild-type or Mutx5 MR1-tetramer staining (± CD8 blockade) of enriched and expanded TRAV1-2$^-$ MR1-tetramer$^+$ cells from 6 donors (out of 20) where staining was affected by the Mutx5 tetramers (gated on CD3$^+$ TRAV1-2$^-$ γδTCR$^+$ cells). Experiment was performed twice with similar results. Red boxes indicate populations with distinct staining profiles for different tetramers.

table S5). The more dominant Vδ-chain contacts encompassed a greater area of the α3 domain of MR1 (BSA: ~660 Å^2) (Fig. 3C). Here, the framework region of Vδ1 and the CDR1δ loop contributed 19 and 25% BSA, respectively, whereas the CDR3δ loop contributed 40% BSA. The CDR3δ loop lies across the α3 domain of MR1 where hydrophobic residues dominated the interactions with MR1 (Fig. 3C). Additionally, the Trp-rich germline-encoded CDR1δ contributed to the interface (Fig. 3C). The α3 domain of human MHC-I binds to natural killer cell receptors (LILRB1 and LILRB2) (*5*–*8*) (fig. S11) and to the CD8 co-receptor (fig. S12) (*9*). The overall G7 γδTCR contact zone on the MR1 α3 domain was more reminiscent of the latter. Thus, interactions mediated primarily between the TCR δ chain and the α3 domain of MR1 underpin G7 γδTCR docking on MR1.

To gauge the generality of the recognition strategy among other MR1-restricted γδTCRs, we undertook an extensive MR1 mutagenesis study (fig. S13). The majority of the α3 domain mutants significantly reduced the staining of the transfected G7 and G83.C5 γδTCRs (Fig. 4A and fig. S14A). These observations were supported by SPR measurements (Fig. 4B and fig. S14, B and C), which confirms the unusual G7 docking topology and also suggests a similar recognition strategy adopted by G83.C5 γδTCR. SAXs analysis of these γδTCRs (Fig. 4C and fig. S11) indicated that the G21 γδTCR interacted with the antigen-binding cleft of MR1. In contrast, ab initio reconstructions derived from the G83.C5 γδTCR–MR1 scattering data revealed an overall shape similar to that of the G7 γδTCR–MR1 crystal structure (Fig. 4C and fig. S11). Thus, two γδTCRs with reduced signaling profiles (Fig. 2, D and E) docked beneath the antigen-binding cleft.

We next generated an α3-domain quintuple-mutant MR1 tetramer (Mutx5) on the basis of residues important for G7 binding. This was used to screen for other MR1 α3 domain–reactive T cells from 20 additional donors. Previous studies have suggested a potential role for the CD8 co-receptor in modulating TCR-mediated MR1 responsiveness (*10*), which could also be affected by the α3-mutant tetramer. Accordingly, we preincubated PBMC with blocking anti-CD8α monoclonal antibody to remove this confounding factor (*11*). These cells were then stained with wild-type or α3-mutant tetramers loaded with Ac-6-FP (Fig. 4D and fig. S15). After eliminating the influence of CD8 coreceptor, a comparison of α3-mutant MR1 tetramer to wild-type MR1 tetramer staining identified a population of α3 domain–dependent γδ T cells in 6 out of 20 donors (Fig. 4D).

We have described a phenotypically diverse population of human γδ T cells that recognizes MR1. These MR1-reactive γδ T cells were found in both healthy and diseased tissues, suggesting a role in physiology and pathology. The prevailing view is that TCRs sit atop the antigen-binding platform and simultaneously co-recognize the presented antigen. Surprisingly, we show that MR1-restricted γδTCRs can adopt diverse binding modes with MR1, including underneath the antigen-binding platform of MR1. Thus, we simultaneously identify a human self-ligand for γδ T cells and transform our understanding of TCR recognition determinants.

REFERENCES AND NOTES

1. J. Rossjohn *et al*., *Annu. Rev. Immunol.* **33**, 169–200 (2015).
2. L. Kjer-Nielsen *et al*., *Nature* **491**, 717–723 (2012).
3. A. J. Corbett *et al*., *Nature* **509**, 361–365 (2014).
4. R. Reantragoon *et al*., *J. Exp. Med.* **210**, 2305–2320 (2013).
5. C. L. Dulberger *et al*., *Immunity* **46**, 1018–1029.e7 (2017).
6. M. Shiroishi *et al*., *Proc. Natl. Acad. Sci. U.S.A.* **103**, 16412–16417 (2006).
7. B. E. Willcox, L. M. Thomas, P. J. Bjorkman, *Nat. Immunol.* **4**, 913–919 (2003).
8. Z. Yang, P. J. Bjorkman, *Proc. Natl. Acad. Sci. U.S.A.* **105**, 10095–10100 (2008).
9. G. F. Gao *et al*., *Nature* **387**, 630–634 (1997).
10. A. Kurioka *et al*., *Front. Immunol.* **8**, 1031 (2017).
11. M. Clement *et al*., *J. Immunol.* **187**, 654–663 (2011).

ACKNOWLEDGMENTS

We thank L. Wakim for assistance in provision of lung tissue; P. E. O'Brien and P. Burton (Centre for Obesity Research) for provision of human gastric tissue; K. Visvanathan (St. Vincent's Hospital, Melbourne) for provision of liver samples; J. Furness and M. Nikfarjam (University of Melbourne) for provision of intestinal tissue; and R. Hicks (Peter MacCallum Cancer Centre) for provision of Merkel cell carcinoma sample. We thank M. Herold for the CRISPR constructs, B. Meehan for assistance with MR1 tetramer production, and K. Loh and S. Gras for technical contributions. The crystallographic research was undertaken on the MX2 beamline at the Australian Synchrotron, part of ANSTO. We thank the staff at the Australian Synchrotron for assistance with data collection, the staff at the Monash Macromolecular Crystallisation Facility, and the staff from the University of Melbourne flow cytometry facilities. **Funding:** This work was supported by program grants (1013667, 1016629, and 1113293) and project grants (APP1159932 and APP1100240) from the National Health and Medical Research Council of Australia (NHMRC) and the Australian Research Council (ARC) (CE140100011). N.A.G. was supported by a Leukaemia Foundation of Australia Postgraduate Scholarship and a Cancer Council Victoria postdoctoral fellowship; J.L.N. is supported by an ARC Future Fellowship (FT160100074); A.J.C. is supported by an ARC Future Fellowship (FT160100083); S.B.G.E. is supported by an ARC DECRA Fellowship; R.B. is supported by an NHMRC CDF Fellowship (1109901); D.G.P. is supported by an NHMRC CDF Fellowship (1144308); A.P.U. is supported by an ARC Future Fellowship (FT140100278); D.I.G. and D.P.F. are supported by NHMRC Senior Principal Research Fellowships (1117766, 1117017); A.W.P. is supported by an NHMRC Principal Research Fellowship; J.R. is supported by an Australian ARC Laureate Fellowship; D.I.G., J.R., and J.M. are supported by a program grant from the National Health and Medical Research Council of Australia (NHMRC) 1113293; A.P.U. is supported by the Cancer Council Victoria (1126866). **Author contributions:** J.L.N. and N.A.G. are joint first authors and contributed to data generation, data analysis, and paper writing; S.H.R., W.A., F.W., B.S.G., Y.K., T.P., J.M.W., J.J.S., A.I.W., A.v.B., M.T.R., S.J.R., R.S., M.L.S.-R., S.L., M.S.D., R.B., T.T., A.W.P., M.N.T.S., and A.P.U. contributed to data generation and analysis; and S.B.G.E., A.J.C., H.H.R., L.L., D.P.F., E.M.G., G.P.W., R.W.T., J.M., and D.G.P. provided key reagents and samples. D.I.G. and J.R. are joint senior authors. They conceived of the study, analyzed data, and cowrote the paper. **Competing interests:** A.J.C., S.B.G.E., D.P.F., L.L., J.R., and J.M. are inventors on patents describing MR1 tetramers and MR1-ligands. **Data and materials availability:** Atomic coordinates and structure factors of the G7 γδTCR–MR1–5-OP-RU ternary complex were deposited in the Protein Data Bank (PDB) under the ID 6MWR. All remaining data are available from the corresponding authors upon request.

SUPPLEMENTARY MATERIALS

science.sciencemag.org/content/366/6472/1522/suppl/DC1
Materials and Methods
Supplementary Text
Figs. S1 to S15
Tables S1 to S6
References (*12*–*26*)

View/request a protocol for this paper from *Bio-protocol*.

12 September 2018; resubmitted 20 September 2019
Accepted 21 November 2019
10.1126/science.aav3900

ORGANIC CHEMISTRY

Foldamer-templated catalysis of macrocycle formation

Zebediah C. Girvin, Mary Katherine Andrews, Xinyu Liu, Samuel H. Gellman*

Macrocycles, compounds containing a ring of 12 or more atoms, find use in human medicine, fragrances, and biological ion sensing. The efficient preparation of macrocycles is a fundamental challenge in synthetic organic chemistry because the high entropic cost of large-ring closure allows undesired intermolecular reactions to compete. Here, we present a bioinspired strategy for macrocycle formation through carbon–carbon bond formation. The process relies on a catalytic oligomer containing α- and β-amino acid residues to template the ring-closing process. The α/β-peptide foldamer adopts a helical conformation that displays a catalytic primary amine–secondary amine diad in a specific three-dimensional arrangement. This catalyst promotes aldol reactions that form rings containing 14 to 22 atoms. Utility is demonstrated in the synthesis of the natural product robustol.

Macrocyclic compounds, containing a ring of 12 or more atoms, play important roles in biology and medicine (*1*–*3*). Engineered macrocycles have engendered new technologies (*4*) and new therapeutic strategies (*5*). Efficient synthesis of macrocycles is challenging because the entropic penalty associated with ring closure allows competition from intermolecular side-reactions, reducing yields of the desired products (*6*–*10*). Preorganization of linear precursors through multipoint coordination of a metal cation, an anion, or a neutral partner can facilitate synthesis of specific macrocycle classes (Fig. 1A), but this strategy depends on noncovalent interaction sites in the linear precursor (*9*–*12*). Intramolecular alkene metathesis can be very effective for formation of large rings (*9*, *13*–*15*). This process features catalytic metal-based activation of terminal alkenes in a linear precursor, but additional coordination between internal functionality and the metal center is necessary (*9*, *13*–*16*). Biosynthetic machinery overcomes the entropic cost of macrocycle formation by holding linear precursors in appropriate conformations, catalyzing the ring-closure reaction, and inhibiting competing intermolecular processes (*17*, *18*). We took inspiration from biological catalysts to develop a macrocyclization catalyst in which a well-folded oligomer activates both ends of a linear precursor and orients the termini for reaction, thereby serving as a template for ring closure through carbon–carbon bond formation.

Our approach uses a foldamer designed to facilitate macrocyclization through aldol condensation by proper orientation of two catalytic groups. We build on pioneering work by Miller *et al.*, who employed related design principles to achieve site-specific catalytic functionalization of complex substrates (*19*). Our work complements the development of small molecules that serve as bifunctional catalysts, such as the recent mimicry of glycotransferase enzymes with cyclic bis-thioureas (*20*) and the recent stereoselective formation of nucleoside phosphoramidates with bis-imidazoles (*21*). Neither of these cases, however, involved macrocycle formation.

Oligomer **1** (Fig. 1B) contains both α- and β-amino acid residues and features an αββ backbone repeat pattern, which favors a helical conformation that has approximately three residues per turn (*22*, *23*). Use of β residues with a five-membered ring constraint, such as the cyclopentane- and pyrrolidine-based residues in **1**, enhances helix stability (*22*). A related α/β peptide containing two pyrrolidine-based residues catalyzes intermolecular crossed aldol condensations involving formaldehyde as the electrophile (*24*). Optimal catalysis required *i*,*i*+*3* spacing of the pyrrolidine residues, which causes alignment of these two catalytic units upon helical folding. α/β-Peptide **1** is distinct from the earlier example in that one of the catalytic units is a primary amine, a difference that proved to be consequential.

The current study began with an unexpected observation. We asked whether α/β-peptide **1** would promote cyclization of C9 dialdehyde **A** to form cyclooctene-1-aldehyde (Fig. 1B). The reaction conditions, based on precedents from Pihko *et al.* and our previous studies (*24*, *25*), included propionic acid and triethylamine as additives and aqueous isopropanol as solvent. The cyclooctene derivative, however, was not observed when 10 mM **A** was allowed to react in the presence of 10 mole % (mol %) **1**, although **A** appeared to be fully consumed within 24 hours. Instead, the foldamer catalyzed formation of a product mixture in which the principal components were cyclodimers. We isolated the major cyclodimer and identified it by two-dimensional (2D) nuclear magnetic resonance (NMR) spectroscopy to be the 16-membered ring *E*,*E* diene **B**. Liquid chromatography–mass spectrometry (LC-MS) revealed initial formation of intermolecular aldol adduct **C**, but the amount of this intermediate remained low throughout the reaction, suggesting rapid cyclization. By contrast, a 1:1 mixture of pyrrolidine and *n*-butylamine (10 mol % each)

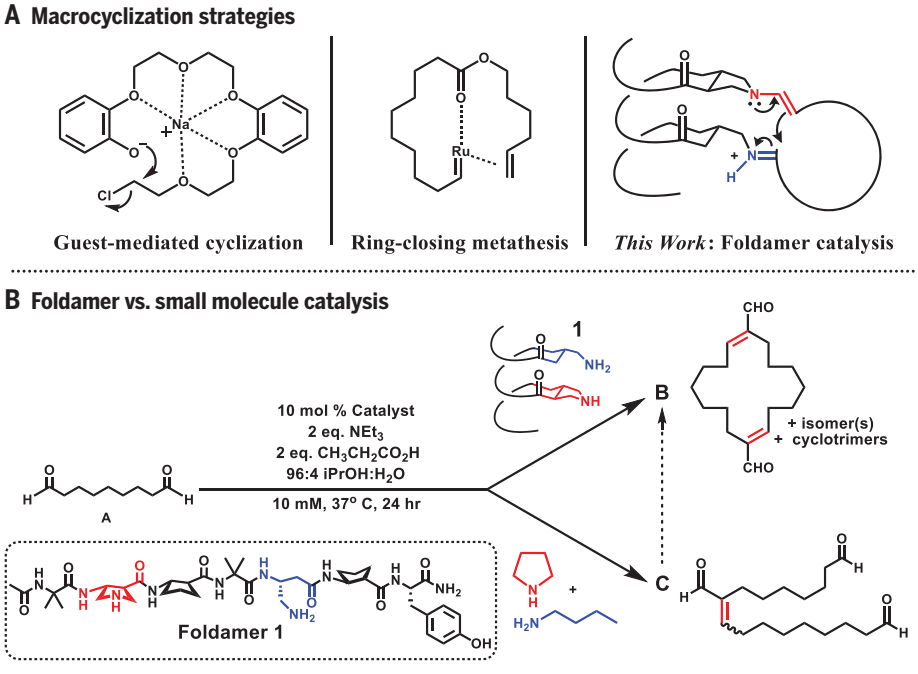

Fig. 1. Macrocyclization strategies. (**A**) Prior approaches and foldamer approach to macrocyclization. (**B**) Divergent reactivity: Foldamer versus small-molecule catalysis. eq., equivalent(s).

Department of Chemistry, University of Wisconsin–Madison, Madison, WI, USA.
*Corresponding author. Email: gellman@chem.wisc.edu

catalyzed slow formation of the linear dimer **C**, with only trace levels of cyclodimer detected after 24 hours. We hypothesized that the foldamer acts by a bifunctional mechanism, serving as a template to overcome the entropic cost of large-ring closure.

To gain further insight on the capabilities of foldamer **1**, we prepared symmetrical dialdehydes **D1** to **D4** (Fig. 2A), each containing a central methoxyphenyl ring that allowed us to monitor starting material, products, and transient intermediates through ultraviolet absorbance. Initial studies focused on **D3**, which can form a 16-membered ring enal, matching the ring size of cyclodimer **B**. When we reacted **D3** with **1**, we observed nearly full conversion to macrocyclic *E*-enal **E3** (full characterization in supplementary material). By contrast, the control reaction with pyrrolidine and *n*-butylamine produced only a trace amount of **E3** after 24 hours (fig. S10).

α/β-Peptide **1** proved to be versatile in terms of product ring size (Fig. 2A). We observed efficient conversion of **D4** to 18-membered ring *E*-enal **E4** and of **D2** to 14-membered ring *E*-enal **E2**. The foldamer-catalyzed reaction of **D1** took longer to reach completion and led to a mixture of *E*-enal **E1** and cyclodimers. Precedents suggest that this outcome arises because of strain that develops upon 12-membered ring formation (*7*, *8*). However, efficient and stereospecific synthesis of the 14-, 16-, and 18-membered ring enals suggests that catalyst **1** is broadly competent for formation of larger rings.

Comparing formation of enal **E3** with α/β-peptide **1** and a set of related oligomers reveals that catalytic efficacy is very sensitive to specific features of foldamer structure (Fig. 2B). As noted above, a control mixture of pyrrolidine and *n*-butylamine was much less effective than α/β-peptide **1** at promoting macrocycle formation. Similarly low reactivity was observed for a pair of monofunctional α/β peptides (**2** + **3**) that provide the secondary and primary amine groups as β-residue side chains in separate molecules. These results are consistent with a bifunctional mechanism involving activation of the two aldehyde groups in a substrate on a single catalyst molecule. A bifunctional mechanism is further supported by the observation that macrocyclization to form **E3** displayed first-order dependence on α/β-peptide **1** (figs. S13 and S14). 2D NMR studies of **1**, conducted in either d_7-isopropanol or d_3-methanol, revealed numerous nuclear Overhauser effects consistent with the expected helical conformation (figs. S31 and S34) and the alignment of the primary and secondary amine side chains, which is essential for bifunctional catalysis.

The spacing between reactive side chains along the foldamer backbone is crucial for catalytic efficacy, as shown by the low yields

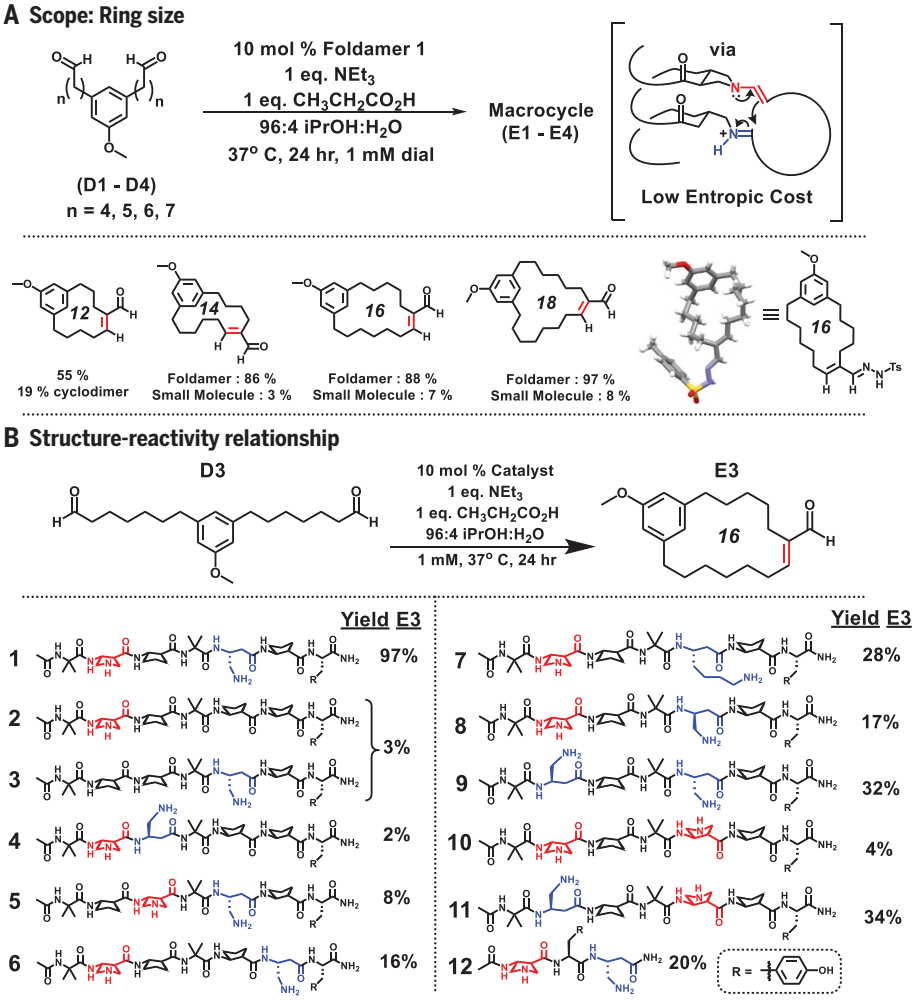

Fig. 2. Scope and structure-reactivity relationship. (**A**) Foldamer-catalyzed macrocyclization: Ring size variation. Isolated yields are reported for foldamer-catalyzed reactions; however, yields for the pyrrolidine–*n*-butylamine catalyst pair ("small molecule") are estimated on the basis of LC-MS data. Ts, *p*-toluenesulfonyl. (**B**) Identification of features critical for foldamer catalysis of macrocyclization. Details are included in the supplementary materials (figs. S8 to S12).

obtained with α/β-peptides **4** to **6**, which are sequence isomers of **1**. When the β residues bearing the reactive amine groups were adjacent in primary sequence (*i*,*i+1* spacing; **4**), macrocyclization was barely detectable. The isomers with *i*,*i+2* and *i*,*i+4* spacing, **5** and **6**, were poor catalysts as well. Because the helical conformation favored by the αββ backbone has three residues per turn (*22*), differences among **1** and sequence isomers **4** to **6** support the conclusion that optimal catalysis requires alignment of the primary and secondary amine groups along the helix axis. When the β residues that provide the reactive groups were properly spaced (*i*,*i+3*) but the linker between the primary amino group and the backbone was lengthened, as in **7**, catalytic activity suffered. Thus, even if the primary and secondary amines are aligned along the helix axis, increased flexibility of the segment between the two amino groups appears to be deleterious. α/β-Peptide **8** is the diastereomer of **1** that differs only in the configuration at the backbone carbon bearing the primary amine side chain, a change expected to diminish helix stability (*26*). We observed only a low yield of enal **E3** with **8**, consistent with high sensitivity of the reaction to the spatial positioning of the amino groups provided by the foldamer scaffold. Overall, this set of comparisons shows that catalytic activity depends on the ability of the α/β-peptide backbone to achieve a specific arrangement of the primary amine–secondary amine diad.

The chemical nature of the amine groups is critical for intramolecular aldol condensation (figs. S35 to S46). α/β-Peptide **9** presents a diad of primary amino groups with the optimal sequence spacing, but the yield of 16-membered ring enal **E3** was substantially lower for this catalyst relative to α/β-peptide **1**. α/β-Peptide **10** presents a secondary amine

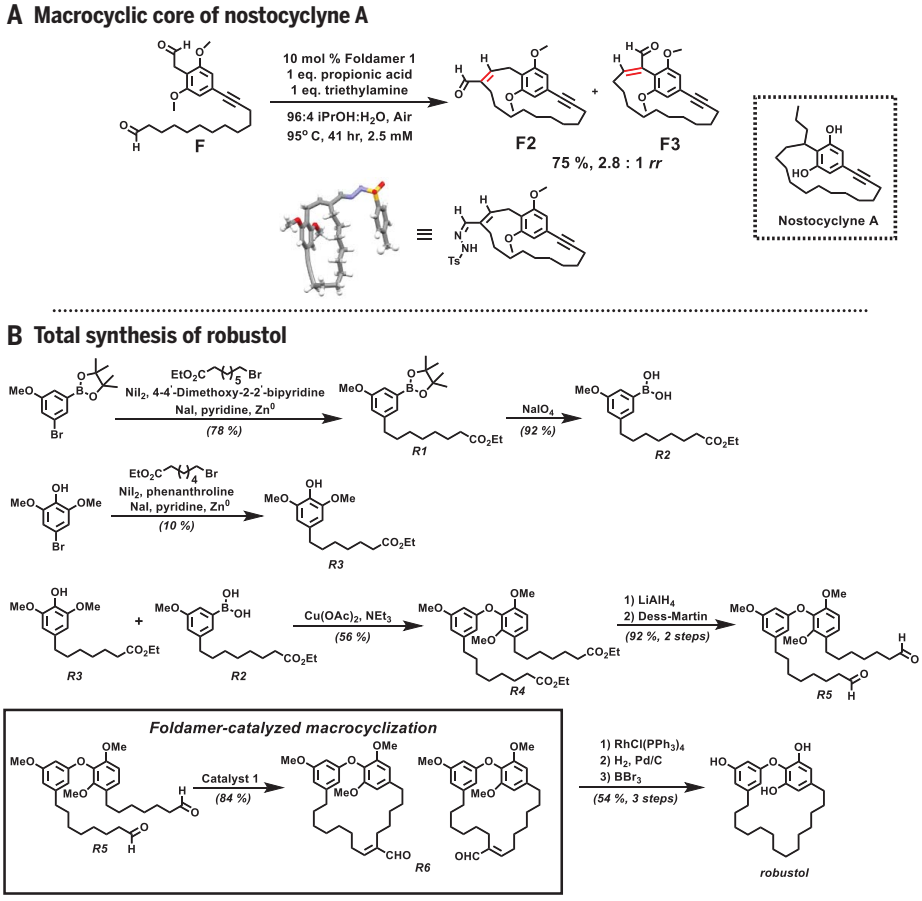

Fig. 3. Applications of foldamer catalysis in total synthesis. (**A**) Foldamer-catalyzed formation of the macrocyclic core of nostocyclyne A. Identity of product F2 was established by means of the crystal structure of the tosylhydrazone derivative. *rr*, regioisomer ratio. (**B**) Total synthesis of robustol. The key step, foldamer-catalyzed closure of the 22-membered ring, is highlighted. Full reaction protocols and product characterization are in the supplementary materials.

diad, and in this case, the macrocyclic product was barely detectable. The variations in catalytic efficacy among **1**, **9**, and **10** may arise because primary amines favor imine adducts with aldehydes (*27*), whereas secondary amines favor enamine adducts (*28*). Macrocycle formation presumably requires the generation of an electrophilic iminium and nucleophilic enamine on a single catalyst scaffold, a combination that is favored by the reactive diad of **1**. Previously, we found that α/β-peptide **10** was an excellent catalyst for intermolecular crossed aldol reactions (*24*). The distinct catalytic profiles of α/β-peptides **1** and **10** show that once a favorable foldamer scaffold is identified, reaction selectivity can be achieved by modifying the catalytic groups.

The modest macrocycle yield obtained with **11** shows that swapping the primary and secondary amine group positions in the α/β-peptide backbone causes erosion of catalytic efficacy. This observation highlights the ability to explore diverse spatial arrangements of reactive groups that is provided by a foldamer scaffold, which is inherently modular. Tripeptide **12** features *i*,*i+2* spacing but is too small to adopt a stable helical conformation. This tripeptide was slightly more effective than the longer α/β-peptide with *i*,*i+2* spacing (**5**), which raises the possibility that a stable folded conformation can cause a modest diminution of intrinsic amine reactivity, perhaps because of steric hindrance.

The efficient foldamer-catalyzed macrocyclization introduced here may be useful for the synthesis of large-ring natural products, analogs of these natural products, and macrocycles of potential therapeutic utility. We could produce the 18-membered ring core of nostocyclyne A (Fig. 3A) (*29*) from dialdehyde **F** with 10 mol % **1**. Because the substrate is unsymmetrical, two macrocyclic *E*-enals are possible. Both were formed in 75% total yield, with a 2.8:1 ratio. The identity of the major isomer was established by a crystal structure of the tosylhydrazone derivative.

We further demonstrated the utility of foldamer-catalyzed macrocyclization by achieving total synthesis of the natural product robustol (*30*), which contains a 22-membered ring (Fig. 3B). This compound is related to the turriane family of natural products, several of which have been prepared by application of macrocycle-closing alkene or alkyne metathesis (*31*). Our route to an appropriate dialdehyde substrate began with two nickel-catalyzed reductive cross-coupling reactions, pioneered by Weix *et al.* (*32*), to prepare boronate ester **R1** and phenol **R3**. Copper-catalyzed Chan-Lam-Evans coupling of these two compounds generated diester **R4** (*33*, *34*), and redox manipulations provided dialdehyde **R5**. The foldamer-catalyzed reaction efficiently generated the desired 22-membered ring skeleton as a mixture of isomers (**R6**). Heating with Wilkinson's catalyst induced decarbonylation (*35*), and the resulting alkene mixture was hydrogenated to produce **R7**. The methyl groups were removed by treatment with excess BBr_3 to yield a single product with an ^1H NMR spectrum matching that of natural robustol (*30*).

Our results suggest that a broad range of macrocycles will be accessible through intramolecular aldol condensations catalyzed by foldamer **1**, with limitations arising when ring closure causes significant internal strain (*7*, *8*). Because polar groups (amine, carboxylic acid, hydroxyl) are abundant in the reaction medium, aldol macrocyclizations catalyzed by α/β-peptide **1** will likely display considerable functional group tolerance. Macrocyclic compounds are of interest for pharmaceutical development, as exemplified by the hepatitis C drug vaniprevir (*36*), and our method should enable synthesis of diverse structures to support discovery of therapeutic agents.

Our use of a foldamer scaffold to achieve optimal arrangement of the primary amine–secondary amine diad was inspired by the role of protein scaffolds in positioning catalytic groups in enzyme active sites (*37*). The prevalence of β-amino acid residues in our foldamer backbone allows us to use residue-based strategies for conformational preorganization (*23*), an opportunity that is not available for catalyst designs based entirely on α-amino acid residues. Well-characterized foldamer scaffolds allow systematic variation of the arrangement of a reactive group set, such as the primary amine–secondary amine diad in **1**, which is useful for catalyst optimization (*24*). Small-molecule scaffolds for bifunctional catalysis (*38*–*40*) may be less amenable to exploration of alternative geometries for a given functional group diad relative to foldamer-based skeletons because small molecules lack the modularity of foldamers. We speculate that the αββ backbone of **1**, and related backbones containing preorganized β- and/or γ-amino acid residues, will provide scaffolds that can be harnessed to enable bifunctional or polyfunctional catalysis of other useful reactions.

REFERENCES AND NOTES

1. E. A. Villar *et al*., *Nat. Chem. Biol.* **10**, 723–731 (2014).
2. K. R. Campos *et al*., *Science* **363**, eaat0805 (2019).
3. D. J. Newman, G. M. Cragg, "Bioactive macrocycles from nature" in *Macrocycles in Drug Discovery*, J. Levin, Ed. (Royal Society of Chemistry, 2014), pp. 1–36.
4. M. Iyoda, J. Yamakawa, M. J. Rahman, *Angew. Chem. Int. Ed.* **50**, 10522–10553 (2011).
5. Å. Rosenquist *et al*., *J. Med. Chem.* **57**, 1673–1693 (2014).
6. T. Gulder, P. S. Baran, *Nat. Prod. Rep.* **29**, 899–934 (2012).
7. C. Galli, L. Mandolini, *Eur. J. Org. Chem.* **2000**, 3117–3125 (2000).
8. M. A. Casadei, C. Galli, L. Mandolini, *J. Am. Chem. Soc.* **106**, 1051–1056 (1984).
9. A. Fürstner, *Top. Catal.* **4**, 285–299 (1997).
10. V. Martí-Centelles, M. D. Pandey, M. I. Burguete, S. V. Luis, *Chem. Rev.* **115**, 8736–8834 (2015).
11. C. J. Pedersen, *J. Am. Chem. Soc.* **89**, 2495–2496 (1967).
12. S. J. Rowan, S. J. Cantrill, G. R. L. Cousins, J. K. M. Sanders, J. F. Stoddart, *Angew. Chem. Int. Ed.* **41**, 898–952 (2002).
13. H. E. Blackwell *et al*., *J. Org. Chem.* **66**, 5291–5302 (2001).
14. X. Shen *et al*., *Nature* **541**, 380–385 (2017).
15. A. Sytniczuk *et al*., *J. Am. Chem. Soc.* **140**, 8895–8901 (2018).
16. J. R. Ludwig, P. M. Zimmerman, J. B. Gianino, C. S. Schindler, *Nature* **533**, 374–379 (2016).
17. D. L. Akey *et al*., *Nat. Chem. Biol.* **2**, 537–542 (2006).
18. F. Kopp, M. A. Marahiel, *Nat. Prod. Rep.* **24**, 735–749 (2007).
19. C. A. Lewis, S. J. Miller, *Angew. Chem. Int. Ed.* **45**, 5616–5619 (2006).
20. Y. Park *et al*., *Science* **355**, 162–166 (2017).
21. D. A. DiRocco *et al*., *Science* **356**, 426–430 (2017).
22. S. H. Choi, I. A. Guzei, L. C. Spencer, S. H. Gellman, *J. Am. Chem. Soc.* **131**, 2917–2924 (2009).
23. J. L. Price, E. B. Hadley, J. D. Steinkruger, S. H. Gellman, *Angew. Chem. Int. Ed.* **49**, 368–371 (2010).
24. Z. C. Girvin, S. H. Gellman, *J. Am. Chem. Soc.* **140**, 12476–12483 (2018).
25. A. Erkkilä, P. M. Pihko, *J. Org. Chem.* **71**, 2538–2541 (2006).
26. E. Krause, M. Bienert, P. Schmieder, H. Wenschuh, *J. Am. Chem. Soc.* **122**, 4865–4870 (2000).
27. A. Erkkilä, I. Majander, P. M. Pihko, *Chem. Rev.* **107**, 5416–5470 (2007).
28. S. Mukherjee, J. W. Yang, S. Hoffmann, B. List, *Chem. Rev.* **107**, 5471–5569 (2007).
29. A. Ploutno, S. Carmeli, *J. Nat. Prod.* **63**, 1524–1526 (2000).
30. J. R. Cannon *et al*., *Aust. J. Chem.* **26**, 2257–2275 (1973).
31. A. Fürstner, F. Stelzer, A. Rumbo, H. Krause, *Chemistry* **8**, 1856–1871 (2002).
32. D. A. Everson, B. A. Jones, D. J. Weix, *J. Am. Chem. Soc.* **134**, 6146–6159 (2012).
33. D. A. Evans, J. L. Katz, T. R. West, *Tetrahedron Lett.* **39**, 2937–2940 (1998).
34. P. Y. S. Lam *et al*., *Tetrahedron Lett.* **39**, 2941–2944 (1998).
35. K. Ohno, J. Tsuji, *J. Am. Chem. Soc.* **90**, 99–107 (1968).
36. J. A. McCauley *et al*., *J. Med. Chem.* **53**, 2443–2463 (2010).
37. S. J. Benkovic, S. Hammes-Schiffer, *Science* **301**, 1196–1202 (2003).
38. C. E. Song, *Cinchona Alkaloids in Synthesis and Catalysis, Ligands, Immobilization and Organocatalysis* (Wiley-VCH, 2008).
39. S.-K. Tian *et al*., *Acc. Chem. Res.* **37**, 621–631 (2004).
40. M. S. Taylor, E. N. Jacobsen, *Angew. Chem. Int. Ed.* **45**, 1520–1543 (2006).

ACKNOWLEDGMENTS

We thank I. Guzei for x-ray structure determination and A. Maza for assistance with high pressure hydrogenation. **Funding:** This research was supported in part by the U.S. National Science Foundation (CHE-1904940). **Author contributions:** Z.C.G. and S.H.G. conceived the study. Z.C.G, M.K.A., X.L., and S.H.G. designed experiments. Z.C.G., M.K.A., and X.L. performed experiments. All authors contributed to data analysis. S.H.G. supervised research and acquired funding. Z.C.G. and S.H.G. wrote the original draft, which was reviewed and edited with input from all authors. **Competing interests:** The α/β-peptide catalysts described here are covered by U.S. patent 7,858,737 B2, on which S.H.G. is a coinventor. This patent covers α/β-peptides containing cyclic β residues. S.H.G. is a cofounder of and has a secondary affiliation with Longevity Biotech, which is pursuing therapeutic applications of α/β-peptides. **Data and materials availability:** Crystallographic parameters are available from the Cambridge Crystallographic Data Centre under references CCDC 1910263 (hydrazone of **E3**) and CCDC 1910264 (hydrazone of **F2**). All other data are available in the main text or supplementary materials. A University of Wisconsin materials transfer agreement applies to materials acquired directly from the authors.

SUPPLEMENTARY MATERIALS

science.sciencemag.org/content/366/6472/1528/suppl/DC1
Materials and Methods
Figs. S1 to S46
Tables S1 to S21
Spectral Data
References (*41*–*62*)

17 April 2019; resubmitted 13 September 2019
Accepted 4 November 2019
10.1126/science.aax7344

MITOCHONDRIAL BIOLOGY

VDAC oligomers form mitochondrial pores to release mtDNA fragments and promote lupus-like disease

Jeonghan Kim[1], Rajeev Gupta[2], Luz P. Blanco[3], Shutong Yang[1], Anna Shteinfer-Kuzmine[2], Kening Wang[4], Jun Zhu[5,7], Hee Eun Yoon[1], Xinghao Wang[3], Martijn Kerkhofs[6], Hyeog Kang[1], Alexandra L. Brown[1], Sung-Jun Park[1], Xihui Xu[1], Eddy Zandee van Rilland[1]*, Myung K. Kim[1], Jeffrey I. Cohen[4], Mariana J. Kaplan[3], Varda Shoshan-Barmatz[2], Jay H. Chung[1]†

Mitochondrial stress releases mitochondrial DNA (mtDNA) into the cytosol, thereby triggering the type I interferon (IFN) response. Mitochondrial outer membrane permeabilization, which is required for mtDNA release, has been extensively studied in apoptotic cells, but little is known about its role in live cells. We found that oxidatively stressed mitochondria release short mtDNA fragments via pores formed by the voltage-dependent anion channel (VDAC) oligomers in the mitochondrial outer membrane. Furthermore, the positively charged residues in the N-terminal domain of VDAC1 interact with mtDNA, promoting VDAC1 oligomerization. The VDAC oligomerization inhibitor VBIT-4 decreases mtDNA release, IFN signaling, neutrophil extracellular traps, and disease severity in a mouse model of systemic lupus erythematosus. Thus, inhibiting VDAC oligomerization is a potential therapeutic approach for diseases associated with mtDNA release.

Mitochondrial stress, such as that triggered by increased mitochondrial reactive oxygen species (mROS), can release mitochondrial DNA (mtDNA) into the cytosol. There, it interacts with and activates a large number of immunostimulatory DNA sensors such as cyclic guanosine monophosphate–adenosine monophosphate synthase (cGAS) that can trigger autoimmunity, including diseases caused by the type I interferon (IFN) response (*1*). Mitochondrial outer membrane permeabilization (MOMP) is required for mtDNA release. To date, only BAX/BAK oligomers, which can form extremely large macropores in the mitochondrial outer membrane (MOM), have been shown to mediate mtDNA release (*2*–*4*). However, the formation of the BAX/BAK macropore generally occurs under conditions that activate BAX/BAK, such as apoptosis or treatment with BAX/BAK activators (*2*–*4*). However, the pores that promote MOMP in live cells or in conditions that do not activate BAX/BAK have not been identified.

Because the voltage-dependent anion channel (VDAC) can oligomerize under oxidative stress conditions, and because VDAC oligomers can form large MOM pores (*5*), we investigated whether VDAC could trigger MOMP in live cells and mediate mtDNA release. VDAC is the most abundant protein in MOM and regulates Ca^{2+} influx, metabolism, inflammasome activation (*6*), and cell death (*7*, *8*). Moreover, the expression of both VDAC1 (the most abundant of the three VDAC isoforms) and VDAC3 is increased in the autoimmune disease systemic lupus erythematosus (SLE) (*9*). In some models of this disease, the trigger is thought to be the release of mtDNA (*10*, *11*).

Previous studies on the mechanism of mtDNA release have used cells that are undergoing apoptosis or have altered mtDNA content (*2*, *12*, *13*), hence the results of such studies are difficult to interpret. To avoid these confounding variables, we studied mouse embryo fibroblasts (MEFs) deficient in endonuclease g (*Endog*), a nuclear-encoded mitochondrial endonuclease (*14*, *15*). *Endog*$^{-/-}$ MEFs have higher levels of cytosolic mtDNA (cmtDNA) relative to wild-type MEFs (Fig. 1A), despite having similar levels of total mtDNA (Fig. 1B) and cellular growth rates (fig. S1A). Consistent with this finding, *Endog*$^{-/-}$ MEFs (Fig. 1, C and D, and fig. S1, B and C) and plasmacytoid dendritic cells (fig. S1D) expressed higher levels of IFN-stimulated gene (ISG) mRNA relative to their wild-type counterparts. ISG expression and phosphorylation of TANK-binding kinase 1 (TBK1) and IFN regulatory factor 3 (IRF3) were significantly reduced in ρ^0 (mtDNA-deficient) cells derived from *Endog*$^{-/-}$ MEFs, relative to cells derived from the parental *Endog*$^{-/-}$ MEFs (Fig. 1, E and F, and fig. S1, E to G). Thus, the cGAS-STING pathway is activated by cmtDNA in *Endog*$^{-/-}$ MEFs (fig. S2, A to I). Increased mROS appeared to cause mtDNA release in *Endog*$^{-/-}$ MEFs because mROS was higher in *Endog*$^{-/-}$ MEFs (fig. S2, J and K). By contrast, the mROS scavenger mito-TEMPO decreased ISG expression in *Endog*$^{-/-}$ MEFs (Fig. 1G).

Under physiological conditions, tissue-culture cells comprise two subpopulations: live cells, which make up the majority of the population, and a small minority of cells undergoing spontaneous apoptosis and caspase activation. Prior studies (*3*, *4*, *16*) and our data (fig. S3A) demonstrate that BAX/BAK activation with ABT-737 in the presence of caspase inhibition increases ISG expression. However, wild-type and *Bax/Bak*$^{-/-}$ MEFs had similar cmtDNA levels (fig. S3B), and knocking down *Endog* robustly induced ISG expression in *Bax/Bak*$^{-/-}$ MEFs, albeit at levels slightly lower than were observed in wild-type MEFs (fig. S3, C and D). Thus, *Endog*$^{-/-}$ MOMP can occur in the absence of BAX/BAK macropores. Moreover, mitochondria in *Endog*$^{-/-}$ MEFs tended to be slightly longer than those in wild-type MEFs rather than being fragmented, as would be expected with BAX/BAK activation (fig. S3E) (*2*, *17*).

We next compared the apoptosis levels in wild-type and *Endog*$^{-/-}$ MEFs because extremely high levels of mROS can lead to apoptosis, and *Endog*$^{-/-}$ MEFs have higher mROS levels than wild-type MEFs (fig. S2, J and K). Wild-type and *Endog*$^{-/-}$ MEFs had similar levels of apoptotic indicators such as caspase activity (fig. S3F), cell viability (fig. S3G), lactate dehydrogenase (LDH) release (fig. S3H), and ethidium homodimer–1 (EthD-1) staining (fig. S3I) either before or after the induction of apoptosis by BAX/BAK. Thus, *Endog*$^{-/-}$ MEFs have levels of mROS stress high enough to promote MOMP and mtDNA release in a BAX/BAK-independent manner but insufficient to promote apoptosis at the cellular level (fig. S3I).

An alternative mediator of MOMP may be VDAC, and indeed, *Vdac1*$^{-/-}$, *Vdac3*$^{-/-}$, and *Vdac1/3*$^{-/-}$ MEFs had lower levels of ISG mRNA and cmtDNA relative to wild-type MEFs (Fig. 2, A and B, and fig. S4, A to C) despite having similar total mtDNA levels (fig. S4D). We excluded VDAC2 from our study because VDAC2 deficiency promotes apoptosis (*8*). Additionally, knockdown of *Endog* increased ISG expression in wild-type and *Bax/Bak*$^{-/-}$ MEFs but not in *Vdac1/3*$^{-/-}$ MEFs (Fig. 2C and fig. S3C), and treatment with the VDAC inhibitor DIDS (*18*) decreased ISG expression in *Endog*$^{-/-}$ MEFs (fig. S4E). In agreement with their reduced type I IFN signaling, *Vdac1/3*$^{-/-}$ MEFs were less resistant to HSV-1 infection than wild-type MEFs (fig. S4, F to H). Thus, both VDAC1 and VDAC3 contribute to both MOMP and mtDNA release.

[1]Laboratory of Obesity and Aging Research, Cardiovascular Branch, National Heart Lung and Blood Institute, Bethesda, MD 20892, USA. [2]Department of Life Sciences and National Institute for Biotechnology in the Negev, Ben-Gurion University of the Negev, Beer-Sheva 84105, Israel. [3]Systemic Autoimmunity Branch, National Institute of Arthritis and Musculoskeletal and Skin Diseases, Bethesda, MD 20982, USA. [4]Medical Virology Section, Laboratory of Infectious Diseases, National Institute of Allergy and Infectious Diseases, Bethesda, MD 20892, USA. [5]Systems Biology Center, National Heart, Lung, and Blood Institute, Bethesda, MD 20892, USA. [7]Mokobio Biotechnology R&D Center, Rockville, MD 20850, USA. [6]Laboratory of Molecular and Cellular Signaling, Department of Cellular and Molecular Medicine, and Leuven Kanker Instituut, KU Leuven, 3000 Leuven, Belgium.
*Present address: Department of Radiology, Beth Israel Deaconess Medical Center, Boston, MA 02215, USA.
†Corresponding author. Email: chungj@nhlbi.nih.gov

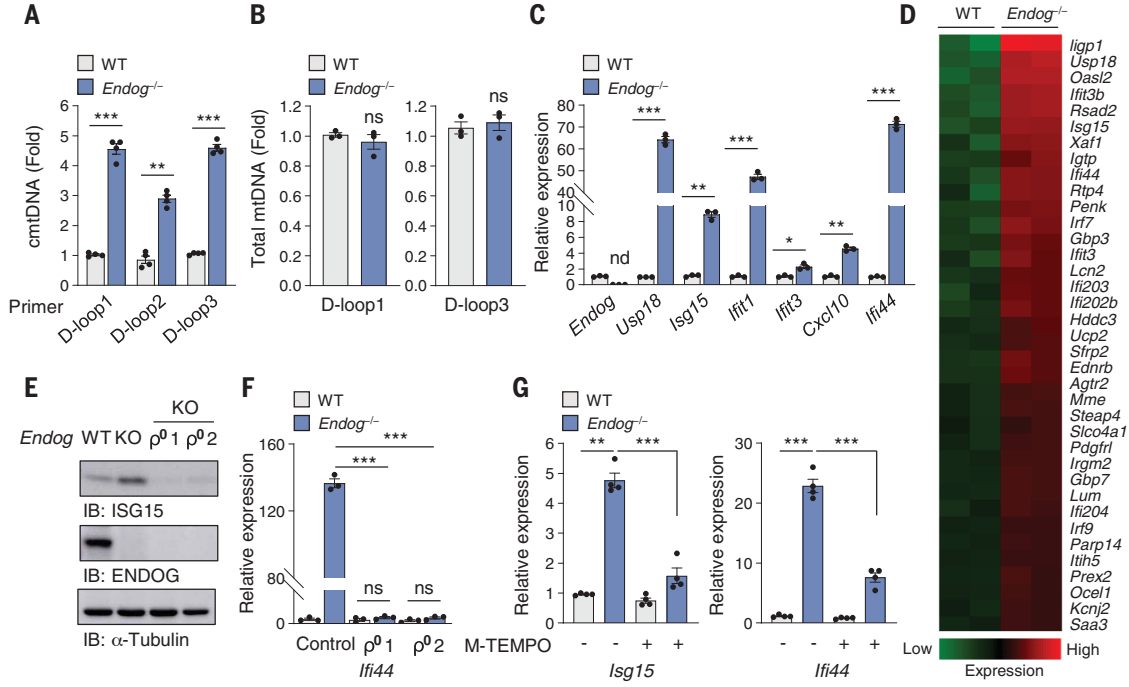

Fig. 1. *Endog* deficiency increases cmtDNA and type I IFN signaling. (**A** and **B**) Quantification of cmtDNA (A) and total mtDNA (B) in wild-type (WT) and *Endog*$^{-/-}$ MEFs. (**C** and **D**) Expression levels of ISG, including *Usp18* (ubiquitin-specific peptidase 18), *Isg15* (interferon-stimulated gene 15), *Ifit1* and *Ifit3* (interferon-induced protein with tetratricopeptide repeats 1 and 3), *Cxcl10* (c-x-c motif chemokine 10), and *Ifi44* (interferon-induced protein 44) (C) and heat map analysis of RNA sequencing data (D) in WT and *Endog*$^{-/-}$ MEFs. (**E** and **F**) ISG expression levels in WT and *Endog*$^{-/-}$ MEFs as well as two independently generated ρ^0 MEFs (ρ^0 1 and ρ^0 2) were determined by immunoblotting (E) and reverse transcription quantitative polymerase chain reaction (RT-qPCR) (F). (**G**) ISG expression was measured in WT and *Endog*$^{-/-}$ MEFs after treatment with 10 μM Mito-TEMPO (M-TEMPO) for 48 hours. Data are means ± SEM of at least three independent experiments. *P < 0.05, **P < 0.01, ***P < 0.005 [two-tailed unpaired Student t test in (A) to (C); one-way analysis of variance (ANOVA) with Tukey post hoc test for multiple comparisons in (F) and (G)]; nd, not detected; ns, not significant.

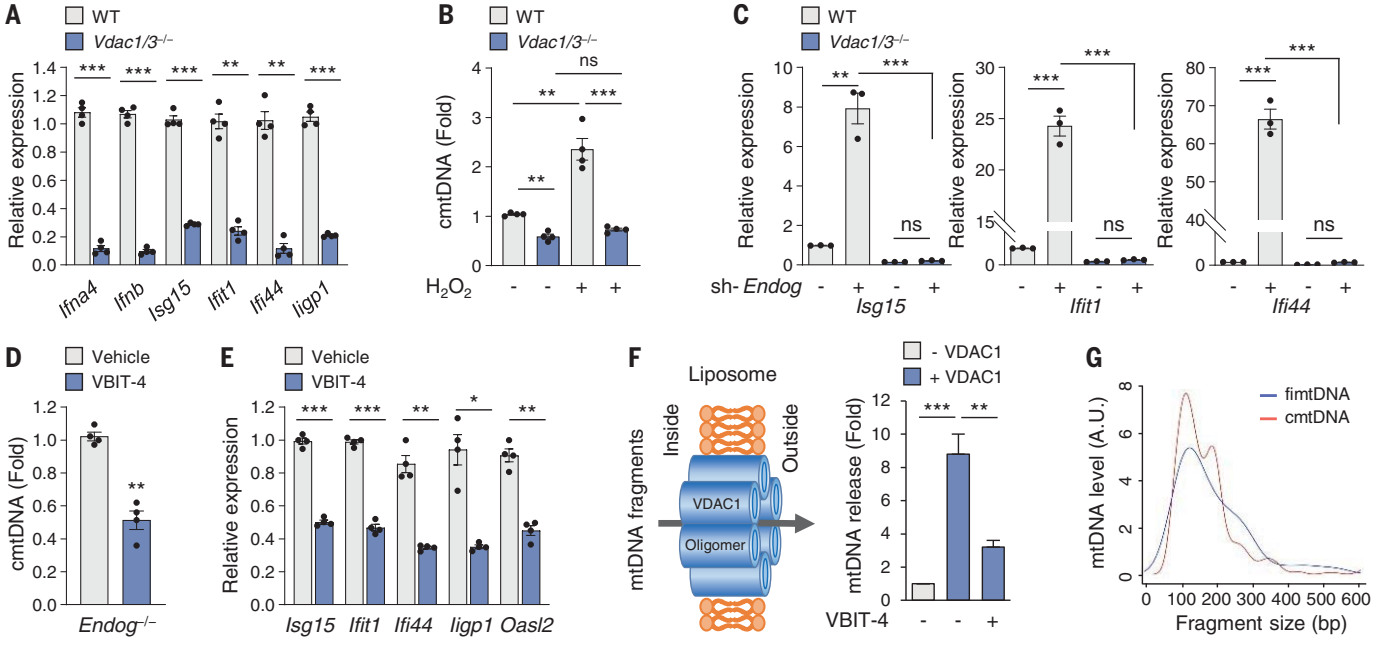

Fig. 2. VDAC oligomerization is required for mtDNA fragment release. (**A**) Expression levels of *Ifna4* and *Ifnb* (interferon alpha-4 and beta) and expression levels of ISG, including *Isg15*, *Ifit1*, *Ifi44*, and *Ligp1* (interferon-inducible GTPase 1), in WT and *Vdac1/3*$^{-/-}$ MEFs. (**B**) cmtDNA levels were determined in WT and *Vdac1/3*$^{-/-}$ MEFs after treatment with 100 μM H_2O_2 for 18 hours. (**C**) ISG expression levels were measured in WT and *Vdac1/3*$^{-/-}$ MEFs after knocking down *Endog*. (**D** and **E**) cmtDNA (D) and expression levels of ISG, including *Isg15*, *Ifit1*, *Ifi44*, *Ligp1*, and *Oasl2* (2′,5′-oligoadenylate synthetase–like 2) (E), which were measured after treatment with 10 μM VBIT-4 in *Endog*$^{-/-}$ MEFs. (**F**) VDAC1 oligomerization–dependent release of mtDNA from mtDNA-loaded liposomes and inhibition by VBIT-4. (**G**) Fragment size distribution of the fimtDNA and cmtDNA. Data are means ± SEM of at least three independent experiments. *P < 0.05, **P < 0.01, ***P < 0.005 [two-tailed unpaired Student t test in (A), (D), (E), and (F); one-way ANOVA with Tukey post hoc test for multiple comparisons in (B) and (C)].

VDAC has been implicated in apoptosis induced by certain stimuli (*7*). However, *Vdac1/3*$^{-/-}$ and wild-type MEFs had similar numbers of cells undergoing apoptosis. This was true both in the basal state and in the presence of H_2O_2 (fig. S5A), which increases cmtDNA (Fig. 2B). In contrast, ABT-737 induced apoptosis in *Vdac1/3*$^{-/-}$ MEFs but not in *Bax/Bak*$^{-/-}$ MEFs (fig. S5B). Thus, VDAC is not required for apoptosis, and presumably MOMP, induced by BAX/BAK activation (fig. S5C).

We initially hypothesized that VDAC regulates mtDNA release by promoting Ca^{2+} influx (*19*), which opens the mitochondrial permeability transition pore (mPTP) in the mitochondrial inner membrane (MIM) in a manner that does not trigger apoptosis at the whole-cell level (*20*, *21*). This would be possible only if the population of affected mitochondria is very small so that the total caspase activity remains near background levels. Chelation of Ca^{2+} with BAPTA decreased ISG expression (fig. S6, A to C), and inhibiting mPTP opening with cyclosporin A (CsA) decreased mtDNA release in both *Endog*$^{-/-}$ MEFs and wild-type mitoplasts as well as ISG mRNA levels in *Endog*$^{-/-}$ MEFs (fig. S6, D to F). Mitochondria deficient in MICU1 (mitochondrial calcium uptake 1) had elevated mROS levels and IFN responses (fig. S6, G to I) (*22*). However, mtDNA release from these mitochondria was still inhibited by DIDS in the absence of Ca^{2+} (fig. S6J). Thus, VDAC may play a Ca^{2+} flux–independent role in mtDNA release. In agreement with this, the highly potent VDAC1 oligomerization inhibitor VBIT-4 (*23*) decreased cmtDNA levels and ISG expression in *Endog*$^{-/-}$ MEFs (Fig. 2, D and E) without inhibiting either Ca^{2+} uptake (fig. S6K) or mPTP opening (fig.

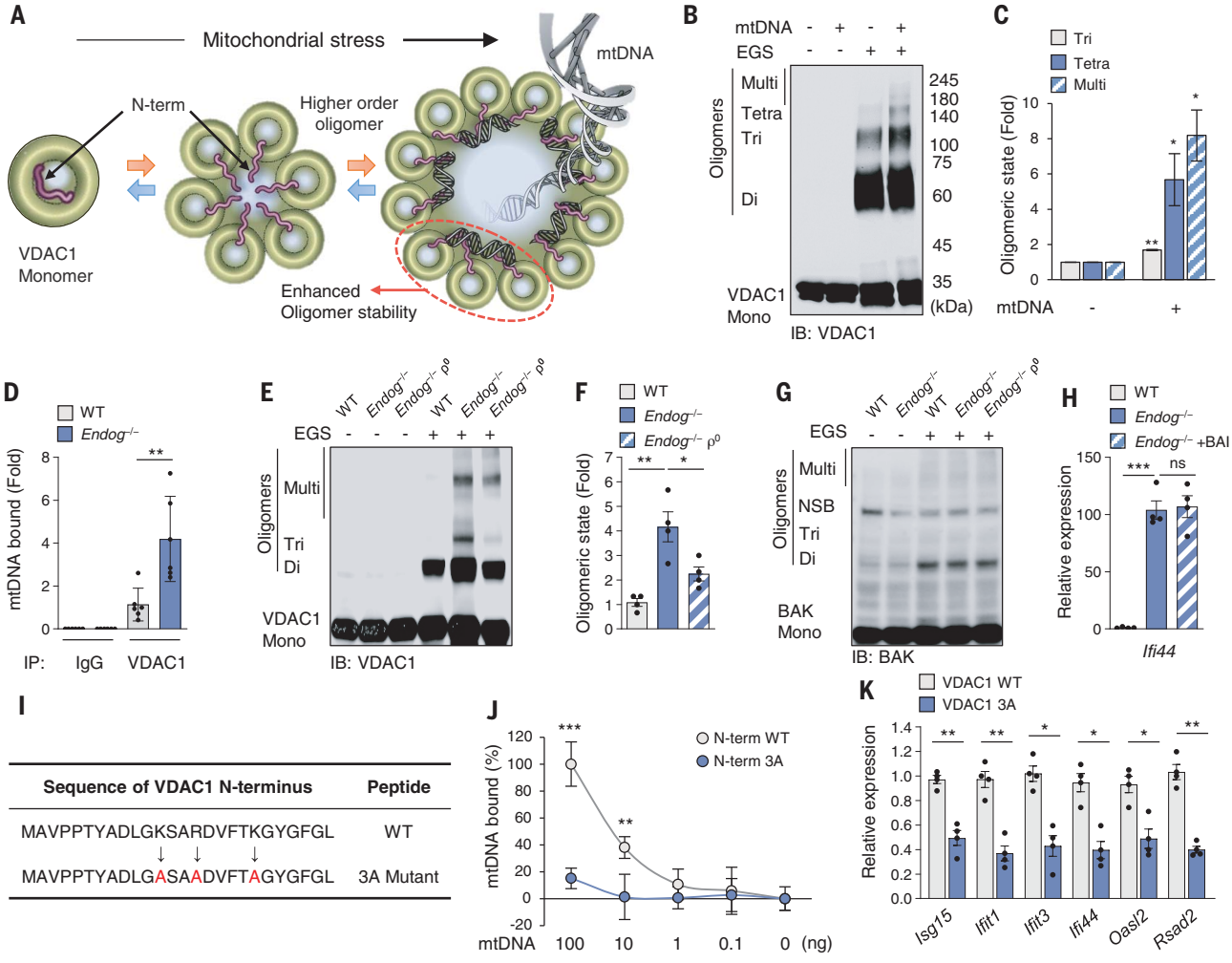

Fig. 3. mtDNA interacts with VDAC1 and stabilizes its oligomeric state. (**A**) Schematic diagram of VDAC1 oligomerization accompanied by the N-terminal domain (red) translocation into the large oligomer pore. We could not characterize VDAC3 in vitro because it tends to form aggregates. (**B** and **C**) mtDNA-induced oligomerization of purified VDAC1 was visualized by immunoblotting after treatment with the cross-linking reagent EGS to stabilize the oligomers during electrophoresis (B). Quantitative analysis of oligomers is shown (C). (**D**) mtDNA binding to VDAC1 in WT and *Endog*$^{-/-}$ MEFs. (**E** to **G**) VDAC1 (E) and BAK (G) oligomerization in WT, *Endog*$^{-/-}$ and *Endog*$^{-/-}$ ρ^0 MEFs was visualized by immunoblotting. The positions of VDAC1 monomers (Mono), dimers (Di), trimers (Tri) and multimers (Multi) are indicated. NSB, nonspecific band. Quantitative analysis of VDAC1 oligomers is shown (F). (**H**) ISG expression was measured in WT and *Endog*$^{-/-}$ MEFs after treatment with the BAX oligomerization inhibitor (BAI) (2 μM) for 24 hours. (**I**) The amino acid sequence of the VDAC1 N-terminal peptide (abbreviations: A, Ala; D, Asp; F, Phe; G, Gly; K, Lys; L, Leu; M, Met; P, Pro; R, Arg; S, Ser; T, Thr; V, Val; Y, Tyr.). The positively charged amino acids were mutated to alanine (red). (**J**) Direct interaction of mtDNA fragments with WT and 3A N-terminal 26 amino acid peptides. (**K**) Expression levels of ISG, including *Isg15*, *Ifit1*, *Ifit3*, *Ifi44*, *Oasl2*, and *Rsad2* (radical *S*-adenosyl methionine domain 2), were measured by RT-qPCR after treatment with 100 μM H_2O_2 for 18 hours in MEFs expressing either WT or 3A VDAC1. Data are means ± SEM of at least three independent experiments. **P* < 0.05, ***P* < 0.01, ****P* < 0.005 [two-tailed unpaired Student *t* test in (C), (D), and (K); one-way ANOVA with Tukey post hoc test for multiple comparisons in (F), (H), and (J)].

S6L) in the mitochondria. We then loaded mtDNA fragments into liposomes with or without membrane-reconstituted VDAC1. The presence of VDAC1 in liposomes increased mtDNA passage across the lipid membrane (Fig. 2F). However, VBIT-4 decreased VDAC1 oligomerization (fig. S7, A and B) as well as mtDNA efflux (Fig. 2F). Thus, VDAC1 oligomers are sufficient to permeabilize lipid membranes for mtDNA passage.

Because the intact mtDNA is large (16 to 17 kb) and is tethered to the MIM in nucleoid complexes (*24*), we hypothesized that short and free (untethered) intra-mtDNA fragments (fimtDNA) that can pass through VDAC oligomer pores preexist in live cells (fig. S8A). To investigate this possibility, we treated mitochondria purified from wild-type MEFs with cytoskeleton (CSK) buffer, which gently permeabilizes mitochondrial membranes and releases fimtDNA while leaving mitochondrial nucleoids intact (*24*). Interestingly, the sequences corresponding to a region within the D-loop in the mitochondrial genome were overrepresented in the fimtDNA pool (fig. S8, A and B). A size-distribution analysis excluding the sequences with 100% homology to both mitochondrial and nuclear genomes indicated that the peak sizes of fimtDNA and cmtDNA are almost identical (~110 bp) (Fig. 2G). Treatment of wild-type MEFs with mito-TEMPO (fig. S8C) or the mTORC1 inhibitor everolimus (fig. S8D), which promotes mitophagy and elimination of damaged mitochondria, decreased fimtDNA. Thus, fimtDNA accumulates preferentially within a subpopulation of mitochondria with elevated mROS, and cmtDNA is derived largely from fimtDNA in live cells (figs. S5C and S8A).

Studies with planar lipid bilayers reconstituted with VDAC1 indicate that the N-terminal domain of VDAC1 can interact directly with mtDNA (fig. S9). The N-terminal domain, which is evolutionarily conserved (fig. S10A), is hydrophilic and is thought to translocate out of the channel when VDAC1 is in an oligomerized state (Fig. 3A) (*25*). This raises the possibility that the negatively charged backbone of mtDNA may interact with multiple VDAC1 molecules simultaneously and may act as a scaffold to stabilize the oligomers

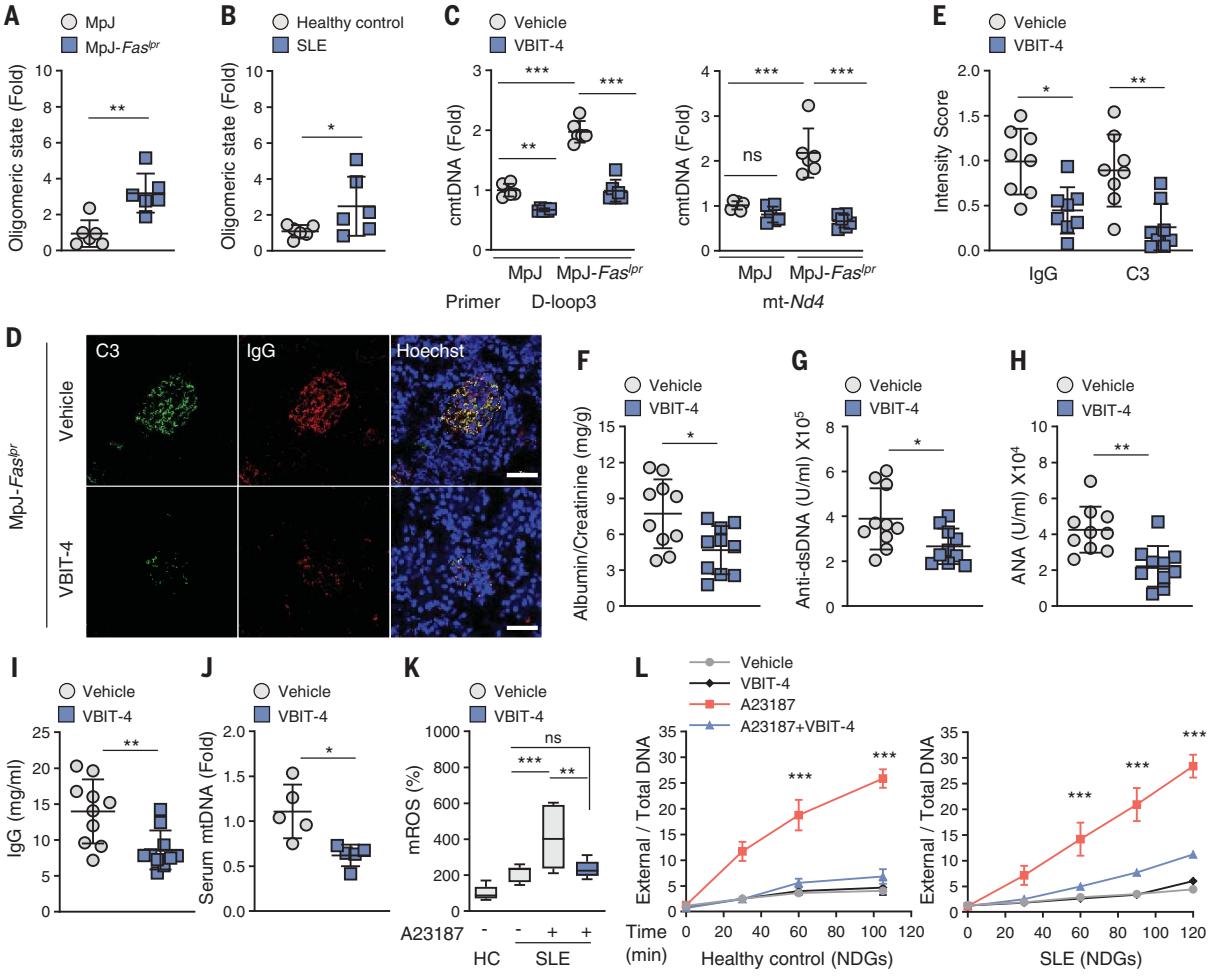

Fig. 4. VDAC1 oligomerization inhibitor VBIT-4 ameliorates lupus-like disease. (**A**) The formation of VDAC1 oligomers in splenocytes of MRL/MpJ-*Fas*^{lpr} lupus-prone mice and MRL/MpJ control mice (see fig. S11B; *n* = 6 in each group). (**B**) Oligomeric state of VDAC1 in PBMCs of healthy control and SLE patients (see fig. S11C; *n* = 6 in each group). (**C**) cmtDNA levels were measured in splenocytes [see (A)] after treatment with 10 μM VBIT-4. (**D**) Kidney glomeruli of VBIT-4–treated mice stained with antibodies to complement C3 (green) and IgG (red). Nuclei were stained with Hoechst (blue). Scale bars, 20 μm. (**E**) Fluorescence intensity of C3 and IgG in (D) (*n* = 8 in each group). (**F** to **I**) Urinary albumin/creatinine ratio (F), serum anti-dsDNA levels (G), ANA levels (H), and IgG levels (I) of VBIT-4–treated mice (*n* = 10 in each group). (**J**) Serum cell-free mtDNA levels of VBIT-4–treated mice (*n* = 5 in each group). (**K**) A23187 (Ca^{2+} ionophore)–induced mROS levels were measured by MitoSOX in PBMCs of healthy controls (HC) and SLE patients (*n* = 3 in each group). (**L**) A23187-induced NET formation by NDGs from HC or SLE subjects was measured by SYTOX-Pico Green plate assay (*n* = 3 in each group). Data are means ± SEM. **P* < 0.05, ***P* < 0.01, ****P* < 0.005 [Student *t* test in (A), (B), (E), (F) to (J), and (L); one-way ANOVA with Tukey post hoc test for multiple comparisons in (C); Mann-Whitney *U* test in (K)].

(Fig. 3A). Indeed, mtDNA increased the formation of VDAC1 trimers and higher-order oligomers (Fig. 3, B and C) in vitro. In agreement with increased cmtDNA in *Endog*$^{-/-}$ MEFs (Fig. 1A), coimmunoprecipitation with antibody to VDAC1 pulled down more mtDNA in *Endog*$^{-/-}$ MEFs than in wild-type MEFs (Fig. 3D). VDAC1 oligomerization was also increased in *Endog*$^{-/-}$ MEFs relative to wild-type MEFs, but was reduced by the elimination of mtDNA in *Endog*$^{-/-}$ MEFs (ρ^0) (Fig. 3, E and F). By contrast, BAK oligomerization was not increased in *Endog*$^{-/-}$ MEFs (Fig. 3G), and BAI, the BAX oligomerization inhibitor (*26*), did not reduce ISG expression in *Endog*$^{-/-}$ MEFs (Fig. 3H). Thus, mtDNA may promote further VDAC1 oligomerization, creating a feedforward cycle.

The N-terminal domain of VDAC1 contains three positively charged residues (Lys^{12}, Arg^{15}, and Lys^{20}) that could potentially interact with the negatively charged backbone of mtDNA (Fig. 3I). Indeed, mtDNA fragments were pulled down by a 26–amino acid VDAC1 N-terminal peptide but not by a VDAC1 N-terminal mutant peptide (3A) in which Lys^{12}, Arg^{15}, and Lys^{20} residues were replaced by alanine (Fig. 3J). We then examined H_2O_2-induced expression of ISG in *Vdac1/3*$^{-/-}$ MEFs with restored expression of wild-type VDAC1, the 3A-mutant VDAC1, or ΔN-terminal VDAC1. Relative to MEFs expressing wild-type VDAC1, ISG expression was reduced in MEFs expressing either the 3A-mutant VDAC1 (Fig. 3K) or ΔN-terminal VDAC1 (fig. S10, B and C). Thus, direct mtDNA-VDAC interactions appear to promote VDAC oligomerization and increase mtDNA release.

An excessive type I IFN response is a hallmark of SLE (*27*). Gene Expression Omnibus (GEO) analysis revealed increased mRNA expression of *VDAC1/3* and decreased expression of *ENDOG* in SLE patients (fig. S11A) (*9*). However, *BAK*, *BAX*, *VDAC2*, and *HSP60* mRNA levels were not changed in SLE patients (fig. S11A). These findings, combined with the observation that type I IFN responses in *Endog*-knockdown MEFs were VDAC1- and VDAC3-dependent (Fig. 2C), suggest that VDAC oligomerization may be associated with SLE. Indeed, splenocytes from MpJ-*Fas*^{lpr} "lupus"-prone mice had more VDAC1 oligomers than did MpJ control mice (Fig. 4A and fig. S11B); the same was true for peripheral blood mononuclear cells (PBMCs) from SLE patients relative to healthy controls (Fig. 4B and fig. S11C). Splenocytes from MpJ-*Fas*^{lpr} mice also had elevated cmtDNA relative to those from MpJ mice, but this was abrogated with VBIT-4 treatment (Fig. 4C).

We next investigated whether VBIT-4 could ameliorate lupus-like symptoms in MpJ-*Fas*^{lpr} mice. VBIT-4 blocked the development of skin lesions and the thickening of the epidermis that accompanies leukocyte infiltration, and suppressed facial and dorsal alopecia without affecting mortality or body weight (fig. S12, A to C). VBIT-4 also decreased spleen and lymph node weights (fig. S12D). Furthermore, ISG mRNA (fig. S12E), renal immune complex deposition (Fig. 4, D and E), proteinuria (Fig. 4F), antibody to double-stranded DNA (dsDNA) (Fig. 4G), antinuclear antibody (ANA) (Fig. 4H), IgG (Fig. 4I), and cell-free mtDNA (Fig. 4J) levels were all reduced by VBIT-4. Cell-free mtDNA plays an immunostimulatory role in human and mouse SLE (*10*, *11*). One potential source of cell-free mtDNA in MpJ-*Fas*^{lpr} mice may be neutrophil extracellular traps (NETs), which are formed in a cell death process termed NETosis (*11*). mROS is an important trigger for NETosis (*11*), and VBIT-4 decreased mROS in neutrophils as well as other immune cells from SLE patients (Fig. 4K and fig. S12F). Furthermore, VBIT-4 suppressed NETosis in low-density granulocytes (LDGs), a distinct class of pro-inflammatory and NETosis-prone neutrophils from SLE patients, and normal-density granulocytes (NDGs) isolated from SLE patients and healthy controls (Fig. 4L and fig. S12G). Thus, VDAC oligomerization increases mROS and NETosis, two proposed important triggers of autoimmunity, in both human neutrophils (healthy and SLE) and during lupus-like disease in mice (fig. S12H).

We propose that the MOMP that mediates mtDNA release and type I IFN response depends on the level of mitochondrial stress. In live cells, VDAC1 oligomer pores, and possibly VDAC3 oligomer pores, play a role in moderate stress responses, whereas BAX/BAK macropores feature in extreme stress and/or apoptosis (fig. S13). The small fragment size and the untethered nature of fimtDNA may facilitate its release via VDAC oligomer pores. Notably, there are other pathways of mtDNA release (*10*, *13*) and SLE is a very heterogeneous disease. Nonetheless, inhibiting VDAC oligomerization may be an alternative therapeutic approach for a wide range of diseases, like SLE and Parkinson's disease (*28*), that are thought to be associated with mtDNA release.

REFERENCES AND NOTES

1. A. P. West, G. S. Shadel, *Nat. Rev. Immunol.* **17**, 363–375 (2017).
2. K. McArthur *et al.*, *Science* **359**, eaao6047 (2018).
3. A. Rongvaux *et al.*, *Cell* **159**, 1563–1577 (2014).
4. M. J. White *et al.*, *Cell* **159**, 1549–1562 (2014).
5. N. Keinan, D. Tyomkin, V. Shoshan-Barmatz, *Mol. Cell. Biol.* **30**, 5698–5709 (2010).
6. R. Zhou, A. S. Yazdi, P. Menu, J. Tschopp, *Nature* **469**, 221–225 (2011).
7. V. Shoshan-Barmatz, Y. Krelin, A. Shteinfer-Kuzmine, *Cell Calcium* **69**, 81–100 (2018).
8. E. H. Cheng, T. V. Sheiko, J. K. Fisher, W. J. Craigen, S. J. Korsmeyer, *Science* **301**, 513–517 (2003).
9. D. R. Fernandez *et al.*, *J. Immunol.* **182**, 2063–2073 (2009).
10. S. Caielli *et al.*, *J. Exp. Med.* **213**, 697–713 (2016).
11. C. Lood *et al.*, *Nat. Med.* **22**, 146–153 (2016).
12. K. Nakahira *et al.*, *Nat. Immunol.* **12**, 222–230 (2011).
13. A. P. West *et al.*, *Nature* **520**, 553–557 (2015).
14. P. Schäfer *et al.*, *J. Mol. Biol.* **338**, 217–228 (2004).
15. C. McDermott-Roe *et al.*, *Nature* **478**, 114–118 (2011).
16. G. Ichim *et al.*, *Mol. Cell* **57**, 860–872 (2015).
17. J. S. Riley *et al.*, *EMBO J.* **37**, e99238 (2018).
18. D. Ben-Hail, V. Shoshan-Barmatz, *Biochim. Biophys. Acta* **1863** (7 Pt A), 1612–1623 (2016).
19. C. P. Baines, R. A. Kaiser, T. Sheiko, W. J. Craigen, J. D. Molkentin, *Nat. Cell Biol.* **9**, 550–555 (2007).
20. N. García, E. Chávez, *Life Sci.* **81**, 1160–1166 (2007).
21. M. Patrushev *et al.*, *Cell. Mol. Life Sci.* **61**, 3100–3103 (2004).
22. J. C. Liu *et al.*, *Cell Rep.* **16**, 1561–1573 (2016).
23. D. Ben-Hail *et al.*, *J. Biol. Chem.* **291**, 24986–25003 (2016).
24. F. J. Iborra, H. Kimura, P. R. Cook, *BMC Biol.* **2**, 9 (2004).
25. S. Geula, D. Ben-Hail, V. Shoshan-Barmatz, *Biochem. J.* **444**, 475–485 (2012).
26. T. P. Garner *et al.*, *Nat. Chem. Biol.* **15**, 322–330 (2019).
27. G. Obermoser, V. Pascual, *Lupus* **19**, 1012–1019 (2010).
28. D. A. Sliter *et al.*, *Nature* **561**, 258–262 (2018).

ACKNOWLEDGMENTS

We thank the NHLBI core facilities, including DNA Sequencing and Genomics core, Bioinformatics and Computational Biology core, Flow Cytometry core, Light Microscopy core, Pathology core, and Biochemistry core. We thank the NIH Fellows Editorial Board for manuscript preparation. **Funding:** Supported by the Intramural Research Program of the National Heart Lung and Blood Institute, National Institute of Arthritis and Musculoskeletal and Skin Diseases, and National Institute of Allergy and Infectious Diseases and by a grant from the National Institute for Biotechnology in the Negev (V.S.-B.) and by a grant of the Korea Health Technology R&D Project through the Korea Health Industry Development Institute (KHIDI), funded by the Ministry of Health and Welfare, Republic of Korea (grant number HI14C1176) and a grant from the KRIBB Research Initiative Program (Korean Biomedical Scientist Fellowship Program), Korea Research Institute of Bioscience and Biotechnology, Republic of Korea. **Author contributions:** J.K. designed and performed the majority of experiments, analyzed the data, interpreted results, and wrote the manuscript; R.G., A.S.-K., and V.S.-B. performed the cross-linking assay, liposome assay, MST, mPTP, VDAC purification, and channel conductance studies and helped write the manuscript; L.P.B., X.W., and M.J.K. performed and analyzed the data for the human sample studies, including NETosis and mROS measurements; K.W. and J.I.C. designed and performed the viral infection study; J.Z. supervised mtDNA sequence analysis; S.Y. and J. Z. performed sequencing and analyzed the data; H.E.Y., M.K., H.K., A.L.B., S.-J.P., X.X., and E.Z.v.R. helped with experiments; M.K.K. and J.H.C. supervised the study, analyzed the data, and wrote the manuscript. **Competing interests:** None declared. **Data and materials availability:** All other data and materials are available from the corresponding author upon request. Gene Expression Omnibus (GEO) database of human SLE patient is supported by National Center for Biotechnology Information (GEO accession number: GSE13887, www.ncbi.nlm.nih.gov/geo/query/acc.cgi?acc = GSE13887).

SUPPLEMENTARY MATERIALS

science.sciencemag.org/content/366/6472/1531/suppl/DC1
Materials and Methods
Figs. S1 to S13
Table S1
References (*29*–*36*)

View/request a protocol for this paper from *Bio-protocol*.

21 September 2018; resubmitted 9 July 2019
Accepted 29 October 2019
10.1126/science.aav4011

Filter Tester

Sartorius Stedim Biotech offers the Sartocheck 5 Plus filter integrity tester for use in downstream processing, which greatly improves the detectability of operator errors, improper test setups, and out-of-tolerance environmental conditions. With the Sartocheck 5 Plus, false-passed and false-failed test results are relegated to the past. This advanced filter tester has been designed to cover the complete range of integrity testing, from small syringe filters up to large multi-round housings and crossflow cassettes, with diffusion rates of up to thousands of mL per min. In addition, the automatic test-time feature for diffusion and water intrusion, along with accelerated bubble-point testing, reduces overall test time. Parallel bubble-point testing is also a significant time saver, enabling up to 10 small filters to be checked with one Sartocheck 5 Plus. User benefits include the biggest, brightest screen currently available on the market (12-in.) for integrity testers, along with an ergonomic interface, easy-to-clean design, improved data integrity, and inherent virus protection.

Sartorius Stedim Biotech
For info: +49-(0)-551-308-0
www.sartorius.com/sartocheck-5

Purification and Maintenance of Cardiomyocytes

AMS Biotechnology (AMSBIO) has introduced human recombinant iMatrix Laminin-211 fragment for the purification and maintenance of cardiomyocytes in culture. As one of the main isoforms present in adult muscle tissue, Laminin-211 is critical for cardiomyocyte function and heart muscle development. AMSBIO iMatrix Laminin-221 is an easy-to-use recombinant fragment that retains the full integrin-binding activity of Laminin-211. The culture of induced pluripotent stem cell (iPSC)-derived heart and muscle cells under feed-free conditions requires the use of extracellular matrix proteins as an anchor to promote adherence and functionality. Laminin-211 fulfils this purpose through its binding of membrane-bound integrin and through activation of intracellular signal cascades. iMatrix Laminin-211 is a high-quality matrix for basic research and drug development and toxicity studies with these critical cell types.

AMS Biotechnology
For info: 617-945-5033
www.amsbio.com/imatrix-recombinant-laminin-e8-fragments.aspx

Antibody Microoptimization Service

Optimizing your antibody conjugates can be time consuming and difficult, and can require significant amounts of antibody and label. Expedeon's Antibody Microoptimization Service is a fast, efficient way to optimize your antibody conjugates using very small quantities of antibody. You provide us with your antibody. By varying parameters such as the degree of antibody activation, the ratio of antibody to label, and the pH of the conjugation, we will generate six different conjugates for you to test in your chosen application. You evaluate and select the best-performing conjugate; then we can either conjugate your bulk antibody material for you or create a custom Lightning-Link kit just for you. With more than 46 labels available for conjugation, we're sure we can meet your needs.

Expedeon
For info: 844-611-3656
www.expedeon.com

T Cell Memory Cell and Cytokine Profiling Kit

The Human T Cell Memory Cell and Cytokine Profiling Kit measures T cells' memory phenotype and function at different stages, while providing information about their health and their role in cytokine secretion. This one-wash assay requires minimal hands-on time and measures both cells and beads. Live immune cells are distinguished from dead cells by staining with a fluorescent membrane integrity dye. Cells are immunophenotyped by staining with a fluorescent antibody panel to separate $CD3^+$ T cells, $CD3^-$ non-T cells, $CD4^+$ T helper cells, and $CD8^+$ T cytotoxic cells. The panel also includes five different T cell surface markers for naive/memory/effector T cell phenotyping: CD45RA, CD45RO, CD27 (long-term survival), CD62L, and CD95. An optimized workflow enables measurement of effector cytokines secreted by activated T cells, including proinflammatory cytokine IFNγ and anti-inflammatory cytokine IL-10 in the same assay well.

Intellicyt
For info: 734-769-1600
intellicyt.com/t-cell-memory-cell-and-cytokine-profiling-kit

24-Pin Liquid Sampler

IonSense introduces the new 24-Pin Module for rapid sampling of liquids from SBS-384 format microtiter plates. The Pin Module is interchangeable with the top bar of our DIP-it Module, and doubles the sampling capacity for sequential analysis of liquids. Each small-diameter metal pin collects a small volume of sample, permitting transfer from the wells to the DART-MS (direct analysis in real time mass spectrometer), where the linear rail presents each pin at a constant speed for analysis. The metal pins are easily cleaned with solvents that are appropriate for removal of the sample, such as methanol water, acetonitrile water, and acid or base solutions.

IonSense
For info: 781-484-1043
ionsense.com

Prisms

Optical Surfaces manufactures large, high-quality prisms for spectroscopic, surveying, and telescope applications. Prisms are solid optics that are ground and polished into geometrical and optically significant shapes where the angle, position, and number of surfaces help define the type and function. Due to variability in shape, size, and number of surfaces, manufacturing of high-quality prisms requires considerable experience and skill. For over 50 years, Optical Surfaces has supplied high-quality, uncoated and coated prisms for spectroscopic applications, including image rotation, inversion, and redirection as well as dispersal of light into its constituent colors. Optical Surfaces produces all types and configurations of prism (Amici/roof, Fresnel biprisms, corner cube retroreflectors, dove, equilateral, isosceles, penta, rhomboid, and wedge) with market-leading tolerances. Prisms are available as single components (up to 450 mm) or as cemented units. Our production team routinely achieves angle accuracy of better than 2 arc seconds, surface accuracy of lambda/20 p-v (peak to valley), 10/5 surface quality, and microroughness of less than 1.2 nm rms (root mean square) on its prisms.

Optical Surfaces
For info: +44-(0)-208-668-6126
www.optisurf.com

Electronically submit your new product description or product literature information! Go to www.sciencemag.org/about/new-products-section for more information.

Newly offered instrumentation, apparatus, and laboratory materials of interest to researchers in all disciplines in academic, industrial, and governmental organizations are featured in this space. Emphasis is given to purpose, chief characteristics, and availability of products and materials. Endorsement by *Science* or AAAS of any products or materials mentioned is not implied. Additional information may be obtained from the manufacturer or supplier.

EMB IEEE Engineering in Medicine & Biology Society

"Your Global Connection to the Biomedical Engineering Community"

Be a part of the growing world of Engineers working in Medicine and Biology…

Become a member: bit.ly/embstryus
More information on www.embs.org

Follow us on social media: SCAN ME!

www.facebook.com/ieeeembs
www.instagram.com/ieeeembs
www.twitter.com/ieeeembs
www.linkedin.com/company/ieeeembs

IEEE

ETH zürich

Professor of Computational Biology

→ The Department of Biology (www.biol.ethz.ch) at ETH Zurich invites applications for the above-mentioned position in the Institute of Molecular Systems Biology (www.imsb.ethz.ch). Together with Life Science Zurich, the Department of Biology offers access to state-of-the-art equipment and outstanding scientific opportunities to participate in interdisciplinary research programmes.

→ The new professor is expected to build a vibrant, world-class research programme in the general field of computational biology with a particular interest into modelling and analysing dynamic interactions between cellular molecules and their phenotypic consequences. Examples are mechanistic modelling of cellular processes, modelling at the single cell or organismic level, analysis of image data in cell biology, analysis of networks involving gene activity, metabolite distribution, or protein interaction in systems biology and medical applications, and genotype to phenotype mapping. The successful candidate is a computer scientist, informatician, engineer, or physicist whose research focus is on addressing biological or clinical questions with, at least in part, computational methods. She or he will engage and contribute to the systems biology teaching programme with an emphasis on quantitative thinking and computational methods (teaching may be in German or English).

→ **Please apply online: www.facultyaffairs.ethz.ch**

→ Applications should include a curriculum vitae, a list of publications, a statement of future research and teaching interests, and a description of the three most important achievements. The letter of application should be addressed **to the President of ETH Zurich, Prof. Dr. Joël Mesot. The closing date for applications is 29 February 2020.** ETH Zurich is an equal opportunity and family friendly employer, strives to increase the number of women professors, and is responsive to the needs of dual career couples.

2019 SANOFI - INSTITUT PASTEUR AWARDS

8TH EDITION

For the 8th edition, the Sanofi - Institut Pasteur Awards foster scientific excellence by rewarding four researchers whose work demonstrates significant breakthroughs for global health.

SANOFI - INSTITUT PASTEUR
2019 AWARDS
FOR BIOMEDICAL RESEARCH

INTERNATIONAL SENIOR ADWARD

Dr. Carl F. NATHAN
Microbiology & Infection

Carl F. Nathan is awarded for his major discoveries in our understanding of host-pathogen relations, such as macrophage activation by interferon gamma which strongly shaped the field of immunology and dramatically influenced treatment of infectious diseases.

INTERNATIONAL JUNIOR ADWARDS

Pr. Ido AMIT
Immunology

Ido Amit is awarded for his breakthrough single cell studies elucidating the diversity of the immune cell types which revolutionized our view in basic immunology and immunotherapy research.

Pr. Andrea ABLASSER
Immunology

Andrea Ablasser is awarded for her major contributions to a fundamental discovery in innate immunity: the role of DNA recognition during infection which has inspired efforts to implement strategies interfering with innate immune responses to treat inflammation-related disorders.

Dr. Marek BASLER
Microbiology & Infection

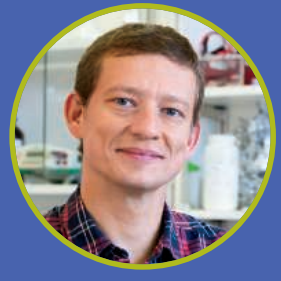

Marek Basler's research has fundamentally advanced our understanding of a very important bacterial nanomachine which delivers effectors in neighboring cells, influencing many areas of microbiology, such as pathogenesis and polymicrobial communities.

SANOFI

Institut Pasteur

FEATURED EMPLOYER
Science Careers online @sciencecareers.org

Focus on Annual Breakthroughs: Fusion and innovation

Zhimin Li
Director of Center for Science and Technology Development Ministry of Education, People's Republic of China

The year 2019 marks the 70th anniversary of the founding of the People's Republic of China (PRC). After 70 years of ups and downs, China has developed into the world's second largest economy and the second largest scientific research output country. As 2020 approaches, we wish to highlight some of the technologies China worked on this year.

Better papers and better AI

The year of 2019 is a memorable year for Chinese science and technology, especially in terms of innovation. Chinese researchers made important discoveries in exploring natural science phenomena, put forward breakthrough ideas in scientific theories and doctrines, and offered original, cutting-edge solutions to major scientific and technological issues that restrict national economic and social development.

On November 19, the Institute of Scientific and Technical Information of China (ISTIC) released the "China Outstanding Paper Output Report." The report shows that from 2009 to October 2019, Chinese scientific and technological personnel published a total of 2.61 million international papers, continuing to rank second in the world, with an increase of 14.7% over the 2018 statistics; In 2018, there were 315,900 outstanding scientific papers, with an increase of 12.4% over 2017. The citation numbers of papers in materials science, chemistry, and engineering technology ranked first in the world. These papers may not be a persuasive indicator, but to a certain extent this shows that China's scientific research output is of high quality, and that China has the ability to participate in international science collaborations.

On October 20, 15 world-leading technological achievements in the Internet were released at the 6th World Internet Conference, including the world's first brain-inspired computing chip from Tsinghua University. Supporting both machine learning algorithms and existing brain-like computing algorithms, this new chip is expected to clear the path for the development of more versatile artificial general intelligence (AGI) and hardware platforms as well as have a huge impact on industry and the economy.

Multiplying fields and talents

Many new disciplines have sprung up in the fields of natural sciences, humanities, and social sciences. In recent years, most of these new disciplines are created through the cross-fusion of the Internet and traditional disciplines, which is of great significance to the progress of disciplines and academic innovation. The "Wuzhen Outlook 2019 Report" released at the 6th World Internet Conference proposed that the deep integration of emerging technologies, such as artificial intelligence (AI), the Internet of Things (IoT), big data, cloud computing, and blockchain will create enormous opportunities to drive a new round of leaping social and economic developments.

Emerging technologies and industries provide a growing demand for inter-disciplinary talent, as well as further integration of these interdisciplinary programs into higher education. China has rearranged the discipline construction of higher education institutions. According to the "List of Self-Set Interdisciplinary Programs for General Colleges and Universities" announced by the Ministry of Education of China, as of May 31, there are 508 interdisciplinary programs independently managed as secondary

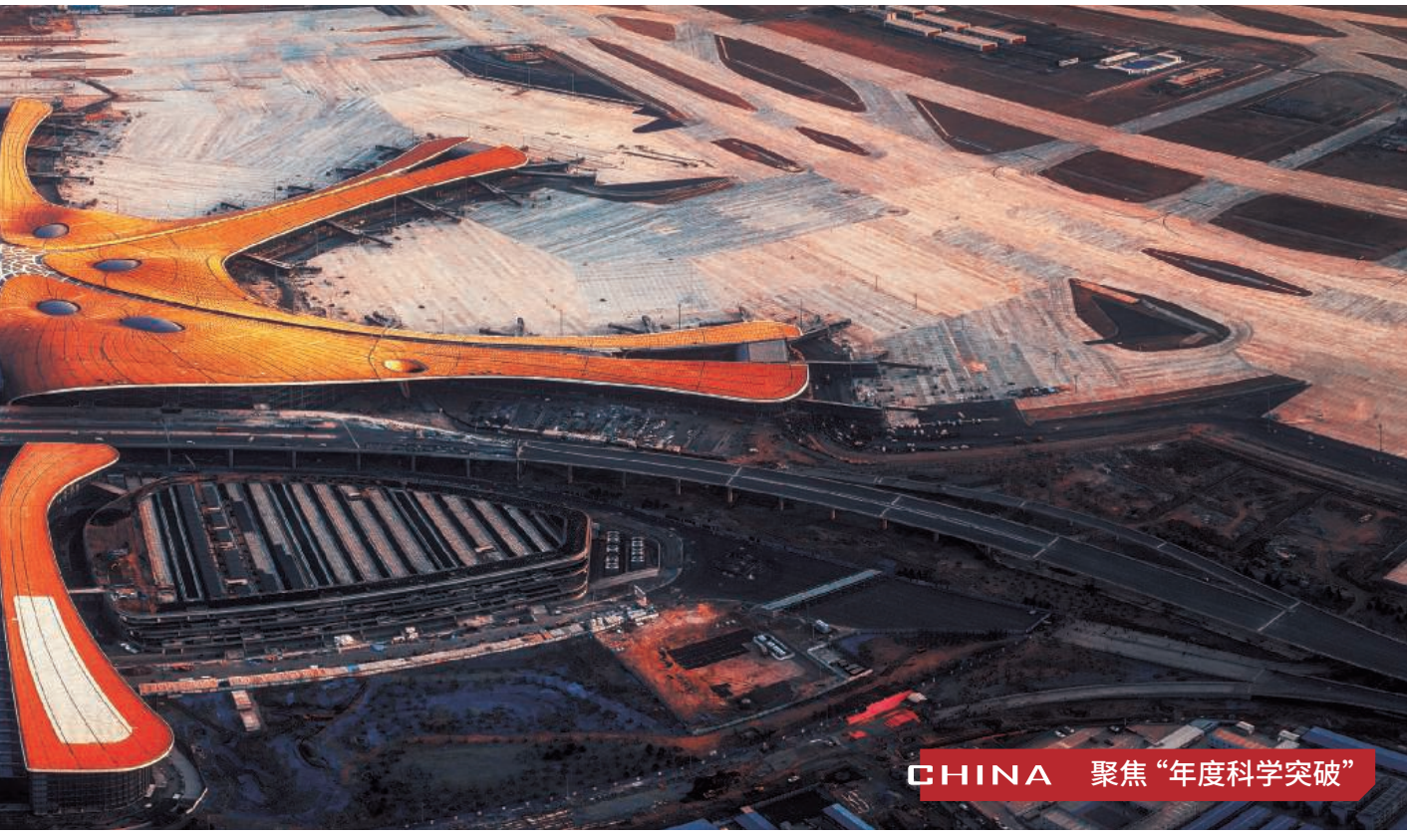

disciplines by universities across the country. Major breakthroughs in scientific frontiers are now mostly the result of multidisciplinary integration. Let us look forward to more scientific breakthroughs and an international talent training mechanism in Chinese universities soon.

Record-high R&D funding

China's breakthroughs in science and technology can be attributed to the continued growth of China's R&D investment. According to data released by the National Bureau of Statistics of China, China has achieved a historic breakthrough in the scale and intensity of its R&D expenditure. The R&D expenditure in 2018 reached 1,965.7 billion yuan (USD 279.2 billion), which was 138 times that of 1991. The intensity of investment in research and development has hit record highs, rising to 2.18% in 2018. In 2019, the China's top three university scientific research funding includes Tsinghua University of 15.375 billion yuan (USD 2.18 billion), Zhejiang University of 13.098 billion yuan (USD 1.86 billion), and Shanghai Jiaotong University of 10.815 billion yuan (USD 1.54 billion). Comparatively the top three in 2018 comprised 5.168 billion yuan (730 million USD) from Tsinghua University, 4.420 billion yuan (USD 630 million) from Zhejiang University, and 3.903 billion yuan (USD 550 million) from Sun Yat-sen University.

Science with heart: improving work–life balance for researchers

In 2019, breakthroughs in China's science and technology policy will speed up the process of integrating knowledge innovation and market transformation. The reform of China's science and technology system has been carried out closely on two main lines: one is to enhance the morale of scientific and technological personnel, and the other is to promote the integration of science and technology with the economy, society, and national security. These two main lines work as an organic whole and exert their strengths in an all-round way.

The most recent policy change by the Chinese government is the "Notice on Nomination of the National Science and Technology Award for 2020" issued by relevant departments on November 29. This "Notice" points out that the country needs to prioritize papers, titles, qualifications, and prizes over citation number. In this spirit, the Natural Science Award will remove the criteria of applicants filling in SCI citations.

At present, China's various industries are booming, providing outstanding talents with unprecedented development space and a platform to display their skills. Talent from all over the world are thriving in China, thanks to generous funding. Chinese universities have developed talent plans with the goal of building first-class universities. Talents are provided with state-of-the art equipment excellent and world-class laboratory conditions. To allow these scientists to conduct research with a peace of mind, universities thoughtfully arrange jobs for spouses and education for children.

China is now undergoing rapid development with numerous opportunities available, and all universities are looking forward to the participation of global talents. Go, go to China!

People in need can contact the talent service agencies of Academic Bridge(**consultant@acabridge.edu.cn**), which provides one-on-one consultations.

Forging Ahead With Challenges and Opportunities :

The School of Mathematics and Statistics at Beijing Institute of Technology

The School of Mathematics and Statistics (SMS) at Beijing Institute of Technology (BIT) comprises a combination of cutting-edge research and excellent teaching across a broad spectrum of mathematics, statistics and their applications. The School of Mathematics and Statistics has had a significant presence in the Chinese mathematical community since the 1960s.

The SMS researchers have made significant progress in their fields and published many important papers in some prestigious academic journals, including Proceedings of the London Mathematical Society, Advances in Mathematics, Mathematische Annalen, Annals of Probability, Stochastic Processes and Their Applications, SIAM Journal on Control and Optimization, etc. The group for algebra and representation theory led by Professor Jun Hu has conducted research in areas ranging from algebraic groups, Lie algebras, quantum groups to Hecke algebras, Schur algebras, KLR algebras and Iwasawa algebras. The researchers in the group have solved several conjectures and open problems, discovered new mathematical structures and fundamental relations, and developed some general frameworks. One such an example is that Jun Hu (with his students) proved Lusztig's conjecture on the Hecke module structure on the space spanned by the involutions in symmetric groups [Advances in Mathematics 287 (2016), 1-30]. Another distinguished research group is the one for probability theory and stochastic analysis, which has conducted research in areas including jump-diffusions and non-local operators, stochastic partial differential equations, and regime-switching jump-diffusion systems. Recently, Dr. Rongchan Zhu and her coauthor have made crucial progress concerning the lattice approximation to the dynamical model [The Annals of Probability 46 (2018), 397-455]. Zhu and her coauthors have also studied the relation between the solutions to the dynamical model constructed by Dirichlet form theory and the SPDE argument [Journal of Functional Analysis 272 (2017), 4263-4303; Communication in Mathematical Physics 352 (2017), 1061-1090]. There are also many other excellent faculty members who have made significant contributions in their fields. For example, Professor Jun-Min Wang, as one of the internationally well-known experts in control theory, has world-leading expertise in Riesz basis approach for control of distributed-parameter systems, particularly for partial differential equations modeling flexible beams and wave equations. He has published more than 70 papers in international journals, such as SIAM Journal on Control and Optimization, IEEE Transactions on Automatic Control, Automatica, and Systems and Control Letters. Dr. Junyong Zhang recently has made some progress in the study of the Strichartz estimates and nonlinear dispersive equations in a conical singular space. For instance, in [Analysis & PDE 9 (2016), 151-192] and [Advances in Mathematics 271 (2015), 91-111], he (with Andrew Hassell) has proved global-in-time Strichartz estimates for Schrödinger and wave equations on non-trapping asymptotically conic manifold.

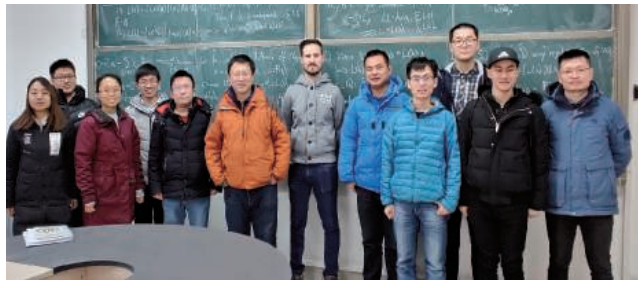

Currently the SMS has a total faculty and staff of 107, including 24 professors, 52 associate professors, 23 assistant professors and 8 staff members. Many of the faculty members are internationally prominent in their research specialties. Among them, there is one scholar supported by the National Natural Science Fund for Distinguished Young Scholars, one scholar supported by the National Natural Science Fund for Outstanding Young Scholars, two Chang Jiang Scholar Chair Professors, five scholars supported by the program for New Century Excellent Talents of the Ministry of Education, and three winners of the "Beijing Excellent Teachers" award.

The SMS at BIT offers vibrant undergraduate and graduate mathematics programs awarding B.S., M.S. and Ph.D. degrees. Students can choose from a diverse range of areas in pure, applied and computational mathematics.The SMS at BIT is one of the leading Chinese schools of mathematics and statistics in offering opportunities for graduate students to work on practical problems with industrial collaborators. During the past 5 years, the undergraduate students have won more than 200 national and international awards in various contests, including the nomination for Outstanding Teams at the Mathematical Contest in Modeling (MCM), the Winning Prize of the S.-T. Yau College Student Mathematics Contests, the First Prize of the Contemporary Undergraduate Mathematical Contest in Modeling (CUMCM), the Outstanding Prize of the First IBM SPSS Innovation Award of CUMC, and the First Prize of the National Undergraduate Mathematical Contest. The SMS has awarded more than 300 Ph.D. degrees so far and these doctorate recipients have made remarkable accomplishments in their respective fields.

For more information, please contact us:
Te: +8610-81384701
Email: sunjing@bit.edu.cn

ADVERTISEMENT

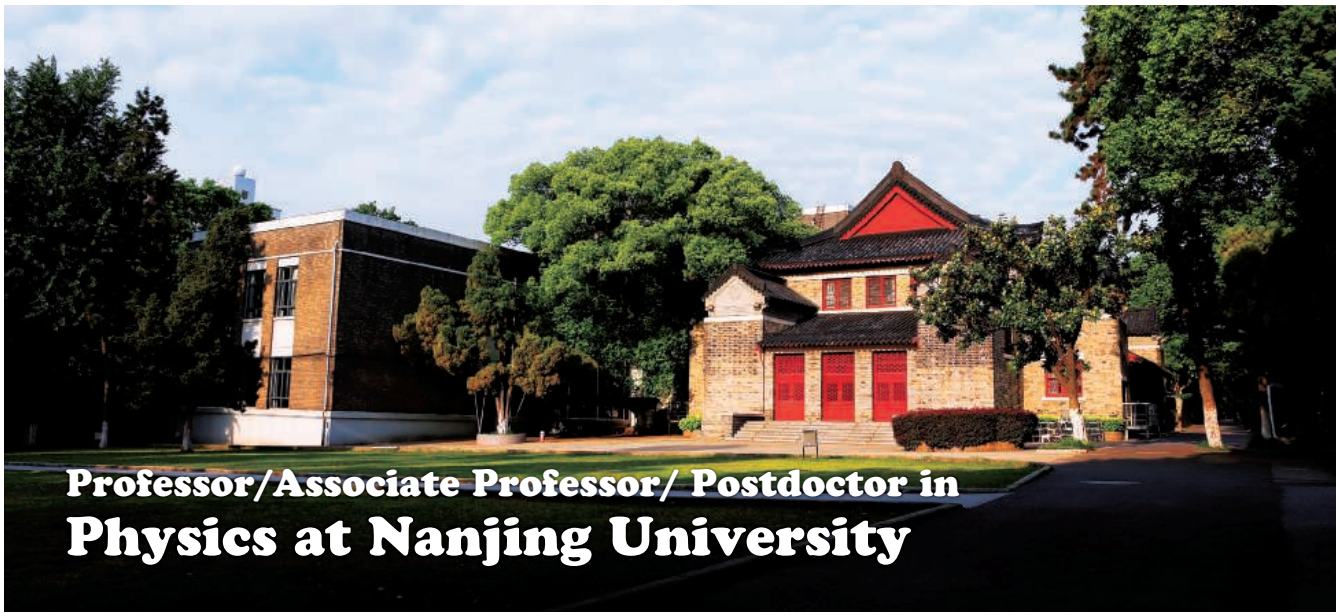

Professor/Associate Professor/ Postdoctor in Physics at Nanjing University

The School of Physics at Nanjing University is one of the first physics departments established in China, dated back to 1920. Over the past hundred years, the School of Physics has contributed significantly to the scientific developments and the modernization of the country, and has itself become one of the best physics departments in China. The school owns the national first-level key discipline of Physics, covering 7 secondary disciplines: Theoretical Physics, Condensed Matter, Optics and Photonics, Acoustics, Particle and Nuclear Physics, Biophysics and Soft Condensed Matter, Atomic, Molecular and Cluster Physics. Currently, the school has 221 faculty members and supporting staff, including 111 professors and 44 associate professors. Among the faculty members, there are 8 academicians of the Chinese Academy of Sciences, 18 ChangJiang professors of Ministry of Education of China and 24 winners of the National Outstanding Young Investigator Prize awarded by the National Nature Science Foundation of China.

The school now has 4 departments and 1 teaching center, including Department of Modern Physics, Department of Physics, Department of Photonics and Quantum Optics, Department of Acoustic Science and Engineering, and Center of Physical Teaching & Experiments. The school has received research funding of over 150 million RMB per year for the past five years. The school has several national and provincial and ministerial laboratories, such as the National Laboratory of Solid State Microstructures (NLSSM), Ministry Key Laboratory of Modern Acoustics, Provincial Key Laboratory for Nanotechnology, Nanjing National Laboratory for Microstructures (under construction), etc. NLSSM was founded in 1984 and was one of the first state key laboratories founded in China. In all of the assessments for state key laboratories, NLSSM always received an "excellent laboratory" assessment. In 2014, the school took the lead in founding the Collaborative Innovation Center of Advanced Microstructures. This is a project in partnership with the physics departments at Fudan University, Shanghai Jiao Tong University, Zhejiang University, the University of Science and Technology of China, and the Hefei Institute of Physical Science of the Chinese Academy of Science.

The School aspires to become one of the most highly ranked physics departments in the world. We extend our warm welcome to distinguished scholars and outstanding young talents to join our efforts from China and beyond. We invite application for tenured/tenure-track faculty positions and postdoctoral positions in the fields of theoretical and experimental condensed matter physics, optics and photonics, acoustics, particle and nuclear physics, biophysics, soft matter physics, atomic and molecular physics, computational physics, as well as artificial intelligence and quantum physics.

Positions and Qualifications

We are seeking outstanding candidates for all levels of faculty positions, including tenured full/associate professors and tenure-track research professors. Candidates should have a Ph.D. in a relevant discipline and an exceptional record of research accomplishments. The individual's work experience and research achievements will determine the position offered.

We are also seeking qualified candidates for postdoctoral position. Candidates should have a Ph.D. in a relevant discipline or expect a Ph.D. within two years, with demonstrated research potential.

Salary and Benefits

All newly hired tenured faculty members will be provided sufficient startup resources and necessary research infrastructures. Annual salaries for tenured full professors range from 500K to 900K RMB (equivalent to US$71200-128200). Annual salaries for tenured associate professors range from 400K to 500K RMB (equivalent to US$57000-71200). Generous housing and start-up packages will also be offered.

Annual salaries for research assistant professors and postdocs range from 200K to 350K RMB (equivalent to US$28500-49800). Rank and salary will be commensurate with work experience and research performance. Two-year initial contracts are renewable. Outstanding performers will be invited to join in faculty.

To apply

Application materials include a cover letter, a full CV with the publication list, a statement of future research plans, and three letters of recommendation. Complete application packages and reference letters should be directed to Prof. Baigeng Wang.

Tel: +86 25 83686486
Email: bgwang@nju.edu.cn
Website: https://physics.nju.edu.cn

Astronomy at Peking University

PKU astronomy encompasses the Department of Astronomy (DoA) and the Kavli Institute for Astronomy and Astrophysics (KIAA), the latter being jointly supported by PKU and the Kavli Foundation, USA. With DoA and KIAA working closely, PKU astronomy has established a high-level international research team through worldwide recruitment. It currently has 25 faculty members (30% are non-Chinese), 30 postdoctoral fellows (60% are non-Chinese), 104 undergraduate students and 59 graduate students. The research includes four major areas of astrophysics: (1) cosmology, galaxy formation and evolution; (2) interstellar medium, stellar and planetary systems; (3) gravitational physics and high-energy phenomena; and (4) computational astrophysics. Recent years have witnessed a number of research findings with considerable international impact.

In 2014, Prof. Fukun Liu and his colleagues found a pair of supermassive black holes in an ordinary galaxy for the first time. This discovery was praised for "really changing the way we think about the universe, and opening up whole new areas for astronomers to study" by international colleagues.

In 2015, Prof. Xuebing Wu's team discovered the most luminous quasar with a central black hole mass of 12 billion solar masses in the early Universe, the most massive black hole discovered at redshift greater than 6. This finding seriously challenged black hole formation and galaxy evolution theories. Published in *Nature*, it was selected as one of the top 10 major scientific achievements of the year in China.

In 2016, Prof. Subo Dong discovered the most luminous supernova ever seen, which may lead to new ideas and new observations of the whole class of superluminous supernovae. Published in *Science*, it was selected as one of the top 10 achievements in astronomical science and technology of the year in China.

In 2015-2016, former PhD student Chengyuan Li published two papers in *Nature*: after finding that intermediate-age star clusters can be composed of a single-generation stellar population, he and his colleagues discovered young populations of stars within globular clusters that have apparently formed from gas flowing in from outside of the clusters themselves.

More achievements are demonstrated by the many prestigious projects and awards, such as the National Key Program for Science and Technology Research and Development sponsored by the Ministry of Science and Technology (MOST) of China, and the Group Innovation Award granted by the National Science Foundation of China. The PKU astronomy group also plays significant roles in the majority of large astronomical research facilities and initiatives involved by China, including NGPS, LAMOST, FAST, QTT, JCMT, TMT, SKA, etc , and serves as key coordinator for the China-US '10+10' program in astronomy, which promotes scientific cooperation and exchange in astronomy between 10 United States universities and 10 Chinese universities.

PKU has become one of the most important platforms for cultivating talent and conducting cutting-edge scientific research in astronomy, generating impact around the world.

Feel free to contact us:
Tel: +86-10-6275-6630
Email: shuyan@pku.edu.cn
http://kiaa.pku.edu.cn/
http://vega.bac.pku.edu.cn/astro/astro.htm

Credit: ESA - C. Carreau.

Credit: ESA/Hubble & NASA. Acknowledgement: Judy Schmidt (geckzilla.com)

Credits: Zhaoyu Li. The background images are from NASA/JPL-Caltech and Misti Mountain Observatory

Credit: Beijing Planetarium / Jin Ma

ADVERTISEMENT

Energy and Resources Engineering at Peking University

The Department of Energy and Resources Engineering (DERE) at Peking University, committed to cutting-edge research on engineering problems related to energy and environment, has a reputation for its research on the development of unconventional fossil energy and renewable energy sources, as well as on the cyclic utilization of resources.

Professor Dongxiao Zhang, the dean of the college, is leading his team to conduct fundamental research on the mechanisms and technologies of unconventional oil and gas development, such as shale gas/oil, coal bed methane and natural gas hydrate. Professor Hailong Lu and his group are dedicated to the fundamental studies of the physical and chemical properties of natural gas hydrates for the development of production and survey technology, providing strong technical support for China's first production test of marine gas hydrate in the South China Sea.

DERE has developed several new energy sources such as new solar cells, lithium battery materials, biomass fuel, and microorganisms (including microalgae) as single-cell factories for biofuels. Xiaowei Zhan and his team created a brand-new nonfullerene acceptor system, the Fused-ring Electron Acceptor (FREA), which is recognized as the best-performing nonfullerene acceptor system and has been adopted by many research groups across the world to fabricate high-performance organic photovoltaics (OPV) with efficiencies exceeding 14%, far superior to fullerene-based OPV (11-12%). The emergence of such a high-performance fullerene acceptor as FREA has begun to marginalize previously predominant acceptors in OPV, inaugurating a new era of OPV technology.

DERE is pioneering new environmental techniques and unconventional resources utilization. Hao Wang and his group has made a breakthrough by developing a nanoscale detection method, i.e. Joints of Interfaces, on the triple-phase contact lines and detected dynamic nanoscale information which was urgently needed for long-standing debates. They created self-driven and aligned moving contact lines on both solid and solution surfaces, which can be used in systems to achieve fast, environmentally friendly, and large-scale fabrication of materials like solar perovskites. They have also developed a smart bubbling scrubber that allows fume gas to be quickly cleaned through interaction with bubbles. Professor Xidong Wang, chair of DERE, is conducting research on the efficient recycling of solid waste resources and residual energy. Various environmentally-friendly material products, by coupling waste resources and residual energy, have been researched, invented, and widely used in industrial production.

DERE has established many laboratories, such as the Beijing Key Laboratory for Advanced Battery Materials and the Beijing Key Laboratory of Solid Waste Utilization, in order to facilitate interdisciplinary research on energy and resources. Outstanding scholars in relevant research areas are warmly welcome to contact DERE at PKU. Feel free to contact us at:

http://en.coe.pku.edu.cn/Energy-Resources-Engineering/index.htm

Tel: +86-10-82529077

Fax: +86-10-82529010

Email: gnyx@pku.edu.cn

Space Sciences at Peking University

The discipline of space sciences was initiated at Peking University in 1959, only two years after the successful launch of the first manmade spacecraft that marked the start of the space era. Peking University has listed space science as one of its key cross-disciplinary sciences. The Institute of Space Sciences and Applied Technology (ISPAT) offers undergraduate and graduate progroams in five major fields of space sciences: solar and heliospheric physics, magnetospheric physics, ionospheric and upper atmospheric physics, space weather, and space exploration.

ISPAT has been conducting high-impact research. For instance, ISPAT is undergoing a NSFC (National Natural Science Foundation of China) Creative Research Group project, led by Prof. Qiugang Zong, to comprehensively investigate the acceleration, transportation, and effects of energetic particles in solar-terrestrial space. ISPAT has achieved a number of scientific breakthroughs in the field of space physics: the discovery of the unusual, isotropic superhalo electrons in the interplanetary space that are probably originated from the magnetic reconnections in solar nano/micro-flares, the establishment of the double-component theory of kinetic turbulence in the solar wind, the proposal of the fast acceleration mechanism of inner-magnetospheric particles via ULF waves, the discovery of the sudden flux drop and subsequent dropout echo of the outer radiation belt electrons that are triggered by interplanetary shocks, the proposal of the drift-echo mechanism to account for a zebra-like pattern of inner radiation belt elections, the discovery of an inverted V-type spectral structure that is generated by the upflowing oxygen ions while accelerated along the magnetic field in the polar regions, etc.

On the other hand, ISPAT has been conducting the design and development of space-borne instrumentation. For instance, the particle radiation detector on board the China-Brazil Earth Resources Satellite has successfully probed the inner radiation belt by monitoring the radiation environment inside the spacecraft. Recently, the Imaging Electron Spectrometer (IES), developed by ISPAT, has been flown on one Beidou Navigation Satellite, to monitor the outer radiation belt and especially explore the wave-particle resonance interactions.

In May 2017, Peking University established the Center of Planetary and Space Sciences upon ISPAT, aiming to provide a world-class research and education platform for space sciences.

ISPAT will expand its efforts in all fields of space sciences, in order to explore the heliopshere - the home of human beings in the universe. Specifically, ISPAT will explore the acceleration and transport of energetic particles from the Sun and in the heliosphere, the solar origin and interplanetary transport of solar wind and coronal mass ejections, as well as the interactions between solar wind and interstellar wind at the outer heliosphere and beyond. It will also conduct comparative planetology studies, especially aiming to investigate the loss of planetary atmosphere and the origin and evolution of planetary magnetic field/magnetosphere.

Since the space-borne instrumentation is a major pacing factor of space sciences, ISPAT will focus on the design and development of the new-generation instrumentation and technology, including the multi-pitch-grid Energetic Neutral Atom Imager that provides the unique way to observe the physics processes in space plasma. ISPAT will also continue participating in China's Mars and Jupiter Exploration Programs, as well as the prospective Magnetosphere-Ionosphere-Thermosphere Coupling Exploration Program (PI: Prof. Suiyan Fu from ISPAT).

For more information, please refer to:

http://www.space.pku.edu.cn/en/

Or Contact Prof. Qiugang ZONG

Email: qgzong@pku.edu.cn,

Tel: +86-10-62767422

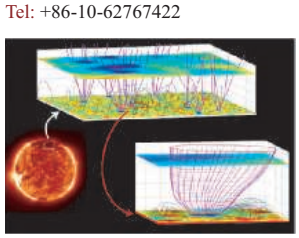

ADVERTISEMENT

ScienceCareers online @sciencecareers.org
OPPORTUNITIES IN CHINA

Zhengzhou University
Seeking for Global Talents to build a First-class University

School Profile

Zhengzhou University is one of the key universities of the national "211 Project", a top-ranking construction university jointly established by the Ministry of Education and Henan Province and. It is a comprehensive university combined of the former Zhengzhou University, Zhengzhou University of Technology, and Henan Medical University in July 2000, covering 12 disciplines class including liberal arts, science, engineering, medicine, and agriculture.

The school has more than 54,000 full-time undergraduate students, over 19,000 postgraduates, and nearly 2,200 international students. It boasts 30 doctoral degree programs for first-level disciplines, 3 doctoral degree programs for professional degrees, 116 Undergraduate majors, and 28 post-doctoral research stations; 3 first-class construction disciplines of clinical medicine, materials science and engineering and chemistry; 6 national key disciplines of pathology and pathobiology, chemical technology, condensed matter physics, material processing engineering, organic chemistry, and ancient Chinese history; 7 disciplines (fields) such as chemistry, materials science, clinical medicine, engineering, pharmacology and toxicology, biology and biochemistry, molecular biology and genetics ranking the top 1% of ESI in the world; 8 national research platforms including the National Engineering Research Center and the Engineering Laboratory. There are more than 5,700 faculty members, including 13 academicians of the 2 academies(the Chinese Academy of Sciences and the Chinese Academy of Engineering), 2 members of the Chinese Academy of Social Sciences, 4 overseas academicians; 8 winners of the "The National Science Fund for Distinguished Young Scholars", 10 Yangtze River scholars, 12 candidates of the National

"Thousand Youth Talents Program"(Introduction Plan of Overseas Chinese High-level Talents), 6 national teaching masters, and 24 national candidates for "Million and Ten Million Talents Projects" . There are also 752 professors. The school has formed a talents team guided by academicians and academic masters, led by "Youth Talents" and "Yangtze River Scholars" as academic leaders, and excellent young doctors as the backbone.

In September 2017, Zhengzhou University was listed in the ranking of national first-class universities and colleges; and in February 2018, it became a jointly established university of the Ministry of Education and Henan Province. At the new historical context, the school positions itself as a comprehensive research-oriented school, proposes a “three-step” development strategy for a first-class university, and strives to become a world-class comprehensive research university by the middle of this century.

The school always gives the priority to talents work and vigorously implements the strategy of strengthening the school with talents. It has formed a talents team guided by academicians and academic masters, led by “Youth Talents” and “Yangtze River Scholars” as academic leaders, and excellent young doctors as the backbone.The construction of Zhengzhou University’s first-class university responses to the call for the economic and social modernization and carries the determination of the Central Plains Rise Strategy and Chinese Nation Rejuvenation. All members form Zhengzhou University will take root in the Central Plains to run a university, seek truths, take the responsibility, and strive for excellence to contribute to the construction of a first-class comprehensive research university.

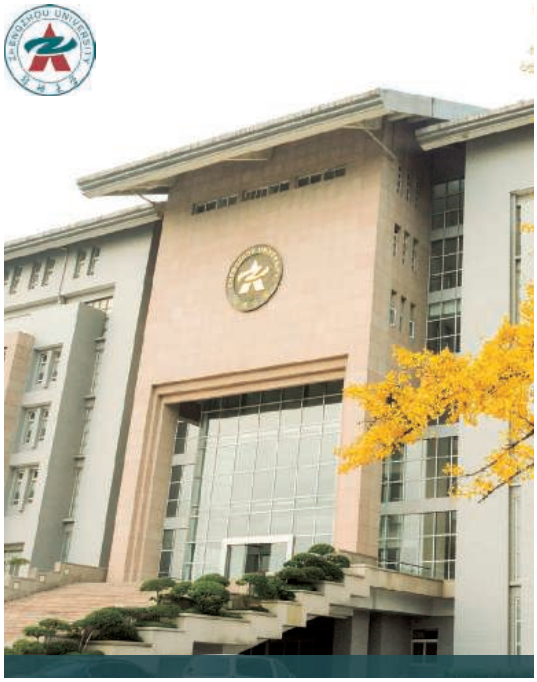

Recruitment Disciplines

Disciplines in Philosophy, Economics, Law, Education, Literature, History, Science, Engineering, Agriculture, Medicine, Management, and Art and others related.

Recruitment Jobs

1.Distinguished Young Talents
Young talents who have great academic development potential and are ready to cooperate.

2.Backbone Teachers
a.Outstanding Doctors: who get good academic records with high-level research achievements.
b. Excellent Doctors: who get good academic records and and promising academic development potential.

3.Post Doctors faculty
Normally fresh postdoc are required.

CONTACT
Mrs Lv (Tel: +86-371-67781085)
Mrs Wang (Tel: +86-371-67781731)
Email: rczp@zzu.edu.cn
Website: www5.zzu.edu.cn/rsc/

Salary and Benefits

Talents Type		Remuneration(Pre-tax)
Distinguished Young Talents		1.Governmental affiliated institutions careers 2.Annual Salary:300 thousand Yuan 3.House Allowance: 300 thousand Yuan 4.Research Founding: 200 thousand~500 thousand Yuan
Backbone Teachers	Outstanding Doctors:	1.Governmental affiliated institutions careers 2.Annual Salary:200 thousand Yuan 3.House Allowance: 200 thousand Yuan 4.Research Founding: 200 thousand Yuan
	Excellent Doctors	1.Governmental affiliated institutions careers 2.Salary for every month measured as lecturers and performance pay 3.House Allowance: 100 thousand Yuan 4.Research Founding: 50~100 thousand Yuan
Post Doctors faculty		1.Governmental affiliated institutions careers 2.Salary for every month measured as lecturers of the 2nd level and annual research performance pay of 60~120 thousand Yuan 3. Research fund: 20~40 thousand Yuan 4.Postdoc apartments or housing subsidy of 1500 Yuan for each month 5. Research Funding or fees subsided from Henan Province Government

The governments of Henan Province and Zhengzhou City will provide funds and prizes, research fees and housing subsidies according to talents types.

Multidisciplinary Faculty Positions at

Zhejiang University Medical Center (ZJUMC)

As a leading education and health institution in China, Zhejiang University integrates medicine-related preponderant disciplines, outstanding talents, and various resources, establishing the foundation of the new medical center (ZJUMC), with a mission to develop a world-class biomedical and clinical innovation hub to tackle unmet medical needs and promote patient health and wellness (for more information, please see www.rand.org/pubs/research_reports/RR2819.html, and the official website of ZJUMC at **www.med-x.zju.edu.cn**).

ZJUMC is located in Hangzhou Future Science & Technology City, a national innovation and entrepreneurship base, neighboring with Alibaba and its DAMO Academy, and Zhejiang LAB. Its innovation ecosystem includes state-of-the-art core facilities, an innovation fund, highly competitive start-up package, and flexible policies. ZJUMC has identified undiagnosed diseases, blood/immune diseases, and major mental illness as its research priorities. Unique features of ZJUMC include:

1.Vibrant interdisciplinary programs that integrate both basic and translational biomedical research in a highly innovative and collaborative environment.

2.Discovery and therapeutic core facilities: multi-omics, single-cell analysis, genome engineering, high-throughput screening, drug discovery, GMP, animal facility, clinical trial facility, big data & medical AI.

3.Institutional member of UDNI (Undiagnosed Diseases Network International).

4.Home of National Frontier Research Center for Brain & Brain-Machine Integration, Ministry of Education of China.

5.Flexible and diverse funding mechanisms (Government fund, AC, VC, industry fund, etc).

6.Abundant clinical resources (Over 15,000 clinical beds, 18M outpatients, 700K inpatients)

ZJUMC is currently recruiting multidisciplinary faculties at several levels: distinguished scholars, physician scientists, academic professors, clinical professors, and junior PIs in the following areas (including but not limited to):

- Genomic Medicine (including genome editing)
- Multi-omics and Disease Phenomics
- Single-cell Technologies
- Stem Cell and Gene/Cell Therapy
- Synthetic Biology
- Precision Diagnosis
- Personalized Medicine
- Disease Modeling
- Clinical Trial
- Bioinformatics
- Big Data and Medical AI

Please kindly send your application including CV, research plan, cover letter and three referees to **shenghongq@zju.edu.cn**. You may also visit http://rsc.zju.edu.cn/talent/english/redir.php?catalog_id=105163&object_id=105158 for more details regarding position description. Application will be open all year round. First round of completed applications will be reviewed starting on December 15, 2019. Additional inquiries may be referred to Zhejiang University Medical Center **(Tel: +86-571-88981475)**.

The Key Lab for Special Functional Materials of Ministry of Education in Henan University

Henan University, founded in 1912, is located in Kaifeng, a famous historical city which had been the capital of Ancient China across eight different dynasties. In 2008, Henan University formally entered the list of the universities which are jointly developed by the provincial government and the Ministry of Education; In 2016, Henan University entered the "111 Plan"; and Since 2017, it has become a "Double Top-ranked" university.

The Key Lab for Special Functional Materials of Ministry of Education was founded in 1986. In 1998, the lab was promoted to be the Provincial Open Laboratory of Key Disciplines in Henan. It has become the Key Laboratory of Henan Province, the Key Laboratory of the Ministry of Education, Henan Engineering Technology Research Center, the Engineering Research Center of the Ministry of Education, the International Joint Laboratory of Henan Province, the National Key Laboratory Base of Universities in Henan Province, Coordinated Innovation Center of Nanoscale Functional Materials and Application in Henan Province, Henan Engineering Laboratory, the National Key Reserve Laboratory in Henan Province, Nation-Local Joint Engineering Research Centre for High-Efficiency Display and Lighting Technology. The total research equipment worth > 80 million RMB. There are around 70 faculty members, including 1 ZhongYuan Scholar, 3 Excellent Young Scholars of the National Science Foundation of China, 1 Thousand Youth Talents Scholar, 4 Distinguished Professors of Henan Province and > 10 Distinguished Professors of Henan University. The lab holds First-Level Doctoral Entitlement and postdoctoral posts for both physics and chemistry. The team initiated "Nano Functional Materials and Applications", which has won support from "the ChangJiang Scholars and Innovation Team Development Plan" by the Ministry of Education.

We are mainly engaging in the fundamental and applied research of nano-materials and devices in the future optoelectronic information, new energy and other fields. Major research area include: i) Quantum dots luminescence display materials and devices, ii) Self-powered electronic/optoelectronic nano-devices, iii) High efficiency thin film photovoltaic materials and technology, and iv) Nano photoelectric biological diagnosis materials and techniques. We strive to cultivating high-end talents and providing original innovation to benefit the development of the regional and national economy. Specifically, we are developing the next-generation display and lighting technology based on quantum-dot light emitting diodes (QLED). It aims at building up the core technologies to support the optoelectronic information industry from Henan to the whole country, especially in the high-efficiency display and lighting industry, and promoting the development of strategic emerging industries.

In accordance with the rapidly growing industry of optoelectronic information, new materials and new energy in the central and western regions of China, we have been establishing wide fields of fundamental research across the design and construction of nanostructured materials, photoelectric transfer characteristics at material surface/interface, photoelectric nano-devices, luminescent quantum dot structural design as well as high efficiency thin-film photovoltaic devices. In particular, we have achieved several world-leading performances on the blue-light QLED and nano-devices. This lab has been granted for > 100 national fundings including the National High Technology Research and Development Program of China, the National Key Basic Research Development Plan, The Key Program of Natural Science Foundation of China, and Innovative Research Team of the Ministry of Education. Besides, > 100 provincial/industrial projects are currently ongoing or have completed in this lab. We have published > 600 research papers on top journals including Nature Photonics, Nano Lett., Adv. Mater., J. Am. Chem. Soc., ACS Nano, Adv. Energy Mater., Adv. Funct. Mater., Appl. Phys. Lett., etc. More than 80 national invention patents have been authorized, some of which have been successfully transferred to industrial applications.

We are recruiting ambitious and outstanding researchers from diverse fields around the globe. Welcome to join us. Together let's build a better future for us and all mankind.

Website: http://lab.henu.edu.cn/
Email: zld@henu.edu.cn

ShanghaiTech University is a young and dynamic higher education institution committed to carrying out China's national development strategy and nurturing the next generation of innovative scientists, inventors and entrepreneurs. With the backing and support of the Shanghai Municipal Government and China Academy of Science, ShanghaiTech's five schools, three research institutes and General Education Center seek cutting-edge solutions to address the challenges that China and the world is facing in the fields of energy, material, environment, human health, and artificial intelligence. As an integral part of the Zhangjiang Comprehensive National Science Center, ShanghaiTech is now leading several frontier research projects and large-scale facilities.
For more information, please visit: www.shanghaitech.edu.cn.

ShanghaiTech is now seeking talents in the following fields
School of Physical Science and Technology: energy, system materials, photon and condensed state, material biology, environmental science and engineering
School of Life Science and Technology: molecular and cell biology, structural biology, neuroscience, immunology, stem cells and regenerative medicine, system biology and biological data, molecular imaging, biomedical engineering
School of Information Science and Technology: computer science, electrical engineering, information engineering, artificial intelligence, network and communication, virtual reality, statistics, big data and data mining.
School of Entrepreneurship and Management: economics, finance, accounting, management, marketing, strategy and entrepreneurship
School of Creativity and Art: innovative design, filmmaking, game design, tech-driven art, big data visualization, creativity, design thinking
Shanghai Institute for Advanced Immunochemical Studies: antibody therapy, Immunotherapy, cell therapy, regeneration medicine
iHuman Institute: bio-imaging, biology, chemistry, computational biology, AI/ML
Institute of Mathematical Sciences: pure mathematics, theory of computing, applied mathematics
Institute of Humanities: Chinese philosophy, Western philosophy, logic, science philosophy, aesthetics, Ancient literature, modern literature, literary theory, comparative literature and world literature, Chinese writing, Chinese history, world history, historical theory, British and American language and literature, French language and literature, German language and literature, Japanese language and literature.

Following positions are opening
1.Tenured and Tenure-track positions: assistant professor, associate professor and full professor.
Successful applicants will have a doctoral degree, and are expected to establish a record for independent, internationally recognized research, supervise students and teach high-quality courses.
2.Research positions: post-doctoral research fellow, research assistant professor, research associate professor and research professor.
Successful applicants will have a doctoral degree, a good research record and great passion for research.
3.Assistant positions: teaching assistant, research assistant, and administrative officer.
Successful applicants will have a Master's degree and relevant working experience.

ShanghaiTech will offer attractive compensation packages, including:
Initial research support package: reasonable start-up funds, research associates and post-doctoral fellows, laboratory space to meet research needs.
Compensation and benefits: highly competitive salary commensurate with experience and academic accomplishments, a comprehensive benefit package.
Subsidized housing: on-campus 80/100/120 m2 faculty apartments available at low rent for tenured and tenure-track faculty, on-campus postdoctoral dormitories, off-campus postdoctoral apartments and municipal apartments subsidized by Shanghai government.
Relocation & travel allowance: reimbursement of expenses for household relocation and family's one-way travel.
Family assistance: support with children's education; affiliated kindergarten, primary and middle schools.

To apply: using this format, please submit a cover letter (Firstname_Lastname_Cover_Letter.pdf), a research plan (Firstname_Lastname_Research_Plan.pdf), and a CV (Firstname_Lastname_CV.pdf) to shanghaitechuniversity@gmail.com

Shaanxi University of Science and Technology (SUST)
Advanced Faculty Positions for Overseas Talents

Shaanxi University of Science and Technology (SUST) located by Ba River and Weiyang Lake in Xi'an, cradle of China's civilization of more than 5000 years, is the only multidisciplinary university specializing in light industry science, technology and engineering in West China. SUST is supported by National University Basic Ability Construction Project-Mid and West, and Shaanxi Province Advanced Level University Construction Project.

Current tenured faculty headcounts amount to 1,200 with approximately 600 with advanced appointments, supervising over 21,000 degree program students including around 3,000 master and PhD degree program students. SUST is home to 6 provincial level top disciplines, 25 key state and province laborites, research bases, engineering and technology research centers, 1 provincial level collaborative innovation center, 1 provincially supported philosophy and humanities special discipline, 5 provincial level model stations of graduate joint education, 6 university level academician workstations.

In January 2017, SUST material science discipline enters the top 1% of ESI ranking for the first time, stepping into international first-rate discipline.

In order to implement "Talent Strengthening SUST Development" strategy more comprehensively and effectively, further enhance the international intensity of faculty, we sincerely invite distinguished talents in the following disciplines to join SUST:

Light Industrial Science & Engineering
(Bio-resources Chemical & Material Engineering)
Materials Science & Engineering
Environmental Science & Engineering
Food & Biological Engineering
Chemistry & Chemical Engineering
Mechanical & Electrical Engineering
Electrical & Information Engineering
Economics & Management
Managerial Science and Engineering

Recruitment Positions

Position Disciplinary Leading Talents (A0) , Distinguished Professors (A1), and National Thousand Youth Talents Plan or Equivalent (A3) are open as well, more details can be found at www.sust.edu.cn.

B0 Position B0 Excellent Young Scholars

1. Qualifications: Applicants should hold a PhD degree or have post-doctoral research experience of top overseas university or research institutions with strong research potential and leadership, and meet one of the following requirements:

(1) Publication of 1 ESI high citation paper, or 2 SCI JCR-Q1 papers, or 5 SCI JCR-Q2 papers or 5 papers with impact factor above 3.0 as the first author in recent 5 years, and experience of primary investigator or co-investigator in important research projects;

(2) 2 years of experience at overseas universities, research institutions or top enterprises with associate (assistant) professorship or post-doctoral fellowship.

2. Salary & Benefits (pre-tax)

1. Relocation

Entitled to buy an apartment on campus (100-120 m2); Relocation allowance: CNY300000.

2. Research Start-up Fund

Science & Engineering: CNY600000; Social Science: CNY300000.

3. Faculty Position & Annual Salary

Level 6 Associate Professorship with minimum annual salary of CNY150000; Master student adviser; Priority in graduate recruiting.

4. Government Talents' Plan Allowance

Applicants can apply for Shaanxi Provincial Hundred Talents Plan with SUST as affiliation. Recipient of Hundred Youth Talents Plan Award can receive a government allowance of 0.5 million which is exempt from income tax.

B1 Position B1 Excellent PhD

1. Qualifications: Applicants should hold a PhD degree or have a post-doctoral experience with top overseas university or research institutions with strong research potential and leadership, and meet one of the following requirements:

(1) Publication of SCI JCR-Q1 paper, or 3 SCI JCR-Q2 papers or 3 papers with impact factor above 3.0, or 6 SCI /EI journal papers as the first author in recent 5 years;

(2) Experience at overseas university, research institution with associate (assistant) professorship or post-doctoral fellowship.

2.Salary & Benefits (pre-tax)

1. Relocation

Entitled to buy an apartment on campus (100-120m^2); Relocation allowance: CNY200000.

2. Research Start-up Fund

Science & Engineering: CNY200000; Social Science: CNY150000.

3. Faculty Position & Annual Salary

Level 7 Associate Professorship with minimum annual salary of CNY120000.

4. Government Talents' Plan Allowance

Applicants can apply for Shaanxi Provincial Hundred Talents Plan with SUST as affiliation. Recipient of Hundred Youth Talents Plan Award can receive a government allowance of 0.5 million, exempt from income tax.

Contact Information

Applicants interested in SUST faculty positions please contact us via information listed below.

SUST Address: Shaanxi University of Science & Technology, Weiyang University Park, Xi'an

SUST Website: www.sust.edu.cn

SUST Recruitment Home Contact: Lv Shaozhong
Contact Number: +86-29-86132873:
Fax: +86-29-86168062
Email: sustrsc@126.com

Recruitment of Global Talents for Guangdong Ocean University

Guangdong Ocean University (GDOU), located in an enchanting southernmost coastal city, Zhanjiang, in the mainland of China, is a key institution co-built by the People's Government of Guangdong Province and the State Oceanic Administration of China. Featuring Ocean and Fisheries Sciences and developing as a comprehensive, multidisciplinary one, GDOU has an integrated academic degree authorization system that provides bachelor's, master's, and doctoral degrees, and has been evaluated "excellent" by the Undergraduate Teaching Evaluation of the Ministry of Education of the P.R. China and crowned as a high-level university of key subject construction in Guangdong Province.

Our university has three campuses of different functions, 806 acres in total, of which the main campus is located at the east side of the National Class 4A Tourist Attraction, Huguangyan, one of the world renowned volcanic geo-parks. This dream campus, being a beautiful place full of trees and flowers, facing sea, and being surrounded by mountains, is home to studying, teaching, and researching.

GDOU prides herself on owning 3 first-class disciplines for doctoral degrees, 9 first-class master's degree programs, 44 secondary master's degree programs, 77 undergraduate majors, 1 comprehensive national reform pilot subject, 4 pilot subjects in the Educational Reform Plan of Excellent Agricultural Talents, 1 national off-campus practical education base for students, 33 research platforms at provincial or ministerial level, 13 provincial demonstration centers of experimental education, 21 key laboratories at department level, etc.

At GDOU, more than 35,000 students from different countries gather around to pursue their dreams. Over 2,500 qualified and brilliant staff and faculty are devoting themselves to teaching, researching, and more at GDOU.

Due to the fast development and establishment, GDOU is now recruiting high-level faculty from both China and abroad.

Disciplines

Sciences, Engineering, Economics, Management, Law, Literature, Education, marine-related disciplines, Art, etc. Please find the details in GDOU website.

Job Requirements

(1) PhD from both overseas and domestic universities/ research institutes;
(2) Be capable of teaching and researching at university.

Contact us

Applicants could send a detailed CV to rcyj@gdou.edu.cn. Please detail your education, work experiences, publications, research interests, etc., and use Applicant's Name + Profession (Field of Research) + Current Institution of Study or Work + Position of interest as the subject of the email.

Tel: (+86) 0759-2383117
Email: rcyj@gdou.edu.cn

GDOU Website: www.gdou.edu.cn
Recruitment: http://zp.ehall.gdou.edu.cn/rsfw/sys/zpglxt/extranet/index.do#/home

Donghua University Welcome Distinguished Scholars from Home and Abroad

Donghua University, located in Shanghai, is one of the state-key universities directly under the Ministry of Education of China. It is a member of Project 211. Textile Science and Engineering is selected as world first-class discipline by the Ministry of Education in 2017.

Donghua University was founded in 1951 as East China Textile College. In 1985, it changed its name to China Textile University, and to its present name, Donghua University in 1999. It is one of the first universities accredited by the Ministry of Education for granting the doctor, master and bachelor degrees. In the fourth-round discipline evaluation in 2017, the discipline of Textile Science and Engineering listed in Class A+. In the ESI rankings, it had six disciplines, Engineering, Chemistry, Materials science, Computer Science, Mathematics and Physics, ranked among the top 1% worldwide.

Currently Donghua University has developed into a distinctive multi-disciplinary university, with engineering as the predominant discipline alongside the coordinated development of engineering, science, management, and the liberal arts disciplines.

Main Disciplines

- Textile Science and Engineering
- Materials science and Engineering
- Control Science and Engineering
- Environmental Science and Engineering
- Chemistry
- Management Science and Engineering
- Mechanical Engineering
- Design

Recruitment Positions

Donghua University Distinguished Research Fellow
Applicant should get PhD degree and have post-doctor experience or obtained assistant professorship or above in prestigious overseas universities; or professors in domestic high-level universities or institutions.

Salary and Benefits

	Annual Salary	House Allowance	Research Funding
Excellent Young Scholars	400,000-500,000	1,000,000-2,000,000	3,000,000-5,000,000
Senior Professors	>650,000	2,000,000-3,000,000	3,000,000-10,000,000

* The units of the above amount are RMB

Distinguished Research Fellow can be directly appointed as professors and doctoral supervisors.

Email: rcb@dhu.edu.cn TEL: +86-02167792043 More details available at http://web.dhu.edu.cn/rcbdhu/

ScienceCareers online @sciencecareers.org
OPPORTUNITIES IN CHINA

华南理工大学 材料科学与工程学院
South China University of Technology School of Materials Science and Engineering

School of Materials Science and Engineering (SMSE), with a history dating back to the 1950s, is developed from the traditional advantage majors in South China Institute of Technology (predecessor of SCUT). SMSE is now composed of several parts: 5 Departments, 5 Institutes, 1 State Key Laboratory (State Key Laboratory of Luminescent Materials and Devices), 1 National Engineering Research Center (National Engineering Research Center for Tissue Restoration and Reconstruction), 1 International School of Advanced Materials. SMSE has a current enrollment of 3219 students, including 1642 undergraduate students, 1095 graduate students and 482 Ph.D candidates. The School currently boasts 220 full-time teachers, among whom 108 are professors, including 7 academicians of CAS and CAE, 6 global highly-cited scientists.

SEEKING GLOBAL TALENTS

先进材料国际化示范学院
South China University of Technology
International School of Advanced Materials

Recruiting Teachers for English Courses Who during Gap Year

Scan to join us

Professor Fei Huang is devoted to the research of organic functional materials and devices for solution processed opto-electronics, including organic solar cells, organic light-emitting didoes etc. He has authored more than 300 publications and filed more than 50 patents. His publications have been cited for more than 18000 times with an H -index of 70 and he was selected as the Highly Cited Researchers from 2016 to 2019 by the Web of Science Group. Dr. Huang was awarded the China National Funds for Distinguished Young Scientists in 2011, the Arthur K. Doolittle Award of ACS in 2014, the Changjiang Distinguished Professor in 2016, and the China National Award for Natural Science (second prize) in 2010 and 2015, respectively.

Professor Wang Yingjun, Ph.D., professor, doctoral supervisor in biomedical materials and tissue engineering. She is the chief scientist of Biomedical Engineering, Director of National Engineering Center for Tissue Restoration and Reconstruction, President of Chinese Society of Biomaterials, Vice President of Chinese Materials Research Society. Elected as the Fellow of Biomaterials Science and Engineering of International Union of Societies for Biomaterials Science and Engineering, Academician of the Chinese Academy of Engineering, Academician of Asia Pacific Academy of Materials.

Professor Zhu Min's research interest includes (1) Hydrogen storage materials; (2) electrode materials for lithium and sodium ion battery; (3) multi-scale and multi-phase structured materials by mechanical alloying and plasma milling; (4) phase transformation and shape memory alloys. He has been chief investigators of more than 30 projects granted by NSFC, Ministry of Science and Technology and the Ministry of Education in the past 30 years. He has published more than 300 papers in peer reviewed international journals, including "Nature Commun.", "Angew. Chemie Int. Ed." ; authored and edited more than 10 books and book chapters and conference proceedings; and give more than 30 invited talks. The citation of his published paper is more than 9000 and the H index is 51. He also own more than 20 patents including 5 PCT patents.

Marine Antifouling Materials. Marine biofouling is the undesirable accumulation of marine microorganisms, plants and animals on submerged surfaces. It is a worldwide problem for marine industries and activities. Marine biofouling can slow the speed and increase the fuel consumption of ships, accelerate metal corrosion and block the seawater pipelines. Professor Guangzhao Zhang's group has been working on marine anti-biofouling for more than 15 years. They proposed the concept of Dynamic Surface Antifouling (DSAF) i.e., a continuously changing surface can effectively prevent marine fouling organisms from landing and adhesion. They have developed a series of DSAF coatings based on degradable polymers polyester-polyurethane, poly(ester-co-acrylate) and hyperbranching polyesters. These coatings exhibit tunable renewability, excellent mechanical properties and long-term antifouling performance (> 5 years). The DSAF coatings have been successfully applied in ships, wave power platforms and underwater detectors. **Their achievements make SCUT the organizer of 20th International Congress on Marine Corrosion and Fouling (Guangzhou, June 21 -26, 2020 (http://www.icmcf2020.com/)**

廣州中醫藥大學

Guangzhou University of Chinese Medicine

Inviting Global Talents

Guangzhou University of Chinese Medicine (GUCM), one of the first four oldest institutions of Chinese Medicine, is currently supported by the National "Double First-rate" plan and the Program of High-level University of Guangdong Province. GUCM is located at the economically developed South China, it offers great opportunities for the researchers who are working in medicine and pharmacy.

High-level talents in the fields of basic or clinical medicine and pharmacy including traditional Chinese medicine, integrative Chinese and Western medicine, acupuncture and rehabilitation medicine, the fields of pharmacology, life sciences, medicinal chemistry and other related research areas are warmly welcome.

Scan and find more information

Tel: +86(020)39358219
+86(020)39356028
Email: rcb@gzucm.edu.cn

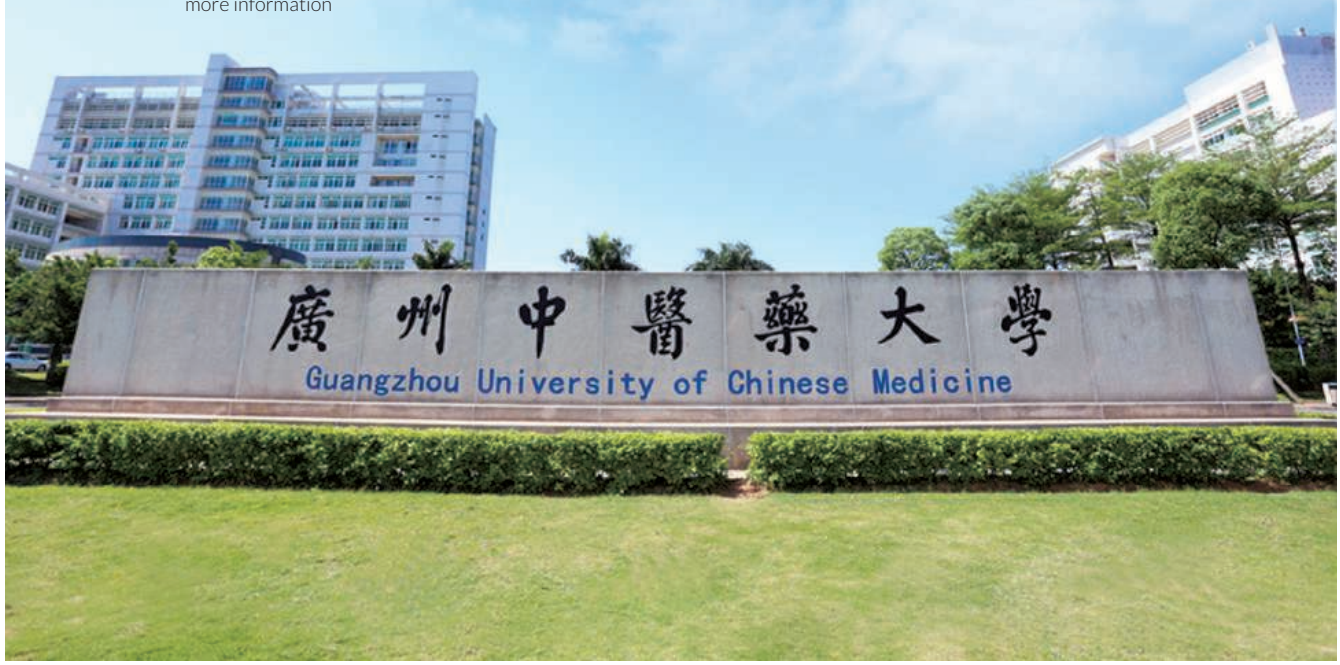

Science Careers online @sciencecareers.org
OPPORTUNITIES IN CHINA

The First Affiliated Hospital of Guangzhou Medical University Wanted

The First Affiliated Hospital of Guangzhou Medical University is a comprehensive 3A hospital, integrating medical treatment, teaching, research, health care, rehabilitation and pre-hospital care together. It harbors Guangzhou Institute of Respiratory Disease, Guangdong key laboratories on orthopedic technique and implant materials and Guangdong key laboratories on urology.

The First Affiliated Hospital of Guangzhou Medical University situated at Pearl River, western to Haizhu square. The Haiyin Branch of First Affiliated Hospital of Guangzhou Medical University located in the south banks of the Pearl River, southern to the Haiyin Bridge. Over 1500 ward beds are available here, serving 37 clinical departments, 18 medical laboratories. The hospital owns over 3300 staffs, including 1 member of Chinese Academy of engineering, 80 experts with outstanding contribution to the state council or province and municipality levels, over 550 senior professionals and over 2600 professionals & technical staffs.

As an affiliated hospital of a university, we focus on professional training as well as discipline construction. We have 6 national clinical key specialties: respiratory medicine, thoracic surgery, urinary surgery, intensive medicine, allergology, and oncology; 1 state key discipline of internal medicine (respiratory disease); 1 national key specialty of drug administration bureau (lung disease treated by traditional Chinese medicine combined with western medicine); 1 national key laboratory (state key laboratory of respiratory diseases); 21 provincial clinical key specialties: respiratory medicine, thoracic surgery.

Positions

- **Chair of academic\clinical department**

Qualifications :Doctors Degree and Senior professionals

- **Clinical Doctor**

Cardiology, Urology, Neurology, Cardiovascular, Anesthesiology, obstetrics, respiratory, Allergy, ICU, Thoracic, Paediatrics, ER, ENT, Ophthalmology, Ultrasonography, Pathology, CT\DR, Radiotherapy, Oncology, Urology
Qualifications, Doctors Degree

- **Research Fellow\ Postdoctor Fellow**

Qualifications, Doctor degree

What we offer:

Research fund, Annual pay, Housing allowance

Please send us your resume in both English and Chinese with a copy of your academic diploma.
Email: rspxkgyfyy@126.com
Tel: 86-020-83062928

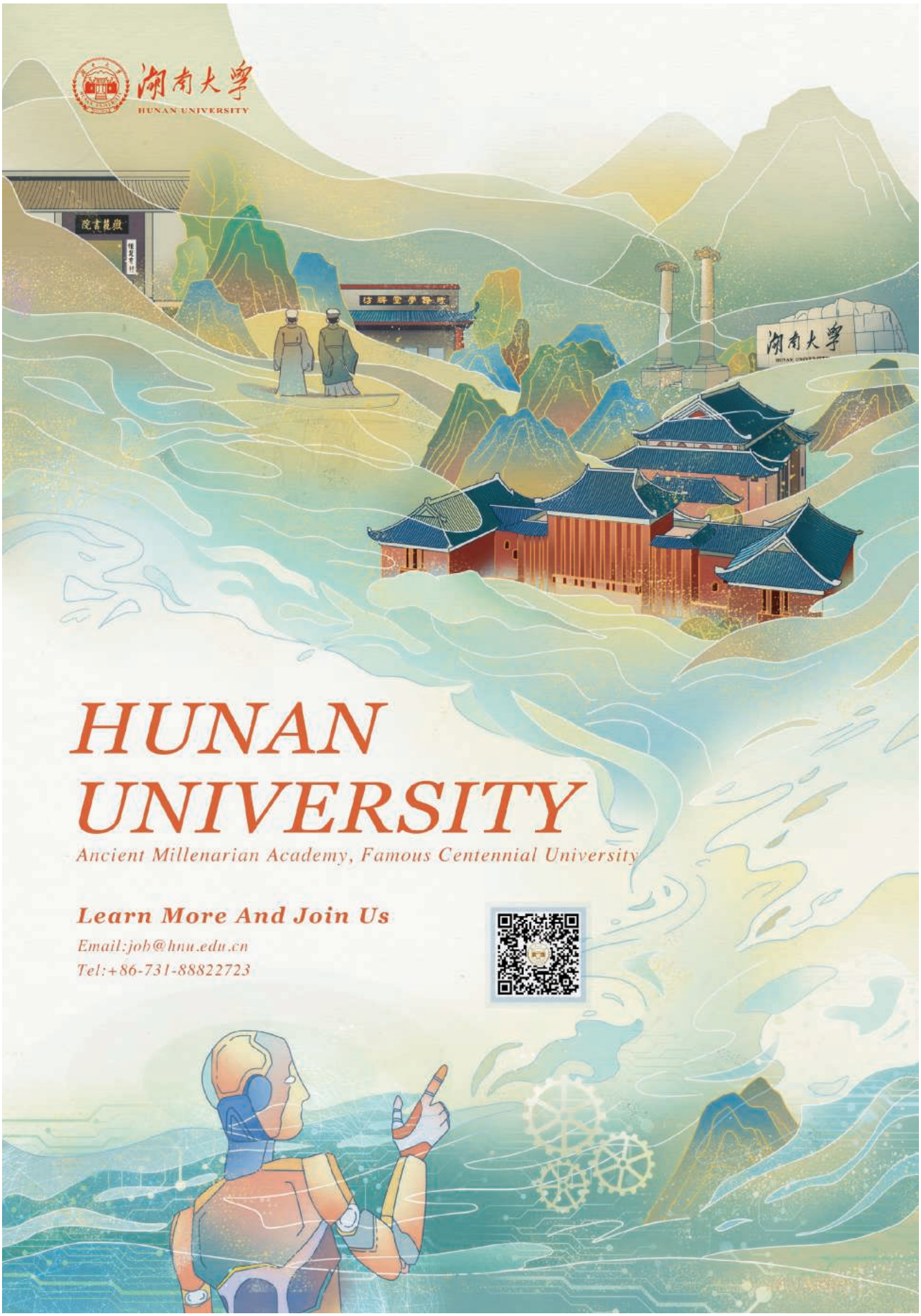

OPPORTUNITIES IN CHINA
ScienceCareers online @sciencecareers.org

Xiangtan University
Calls for Global Talents

Xiangtan University (XTU), located in the hometown of Chairman Mao Zedong, was established in 1958. And the great leader Mao Zedong initiated the university's establishment, inscribed the name of the university, and bade university administrators to "do their best to make a success of it".Now XTU has a comprehensive range of academic disciplines covering 9 categories including literature, history, philosophy, science, engineering, economics, management, law, and art. Of all the disciplines, four (chemistry, materials science, engineering, and mathematics) have ranked among the top 1% of the global universities and research institutions on ESI, and seven have entered the ShanghaiRanking's Global Ranking of Academic Subjects 2019. Besides, XTU ranks 43rd among Chinese universities in the Times Higher Education (THE) World University Rankings 2019, and it is one of the few universities in China listed in both the THE World University Rankings and the US News Global University Rankings.

XTU has long been holding the developmental philosophy of "talent strategy", and is committed to building a greater platform for talented staff. And we sincerely invites talented, driven candidates to join us, and together to create a glorious future.

Subject Areas for Recruitment: philosophy, theoretical economics, applied economics, law, political science, Marxist theory, Chinese language and literature, journalism and communication, foreign language and literature, Chinese history, world history, mathematics, physics, chemistry, statistics, mechanics, mechanical engineering, material science and engineering, power engineering and engineering thermal physics, electrical engineering, electronic science and technology, information and communication engineering, control science and engineering, computer science and technology, civil engineering, chemical engineering and technology, environmental science and engineering, management science and engineering, business administration, public management, and library information and archive management.

Professional Title and Education Requirement: The candidates are expected to hold associate professorship or above. Or they should have a PhD degree.

Contact Person: Mr. Chen; Ms. Zhang
Tel: (+86) 0731-58292074
E-mail: rcb@xtu.edu.cn

湘潭大學

Introduction of Changsha University of Science and Technology

Boasting of a history of over 60 years, Changsha University of Science and Technology (CSUST) evolves into an engineering-centered multidisciplinary university, integrating engineering, science, management, economics, liberal arts, law, philosophy, and fine arts with a stronghold in undergraduate education and a capacity of post-doctoral science and research workstations, conferment of Doctor's Degree and recommendation of postgraduates for Master's Degree. The university is honored with “basic capacity-building project college/university in the central and western regions”. It is also acknowledged as one of top tier construction universities in Hunan (Type A).

With over 60 years of development, the university has accumulated a culture with the core value "erudition, practice, integrity and innovation" and in particular, "Pave Stone Spirit". Since the establishment of the university, more than 400,000 senior professionals have been trained in transportation, electricity, water engineering, light industry and other sectors for regional economic and social development.

It is located on Jinpenling and Yuntang campuses, with an area of around 200 hectares and a total floor space of 1.2 million square meters. The university has a collection of more than 3.5172 million printed books, 800.26 thousand copies of eBooks, and 956 kinds of Chinese and foreign academic journals. The university has a science search station in accordance with the Ministry of Education standard and a power science search station of the China Electrical Engineering Society. It is also a alliance member of China University Intellectual Property Info Service Center.

The university has 19 teaching faculties, an independent/affiliated college and a continuing education faculty. It has a total of 69 undergraduate majors. The university has 6 key disciplines that have been included in part of the plan to construct top tier university in the Hunan region. The engineering subject has ranked among top 1% of ESI worldwide. It has 5 post-doctoral workstations, 6 primary disciplines and 33 sub-disciplines for doctoral degrees, 25 primary disciplines for master’s degrees. There are more than 39,000 full-time registered students, among which around 5,600 are doctoral or master students.

Upholding the strategy of Talent First, the university is staffed with 1986 full-time teachers, among whom, 313 professors and 657 associate professors; one accredited academician of the Chinese Academy of Engineering (CAE) and two other CAE academicians that hold concurrent posts in CSUST. Nearly 300 talents are included in the talent project candidates on provincial and ministerial level.

In recent five years, the university has won 30 provincial awards for teaching achievements, 5 national science and technology advancement awards. The university has engaged in over 388 national projects, with a number of 774 service invention patents authorizations.

CSUST adheres to the open education initiative by establishing international exchange and cooperation with world partners. We have established exchange and cooperation with some 70 institutions of higher learning and research institutions from more than 20 countries or regions.

To cater to the growing development of the university, we are reaching out for outstanding Ph.D. graduates and capable talents of all kinds to join with us. The university has implemented the "Huxiang Scholar" talent plan, with tailored posts open on three levels in six categories. We offer competitive salary and incentives, we render scientific research support, and we provide housing subsidies and talent backup services. We sincerely welcome outstanding talents of all kinds from home and abroad to join this course with us.

Reach us via the following contacts:
Tel: (+86) 0731-85258354
Email: cslgzhp@126.com
University official website:
www.csust.edu.cn

Scan the QR code to apply

ScienceCareers online @sciencecareers.org
OPPORTUNITIES IN CHINA

Clinical Research at the Xiangya Hospital of Central South University

The Xiangya Hospital of Central South University is recruiting talents from all over the world with competitive salaries and benefits. The goal is to establish a national-level regional medical center and a top research hospital with international influence.

Xiangya Hospital, Central South University, is one of the top general hospitals in China. It was founded in 1906 by Yale-China Association. The hospital has long enjoyed the reputation of "South Xiangya", which indicated the best hospital in southern China. The hospital has 3,500 in-patients beds, 88 clinical departments, serving more than 100 million patients annually. The hospital advocates for clinical research and provides decent funding for disciplines construction, and scientific and technological innovation every year. Welcome to join us!

An Innovative Closed-loop Research & Implementation Model for Skin-health (chenxiangck@126.com)

In line with the "Healthy China Action Plan" to move from disease treatment to health improvement and disease prevention in 2019, Dr. Xiang Chen and his dermatology group in Xiangya Hospital, Central South University, has already been advocating for and practicing "multi-facet skin-health research & implementation" for years.

"Our mission is not only to translate innovative basic research to effective clinical applications, but also to integrate population-level evidence and campaign to improve skin-health among Chinese population," said Dr. Xiang Chen, who also is the vice president of Central South University, "equipped with diverse talents from basic science, translational research, clinical practice, public health and information-engineering, our team has established a closed-loop research & implementation model for skin-health."

Chen's team, consisted of three independent research institutes, has committed to three major skin conditions: skin tumors, psoriasis, and skin allergies for over 20 years. In basic/translational research, the team has received over 50 grants and 30 patents and produced over 100 high-impacted articles. In clinical practice, the use of health-care big-data and comprehensive follow-up systems has been integrated into their numerous clinical research projects since 2006. Furthermore, the team launched four prospective cohorts aiming to answer the epidemiological changes of skin disease in China. Supported by two international grants, the team also helped to train primary care practitioners (PCPs) for essential dermatological skills besides epidemiological surveys. Chen's team developed the first dermatology internet hospital in China in 2018 to serve as a platform for teledermatology, e-training system, and the network for PCPs, which has accelerated the process of promoting the general skin health in China.

From Bench Side to Bedside: Prevention and Treatment of Osteoarthritis (lei_guanghua@csu.edu.cn)

Osteoarthritis (OA) is the most common joint disorder that represents a major socioeconomic burden worldwide; however, no disease-modifying strategies have been proven useful to date.

Guanghua Lei, the president of Xiangya Hospital, Central South University, deputy director of National Clinical Research Center of Geriatric Disorders, and director of Hunan Key Laboratory of Joint Degeneration and Injury, has long been committed to the pathogenesis, treatment and prognosis of OA. Lei's team has conducted two large-sample and population-based cohorts with comprehensively collected biological samples to explore the etiology and risk factors of OA. Also, sophisticated platforms for the establishment, intervention and detection of cell/animal models have been constructed to investigate the pathogenesis of OA and develop new disease-modifying drugs and biomaterial-based therapies. In addition, they have done several big data researches on OA-related pharmacoepidemiology as well as health policies and have conducted several randomized controlled trials.

In recent years, Lei's team discovered that tramadol prescription may be associated with increased all-cause mortality compared with commonly prescribed nonsteroidal anti-inflammatory drugs (NSAIDs). They also compared the efficacy and safety of topical NSAIDs and found that topical NSAIDs are effective to reduce pain and improve function in OA without increasing local or systemic adverse effects. "We expect preemptive prevention, medical diagnosis and treatment in preclinical OA to improve the quality of life for people worldwide," said Guanghua Lei.

Cross Talking between Bone Metabolism and Glucose Metabolism (xianghangluo@hotmail.com)

Endocrine Research Center and Endocrinology Department of Xiangya Hospital of Central South University is a young and energetic clinical research team. This team is led by Prof. Luo Xianghang, and the Chief PI is Dr. Li Changjun. Luo's team focuses on the pathogenesis and prevention of metabolic endocrine diseases, and has achieved excellent results in the areas of osteoporosis and diabetes. The research team has cloned causative genes of metabolic bone disease, and proposed the mechanism of bone-derived exosomes regulating insulin resistance. In modern society, the impact of population ageing becomes more and more apparent. Diabetes and osteoporosis have become the two major aging-related diseases, incidence rates continuing to rise globally. "Life lies in movement. As the biggest moving organ, bone makes body more active by regulating organism metabolism. We are committed to discovering the endocrine mechanism of cross talking between bone and glucose metabolism, and exploring new targets and drugs effectively preventing osteoporosis and diabetes." explained Luo Xianghang, "We can take advantage of data from clinical patients to obtain meaningful results, and find the mutual regulation mechanism between bone and glucose metabolism, thus improving clinical outcomes."

"We warmly invite outstanding scientific researchers to join our team, and work together to contribute to the prevention and treatment of diabetes, obesity and osteoporosis." Said Xianghang Luo.

ADVERTISEMENT

SJTU Global Recruiting Program

Shanghai Jiao Tong University (SJTU) is one of the higher education institutions which enjoy a long history and a world-renowned reputation in China. Through some 120 years' unremitting efforts, SJTU has become a comprehensive, research-oriented, and internationalized top university in China.

SJTU now has 30 schools/departments, 31 research institutions, 13 affiliated hospitals, with around 50,000 students and over 3,000 full-time teachers, including the leading number of academic masters such as academicians of the Chinese Academy of Sciences and the Chinese Academy of Engineering, candidates for overseas talent programs and winners of National Outstanding Youth Fund among institutes of higher education in China.

Today SJTU has 67 undergraduate programs, 42 first-level disciplines authorized to offer doctorate degree, 57 first-level disciplines authorized to offer master degree. According to Thomson Reuter's Essential Science Indicator (ESI), SJTU has 19 disciplines listed World Top 1%, with 6 disciplines ranking World Top 0.1% and Engineering ranking World Top 0.01%. In 2019 QS World University Rankings by Subject, SJTU has 25 subjects ranking World Top 100, of which 10 subjects rank World Top 50. By the year of 2018, SJTU has led the country for the 9th consecutive year in terms of both the project number and the amount of money issued by National Natural Science Foundation of China. SJTU also ranks No.1 among all Chinese universities in the total number of published SCI papers and China excellent highly-cited papers.

Shanghai Jiao Tong University, carrying the mission of preserving cultural heritage, and seeking for the truth, bearing the responsibility of invigorating the Chinese nation and developing for the benefits of mankind, today this centennial university is sailing for the aim of becoming a comprehensive, research-oriented and internationalized world-class university. SJTU will provide free academic environment, strong research support and competitive compensation package for the talents. SJTU, your stage to becoming academic master!

Recruiting Position

Chair Professor/Distinguished Professor/Tenured Professor/ Chief Researcher/Tenure-track Associate Professor

Work and Life Treatment

(1) Remuneration: With reference to the corresponding positions in the world's top universities, selected candidates will be provided with competitive remuneration and welfare benefits;
(2) Doctoral Students: A guaranteed number of doctoral students to be enrolled each year;
(3) Start-up Fund: Negotiable according to actual research demand;
(4) Housing: Assistance will be given in solving housing problem with furnished interim apartment provided;
(5) Healthcare: Health service will be provided depending on medical resources from 13 affiliated hospitals;
(6) Children's schooling: Children of pre-school and compulsory education age can be arranged to attend kindergartens and schools affiliated to SJTU.

Application Materials:

(1) Cover letter for the position that you are applying for;
(2) CV (with publication list);
(3) No less than 5 representative papers;
(4) Expertise and academic results.

How to Apply:

All the materials needed for application should be integrated into a PDF document named "name-position-department/school/discipline", to be sent to the email of Talent Resources Department (ccy@sjtu.edu.cn).

To Meet in Shandong for a Win-win Future

Benefiting from its long history and outstanding culture, Shandong Province, the hometown of Confucius and Mencius, is well-known around the world for “One Mountain, One Water & One Sage”, as Confucius was born here, Mount Tai rises here, and the Yellow River flows into the sea here. Entering the new era, Shandong Province has been implementing the new development concept and undergoing a complete system remolding in the quality, structure, system, mechanism and development environment, showing a new vitality of innovation, and ushering in an unprecedented opportunity for innovation, entrepreneurship and creation.

Deng Yunfeng
Director-General of
Shandong Provincial
Education Department

At present, the higher education in Shandong Province is at a crucial stage of accelerating "Double First-Class" initiative and comprehensively promoting high-quality development. We have clear tasks and goals, which are to deepen the reforms, open wider to the outside world, strengthen the distinctive features and focus on the priorities, and in about 10 years, 2-3 colleges and universities can reach the world first-class level in a number of fields, around 20 can reach the domestic first-class level in the same type of colleges and universities, around 40 disciplines can reach the domestic first-class level, and the number of high-level talents can be doubled. Therefore, we are committed to building a high-level development platform. In 2019, we established Nishan World Center for Confucianism Studies and are preparing to construct the Rehabilitation University; There are 53 first-class disciplines in our 146 universities; 6 universities get into Top 100 of ESI on comprehensive ranking of Chinese universities; 72 disciplines in 21 universities enter Top 1% of ESI. We’re striving to increase the supply of effective institutions and provide more high-quality talent support policies, relaxed scientific research environment, comfortable living conditions and complete service system. With the unique personality of honesty and hospitability, people in Shandong are trying their best to provide more dream pursuers with the stage of innovation and entrepreneurship to achieve their success.

Welcome to make win-win progress in Shandong Province, the “Dream Factory” in the new era of high-quality development. Let’s sow the seeds of cooperation, reap the fruits of common development and create an even brighter future together!

ADVERTISEMENT

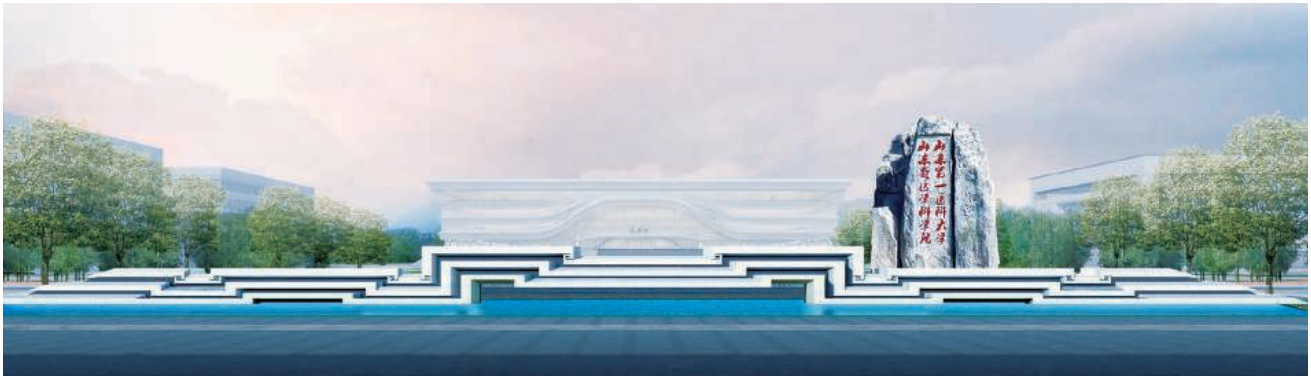

Science and education integration creates a fertile ground of innovation

"Shandong First Medical University aims to build up an application- and research-oriented university which will rank the first-class in China and exert an important influence in the world." Jinxiang Han, executive deputy secretary of Shandong First Medical University said. In February 2019, Shandong First Medical University was formally established by integratingTaishan Medical University, Shandong Academy of Medical Sciences, Shandong Provincial Hospital, Shandong Provincial Qianfoshan Hospital, and other high-level institutes.Shandong First Medical University is one of the government's key construction projects, and the largest medical scientific research institution in Shandong Province.

Jinxiang Han said, "The university has several-high-level interdisciplinary teams led by 5 academicians of the Chinese Academy of Engineering. It has over 40 series of high-level innovation platforms including the National Key Laboratory Construction Base co-sponsored by province and ministry, the Key Laboratory of National Health Commission, and the Provincial Key Laboratory. There are 13 affiliated hospitals, including 9 first-class tertiaryhospitals." At present, the university is building a first-class sci-tech innovation center in China, and hasinvested RMB235 million to support 67 research teams and innovation platforms which areguidedby academician,leader and potentialtalents. The ultimate goal is to establish a comprehensive system for disease diagnosis and controlbased on Shandong characteristics. According to the latest ESI indicesannouncedin November, three disciplines of clinical medicine, pharmacology and toxicology, biology and biochemistry of Shandong First Medical University have ranked Top1%globally. In the ESIcomprehensive'sstrength ofthe universities of Chinese mainland, Shandong First Medical University ranks the 90th, as well as the 13th among the independent medical universities in the country. The clinical medicine discipline has been rankedthe top 1% of the ESI world for six consecutive years, and ranks 714thworldwidely."

The rapid development of Shandong First Medical University provides a brand-new business platform for people with lofty ideals. Jinxiang Han said, "Shandong First Medical Universityis eagerly seeking high-leveltalents with open minds with world-class and highly competitive remuneration. We also provide considerate and personalized services in accommodation, children's education, medical services, and other living facilities. The talents can dive into research and grow rapidly here."

ADVERTISEMENT

Northeast Forestry University Invites Excellent Talents at Home and Abroad

東北林業大學

Established in 1952 and located in Harbin – the beautiful "Ice City", Northeast Forestry University is in national "211 Project" directly under the Ministry of Education of the People's Republic of China and key construction projects of "Advantage Discipline Innovation Platform". It is a multidisciplinary university integrating agriculture, science, industry, economics, management, culture, law, medicine and art with forestry science as its advantage and forestry engineering as its feature.

I. Recruitment of high-level talents

Relevant support policies for talents

NEFU vigorously implements the "5211" talent introduction plan, and provides a guarantee of talent for realizing the grand goal of building NEFU into a world-class forestry university and comprehensively promoting the construction of the "Double First class" university.

The level and treatment of imported talents (house purchase subsidy and personal emolument are both pre-tax) are as follows:

1. Leading Talents or Teams

Academicians of the Chinese Academy of Sciences, academicians of the Chinese Academy of Engineering, and foreign academicians of famous overseas academic institutions; Or someone who has obtained important scientific research results recognized by domestic and foreign counterparts, and has quite strong competitiveness and wide academic influence in the industry.

Remuneration: it depends on the talents' condition

2. Distinguished Young Scholars

Scholars with a PhD who have published high-level academic papers in the top academic journals in the field; Outstanding young scholars at home and abroad who have the potential to get awards of talent programs such as Recruitment Program of Global Experts, National Science Fund for Distinguished Young Scholars, Changjiang Scholars Program, Young overseas high-level talents introduction plan, and National special support program for high-level talents, etc.; Scholars with a title at or above the level of associate professor from well-known overseas universities, or researchers with the same title as those from overseas well-known research academy (institute).

Remuneration: Appointment as professor; Annual salary system, starting from RMB 300, 000 a year, Subsidies for house purchase starting from RMB500, 000. Start-up funds for scientific research in natural science and acquisition expenses of equipment starting from RMB 2, 000, 000, Start-up funds for scientific research in humanities and social science starting from RMB 300, 000.

3. Excellent Young Scholars

Scholars with a PhD who have published high-level academic papers in the influential academic journals in the field; Outstanding young scholars at home and abroad who have the potential to get awards of projects such as Provincial Science Fund for Distinguished Young Scholars, Longjiang Scholars and Provincial Outstanding Young and Middle-aged experts, etc.

Remuneration: Appointment as professor or associate professor; House purchase subsidies are from RMB 150, 000 to RMB 300, 000; Start-up funds for scientific research in natural science and acquisition expenses of equipment range from RMB 300, 000 to RMB 1, 000, 000; Start-up funds for scientific research in humanities and social science range from RMB 100, 000 to RMB 300, 000 Implementation of the national wage and school allowance standard and additional post subsidy RMB 1000 per month in the first 2 years during the first employment period;.

4. Young Backbone

A doctorate holder who is from a well-known university at home or abroad or who has been engaged in teaching or scientific research in a well-known academic institution at home or abroad for more than 3 years. Young backbone who has published high-level academic papers in the outstanding academic journals in the field, who has the ability to obtain the National Natural Science Foundation or the National Foundation for Philosophy and Social Sciences, and who has great development potential in academic and scientific research, etc.

Remuneration: Appointment as associate professor or lecturer; House purchase subsidies are from RMB 80, 000 to RMB 150, 000; Start-up funds for scientific research in natural science and acquisition expenses of equipment range from RMB 150, 000 to RMB 300, 000; Start-up funds for scientific research in humanities and social science range from RMB 50, 000 to RMB 100, 000 Implementation of the national wage and school allowance standard and additional post subsidy RMB 1000 per month in the first 2 years during the first employment period.

5. Excellent Young Teachers

The excellent young teacher whose moral quality is high, with outstanding achievements and good academic development potential. The first degree should be a full-time undergraduate degree from a well-known university, and applicants should possess a doctoral candidate education background and a degree at a non-equivalent education level; A non-foreign language teacher should be proficient in a foreign language, and a foreign language teacher should reach level 8 of a professional foreign language. In principle, doctoral education background and degree are required.

Remuneration: The position of appointment shall be executed in accordance with the relevant documents; Implementation of the national wage and school allowance standards; House purchase subsidies are RMB 50, 000; Start-up funds for scientific research in natural science range from RMB 50, 000 to RMB 150, 000; Start-up funds for scientific research in humanities and social science range from RMB 30, 000 to RMB 50, 000.

NEFU recruits the flexible talents, and the treatment of flexible talents depends on the circumstances.

Contact Information

Zhang Ran (Tel: +86-0451-82191327)
Chen Lijun (Tel: +86-0451-82192089)
Please submit your resume to
nefumoe@vip.163.com

II. Recruitment of Full-time postdoctoral

Someone who high moral quality, outstanding achievements and good academic development potential, and could do full-time post-doctoral research in our university. Received a doctorate from a well-known university or research institution at home and abroad, and the doctoral time is generally no more than 3 years.

Contact information

Bai Xiaoting (+86-0451-82192070)
Please submit your resume to
nefubgb@nefu.edu.cn

Sincerely invite talents from all over the world to create a bright future in ZJOU

Zhejiang Ocean University 2020 High-level Talents Recruitment Announcement

Founded in 1958, Zhejiang Ocean University (ZJOU) is a research and teaching type university with marine characteristics jointly built by the Ministry of Natural Resources and People's Government of Zhejiang Province. ZJOU consists of 10 schools, 1 independent college and the teaching and research institutions such as Zhejiang Marine Fisheries Research Institute, etc. It is the construction unit of "International Characteristic University" of Zhejiang Province and has a sino-foreign cooperative school— ZJOU Pisa Ocean Graduate School. The university has 9 provincial first-level disciplines, of which Fisheries ranked the third and Marine Science the fourth in Soft Science China's Best Discipline Ranking of 2018. It has 9 discipline master's degree programs, 5 professional master's degree programs as well as the equivalent master's degree programs. ZJOU offers 48 undergraduate programs, including 2 state-level specialties, and 21 are among the list of dominant and characteristic specialties in Zhejiang Province. ZJOU boasts 10 dual-employed academicians, 35 national experts (honored as National Distinguished Experts, Experts Awarded the State Council Special Allowance) and 80 provincial talents as well. In the past five years, ZJOU has won 3 second prizes of the National Science and Technology Progress Award, including 2 of them as the first completed units. It has built national research platforms such as the National Research Center for Marine Facility Aquaculture Engineering and Technology, the National-Local Joint Engineering Laboratory of Exploitation and Utilization of Marine Biological Germplasm Resources, the International Science and Technology Cooperation Base of Marine Areas , etc. ZJOU has 2 maritime research vessels, of which "Zhehaike No. 1" has become one of the National Maritime Research Vessels.

"A good wind makes the right time to set sail." Party Secretary of ZJOU — Xiaojun Yan (IEAS Academician; Science and Technology Innovation Leading Talent of National "Ten Thousand Project") together with the President of ZJOU — Jianmeng Chen (Innovative Team leader of "Changjiang Scholar and Innovative Team Development Project" of the Ministry of Education"; National Talent of "New Century Hundred-Thousand-Ten Thousand Talents Program") warmly welcome your arrival!

Key required disciplines
Marine science,Fisheries,-Food science and Engineering,Naval Architecture and Ocean Engineering,-Mechanical Engineering,Transportation Engineering,Port and Coastal Engineering,Hydraulic Engineering,Oil and Gas Engineering, Mathematics,Computer Science and Technology,Environmental Science and Engineering, Business Administration, Education and other related disciplines.

CONTACT:
Telphone: 0580-2550017 (Ms. Dong, Ms. Xu)
E-mail: rsc@zjou.edu.cn
Website: www.zjou.edu.cn
Address: No.1, Haida South Road, Lincheng Dinghai District, Zhoushan, Zhejiang Province
Zip code: 316022

Introduction to Fujian Medical University (FJMU)

Fujian Medical University (FJMU) was founded in 1937 and is currently located in Fuzhou, the capital city of Fujian Province. It belongs to the list of "Establishment of Double First-Rate Universities in Fujian" and has been ranked 17th of "2019 Best Medical Universities in China" according to Shanghai Ranking Consultancy.

FJMU consists of two main campuses, occupying an area of 1,500 acres. It has 21 colleges/divisions and offers 27 different undergraduate majors. There are over 11,400 faculty members and medical staff (including affiliated hospitals), 1,574 of whom are full-time teachers including 491 professors, 578 associate professors and 330 national or provincial high-level talents. of note, 42.31% of the full-time teachers have doctorate degrees. There are more than 16,000 full-time students in the University. FJMU has 6 affiliated hospitals, 5 clinical medical schools, 15 non-administratively affiliated hospitals, 23 clinical teaching hospitals and 94 professional practice teaching bases. It cooperates with more than 120 national or overseas universities and research institutions at multi-disciplinary and multi-dimensional levels.

Since its founding FJMU has cultivated and delivered more than 150,000 talents for the nation and local communities, and many alumni have become the leaders and backbones of the medical and health system in China, especially in Fujian Province. FJMU is committed to building influential and high-level discipline and research platforms. There are 6 first-class and doctorate-conferring disciplines that include Clinical Medicine, Basic Medicine, Dental Sciences, Public Health and Preventive Medicine, Pharmacy, and Nursing; 2 specialty doctoral degree programs in Clinical Medicine and Dental Sciences respectively; 8 first-class and master degree-conferring disciplines; 6 specialty master degree programs. There are also 2 postdoctoral training programs in Clinical and Basic medicine, 4 post-doctoral work stations, and 3 academician work stations. The total number of medical doctorate programs in FJMU ranks 8th among the nation's independent medical schools (including military medical colleges). Clinical Medicine program in FJMU has been ranked top 0.3% by Essential Science Indicators (ESI).

FJMU has 64 provincial or ministerial-level scientific research platforms, such as the National Collaboration Center in Immuno-Oncology, Key Laboratory of Ministry of Education for Gastrointestinal Cancer, Fujian Center for Safety Evaluation of New Drugs, Fujian Provincial Center For New Drug Development, Key Laboratory of Fujian Province, Key Laboratory of Universities in Fujian Province, Special and Novel Intelligent Library for Fujian Universities. Since 2016, FJMU has undertaken more than 3,200 scientific research projects funded by various resources, published more than 3,900 SCI papers and has been granted 95 national invention patents, obtained 75 awards including the Chinese Medical Science and Technology Award, Fujian Province Science and Technology Progress Award, Fujian Medical Science and Technology Award (The above information is updated to August of 2019).

We sincerely welcome overseas scholars to visit us and carry out academic exchanges. Should you have interest, please feel free to contact us and we may cover some travel expenses allowed by the University policy.

Contacts:

Ms. Zeng, Ms. Wang
Tel: 86-0591-22862961
E-mail: fmuszk@mail.fjmu.edu.cn or 123328705@qq.com
Website: www.fjmu.edu.cn
Address: 1 Xuefu North Road, University Town, Fuzhou, Fujian, P.R.C.

Recruitment Program of Nanchang Hangkong University for Overseas High-level Talents

Nanchang Hangkong University (NCHU) is an institution of higher learning jointly built by People's Government of Jiangxi Province and State Administration of Science, Technology and Industry for National Defence, staying committed to building a distinctive and high-level university ranking first-class in the province and nationally renowned. Founded in 1952, NCHU is one of the first-batch universities entitled to award bachelor's degree in China, entitled to award master's degree in 1990 and recognized as the to-be institution for the program construction of doctoral degree in 2009.

Principal: Luo Shenglian

NCHU currently has more than 2,000 faculty members, among which over 1,500 faculty members are full-time teachers, including 1,300 teachers having doctoral or master's degrees, accounting for 92% of the total full-time teachers. NCHU has more than 30 doctoral supervisors, over 60 master's supervisors, 7 double-employed academicians from Chinese Academy of Sciences and Chinese Academy of Engineering and 30 state-level talents including the winner of the National Science Fund for Distinguished Young Scholars, leading talents in scientific and technological innovation of National Thousand Talents Program and National Ten-thousand Talents Program, candidates for National Millions of Talents Program, the winner of the Science Fund for Outstanding Youth, candidates for the Hundred Talents Program of CAS, talents enjoying the special government allowance of the State Council, national outstanding teachers, young and middle-aged leading talents in scientific and technological innovation of the Ministry of Science and Technology, candidates for the New Century Excellent Talent Supporting Program of the Ministry of Education, Master of Chinese Arts and Crafts, etc. NCHU also has 322 province-level talents, including candidates for the Millions of Talents Program of Jiangxi Province, talents enjoying the special allowance of provincial government, candidates for 555 Ganpo Talents Program of Jiangxi Province, specially-employed professor of Jinggang Scholar Program, technological leaders in major academic disciplines of Jiangxi Province, candidates for the Double-thousand Program of Jiangxi Province, candidates for Youth Jinggang Scholar Program, renowned teachers of Jiangxi Province, candidates for Young Scientist Cultivation Program of Jiangxi Province, candidates for Cultivation Program of Outstanding Youth, candidates for Cultural Famous Masters of Jiangxi Province, leading talents in philosophy of Jiangxi universities and colleges, academic leaders in culture and art of Jiangxi Province, academic leaders at provincial (ministerial) level, young and middle-aged core teachers at provincial (ministerial) level, etc.

Since the 12th Five-year Plan, members of NCHU have published nearly 9,000 articles in the academic journals at home and abroad, including 3,095 articles included in document-retrieval systems SCI, EI and ISTP and 280 articles included in CSSCI document-retrieval system. 1433 patents of NCHU have been authorized as the national patents, including 666 patents of invention, 209 published works and 274 textbooks. NCHU has received the approvals of 1 program of National Science Fund for Distinguished Young Scholars, 2 programs of Fund for Outstanding Youth, 392 programs of the national natural science funds of other kinds and 30 programs of the National Social Science Fund of China. NCHU is also responsible for more than 20 programs including the major bidding program of the Ministry of Education in philosophy and social sciences, the general program of the Ministry of Education in humanities, educational and technological programs, excellent talents programs, etc., undertaking and participating in nearly 20 programs including national science and technology major projects (and sub-projects) and sub-projects of "973 Program" and "863 Program", and is in charge of over 200 programs for national defense research and more than 1,000 programs at provincial or ministerial level, including the science and technology major projects of Jiangxi Province. NCHU has been awarded 1 National Prize for Progress in Science and Technology (participating) and 1 Third Prize for Outstanding Achievements in Humanities and Social Sciences Research in Chinese Universities. 116 awards at provincial or ministerial level have also been awarded to NCHU. Prof. Luo Shenglian was awarded the Prize of HO LEUNG HO LEE Foundation for Innovation in Science and Technology in 2012 and was listed in the Highly-cited Researchers for 2 consecutive years. The disciplines of NCHU, including material science, engineering science and chemistry has ranked in the top 1% of ESI global ranking, entering the ranks of international high-level disciplines.

Talent Demand

Doctors in hylology, materials science and engineering and related majors, and doctors in universities (research institutions) of aeronautics and astronautics are preferredDoctors in majors related to machine manufacturing, Doctors in majors related to aero-engine, Doctors in majors related to aircraft design, Doctors in majors related to aeronautical maintenance, Doctors in majors related to flight technology (aviator), Doctors in majors related to traffic engineering or masters with senior professional title, Doctors in computer science and technology, control science and engineering, information and communication engineering, and other related majors, Business administration, industrial engineering, management science and engineering, economics, accounting, Doctors in Art, philosophy (aesthetics).

Introduction Method

Full-time introduction, signing employment contract with NCHU.

Contact Method

Department of Personnel of NCHU
Teacher Yang, Teacher Chen
Tel: +0791-83863092, +0791-83863706
E-mail: hr@nchu.edu.cn
Website: www.nchu.edu.cn

OPPORTUNITIES IN CHINA
ScienceCareers online @sciencecareers.org

Announcement of Recruitment

——ECJTU Welcomes Talents from Home and Abroad

I. Introduction

East China Jiaotong University（ECJTU）, as a multi-disciplinary teaching-and-research-oriented institution in China, features transportation engineering with focus on railway-related disciplines. Dually co-constructed by China Railway Corporation and Jiangxi Provincial People's Government, and the State Railway Administration and the local government, ECJTU has grown into a provincially key university, accredited as a participant to the "Central-western Chinese Universities Capacity-building Project" and an institution offering doctoral degree programs. ECJTU is now composed of 18 schools, offering a complete range of disciplines, including science, engineering, economics, management, literature, law, education, and art.

At present, the university has nearly 2000 staff and faculty members, with 1150 full-time teachers, more than 550 professors and associate professors. Meanwhile, it boasts over 160 excellent members receiving honorable titles at provincial level and above, like the "Double-hired Academicians", specially-appointed professors of the Ministry of Education's "Changjiang Scholars Program", winners of the "National Science Fund for Outstanding Young Scholars" under the Natural Science Foundation of China, members for the "Ten-Thousand Talent Project" for technological and innovative pioneers, awardees for the"Hundred, Thousand and Ten-thousand Talent Project",, receivers of the State Council Special Allowance, members of "the Program for New Century Excellent Talents" of the Ministry of Education, the "Young and Middle-aged Leading Talents in Science Technology" of the Ministry of Science and Technology, "Nationally Excellent Teachers" , "Nationally Excellent Educators" distinguished professors of "Jingangshan Scholars, candidates for "Double Thousand Plan" and "the 555 Ganpo Talent Project, etc. One group is listed as key innovation team of "Promotion Project for Innovation Talents", given by the Ministry of Science and Technology.

Located in Nanchang City, the capital of Jiangxi Province in China, also called "the place of raising military flags" in honor of the establishment of People's Liberation Army there, ECJTU nestles near a mountain, with a river running besides and a few lakes dotted inside. Like a wonderful landscape with blooming flowers and exuberantly growing trees scattered here and there, and birds chirping inside at times, the campus is an ideal place for teaching, learning and living. Among the school size of nearly 3000 mu (200 hectares), the area of buildings of all kinds exceeds 750,000 square meters. Apart from CNY 404 million valued teaching and research equipment, the university also has built its library into a first-class Chinese retrieval station for academic journals and documents, with a collection of 2.29 million volumes of books and journals, and over 2.33 million volumes of electronic documents.

During the Period of 13th Five-Year Plan, the whole staff and all the students of the university are determined to keep sailing on the voyage to shape the school into a nationally renowned "Jiaotong University" (university of transport and communications) with distinctive features and prominent advantages. We sincerely invite suitable talents both at home and abroad to join us at ECJTU!

II. Talents Recruitment Plan

ECJTU is seeking for 1 hundred full-time teachers (Applicants with PhDs).

III. Salaries & Benefits

ECJTU offers talents salaries and benefits under annual salary system which is provincially competitive, providing salaries of 5 categories and 9 levels (annual salary ranging from RMB 300 thousand to 1.6 million) with corresponding performance requirements, in order to help high-level talents find suitable options.

Standards for Salaries & Benefits

IV. Research Funding

The university has greatly increased its reword for marked scientific research achievements. Various funds are established to reword or subsidize high-level scientific research projects and similar platforms. Special emphasis is laid on the rewarding for declaration and approval of the projects at national level, those of young scholars and other similar ones, with a sum up to RMB 600,000.

Standards for Research Funding

V. Discipline Platform

ECJTU runs 3 doctoral programs and 21 master programs in the primary disciplines. Transportation Engineering, Control Science and Engineering and Civil Engineering are the first-class disciplines in Jiangxi Province, and 4 disciplines are known as the leading ones of Jiangxi Disciplinary Union. ECJTU boasts 35 scientific research platforms at or above the provincial level, including National and Local Joint Engineering Research Center of Safety Guarantee Technology for Operation and Maintenance of Rail Transport Infrastructure, National and Local Joint Engineering Research Center of Fruit Intelligent Photoelectric Detection Technology and Equipment, and Engineering Research Center of Railway Environmental Vibration and Noise, Ministry of Education.

ECJTU Scientific Research Platform

VI.Contact Details

Colleges	Contact	E-mail
School of Civil Engineering and Architecture	Ms. Pan	Tumu@ecjtu.edu.cn
School of Electrical and Automation Engineering	Mr. Wei	dianqi@ecjtu.edu.cn
School of Mechatronics& Vehicle Engineering	Mr. Chen	Jidian@ecjtu.edu.cn
School of Science	Ms. Zhou	Lixueyuan@ecjtu.edu.cn
School of Transportation and Logistics	Mr. Guo	Jiaotong@ecjtu.edu.cn
School of Information Engineering	Ms. Li	Xinxi@ecjtu.edu.cn
School of Economics and Management	Mr. Han	Jdmba@126.com
School of Arts	Ms. Li	Yishu@ecjtu.edu.cn
School of Material Science and Engineering	Mr. Chen	Cailiao@ecjtu.edu.cn
School of Physical Education	Mr. Hu	Tiyu@ecjtu.edu.cn
School of Marxism	Mr. liu	337506393@qq.com
School of Foreign Languages	Ms. Xiong	Waiyu@ecjtu.edu.cn
School of Humanities and Social Science	Ms. Wang	Renwen@ecjtu.edu.cn
School of Software	Mr. Xiong	ruanjian@ecjtu.edu.cn

Human Resource Contact: Mr. Jiang
Email: rscecjtu@126.com
Tel: +86-791-87046804
Website: www.ecjtu.edu.cn
Address: No. 808 Shuanggang East Street, Nanchang Economic and Technological Development Zone, Nanchang City, Jiangxi Province.
Zip code: 330013

Anhui Normal University Warmly Welcomes Talents from Home and Abroad

Anhui Normal University (AHNU) is the earliest institution of higher education established in Anhui Province. It is located in Wuhu, a state-level open city hailed as “the embodiment of Anhui customs and the city of thousand lakes". AHNU is a university jointly established by the Anhui Provincial People's Government and China’s Ministry of Education, a member of National Basic Ability Construction Project of Western and Central China, a provincial key comprehensive university that is given priority by the Anhui Provincial Party Committee and the Provincial Government, and also one of the “Local High-level Universities” in Anhui Province.

The university currently has 8 primary-level disciplines authorized to confer doctoral degrees, 6 post-doctoral mobile stations, 18 provincial key disciplines, 3 major provincial discipline construction projects, and 88 undergraduate majors. There is a key research institute of humanities and social sciences at universities and a provincial key laboratory (cultivation) jointly established by China’s Ministry of Education and Anhui Province, a key laboratory and a center for regional studies approved by the Ministry of Education. There are more than 2,380 faculty members, including more than 1,590 full-time teachers, over 330 professors, and 600-odd associate professors.

Position Requirements

1. High-level talents such as leading talents in their own disciplines.
2. Outstanding doctors from well-known universities at home and abroad or outstanding young scholars engaged in postdoctoral research.

Disciplines Recruiting Talents

1. Liberal Arts: Chinese Language and Literature, Theory of Literature and Art, Philosophy, Foreign Language and Literature, Journalism and Communication, Law, History, Economics, Marxist Theory, Education, Management, etc.
2. Science: Mathematics, Physics, Chemistry, Geography, Biology, Ecology, Statistics, etc.
3. Engineering: Optics, Materials Science, Computer Science and Technology, Environmental Science and Engineering, Food Science and Engineering, etc.
4. The Field of Art: Sports, Design, Art, Music, etc.

Salary and Benefits

1. Support funds. Resettlement fees, scientific research support funds and other funds will be provided according to the university's talent introduction policy. The salary and benefits of exceptional talents are determined by the "One Person, One Discussion" system.
2. Spouse placement. For high-level talents, especially exceptional or urgently needed doctors, the school will arrange their spouses who work in different places in an appropriate manner, or give a one-time financial subsidy for resettlement.
3. Education for children. Children from enrolled teachers can enjoy the best kindergartens, primary schools and middle schools in Anhui Province.
4. Housing. The university offers relocation houses.
5. Meanwhile, relevant talent subsidies of Wuhu Municipal Government will be provided.

Application Procedures

1. Please send your resume to ruixh2007@QQ.com.
2. If there is any ambiguity, you can directly contact the Human Resources Office of Anhui Normal University.

Contact Person: Mr. Rui; Contact Number: 0553-5910165.

ScienceCareers online @sciencecareers.org

GOVERNMENT OF INDIA

Ministry of Human Resource Development (Department of Higher Education) Technical Section - I

Appointment of Director, IIT Bhubaneswar, Director, IIT Patna & Director, IIT Ropar

Applications are invited for appointment to the post of Director of Indian Institute of Technology (IIT) at Bhubaneswar, Patna and Ropar. The Director of an IIT is the academic and administrative head of the Institution. He/she is expected to have a minimum of 5 years' administrative experience and leadership qualities to head an Institute of National importance. The candidate/person should be a Ph.D. with first class or equivalent at the preceding degree, preferably in a branch of Engineering.

In exceptional cases, candidates with Science, Mathematics or Management degrees may be considered. He/she should have an outstanding academic record throughout and a minimum of

10 years teaching experience as a Professor in a reputed Engineering or Technology Institute or University and should have guided Ph.D students. The applicant should preferably be less than

60 years of age on the last date of receipt of the applications. The post carries a fixed pay of

Rs. 2,25,000/- (Revised) per month, with allowances as per rules.

2. Interested individuals may apply giving their detailed resume in the prescribed format clearly bringing out research, teaching, industry-academia collaborations and administrative achievements, alongwith a two-page justification in support of their candidature, a two-page vision statement for the institution and contact details of at least two distinguished individuals well acquainted with their work. The application typed in the prescribed format along with enclosures may be sent by Registered/Speed Post to **The Under Secretary (TS.1), Department of Higher Education, Ministry of Human Resource Development, Room No. 428 "C" Wing, Shastri Bhawan, New Delhi -110 001** so as to reach the Ministry **on or before 15th January, 2020**. The detailed advertisement and the format of application is available on the website (**www.mhrd.gov.in**)

The 2020 (36th) International Prize for Biology

Calling for Nominations

The 2020's research field: **Biology of Environmental Responses**

Please access: http://www.jsps.go.jp/english/e-biol

Deadline: April 10, 2020

- The International Prize for Biology was established in 1985 to commemorate the 60-year reign of Emperor Showa and his longtime devotion to biological research.
- The Prize is awarded each year to an individual who has made an outstanding contribution to the advancement of basic research in a field of biology.
- The Prize shall consist of a medal and a prize of 10 million yen.
- The 35th award ceremony was held in Tokyo in November 2019 in the presence of their Imperial Highnesses Crown Prince and Crown Princess Akishino.

Recent Years Prize Winners

2019
Dr. Naomi E. Pierce
(Biology of Insects)

2018
Dr. Andrew H. Knoll
(Paleontology)

2017
Dr. Rita R. Colwell
(Marine Biology)

JAPAN SOCIETY FOR THE PROMOTION OF SCIENCE
日本学術振興会

UNIVERSITY OF WYOMING

Assistant Professor Zoology and Physiology (19004940)

The Department of Zoology and Physiology at the University of Wyoming invites applications for a full-time tenure-track faculty member in Animal Biology. The position is at the Assistant Professor rank at the University of Wyoming at Casper. We seek candidates with a PhD in the biological sciences with undergraduate teaching experience that will involve undergraduate students in a field/laboratory-based research program using animals to address fundamental biological questions. The successful candidate will be expected to teach courses in conservation biology, ecology, evolution, and vertebrate biology and to contribute to the NIH funded Wyoming IDeA Networks for Biomedical Excellence (INBRE) program (http://www.uwyo.edu/wyominginbre).

MINIMUM QUALIFICATIONS: • Doctorate degree in Biology related field by date of appointment - Ability to teach introductory and upper division courses in some combination of conservation biology, ecology, evolution, vertebrate biology (mammalogy and possibly either ornithology, herpetology, or ichthyology) • A field- and/or lab-based research program that incorporates undergraduate student participation • Ability to mentor undergraduate and potentially graduate students in research **DESIRED QUALIFICATIONS:** • Expertise in research involving vertebrate animals utilizing contemporary approaches combining field and laboratory study. • Evidence of teaching effectiveness **REQUIRED MATERIALS:** Complete the online application and upload the following for a complete application: cover letter, research (1 page) and teaching statements (1 page), C.V. and contact information for four work-related references. To Apply: **https://uwyo.taleo.net/careersection/00_ex/jobdetail.ftl?job=19004940&tz=GMT-07%3A00&tzname=**. Review of applications will begin January 5, 2020 and continue until the position is filled.

HIRING STATEMENT: *UW is an Affirmative Action/Equal Opportunity Educator and Employer. We are committed to a multicultural environment and strongly encourage applications from women, minorities, veterans and persons with disabilities. In compliance with the ADA Amendments Act (ADAAA), if you have a disability and would like to request an accommodation to apply for a position, please call 307-766-2377 or email jobapps@uwyo.edu.*

MERCK
INVENTING FOR LIFE

MAKE A GROUNDBREAKING DISCOVERY: **YOU CAN CHANGE LIVES AS PART OF OUR POSTDOC RESEARCH PROGRAM.**

As a global health leader in prescription medicines, vaccines, and animal health products, Merck has channeled the power of invention to transform lives for more than 125 years. Fostering a culture of applied curiosity and empowerment, we use our minds to take on the work's most challenging health issues with intellectual prowess. Here is your chance to do the same:

THE MERCK POSTDOCTORAL RESEARCH FELLOW PROGRAM AT MERCK RESEARCH LABORATORIES (MRL)

The world's finest minds are welcome to participate in this unique program, taking place within state-of-the-industry Research & Development locations across the United States and around the world.

Be a force for transformative innovation with Merck. In addition to an opportunity to enhance lives, we offer the competitive salary and benefits you would expect of an industry leader.

Positions open on **January 13, 2020**.
For more information, visit **jobs.merck.com**.

Merck is an equal opportunity employer. Minority/Female/Disability/Veteran-proudly embracing diversity in all its manifestations.

INVENT.
IMPACT.
INSPIRE.

Who's the Top Employer for 2019?

Science Careers' annual survey reveals the top companies in biotech & pharma voted on by *Science* readers.

Read the article and employer profiles and listen to podcasts at sciencecareers.org/topemployers

Science 2019
TOP EMPLOYERS

We need you to build the world of tomorrow.

From 3 December 2019 to 7 January 2020, CNRS is recruiting 250 new researchers.

carrieres.cnrs.fr/en

&cnrs

80 years of building new worlds through knowledge

HUMAN FRONTIER SCIENCE PROGRAM

CALL FOR LETTERS OF INTENT FOR RESEARCH GRANTS:

AWARD YEAR 2021

Initiation deadline: 19 March 2020
Submission deadline: 30 March 2020

The Human Frontier Science Program (HFSP) supports innovative basic research into fundamental biological problems that applies novel and interdisciplinary approaches and includes scientific exchanges across national and disciplinary boundaries.

HFSP research projects extend the frontiers of knowledge. Successful applications will entail risk and aim to develop novel lines of research for each participating partner that must be different from their ongoing research. The participation of scientists from outside the traditional life sciences such as biophysics, chemistry, computational biology, computer science, engineering, mathematics, nanoscience or physics is considered a key requisite in HFSP grant applications.

To stimulate novel, daring ideas and innovative approaches, preliminary results are not required in HFSP research grant applications. Special emphasis is placed on encouraging scientists early in their careers to participate in the Program Grants. Applicants are expected to develop new lines of research through the collaboration.

Awards are for 3 years and made to international (preferably intercontinental) teams of 2 – 4 members. Research Grants (**Program Grants**) are for independent scientists at all stages of their careers. Grants are also available for teams of early career researchers (**Young Investigator Grants**) who are all within 5 years of establishing an independent laboratory and within 10 years of obtaining their PhDs. The amount is dependent upon team size, up to $450,000 per year. The principal applicant must be located in one of the HFSP member countries; co-investigators may be located in any country.

Applicants are advised to use the quiz on the HFSP website to check their eligibility and to read the guidelines carefully (www.hfsp.org). Starting end of January 2020 principal applicants can initiate an application via the HFSP Extranet until March 19, 2020. Submission deadline for the letter of intent is March 30, 2020.

Specific enquiries: grant@hfsp.org

By **Firdous A. Khan**

Learning to teach

While preparing to teach my first lecture as a new faculty member, I told myself: "You have many research presentations under your belt; you'll nail this!" It didn't take long for me to realize that I was way off base. A few minutes in, the students looked tired, distracted, and in no mood to listen—a stark contrast to my research talk audiences, which *seemed* attentive at least. At one point, I noticed a few students giggling. "Do I look or talk funny?" I wondered. When I saw that the giggling students were on Facebook, I was relieved. But later I realized that, too, was a sign that I had failed to command their attention.

In grad school, I had served as a teaching assistant, helping guide undergraduate students during hands-on lab sessions. But I was never responsible for teaching a class on my own, and I never had any formal training.

When I became a faculty member, I had to take on a daunting course load, teaching 50 lectures and as many labs per semester. It felt as though I'd been dropped in the deep end of a pool with no swimming lessons. Class by class, my doubts about my teaching abilities mounted, along with my fears that students were not absorbing the key details in my lectures.

I started to reflect on my own experiences as a student and tried to recall the things that helped me learn, as well as the things that didn't. The researcher in me also began to search for scientific evidence to guide me. I sought help from experts in pedagogy, as well as colleagues who had more teaching experience than I did. They told me about tools that they used during lectures and resources on campus for new teachers.

Within 1 year, there was a marked change in my teaching. I began to use new skills and tools that kept my students engaged. One student wrote in a teaching evaluation that my approach to teaching "made the information exciting" and "challenged students to pay attention." Teaching gradually became a source of satisfaction rather than anxiety.

Here are some of the lessons that have helped me become a more effective teacher.

"Actively engaging students is essential for holding their attention."

SEEK HELP. Teaching is a skill and as such needs to be learned. Many scientists assume that their graduate degree or postdoctoral experience qualifies them to be a teacher. The reality is far from that. Most universities have support systems for new teachers, but it is usually up to the instructor to actively seek help. I'd recommend taking formal university courses on teaching methods and participating in workshops. They can help you build networks with fellow educators, swap ideas, and share challenges.

KEEP IT INTERACTIVE. Actively engaging students is essential for holding their attention and nurturing critical thought. In a small class, asking students to partner with a classmate to brainstorm an answer to a question can help keep them focused. Then, you can bring everyone together and ask the students to share their ideas. Bigger classes pose a greater challenge, but there, too, the right tools can help engage students. For instance, you can ask multiple choice questions and use electronic clickers to register the students' responses. Or you can tell the students to pass a soft toy around the classroom, each taking a turn to ask or answer a question when the toy comes to them.

BE COMPASSIONATE. Students are more likely to learn if they feel the teacher genuinely cares about them and respects them. So treat every student with understanding and compassion, and make it clear to them that they can come to you for help. It is also important to be mindful of the diversity in student backgrounds and approaches to learning. Some students may not feel comfortable raising their hand in lecture, for instance, so I use an anonymous Google document where they can leave questions for me.

Teaching isn't always easy or intuitive, but it's your responsibility to help your students learn. Put in the time to create an environment that maximizes learning for everyone. ■

Firdous A. Khan is an associate professor at St. George's University in Grenada.

ILLUSTRATION: ROBERT NEUBECKER

Published by AAAS